nanomaterials

Recent Progress in Antimicrobial Nanomaterials

Edited by
Ana María Díez-Pascual

Printed Edition of the Special Issue Published in *Nanomaterials*

www.mdpi.com/journal/nanomaterials

Recent Progress in Antimicrobial Nanomaterials

Recent Progress in Antimicrobial Nanomaterials

Editor

Ana María Díez-Pascual

MDPI • Basel • Beijing • Wuhan • Barcelona • Belgrade • Manchester • Tokyo • Cluj • Tianjin

Editor
Ana María Díez-Pascual
Alcalá University
Spain

Editorial Office
MDPI
St. Alban-Anlage 66
4052 Basel, Switzerland

This is a reprint of articles from the Special Issue published online in the open access journal *Nanomaterials* (ISSN 2079-4991) (available at: https://www.mdpi.com/journal/nanomaterials/special_issues/antimicro_nano).

For citation purposes, cite each article independently as indicated on the article page online and as indicated below:

LastName, A.A.; LastName, B.B.; LastName, C.C. Article Title. *Journal Name* **Year**, *Volume Number*, Page Range.

ISBN 978-3-03943-959-1 (Hbk)
ISBN 978-3-03943-960-7 (PDF)

Contents

About the Editor

Ana María Díez-Pascual graduated with a degree in Chemistry in 2001 (awarded the Extraordinary Prize) from Complutense University (Madrid, Spain), where she also carried out her Ph.D. studies (2002–2005) on the dynamic and equilibrium properties of fluid interfaces under the supervision of Prof. Rubio. In 2005, Dr. Diez-Pascual worked at the Max Planck Institute of Colloids and Interfaces (Germany) with Prof. Miller on the rheological characterization of water-soluble polymers. From 2006 to 2008, she was a Postdoctoral Researcher at the Physical Chemistry Institute of the RWTH Aachen University (Germany), where she worked on the layer-by-layer assembly of polyelectrolyte multilayers onto thermoresponsive microgels. Dr. Diez-Pascual then moved to the Institute of Polymer Science and Technology (Madrid, Spain) and participated in a Canada–Spain joint project to develop carbon nanotube (CNT)-reinforced epoxy and polyetheretherketone composites for transport applications. Currently, Dr. Diez-Pascual is a Permanent Professor at Alcala University (Madrid, Spain), where she focuses on the development of polymer/nanofiller systems for biomedical applications. She has participated in 25 research projects (15 international and 10 national, of which 3 have been with private companies, and she was the principal investigator in 6 of the projects). She has published 112 SCI articles (97% in Q1 journals) and has an h-index of 41 and more than 3500 total citations. More than 50% of her articles are in journals with an impact factor of $\geq$4.8, such as *J. Mater. Chem, Carbon*, and *J. Phys. Chem. C*. She is the first and corresponding author of two invited reviews in Prog. Mater. Sci. and a frequent reviewer for journals published by ACS, MDPI, and Elsevier. Dr. Diez-Pascual has published 22 book chapters and 2 monographs and edited 5 books; she is the first author of an international patent. She has contributed to 65 international conferences (49 oral communications, including 6 by invitation) and has been a member of the organizing committee in 3 workshops and 1 national meeting. She has been invited to present seminars at prestigious international research centers, such as Max Planck in Germany, NRC in Canada, and the School of Materials in Manchester, UK. She was awarded the TR35 2012 Prize by the Massachusetts Institute of Technology (MIT) for her innovative work in the field of nanotechnology.

nanomaterials

MDPI

Editorial

Recent Progress in Antimicrobial Nanomaterials

Ana Maria Díez-Pascual

Department of Analytical Chemistry, Physical Chemistry and Chemical Engineering, Faculty of Sciences, Institute of Chemistry Research "Andrés M. del Río" (IQAR), University of Alcalá, Ctra. Madrid-Barcelona, Km. 33.6, 28871 Alcalá de Henares, Madrid, Spain; am.diez@uah.es; Tel.: +34-918-856-430

Received: 23 October 2020; Accepted: 13 November 2020; Published: 23 November 2020

Bacterial infections are a well-known and serious problem in numerous areas of everyday life, causing death, pain, and huge added costs to healthcare worldwide. They also cause major issues in many other industries, such as textiles, water treatment, marine transport, medicine, and food packaging. Despite strong efforts by academic researchers and industries, a universal solution for controlling bacterial adhesion and proliferation has not yet been found. Over the last years, many novel antibacterial nanomaterials have been developed, and some of them are already applied in hospitals and public buildings. This Special Issue, with a collection of nine original contributions and two reviews, provides selected examples of the latest advances in the field of antibacterial nanomaterials and their applications in various fields.

Recent advances in nanoscience and nanotechnology have led to the development of advanced functional nanomaterials with unique chemical and physical properties. The large surface-area-to-volume ratio of nanoparticles (NPs) opens many possibilities for developing bactericidal agents to treat deadly microbial infections. In particular, metal and metal-oxide NPs have attracted great attention as promising candidates for antibacterial agents [1,2]. The key mechanisms for the antibacterial activities of these NPs include: (a) oxidative stress due to reactive oxygen species (ROS) generation [3], in which the oxidation in bacteria cells induces peroxidation of the lipid membrane, thus destructing proteins and DNA.;(b) the release of metal ions release from metal or metal-oxide NPs penetrating over bacteria cell walls that directly interact with amino and carboxylic acid groups of proteins and nucleic acids, resulting in cell death [4]; (c) membrane disruption due to accumulation of the NPs at the bacterial membrane followed by NP internalization.

Silver nanoparticles (AgNPs) have been applied as antibacterial agents for textile fabrics, healthcare products, cosmetics, coatings, and wound dressings, owing to their effective bactericidal action. Furthermore, they are employed in clinical practice for an extensive range of treatments, such as burns, chronic ulcers, and diabetic wounds that have developed antibiotic resistance. In addition to anti-inflammatory effects, AgNPs-treated wounds have revealed abundant collagen deposition able to accelerate wound healing [5]. However, AgNPs are toxic for several human cell lines and induce dose-, size-, and time-dependent cytotoxicity, especially those with sizes of ≤10 nm [6]. To overcome these disadvantages, their immobilization onto various supporting materials, such as metal oxides, activated carbon, graphene oxide, polymers, etc., have been investigated [7]. The modification of AgNPs with titanate nanotubes (TNT) leads to changes in their physicochemical characteristics, such as size, shape, stability, and oxidation state, leading to improved antibacterial, photocatalytic, and catalytic activities. Immobilization onto polysaccharides such as carboxymethyl-cellulose (CMC) with different degrees of substitution and molecular weight has also been reported [8], and it was found that the particle size distribution and morphology of AgNPs are conditioned by the number of functional groups available for their immobilization. Accordingly, smaller particle sizes were obtained for CMC with a higher degree of substitution, resulting in increased antibacterial activity and cytotoxicity of the samples.

Compared to other types of nanoparticles, titanium dioxide (TiO_2) is particularly attractive for photocatalytic bactericidal activity, owing to its somewhat low cost, natural abundance, and improved

chemical stability [9]. It is an n-type semiconductor due to the presence of oxygen vacancies that favor the formation of Ti^{3+} centers, acting as electron donors [10]. Furthermore, these vacancies can influence charge transport and electron–hole recombination processes by trapping charge carriers in the defect sites. To achieve antibacterial inactivation under visible light, TiO_2 NPs can be doped with metal and nonmetal elements, modified with carbonaceous nanomaterials, coupled with other metal-oxide semiconductors, or deposited onto fibrous materials [11,12]. The modification of TiO_2 NPs with carbon-based nanomaterials, such as nanotubes or graphene, also results in efficient ROS formation under visible-light irradiation [13]. By incorporating TiO_2 NPs into polymers such as chitosan or epoxidized vegetable oils [14], the resulting polymer nanocomposites exhibit excellent antimicrobial properties that can have applications in fruit/food wrapping films, self-cleaning fabrics, medical scaffolds, antimicrobial coatings, and wound dressings.

Copper-containing compounds, such as $CuSO_4$ and $Cu(OH)_2$, are used as conventional antibacterial agents. In addition, aqueous copper solutions, complex copper species, or copper-containing polymers are used as antifungal compounds. On the other hand, liposomes are nanovesicles made with phospholipids traditionally used as delivery vehicles because phospholipids facilitate cellular uptake. Their carrier capacity and hydrophilic/hydrophobic balance are beneficial for developing hybrid nanostructures based on metallic NPs. Thus, with the aim to improve the effectiveness of traditional bactericide agents, nanovesicular systems have been loaded with Cu NPs electrosynthesized in organic media [15]. The nanovesicles have been synthesized by the thin-film hydration technique in aqueous media, using phosphatidylcholine and cholesterol as membrane stabilizers. Several quaternary ammonium salts were tested as stabilizing surfactants for the synthesis and insertion of CuNPs. These are attached mainly to the membrane, probably due to the attraction of their hydrophobic shell to the phospholipid bilayers. It was found that the stability of the liposomes increased upon increasing NP loading, signifying a charge-stabilization effect in a novel material that can fight against antibiotic-resistant biofilms. The use of nanovesicles is of great interest since their size is in the order of 100 to 1000 nm, whereas safety regulations apply for ultrafine NPs [16].

Zinc oxide (ZnO) nanostructures are widely used materials capable of antimicrobial action [17]. With a wide bandgap of 3.4 eV and large exciton-binding energy of 60 meV at room temperature, they are widely used for optical devices [18]. These environmentally friendly materials possess a large volume-to-area ratio, crystalline structure, radiation hardness, good mechanical properties, and high thermal conductivity and are highly suitable as catalysts, gas sensors, or reinforcing fillers in polymers [19]. They can be obtained by several methods, including physical and chemical approaches. Bearing in mind the recent growth in environmentally friendly and low-cost synthetic routes for nanomaterial synthesis, electrochemical techniques represent a valid alternative to biogenic synthesis. In this regard, the aqueous electrosynthesis of ZnO nanomaterials (both rod-like and flower-like structures) with different aspect ratios based on the use of alternative stabilizers such as benzyl-hexadecyl-dimethylammonium chloride (BAC) and poly-diallyl-(dimethylammonium) chloride (PDDA) has been reported [20]. The combination of UV–vis, FTIR, and XPS spectroscopies demonstrated the whole conversion of the raw colloidal materials into stoichiometric ZnO species with moderate morphological modification. Both BAC- and PDDA-modified nanomaterials showed a strong antimicrobial efficacy against *B. subtilis*, as demonstrated by agar diffusion tests. This approach is an efficient alternative to current methodologies to produce elongated ZnO nanomaterials in an aqueous solution with cationic capping agents, leading to higher yields and milder preparation conditions. Application of these ZnO nanostructures in transistor devices (PDDA-capped) and for cultural heritage preservation (BAC-capped) is foreseen.

Layer-by-layer (LbL) assemblies, based on the alternated adsorption of oppositely charged compounds, is a versatile approach that allows control at the nanoscale [21]. A wide range of LbL antimicrobial coatings comprising polymers, nanoparticles, enzymes, peptides, biological molecules, and antibiotics as building units have been reported [22]. Their antimicrobial action is based on bioadhesion resistance, contact-killing, release-killing, or a combination of such mechanisms [23].

LbL assemblies comprising poly(allylamine hydrochloride) and poly(sodium 4-styrene sulfonate) showed significant antimicrobial activity via contact killing, and poly (L-lysine)/poly (L-glutamic acid) multilayers with the top bilayers bearing the pegylated polyanion drastically suppressed the adsorption of *E. coli* [24]. LbL assemblies comprising two naturally occurring antimicrobials, lysozyme, and chitosan, together with Nafion, a synthetic ionomer-bearing hydrophilic sulfonic acid group, has recently been reported [25]. Owing to its chemical composition, Nafion forms proton-exchange membranes with utmost structural and chemical stability highly suitable for fuel cell applications. Although the surface charges of Nafion were neutralized and even overcompensated by the adsorption of positively charged molecules, the coatings displayed noticeable antimicrobial activity against *E. coli* and *S. aureus*. It is envisaged that the synergistic effect of Nafion and conventional antimicrobial agents can generate highly effective platform coatings with enhanced bactericidal action.

Polyhydroxyalkanoates (PHAs) are a class of biocompatible and biodegradable polymers belonging to the family of natural polyesters synthesized by bacterial fermentation from renewable resources such as cane sugar [26], widely used in a variety of applications ranging from nanotechnology, medical, tissue engineering, and packing industries [27]. However, PHAs possess limited applications in the biomedical field due to their brittleness and poor mechanical properties. To improve the mechanical and thermal properties of PHAs, they can be copolymerized with different monomers such as 3-hydroxyhexanoate (HHx), providing better flexibility and biodegradability compared to raw PHAs [28]. Furthermore, blending with other biopolymers such as chitosan (Ch) can lead to improved physicochemical properties [29].

Other natural compounds that have a low environmental impact are also receiving widespread attention. In particular, plant-derived bioactive substances have been applied as natural preservatives (e.g., essential oils) in the food industry due to their antifungal properties [14]. Eugenol (1,2-methoxy-4-(2-propenyl)-phenol), a main component of the herbal oil from basil, has been categorized as GRAS (generally recognized as safe) food additive since it is beneficial for the food field due to its antimicrobial properties against a comprehensive range of microorganisms [30]. However, eugenol is highly volatile and has poor water solubility, which limits its applications. Caseins, the main component of milk proteins in bovine milk, is a cheap and commercially available food-grade additive. The amphiphilic nature of caseins makes them suitable for encapsulating compounds of poor water solubility. In this regard, eugenol-entrapped casein nanoparticles have been prepared via a low-energy and simple self-emulsifying technique [31]. A mass ratio of 5:1 of caseins/eugenol yielded the best encapsulation efficiency and stability. This encapsulation with casein noticeably enhances the antifungal efficacy against anthracnose. These results indicate that EC-NPs nanoparticles could be used as an economical and simple-manufactured preservative for postharvest fruits against microbial spoilage.

On the other hand, hexagonal boron nitride (hBN) nanostructures exhibit comparable or even better properties than their carbon counterparts and are stable under oxidative conditions up to 1000 °C. They display a very high Young's modulus (up to 1.3 TPa), piezoelectricity, hydrogen storage capacity, superhydrophobicity, lubricant behavior, and good biocompatibility, which makes them suitable for biomedical applications including drug delivery, biosensors, biomaterials, and neutron capture therapy [32]. The potential antibacterial effect and cell viability efficacy of PHA/Ch-hBN nanocomposites loaded with three different concentrations of hBN nanoparticles have been recently investigated [33]. Nanocomposites were prepared through a simple solvent casting technique. The fabricated PHA/Ch-hBN nanocomposites demonstrated effective antimicrobial against *S. Aureus* and *E. Coli*, and good biocompatibility properties that would be suitable for biomedical applications.

Synthetic bactericidal patterned surfaces that are capable of killing the bacteria via mechanical mechanisms have recently been developed via nano-/microfabrication techniques [34]. Different design parameters are known to affect the bactericidal activity of nanopatterns. Evaluating the effects of each parameter, isolated from the others, requires systematic studies. A recent article has evaluated the influence of the interspacing and disordered arrangement of nanopillars on the bactericide properties of nanopatterned surfaces [35]. Electron beam induced deposition (EBID) was used to

manufacture the nanopatterns with accurately controlled dimensions as well as disordered versions of them. The killing efficiency of the nanopatterns against *S. Aureus* increased by decreasing the interspace, achieving the highest efficiency on the nanopatterns with 100 nm interspacing. In contrast, the disordered nanopatterns did not influence the killing efficiency significantly, as compared to their ordered correspondents. Thus, optimizing the design of nanopatterns should focus on the interspacing as an important parameter affecting the bactericidal properties.

References

1. Hajipour, M.J.; Fromm, K.M.; Ashkarran, A.A.; Jimenez de Aberasturi, D.; de Larramendi, I.R.; Rojo, T.; Serpooshan, V.; Parak, W.J.; Mahmoudi, M. Antibacterial properties of nanoparticles. *Trends Biotechnol.* **2012**, *30*, 499–511.
2. Díez-Pascual, A.M.; Xu, C.; Luque, R. Development and characterization of novel poly(ether ether ketone)/ZnO bionanocomposites. *J. Mater. Chem. B* **2014**, *2*, 3065–3078.
3. Díez-Pascual, A.M.; Díez-Vicente, A.L. High-Performance Aminated Poly(phenylene sulfide)/ZnO Nanocomposites for Medical Applications. *ACS Appl. Mater. Interfaces* **2014**, *6*, 10132–10145.
4. Regmi, C.; Joshi, B.; Ray, S.K.; Gyawali, G.; Pandey, R.P. Understanding mechanism of photocatalytic microbial decontamination of environmental wastewater. *Front. Chem.* **2018**, *6*, 33. [PubMed]
5. Ezhilarasu, H.; Vishalli, D.; Dheen, S.T.; Bay, B.-H.; Srinivasan, D.K. Nanoparticle-Based Therapeutic Approach for Diabetic Wound Healing. *Nanomaterials* **2020**, *10*, 1234.
6. Liao, C.; Li, Y.; Tjong, S.C. Bactericidal and cytotoxic properties of silver nanoparticles. *Int. J. Mol. Sci.* **2019**, *20*, 449.
7. Jose, M.; Sienkiewicz, P.; Szymanska, K.; Darowna, D.; Moszynski, D.; Lendzion-Bielun, Z.; Szymanski, K.; Mozia, S. Influence of Preparation Procedure on Physicochemical and Antibacterial Properties of Titanate Nanotubes Modified with Silver. *Nanomaterials* **2019**, *9*, 795.
8. Martínez-Rodríguez, M.Á.; Madla-Cruz, E.; Urrutia-Baca, V.H.; de la Garza-Ramos, M.A.; González-González, V.A.; Garza-Navarro, M.A. Influence of Polysaccharides' Molecular Structure on the Antibacterial Activity and Cytotoxicity of Green Synthesized Composites Based on Silver Nanoparticles and Carboxymethyl-Cellulose. *Nanomaterials* **2020**, *10*, 1164.
9. Liao, C.; Li, Y.; Tjong, S.C. Visible-Light Active Titanium Dioxide Nanomaterials with Bactericidal Properties. *Nanomaterials* **2020**, *10*, 124.
10. Díez-Pascual, A.M.; Díez-Vicente, A.L. Nano-TiO_2 Reinforced PEEK/PEI Blends as Biomaterials for Load-Bearing Implant Applications. *ACS Appl. Mater. Interfaces* **2015**, *7*, 5561–5573.
11. Frolov, G.; Lyagin, I.; Senko, O.; Stepanov, N.; Pogorelsky, I.; Efremenko, E. Metal Nanoparticles for Improving Bactericide Functionality of Usual Fibers. *Nanomaterials* **2020**, *10*, 1724.
12. Díez-Pascual, A.M. Antibacterial Activity of Nanomaterials. *Nanomaterials* **2018**, *8*, 359.
13. Díez-Pascual, A.M. Antibacterial Action of Nanoparticle Loaded Nanocomposites Based on Graphene and Its Derivatives: A Mini-Review. *Int. J. Mol. Sci.* **2020**, *21*, 3563.
14. Díez-Pascual, A.M.; Díez-Vicente, A.L. Development of Linseed Oil/TiO_2 Green Nanocomposites as Antimicrobial Coatings. *J. Mater. Chem. B* **2015**, *3*, 4458–4471.
15. Sarcina, L.; García-Manrique, P.; Gutiérrez, G.; Ditaranto, N.; Cioffi, N.; Matos, M.; Blanco-López, M.C. Cu Nanoparticle-Loaded Nanovesicles with Antibiofilm Properties. Part I: Synthesis of New Hybrid Nanostructures. *Nanomaterials* **2020**, *10*, 1542.
16. Boros, B.V.; Ostafe, V. Evaluation of ecotoxicology assessment methods of nanomaterials and their effects. *Nanomaterials* **2020**, *10*, 610.
17. Díez-Pascual, A.M.; Díez-Vicente, A.L. Development of Nanocomposites Reinforced with Carboxylated Poly(ether ether ketone) Grafted to Zinc Oxide with Superior Antibacterial Properties. *ACS Appl. Mater. Interfaces* **2014**, *6*, 3729–3741.
18. Díez-Pascual, A.M.; Diez-Vicente, A.L. Epoxidized Soybean Oil/ZnO Biocomposites for Soft Tissue Applications: Preparation and Characterization. *ACS Appl. Mater. Interfaces* **2014**, *6*, 17277–17288.
19. Díez-Pascual, A.M.; Diez-Vicente, A.L. Wound Healing Bionanocomposites Based on Castor Oil Polymeric Films Reinforced with Chitosan-Modified ZnO Nanoparticles. *Biomacromolecules* **2015**, *16*, 2631–2644.

20. Sportelli, M.C.; Picca, R.A.; Izzi, M.; Palazzo, G.; Gristina, R.; Innocenti, M.; Torsi, L.; Cioffi, N. ZnO Nanostructures with Antibacterial Properties Prepared by a Green Electrochemical-Thermal Approach. *Nanomaterials* **2020**, *10*, 473.
21. Díez-Pascual, A.M.; Wong, J.E. Effect of layer-by-layer confinement of polypeptides and polysaccharides onto thermoresponsive microgels: A comparative study. *J. Colloid Int. Sci.* **2010**, *347*, 79–89.
22. Wong, J.E.; Díez-Pascual, A.M.; Ritchering, W. Layer-by-Layer Assembly of Polyelectrolyte Multilayers on Thermoresponsive P(NiPAM-co-MAA) Microgel: Effect of Ionic Strength and Molecular Weight. *Macromolecules* **2009**, *42*, 1229–1238.
23. Zhu, X.; Loh, X.J. Layer-by-layer assemblies for antibacterial applications. *Biomater. Sci.* **2015**, *3*, 1505–1518. [PubMed]
24. Boulmedais, F.; Frisch, B.; Etienne, O.; Lavalle, P.; Picart, C.; Ogier, J.; Voegel, J.C.; Schaaf, P.; Egles, C. Polyelectrolyte multilayer films with pegylated polypeptides as a new type of anti-microbial protection for biomaterials. *Biomaterials* **2004**, *25*, 2003–2011.
25. Gibbons, E.N.; Winder, C.; Barron, E.; Fernandes, D.; Krysmann, M.J.; Kelarakis, A.; Parry, A.V.S.; Yeates, S.G. Layer by Layer Antimicrobial Coatings Based on Nafion, Lysozyme, and Chitosan. *Nanomaterials* **2019**, *9*, 1563.
26. Díez-Pascual, A.M.; Díez-Vicente, A.L. Poly(3-hydroxybutyrate)/ZnO bionanocomposites with improved mechanical, barrier and antibacterial properties. *Int. J. Mol. Sci.* **2014**, *15*, 10950–10973. [PubMed]
27. Díez-Pascual, A.M.; Díez-Vicente, A.L. ZnO-Reinforced Poly(3-hydroxybutyrate-co-3-hydroxyvalerate) Bionanocomposites with Antimicrobial Function for Food Packaging. *ACS Appl. Mater. Interfaces* **2014**, *6*, 9822–9834. [PubMed]
28. Díez-Pascual, A.M.; Díez-Vicente, A.L. Electrospun fibers of chitosan-grafted polycaprolactone/poly (3-hydroxybutyrate-co-3- hydroxyhexanoate) blends. *J. Mater. Chem. B* **2016**, *4*, 600–612.
29. Karbasi, S.; Khorasani, S.N.; Ebrahimi, S.; Khalili, S.; Fekrat, F.; Sadeghi, D. Preparation and characterization of poly (hydroxy butyrate)/chitosan blend scaffolds for tissue engineering applications. *Adv. Biomed. Res.* **2016**, *5*, 177.
30. Garg, A.; Singh, S. Enhancement in antifungal activity of eugenol in immunosuppressed rats through lipid nanocarriers. *Colloids Surf. B Biointerfaces* **2011**, *87*, 280–288.
31. Xue, Y.; Zhou, S.; Fan, C.; Du, Q.; Jin, P. Enhanced Antifungal Activities of Eugenol-Entrapped Casein Nanoparticles against Anthracnose in Postharvest Fruits. *Nanomaterials* **2019**, *9*, 1777.
32. Díez-Pascual, A.M.; Díez-Vicente, A.L. PEGylated boron nitride nanotube-reinforced poly(propylene fumarate) nanocomposite biomaterials. *RSC Adv.* **2016**, *6*, 79507–79519.
33. Mukheem, A.; Shahabuddin, S.; Akbar, N.; Miskon, A.; Muhamad Sarih, N.; Sudesh, K.; Ahmed Khan, N.; Saidur, R.; Sridewi, N. Boron Nitride Doped Polyhydroxyalkanoate/Chitosan Nanocomposite for Antibacterial and Biological Applications. *Nanomaterials* **2019**, *9*, 645.
34. Gates, B.D.; Xu, Q.; Stewart, M.; Ryan, D.; Willson, C.G.; Whitesides, G.M. New approaches to nanofabrication: Molding, printing, and other techniques. *Chem. Rev.* **2005**, *105*, 1171–1196.
35. Modaresifar, K.; Kunkels, L.B.; Ganjian, M.; Tümer, N.; Hagen, C.W.; Otten, L.G.; Hagedoorn, P.-L.; Angeloni, L.; Ghatkesar, M.K.; Fratila-Apachitei, L.E.; et al. Deciphering the Roles of Interspace and Controlled Disorder in the Bactericidal Properties of Nanopatterns against *Staphylococcus aureus*. *Nanomaterials* **2020**, *10*, 347.

nanomaterials

MDPI

Review

Nanoparticle-Based Therapeutic Approach for Diabetic Wound Healing

Hariharan Ezhilarasu [1], Dinesh Vishalli [2], S. Thameem Dheen [1], Boon-Huat Bay [1] and Dinesh Kumar Srinivasan [1,*]

[1] Department of Anatomy, Yong Loo Lin School of Medicine, National University of Singapore, Singapore 117594, Singapore; anthe@nus.edu.sg (H.E.); antstd@nus.edu.sg (S.T.D.); antbaybh@nus.edu.sg (B.-H.B.)

[2] Faculty of Medical Sciences, Krishna Institute of Medical Sciences "Deemed to be University", Karad, Maharashtra 415539, India; vishallidinesh@gmail.com

* Correspondence: dineshkumar@nus.edu.sg; Tel.: +65-66015996

Received: 2 June 2020; Accepted: 22 June 2020; Published: 25 June 2020

Abstract: Diabetes mellitus (DM) is a common endocrine disease characterized by a state of hyperglycemia (higher level of glucose in the blood than usual). DM and its complications can lead to diabetic foot ulcer (DFU). DFU is associated with impaired wound healing, due to inappropriate cellular and cytokines response, infection, poor vascularization, and neuropathy. Effective therapeutic strategies for the management of impaired wound could be attained through a better insight of molecular mechanism and pathophysiology of diabetic wound healing. Nanotherapeutics-based agents engineered within 1–100 nm levels, which include nanoparticles and nanoscaffolds, are recent promising treatment strategies for accelerating diabetic wound healing. Nanoparticles are smaller in size and have high surface area to volume ratio that increases the likelihood of biological interaction and penetration at wound site. They are ideal for topical delivery of drugs in a sustained manner, eliciting cell-to-cell interactions, cell proliferation, vascularization, cell signaling, and elaboration of biomolecules necessary for effective wound healing. Furthermore, nanoparticles have the ability to deliver one or more therapeutic drug molecules, such as growth factors, nucleic acids, antibiotics, and antioxidants, which can be released in a sustained manner within the target tissue. This review focuses on recent approaches in the development of nanoparticle-based therapeutics for enhancing diabetic wound healing.

Keywords: nanoparticle; drug delivery system; diabetes mellitus; wound healing; diabetic foot ulcer; pathophysiology

1. Introduction

Diabetes mellitus (DM) is a chronic health problem that is prevalent among the human population. DM is an endocrine disorder which is distinguished by the state of hyperglycemia (higher level of glucose in the blood), and is classified into Type 1 DM and Type 2 DM. Factors associated with a steady increase in DM are aging populations, dietetic revolutions and sedentary lifestyles [1,2]. On the basis of 2019 prevalence data from the International Diabetes Federation (IDF), the estimated number of adults (20–79) with DM worldwide is 463 million, which is expected to increase to 578.4 million by 2030 and 700.2 million by 2045 [3]. It is anticipated that DM may increase in developing countries as compared to developed countries (Figure 1). In 2019, IDF revealed that the number of deaths resulting from DM and its complications was 4.2 million worldwide [3]. It is projected that the annual global health expenditure on DM in 2019 is USD 760 billion, which will reach USD 825 billion by 2030 and USD 845 billion by 2045 [3]. Therefore, DM has emerged as one of the serious health threats with a huge socioeconomic burden.

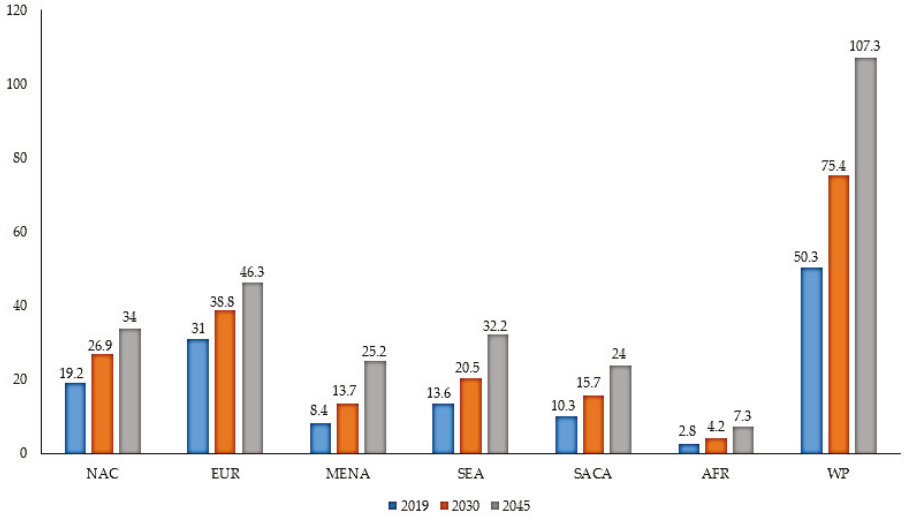

Figure 1. Prevalence of DM (millions) by IDF regions in adults (>65 years) in 2019, 2030 and 2045 [3]. IDF: International Diabetes Federation; NAC: North America and Caribbean; EUR: Europe; MENA: Middle East and North Africa; SEA: South-East Asia; SACA: South and Central America; AFR: Africa; WP: Western Pacific.

DM increases the risk of infection and delays wound healing due to impairment of metabolic activity. As DM advances, a complication that may occur is diabetic foot ulcers (DFUs), a chronic wound that affects the lifestyle of patients and consequently, heightening the risk of mortality [1]. Worldwide, 9.1 to 26.1 million people with DM develop DFU annually. Individuals with DM stand a 25% chance of risk for DFU, and sadly, many cases must ultimately opt for amputation as the treatment modality. Fifty percent DFU amputees have an average 3-year survival rate as a result of infection and unsolved arterial injury, while for post-treatment patients with healed DFU, 50% to 70% may have recurrence within 5 years [1,4,5]. Though DFU is preventable, it puts a massive burden on patients and health care services. A cautious lifestyle as a preventive front, timely assessment and high-level treatments by a multi-disciplinary group of specialists are effective approaches for DFU management [6].

1.1. Pathophysiology of Diabetic Foot Ulcer (DFU)

Peripheral arterial disease (PAD), neuropathy, ischemia, and infection are the key factors influencing the development of DFU. Figure 2 shows a flow diagram depicting the factors that contribute to the pathophysiology of DFU [7].

1.2. Neuropathy

DFU may develop as a result of neuropathy caused by hyperglycemia [8]. The hyperglycemic condition increases stimulation of the enzymes, aldose reductase and sorbitol dehydrogenase, which lead to conversion of intracellular glucose to sorbitol and fructose. The accumulation of converted glucose products results in a decrease in the synthesis of nerve cell myoinositol [9]. In addition, the chemical change associated with glucose induces depletion of nicotinamide adenine dinucleotide phosphate (NADP), which is essential for the detoxification of reactive oxygen species (ROS) and for the synthesis of the vasodilator, nitric oxide (NO). There is a subsequent upsurge in oxidative stress on the nerve cells and an increase in vasoconstriction leading to ischemia, which will cause nerve cell damage and cell death [10,11]. Neuropathy affects all the components of the nervous

system, viz., sensory, motor and autonomic. In autonomic neuropathy, the foot becomes dry as it loses the ability to moisturize its surface due to decreased secretory functions of the sebaceous and sweat glands, thereby encouraging infections to spread [5,8].

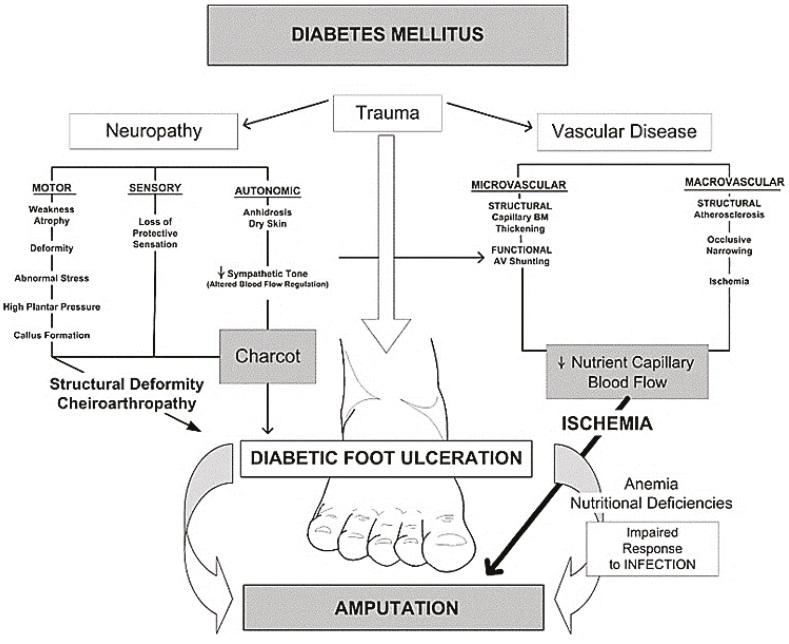

Figure 2. Pathophysiology of DFU. Reproduced from [7], with permission from Elsevier, 2006.

1.3. Peripheral Arterial Disease (PAD)

DFUs are also known to be caused by the complications of PAD. Multiple factors other than DM are associated with greater risk of PAD including age, smoking, hypertension, hyperlipidemia, inflammatory markers, and renal dysfunction [12]. Diabetic vascular complications are divided into microvascular and macrovascular disease. In the diabetic state, due to the upsurge in glucose, endothelial cellular dysfunction and smooth muscle abnormalities develop as a consequence of a reduction in endothelium-derived vasodilators, leading to constriction of blood arteries in the foot [13]. Furthermore, atherosclerosis with thickening of blood capillaries and hardening of arteriolar walls, cause blockage in major arteries such as femoro-popliteal and aortoiliac vessels, resulting in ischemia [2].

2. Normal and Diabetic Wound Healing

Wound healing is a complex process with dynamic interactions of different cell types, extracellular matrix (ECM), cytokines and growth factors. The fundamental steps of wound healing include hemostasis, inflammation, cell movement, and proliferation, followed by wound compression and further remodeling [14]. Any bleeding associated with penetration of skin to the dermis layer by trauma is considered as a wound [15]. The first step in initiating the wound healing process is hemostasis, a clotting process involving the coagulation cascade that leads to cessation of bleeding. The first subset of cells that enter the injury site are platelets, which release several growth factors such as platelet derived growth factor (PDGF), transforming growth factor beta (TGF-β), endothelial growth factor (EGF), and fibroblast growth factor (FGF), which support the inflammation process [16,17]. The inflammatory phase occurs immediately after hemostasis and is characterized by vascular delivery of inflammatory agents and migration of cells into the injury site. Release of inflammatory mediators,

such as prostaglandins, histamine and leukotrienes by mast cells, which stimulates angiogenesis and permeability to allow cells and molecules from the blood stream to enter the wound site [18,19]. Neutrophils, monocytes and lymphocytes are white blood cells that invade the injury site. Neutrophils combat microbial infections and macrophages, stimulate angiogenesis by secretion of TGF-β, vascular endothelial growth factor (VEGF) and FGF, and produce tumor necrosis factor alpha (TNF-α), which breakdown necrotic tissue, facilitating the proliferation of fibroblasts that deposit collagen for tissue granulation [20,21]. Wound contraction begins 2 weeks after a dermal wound. During tissue granulation, fibroblasts differentiates to myofibroblasts phenotype, with enhanced alpha smooth muscle actin (α-SMA) cytoskeleton, which plays a vital role in wound closure. Re-epithelialization of tissue occurs when the wound bed is covered by new tissue and keratinocytes migrate, differentiate and proliferate to generate a stratified epidermis along the superficial area of injury, providing cover for newly formed tissue [22,23]. The last phase in the wound healing process (which lasts 6 to 24 months) is wound remodeling. In this phase, granulation tissue forms accompanied by replacement of the ECM with type I collagen (substituting collagen III) mediated via PDGF and TGF-β [24,25] (Figure 3).

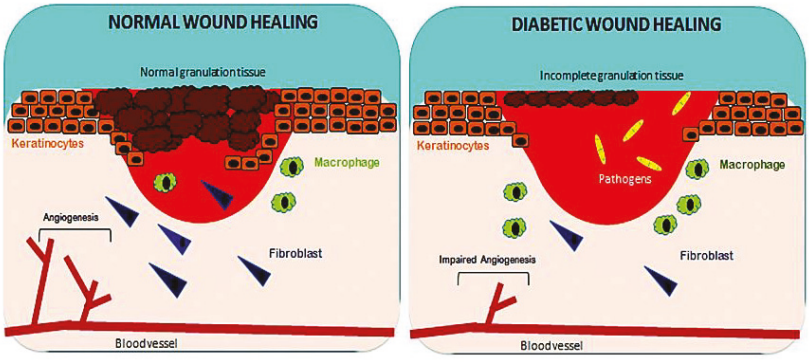

Figure 3. Factors affecting normal and diabetic wound healing. Reproduced from [1], with permission from Royal Society of Chemistry, 2017.

In diabetic wounds, a larger number of inflammatory macrophages continue to stay at the site of injury for a longer period, compared to normal wound healing. These macrophages produce an increased ratio of pro-inflammatory cytokines, such as TNF-α and interleukin 6 (IL-6) and elaborate ROS causing persistent inflammation, which lead to stimulation of proliferative factors for successful wound healing. However, the common cytokine cascade is perturbed due to inefficient efferocytosis (phagocytosis of apoptotic cells) by macrophages, related to the higher burden of apoptotic cells. Increased ratio of pro-inflammatory cytokines (IL-1β and TNF-α) and matrix metalloproteinase-9 (MMP-9) with decreased anti-inflammatory signals (CD206, IGF-1, TGF-β and IL-10) will lead to abnormal apoptosis of fibroblasts and keratinocytes, together with decreased angiogenesis [26–28]. In diabetic wound healing, fibroblasts do not properly differentiate into myofibroblasts, leading to reduced mechanical tension of ECM, and subsequently poor wound closure due to lack of α-SMA [28–30]. In impaired wound healing, a non-equilibrium balance between MMPs that degrade the disorganized collagen in normal wound healing and tissue inhibitor of metalloproteinases (TIMPs), lead to abnormal ECM degradation and deposition. Lower expression of TIMPs and higher expression of MMPs are due to the persistently high levels of pro-inflammatory cytokines and pro-fibrotic cytokines. In a chronic wound, levels of MMPs are raised 60 times more than that for acute wound healing [30]. Increase in protease activity in tissue reconstruction enhances degradation of ECM, growth factors and collagen deposition, which are crucial for effective wound healing [31,32]. All these factors, together with a dysregulated molecular and cellular wound microenvironment that is not conducive to normal healing responses, culminate in impaired healing of diabetic ulcer [1] (as illustrated in Figure 3).

3. Therapeutic Modalities for Diabetic Foot Ulcers

Chronic wounds remain a significant public health problem. Alterations in normal physiological healing processes caused by aging or diabetes, lead to impaired tissue repair and the development of chronic and non-healing wounds. Understanding the unique features of the wound environment will be required to develop new therapeutics that impact these disabling conditions. Although there are numerous strategies for the treatment of DFU, it remains a major challenge to optimize the therapeutic approach in the clinical healthcare setting [33]. Systemic delivery, the most common approach for administering drugs to patients, relies on adequate perfusion of the target tissue and blood supply, that many chronic wounds lack. Moreover, there may be significant potential harmful side-effects to non-target tissues. On the other hand, topical delivery is primarily intended for a local effect which can potentially eliminate the need for systemic administration of drug therapies, minimize the total dose required to reach the target site, and reduce off-target adverse effects [34,35]. Wound care has traditionally relied on dressings, including both natural and synthetic materials and drugs, to sustain a warm and moist surrounding for conducive wound healing, while diminishing bacterial infection [35]. Topical delivery of free siRNA, proteins, antibiotics, and nucleic acids, may lead to degradation of these encapsulated compounds by endogenous enzymes produced in chronic wounds, increased drug clearance due to rapid half-life, toxicity to tissues or organs, and uncontrolled delivery of drugs, leading to under dosage or over dosage and inappropriate immune responses [36,37]. Moreover, topical application of therapeutic drugs offers a poor solution with regard to diabetic wound healing due to the development of bacterial resistance against antibiotics [38].

Other diabetic wound healing therapies, such as bioengineered grafts, face the problems of decreased angiogenesis and physiological rejection. Growth factor therapy may encounter problems associated with breakdown of growth factor at wound site, synthetic hydrophobic polymer dressings with ineffective release of bioactive components, silver dressings with cellular toxicity at specific concentrations, and natural polymer dressings may give rise to allergic reactions [39]. Commercially available hydrofiber and hydropolymer dressings, as well as alginates, are not suitable for dry wounds. On the other hand, hydrocolloidal dressings require a secondary dressing to prevent contamination and also not an option for substantial draining wounds. Foam dressings may cause dehydration of wounds, which arrest epithelialization of the ulcer. Currently, there is no experimental verification of a single type of wound dressing that is effective in eliminating every limitation posed by DFU [40].

4. Nanotechnology Based Drug Delivery System

New drug-delivery systems (DDSs) may enhance the current and future therapies for this challenging clinical problems [35]. Recently, nanotechnology has become one of the most focused research areas for the treatment of DM patients and its associated complications. The advantage of nanomaterials (with a range of 1–100 nm) are versatility in use, controlled size, and tunability of physiochemical properties. Nanomaterials with a larger surface area to volume ratio allow for cell adhesion, and possibly can encapsulate a greater number of surface functionalized active components to accelerate specific regenerative functions [41]. The nanotechnology-based wound healing methods confer advantages such as topical drug delivery, cell specificity, and sustainable and controlled release of encapsulated drugs for a required period until the wound heals [34,42]. In the case of wound healing, nanoparticles are ideal for topical delivery, supporting better interactions with the biological target and increased penetration at the wound sites. Besides, encapsulated drugs could be delivered in a sustained manner and delivery rate could be suitably altered by changing the nanoparticle distribution. Thus, wound healing treatments incorporating the nanotherapeutics approach for delivery of therapeutic biomolecules, paves the way for an excellent opportunity to tackle the complexity of diabetic wound healing by [43,44].

Conceptually, topical delivery of nanotherapeutics has major advantages for chronic wounds such as diabetic wound, by promoting effective wound healing and skin regeneration due to: (a) multifactorial factors and cell-type specificity and (b) use of therapeutic agent for a limited time or until the wound

has healed. Nanotechnology-based materials act as smart nanomaterials in the form of nanofibers and hydrogel, foams loaded with nanoparticles which can encapsulate antibiotics, growth factors, peptides, nucleic acids and extracellular substrates, with the possibility of combined delivery of two different therapeutic agent with dissimilar characteristics to enhance the healing process, that include liposomes, polymeric nanoparticles, inorganic nanoparticles, lipid nanoparticles, nanofibrous structures, and nanohydrogel [34,39,45–47] (as shown in Figure 4).

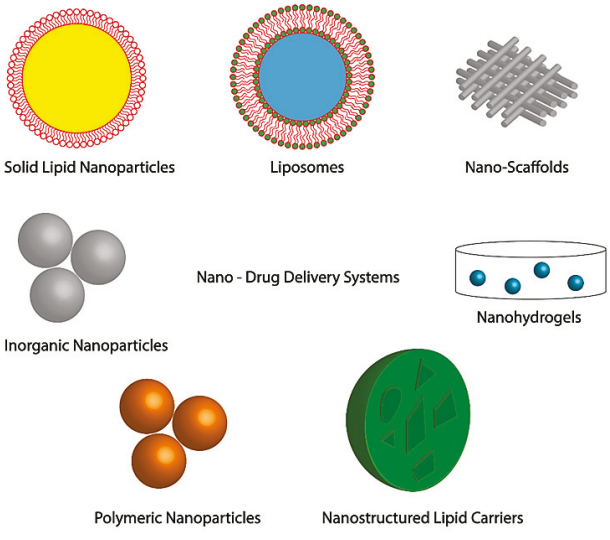

Figure 4. Nano-DDSs in skin regeneration and wound treatment. Adapted from [46], with permission from Springer Nature, 2019.

Drugs are absorbed, dispersed or dissolved around the nanoparticle, and confined in an aqueous core with shell like surroundings, or alternatively the drug can be covalently bound to the surface matrix of nanoparticles [48]. In the biological system, the drugs loaded in the nanoparticles will be released by diffusion, dissolution, reduction and distension. Furthermore, nanoparticles can be encapsulated in nanofiber, hydrogel, foam, films and nanocrystals as a nanocomposite system along with other drugs (Figure 5), which allows for synergistic effect between nanoparticles and the drug of interest, creating a new concept of wound dressing that promotes enhanced wound healing [49]. Such dressings have increased porosity surface-to-volume ratio, and their structure simulates the topographic appearance of endogenous ECM, allowing attachment and spreading of both fibroblasts and keratinocytes, thereby facilitating collagen synthesis and re-epithelialization of wounds [41].

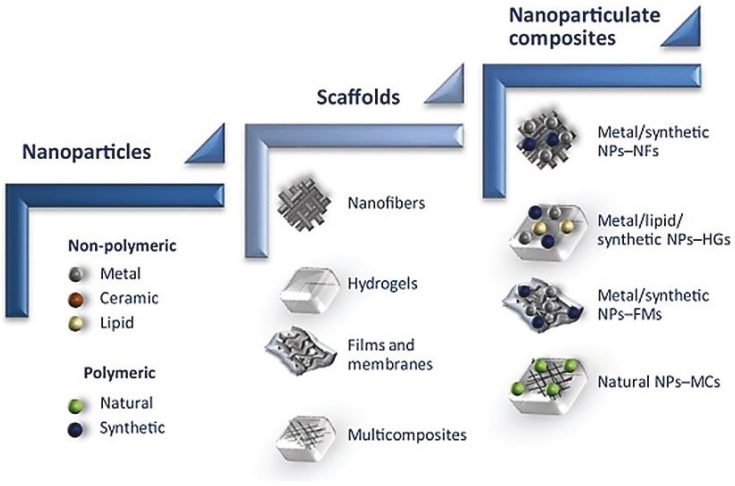

Figure 5. Schematic of nanomaterial, from nanoparticle to nanoparticulate system for wound regeneration. NFs—Nanofibers, NPs—Nanoparticles, HGs—Hydrogel, FMs—Films and membrane, MCs—Multicomposites. Reproduced from [49], with permission from Elsevier, 2017.

5. Nanoparticle Delivery of Therapeutic Drugs for Diabetic Wound Healing

It is well established that delivering of therapeutic active components such as growth factors, nitric oxide, nucleic acid, antioxidants, and antibiotics to damaged tissue, can stimulate cell proliferation, migration, angiogenesis, and collagen secretion, and inhibit microbes, thereby influencing healing of chronic wounds [50]. Nanofibers have received much attention because of their structural similarity, which closely mimics the native ECM environment [51,52]. Nanofibers promote wound healing by providing characteristics of high surface area to volume ratio, tunable mechanical properties, increased porosity, and ability to encapsulate nanoparticles and bioactive compounds for controlled release, which can support the cells to actively interact with the matrix during functionalization and remodeling [53,54]. Hydrogels are hydrophilic 3D polymer networks with established applications in tissue engineering and drug delivery. Hydrogels with high water content, tunable viscoelasticity and biocompatibility have been intensively explored to enable topical delivery of bioactive molecules [55,56]. More importantly, nanoparticle and biomolecules can be incorporated in hydrogels and thus, opens the door to more advanced topical drug delivery with unique benefits such as improved tissue localization, minimized burst release and controlled sequential drug release, by preserving its structural integrity of nanoparticle [57]. Non-polymeric nanoparticles such as silver nanoparticles (AgNPs) and gold nanoparticles (AuNPs) are widely used as therapeutic agents, primarily for their anti-infective and anti-inflammatory effects [58]. There is an unmet need for a novel antibiofilm approach and effective antimicrobial compounds, and silver nanotechnology-based therapeutics has captured the attention of health care providers for enhancing health care [59]. AgNPs are used in clinical practice for a wide range of treatments such as burns, chronic ulcers and diabetic wounds that have developed antibiotic resistance and hospital acquired bacterial infection. In addition to anti-inflammatory effects, AgNPs treated wounds have shown abundant collagen deposition that could accelerate wound healing [60,61]. Biocompatible AuNPs are extensively used in tissue regeneration, targeted drug delivery and wound healing. Unlike Ag nanomaterials, Au nanomaterials as a single material alone does not have any antimicrobial activity. Thus, AuNPs must be incorporated with other biomolecules to be used for effective biological functions [62,63]. Zinc (Zn) can be used for treating type 1 and type 2 DM, owing to its role in the function of >300 enzymes that are necessary to maintain metabolic homeostasis in the body. Zn reduces blood sugar levels by inhibiting glucose absorption and raising glucose absorption

by skeletal muscles and adipose tissues [64]. Zinc oxide (ZnO) nanoparticles have been explored as drug delivery carriers and therapeutic approaches for human biomedical applications because of the fact of their biocompatibility [65]. ZnO nanoparticles have exhibited therapeutic activities against melanoma, diabetes, bacterial infection, and inflammation, and have shown potential for wound healing applications [66]. Ceramic nanoparticles containing inorganic components have fundamental therapeutic ability and can transport drugs to injury sites [67]. Lipid-based nanoparticles, in addition to being safe, are extensively used to deliver both hydrophilic and hydrophobic drugs. Liposomes sustain long term release of drugs by reducing the toxicity exerted by huge release of drugs via conventional administration [68]. In the case of polymeric nanoparticles, chitosan is a natural polymer to use, due to its biocompatibility and antimicrobial activity. It is possible to encapsulate a wide range of natural components such as aloe vera, vitamin E and curcumin, which have potential beneficial effects on skin wound healing [69,70]. PLGA or poly (lactic-*co*-glycolic acid), poly (ε-caprolactone) (PCL), poly (lactic acid) (PLA), and poly (ethylene glycol) (PEG) are synthetic polymers approved by Food and Drug Administration (FDA). Among these polymers, PLGA is considered the best biodegradable polymer due to its ability to release lactate, a degradation byproduct. PLGA nanoparticles have been reported to stimulate cell proliferation and shorten the duration of wound healing in diabetic rats and despite moderate drug loading may be a promising delivery system for growth factors [71,72].

The type of therapeutics that can be delivered by nanoparticles are given below.

5.1. Growth Factors

Growth factors are physiologically active proteins involved in cell proliferation, migration, differentiation, and metabolism. Physiologically, every healing process is regulated by growth factors and cytokines. Growth factors bind to a specific receptor and stimulate a series of molecular mechanisms that are essential for cell function [73]. In the wound healing process, growth factors play an important role by stimulating inflammatory response, angiogenesis, granulation of tissue, and modelling. It is well established that in a diabetic wound, the availability of growth factors will decrease due to the pathophysiology [74,75]. External administration of growth factors can be given, but proteases present in the wound bed can easily degrade these growth factors physiologically. Furthermore, the short half-life of growth factors and their reasonably large size, together with toxicity at an elevated systemic dosage, shows that conventional delivery techniques of growth factor in a free form are not appropriate to transport growth factors effectively in the wound bed. In addition, as various biomolecules are engaged in wound healing progression, sometimes it may be inadequate to utilize a single growth factor to accelerate wound closure in diabetic ulcers [76,77]. With these problems, encapsulation of growth factors in nanoparticles have been widely used to overcome the limitation of protein administration by improving the half-life, encapsulation of more than one biomolecule, and protection against degradation by proteases in the wound bed through protective characteristics of nanoparticles [78]. Nanoparticle-loaded recombinant human EGF (rhEGF) has been shown to provide faster healing of wound compared to free rhEGF administration in rats, due to the sustained release of rhEGF [79]. Nanoparticle-loaded VEGF have been observed to induce faster acceleration of wound closure in both diabetic and non-diabetic mice, as compared to PLGA nanoparticle and VEGF alone [80]. Gainza et al. fabricated rhEGF loaded solid lipid nanoparticles (SLN) and nanostructure lipid carrier (NLC) using the emulsion ultrasonication method. The same investigators showed that SLN-rhEGF and NLC-rhEGF significantly increased wound closure in diabetic mice compared to free rhEGF and alginate microspheres with rhEGF, suggesting that there is controlled release of rhEGF from lipid nanoparticle without loss of rhEGF bioactivity after encapsulation [81]. In another study, Losi et al. reported that poly(ether)urethane-polydimethylsiloxane/fibrin-based scaffold containing PLGA nanoparticles loaded with VEGF and basic fibroblast growth factor (bFGF) (scaffold/growth factor-loaded NPs) stimulated significant granulation tissue formation, collagen secretion and re-epithelialization, thereby promoting considerable increase in wound closure rate in diabetic mice, as compared to scaffold with PLGA nanoparticles without growth factors and controls. The same authors further suggested that

the observed results may be due to: (i) controlled delivery of growth factor from the encapsulated nanoparticles, (ii) simultaneous delivery of more than one growth factor, and (iii) administration of growth factor protecting from enzymatic hydrolysis by encapsulating in nanoparticles [82]. In another study, chitosan-based hydrogel carrying human epidermal growth factor was conjugated with sodium carboxymethyl chitosan nanoparticles (NaCMCh-rhEGF) for controlled release of growth factor in an excision wound model on diabetic rats. The in vitro results demonstrated that the NaCMCh-rhEGF stimulated higher cell viability, thereby reducing the wound area significantly on day 15 in comparison to free rhEGF and controls [83]. Lai et al. fabricated a collagen (Col)- hyaluronic acid (HA) electrospun nanofibrous scaffold encapsulated with gelatin nanoparticles that can release multiple angiogenic growth factors such as VEGF, PDGF, bFGF, and EGF at the excision wound site. Topical application of Col-HA membrane with four kinds of growth factors (Col-Ha w/4GF) on the diabetic wound bed accelerated complete healing of excision wound in rats along with elevated collagen synthesis, re-epithelialization and vascularization compared to control animals [84]. Furthermore, Li et al. conjugated keratinocyte growth factor (KGF) with AuNPs to determine the stability and binding affinity of KGF for diabetic wound healing. The result showed that by KGF-AuNPs conjugation, KGF retained its bioactive affect at the wound site at greater stability and resistance against proteolytic degradation to promote keratinocytes proliferation and migration and generated greater binding effect to its physiological receptor than unmodified KGF. Moreover, KGF-AuNPs at wound site supported re-epithelialization and wound contraction along with elevated expression of Col-I, α-SMA and TGF-β1. These observed conditions lead to accelerated wound healing by fabricated KGF-AuNPs when compared to controls [85]. Recently, the safety and efficiency of topically administered exogenous growth factors (VEGF or bFGF) in the healing of chronic diabetic wounds were examined in clinical trials, where local administration of growth factors was proven to be well tolerated. However, the free form of exogenous growth factor administration has encountered problems such as rapid leakage from the wound bed, short biological half-life and the rapid enzymatic degradation, which makes it difficult to achieve effective concentration to treat diabetic ulcer, leading to inefficacy of the treatment [86,87]. The afore-mentioned growth factor delivery by nanoparticles (as summarized in Table 1) has also addressed the common clinical barriers, which include achieving a sustained and controlled release of biomolecule proteins, distributing concurrently more than one growth factor, and protecting the growth factors against enzymatic hydrolysis when administrated at the wound site, suggesting promising future clinical application of growth factor-loaded nanoparticles for diabetic wound healing.

5.2. Nucleic Acid

Nucleic acid encapsulated particulate combines gene therapy and nanotechnology to knockdown or express a specific gene for successful healing of a chronic wound [88]. Gene delivery to injury site supports expressing specific proteins which can accelerate healing of chronic wounds. For instance, VEGF for induction of angiogenesis in chronic wound has been transfected by viral vectors in diabetic patients and the effect in wound healing observed [89]. However, the use of non-viral vectors such as nanoparticles to deliver nucleic acid is a better choice as viral vectors can cause immune response and should always be treated with caution [90,91]. siRNA permits knockdown of gene expression by selectively targeting genes such as *MMP, ganglioside-monosialic acid 3 synthase (GM3S)* and *TNF-α*, which are overexpressed in chronic wounds. In vivo delivery of siRNA requires a carrier for transport into cells to protect against physiological nucleases. Nanoparticle-based technology has enabled targeted transport of siRNA and prevention from degradation [92,93]. Clinical studies delivering siRNA to cure several diseases have been promising, yet primary clinical trials were unsuccessful due to inadequate efficacy or significant off-target effects. RNAi technology demands additional refinement prior to widespread clinical use. Barriers for successful siRNA delivery for efficient therapy are degradation of siRNAs by enzymes in the wound environment and siRNAs not readily taken up by the cells due to electrostatic constraints, as the negatively charged cell wall will not easily allow penetration of negatively charged siRNAs into the cells. To address these problems, a wide variety of delivery

systems have been pre-clinically tested using nanoparticles. Delivery vehicles for siRNAs such as those mentioned below have attained varying degrees of efficacy, with topical dosing and intravenous formulations, and are currently at the forefront of testing for clinical use [94,95].

(a) Ganglioside GM3 siRNA: Ganglioside GM3 is a monosialodihexosylganglioside produced by the enzyme GM3 synthase (GM3S). GM3S is key intermediary of insulin resistance which has proven to be highly expressed in human diabetic foot skin, diabetes stimulated obese mouse, hyperglycemic mouse, and mouse keratinocytes exposed to high glucose [96,97]. Randeria et al. showed that knockdown of GM3S expression in diabetic mice by AuNPs conjugated with GMS3 siRNA-based spherical nucleic acids (SNAs) reverse impaired wound healing in diabetic mice with no obvious toxicity [98].

(b) TNF-α siRNA: TNF-α is an inflammatory cytokine and it is required in limited amounts to accelerate wound healing as TNF-α is required for fibroblast proliferation, migration and wound remodeling. However, in the case of diabetic wound, uncontrolled production of TNF-α blocks the normal process of wound healing by increasing cell apoptosis, ROS and matrix degradation [99,100]. Kasiewicz et al. fabricated lipid nanoparticles encapsulated with specific TNF-α siRNA to accelerate wound healing in diabetic mice [101]. The same investigators demonstrated that topical application of lipid nanoparticles loaded with TNF-α siRNA in the diabetic wound of mice downregulated TNF-α expression by 40–50% with closure of wound significantly faster than control wound.

(c) Keap1 (Kelch-like erythroid cell-derived protein with CNC homology-associated protein 1) siRNA: In the absence of oxidative stress, the nuclear factor erythroid 2–related factor 2 (Nrf2) binds to Keap1 (in the cytoplasm, which subsequently lead to Nrf2 degradation by ubiquitination). However, in the presence oxidative stress, keap1 is covalently modified in some region that prevents degradation of Nrf2. Following which, Nrf2 enters the nucleus by dissociating from the repressor site of Keap 1 and binds to the antioxidant response element (ARE) in the promotor region of a wide variety of genes responsible for preventing oxidative stress and protein instability, as well as proteasome integrity [102]. ARE is situated in the promoter area of genetic materials that encode many antioxidant and phase II detoxifying enzymes. These enzymes are essential for cellular protection by increasing the elimination of cytotoxic electrophiles and ROS [103]. Chronic hyperglycemia in diabetes causes imbalance of ROS and over production of Keap1, leading to degradation of Nrf2, which regulates diabetic oxidative stress [104,105]. Rabbani et al. has developed a liposome and protein hybrid nanoparticulate delivery system loaded with siRNA specific to Keap1, which can accelerate diabetic wound with severe oxidative stress [94].

(d) miR-146a: The hyperglycaemic state also activates redox-sensitive transcription factors, mainly NFkB, which leads to over production of pro-inflammatory cytokines such as IL-6 and IL-8 that delay wound healing by extending the inflammation period [106,107]. Cerium oxide nanoparticles (CNP) can act as a therapeutic agent for oxidative stress as CNP has an ability to scavenge free radicals [108,109]. The initial inflammatory response to injury is essential to activate normal wound healing while sustained inflammatory response impairs wound healing associated with diabetic wounds [110]. Zgheib et al. has designed microRNA (miR-146a) loaded CNPs for diabetic wound healing [111]. miR-146a has been reported to negatively regulate the production of pro-inflammatory cytokines, implying that miR-146a can act as a molecular brake in the inflammatory response [112,113]. miR-146a suppresses interlukin-1 receptor associated kinase 1 (IRAK1) and tumor necrosis factor receptor associated kinase 6 (TRAF6), which induces overexpression of IL-6 and IL-8 [114,115]. Down regulation of miR-146a, which influences the upregulation of its target gene IRAK1 and TRAF6, has been observed in diabetic wounds [116]. CNP-miR-146a has been reported to be effective for diabetic wound healings [111]. The use of nanoparticles as a delivery system for siRNA (as summarized in Table 2) may be able to overcome the boundaries of existing methods of free siRNA delivery at wound site because of the capability for encapsulation, controlled release, specific targeting, stability, and bioavailability.

Table 1. Nanoparticles-based therapeutic incorporated with growth factors for diabetic wound healing.

Type of Nanoparticles	Incorporated Growth Factors	In-Vitro Model	In-Vivo Model	Results	Route of Administration	Ref.
SLN and NLC nanoparticles	rhEGF	Fibroblasts, keratinocytes	8 mm in diameter skin wound was created in diabetic male db/db mice	rhEGF loaded lipid nanoparticles exhibited higher fibroblast and keratinocyte proliferation and greater resolution of inflammation re-epithelialization and significant wound closure compared to free rhEGF	Topical SLN-rhEGF and NLC-rhEGF dressing of nanoparticles at wound site	[81]
PLGA nanoparticles	VEGF, bFGF	–	8 mm in diameter skin wound was created in diabetic male db/db mice	VEGF and bFGF loaded nanoparticles treated wound stimulated significant granulation tissue formation, collagen secretion and re-epithelialization, and accelerated wound closure compared to controls and NPs without biomolecules	Topical dressing of nanoparticles incorporated polydimethylsiloxane/ fibrin-based scaffold at wound site	[82]
NaCMCh nanoparticles	rhEGF	Fibroblast	20 mm in diameter skin wound was created in diabetic male Sprague–Dawley rats	Nanoparticles-treated cells showed higher cell viability with enhanced wound healing rate when compared to controls and free rhEGF	Topical dressing of nanoparticles incorporated chitosan-based hydrogel at wound site	[83]
Gelatin nanoparticles	VEGF, PDGF, bFGF, EGF	Human umbilical vein endothelial cells (HUVEC)	15 mm in diameter skin wound was created in diabetic male Sprague–Dawley rats	Gelatin nanoparticles loaded with multiple angiogenic growth factors showed high cell proliferation and accelerated complete healing along with enhanced collagen synthesis, re-epithelialization and vascularization compared to controls	Topical dressing of drug loaded collagen/ hyaluronic acid nanofibrous scaffold at wound site.	[84]
AuNPs	KGF	Keratinocytes	10 mm in diameter skin wound was created in diabetic rats	KGF-AuNPs increased healing effect compared to free KGF and nanoconjugate promoted re-epithelialization and wound contraction along with elevated expression of Col-I, α-SMA and TGF-β1, leading to accelerated wound healing compared to controls	Topical gelatin hydrogel dressing encapsulated with KGF-AuNPs	[85]

5.3. Antibiotics

The most common characteristic of prolonged chronic wound healing is infection. In diabetic wounds, surface infections lead to the development of biofilms superficially within the wound, disrupting normal physiological wound healing [117]. Contamination by pathogens in a wound can evolve into colonization of bacteria, leading to localized infection and even systemic infection, sepsis and multi-organ dysfunction [118]. The presence of a biofilm leads to prolonged inflammation by stimulation of NO, cytokines and free radicals [119]. Hence, an effective treatment is required to deliver antimicrobial drugs to infected wounds for normal wound healing. In this regard, nanoparticles can be utilized to specifically target and eliminate pathogens. The antimicrobial effect of nanoparticles comprises destruction of cell membranes, impediment of enzyme pathways, modifications of microbial cell wall and nucleic materials pathway, and as a delivery system.

AgNPs have demonstrated a huge potential for different biomedical applications, such as in detection and diagnosis, drug delivery, coating of biomaterials, devices for novel antimicrobial agents and in regeneration materials [59]. For instance, AgNPs are known to have antimicrobial activity, which when incorporated with EGF, promotes re-epithelization, resulting in wound healing in diabetic mice [120]. AgNPs embedded in cellulose nanocrystals (CNCs) isolated from *syzygium cumini* leaves (which help to preserve the moist environment in the wound) has accelerated wound healing in diabetic mice [121].

Nanoparticle encapsulation with antimicrobial drug has developed as a novel and capable alternative to address diabetic wound infection with minimal undesirable side effects [122]. A major challenge faced in antibiotic therapy is antibiotic resistance. According to the World Health Organization (WHO), Methicillin-resistant *Staphylococcus aureus* (MRSA) infections have caused a higher mortality in patients by 64% compared to the non-resistant form [123]. To overcome the challenges of multi-drug resistant bacteria and to restore the efficacy of antibiotics, Kalita et al. designed lysozyme capped gold nanoclusters (AUNC-L) functionalized with a widely used β-lactam antibiotic, ampicillin, as a model drug to combat MRSA resistance against ampicillin and to accelerate diabetic wound with MRSA persistent infection [117]. Free ampicillin has failed to reduce MRSA infection on diabetic wounds while AUNC-L-Amp has accelerated wound healing by eliminating the MRSA persisted infection within the wound [117]. This same study showed that metallic nanoclusters in combination with antibiotics, augment their antibacterial properties and thereby mitigate the cytotoxicity of both the agents by reducing the necessity for high drug dosages. For the development of nano-antibiotics against microbial pathogens, toxicity of non-natural materials is a limiting step for utilization in clinical application.

The emergence of bacterial resistance to conventional antibiotics represents a general challenge in clinical trials. Dai et al. developed an AgNPs-coated ε-Polylysine (EPL-g-butyl@AgNPs) bacterial binding nanocomposite, in which ε-Polylysine was used to coat AgNPs so as to act as bacterial affinity ligand to combat multiple-drug resistance bacteria. The nanocomposites and levofloxacin were introduced in the culture of Gram-negative (*P. aeruginosa*) and Gram-positive (*S. aureus*) bacteria, respectively. After 30 passages, MIC remained the same for EPL-g-butyl@AgNPs, while the MIC value of levofloxacin increased from 0.64 to 78 μg mL^{-1} against *S. aureus* and from 3.2 to 156 μg mL^{-1} against *P. aeruginosa*. Compared with the antibiotic, no antimicrobial resistance was detected against the EPL-g-butyl@AgNPs nanocomposite, providing a promising solution to control and prevent drug resistance. Furthermore, the same investigators proved that EPL-g-butyl@AgNPs offer effective antibacterial effect and wound-healing acceleration in diabetic rats by the synergetic effect of ε-Polylysine and AgNPs [124] (Figure 6).

Table 2. Nanoparticles-based therapeutics encapsulated with nucleic acids for diabetic wound healing.

Type of Nanoparticles	Encapsulated Nucleic Acids	In-Vitro Analysis	In-Vivo Model	Results	Route of Administration	Ref.
Cationic lipid nanoparticles	Keap1 siRNA	Knockdown of Keap1 via LPP-10 correlated with an increased protein expression of Nrf2, a critical transcription factor in maintenance of cell integrity	10 mm in diameter skin wound was created in diabetic mice	Nanoparticles treatment complexing siKeap1, restored Nrf2 antioxidant function, accelerated diabetic tissue regeneration, and augmented reduction oxidation homeostasis in the wound environment	Topical administration to wound	[94]
AuNPs	GM3S siRNA based SNAs	GM3S loaded nanoparticles treated wounds were completely closed in hyperglycemic conditions and almost closed in normoglycemic medium	6 mm in diameter skin wound was created in diet- induced obese C57BL/6 diabetic mice	Nanoparticles treated wound stimulated granulation of tissue area, vascularization, and IGF1 and EGF receptor phosphorylation are elevated in GM3S SNA-treated wounds that accelerated active wound closure compared to free GM3S siRNA	Topical administration to wound	[98]
Lipid nanoparticles	TNF-α siRNA	-	8 mm in diameter skin wound was created in diabetic C57BL/6 mice	Nanoparticles in diabetic mice accelerated TNF-α knockdown of diabetic wound that elevated the wound closure rate within 13 days, which was statistically faster than control wounds, which remained open on Day 16	Topical administration to wound	[101]
CNPs	miR-146a	-	8 mm in diameter skin wound was created in Db/Db mice	CNP-miR-146a improves wound healing in diabetic mice wound model without compromising wound strength and elasticity	Topical administration to wound	[111]

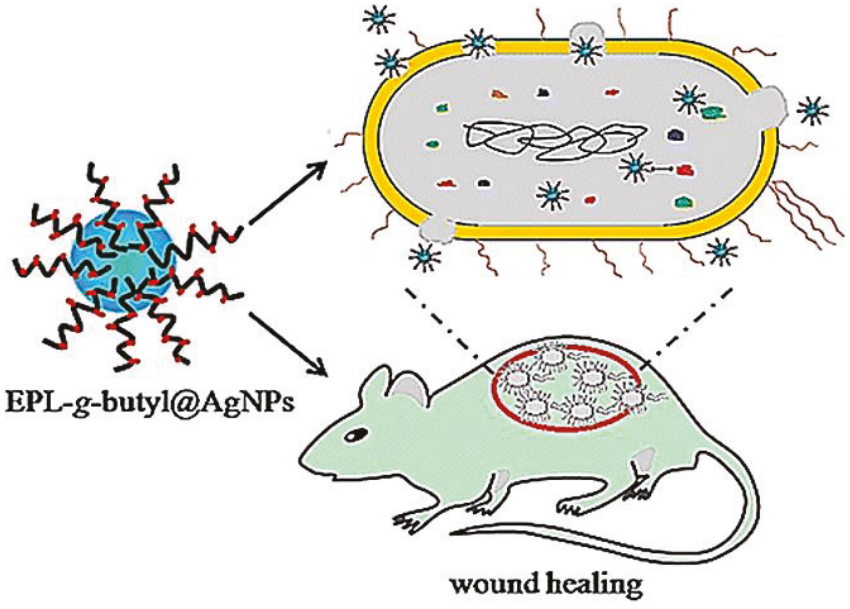

Figure 6. Nanocomposite (EPL-g-butyl@AgNPs) shows effective antibacterial activity against both Gram-negative (*P. aeruginosa*) and Gram-positive (*S. aureus*) bacteria without the emergence of bacterial resistance, which effectively promoted infected wound healing in diabetic rats. Reproduced from [124], with permission from American Chemical Society, 2016.

According to the American Diabetes Association, 25% of hyperglycaemic patients experience delayed wound healing. Chronic wound infections are frequently polymicrobial, whereby several microorganisms share a common niche [125]. Polymicrobial wound infections usually necessitate increased doses of antibiotics and fungicides. Yet, continued antimicrobial treatments are related with possible systemic side effects and possible risk of developing drug-resistant microorganisms. Hence, Thattaruparambil-Raveendran et al. has developed chitosan (CH) bandages using fibrin nanoparticles (FNPs) encapsulated with antimicrobial agents, such as ciprofloxacin and fluconazole (cFNPs+fFNPs−CH) and demonstrated significant reduction in microbial contamination with accelerated wound healing, as compared to control animals with topical application of cFNPs+fFNPs−CH in vivo. Also, this same study analyzed the antimicrobial ability of the bandages containing nanoparticles-loaded antibiotics against a co-culture of *S. aureus*, *E. coli*, and *C. albicans*, to mimic the clinical scenario of polymicrobial infection in chronic wounds. The findings verified that the chitosan bandages had significant antimicrobial property towards co-cultures of bacteria and fungi, indicating that this bandage is a potential candidate for clinical applications for diabetic wound healing [126]. Liang et al. established a glycidyl methacrylate functionalized quaternized chitosan (QCSG) and gelatin methacrylate (GM) hydrogel, encapsulated with graphene oxide (GO), for drug-resistant bacterial infective wound healing. Development of injectable conductive nanocomposite hydrogel dressings based on GO and cationic polymer for wound healing is highly promising as the QCSG/GM/GO hydrogels demonstrated 95% killing ratio against *S. aureus* and *E. coli*, and for clinical drug-resistant bacterium MRSA, the bacterial killing ratio is also higher than 90%. Based on the known photothermal effectiveness of these hydrogels, near-infrared light-assisted photothermal antimicrobial activity was analyzed. Infrared irradiation of QCSG/GM/GO hydrogel for more than 10 min had killing ratios of almost 100% for all three bacteria, affirming the effective near-infrared-assisted photothermal antibacterial properties of QCSG/GM/GO hydrogels. In order to evaluate the continuous

drug release ability of hydrogels, an inhibition zone assay was conducted to assess the antimicrobial activity of the doxycycline that was released from hydrogels. Inhibition for *S. aureus* and MRSA lasted for 9 days, which further confirmed sustained drug release of the hydrogels. Cell compatibility data demonstrated higher L929 cell viability with increase in incubation time for the hydrogel groups. It was noted that IL-6 expression (a biological cytokine plays a significant role in inflammatory response and secreted by several types of cells) in the wounds of the hydrogel-treated group was lower than that of the Tegaderm group on the third day, while inflammation was significantly reduced on the 7th day. Moreover, injectable QCSG/GM/GO hydrogels with antibiotics accelerated infectious skin defect wounds compared to commercially available Tegaderm with an increase in collagen deposition and re-epithelialization [127].

Bacterial infection and prolonged inflammation is a very important factor in preventing successful clinical intervention for diabetic wound healing. The above discussed research studies evaluated the antibacterial property of nanoparticles loaded with antibiotics (summarized in Table 3). The findings that showed the effective antibacterial property of nanoparticulate systems against major drug-resistant bacteria may give rise to novel clinical applications in the near future.

5.4. Antioxidants

In the inflammatory phase of wound healing, neutrophils, leucocytes, and monocytes will be attracted to the wound sites by biologically active mediators and then attack the microorganisms and foreign debris via phagocytosis, which will lead to the production of ROS [128]. The antioxidant system in the cell evolves to play central roles in scavenging these free radicals to maintain redox homeostasis or the equilibrium between free radicals and antioxidants [129]. ROS including superoxide (O_2-), hydrogen peroxide (H_2O_2), hydroxyl radical, and other reactive oxygen derivatives, are very lethal and cause extensive damage to protein, DNA and lipids, thereby affecting normal cellular functioning [130]. ROS is produced in the cell as an unavoidable by-product of oxidative phosphorylation [131]. ROS is constantly being generated at basal levels. However, they are unable to cause damage, as they are being scavenged by different antioxidant mechanisms [132]. As high levels of ROS can damage cells by oxidizing lipids and proteins, the levels are tightly controlled by the presence of ROS scavenging enzymes and small molecule antioxidants [133]. Altered redox signaling (non-equilibrium between free radicals and antioxidants) that leads to oxidative stress is widely accepted as a contributor to the development of diabetic complications, including cardiovascular disease, nephropathy and retinopathy [134,135]. Accumulation of ROS leads to significant destruction of endogenous stem cells, growth factors, and nucleic acids in the wounded tissue, thus greatly affecting their regenerative potential, causing delayed wound healing [136].

Table 3. Nanoparticles-based therapeutics incorporated with an antibiotic for diabetic wound healing.

Type of Nanoparticles	Incorporated Antibiotics	Antibacterial Assay	In Vitro Analysis	In Vivo Model	Results	Route of Administration	Ref.
AUNC-L	Ampicillin	50–89-fold increase in antibacterial activity of nanoclusters compared to Free-Amp in terms of zone of inhibition against 9 non-resistant bacterial pathogens	Cyto-compatibility study of nanoclusters with human blood cells and fibroblast shows higher cell viability compared to free ampicillin	1.5 cm in diameter skin wound was created in diabetic male Wistar rats followed by MRSA infection	Nanoclusters eradicated MRSA infections from diabetic wound which accounts for pronounced and faster wound healing	Topical application of nanoclusters to wound	[117]
AgNPs coated ε-Polylysine nanocomposites	ε-polylysine	4.7 μg mL^{-1} of nanocomposite inhibited antibiotic resistant Gram-negative and Gram-positive bacteria	Fibroblast cells maintained a viability of 80% after 2 days treatment with nanoparticles	1.5 cm in diameter skin wound was created in diabetic male Wistar rats followed by inoculation with *P. aeruginosa* and *S. aureus*	Nano-composite modulated inflammation of cells primes to wound healing acceleration without side effects on dermal tissues, eliminating the infection in wound	Topical application of nanoparticles with antibiotic to wound	[124]
FNPs	Ciprofloxacin, fluconazole	The nanoparticles loaded bandages showed promising inhibitory activity against individual and co-culture *S. aureus*, *E. coli*, and *C. albicans*	Toxicity of the bandages studied against the human dermal fibroblast cell line proved its cyto-compatibility	1.5 cm in diameter skin excisional infected wounds model was created in diabetic female Sprague–Dawley rats by inoculation of *S. aureus*, *E. coli*, and *C. albicans*	The bandages with nanoparticles showed a significant reduction in microbial populations in the poly-microbial infected rat wound model which accelerated wound healing	Topical dressing of bandage with nanoparticles loaded antibiotic to wound	[126]

Nanoparticles-based treatment has shown promising results in promoting antioxidant activities in diabetic rodents for effective wound healing. Bairagi et al. has developed PLGA nanoparticles encapsulated with ferulic acid (FA; 4-hydroxy-3-methoxycinnamic acid) to study its effect in diabetic wound healing. FA is a phenolic compound and a natural antioxidant with a potential synergistic therapeutic effect in diabetic wound healing due to its hypoglycemic, free radical scavenging, angiogenic, antibacterial, and neurogenic effects. In this same study, the investigators demonstrated that FA-loaded polymeric nanoparticles dispersion (oral administration) and FA-loaded polymeric nanoparticles-based hydrogel (topical administration) treated wounds had faster epithelization of the wound, leading to effective wound closure on day 14 as compared with the diabetic wound group [137]. The formation of advanced glycation end products (AGEs) has been recognized as an important pathophysiological mechanism in the development of diabetic ulcers; the binding of circulatory AGE to RAGE (receptor for AGEs) on different cell types leads to impaired function of growth factors. Glycation is an important pathway in the pathogenesis of microvascular and macrovascular complications of DFUs. AGE and RAGE result in oxidative stress and cause abnormal angiogenesis in wound healing [138]. In type 2 diabetic skin tissues, the expression of both AGE and RAGE were increased when compared with normal skin tissues. Moreover, a study on human dermal fibroblasts demonstrated that cell arrest and apoptosis was increased [139]. The levels of nitric oxide were increased in glycated soluble protein (AGE-BSA) treated kidney cell lines, suggesting oxidative stress [140]. The blockage of RAGE by intraperitoneal soluble RAGE, significantly suppressed the TNF-α and IL-6 while enhancing cutaneous wound closure in db/db mice [141]. A previous study reported that an antioxidant, epigallocatechin gallate (EGCG) decreased RAGE mRNA and protein expression in AGE-treated human mesangial cells [142]. EGCG also attenuated AGE-induced RAGE in neuronal cells [143,144], and alpha-lipoic acid (ALA) is a scavenger of many ROS [144]. Chen et al. demonstrated that the combination of antioxidants EGCG, ALA and AuNPs in specific concentrations significantly decreased expression of the RAGE protein within cultured fibroblasts (Hs68) and diabetic wound healing in a mouse model. In this study, the authors showed that a mixture of AuNP, EGCG and ALA (AuEA) significantly decreased AGE-induced RAGE protein expression in fibroblasts (Hs68). Furthermore, topical AuEA application decreased RAGE expression in diabetic mouse skin, which suggests that a combination of EGCG, ALA and AuNPs considerably accelerated diabetic wound healing through anti-inflammatory and angiogenesis via modulation of antioxidants [145]. Similarly, topical gas-injection of a EGCG and AuNP liquid mixture (AuE) using the GNT GoldMed™ liquid DDS showed a significantly higher rate of wound closure on wild-type and streptozotocin-induced diabetic mouse skin, associated with increased epidermal growth factor receptors and VEGF, which stimulate wound recovery and the new tissue formation. Besides, collagen I, III and hyaluronic acid protein expressions increased in the wound area. These are essential factors of physiological matrix and wound healing [146]. In another study, Ponnanikajamideen et al., using the leaf extract powder of a plant, *Chamaecostus Cuspidatus*, and fabricated green synthesized AuNPs, showed 50% inhibition of free radicals by green synthesized AuNPs without inducing any lethal effects in a mouse model, with restoration of blood glucose, glycogen and insulin levels in the diabetic mice after 21 days of treatment [147]. He et al. fabricated PCL and quaternized chitosan-*g*-polyaniline (QCSP) nanofibers to promote wound healing [128]. The nanofibrous wound dressings displayed comparable mechanical characteristics to soft tissue, free radical scavenging capability, antimicrobial property and biocompatibility. Their data suggested that the antioxidant capability of PCL/QCSP15 nanofibers heightened with increasing concentration of QCSP and almost 70% of free radicals can be cleared by 6 mg mL^{-1} of PCL/QCSP15 dispersion liquid, and the scavenging efficacy for DPPH has shown more than 80% when the content of PCL/QCSP15 dispersion liquid reached 8 mg mL^{-1}. Furthermore, wounds that received treatment by PCL/QCSP15 nanofiber dressing showed elevated collagen secretion, granulation tissue thickness and enhanced angiogenesis, leading to accelerated wound closure compared to commercially available Tegaderm [128]. As DFU remain a complex problem in clinical settings, the above discussed studies (highlighted in Table 4) strongly support the beneficial effects of anti-oxidants and nanoparticles on diabetic patients with cutaneous wounds and clearly provide a basis for the potential therapeutic application of AuEA, PLGA nanoparticles in chronic wound therapy.

Table 4. Nanoparticles-based therapeutics incorporated with antioxidants for diabetic wound healing.

Type of Nanoparticles	Incorporated Antioxidants	In Vitro Analysis	In Vivo Model	Results	Route of Administration	Ref.
PLGA nanoparticles	FA	-	2.5 cm in length skin wound was created in diabetic Wistar rats of either sex	FA nanoparticles topical and oral treatment is effective in promoting wound healing in diabetic rats	Oral administration of nanoparticles and topical administration of hydrogel containing nanoparticles	[137]
AuNPs	EGCG, ALA	Antioxidant loaded nanoparticles group significantly decreased RAGE expression in AGE-treated fibroblast cells	1 cm in diameter skin wound was created in diabetic male BALB/c mice	Nanoparticles loaded with antioxidant significantly increased the rate of diabetic wound healing by decreasing RAGE expression than control and free antioxidants	Topical application of nanoparticles containing antioxidant on wound	[145]
AuNPs	EGCG	-	1 cm in diameter skin wound was created in diabetic male BALB/c mice	Epidermal growth factor receptor and collagen I and III protein expression, and hyaluronic acid expression increased considerably which significantly increases the rate of wound healing both in wild-type and diabetic mice	Nanoparticles containing liquid by gas-injection applied directly to the wound	[146]
AuNPs	Green synthesis of AuNPs by *Chamaecostus Cuspidatus*	-	Blood sampling in Wistar male diabetic mice	Nanoparticles with nontoxic effects showed 50% inhibition of free radicals with restoration of blood glucose, glycogen, and insulin levels in the diabetic mice	Intraperitoneal administration of green synthesized nanoparticle	[147]

6. Regulatory Pathway for Nanomaterial

Nanotechnology is an emerging technology that can be used in a broad array of FDA-regulated products. There are two main points for consideration when providing an initial screening tool that can be applied to FDA-regulated nanotechnology products. 1. Whether an engineered material is in nanoscale range of 1 to 100 nm with at least one external dimension. 2. Whether an engineered material demonstrates properties involving physical characteristics or biological effects that are attributable to its dimensions, even if these dimensions fall outside the nanoscale range, up to 1 µm (1000 nm). FDA regulatory framework and review process adequately identify and manage potential risk associated with the use of nanomaterials in products [148,149]. The safety assessment and the toxicity and biocompatibility of nanomedicines go through the same FDA regulatory process as drugs that do not contain nanotechnology products. Primary development of a nanotech product is at the nexus of basic and preclinical research, where further development often includes collaborations among academic supervisor and industrial researchers. Primary studies may be initial tests for its translational potential and will offer a base for further preclinical development, which involves tests that meet the regulatory requirements for investigational new drug (IND) applications, new drug applications (NDAs), and abbreviated new drug applications (ANDAs) by the United States FDA [150]. After gaining the status of a new research drug, to administer an investigation drug or biologic to humans from IND, nanomedicines or nano DDSs, investigations are initiated to evaluate their safety and efficacy in humans by clinical trials. These clinical trials are divided into three phases: phase 1 (mainly assesses safety), phase 2 (mainly determines efficacy) and phase 3 (safety, efficacy and dosage are evaluated). After obtaining approval in these three phases, the IND can be filed by the FDA to request endorsement of the new nanomedicine or nano DDSs [151,152]. FDA regulations, as well, specifically address nanomaterials safety, for which it is essential to explore the properties to understand the mechanisms by which nanomaterials communicate with biological systems to identify exposure, hazards and their possible risks [153]. Biocompatibility is an essential property in the design of nanomaterial-based DDSs. Biocompatibility is defined as material that has the potential to perform the desired function in a specific application and its surface would not elicit any undesired response from the organisms [154]. Pre-clinical evaluation of nanomaterials goes through a complete biocompatibility testing that includes in vivo studies followed by essential in vitro assays to prove its biocompatibility, so as to avoid toxicology concerns [155]. The pharmacokinetics and distribution of nanoparticles in the body depends on their surface physicochemical characteristics, shape and size. For example, nanoparticles that are 10 nm in size, are observed in blood, liver, spleen, kidney, testis, thymus, heart, lung, and brain, whilst larger particles are found only in the spleen, liver, and blood [156]. The surface properties of nanoparticles also affect their distribution in these organs, since combination with serum proteins available in the systemic circulation may influence cellular uptake. It should be reiterated that a biocompatible material does not elicit any physiological immune response. One of the reasons that an immune response is triggered is due to possible adsorption by body proteins, therefore, evaluation of an in vivo protein profile is essential to address the biological interactions and to establish its biocompatibility [157]. Lastly, clearance of nanoparticles is also dependent on size and surface of nanoparticles. Nanoparticles that are below 10 nm size are promptly cleared by renal excretion, whereas nanoparticles larger than 200 nm are efficiently taken up by mononuclear phagocytic system located in the liver, spleen, and bone marrow [158]. Studies are therefore required to address how nanomaterials penetrate cells and tissues, and the respective biodistribution, degradation, and excretion before translation into clinical applications.

7. Clinical Status of Nanomedicine

Several agents for promoting tissue healing, such as growth factors, small molecules, and siRNA-based therapeutics, have shown promising results in improving wound healing in preclinical trials. Despite recent advances, challenges in retention and duration of the therapeutic effect in the harsh wound environment, has limited the pace for clinical implementation. Nanoparticle formulations,

nanofibrous scaffold and hydrogel-related treatments are being devised to overcome this limitation. Ultimately, these technologies will require additional validation by testing in larger animal models, particularly the porcine model, before the consideration of a clinical setting [35,159]. AgNPs have been used for numerous clinical trials in the therapy of wounds, especially burns and chronic wounds (diabetic wounds). Currently, there are some commercially available dressings containing AgNPs [160]. Among the different polymers developed to fabricate polymeric nanoparticles, PLGA is one of the most successfully used synthetic polymers, with FDA approval for clinical use in humans as a DDS, due to the following desirable properties: (1) well-described formulations and methods of production adapted to various types of drugs, ranging from small molecules to macromolecules; and (2) ability to protect drugs from degradation and the possibility of sustained release [161]. Recombinant human-PDGF (rhPDGF), the only FDA-approved growth factor available for clinical use, has been shown in clinical trials to increase the incidence of complete wound closure and decrease the time to achieve complete wound healing [162]. The only siRNA delivery depot in clinical pipeline is the siG12D LODER therapeutic to combat non-resectable pancreatic dual adenocarcinoma [163]. In the market, modern wound bandage materials that are effective for skin regeneration have arrived. Despite the demand for the use of improved dressing materials for wound healing, many of the wound healing material that are applied clinically rely on safety data and experience rather than the efficacy rate. Inorganic-based Au, copper, ZnO, cerium oxide, and silica nanoparticles are still under clinical investigation [164].

8. Future Perspective

The usage of nanoparticle-based treatments by incorporation of therapeutic drugs and siRNAs, is an exciting and novel field for wound treatment, with unlimited prospects and opportunities. Nanoparticle-based remedies involve delivery of therapeutic drugs that promote wound healing, due to the integral properties of the nanoparticles as efficient delivery systems. There are promises of achieving greater efficacy and specificity, with a smaller amount of systemic side effects. In addition, compared to conventional antibiotics, nanoparticle-based antimicrobial treatment is more likely to eradicate bacteria developing resistance. However, the adverse biological effects elicited by nanoparticles should be further investigated and the development of nanoparticle-based therapies should be undertaken with a reasonable amount of caution, bearing in mind nanosafety concerns. Working towards improving the efficacy of nanoparticle wound treatments should go hand in hand with investigating the long and short-term effects of nanoparticle-based treatments, as well as the mechanisms underpinning them. The current approach of exploiting nanotechnology for the treatment of diabetic wound healing is occurring at an exponential rate. Further research and development efforts in this emerging field will have a positive impact on the treatment of wound regeneration, especially chronic wounds, which pose a significant burden on the quality of life and healthcare. Therefore, it is likely that nanotechnology-based remedies will possibly be the next frontier poised for breakthroughs in meeting the clinical needs of chronic wound healing.

9. Conclusions

Wound healing is an intricate three-staged process involving inflammation, proliferation and remodeling. The physiology of the healing process is perturbed in the case of DFU by both internal and external factors, such as altered cellular and cytokines response, poor vascularization, and infection by microorganisms. This overview focusing on nanoparticle-based therapeutics that deliver peptides; nucleic acids; antibiotics; and antioxidants incorporated in polymeric and natural nanostructures, hydrogels and nanofibers, have revealed promising results on re-epithelialization, deposition of collagen fibers, tissue regeneration, and ultimately a faster rate of wound closure in chronic diabetic wounds. Moreover, studies have clearly shown the effective antibacterial property of nanoparticulate systems against major drug-resistant bacteria. The combination of nanoparticles and biopolymers as a nanocomposite have a greater effect in speeding up tissue repair and wound healing. The use of nanomaterials for wound healing has been widely explored, although it is still

far from commercialization and routine clinical practice. However, the studies collated in this review may provide more insight for pre-clinical testing of nanoparticle-based therapeutics for DFU, before instituting the relevant clinical trials and further commercialization. The overall outlook of nanoparticle DDSs is promising, as they are being developed not only for treatment of diabetic wounds, but many other diseases including cancer.

Author Contributions: Conceptualization, H.E., D.K.S.; writing—original draft preparation, H.E.; design figures (1 & 4) and tables, H.E., D.V.; writing—review and editing, D.K.S., B.-H.B., S.T.D.; supervision, project administration, funding acquisition, D.K.S. All authors have read and agreed to the published version of the manuscript.

Funding: This work was funded (DKS) by Singapore Ministry of Education Academic Research Fund Tier 1 Grant (R-181-000-184-114).

Conflicts of Interest: The authors declare no conflict of interest.

Abbreviations

AGEs: Advanced glycation end products; AgNPs, Silver nanoparticles; ALA, Alpha lipoic acid; α-SMA, Alpha smooth muscle actin; ANDAs, Abbreviated new drug applications; ARE, Antioxidant response element; AuE, Gold nanoparticle liquid mixture; AuEA, Gold nanoparticle + EGCG and ALA; AUNC-L, Lysozyme capped gold nanoclusters; AuNPs, Gold nanoparticles; bFGF, Basic fibroblast growth factor; *C. albicans, Candida albicans*; CNCs, Cellulose nanocrystals; CNP, Cerium oxide nanoparticles; CH, Chitosan; cFNPs+fFNPs−CH, CH bandage using fibrin nanoparticles encapsulated with ciprofloxacin and fluconazole; Col, Collagen; DDSs, Drug-delivery systems, DFU, Diabetic foot ulcer; DM, Diabetes mellitus; EGF, Endothelial growth factor; EGCG, Epigallocatechin gallate; EPL-g-butyl@AgNPs, Silver nanoparticle coated ε-Polylysine; ECM, Extracellular matrix; *E. coli, Escherichia coli*; FA (4-hydroxy-3-methoxycinnamic acid), Ferulic acid; FNPs, Fibrin nanoparticles; FGF, Fibroblast growth factor; FDA, Food and Drug Administration; GM, Gelatin methacrylate; GM3S, Ganglioside-monosialic acid 3 synthase; GF, Growth factor; GO, Graphene oxide; HA, Hyaluronic acid; HUVEC, Human umbilical vein endothelial cells; H_2O_2, Hydrogen peroxide; IDF, International Diabetes Federation; IL-6, Interleukin 6; IND, Investigational new drug; IRAK1, Interlukin-1 receptor associated kinase 1; Keap1, Kelch-like erythroid cell-derived protein with CNC homology-associated protein 1; KGF, Keratinocyte growth factor; miR, Micro RNA; MMP, Matrix metalloproteinase; MRSA, Methicillin-resistant *Staphylococcus aureus*; NaCMCh, Sodium carboxymethyl chitosan; NADP, Nicotinamide adenine dinucleotide phosphate; NDAs, New drug applications; NLC, Nanostructure lipid carrier; NO, Nitric oxide; Nrf2, Nuclear factor erythroid 2–related factor 2; O_2-, Superoxide; PAD, Peripheral arterial disease; *P. aeruginosa, Pseudomonas aeruginosa*; PDGF, Platelet derived growth factor; PCL, Poly (ε-caprolactone); PEG, Poly (ethylene glycol); PLA, Poly (lactic acid); PLGA, Poly (lactic-co-glycolic acid); QCSG, Glycidyl methacrylate functionalized quaternized chitosan, QCSP, Quaternized chitosan-g-polyaniline; RAGE, receptor for AGEs; rhEGF, Recombinant human EGF; rhPDGF, Recombinant human-PDGF; ROS, Reactive oxygen species; *S. aureus, Staphylococcus aureus*, SLN, Solid lipid nanoparticles; SNAs, SiRNA-based spherical nucleic acids; TGF-β, Transforming growth factor beta; TIMPs, Tissue inhibitor of metalloproteinases; TNF-α, Tumor necrosis factor alpha; TRAF6, Tumor necrosis factor receptor associated kinase 6; VEGF, Vascular endothelial growth factor; WHO, World Health Organization; Zn, Zinc; ZnO, Zinc oxide.

References

1. Kasiewicz, L.N.; Whitehead, K.A. Recent advances in biomaterials for the treatment of diabetic foot ulcers. *Biomater. Sci.* **2017**, *5*, 1962–1975. [CrossRef] [PubMed]
2. Noor, S.; Zubair, M.; Ahmad, J. Diabetic foot ulcer-A review on pathophysiology, classification and microbial etiology. *Diabetes Metab. Syndr.* **2015**, *9*, 192–199. [CrossRef] [PubMed]
3. International Diabetes Federation. IDF Diabetes Atlas 9th Edition 2019, Global Estimates for the Prevalence of Diabetes for 2019, 2030 and 2045. Available online: http://www.diabetesatlas.org/ (accessed on 30 May 2020).
4. Armstrong, D.G.; Boulton, A.J.M.; Bus, S.A. Diabetic Foot Ulcers and Their Recurrence. *New Engl. J. Med.* **2017**, *376*, 2367–2375. [CrossRef] [PubMed]
5. Forlee, M. What is the diabetic foot? The rising prevalence of diabetes worldwide will mean an increasing prevalence of complications such as those of the extremities. Available online: http://www.cmej.org.za/index.php/cmej/article/view/1770 (accessed on 23 June 2020).
6. Wu, S.C.; Driver, V.R.; Wrobel, J.S.; Armstrong, D.G. Foot ulcers in the diabetic patient, prevention and treatment. *Vasc. Health Risk Manag.* **2007**, *3*, 65–76.
7. Frykberg, R.G.; Zgonis, T.; Armstrong, D.G.; Driver, V.R.; Giurini, J.M.; Kravitz, S.R.; Landsman, A.S.; Lavery, L.A.; Moore, J.C.; Schuberth, J.M.; et al. Diabetic foot disorders. A clinical practice guideline (2006 revision). *J. Foot Ankle. Surg.* **2006**, *45*, S1–S66. [CrossRef]

8. Bowering, C.K. Diabetic foot ulcers. Pathophysiology, assessment, and therapy. *Can. Fam. Phys.* **2001**, *47*, 1007–1016.
9. Tang, W.H.; Martin, K.A.; Hwa, J. Aldose reductase, oxidative stress, and diabetic mellitus. *Front. Pharmacol.* **2012**, *3*, 87. [CrossRef]
10. Clayton, W.; Elasy, T.A. A Review of the Pathophysiology, Classification, and Treatment of Foot Ulcers in Diabetic Patients. *Clin. Diabetes* **2009**, *27*, 52–58. [CrossRef]
11. Simmons, Z.; Feldman, E.L. Update on diabetic neuropathy. *Curr. Opin. Neurol.* **2002**, *15*, 595–603. [CrossRef]
12. Juster-Switlyk, K.; Smith, A.G. Updates in diabetic peripheral neuropathy. *F1000Research* **2016**, *5*, 738. [CrossRef]
13. Avogaro, A.; Albiero, M.; Menegazzo, L.; de Kreutzenberg, S.; Fadini, G.P. Endothelial dysfunction in diabetes: The role of reparatory mechanisms. *Diabetes Care* **2011**, *34*, S285–S290. [CrossRef] [PubMed]
14. Gonzalez, A.C.; Costa, T.F.; Andrade, Z.A.; Medrado, A.R. Wound healing—A literature review. *An. Bras. Dermatol.* **2016**, *91*, 614–620. [CrossRef] [PubMed]
15. Iqbal, A.; Jan, A.; Wajid, M.A.; Tariq, S. Management of Chronic Non-healing Wounds by Hirudotherapy. *World J. Plast. Surg.* **2017**, *6*, 9–17. [PubMed]
16. Cañedo-Dorantes, L.; Cañedo-Ayala, M. Skin Acute Wound Healing: A Comprehensive Review. *Int. J. Inflamm.* **2019**, *2019*, 3706315. [CrossRef] [PubMed]
17. Nurden, A.T. Platelets, inflammation and tissue regeneration. *Thromb. Haemost.* **2011**, *105*, S13–S33. [CrossRef] [PubMed]
18. Ng, M.F. The role of mast cells in wound healing. *Int. Wound J.* **2010**, *7*, 55–61. [CrossRef]
19. Theoharides, T.C.; Kempuraj, D.; Tagen, M.; Conti, P.; Kalogeromitros, D. Differential release of mast cell mediators and the pathogenesis of inflammation. *Immunol. Rev.* **2007**, *217*, 65–78. [CrossRef]
20. Shah, J.M.; Omar, E.; Pai, D.R.; Sood, S. Cellular events and biomarkers of wound healing. *Indian J. Plast. Surg.* **2012**, *45*, 220–228.
21. Guo, S.; Dipietro, L.A. Factors affecting wound healing. *J. Dent. Res.* **2010**, *89*, 219–229. [CrossRef]
22. Li, J.; Chen, J.; Kirsner, R. Pathophysiology of acute wound healing. *Clin. Dermatol.* **2007**, *25*, 9–18. [CrossRef]
23. Van De Water, L.; Varney, S.; Tomasek, J.J. Mechanoregulation of the Myofibroblast in Wound Contraction, Scarring, and Fibrosis: Opportunities for New Therapeutic Intervention. *Adv. Wound Care* **2013**, *2*, 122–141. [CrossRef] [PubMed]
24. Marshall, C.D.; Hu, M.S.; Leavitt, T.; Barnes, L.A.; Lorenz, H.P.; Longaker, M.T. Cutaneous Scarring: Basic Science, Current Treatments, and Future Directions. *Adv. Wound Care* **2018**, *7*, 29–45. [CrossRef] [PubMed]
25. Monaco, J.L.; Lawrence, W.T. Acute wound healing an overview. *Clin. Plast. Surg.* **2003**, *30*, 1–12. [CrossRef]
26. Patel, S.; Srivastava, S.; Singh, M.R.; Singh, D. Mechanistic insight into diabetic wounds: Pathogenesis, molecular targets and treatment strategies to pace wound healing. *Biomed. Pharmacother.* **2019**, *112*, 108615. [CrossRef]
27. Cho, H.; Blatchley, M.R.; Duh, E.J.; Gerecht, S. Acellular and cellular approaches to improve diabetic wound healing. *Adv. Drug Deliv. Rev.* **2019**, *146*, 267–288. [CrossRef]
28. Xu, F.; Zhang, C.; Graves, D.T. Abnormal cell responses and role of TNF-α in impaired diabetic wound healing. *Biomed. Res. Int.* **2013**, *2013*, 754802. [CrossRef]
29. Chitturi, R.T.; Balasubramaniam, A.M.; Parameswar, R.A.; Kesavan, G.; Haris, K.T.; Mohideen, K. The role of myofibroblasts in wound healing, contraction and its clinical implications in cleft palate repair. *J. Int. Oral. Health* **2015**, *7*, 75–80.
30. Nguyen, T.; Mobashery, S.; Chang, M. *Roles of Matrix Metalloproteinases in Cutaneous Wound Healing*; IntechOpen Ltd.: London, UK, 2016; pp. 37–71.
31. McCarty, S.M.; Percival, S.L. Proteases and Delayed Wound Healing. *Adv. Wound Care* **2013**, *2*, 438–447. [CrossRef]
32. Ayuk, S.M.; Abrahamse, H.; Houreld, N.N. The Role of Matrix Metalloproteinases in Diabetic Wound Healing in relation to Photobiomodulation. *J. Diabetes Res.* **2016**, *2016*, 2897656. [CrossRef]
33. Gottrup, F.; Apelqvist, J. Present and new techniques and devices in the treatment of DFU: A critical review of evidence. *Diabetes Metab. Res. Rev.* **2012**, *28*, 64–71. [CrossRef]
34. Goyal, R.; Macri, L.K.; Kaplan, H.M.; Kohn, J. Nanoparticles and nanofibers for topical drug delivery. *J. Control. Release* **2016**, *240*, 77–92. [CrossRef] [PubMed]

35. Whittam, A.J.; Maan, Z.N.; Duscher, D.; Wong, V.W.; Barrera, J.A.; Januszyk, M.; Gurtner, G.C. Challenges and Opportunities in Drug Delivery for Wound Healing. *Adv. Wound Care* **2016**, *5*, 79–88. [CrossRef] [PubMed]
36. Pan, R.; Xu, W.; Yuan, F.; Chu, D.; Ding, Y.; Chen, B.; Jafari, M.; Yuan, Y.; Chen, P. A novel peptide for efficient siRNA delivery in vitro and therapeutics in vivo. *Acta Biomater.* **2015**, *21*, 74–84. [CrossRef] [PubMed]
37. Yoo, J.-W.; Irvine, D.J.; Discher, D.E.; Mitragotri, S. Bio-inspired, bioengineered and biomimetic drug delivery carriers. *Nat. Rev. Drug Discov.* **2011**, *10*, 521–535. [CrossRef]
38. Lipsky, B.A.; Hoey, C. Topical antimicrobial therapy for treating chronic wounds. *Clin. Infect. Dis.* **2009**, *49*, 1541–1549. [CrossRef]
39. Hamdan, S.; Pastar, I.; Drakulich, S.; Dikici, E.; Tomic-Canic, M.; Deo, S.; Daunert, S. Nanotechnology-Driven Therapeutic Interventions in Wound Healing: Potential Uses and Applications. *ACS Cent. Sci.* **2017**, *3*, 163–175. [CrossRef]
40. Baltzis, D.; Eleftheriadou, I.; Veves, A. Pathogenesis and treatment of impaired wound healing in diabetes mellitus: New insights. *Adv. Ther.* **2014**, *31*, 817–836. [CrossRef]
41. Mordorski, B.; Rosen, J.; Friedman, A. Nanotechnology as an innovative approach for accelerating wound healing in diabetes. *Diabetes Manag.* **2015**, *5*, 329–332. [CrossRef]
42. Jackson, J.E.; Kopecki, Z.; Cowin, A.J. Nanotechnological Advances in Cutaneous Medicine. *J. Nanomater.* **2013**, *8*, 808234. [CrossRef]
43. Andreu, V.; Mendoza, G.; Arruebo, M.; Irusta, S. Smart Dressings Based on Nanostructured Fibers Containing Natural Origin Antimicrobial, Anti-Inflammatory, and Regenerative Compounds. *Materials* **2015**, *8*, 5154–5193. [CrossRef]
44. Korrapati, P.S.; Karthikeyan, K.; Satish, A.; Krishnaswamy, V.R.; Venugopal, J.R.; Ramakrishna, S. Recent advancements in nanotechnological strategies in selection, design and delivery of biomolecules for skin regeneration. *Mater. Sci. Eng. C Mater. Biol. Appl.* **2016**, *67*, 747–765. [CrossRef] [PubMed]
45. Zarrintaj, P.; Moghaddam, A.S.; Manouchehri, S.; Atoufi, Z.; Amiri, A.; Amirkhani, M.A.; Nilforoushzadeh, M.A.; Saeb, M.R.; Hamblin, M.R.; Mozafari, M. Can regenerative medicine and nanotechnology combine to heal wounds? The search for the ideal wound dressing. *Nanomedicine* **2017**, *12*, 2403–2422. [CrossRef] [PubMed]
46. Wang, W.; Lu, K.J.; Yu, C.H.; Huang, Q.L.; Du, Y.Z. Nano-drug delivery systems in wound treatment and skin regeneration. *J. Nanobiotechnol.* **2019**, *17*, 82. [CrossRef] [PubMed]
47. Johnson, N.R.; Wang, Y. Drug delivery systems for wound healing. *Curr. Pharm. Biotechnol.* **2015**, *16*, 621–629. [CrossRef] [PubMed]
48. Gelperina, S.; Kisich, K.; Iseman, M.D.; Heifets, L. The potential advantages of nanoparticle drug delivery systems in chemotherapy of tuberculosis. *Am. J. Respir. Crit. Care Med.* **2005**, *172*, 1487–1490. [CrossRef] [PubMed]
49. Berthet, M.; Gauthier, Y.; Lacroix, C.; Verrier, B.; Monge, C. Nanoparticle-Based Dressing: The Future of Wound Treatment? *Trends Biotechnol.* **2017**, *35*, 770–784. [CrossRef] [PubMed]
50. Goh, E.T.; Kirby, G.; Jayakumar, R.; Liang, X.J.; Tan, A. Accelerated Wound Healing Using Nanoparticles. In *Nanoscience in Dermatology*; Hamblin, M.R., Avci, P., Prow, T.W., Eds.; Elsevier Inc.: Amsterdam, The Netherlands, 2016.
51. Ezhilarasu, H.; Ramalingam, R.; Dhand, C.; Lakshminarayanan, R.; Sadiq, A.; Gandhimathi, C.; Ramakrishna, S.; Bay, B.H.; Venugopal, J.R.; Srinivasan, D.K. Biocompatible Aloe vera and Tetracycline Hydrochloride Loaded Hybrid Nanofibrous Scaffolds for Skin Tissue Engineering. *Int. J. Mol. Sci.* **2019**, *20*, 5174. [CrossRef]
52. Ramalingam, R.; Dhand, C.; Leung, C.M.; Ezhilarasu, H.; Prasannan, P.; Ong, S.T.; Subramanian, S.; Kamruddin, M.; Lakshminarayanan, R.; Ramakrishna, S.; et al. Poly-ε-Caprolactone/Gelatin Hybrid Electrospun Composite Nanofibrous Mats Containing Ultrasound Assisted Herbal Extract: Antimicrobial and Cell Proliferation Study. *Nanomaterials* **2019**, *9*, 462. [CrossRef]
53. Shan, X.; Liu, C.; Li, F.; Ouyang, C.; Gao, Q.; Zheng, K. Nanoparticles vs. nanofibers: A comparison of two drug delivery systems on assessing drug release performance in vitro. *Des. Monomers Polym.* **2015**, *18*, 678–689. [CrossRef]
54. Ezhilarasu, H.; Sadiq, A.; Ratheesh, G.; Sridhar, S.; Ramakrishna, S.; Ab Rahim, M.H.; Yusoff, M.M.; Jose, R.; Reddy, V.J. Functionalized core/shell nanofibers for the differentiation of mesenchymal stem cells for vascular tissue engineering. *Nanomedicine* **2019**, *14*, 201–214. [CrossRef]

55. Gao, W.; Vecchio, D.; Li, J.; Zhu, J.; Zhang, Q.; Fu, V.; Thamphiwatana, S.; Lu, D.; Zhang, L. Hydrogel containing nanoparticle-stabilized liposomes for topical antimicrobial delivery. *ACS Nano* **2014**, *8*, 2900–2907. [CrossRef] [PubMed]
56. Slaughter, B.V.; Khurshid, S.S.; Fisher, O.Z.; Khademhosseini, A.; Peppas, N.A. Hydrogels in regenerative medicine. *Adv. Mater.* **2009**, *21*, 3307–3329. [CrossRef] [PubMed]
57. Chai, Q.; Jiao, Y.; Yu, X. Hydrogels for Biomedical Applications: Their Characteristics and the Mechanisms behind Them. *Gels* **2017**, *3*, 6. [CrossRef] [PubMed]
58. Mauricio, M.D.; Guerra-Ojeda, S.; Marchio, P.; Valles, S.L.; Aldasoro, M.; Escribano-Lopez, I.; Herance, J.R.; Rocha, M.; Vila, J.M.; Victor, V.M. Nanoparticles in Medicine: A Focus on Vascular Oxidative Stress. *Oxid. Med. Cell Longev.* **2018**, *2018*, 6231482. [CrossRef] [PubMed]
59. Paladini, F.; Pollini, M. Antimicrobial Silver Nanoparticles for Wound Healing Application: Progress and Future Trends. *Materials* **2019**, *12*, 2540. [CrossRef] [PubMed]
60. Chaloupka, K.; Malam, Y.; Seifalian, A.M. Nanosilver as a new generation of nanoproduct in biomedical applications. *Trends Biotechnol.* **2010**, *28*, 580–588. [CrossRef]
61. Alarcon, E.C.; Griffith, M.; Udekwu, K.I. *Silver Nanoparticle Applications*; Springer International Publishing: Cham, Switzerland, 2015.
62. Akturk, O.; Kismet, K.; Yasti, A.C.; Kuru, S.; Duymus, M.E.; Kaya, F.; Caydere, M.; Hucumenoglu, S.; Keskin, D. Collagen/gold nanoparticle nanocomposites: A potential skin wound healing biomaterial. *J. Biomater. Appl.* **2016**, *31*, 283–301. [CrossRef]
63. Ding, Y.; Jiang, Z.; Saha, K.; Kim, C.S.; Kim, S.T.; Landis, R.F.; Rotello, V.M. Gold nanoparticles for nucleic acid delivery. *Mol. Ther.* **2014**, *22*, 1075–1083. [CrossRef]
64. El-Gharbawy, R.M.; Emara, A.M.; Abu-Risha, S.E. Zinc oxide nanoparticles and a standard antidiabetic drug restore the function and structure of beta cells in Type-2 diabetes. *Biomed Pharm.* **2016**, *84*, 810–820. [CrossRef]
65. Huang, X.; Zheng, X.; Xu, Z.; Yi, C. ZnO-based nanocarriers for drug delivery application: From passive to smart strategies. *Int. J. Pharm.* **2017**, *534*, 190–194. [CrossRef]
66. Jin, S.E.; Jin, H.E. Synthesis, Characterization, and Three-Dimensional Structure Generation of Zinc Oxide-Based Nanomedicine for Biomedical Applications. *Pharmaceutics* **2019**, *11*, 575. [CrossRef] [PubMed]
67. Yang, L.; Sheldon, B.; Webster, T. Nanophase ceramics for improved drug delivery: Current opportunities and challenges. *Am. Ceram. Soc. Bull.* **2010**, *89*, 24–32.
68. Kraft, J.C.; Freeling, J.P.; Wang, Z.; Ho, R.J. Emerging research and clinical development trends of liposome and lipid nanoparticle drug delivery systems. *J. Pharm. Sci.* **2014**, *103*, 29–52. [CrossRef] [PubMed]
69. Lin, Y.H.; Lin, J.H.; Hong, Y.S. Development of chitosan/poly-γ-glutamic acid/pluronic/curcumin nanoparticles in chitosan dressings for wound regeneration. *J. Biomed. Mater. Res. B Appl. Biomater.* **2017**, *105*, 81–90. [CrossRef] [PubMed]
70. Blažević, F.; Milekić, T.; Romić, M.D.; Juretić, M.; Pepić, I.; Filipović-Grčić, J.; Lovrić, J.; Hafner, A. Nanoparticle-mediated interplay of chitosan and melatonin for improved wound epithelialisation. *Carbohydr. Polym.* **2016**, *146*, 445–454. [CrossRef] [PubMed]
71. Chereddy, K.K.; Vandermeulen, G.; Préat, V. PLGA based drug delivery systems: Promising carriers for wound healing activity. *Wound Repair Regen.* **2016**, *24*, 223–236. [CrossRef] [PubMed]
72. Sharma, S.; Parmar, A.; Kori, S.; Sandhir, R. PLGA-based nanoparticles: A new paradigm in biomedical applications. *TrAC Trends Anal. Chem.* **2016**, *80*, 30–40. [CrossRef]
73. Stone, W.L.; Varacallo, M. Physiology, Growth Factor. In *StatPearls*; StatPearls Publishing LLC.: Treasure Island, FL, USA, 2020.
74. Barrientos, S.; Stojadinovic, O.; Golinko, M.S.; Brem, H.; Tomic-Canic, M. PERSPECTIVE ARTICLE: Growth factors and cytokines in wound healing. *Wound Repair Regen.* **2008**, *16*, 585–601. [CrossRef]
75. Ulubayram, K.; Cakar, A.N.; Korkusuz, P.; Ertan, C.; Hasirci, N. EGF containing gelatin-based wound dressings. *Biomaterials* **2001**, *22*, 1345–1356. [CrossRef]
76. Mast, B.A.; Schultz, G.S. Interactions of cytokines, growth factors, and proteases in acute and chronic wounds. *Wound Repair Regen.* **1996**, *4*, 411–420. [CrossRef]
77. Mark Saltzman, W.; Baldwin, S.P. Materials for protein delivery in tissue engineering. *Adv. Drug Deliv. Rev.* **1998**, *33*, 71–86. [PubMed]

78. Park, J.W.; Hwang, S.R.; Yoon, I.S. Advanced Growth Factor Delivery Systems in Wound Management and Skin Regeneration. *Molecules* **2017**, *22*, 1259. [CrossRef] [PubMed]
79. Chu, Y.; Yu, D.; Wang, P.; Xu, J.; Li, D.; Ding, M. Nanotechnology promotes the full-thickness diabetic wound healing effect of recombinant human epidermal growth factor in diabetic rats. *Wound Repair Regen.* **2010**, *18*, 499–505. [CrossRef] [PubMed]
80. Chereddy, K.K.; Lopes, A.; Koussoroplis, S.; Payen, V.; Moia, C.; Zhu, H.; Sonveaux, P.; Carmeliet, P.; des Rieux, A.; Vandermeulen, G.; et al. Combined effects of PLGA and vascular endothelial growth factor promote the healing of non-diabetic and diabetic wounds. *Nanomedicine* **2015**, *11*, 1975–1984. [CrossRef] [PubMed]
81. Gainza, G.; Pastor, M.; Aguirre, J.J.; Villullas, S.; Pedraz, J.L.; Hernandez, R.M.; Igartua, M. A novel strategy for the treatment of chronic wounds based on the topical administration of rhEGF-loaded lipid nanoparticles: In vitro bioactivity and in vivo effectiveness in healing-impaired db/db mice. *J. Control. Release* **2014**, *185*, 51–61. [CrossRef] [PubMed]
82. Losi, P.; Briganti, E.; Errico, C.; Lisella, A.; Sanguinetti, E.; Chiellini, F.; Soldani, G. Fibrin-based scaffold incorporating VEGF- and bFGF-loaded nanoparticles stimulates wound healing in diabetic mice. *Acta Biomater.* **2013**, *9*, 7814–7821. [CrossRef] [PubMed]
83. Hajimiri, M.; Shahverdi, S.; Esfandiari, M.A.; Larijani, B.; Atyabi, F.; Rajabiani, A.; Dehpour, A.R.; Amini, M.; Dinarvand, R. Preparation of hydrogel embedded polymer-growth factor conjugated nanoparticles as a diabetic wound dressing. *Drug Dev. Ind. Pharm.* **2016**, *42*, 707–719. [CrossRef] [PubMed]
84. Lai, H.J.; Kuan, C.H.; Wu, H.C.; Tsai, J.C.; Chen, T.M.; Hsieh, D.J.; Wang, T.W. Tailored design of electrospun composite nanofibers with staged release of multiple angiogenic growth factors for chronic wound healing. *Acta Biomater.* **2014**, *10*, 4156–4166. [CrossRef]
85. Li, S.; Tang, Q.; Xu, H.; Huang, Q.; Wen, Z.; Liu, Y.; Peng, C. Improved stability of KGF by conjugation with gold nanoparticles for diabetic wound therapy. *Nanomedicine* **2019**, *14*, 2909–2923. [CrossRef]
86. Uchi, H.; Igarashi, A.; Urabe, K.; Koga, T.; Nakayama, J.; Kawamori, R.; Tamaki, K.; Hirakata, H.; Ohura, T.; Furue, M. Clinical efficacy of basic fibroblast growth factor (bFGF) for diabetic ulcer. *Eur. J. Dermatol.* **2009**, *19*, 461–468. [CrossRef]
87. Hanft, J.R.; Pollak, R.A.; Barbul, A.; van Gils, C.; Kwon, P.S.; Gray, S.M.; Lynch, C.J.; Semba, C.P.; Breen, T.J. Phase I trial on the safety of topical rhVEGF on chronic neuropathic diabetic foot ulcers. *J. Wound Care* **2008**, *17*, 30–32, 34–37. [CrossRef] [PubMed]
88. Wang, C.; Ma, L.; Gao, C. Design of gene-activated matrix for the repair of skin and cartilage. *Polym. J.* **2014**, *46*, 476–482. [CrossRef]
89. Kwon, M.J.; An, S.; Choi, S.; Nam, K.; Jung, H.S.; Yoon, C.S.; Ko, J.H.; Jun, H.J.; Kim, T.K.; Jung, S.J.; et al. Effective healing of diabetic skin wounds by using nonviral gene therapy based on minicircle vascular endothelial growth factor DNA and a cationic dendrimer. *J. Gene Med.* **2012**, *14*, 272–278. [CrossRef] [PubMed]
90. Dizaj, S.M.; Jafari, S.; Khosroushahi, A.Y. A sight on the current nanoparticle-based gene delivery vectors. *Nanoscale Res. Lett.* **2014**, *9*, 252. [CrossRef] [PubMed]
91. Nayerossadat, N.; Maedeh, T.; Ali, P.A. Viral and nonviral delivery systems for gene delivery. *Adv. Biomed. Res.* **2012**, *1*, 27. [CrossRef] [PubMed]
92. Kasiewicz, L.N.; Whitehead, K.A. Silencing TNFα with lipidoid nanoparticles downregulates both TNFα and MCP-1 in an in vitro co-culture model of diabetic foot ulcers. *Acta Biomater.* **2016**, *32*, 120–128. [CrossRef]
93. Jozic, I.; Daunert, S.; Tomic-Canic, M.; Pastar, I. Nanoparticles for Fidgety Cell Movement and Enhanced Wound Healing. *J. Invest. Dermatol.* **2015**, *135*, 2151–2153. [CrossRef]
94. Rabbani, P.S.; Zhou, A.; Borab, Z.M.; Frezzo, J.A.; Srivastava, N.; More, H.T.; Rifkin, W.J.; David, J.A.; Berens, S.J.; Chen, R.; et al. Novel lipoproteoplex delivers Keap1 siRNA based gene therapy to accelerate diabetic wound healing. *Biomaterials* **2017**, *132*, 1–15. [CrossRef]
95. Zhou, J.; Shum, K.T.; Burnett, J.C.; Rossi, J.J. Nanoparticle-Based Delivery of RNAi Therapeutics: Progress and Challenges. *Pharmaceuticals* **2013**, *6*, 85–107. [CrossRef]
96. Wang, X.Q.; Lee, S.; Wilson, H.; Seeger, M.; Iordanov, H.; Gatla, N.; Whittington, A.; Bach, D.; Lu, J.Y.; Paller, A.S. Ganglioside GM3 depletion reverses impaired wound healing in diabetic mice by activating IGF-1 and insulin receptors. *J. Invest. Dermatol.* **2014**, *134*, 1446–1455. [CrossRef]

97. Tagami, S.; Inokuchi Ji, J.; Kabayama, K.; Yoshimura, H.; Kitamura, F.; Uemura, S.; Ogawa, C.; Ishii, A.; Saito, M.; Ohtsuka, Y.; et al. Ganglioside GM3 participates in the pathological conditions of insulin resistance. *J. Biol. Chem.* **2002**, *277*, 3085–3092. [CrossRef] [PubMed]
98. Randeria, P.S.; Seeger, M.A.; Wang, X.Q.; Wilson, H.; Shipp, D.; Mirkin, C.A.; Paller, A.S. siRNA-based spherical nucleic acids reverse impaired wound healing in diabetic mice by ganglioside GM3 synthase knockdown. *Proc. Natl. Acad. Sci. USA* **2015**, *112*, 5573–5578. [CrossRef] [PubMed]
99. Liu, R.; Bal, H.S.; Desta, T.; Behl, Y.; Graves, D.T. Tumor necrosis factor-alpha mediates diabetes-enhanced apoptosis of matrix-producing cells and impairs diabetic healing. *Am. J. Pathol.* **2006**, *168*, 757–764. [CrossRef] [PubMed]
100. Frank, J.; Born, K.; Barker, J.H.; Marzi, I. In Vivo Effect of Tumor Necrosis Factor Alpha on Wound Angiogenesis and Epithelialization. *Eur. J. Trauma* **2003**, *29*, 208–219. [CrossRef]
101. Kasiewicz, L.N.; Whitehead, K.A. Lipid nanoparticles silence tumor necrosis factor α to improve wound healing in diabetic mice. *Bioeng. Transl. Med.* **2019**, *4*, 75–82. [CrossRef] [PubMed]
102. Ambrozova, N.; Ulrichova, J.; Galandakova, A. Models for the study of skin wound healing. The role of Nrf2 and NF-κB. *Biomed. Pap. Med. Fac. Univ. Palacky Olomouc. Czech. Repub.* **2017**, *161*, 1–13. [CrossRef]
103. Lee, J.M.; Johnson, J.A. An important role of Nrf2-ARE pathway in the cellular defense mechanism. *J. Biochem. Mol. Biol.* **2004**, *37*, 139–143. [CrossRef]
104. auf dem Keller, U.; Kümin, A.; Braun, S.; Werner, S. Reactive oxygen species and their detoxification in healing skin wounds. *J. Investig. Dermatol. Symp. Proc.* **2006**, *11*, 106–111. [CrossRef]
105. Braun, S.; Hanselmann, C.; Gassmann, M.G.; auf dem Keller, U.; Born-Berclaz, C.; Chan, K.; Kan, Y.W.; Werner, S. Nrf2 transcription factor, a novel target of keratinocyte growth factor action which regulates gene expression and inflammation in the healing skin wound. *Mol. Cell Biol.* **2002**, *22*, 5492–5505. [CrossRef]
106. Zgheib, C.; Hodges, M.M.; Hu, J.; Liechty, K.W.; Xu, J. Long non-coding RNA Lethe regulates hyperglycemia-induced reactive oxygen species production in macrophages. *PLoS ONE* **2017**, *12*, e0177453. [CrossRef]
107. Matough, F.A.; Budin, S.B.; Hamid, Z.A.; Alwahaibi, N.; Mohamed, J. The role of oxidative stress and antioxidants in diabetic complications. *Sultan Qaboos. Univ. Med. J.* **2012**, *12*, 5–18. [CrossRef] [PubMed]
108. Chigurupati, S.; Mughal, M.R.; Okun, E.; Das, S.; Kumar, A.; McCaffery, M.; Seal, S.; Mattson, M.P. Effects of cerium oxide nanoparticles on the growth of keratinocytes, fibroblasts and vascular endothelial cells in cutaneous wound healing. *Biomaterials* **2013**, *34*, 2194–2201. [CrossRef] [PubMed]
109. Das, S.; Dowding, J.M.; Klump, K.E.; McGinnis, J.F.; Self, W.; Seal, S. Cerium oxide nanoparticles: Applications and prospects in nanomedicine. *Nanomedicine* **2013**, *8*, 1483–1508. [CrossRef] [PubMed]
110. Garash, R.; Bajpai, A.; Marcinkiewicz, B.M.; Spiller, K.L. Drug delivery strategies to control macrophages for tissue repair and regeneration. *Exp. Biol. Med.* **2016**, *241*, 1054–1063. [CrossRef]
111. Zgheib, C.; Hilton, S.A.; Dewberry, L.C.; Hodges, M.M.; Ghatak, S.; Xu, J.; Singh, S.; Roy, S.; Sen, C.K.; Seal, S.; et al. Use of Cerium Oxide Nanoparticles Conjugated with MicroRNA-146a to Correct the Diabetic Wound Healing Impairment. *J. Am. Coll. Surg.* **2019**, *228*, 107–115. [CrossRef]
112. Li, S.; Tan, H.Y.; Wang, N.; Zhang, Z.J.; Lao, L.; Wong, C.W.; Feng, Y. The Role of Oxidative Stress and Antioxidants in Liver Diseases. *Int. J. Mol. Sci.* **2015**, *16*, 26087–26124. [CrossRef]
113. Mulholland, E.J.; Dunne, N.; McCarthy, H.O. MicroRNA as Therapeutic Targets for Chronic Wound Healing. *Mol. Ther. Nucleic Acids* **2017**, *8*, 46–55. [CrossRef]
114. Feng, Y.; Chen, L.; Luo, Q.; Wu, M.; Chen, Y.; Shi, X. Involvement of microRNA-146a in diabetic peripheral neuropathy through the regulation of inflammation. *Drug Des. Devel. Ther.* **2018**, *12*, 171–177. [CrossRef]
115. Lo, W.Y.; Peng, C.T.; Wang, H.J. MicroRNA-146a-5p Mediates High Glucose-Induced Endothelial Inflammation via Targeting Interleukin-1 Receptor-Associated Kinase 1 Expression. *Front. Physiol.* **2017**, *8*, 551. [CrossRef]
116. Xu, J.; Wu, W.; Zhang, L.; Dorset-Martin, W.; Morris, M.W.; Mitchell, M.E.; Liechty, K.W. The role of microRNA-146a in the pathogenesis of the diabetic wound-healing impairment: Correction with mesenchymal stem cell treatment. *Diabetes* **2012**, *61*, 2906–2912. [CrossRef]
117. Kalita, S.; Kandimalla, R.; Bhowal, A.C.; Kotoky, J.; Kundu, S. Functionalization of β-lactam antibiotic on lysozyme capped gold nanoclusters retrogress MRSA and its persisters following awakening. *Sci. Rep.* **2018**, *8*, 5778. [CrossRef] [PubMed]

118. Leaper, D.; Assadian, O.; Edmiston, C.E. Approach to chronic wound infections. *Br. J. Dermatol.* **2015**, *173*, 351–358. [CrossRef] [PubMed]
119. Järbrink, K.; Ni, G.; Sönnergren, H.; Schmidtchen, A.; Pang, C.; Bajpai, R.; Car, J. Prevalence and incidence of chronic wounds and related complications: A protocol for a systematic review. *Syst. Rev.* **2016**, *5*, 152. [CrossRef] [PubMed]
120. Choi, H.J.; Thambi, T.; Yang, Y.H.; Bang, S.; Kim, B.S.; Pyun, D.G.; Lee, D.S. AgNP and rhEGF-incorporating synergistic polyurethane foam as a dressing material for scar-free healing of diabetic wounds. *RSC Adv.* **2017**, *7*, 13714–13725. [CrossRef]
121. Singla, R.; Soni, S.; Patial, V.; Kulurkar, P.M.; Kumari, A.; S, M.; Padwad, Y.S.; Yadav, S.K. Cytocompatible Anti-microbial Dressings of Syzygium cumini Cellulose Nanocrystals Decorated with Silver Nanoparticles Accelerate Acute and Diabetic Wound Healing. *Sci. Rep.* **2017**, *7*, 10457. [CrossRef]
122. Salouti, M.; Ahangari, A. Nanoparticle based drug delivery systems for treatment of infectious diseases. In *Application of Nanotechnology in Drug Delivery*; Sezer, A.D., Ed.; IntechOpen Ltd.: London, UK, 2014; pp. 155–194.
123. Ling, L.L.; Schneider, T.; Peoples, A.J.; Spoering, A.L.; Engels, I.; Conlon, B.P.; Mueller, A.; Schäberle, T.F.; Hughes, D.E.; Epstein, S.; et al. A new antibiotic kills pathogens without detectable resistance. *Nature* **2015**, *517*, 455–459. [CrossRef]
124. Dai, X.; Guo, Q.; Zhao, Y.; Zhang, P.; Zhang, T.; Zhang, X.; Li, C. Functional Silver Nanoparticle as a Benign Antimicrobial Agent That Eradicates Antibiotic-Resistant Bacteria and Promotes Wound Healing. *ACS Appl. Mater. Interfaces* **2016**, *8*, 25798–25807. [CrossRef]
125. Brogden, K.A.; Guthmiller, J.M.; Taylor, C.E. Human polymicrobial infections. *Lancet* **2005**, *365*, 253–255. [CrossRef]
126. Thattaruparambil Raveendran, N.; Mohandas, A.; Ramachandran Menon, R.; Somasekharan Menon, A.; Biswas, R.; Jayakumar, R. Ciprofloxacin- and Fluconazole-Containing Fibrin-Nanoparticle-Incorporated Chitosan Bandages for the Treatment of Polymicrobial Wound Infections. *ACS Appl. Bio. Mater.* **2019**, *2*, 243–254. [CrossRef]
127. Liang, Y.; Chen, B.; Li, M.; He, J.; Yin, Z.; Guo, B. Injectable Antimicrobial Conductive Hydrogels for Wound Disinfection and Infectious Wound Healing. *Biomacromolecules* **2020**, *21*, 1841–1852. [CrossRef]
128. He, J.; Liang, Y.; Shi, M.; Guo, B. Anti-oxidant electroactive and antibacterial nanofibrous wound dressings based on poly (ε-caprolactone)/quaternized chitosan-graft-polyaniline for full-thickness skin wound healing. *Chem. Eng. J.* **2020**, *385*, 123464. [CrossRef]
129. Tauler Riera, P. Redox Status. In *Encyclopedia of Exercise Medicine in Health and Disease*; Mooren, F.C., Ed.; Springer: Berlin/Heidelberg, Germany, 2012; pp. 751–753.
130. Apel, K.; Hirt, H. Reactive oxygen species: Metabolism, oxidative stress, and signal transduction. *Annu. Rev. Plant Biol.* **2004**, *55*, 373–399. [CrossRef] [PubMed]
131. Lieburg-Apers, D.C.; Willems, P.H.; Koopman, W.J.; Grefte, S. Interactions between mitochondrial reactive oxygen species and cellular glucose metabolism. *Arch. Toxicol.* **2015**, *89*, 1209–1226. [CrossRef] [PubMed]
132. Das, K.; Roychoudhury, A. Reactive oxygen species (ROS) and response of antioxidants as ROS-scavengers during environmental stress in plants. *Front. Environ. Sci.* **2014**, *2*, 53. [CrossRef]
133. Birben, E.; Sahiner, U.M.; Sackesen, C.; Erzurum, S.; Kalayci, O. Oxidative stress and antioxidant defense. *World Allergy Organ. J.* **2012**, *5*, 9–19. [CrossRef] [PubMed]
134. Montezano, A.C.; Dulak-Lis, M.; Tsiropoulou, S.; Harvey, A.; Briones, A.M.; Touyz, R.M. Oxidative stress and human hypertension: Vascular mechanisms, biomarkers, and novel therapies. *Can. J. Cardiol.* **2015**, *31*, 631–641. [CrossRef]
135. Giacco, F.; Brownlee, M.; Schmidt Ann, M. Oxidative Stress and Diabetic Complications. *Circ. Res.* **2010**, *107*, 1058–1070. [CrossRef]
136. Wu, H.; Li, F.; Shao, W.; Gao, J.; Ling, D. Promoting Angiogenesis in Oxidative Diabetic Wound Microenvironment Using a Nanozyme-Reinforced Self-Protecting Hydrogel. *ACS Cent. Sci.* **2019**, *5*, 477–485. [CrossRef]
137. Bairagi, U.; Mittal, P.; Singh, J.; Mishra, B. Preparation, characterization, and in vivo evaluation of nano formulations of ferulic acid in diabetic wound healing. *Drug Dev. Ind. Pharm.* **2018**, *44*, 1783–1796. [CrossRef]
138. Huijberts, M.S.P.; Schaper, N.C.; Schalkwijk, C.G. Advanced glycation end products and diabetic foot disease. *Diabetes Metab. Res. Rev.* **2008**, *24*, S19–S24. [CrossRef]

139. Niu, Y.; Xie, T.; Ge, K.; Lin, Y.; Lu, S. Effects of extracellular matrix glycosylation on proliferation and apoptosis of human dermal fibroblasts via the receptor for advanced glycosylated end products. *Am. J. Dermatopathol.* **2008**, *30*, 344–351. [CrossRef] [PubMed]
140. Peres, G.B.; Schor, N.; Michelacci, Y.M. Impact of high glucose and AGEs on cultured kidney-derived cells. Effects on cell viability, lysosomal enzymes and effectors of cell signaling pathways. *Biochimie* **2017**, *135*, 137–148. [CrossRef] [PubMed]
141. Goova, M.T.; Li, J.; Kislinger, T.; Qu, W.; Lu, Y.; Bucciarelli, L.G.; Nowygrod, S.; Wolf, B.M.; Caliste, X.; Yan, S.F.; et al. Blockade of receptor for advanced glycation end-products restores effective wound healing in diabetic mice. *Am. J. Pathol.* **2001**, *159*, 513–525. [CrossRef]
142. Liang, Y.J.; Jian, J.H.; Liu, Y.C.; Juang, S.J.; Shyu, K.G.; Lai, L.P.; Wang, B.W.; Leu, J.G. Advanced glycation end products-induced apoptosis attenuated by PPARdelta activation and epigallocatechin gallate through NF-kappaB pathway in human embryonic kidney cells and human mesangial cells. *Diabetes Metab. Res. Rev.* **2010**, *26*, 406–416. [CrossRef] [PubMed]
143. Lee, S.J.; Lee, K.W. Protective effect of (-)-epigallocatechin gallate against advanced glycation endproducts-induced injury in neuronal cells. *Biol. Pharm. Bull.* **2007**, *30*, 1369–1373. [CrossRef] [PubMed]
144. Lateef, H.; Aslam, M.N.; Stevens, M.J.; Varani, J. Pretreatment of diabetic rats with lipoic acid improves healing of subsequently-induced abrasion wounds. *Arch. Dermatol. Res.* **2005**, *297*, 75–83. [CrossRef]
145. Chen, S.A.; Chen, H.M.; Yao, Y.D.; Hung, C.F.; Tu, C.S.; Liang, Y.J. Topical treatment with anti-oxidants and Au nanoparticles promote healing of diabetic wound through receptor for advance glycation end-products. *Eur. J. Pharm. Sci.* **2012**, *47*, 875–883. [CrossRef]
146. Huang, Y.-H.; Chen, C.-Y.; Chen, P.-J.; Tan, S.-W.; Chen, C.-N.; Chen, H.-M.; Tu, C.-S.; Liang, Y.-J. Gas-injection of gold nanoparticles and anti-oxidants promotes diabetic wound healing. *RSC Adv.* **2014**, *4*, 4656–4662. [CrossRef]
147. Ponnanikajamideen, M.; Rajeshkumar, S.; Vanaja, M.; Annadurai, G. In Vivo Type 2 Diabetes and Wound-Healing Effects of Antioxidant Gold Nanoparticles Synthesized Using the Insulin Plant Chamaecostus cuspidatus in Albino Rats. *Can. J. Diabetes* **2019**, *43*, 82–89. [CrossRef]
148. Chen, L.; Remondetto, G.E.; Subirade, M. Food protein-based materials as nutraceutical delivery systems. *Trends Food Sci. Technol.* **2006**, *17*, 272–283. [CrossRef]
149. Administration, D. Guidance for industry considering whether an FDA-regulated product involves the application of nanotechnology. *Biotechnol. Law Rep.* **2011**, *30*, 613–616.
150. Tyner, K.M.; Zou, P.; Yang, X.; Zhang, H.; Cruz, C.N.; Lee, S.L. Product quality for nanomaterials: Current U.S. experience and perspective. Wiley Interdiscip. *Rev. Nanomed. Nanobiotechnol.* **2015**, *7*, 640–654. [CrossRef] [PubMed]
151. Sainz, V.; Conniot, J.; Matos, A.I.; Peres, C.; Zupančič, E.; Moura, L.; Silva, L.C.; Florindo, H.F.; Gaspar, R.S. Regulatory aspects on nanomedicines. *Biochem. Biophys. Res. Commun.* **2015**, *468*, 504–510. [CrossRef] [PubMed]
152. Ventola, C.L. Progress in nanomedicine: Approved and investigational nanodrugs. *Pharm. Ther.* **2017**, *42*, 742–755.
153. Juillerat-Jeanneret, L.; Dusinska, M.; Fjellsbo, L.M.; Collins, A.R.; Handy, R.D.; Riediker, M. Biological impact assessment of nanomaterial used in nanomedicine. Introduction to the NanoTEST project. *Nanotoxicology* **2015**, *9*, 5–12. [CrossRef]
154. Anderson, J.M. Biocompatibility. *Polym. Sci. A Compr. Ref. 10 Vol. Set* **2012**, *9*, 363–383.
155. Hussain, S.M.; Warheit, D.B.; Ng, S.P.; Comfort, K.K.; Grabinski, C.M.; Braydich-Stolle, L.K. At the crossroads of nanotoxicology in vitro: Past achievements and current challenges. *Toxicol. Sci.* **2015**, *147*, 5–16. [CrossRef]
156. De Jong, W.H.; Hagens, W.I.; Krystek, P.; Burger, M.C.; Sips, A.J.A.M.; Geertsma, R.E. Particle size-dependent organ distribution of gold nanoparticles after intravenous administration. *Biomaterials* **2008**, *29*, 1912–1919. [CrossRef]
157. Keck, C.M.; Müller, R.H. Nanotoxicological classification system (NCS)—A guide for the risk-benefit assessment of nanoparticulate drug delivery systems. *Eur. J. Pharm. Biopharm.* **2013**, *84*, 445–448. [CrossRef]
158. Han, H. The effect of nanoparticle size on in vivo pharmacokinetics and cellular interaction. *Nanomedicine* **2016**, *11*, 673–692.

159. Layliev, J.; Wilson, S.; Warren, S.M.; Saadeh, P.B. Improving Wound Healing with Topical Gene Therapy. *Adv. Wound Care* **2012**, *1*, 218–223. [CrossRef] [PubMed]
160. Naderi, N.; Karponis, D.; Mosahebi, A.; Seifalian, A.M. Nanoparticles in wound healing; from hope to promise, from promise to routine. *Front. Biosci.* **2018**, *23*, 1038–1059.
161. Gunatillake, P.A.; Adhikari, R. Biodegradable synthetic polymers for tissue engineering. *Eur. Cell Mater.* **2003**, *5*, 1–16. [CrossRef] [PubMed]
162. Li, W.; Tsen, F.; Sahu, D.; Bhatia, A.; Chen, M.; Multhoff, G.; Woodley, D.T. Extracellular Hsp90 (eHsp90) as the actual target in clinical trials: Intentionally or unintentionally. *Int. Rev. Cell Mol. Biol.* **2013**, *303*, 203–235.
163. Khvalevsky, E.Z.; Gabai, R.; Rachmut, I.H.; Horwitz, E.; Brunschwig, Z.; Orbach, A.; Shemi, A.; Golan, T.; Domb, A.J.; Yavin, E.; et al. Mutant KRAS is a druggable target for pancreatic cancer. *Proc. Natl. Acad. Sci. USA* **2013**, *110*, 20723–20728. [CrossRef]
164. Nethi, S.K.; Das, S.; Patra, C.R.; Mukherjee, S. Recent advances in inorganic nanomaterials for wound-healing applications. *Biomater. Sci.* **2019**, *7*, 2652–2674. [CrossRef]

nanomaterials

MDPI

Review

Visible-Light Active Titanium Dioxide Nanomaterials with Bactericidal Properties

Chengzhu Liao [1,*], Yuchao Li [2] and Sie Chin Tjong [3,*]

[1] Department of Materials Science and Engineering, Southern University of Science and Technology, Shenzhen 518055, China
[2] Department of Materials Science and Engineering, Liaocheng University, Liaocheng 252000, China; liyuchao@lcu.edu.cn
[3] Department of Physics, City University of Hong Kong, Tat Chee Avenue, Kowloon, Hong Kong 999077, China
* Correspondence: liaocz@sustech.edu.cn (C.L.); aptjong@gmail.com (S.C.T.)

Received: 6 December 2019; Accepted: 6 January 2020; Published: 9 January 2020

Abstract: This article provides an overview of current research into the development, synthesis, photocatalytic bacterial activity, biocompatibility and cytotoxic properties of various visible-light active titanium dioxide (TiO_2) nanoparticles (NPs) and their nanocomposites. To achieve antibacterial inactivation under visible light, TiO_2 NPs are doped with metal and non-metal elements, modified with carbonaceous nanomaterials, and coupled with other metal oxide semiconductors. Transition metals introduce a localized d-electron state just below the conduction band of TiO_2 NPs, thereby narrowing the bandgap and causing a red shift of the optical absorption edge into the visible region. Silver nanoparticles of doped TiO_2 NPs experience surface plasmon resonance under visible light excitation, leading to the injection of hot electrons into the conduction band of TiO_2 NPs to generate reactive oxygen species (ROS) for bacterial killing. The modification of TiO_2 NPs with carbon nanotubes and graphene sheets also achieve the efficient creation of ROS under visible light irradiation. Furthermore, titanium-based alloy implants in orthopedics with enhanced antibacterial activity and biocompatibility can be achieved by forming a surface layer of Ag-doped titania nanotubes. By incorporating TiO_2 NPs and Cu-doped TiO_2 NPs into chitosan or the textile matrix, the resulting polymer nanocomposites exhibit excellent antimicrobial properties that can have applications as fruit/food wrapping films, self-cleaning fabrics, medical scaffolds and wound dressings. Considering the possible use of visible-light active TiO_2 nanomaterials for various applications, their toxicity impact on the environment and public health is also addressed.

Keywords: antibacterial activity; photocatalyst; titania; nanomaterial; doping; *Staphylococcus aureus*; *Escherichia coli*; reactive oxygen species; silver nanoparticle; visible light

1. Introduction

The overuse of antimicrobials in humans, animal husbandry and aquafarming gives rise to the development of dangerous, antibiotic-resistant bacteria [1,2]. Infections caused by antibiotic-resistant bacteria are now emerging as worldwide public health challenges. Medicines find it harder to treat infections, increasing the risk of mortality and morbidity. For instance, Staphylococci such as *Staphylococcus aureus* (*S. aureus*) and *Staphylococcus epidermidis* (*S. epidermidis*), that cause orthopedic infections (e.g., osteomyelitis), have developed into methicillin-resistant *S. aureus* (MRSA) and methicillin-resistant *S. epidermidis* (MRSE). MRSA is capable of forming biofilms on medical devices, giving rise to antibiotic resistance [3,4]. Osteomyelitis is a bone infection induced by *Staphylococci*, leading to progressive bone loss and tissue damage. Moreover, multidrug-resistant (MDR) bacteria spread not only between hospital inpatients, but also through food chains and potable water [5].

Accordingly, researchers have concentrated on developing antimicrobial nanomaterials as alternatives to conventional antibiotics [6–9].

Current developments in nanoscience and nanotechnology have led to the creation of advanced functional nanomaterials with unique chemical, physical, and biological properties [9–17]. Nanomaterials with large, specific surface area-to-volume ratios enhance surface chemical reactivity due to the size reduction at the nanoscale. Thus, nanomaterials have opened up new opportunities for developing bactericidal agents to treat deadly microbial infections [18]. In particular, metal and metal oxide nanoparticles (NPs) have attracted great attention as promising candidates for antibacterial agents [19,20]. The main mechanisms of the antibacterial activities of those nanoparticles proposed in the literature include: (a) oxidative stress induction associated with the generation of reactive oxygen species (ROS) [21], where the oxidation process in bacterial cells causes peroxidation of the lipid membrane, thereby damaging proteins and DNA; (b) released metal ions from metal or metal oxide NPs penetrating through bacterial cell walls, directly interacting with the –SH, –NH and –COOH groups of nucleic acid and protein and eventually causing cell death [15,22]. For example, silver nanoparticles (AgNPs) have been employed as antibacterial agents for textile fabrics, healthcare products, cosmetics, coatings and wound dressings, because they exhibit relatively high bactericidal activity [15,23–27]. However, AgNPs are toxic for several human cell lines. This is because they induce a dose-, size- and time-dependent cytotoxicity, especially those with sizes of ≤10 nm [15].

Compared to other types of nanoparticles, titanium dioxide is particularly attractive for photocatalytic bactericidal activity because of its relatively low cost, natural abundance and superior chemical stability. Titanium dioxide (TiO_2), generally known as titania, is an n-type semiconductor due to the presence of oxygen vacancies [28,29]. Those oxygen vacancies favor the formation of unpaired electrons or Ti^{3+} centers, thus acting as electron donors in the electronic structure of TiO_2 [28]. Furthermore, oxygen vacancies can influence the charge transport and electron–hole recombination processes by trapping charge carriers in the defect sites [30–33]. Titania also has a high dielectric permittivity (κ = 50–80) that finds application as a gate insulator in the microelectronic industry. However, TiO_2 with a bandgap of 3.2 eV suffers from a large leakage current and low dielectric breakdown field. In contrast, HfO_2 with a larger bandgap (5.3–5.7 eV) is widely used as a high-κ gate dielectric material in the microelectronic sector [34].

By irradiating photocatalytic semiconductors with a photon of sufficient energy (≥band gap energy), an electron in the valence band (VB) is excited to the conduction band (CB), leaving a positive hole in the VB. These charge carriers migrate to the photocatalyst surface and can generate highly reactive oxygen species (ROS) such as hydroxyl ($^{\bullet}OH$) and superoxide anion (O_2^-) radicals, and hydrogen peroxide (H_2O_2) through the oxidative or reductive path with surface-adsorbed water and oxygen (Figure 1). Hydroxyl and superoxide species are highly reactive due to the presence of unpaired valence shell electrons, and can cause oxidative damage to biomolecules such as proteins, lipids and nucleic acids [25,35,36].

Matsunaga et al. first reported the antimicrobial and photoelectrochemical activities of platinum-loaded titanium oxide (TiO_2/Pt) powders for killing Lactobacillus acidophilus, *Saccharomyces cerevisiae* and *Escherichia coli* (*E. coli*) in 1985 [37]. Nano-TiO_2 exhibits excellent photocatalytic bactericidal activity against viruses and MDR bacteria under UV irradiation [38]. Accordingly, extensive efforts have been carried out by researchers to improve the photocatalytic bactericidal activity of TiO_2 nanomaterials. TiO_2 nanostructures have a wide spectrum of industrial, environmental and energy applications, including water purification, food preservation, degradation of dyes, chemical sensors, dye-sensitized solar cells, and antimicrobial agents. [39–57]. In particular, visible light-responsive TiO_2 doped with metals and non-metals exhibit bactericidal activity against a wide variety of bacterial species including Gram-negative *E. coli*, Acinetobacter baumannii, Shigella flexneri, and Gram-positive *S. aureus*, Bacillus subtilis, Listeria monocytogenes, as well as Bacillus anthracis spores [58]. Those photocatalysts can be used for the disinfection of pathogenic bacteria, thereby preventing the spread of microbe-related diseases. Recently, Markov and Vidaković reviewed

antimicrobial testing methods of TiO_2 photocatalysts, including thin-film technique, petri-dish system, and polytetrafluoroethylene membrane-separated system. They also addressed the calculation methods for assessing the antimicrobial efficacy of TiO_2 photocatalysts [35]. To avoid mechanical damage to TiO_2 NPs, they are embedded in the polymeric matrices to form antibacterial nanocomposites [59–65]. The beneficial effects of polymers as the matrix materials of functional composites include ease of processing and good moldability, and they are inexpensive with a low density [66–72].

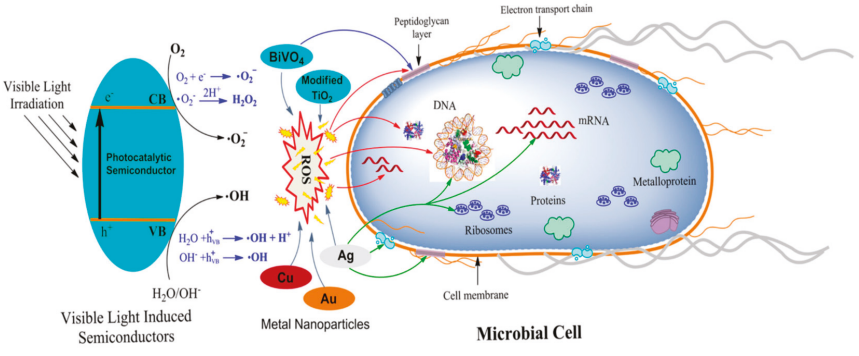

Figure 1. The possible mechanisms of antibacterial activities exhibited by different metal nanoparticles (NPs) and photocatalytic semiconductors. The activation of the photocatalytic semiconductor by visible light is depicted on the left-hand side of the figure. Reactive oxygen species created by various semiconductors destruct bacterial cell components, as indicated by red arrows. Ag, Cu, and Au nanoparticles also generate reactive oxygen species (ROS) for bacterial killing. The green arrow represents targets of Ag. Reproduced with permission from [22]. Copyright Frontiers, 2018.

Apart from bactericidal activity, TiO_2 NPs also find attractive application in biomedical fields as photodynamic therapeutic agents for destroying human cancer cells from the skin to the internal organs under ultraviolet (UV) and visible light illumination [36]. This is due to the ROS created by TiO_2. NPs can damage cellular respiration in mitochondria, thus releasing electron-transfer proteins and causing cell death. Moreover, light-activated TiO_2 NPs can lead to DNA fragmentation as a result of the electron transfer mechanism. This approach shows promise for reprograming gene-coding either by deleting or by inserting gene codons. In addition, TiO_2 nanotubes can be used for light-controlled delivery of drugs for treating the diseased tissues upon UV irradiation [36]. This article provides an update review on the current development, synthesis, photocatalytic bacterial inactivation, and cytotoxicity of TiO_2 NPs and their nanocomposites, especially in a rapidly growing field of research, over the past five years.

2. Crystal Structure of Titania

Titanium dioxide generally exists naturally in three crystalline structures, i.e., anatase, rutile, and brookite [42,43]. Anatase exhibits the tetragonal structure with a space group of $I4_1/amd$ (I: body centered). Body-centered tetragonal anatase has lattice parameters of a = 3.7845 Å and c = 9.5143 Å. Rutile belongs to the P42/mnm (P: primitive) space group, with the primitive tetragonal lattice having lattice parameters a = 4.5937 Å, and c = 2.9587 Å. Brookite is orthorhombic with a space group of Pbca, having lattice parameters of a = 9.1819 Å, b = 5.4558 Å, and c = 5.1429 Å, as shown in Figure 2. [43,73,74]. These polymorphs are formed by linking the chains of distorted TiO_6 octahedra through corner- and edge-sharing in different ways. In the TiO_6 octahedra, titanium cations (Ti^{4+}) are coordinated to six oxygen anions (O^{2-}). The octahedron shares two, three, and four edges with adjacent octahedra to give rutile, brookite and anatase, respectively [42]. Anatase and brookite are metastable, and transform irreversibly to a stable rutile phase by heating at 500–700 °C. Moreover, anion fluorine dopant also

stabilizes anatase at elevated temperatures (>1000 °C) [75]. Generally, anatase TiO_2 is more photoactive than rutile and brookite. Anatase TiO_2 absorbs ultraviolet light (UV) to create an electron–hole pair necessary for photocatalytic reaction. In the process, electron is excited from the valence band to the conduction band, leaving a positively charged hole in the valence band. This photogenerated electron–hole pair displays a high reducing and oxidizing capability. In this respect, the electron in the conduction band reacts with molecular oxygen to produce superoxide ion (O_2^-) via a reductive process, while the hole in the valence band oxidizes adsorbed water or hydroxyl ions at the titania surface into hydroxyl radicals ($^{\bullet}OH$) [76]. The photocatalytic activity of TiO_2 depends mainly on the crystal structure, shape, particle size and surface area. The equilibrium shape of anatase consists of a truncated bipyramid constructed by {101} and {001} facets. According to the Wulff construction, the {001} facets constitute nearly 6% of the total exposed surface of anatase TiO_2, while stable {101} facets contribute to more than 94% of the surface area [42]. However, the {001} facets of anatase TiO_2 have a higher photocatalytic performance than {101} facets [77–79]. TiO_2 NPs with a larger surface area and smaller size than their bulk counterparts generate more ROS during photoexcitation [80]. Xu et al. indicated that anatase TiO_2 NPs exhibit a higher phototoxicity and cytotoxicity in human keratinocyte cells than rutile TiO_2 NPs [81]. Recently, Bartlet et al. indicated that one-dimensional titania nanotubes prepared by electrochemical anodization exhibit superhydrophobic behavior with a large water contact angle of >150°. Such superhydrophobic titania nanotubes reduced bacterial adhesion on their surfaces [82].

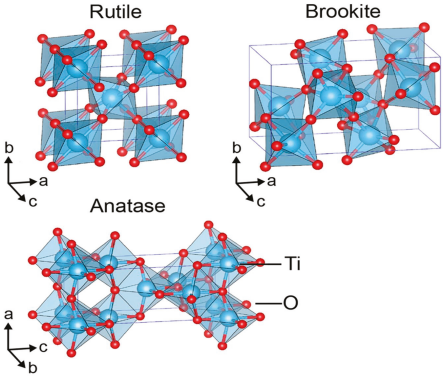

Figure 2. Connecting the chains of distorted TiO_6 octahedra by sharing edges and corners in different ways to form rutile, brookite and anatase polymorphs. Titanium atoms are blue; oxygen atoms are red. Reproduced with permission from [42]. Copyright Nature Publishing Group, 2017.

3. Visible-Light Active TiO_2

TiO_2 NPs with a large bandgap (anatase = 3.2 eV and rutile = 3.0 eV) can only be activated by UV light, which accounts for less than 5% of the solar spectrum compared to 45% of visible light [83]. The low photocatalytic efficiency of titania under visible light limits its practical applications. Extending the utilization of solar energy to the visible region has motivated researchers to improve the visible-light photocatalytic performance of TiO_2 NPs. Moreover, TiO_2 NPs have another drawback, due to a rapid recombination of photogenerated electron–hole pairs. Recombination occurs when the excited electron returns to the valence band without interacting with the adsorbed species under UV irradiation. Accordingly, the energy of recombination is dissipated in the form of light or heat. Therefore, it deems necessary to enhance the photocatalytic activity of TiO_2 NPs by reducing both the bandgap and the recombination of electron–hole pairs under visible light irradiation. Many attempts have been made by researchers to design and synthesize visible light-active TiO_2 photocatalysts. These include metal and non-metal doping, coupling with semiconductors, and modification with graphene oxide or carbon

nanotube [84–104]. The incorporation of those dopants into titania affects its electronic band structure greatly, thereby promoting visible light absorption and a red shift in the bandgap.

3.1. Metal Doping

The VB of titania is composed of hybridized states of O-2p and Ti-3d orbitals, while the CB consists of primarily Ti-3d orbitals. The electronic and optical properties of titania can be modified by doping. In this context, titanium or oxygen ions' sites of titania lattice can be substituted with either metal or nonmetal dopants to alter their optical and photocatalytic properties. The cationic doping of titania with transition metals, rare earth metals and noble metals is typically used to improve its photocatalytic performance under visible light excitation. The presence of metal ion dopants can alter the charge transfer properties of TiO_2, thus improving the separation efficiency of photogenerated carriers, and producing a shift in its absorption edge to the visible regime. The dopant energy level is located below the CB of TiO_2, acting as an electron or hole trap, and thus allowing more carriers to transport to the surface. The photocatalytic activity of metal-doped titania depends on several factors, including the dopant concentration, type of metal dopant, d-electron configuration and energy band level of dopant in the titania lattice [105]. Although metal dopants facilitate a red shift in optical absorption edges of titania, they can induce defect states, acting as carrier recombination centers, especially at very high dopant contents. Thus, the occurrence of a rapid recombination rate of photogenerated charge carriers arises from a reduction in the distance between the trapping sites by increasing the number of dopant ions.

Doping TiO_2 with transition metals influences its electronic energy levels and narrows the bandgap, resulting in a shift in the absorption spectrum of titania to longer wavelengths. Titania can be self-doped with Ti^{3+} ions to improve its visible-light absorption and avoid the incorporation of other impurities into its lattice. The introduction of Ti^{3+} energy level and the creation of an oxygen vacancy (O_{vac}) in the bandgap are responsible for the shift in optical adsorption of TiO_2 into the visible light region. As such, the electrons in the VB can be excited to the O_{vac}–Ti^{3+} defect states, and electrons from these defect sites can be excited to the CB upon visible light illumination [106,107]. In this respect, the O_{vac}–Ti^{3+} sites can trap photogenerated electrons under visible light, thereby inhibiting the recombination of electron–hole pairs and improving photocatalytic activity accordingly. Generally, oxygen vacancy is not stable in air, and it remains a challenge to develop a stable Ti^{3+} self-doped titania with a high photocatalytic performance [108].

Apart from Ti^{3+} ions, other transition metals, such as copper (Cu), vanadium (V), chromium (Cr), manganese (Mn), iron (Fe) and nickel (Ni), are typically employed to enhance the visible-light photocatalytic activity of titania [88–95,109–115]. The redshift effectiveness takes the following order: V > Cr > Mn > Fe > Ni [86]. The substitution of Ti^{4+} in the TiO_2 lattice by transition metal ions creates a new energy state in the bandgap of TiO_2. Therefore, the localized d-electron state of transition metals introduced in the bandgap captures the excited electrons from the titania valence band, thereby suppressing the recombination of charge carriers. Figure 3a shows the typical charge transfer reactions involved during photocatalysis of Mn-doped TiO_2. Mn^{2+} displays an electronic configuration of $3d^5$ and changes to $3d^6$ (Mn^+) by trapping electrons, while it changes to $3d^4$ (Mn^{3+}) as it traps the holes. Both Mn^+ and Mn^{3+} species are unstable, and react with adsorbed O_2 and surface hydroxyl molecules to yield ROS [92]. Similarly, Fe^{3+} ions of Fe-doped TiO_2 can also act as hole and electron traps in prohibiting the recombination of the electron–hole pair and promoting ROS generation [84–86]. These result in a red shift in the absorption edge and thus enhance photocatalytic activity (Figure 3b) [95]. Doping TiO_2 with vanadium, molybdenum (Mo) and tungsten can also shift its absorption edge to the visible region [111,112]. By doping TiO_2 NPs with 1% and 2% Mo, the bandgap of TiO_2 NPs decreases from 3.05 to 2.94 and 2.73 eV, respectively. The ionic radius of Mo^{6+} is 0.062 nm, while that of Ti^{4+} is 0.068 nm. As such, Mo ions can readily replace Ti^{4+} in the TiO_2 lattice, as they have approximately the same ionic radii, resulting in a narrower bandgap [112]. This facilitates the charge transfer between the VB and Mo-3d orbitals, thereby promoting photocatalytic activity under visible light [112].

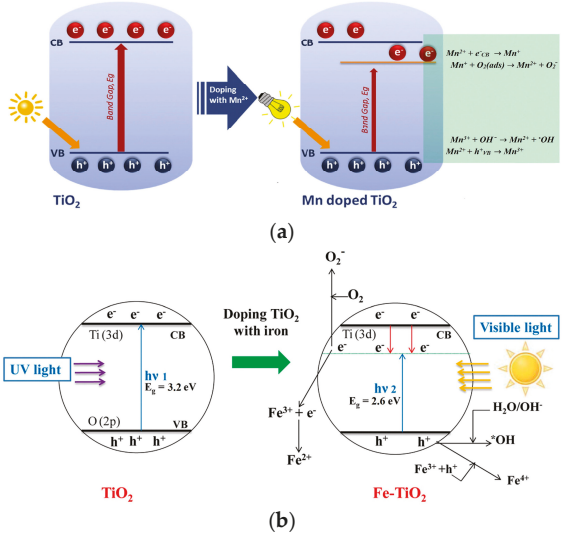

Figure 3. The charge transfer processes between excited electrons from the valence band of TiO_2 with (**a**) Mn^{2+} ions of Mn-doped TiO_2, and (**b**) Fe^{3+} ions of Fe-doped TiO_2. CB and VB are the conduction and valence bands of TiO_2, respectively. Reproduced with permission from [92,95], respectively. Copyright Elsevier, 2017; Copyright American Chemical Society, 2013.

From the literature, rare earth metal ions are effective in extending the recombination time of charge carriers and improving their separation efficiency. Rare earth metals, such as cerium (Ce), lanthanide (La), erbium (Er) and ytterbium (Yb), with 4f, 5d, and 6s electrons are good dopants for modifying the electronic structure and optical properties of titania [116,117]. Rare earth dopants introduce several impurity energy levels due to the introduction of orbitals between the conduction and valence bands. Moreover, lattice defects are generated in titania as a result of a large mismatch of both the charge and ionic radius between the dopant and Ti cations. The impurity energy levels act as trapping centers for photogenerated electrons and holes, thereby favoring charge separation and reducing the electron–hole recombination [118–121]. Among these, the La dopant in titania is studied most frequently, followed by Ce doping, in recent years [116–122]. Kasinathan et al. reported that cerium doping suppresses the recombination of photogenerated electron–hole pairs in titania and promotes a red-shift in its band gap transition. As such, Ce-TiO_2 had strong antibacterial activity against *E. coli* due to its strong oxidation activity and superhydrophilicity [121].

Generally, two or more types of metal cations can be incorporated into the TiO_2 lattice to further improve its photocatalytic performance. This is typically termed the 'co-doping'. The enhancement in the photocatalytic activity of co-doped TiO_2 is attributed to the synergistic effect of the dopants in increasing visible light absorption, thus facilitating electron–hole generation and suppressing the recombination rate [90,113–115]. Very recently, Aviles-Garcia et al. synthesized W and Mo co-doped TiO_2, and reported that the nanocomposite with the W:Mo = 1:1 ratio having a bandgap of 2.87 eV exhibits a synergistic effect between the dopants to generate more hydroxyl radicals for degrading 4-chlorophenol. This is because both the $W6^+$ and Mo^{6+} ions are effective in trapping photogenerated electrons, thus extending the lifetime of electron–hole pairs and reducing their recombination rate. The holes can react with the adsorbed H_2O or –OH groups on the TiO_2 surface, giving rise $_{to}$ hydroxyl radicals. The photocatalytic reactions can be expressed as follows [114]

$$\text{W/Mo-TiO}_2 + h\nu \rightarrow \text{e}^- + \text{h}^+ \quad (1)$$

$$W^{6+} + e^- \rightarrow W^{5+} \quad (2)$$

$$Mo^{6+} + e^- \rightarrow Mo^{5+} \quad (3)$$

$$H_2O + h^+ \rightarrow {}^{\bullet}OH + H^+ \quad (4)$$

$$OH^- + h^+ \rightarrow {}^{\bullet}OH. \quad (5)$$

The visible light response of titania can also be achieved by doping with noble metals such as gold (Au), silver (Ag), platinum (Pt) and palladium (Pd) [123–126]. As recognized, a collective oscillation of conduction electrons can be induced in metal NPs by irradiating with light. This is because the collective oscillation of surface electrons resonates with the electromagnetic field of the incident light. This behavior is generally termed as the localized surface plasmon resonance (LSPR). LSPR covers a wide range of solar spectrum, particularly in the visible and near-infrared (NIR) regions [127,128]. After excitation, LSPR decays non-radiatively into hot electrons and holes through Landau damping, generating highly energetic charge carriers that are typically termed 'hot carriers' [129]. This ultrafast relaxation renders the hot carriers capable of rapidly separating and transferring into semiconductors to drive chemical reactions on adsorbed molecules [128–131]. The LSPR effect is more pronounced for Au and Ag nanoparticles compared with other metals.

Employing plasmonic NPs on semiconductors is considered to be effective in improving their photocatalytic performance. In this respect, noble metal NPs act as electron donors for titania by injecting hot electrons into the conduction band of TiO_2 under visible light [132]. The holes created in plasmonic AgNPs can capture conduction electrons of TiO_2, thereby reducing the charge recombination in titania. Therefore, plasmonic oscillation from Au and Ag nanoparticles to TiO_2 under visible light has received considerable attention in recent years [133–138]. Moreover, AgNPs with well-established antibacterial properties are particularly attractive dopants for titatia in addition to their LSPR effect [15]. Figure 4 shows the UV-visible spectra of pristine TiO_2 and Ag/TiO_2 nanocomposites with different AgNP contents [126]. Pristine TiO_2 exhibits a strong UV light absorption band due to the excitation of the electron–hole pair across the bandgap. The Ag/TiO_2 nanocomposites display higher absorption values in the UV region, and the absorption intensity increases with increasing AgNP concentrations. The introduction of AgNPs into TiO_2 results in an increase in the absorption towards the visible light region, i.e., 400–650 nm wavelength. This arises from the LSPR effect of AgNPs that promotes the absorption of Ag/TiO_2 nanocomposites in the visible regime.

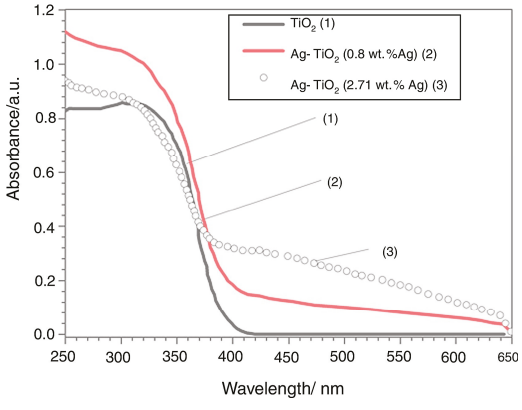

Figure 4. Ultraviolet-visible diffuse reflectance spectra of TiO_2 and its nanocomposites. Reproduced with permission from [126]. Copyright Elsevier, 2019.

When a metal comes into contact with a semiconductor of a different work function, a large potential barrier is established at their interface, which is usually known as the Schottky barrier [137].

Such a barrier at the AgNPs/titania junction improves the charge separation or suppresses the charge recombination greatly [135,138]. Under UV irradiation and in the absence of plasmonic oscillation, electron transfer from the TiO_2 conduction band to AgNPs is thermodynamically favorable, as the Fermi level of titania is higher than that of AgNPs. From this perspective, excited electrons are transferred from titania to AgNPs across the Schottky barrier at the Ag/TiO_2 interface. Accordingly, AgNPs serve as an excellent electron accumulator, thus suppressing the charge recombination process. Under visible light irradiation, AgNPs experience the LSPR effect, and excite the conduction electrons for transfer to TiO_2 to create ROS, as mentioned previously (Figure 5).

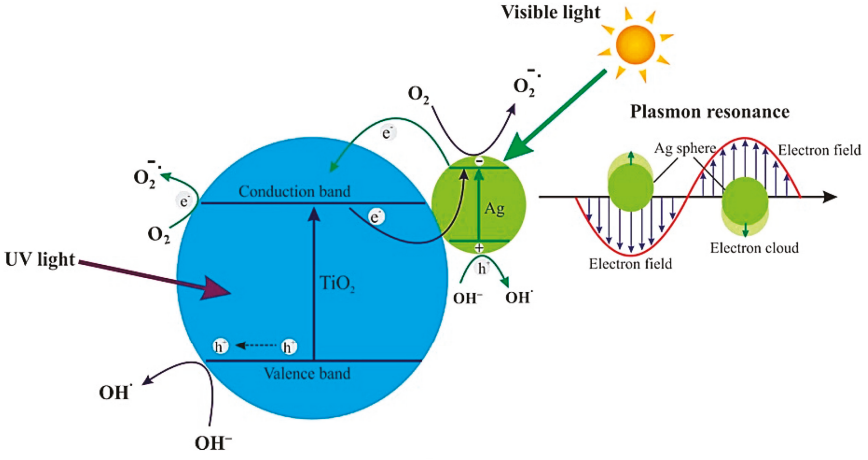

Figure 5. The creation of reactive oxygen species in Ag/TiO_2 nanomaterials due to the localized surface plasmon resonance (LSPR) effect of AgNPs under visible light. After excitation, LSPR decays into hot electrons and holes through Landau damping, creating highly energetic charge carriers. On the other hand, AgNPs serve as an excellent electron accumulator for TiO_2 under UV irradiation. Reproduced with permission from [138]. Copyright MDPI, 2019.

3.2. Carbonaceous Nanomaterials Modified Titania

Pure and high-quality graphene is an excellent electrical conductor as it has no bandgap. Graphene consists of a monolayer of sp^2-bonded carbon atoms that are tightly organized into a two-dimensional (2D) honeycomb structure. Graphene has been reported to possess an excellent electrical mobility of 2×10^5 cm^2 V^{-1} s^{-1}, a superior light transparency of 97.7%, a high specific surface area of 2600 m^2 g^{-1}, and good antibacterial activity [14,139,140]. In this context, graphene and its derivatives, such as graphene oxide (GO) and reduced graphene oxide (rGO), find attractive applications in electronic and optoelectronic devices, energy storage devices, chemical sensors and biomedical implants [141–143]. Moreover, a graphene sheet with a lateral dimension of several micrometers can serve as a template for anchoring TiO_2 NPs onto its surface [102,144–146].

Large-area graphene sheets can be synthesized from chemical vapor deposition (CVD) [147]. However, the CVD approach is still an expensive process for manufacturing high-quality graphene sheets. To tackle this, GO can be prepared at a large scale by exposing the graphite flakes in a strong oxidizing solution, i.e., a mixture of sulfuric acid, sodium nitrate, and potassium permanganate, using a modified Hummers process [148]. As a result, GO bears oxygen functional groups having hydroxyl and epoxide on the graphene basal plane, with carboxyl and carbonyl groups at the edges [149]. Those oxygenated groups damage the conjugated structure of graphene, leading to poor electrical conductivity. To resume its electrical conducting properties, reducing agents, such as hydrazine and sodium borohydride, are used to reduce GO to form rGO [150]. The aforementioned reductants are toxic, so green reductants such as L-ascorbic acid, D-glucose and tea polyphenol can be used to

reduce GO to rGO [151]. Generally, all chemical reductants cannot remove oxygenated groups of GO completely, rendering rGO with a certain degree of residual oxygen levels. Accordingly, GO would change from insulating to conducting behaviors by regulating the C/O ratios. GO and rGO with a tunable band gap of 4.3–2.4 eV is dependent upon the oxygen level; the bandgap generally increases with increasing O levels [152]. In contrast, pure graphene exhibits no bandgap with excellent electron mobility.

For novel graphene/TiO_2 nanostructures, the migration of photogenerated charge carriers from TiO_2 to graphene or vice-versa depends upon the interfacial contact between them, and the photon energy or wavelength [153]. As is known, uniformly dispersed TiO_2 NPs on a large-area graphene sheet and a close interfacial interaction between them are essential for efficient charge transport across the interface (Figure 6a). Under UV irradiation, photoexcited electrons from titania are injected into graphene as the conduction band minimum of TiO_2 is higher than the Fermi level of graphene [32]. As such, highly conductive graphene acts as an electron acceptor for titania, and provides a network to facilitate the rapid transfer of excited electrons. These promote the separation between electron–hole pairs and inhibit their recombination [154]. Under visible light illumination, electrons located in high-energy graphene states are delocalized into the conduction band of TiO_2. Consequently, electrons react with oxygen adsorbed on the TiO_2 surface to form superoxide anion (Figure 6b) [153]. In general, a few layer graphene sheets of rGO/TiO_2 photocatalyst facilitate a red shift in the optical absorption, thereby narrowing its bandgap and enhancing its photocatalytic efficiency [144,146]. Figure 7 shows the UV-vis spectra of anatase TiO_2 and rGO/TiO_2 nanocomposite. The inset displays the Tauc plot of the modified Kubelka–Munk (KM) function with a linear extrapolation to produce respective bandgap values of TiO_2 and rGO/TiO_2 materials, i.e., 3.2 eV and 2.9 eV.

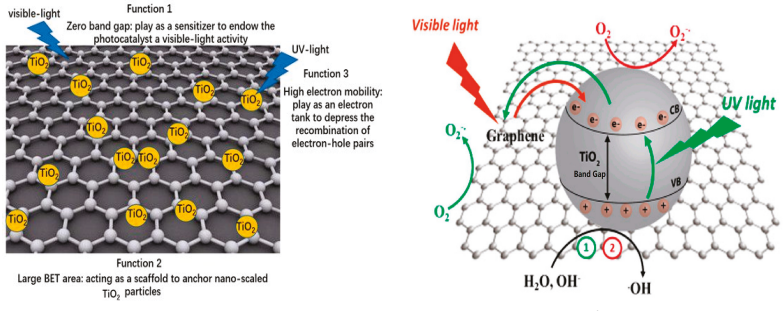

Figure 6. Schematics displaying the (**a**) roles of graphene layers of graphene/TiO_2 composite in photocatalysis, and (**b**) charge transfer mechanism under ultraviolet or visible light irradiation. Reproduced with permission from [145,153], respectively. Copyright MDPI, 2018 and 2017.

A single-walled carbon nanotube (SWNT) is formed by rolling-up a graphene sheet into a cylindrical or turbular shape, while several sheets rolls into a multi-walled nanotube (MWNT). The MWNTs with a large surface-area-to-volume ratio and remarkable electrical conductivity serve as the template for anchoring TiO_2 NPs, facilitating the separation of electron–hole pairs and inhibiting the charge recombination by trapping photoexcited electrons from titania [154]. Accordingly, the bandgap of TiO_2 NPs reduces from 3.25 to 2.71 eV with an increase in MWNTs content. This leads to a shift in the absorption edge into the visible region. The Ti–O–C bond extends the light absorption to longer wavelengths [155–157].

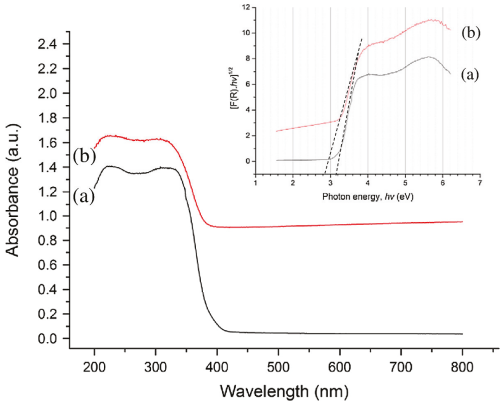

Figure 7. UV–vis diffuse reflectance spectra of (**a**) anatase TiO_2 and (**b**) nanostructured rGO/TiO_2. Inset: plot of transformed KM function $[F(R).h\nu]^{1/2}$ vs. $h\nu$ for bandgap determination of anatase TiO_2 and rGO/TiO_2; R is reflectance and $h\nu$ is photon energy. Reproduced with permission from [146]. Copyright Springer, 2013.

3.3. Non-Metal Doping

Metal doping has some drawbacks for enhancing the visible light response of titania. These include transition metals of high contents, which may serve as recombination sites for photogenerated charge carriers, the low thermal stability of photocatalysts, the formation of secondary phases and dopant insolubility [105,158,159]. Therefore, significant improvement in the photocatalytic performance of metal-doped titania can be achieved only at a low metal dopant concentration. Above an optimal dopant content, photocatalytic activity decreases owing to a higher recombination rate of charge carriers. Non-metal elements such as carbon, nitrogen and boron, with an atomic radius close to that of the O atom, can be utilized as anionic dopants for replacing lattice oxygen anions [76,97,159–164]. In this respect, non-metal doping appears to be an alternative route for enhancing visible light efficiency, due to the introduction of a new valence band associated with their localized 2p states lying above the valence band of TiO_2 (Figure 8). As such, non-metal doping generates a hybridization of O-2p and N-2p orbitals, giving rise to an upshift in the valence band position. By irradiating with visible light, electrons are excited from the localized N-2p states to the CB, leaving behind holes on the localized states. The exception is fluorine with the highest electronegativity, having filled states below the O-2p valence band, leading to the formation of Ti^{3+} ions as of result of the charge compensation [165].

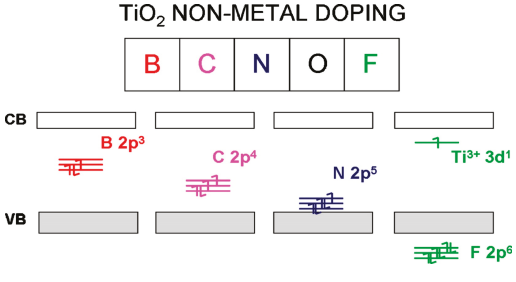

Figure 8. Electronic band structure of titania due to non-metal doping. CB and VB represent conduction band and valence band, respectively. Reproduced with permission from [160]. Copyright Elsevier, 2013.

Among anionic dopants, nitrogen is widely employed to enhance the visible light response of titania. The N atom can occupy either the substitutional or interstitial site of the titania lattice. In

the former case, the N atom substitute the O atom to yield $TiO_{2-x}N_x$, so that the doping energy state (N-2p) lies just above the valence band. Substitutional N doping reduces the bandgap of titania slightly, from 3.20 to ~3.06 eV. The interstitial N-doping reduces the bandgap to ~2.46 eV, in which the doping energy level lies in the midgap, i.e., at 0.74 eV above the valence band [166–168]. In an earlier study by Asahi et al., N-doping into substitutional sites of TiO_2 is reported to be essential for bandgap reduction and efficient photocatalytic activity [166]. For the C-doped TiO_2 photocatalyst, carbon dopant may replace oxygen or Ti in the substitutional lattice site. It may also occupy the interstitial site [169]. Therefore, C-doped TiO_2 can have different photocatalytic behaviors, depending on the synthesis process employed. Density functional theory (DFT) calculations predict that substitutional (to oxygen) carbon and oxygen vacancies are formed at low carbon contents and oxygen-poor conditions. Under oxygen-rich conditions, interstitial and substitutional (to Ti) C atoms are favored [170]. Similarly, the B dopant can substitute for either the O or Ti atom, or can occupy the interstitial position. DFT simulations indicate that a B substitution for Ti is unlikely to take place. In contrast, the boron atom tends to either replace an oxygen atom or occupies the interstitial site [171]. From the X-ray photoelectron spectroscopic (XPS) results, Patel et al. reported that B preferentially occupies the interstitial site at low concentrations (up to 1%), while it occupies the substitutional O site as the concentration increases (≥2%) [172].

Recently, Sotelo-Vazquez et al. reported that phosphorus (P)-doping can result in the formation of both cationic (P^{5+}) and anionic (P^{3-}) states of anatase TiO_2 films on the basis of XPS results. The P^{3-} state of P-doped TiO_2 exhibited inferior photocatalytic activity compared to undoped TiO_2 film. Transient absorption spectroscopic results revealed that charge carrier concentrations increased by several orders of magnitude in films containing P^{5+} species [173]. From the XPS measurements, Gopal et al. demonstrated that the P dopant exists in a P^{5+} state which can replace part of Ti^{4+} through the formation of Ti–O–P bonds, i.e., forming P cation-doped TiO_2 [174]. As a result, the photocatalytic activity of P-doped titania for degrading methylene blue was much enhanced and superior to undoped TiO_2. Moreover, X-ray diffraction results indicated that P-dopant increases the thermal stability of TiO_2 NPs, and retards the phase transition from anatase to rutile.

From the literature, fluorine doping stabilizes anatase TiO_2 at elevated temperatures up to 1200 °C [75]. The substitution of fluorine for oxygen in TiO_2 NPs leads to the creation of an oxygen vacancy [175]. Fluorine doping converts Ti^{4+} to Ti^{3+} in TiO_2 NPs by charge compensation. The presence of Ti^{3+} suppresses the recombination of the electron–hole pairs and enhances the photocatalytic activity accordingly [165]. Co-doping TiO_2 NPs with F and N is considered to be very effective in tuning the bandgap to further enhance visible-light photocatalytic activity. Multiple charge transfer transitions occur in the Ti^{3+} localized state, oxygen vacancy and N midgap state of the F–N, co-doped TiO_2 NPs [176]. Table 1 summarizes visible-light active TiO_2 NPs doped with metals and non-metals.

3.4. Coupling of Semiconductors

The poor photocatalytic efficiency of titania under visible light can be overcome through the formation of a heterojunction structure by coupling with other semiconductors with a suitable energy band level. Titania can be coupled with metal oxides (e.g., Cu_2O, Fe_2O_3, WO_3) and chalcogenides (e.g., CdS, MoS_2 and WS_2) to form a heterojunction for the charge separation in enhanced visible light absorption. Those coupled semiconductors acting as sensitizers should be nontoxic, and exhibit visible light photocatalytic activity, with a bandgap smaller than that of titania [177–183]. In this respect, photoexcited electrons in the CB and holes in the VB of a sensitizer semiconductor can be transferred to the CB and VB of TiO_2 NPs [180]. Zinc oxide with good antimicrobial property is unsuitable to form visible-light active ZnO/TiO_2 nanostructures due to its wide bandgap of 3.37 eV. Cadmium sulfide is toxic and carcinogenic, so it is unfavorable to form CdS/TiO_2 heterojunction for practical applications. Nontoxic molybdenum disulfide (MoS_2) with a direct band-gap of 1.9 eV can be coupled with titania to form MoS_2/TiO_2 nanocomposites, having excellent visible photocatalytic activity [181]. Oxide semiconductors, such as α-Fe_2O_3 and Cu_2O with a respective small bandgap of 2.2 eV and 2.17 eV,

can also form composite photocatalysts, with TiO_2 having good antibacterial properties under visible light [177,179,182,183]. Inexpensive and nontoxic Cu_2O, with its efficient electron injection to the conduction band of TiO_2, is particularly suitable for forming heterojunction photocatalysts [182,183].

Table 1. Visible-light active TiO_2 NPs doped with metals and non-metals.

Dopants	New Band (Gap) State Created	Reference
Metals		
Ti	Ti^{3+}, oxygen vacancy	[106,107]
Mn	Mn^{2+}	[92]
Fe	Fe^{3+}	[93,95]
Ni	Ni^{2+}	[110]
Cu	Cu^{2+}	[109]
V	V^{4+}	[88]
Mo	Mo^{6+}	[111,112]
Ce	Ce^{3+}	[121,122]
Mo and W	Mo^{6+}, W^{6+}	[114]
V and Co	V^{4+}, Co^{2+}	[90]
Fe and Co	Fe^{3+}, Co^{2+}	[115]
Non-Metals		
N	N midgap	[166]
P	P^{5+}	[173,174]
F	Ti^{3+}, oxygen vacancy	[165,175]
F and N	Ti^{3+}, oxygen vacancy, N midgap	[176]

4. Synthesis of Titania Nanomaterials

Titania can be fabricated in the form of thin films, powders, or nanocrystals. Physical deposition techniques such as thermal evaporation, reactive sputtering and pulsed laser deposition, chemical gas-phase atomic layer deposition (ALD) process, and wet chemical deposition methods such as dip-coating, spin-coating, spray coating and sol-gel, have been employed by researchers to prepare TiO_2 thin films [184–189]. Those homogeneous films deposited by physical deposition techniques are beneficial for use in dye-sensitized solar cells, microelectomechanical systems and electroluminescent devices [185,189]. In ALD, chemical precursors react sequentially on various substrate surfaces including carbon nanotubes, forming nanometer-sized films of metal oxides (e.g., TiO_2 and HfO_2) [190–192]. It offers the advantages of nanometer-level control of both thickness and film composition. For bactericidal applications, wet chemical processing is the most convenient, simple and effective synthesis route for preparing TiO_2 NPs and nanocomposites. Moreover, the solution chemical synthesis process is capable of producing titania nanomaterials in larger quantities in comparison with the physical processing route. Solution processing techniques include the sol-gel, wet impregnation, photoreduction, hydrothermal and solvothermal processing, electrochemical anodization and electrospinning.

4.1. Solution Processing Route

4.1.1. Sol-Gel Method

Titania colloids can be synthesized through the hydrolysis and condensation reaction of titanium alkoxide in the presence of water, and these reactions are catalyzed by an acid [193–196]. The sol-gel process involves the transformation of metal alkoxide or metal salt into a solid by adding an excess of water to give a metal–oxo linkage (M–O–M). The hydrolysis facilitates the formation of original nuclei TiO_2, and the subsequent condensation promotes the growth of a crosslinked network of TiO_2 nuclei. This strategy allows the formation of TiO_2 NPs with a high level of chemical purity [196,197]. From an earlier study of Padmanabhan et al., the sol-gel process involved the reaction of titanium

tetraisopropoxide (TTIP) with trifluoroacetic acid (TFA), followed by hydrolysis, gelation, drying, and finally calcination at high temperatures. The sol was dried at 90 °C to obtain the gel, and then calcined at 500–900 °C to remove organic substances to form nano-TiO_2 with a high photocatalytic activity [194]. In a recent study, Lusvard et al. employed different precursors and procedures for synthesizing TiO_2 NPs with the preparation conditions compatible with the industrial scale for water purification [196]. Three different kinds of precursors were utilized for the synthesis of TiO_2 NPs, including: titanium tetrachloride ($TiCl_4$) and ethanol, titanium isopropoxide ($C_{12}H_{28}O_4Ti$) and urea ($CO(NH_2)_2$), as well as titanium isopropoxide, isopropyl alcohol (C_3H_8O), acetic acid (CH_3COOH) and methanol (CH_3OH). They reported that TiO_2 NPs, synthesized from molar TTIP: urea in a ratio of 2:1 at 50 °C, have the best photocatalytic activity for degrading methyl blue and bromothymol blue [196].

For fabricating metal-doped TiO_2 nanopowders, an additional metal source reagent is needed, and added to titanium precursors during the sol-gel process [197–200]. For instance, Marami et al. prepared Fe-doped TiO_2 powders by introducing $FeSO_4{\cdot}7H_2O$ into the TTIP, and the ethanol solution followed with the addition of acetic acid under vigorous stirring. Thereafter, the temperature of mixture was increased to 70 °C, and ethylene glycol was added, acting as a stabilizer. The product was dried and finally calcined at 600 °C for 4 h to yield Fe-doped TiO_2 nanopowders [198]. In the case of Ag-doped TiO_2, a desired amount of silver salt precursor, i.e., silver nitrate was added to the TTIP−methanol solution [50,199]. Reducing agents such as $NaBH_4$ are employed to reduce silver ions to AgNPs. For the synthesis of N-doped TiO_2, an organic compound with nitrogen (such as trimethylamine, 1,3-diaminopropane, ethylmethylamine), or ammonium salt bearing nitrogen (e.g., ammonium carbonate, ammonium chloride, ammonium nitrate), is added to the sol-gel solution during the synthesis process [200–204].

4.1.2. Hydrothermal/Solvothermal Synthesis

The hydrothermal/solvothermal method is a useful tool for fabricating TiO_2 nanostructures involving chemical reactions in a solvent (water/nonaqueous) medium at an elevated temperature >100 °C and a pressure higher than 1 atm, within a closed system using an autoclave. As the sol-gel process generally produces amorphous or low crystalline materials, a subsequent annealing at high temperatures for crystallization is needed. In this context, hydrothermal or solvothermal processing is beneficial for improving the crystallinity of titania synthesized by the sol-gel technique. For example, Yanagizawa and Ovenstone investigated the effect of hydrothermal treatment on the crystallinity and phase structure of sol-gel prepared, TiO_2 amorphous powders [205]. In their study, hydrothermal treatment was performed at 250 °C for 1 h in the presence of several inorganic salts under acidic and basic conditions. Acidic conditions led to the formation of anatase, brookite, and rutile, whereas basic conditions and/or the presence of sulfate ions favored the crystallization of anatase [205]. In addition, the hydrothermal approach can also be used to synthesize rGO/TiO_2 nanocomposites [206].

The organic solvents in solvothermal treatment help to control the morphology of synthesized nanocrystals. Thus, this process enables better control of the shape, size distribution and crystallinity of TiO_2 NPs in comparison with the hydrothermal method. TiO_2 nanostructures of different morphologies can be obtained and tailored by manipulating several processing parameters, including the type of solvent and titanium precursor, molar ratio of reagents, addition of surfactant, reaction temperature and time [207–212]. For instance, TiO_2 nanorods can be synthesized in TTIP, benzyl alcohol (BzOH) and acetic acid (AA) at 150 °C for 8 h. The molar ratio of TTIP/AA is kept at 1: 4 [208]. Recently, Falentin-Daudré et al. synthesized highly crystalline sphere and rod-shaped TiO_2 nanostructures using TTIP, benzyl alcohol (BzOH) and AA reagents. The shape of the TiO_2 nanostructure can be tuned by varying the concentration molar ratios of TTIP/BzOH and AA/BzOH (Figure 9) [209]. The X-ray diffraction patterns for TiO_2 nanospheres and nanorods display well-defined peaks associated with pure anatase, thus revealing TiO_2 nanospheres and nanorods with a high crystallinity.

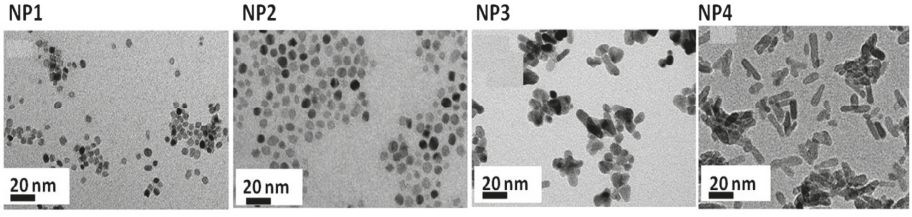

Figure 9. Transmission electron micrographs of solvothermally synthesized TiO_2 with nanospheres (NP1–NP2) and nanorods (NP3–NP4) morphologies. Reproduced with permission from [209]. Copyright Elsevier, 2017.

For preparing rGO/TiO_2 nanocomposite, Tan et al. first obtained a mixed solution of tetrabutyl titanate, ethylene glycol and acetic acid, and then added it dropwise into a chilled GO solution under vigorous stirring. Thereafter, an autoclave filled with the GO–TiO_2 solution was heated at 180 °C for 8 h. The greyish-black precipitate was obtained by centrifugation [146]. During the solvothermal synthesis, GO was reduced to rGO accordingly. Figure 10a,b show the respective field-emission scanning electron microscopic (FESEM) image and transmission electron micrograph (TEM) of the rGO/TiO_2 nanocomposite. It is apparent that titania nanoparticles with an average size of 12 nm are dispersed and anchored on the rGO surface. The high-resolution TEM (HRTEM) images of a selected rGO-TiO_2 heterojunction are shown in Figure 10c,d. The lattice fringes can be seen in titania nanoparticles, especially in the high magnification image shown in Figure 10d, implying that the TiO_2 nanocrystals exhibit good crystallinity. The lattice spacing of TiO_2 is determined to be 0.35 nm, which corresponds to the (101) plane of anatase TiO_2. Moreover, the rGO–TiO_2 interface is clean and free from the impurity products. The intimate connection enables photoinduced electrons to flow readily from rGO to TiO_2 NPs, thereby enhancing the photocatalytic activity.

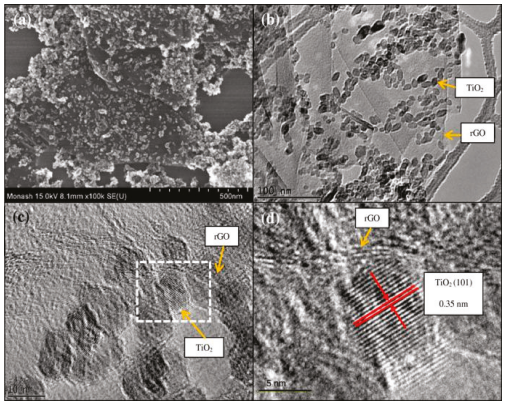

Figure 10. (**a**) Field-emission scanning electron image and (**b**) transmission electron micrograph of the solvothermally synthesized rGO/TiO_2 nanocomposite. (**c**,**d**) Enlarged images of high-resolution transmission electron micrographs showing the lattice fringes of TiO_2 and a clean interface between TiO_2 and rGO. Reproduced with permission from [146]. Copyright Springer, 2013.

4.1.3. Electrochemical Anodization

Transition metals like iron and chromium can form a thin oxide film on their surface upon electrochemical polarization in the anodic region [213,214]. Therefore, titanium and its alloys can also form anodic films on their surfaces during the anodizing process. Ti-based alloys are widely used as load-bearing bone prostheses and dental implants in clinical sectors. However, bacterial

infection due to biofilm formation is the main cause of implant failures. In recent years, there has been a clinical demand for functional Ti-prostheses with enhanced bone cell adhesion/growth, and excellent antibacterial properties. To improve the biocompatibility of Ti-implants with the host-tissues, titania coating is formed on their surfaces through the anodization technique [215]. One-dimensional titania nanotubes' (TNTs) high surface area to volume ratio and enhanced bone–cell adhesion ability makes them suitable for biomedical applications [216–219]. TNTs promote the osseointegration of bone implants more effectively than titanium alloys. Compared with TiO_2 NPs, TNTs bear a stronger negative surface charge [55], enabling them to repel bacteria with a negatively charged membrane. Thus, TNTs show bactericidal effects to a lesser degree. By incorporating AgNPs into TNTs, the bactericidal performance of anodized Ti-alloys is improved significantly [218]. The TNTs fabricated from the sol-gel or hydrothermal methods are randomly oriented [220]. In contrast, ordered and self-organized titania nanotubes can be prepared by electrochemical anodization [219]. Anodization offers the additional advantages of simplicity, and ease of fabrication and scaling-up. The tube diameter, length and wall thickness can be properly manipulated by processing parameters including electrolyte composition, applied voltage, pH, temperature, and time [221]. In general, the applied voltage regulates the nanotube diameter, and the anodizing time controls the tube length.

Titanium anodization can be simply performed in a two-electrode cell system connected to a power supply (Figure 11a). The oxide film formation involves an anodic oxidation of metal at the metal surface, outward migration of Ti^{4+} ions toward the metal/oxide interface and field-assisted dissolution of oxide at the oxide/electrolyte interface [219]. The oxide layer generally has a low conductivity, which restricts the migration of oxygen and Ti ions accordingly. As such, continued oxide growth is assisted by an electric field, and a compact oxide layer is formed on the Ti surface. The electrochemical reactions occurring during anodization are given as follows

$$Ti + 2H_2O + 4e \rightarrow TiO_2 + 4H^+ \text{ Anodic oxidation,} \quad (6)$$

$$4H^+ + 4e \rightarrow 2H_2 \text{ Cathodic reaction.} \quad (7)$$

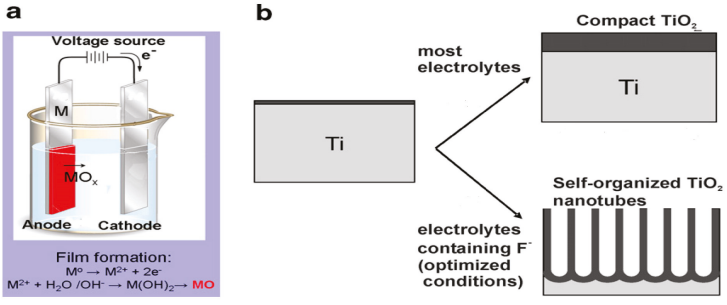

Figure 11. Schematic illustration displaying (**a**) the set-up for anodization and (**b**) frmation of compact titania layer on the Ti substrate in electrolytes without fluoride, and self-organized titania nanotube arrays in electrolytes with fluoride. Reproduced with permission from [222]. Copyright Elsevier, 2007.

To form TNTs on Ti foil substrate, aqueous fluoride-containing electrolytes such as $(NH_4)_2HPO_4/NH_4F$ or $(NH_4)_2SO_4/NH_4F$, and organic electrolytes, e.g., ethylene glycol, formamide, or dimethylsulfoxide containing F^- anions, are needed (Figure 11b). The presence of F^- anions in the electrolyte results in the chemical dissolution of oxide at the electrolyte/oxide interface to yield $[TiF_6]^{2-}$ and F^{--}rich layers. In other words, F^- ions etch the oxide layer to form water-soluble $[TiF_6]^{2-}$ complexes. The chemical reaction associated with the F^- ions etching is given by [222]

$$TiO_2 + 6F^- + 4H^+ \rightarrow [TiF_6]^{2-} + 2H_2O \quad (8)$$

Accordingly, small pits are produced at the electrolyte/oxide interface due to the chemical dissolution of oxide. These pits gradually grow into nanopores, as shown in Figure 12a,b. The pores grow into tubular features and form TNT arrays as the anodizing process continues to its final stage (Figure 12c,d). The growth of TNT arrays is described as the competition between electrochemical oxide formation and chemical dissolution of oxide by F^- ions of sufficient concentrations [222–224]. Figure 13a,b shows the formation of TNT arrays by anodizing Ti in a mixed ethylene glycol/NH_4F and water solution [223,225]. At a low applied voltage of 5 V, an SEM image shows the formation of the rough Ti surface together with inhomogeneous TNTs. However, uniform and well-aligned TNTs are produced by increasing the applied voltage from 15 to 20 V (Figure 13a). The as-anodized TiO_2 nanotubes generally exhibit an amorphous structure. Therefore, post-annealing treatment is typically performed to enhance their crystallinity.

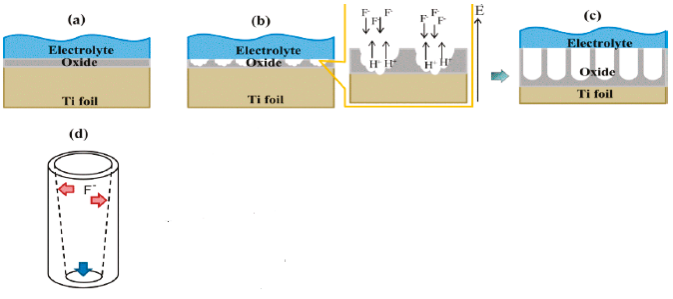

Figure 12. Schematic showing the formation of titania nanotube (TNT) arrays: (**a**) an initial development of a compact oxide layer on the surface of Ti, (**b**) small pits formation due to the etching of oxide by F^- ions, (**c**) local growth of nanopores into well-aligned TNT arrays, and (**d**) the shape and wall thickness of a nanotube. Reproduced with permission from [223]. Copyright MDPI, 2019.

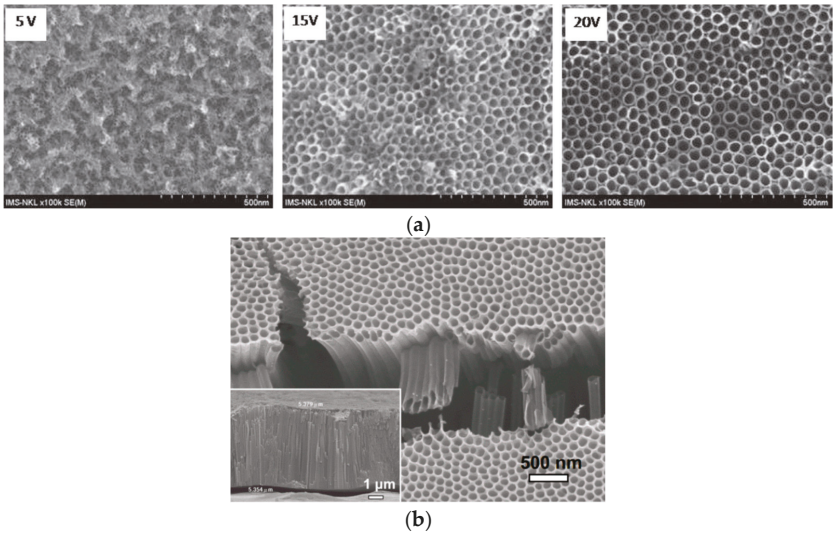

Figure 13. (**a**) Top-view scanning electron micrographs of TNT arrays prepared by anodizing Ti in a mixed ethylene glycol/NH_4F and water solution under applied voltages of 5, 15 and 20 V for 5 h. Reproduced with permission from [225]. Copyright IOP Publishing, 2014. (**b**) Cross-sectional SEM image (inset) and top view of TNTs fabricated by anodizing Ti in a mixed ethylene glycol/NH_4F and water solution at 30 V for 1 h. Reproduced with permission from [223]. Copyright MDPI, 2019.

To introduce AgNPs into TNTs, Lan et al. deposited a thin Ag layer on anodized TNTs via electron-beam evaporation. AgNPs were directly coated onto inner- and outer-tube surfaces [226]. Figure 14A is the TEM image of AgNP-decorated TNTs, showing the uniform distribution of AgNPs along the tubes. High-magnification TEM images reveal that the sizes of AgNPs range from 5 to 20 nm (Figure 14B,C). The corresponding energy dispersive X-ray spectrum (EDS) reveals the presence of Ag in addition to Ti from the TNT (Figure 14D). Alternatively, the wet chemical synthesis route using TNT and silver nitrate mixed solution can yield Ag-decorated TNTs. Thereafter, UV illumination is employed to reduce Ag^+ ions to AgNPs through the photoreduction process without using reducing agents. As such, photo-assisted deposition can bind AgNPs closely to TNTs [53].

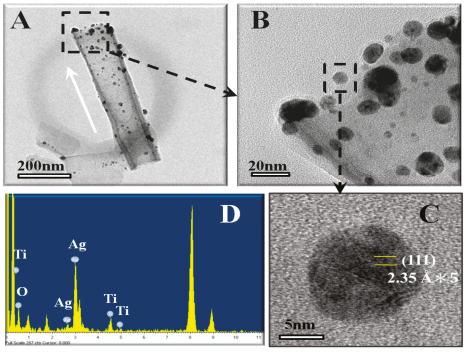

Figure 14. (**A**) TEM image of a single, Ag-decorated TiO_2 nanotube with a diameter of 100 nm. The white arrow indicates the growth direction of a nanotube. (**B**) High-magnification image of the selected are, as marked by a dashed square in (**A**). (**C**) Enlarged view of a single AgNP, and (**D**) the corresponding EDS spectrum of AgNP and TiO_2 nanotubes. Reproduced with permission from [226]. Copyright Public Library of Science, 2013.

4.1.4. Electrospinning

Electrospinning is a simple and versatile tool to form microfibers and nanofibers (NFs) from different materials including polymers, metal oxides and their nanocomposites. This process has been used extensively for fabricating nanofibers derived from polymers and polymer nanocomposites [27,72,227,228]. In the process, a high electric field is applied to the polymer/solvent solution. Beyond a critical voltage, the repulsive electrostatic force overcomes the surface tension of the polymer droplet, resulting in the ejection of a charged jet from the nozzle towards the collector. Several processing parameters affect the fiber diameter and porosity of electrospun polymer mats, including the type of solvent used, polymer concentration, applied voltage, flow rate, needle-to-collector distance, etc. [227,228]. Very recently, Feng et al. incorporated commercial Degussa P25 (70–80% anatase and 20–30% rutile) with a diameter of 20 nm into polylactic acid (PLA) using the electrospinning method [229]. They reported that the PLA/TiO_2 composite nanofibers with 0.75 wt% TiO_2 exhibit good bactericidal activity upon exposure to UV-A (360 nm) radiation.

In general, two approaches have been employed to prepare electrospun metal oxide NFs, i.e., a polymer-assisted spinning method and direct electrospinning without using a polymer [230–234]. The former strategy involves the mixing of metal alkoxide sol with a polymer solution in which the polymer controls the rheology during electrospinning. Without a polymer solution, the viscosity of the sol varies with time, causing a difficulty in controlling the rheological properties of a sol. In addition, the diameter of the as-spun ceramic fibers falls in the micrometer scale [232]. To improve solution spinnability, poly (vinyl pyrrolidone) (PVP) is added to the sol to obtain continuous ceramic NFs. As such, the diameter of titania fibers can be tuned from the micrometer to nanometer scale by regulating

the concentration of PVP and the Ti alkoxide to PVP ratio. For example, Tekmen et al. electrospun TiO_2 with a diameter of 54–78 nm, employing a mixture solution of PVP and TTIP [231].

Albetran et al. studied the effect of calcination treatment on the bandgap reduction in electrospun titania nanofibers exposed to pure argon, air, and air–argon mixtures at 900 °C [233]. The spinning solution was prepared by mixing TTIP, ethanol, and acetic acid in a fixed volume ratio of 3:3:1, followed by the addition of 12 wt% PVP. The nanofibers heated in 100% argon exhibit an uneven or rough surface in comparison with the as-spun amorphous fibers due to the formation of crystalline grains of anatase and rutile (Figure 15a,b). In general, the anatase phase is stable in TiO_2 up to 500–700 °C, and transforms to rutile with an increase in temperature [75]. Calcination at 900 °C led to a reduction in the diameter of NFs due to the removal of PVP and the densification of TiO_2. The degree of crystallinity of calcined titania NFs was 73.4%. Moreover, calcination of the as-spun NFs in 100% argon induced the formation of a high amount of oxygen vacancies, thereby creating a localized state below the conduction band, and reducing the bandgap accordingly. The creation of oxygen vacancies was reported to be effective to enhance visible light absorption as the oxygen vacancy states were located 0.75 to 1.18 eV below the conduction band minimum of TiO_2. Those oxygen vacancies were generated in titania by heating in an oxygen-poor environment, such as a N_2, Ar or a vacuum at elevated temperatures (>400 °C) [235]. From Figure 15c, the as-spun mat calcined at 900 °C in a 100% argon atmosphere had the highest absorbance in the visible light region compared with the as-spun mats with and without calcination in air and air–argon gaseous mixtures. The bandgap of as-electrospun amorphous nanofibers determined from the UV-vis spectra reduced from 3.33 to 3.09, 2.91 and 2.18 eV through calcination in air, 25% air/75% argon and 100% argon, respectively. Nasr et al. electrospun (2%–7 wt%) rGO/TiO_2 NFs, followed by annealing at 500 °C [236]. The rGO sheets reduced the bandgap of TiO_2 NFs from 3.2 to 2.9 eV, thus suppressing the recombination of electron–hole pairs, and increasing visible-light photocatalytic activity for degrading methylene blue. Very recently, Chapman et al. successfully obtained TiO_2 NFs with average diameters of ~70 nm without using a polymer through mixing an alkoxide precursor, solvent, water, and an acid [234]. They introduced TTIP in ethanol, aged under nitric acid condition, and then added *N*,*N*-dimethylformamide to obtain a sol needed for the continuous spinning of TiO_2 NFs.

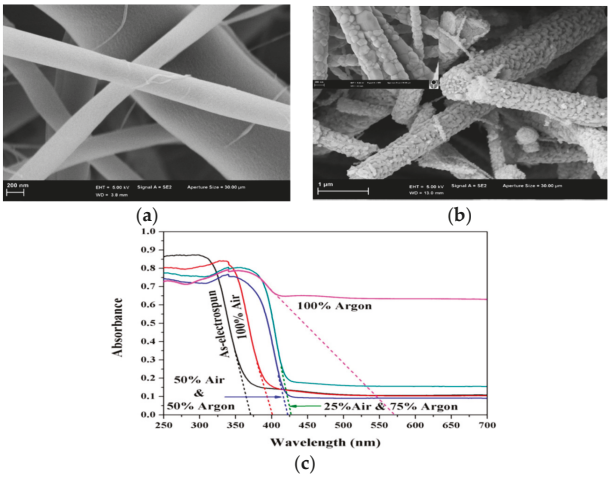

Figure 15. Scanning electron micrographs of (**a**) electrospun titania nanofibers before heating, and (**b**) after heating in 100% argon atmosphere at 900 °C. (**c**) UV-visible spectra of as-spun titania nanofibers without calcination, and with calcination at 900 °C in 100% air, 50% air–50% argon, 25% air–75% argon and 100% argon. Reproduced with permission from [233]. Copyright Elsevier, 2016.

5. Bactericidal Activities

Titania NPs are negatively charged at the point of zero charge (pzc) at pH = 6.2. Therefore, they exhibit low bactericidal activity in neutral and alkaline solutions by repelling negatively charged bacteria in the absence of light. At acidic pH, positively charged TiO_2 NPs strongly interact with the bacterial cells, resulting in bacterial membrane penetration and inducing oxidative damage accordingly [57]. Kiwi et al. reported that TiO_2 NPs tend to kill *E. coli* by direct contact in the dark condition, thus damaging their cell walls, due to the electrostatic attraction between the TiO_2 NPs and the negatively charged bacterial cell wall at a pH close to but below pzc [237]. On the contrary, the bactericidal effect is caused by the creation of ROS species on the TiO_2 NPs under UV irradiation. This means that the bactericidal activity is due to the radiation itself and is not caused by the titania NPs [238]. TiO_2 NPs can kill multidrug-resistant bacteria such as MRSA, vancomycin-resistant Enterococcus faecalis (VRE) and *P. aeruginosa* through the reactive radicals generated by electron–hole pairs upon UV excitation [239,240]. The photocatalytic inactivation of MRSA and VRE strains depends on the power and irradiation time of UV-A light [239]. Therefore, the disinfection process requires a high-power UV source to excite TiO_2 NPs. Apparently, TiO_2 NPs do not reach their full potential for bactericidal applications owing to their ineffective photoexcitation under visible light irradiation. As a result, TiO_2 NPs have limited efficiency against microorganisms in indoor environments where the fraction of UV light is small. From this perspective, the development of a visible-light active TiO_2 with excellent antibacterial performance is of crucial importance in medical and industrial sectors.

5.1. Metal Doping

Transition metals like Cr, Fe, Ni, Cu, and RE metals can be used to enhance the photocatalytic activity of nanocrystalline titania, and this in turn improves its bactericidal performance. Those metal cations substitute Ti^{4+} ions in the titania lattice, leading to a reduction in the bandgap and promoting the formation of charge carriers under visible light. As a result, ROS are generated on the titania surface, and they are very effective at killing bacteria through lipid peroxidation, the depletion of glutathione, DNA damage and the final disintegration of the cell membrane. This results in a leakage of cellular contents, thus causing cell lysis and eventual cell death [241,242]. Negatively charged superoxide and hydroxyl radicals generally reside on the membrane and do not penetrate into the bacterial cytoplasm, while electrically neutral H_2O_2 can pass through the cell membrane. Hydrogen radicals can abstract hydrogen atoms from the fatty acids of bacterial membrane lipids, causing lipid peroxidation and damaging the respiratory electron transport chain located in the membrane [242]. As is known, most transition and RE metals are toxic to humans. In terms of environmental and public health considerations, Cu is more suitable than other transition metals and RE metals for doping nanocrystalline titania. Copper metal is widely used in hospitals for preventing spread of bacteria among the patients because of its antimicrobial activity [243]. Therefore, copper can be used to dope titania for antibacterial purposes [244–247]. As an example, TiO_2–Cu films exhibit bacterial inactivation for *E. coli* and MRSA under indoor visible light irradiation [244,245].

5.1.1. Doped Titania NPs

Yadav et al. fabricated Ni-doped TiO_2 NPs using the sol-gel process through the addition of $NiSO_4(H_2O)_6$ to a mixture solution containing TTIP, acetic acid and sodium dodecyl sulfate. The resulting powders were dried and calcined at 500 °C for 5 h [248]. Figure 16a,b shows the photocatalytic bactericidal activity against *E. coli* and *S. aureus* of Ni-doped TiO_2 NPs with 1.0 mol %, 2.0 mol % and 3.0 mol % Ni dopants, denoting Ni1–TiO_2, Ni2–TiO_2 and Ni3–TiO_2, respectively. In dark (with doped TiO_2 NPs) and visible light (without doped TiO_2 NPs) environments, both bacterial strains grow into a high density of cell populations, expressed as colony-forming units (CFU)/mL. The photocatalytic inactivation of *E. coli* and *S. aureus* takes place by illuminating Ni-doped TiO_2 NPs with visible light. The Ni3–TiO_2 sample shows the highest photocatalytic inactivation because it can generate a higher

ROS level with an increase in Ni content. Moreover, the photocatalytic inactivation efficiency of Ni-doped TiO_2 NPs toward Gram-positive *S. aureus* is somewhat faster than Gram negative *E. coli*. In the case of Gram-negative salmonella abony, complete inactivation takes 360 min of light irradiation (data not shown). The time required for the full inactivation of S. abony is higher than that for *E. coli* inactivation. Using the same approach, they also fabricated Cu-doped TiO_2 NPs with 1.0 mol %, 2.0 mol % and 3.0 mol % Cu by adding different concentrations of $CuSO_4 \cdot 5H_2O$ to a solution containing TTIP and acetic acid. The catalysts were calcined in air at 500 °C for 5 h [247]. The 3%Cu/TiO_2 NPs photocatalyst exhibits a higher bactericidal activity than those doped with 1.0 mol %, and 2.0 mol % Cu. The 3%Cu/TiO_2 NPs catalyst shows 100% inhibition for *S. aureus* within 120 min, but it requires 240 min for the complete inactivation of *E. coli*. This implies that the rate of bacterial inactivation for *E. coli* is much slower than for *S. aureus*. This is caused by a difference in the cell wall structures between these two bacterial strains. As is known, bacteria exhibit a negative charge on their cell wall surface. The cell wall of Gram-positive bacteria is relatively porous and thick (20–80 nm) consisting of several layers of peptidoglycan, interspersed with teichoic and lipoteichoic acids. Peptidoglycan is negatively charged due to the presence of carboxyl and amino groups [249]. In contrast, the cell wall of Gram-negative bacteria is thinner (<10 nm) with a single peptidoglycan layer, surrounded by an outer membrane with a very complex structure. Lipopolysaccharides (LPS) and lipoproteins are located in the outer leaflet, while phospholipids are found in the inner leaflet of the outer membrane. The phosphate groups of LPS increase the overall negative charge. Thus Gram-negative bacteria have a higher negative charge than Gram-positive bacteria [250–252]. The structural variations in the cell walls between these two bacterial strains lead to their different interactions with photocatalysts. As such, Gram-negative bacteria is more resistant to attack from the superoxide anion and hydroxy radical with a negative charge. Moreover, LPS also creates a permeability barrier at the cell surface, thus contributing to its resistance against many antibiotics and substances [250–252].

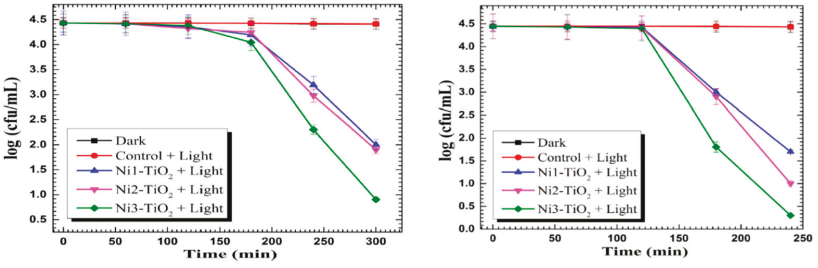

Figure 16. Inactivation of (**a**) *E. coli* and (**b**) *S. aureus* by Ni-doped TiO_2 NPs as a function of time. Reproduced with permission from [248]. Copyright Elsevier, 2014.

Very recently, Pillai and coworkers prepared Cu-doped TiO_2 NPs by adding a copper sulfate solution to a mixture solution containing TTIP, and isopropanol [109]. The resulting gel was dried, and doped titania powders were calcined at 500, 600, 650 and 700 °C, respectively. Pure TiO_2 powders were prepared from TTIP and isopropanol without copper sulphate addition. The obtained TiO_2 powders were calcined at 500 and 700 °C to yield anatase and rutile, respectively. Their results showed that Cu doping is very effective to retain the anatase phase of TiO_2 at calcined temperatures up to 650 °C. X-ray Photo-electron Spectroscopy (XPS) spectra reveals the presence of Cu^+ and Cu^{2+} in Cu-doped TiO_2 where the Cu^+ state predominates. Figure 17a,b shows the photocatalytic bactericidal activity of 0.5 wt% Cu/TiO_2, anatase TiO_2 and rutile TiO_2 against *E. coli* and *S. aureus* under dark and visible light illumination, respectively. In the dark, both bacteria strains grow quickly and their survival rate reaches a high plateau value. However, a 5-Log pathogen reduction (99.999%) is observed in both bacterial strains exposed to 0.5 wt% Cu/TiO_2 following visible light irradiation for 30 min (Figure 18).

In this respect, 0.5 wt% Cu/TiO_2 photocatalyst exhibits a strong antibacterial effect against *E. coli* and S. aureous under visible light irradiation. The enhanced antibacterial performance of 0.5 wt% Cu/TiO_2 photocatalyst calcined at 650 °C is attributed to the formation of a heterojunction between TiO_2 and Cu_2O, inducing hydroxyl radicals through the interfacial charge carrier transfer mechanism, to the copper ions killing effect. The replacement of Ti^{4+} with Cu^{2+} also induces the creation of oxygen vacancies. This gives rise to the high absorption rate of visible light as a result of a bandgap reduction from 3.17 to 2.8 eV. It is noted that some Cu^+ ions may react with a transient metabolic byproduct of cellular respiration, i.e., H_2O_2 through the Fenton reaction, resulting in the formation of hydroxyl radicals and Cu^{2+} ions. The Fenton reaction for generating hydroxyl radicals due to the presence of Cu^+ ions is given by [246]

$$Cu^+ + H_2O_2 \rightarrow Cu^{2+} + OH^- + {}^{\bullet}OH. \quad (9)$$

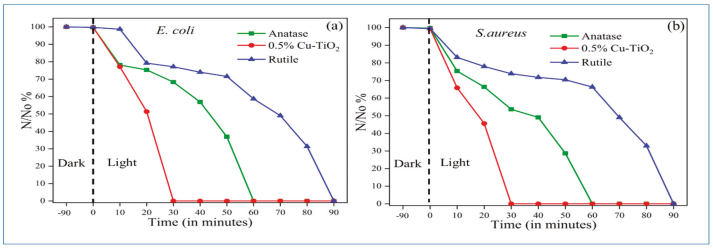

Figure 17. Photocatalytic inactivation of (**a**) *E. coli* and (**b**) *S. aureus* with 0.5% Cu/TiO_2 calcined at 650 °C, pure anatase and rutile specimens. N/N_o is the reduction in the concentration of the bacteria. Reproduced with permission from [109]. Copyright MDPI, 2018.

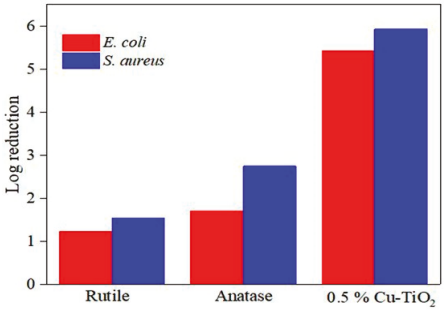

Figure 18. Photocatalytic bactericidal efficacy of 0.5% Cu/TiO_2, pure anatase and rutile with *E. coli* and *S. aureus* upon visible light irradiation for 30 min. Reproduced with permission from [109]. Copyright MDPI, 2018.

Silver nanoparticles with an additional function as a bactericidal agent can be used to modify titania photocatalyst to further enhance its antibacterial performance. From the literature, AgNPs exhibit excellent antibacterial activity against various microorganisms, including *S. aureus*, MRSA, Bacillus subtilis, *E. coli*, *Pseudomonas aeruginosa*, *Klebsiella pneumonia*, and *Acinetobacter baumanii* [253]. Whether metallic Ag^0 or ionic Ag^+ released from AgNPs exerts killing effects on bacteria is still unknown [15,253–255]. The former mechanism involves the adhesion of AgNPs to the cell membrane, leading to membrane damage, the generation of oxidative stress and leakage of cellular contents. Moreover, AgNPs can move into the cytoplasm and interact with biomolecules such as protein and DNA. In some cases, they inactivate and destabilize ribosome, thus inhibiting protein synthesis and generating ROS accordingly. In the case of silver-ion induced toxic effects, released silver ions would interact with the thiol groups of respiratory chain proteins on the membrane, resulting in the disruption

of the bacterial cell wall and the creation of ROS. The electron transport chain for bacterial respiration is located at the bacterial cytoplasmic membrane, since bacteria have no mitochondria (Figure 1). Silver ions can also penetrate into the cytoplasm and react with the thiol groups of cytoplasmic proteins [15,253–255].

As mentioned, AgNPs can induce a collective oscillation of surface electrons under visible light irradiation, thereby creating a hot electron–hole pair and inducing ROS for bacterial inactivation. Thus, AgNPs serve as electron donors for titania, since plasmonic hot electrons are injected into the conduction band of TiO_2 and trigger a photocatalytic disinfection reaction to generate superoxide anion, as shown in Figure 6. Accordingly, AgNPs play the dual role of antibacterial agent and electron donor for Ag-doped TiO_2 NPs [124]. Gupta et al. fabricated Ag-doped TiO_2 NPs with 3% and 7% AgNPs using the sol-gel process. The resulting powders were dried in an oven followed by annealing at 450 °C for 30 min [256]. The photocatalytic activities of the as-synthesized TiO_2, annealed TiO_2, and annealed Ag-doped TiO_2 materials were assessed against Gram negative *E. coli*, Pseudomonas aeruginosa and Gram positive *S. aureus* under visible light. Figure 19a,b shows the viability of *E. coli* and *S. aureus* versus the concentration of catalyst nanoparticles, respectively. The as-synthesized TiO_2 NPs with an amorphous structure inactivates some *E. coli* and *S. aureus* because their negatively charged surface can repel bacteria, resulting in a net negative charge on the cell wall [57]. Annealing treatment at 450 °C induces the crystallization of the anatase phase in TiO_2 NPs. The bactericidal performance of annealed Ag-doped TiO_2 NPs is markedly improved in comparison with the as-synthesized and annealed TiO_2 NPs. The Ag-doped TiO_2 NPs with 7% AgNPs exhibits toxicity to both bacterial strains at 60 mg/30 mL, and at 40 mg/30 mL culture in the case of *P. aeruginosa*.

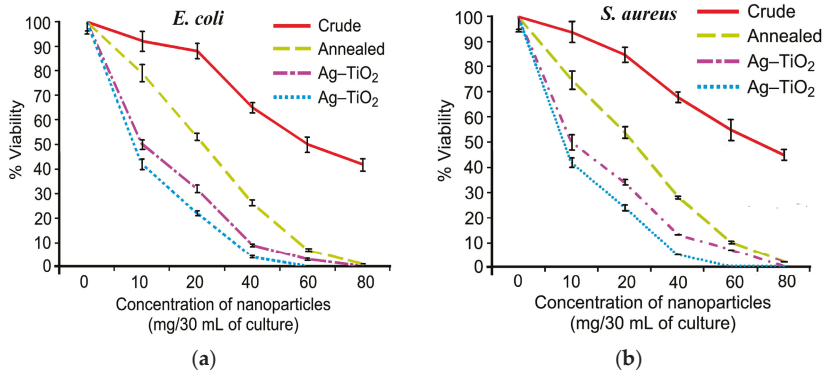

Figure 19. Viability of (**a**) *E. coli* and (**b**) *S. aureus* against the concentration of as-synthesized TiO_2 NPs, annealed TiO_2 NPs, and Ag-doped TiO_2 NPs with 3% AgNPs (dash–dot curve) and 7% AgNPs (dot curve; blue). Reproduced with permission from [256]. Copyright Beilstein-Institut, 2013.

5.1.2. Doped Titania Nanotubes

The photocatalytic activity of one-dimensional TNTs is considerably higher than that of TiO_2 NPs because of their large surface area, high aspect ratio, and good light-harvesting properties [257,258]. Recently, Podporska-Carroll et al. reported that TNTs exhibit very high bactericidal efficiency against *E. coli* (97.53%) and *S. aureus* (99.94%) under 24 h of UV irradiation [259]. Moreover, anodic TNTs exhibit a higher photocatalytic inactivation of bacteria than commercial Degussa P25 TiO_2 powders. To extend the optical absorbance to the visible-light region and improve bactericial performance in this optical regime, noble metal dopants are added to TNTs accordingly. For instance, Viet et al. demonstrated that the 2 wt% Ag/TNTs photocatalyst exhibits higher bactericidal activity against *S. aureus* than pristine TNTs when exposed to sunlight at noontime [53].

Rtimi and coworkers prepared TNTs of different diameters by varying applied voltages from 20 V–70 V during anodizing process. The anodized TNTs were air-dried, annealed for 3 h at 400 °C, and then immersed in a 0.1 M $AgNO_3$; Ag^+ ions were reduced to AgNPs on TNTs using the photoreduction method [260]. A low voltage of 20 V was not favorable for the formation of TNTs. The average diameters of TNTs under applied voltages of 40, 50, 60 and 70 V were 59.6, 93.6, 96.6 and 100. 9 nm, respectively. The tube diameter increased with increasing applied voltage. Figure 20a shows the bacterial survival rate of *E. coli* on pristine TNTs and Ag-decorated TNTs of different diameters upon exposure to solar-simulated light (50 mW/cm^2). The used light intensity corresponds with the overcast daylight dose. Pristine TiO_2–NTs inactivate 1.6log E coli within 180 min. Negatively charged TNTs tend to repel *E. coli* with a negative surface charge, giving rise to a low level of antibacterial activity. From this figure, a stronger *E. coli* inactivation can be achieved by increasing the diameter of TNTs. The Ag/TNTs with diameters of 96.6 nm and 100.9 nm exhibit excellent bacterial inactivation compared with neat TNTs. These two samples require 90 min for inactivating 99.99% *E. coli* upon exposure to solar-simulated light. The bacterial inactivation is attributed to the generation of ROS as a result of the plasmonic oscillation of surface electrons of AgNPs caused by solar-simulated light irradiation. This, in turn, leads to the generation of an electron–hole pair in TNTs to create ROS (Figure 20b). Free radicals abstract electrons from the lipid molecules of bacterial membrane, leading accordingly to lipid peroxidation and membrane damage.

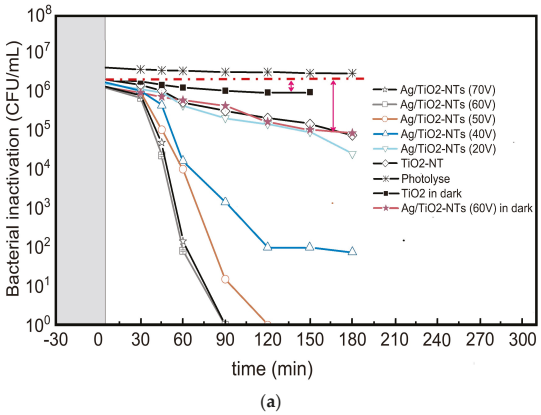

(**a**)

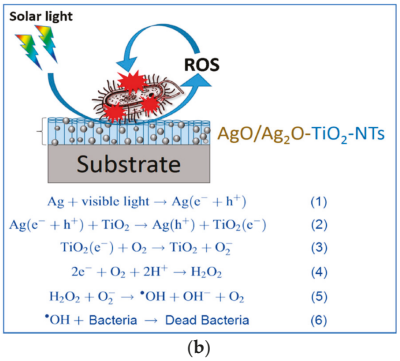

(**b**)

Figure 20. (**a**) Bacterial inactivation on neat TiO_2–NT and Ag/TNTs photocatalysts exposed to solar-simulated light (50 mW/cm^2, 310–800 nm). Error bars: standard deviation; $n = 5$. (**b**) Bacterial inactivation mechanism of Ag/TNTs, as described by Reaction (1–6). Reproduced with permission from [260]. Copyright Elsevier, 2018.

The AgNPs of silver-decorated TNTs also play the role of antibacterial agent through the released Ag^+ ions. Uhm et al. fabricated Ag-doped TNTs by depositing a thin silver layer onto anodized TNTs via magnetron sputtering for different time periods [261]. The TNTs samples coated with silver for 60, 120 and 180 s were designated as ANS 60, ANS 120 and ANS 180, respectively. A longer sputtering time induced more AgNPs formation on the nanotubes, as expected. To assess the silver-ion induced toxic effect on the *S. aureus*, Ag^+ ion, released in phosphate-buffered saline (PBS) and plate counting methods was employed in their study (Figure 21a,b). From Figure 21a, all Ag-doped TNTs samples showed excellent antibacterial activity compared to commercially pure Ti (cpTi) and pristine TNTs. This was attributed to the released Ag^+ ions from the Ag-doped TNTs for bacterial inactivation (Figure 21b). Such an antibacterial effect was unrelated to photoactivity. A profound difference in bacterial reduction in terms of CFU was seen between neat TNTs and Ag-doped TNTs.

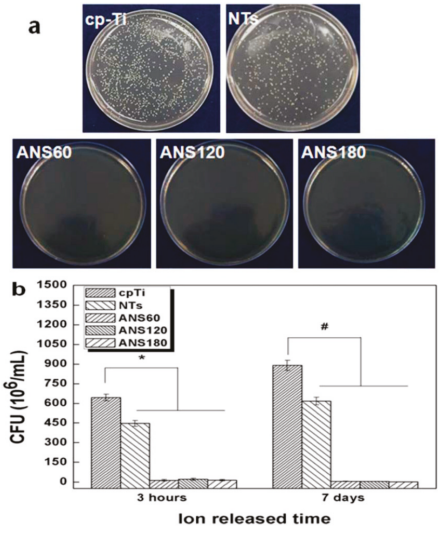

Figure 21. (a) Photographs showing the spread of *S. aureus* on commercially pure titanium (cpTi), titanium nanotubes (NTs) and Ag-doped TNTs samples. (**b**) Antibacterial efficacy of all samples immersed in PBS for 3 h and 7 d. The error bars are the standard deviation ($n = 5$); * denotes $p < 0.05$ compared with cp-Ti at a 3 h ion extraction time, # denotes $p < 0.05$ compared with cp-Ti at 7 days ion extraction time. Reproduced with permission from [261]. Copyright Wiley, 2014.

5.2. Non-Metal Doping

Non-metal dopants such as nitrogen, carbon, and boron are typically employed to replace lattice oxygen anions of titania, in order to narrow its bandgap and extend the optical absorption edge to the visible regime, thereby increasing photocatalytic activity. This in turn leads to an improvement in its antibacterial properties under visible light [161,202,246,262–265]. The visible light response originates from the presence of localized energy levels of the dopant lying above the valence band, thus shifting the VB level upward (Figure 8) [97,159–164]. Among those dopants, nitrogen has a size comparable to oxygen, so it can be readily doped into the TiO_2 lattice in either substitutional or interstitial sites. The N-2p orbital hybrids with the O-2p state, leading to the band gap narrowing. Recently, Ananpattarachai et al. prepared N-doped TiO_2 NPs using the sol-gel technique with diethanolamine acting as the N source. For the purposes of comparison, they also prepared Ni-doped TiO_2 NPs by adding $NiSO_4(H_2O)_6$ to the Ti-sol. The as-synthesized N- and Ni- doped TiO_2 NPs powders were calcined at 600 °C [161]. The bandgaps of N-doped TiO_2 NPs and Ni-doped TiO_2 NPs were determined to be 2.1 eV and 2.97 eV, respectively. The antibacterial activities of the photocatalysts

were assessed using *S. aureus* and *E. coli* strains under visible light irradiation. Figure 22 shows the photocatalytic inactivation of *S. aureus* with neat TiO_2, N-doped TiO_2 NPs and Ni-doped TiO_2 NPs. Apparently, N-doped TiO_2 NPs are more effective than Ni-doped TiO_2 NPs for *S. aureus* inactivation due to their smaller bandgap. Nearly 90% of *S. aureus* cells are inactivated by N-doped TiO_2 NPs within 300 min. The complete inactivation time for *S. aureus* is 360 min. In contrast, the complete inactivation time for *E. coli* is 420 min (not shown). Figure 23 displays the photocatalytic inactivation of *S. aureus* with different concentrations of N-doped TiO_2 NPs and Ni-doped TiO_2 NPs. The survival of *S. aureus* with N-doped TiO_2 NPs under visible light is smaller than with Ni-doped TiO_2 NPs. Figure 24 shows the photocatalytic inactivation of *E. coli* with different concentrations of N-doped TiO_2 NPs. The inactivation efficacy of Gram-positive *S. aureus* using N-doped TiO_2 NPs is higher than that of Gram-negative *E. coli* under visible light illumination. According to the literature, carbon dopant is also beneficial in improving the visible light absorption of TiO_2 NPs and photocatalytic inactivation of anthrax, a fatal bacterial disease that occurs in animals and can transmit to humans, and is caused by Gram-positive Bacillus anthracis [264].

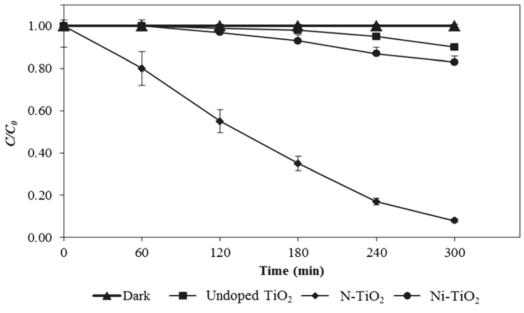

Figure 22. Survival ratio (C/Co) of *S. aureus* with neat TiO_2, N-doped TiO_2 NPs and Ni-doped TiO_2 NPs under an 18 W visible light irradiation for different time periods. *S. aureus* without TiO_2 in the dark is used as a control. Statistically significant at $p < 0.05$. Reproduced with permission from [161]. Copyright Springer, 2016.

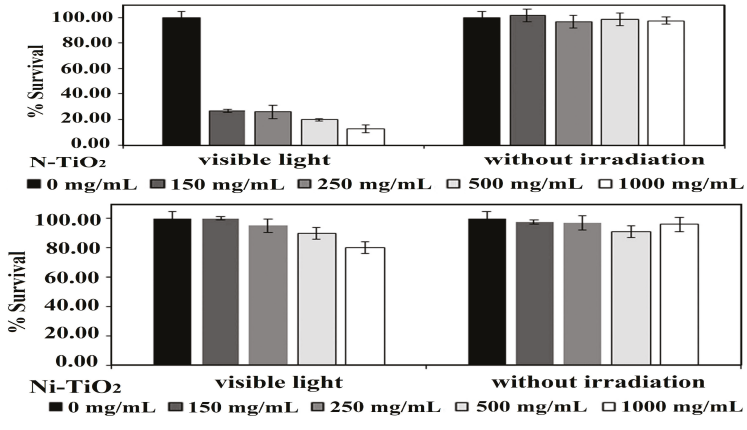

Figure 23. Photocatalytic inactivation of *S. aureus* with N- and Ni-doped TiO_2 NPs of different contents under visible light. Statistically significant at $p < 0.05$. Reproduced with permission from [161]. Copyright Springer, 2016.

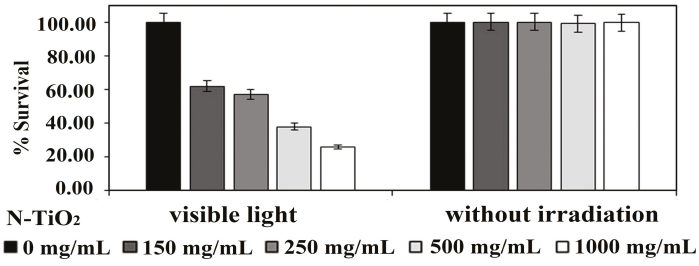

Figure 24. Photocatalytic inactivation of *E. coli* with N-doped TiO_2 NPs of different concentrations under an 18 W visible light. Statistically significant at $p < 0.05$. Reproduced with permission from [161]. Copyright Springer, 2016.

He et al. fabricated N-doped TiO_2 NPs (30 nm) using the sol-gel technique. The photocatalytic and bactericidal behaviors of N-doped TiO_2NPs against *E. coli* under dark and simulated-sunlight conditions were investigated [265]. The bacterial inactivation of this catalyst reaches 90% under simulated sunlight for 2 h, much higher than in the dark. Figure 25 displays photographs of neat TiO_2 and N-doped TiO_2 NPs treated with *E. coli* in the dark for 24 h, and under visible light for 2 h. Bacteria grows into colonies on these samples in the dark (top panel). However, N-doped TiO_2 can inactivate *E. coli* by irradiating with simulated-sunlight for 2 h (bottom panel).

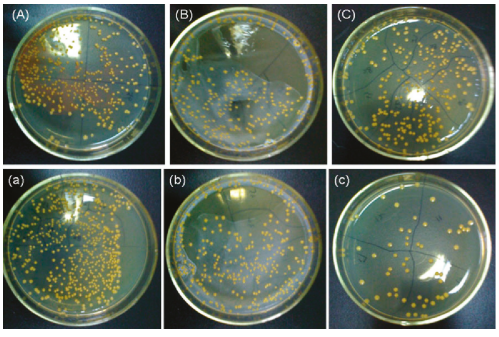

Figure 25. Photographs of *E. coli* colonies developed on agar plates treated with (**A**) control, (**B**) TiO_2 and (**C**) N-doped TiO_2 samples in the dark for 24 h. (**a**–**c**) are the images of *E. coli* colonies under visible light irradiation for 2 h. (**a**): control, (**b**): neat TiO_2, and (**c**) N-doped TiO_2. Reproduced with permission from [265]. Copyright Springer, 2013.

From the literature, fluorine doping does not shift the bandgap of TiO_2. Fluorine dopant stabilizes anatase TiO_2 up to 1200 °C [75,266]. The replacement of lattice oxygen with fluorine in TiO_2 converts Ti^{4+} to Ti^{3+} as a result of the charge compensation between F^- and Ti^{4+} [165]. The Ti^{3+} ions suppress the recombination rate of photogenerated charge carriers, thereby enhancing photocatalytic activity. The substitution of fluorine for oxygen in the titania lattice gives rise to a dramatic increase in oxygen vacancy concentrations [175,267]. The visible-light photocatalytic activity of F-doped TiO_2 can be further enhanced by co-doping with N [268]. Thus, the co-doping approach is an effective route to tune the energy band level of TiO_2 NPs to enhance photocatalytic reactions. Figure 26a shows the charge-transfer mechanism for visible-light excitation of N−F co-doped TiO_2. A series of charge transfer events take place during visible light irradiation. In the process, electrons are excited from the N midgap state to the conduction band, and the corresponding holes generated in the N-state are filled by electrons from the Ti^{3+} level. Oxygen vacancies (O_{vac}) also donate electrons to the empty N-state. Moreover, the conduction band can transfer electrons to the oxygen vacancies. This cascade effect

facilitates the continuous generation of superoxide anion and hydroxide radical species [268,269]. The ROS then cause the destruction and death of microorganisms accordingly.

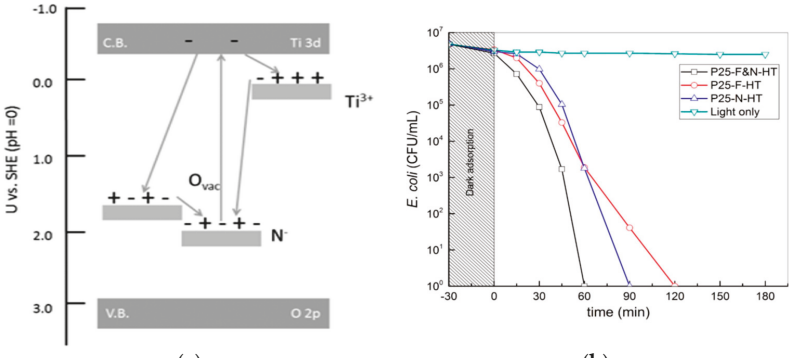

Figure 26. (**a**) Visible light excitation of N−F codoped TiO_2 and subsequent filling of empty N state by electron transfer from either Ti^{3+} or oxygen vacancies (O_{vac}). Reproduced with permission from [268]. Copyright American Chemical Society, 2014. (**b**) Survival rate of *E. coli* treated with N-doped P25 (P25-N-HT), F-doped P25 (P25-F-HT) and (3) F-N codoped P25 (P25-F&N-HT) under simulated light illumination. Reproduced with permission from [270]. Copyright MDPI, 2017.

Milosevic et al. fabricated N-doped and F-doped TiO_2 by wet milling Aeroxide® P25 (21 nm) powders in the presence of glycine (N source) or polytetrafluoroethylene (PTFE; fluorine source), respectively [270]. For the preparation of F−N-co-doped P25, both glycine and PTFE were added during wet milling. The resulting N-doped P25 was heat-treated at 500 °C for 1 h, while F-doped P25 and F−N-doped P25 were calcined at 600 °C for 1 h. Figure 26b shows the survival rate of *E. coli* treated with F-doped P25, N-doped P25, and F−N-co-doped P25 under visible light irradiation. The complete bacterial inactivation times for F-doped P25, N-doped P25 and F−N-co-doped P25 catalysts are 120 min, 90 min and 60 min, respectively. Apparently, codoping P25 with F and N leads to the F−N-doped P25 catalyst with the best bactericidal performance. This is attributed to a synergistic effect between F and N dopants, creating a series of charge transfer reactions, thereby inducing ROS for bacterial inactivation (Figure 26a). In another study, Milosevic et al. prepared F-doped TiO_2 NPs by means of solution precipitation through the hydrolysis of titanium oxychloride, using urea and ammonia as the precipitation agents, and potassium fluoride as the fluorine source. This was followed by wet milling in glycine, and the resulting F−N-doped TiO_2 powders were calcined at 500 °C for 1 h [271]. The complete bacterial inactivation times for F-doped TiO_2 and F-N codoped TiO_2 are 75 min and 60 min, respectively.

5.3. Graphene and MWNT Modified Titania Nanocomposites

A graphene sheet with sharp edges can act as a 'nanoknife' for killing microorganisms during the direct contact of bacteria with the sheet edges. In addition, graphene with a lateral dimension of several micrometers can effectively wrap and isolate bacteria from the environment, thus stopping the supply of nutrients [272,273]. A direct contact of the bacterial cell wall with graphene may also lead to the induction of oxidative stress, resulting in the physical disruption of lipid bilayers and the generation of ROS [274,275]. In this respect, the inclusion of rGO to TiO_2 NPs can produce novel photocatalysts with improved antibacterial performance. There are few studies in the literature reporting bacterial inactivation of rGO/TiO_2 photocatalysts [101,102,276,277].

More recently, Wanag et al. fabricated (0.5–2.5 wt%) rGO/TiO_2 NPs using hydrothermal process at 180 °C for 4 h. The resulting products were finally heated in a furnace at 100 °C for 4 h [101].

Figure 27A,B shows the survival rate of *E. coli* treated with (0.5–2.5 wt%) rGO/TiO_2 NPs in the dark and under artificial solar light irradiation, respectively. Little change in the bacterial populations is seen in the dark condition. The complete bacterial inactivation times for TiO_2 NPs, 0.5% rGO/TiO_2 NPs, 1.5% rGO/TiO_2 NPs, and 2.5% rGO/TiO_2 NPs samples are 105, 90, 75 and 85 min, respectively. It appears that the 1.5% rGO/TiO_2 NPs photocatalyst exhibits the best bacterial inactivation effect.

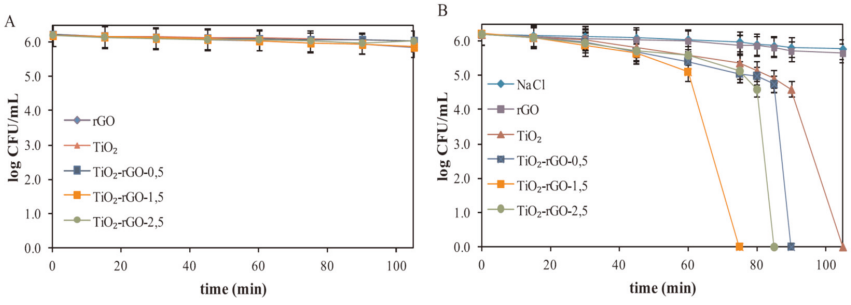

Figure 27. Inactivation of *E. coli* in the presence of rGO, TiO_2 and (0.5–2.5 wt%) rGO/TiO_2 samples in (**A**) dark contition and (**B**) under artificial solar light irradiation. Reproduced with permission from [101]. Copyright Elsevier, 2018.

Nica et al. determined the minimum inhibitory concentration (MIC) and minimum biofilm eradication concentration (MBEC) values of rGO/1%Fe–N-doped TiO_2 nanocomposites prepared by a hydrothermal synthesis of mixed 1%Fe–N-doped TiO_2 and GO solutions at 150 °C for 2 h [277]. Two different precipitation strategies were adopted to yield 1%Fe–N-doped TiO_2 powders. Sample A solution was prepared through a simultaneous precipitation of Ti^{3+} and Fe^{3+} ions by mixing desired amounts of $TiCl_3$ and $FeCl_3.6H_2O$ in water, with a subsequent addition of NH_4OH to maintain an alkaline pH of 9. This solution was hydrothermally treated at 200 °C for 2 h, and the resulting powders were calcined at 400 °C for 2 h. Sample B solution was made via a sequential precipitation of these two cations. The Ti^{3+} ions were first precipitated and oxidized to Ti^{4+} followed by the addition of Fe^{3+} ions in an alkaline reaction medium. The purpose of this was to attain a higher iron concentration on the surfaces of synthesized powders [242]. The antibacterial activity of rGO/1%Fe–N-doped TiO_2 nanocomposites was assessed with *S. aureus*, *E. coli*, *P. aeruginosa* and Candida albicans (a type of fungus). Figure 28 shows the the MIC and MBEC values of rGO/1%Fe–N-doped TiO_2 nanocomposites irradiated with visible light. MIC is generally defined as the lowest antimicrobial agent concentration inhibiting visible growth of bacteria, whereas MBEC is the lowest concentration of an antimicrobial agent needed to kill a bacterial biofilm [278,279]. Compared with commercial P25, rGO/1%Fe–N-doped TiO_2 nanocomposites made from the respective Sample A and Sample B solutions exhibit a much higher antibacterial activity under visible light exposure than Gram-positive *S. aureus*, Gram-negative *E. coli*, and *P. aeruginosa*. The MIC value of rGO/doped TiO_2 nanocomposites for *E. coli* and *S. aureus* is 2.5 µg/mL, four times smaller than that of P25.

Akhavan et al. prepared MWNT/TiO_2 thin films with 2–40 wt% MWNTs by sol-gel technique. The films were deposited on the glass slides by the dip coating method followed by annealing at 450 °C in air for 1 h to yield anatase phase, thereby forming Ti–C and Ti–O–C bonds [155]. The 20 wt% MWNT/doped TiO_2 film inactivated *E. coli* completely under visible light irradiation for 60 min. They attributed bactericidal effects of 20 wt% MWNT/doped TiO_2 nanocomposite to an efficient charge transfer between the MWNTs and TiO_2 due to the formation of a Ti–C and Ti–O–C bond, and a reduction in the electron–hole recombination rate, leading to an increase in the production of hydroxyl radicals for photocatalytic inactivation. Very recently, Koli et al. fabricated (0.1–0.5 wt%) MWNT/doped TiO_2 nanocomposites using the solution-mixing method. The final products were centrifuged and calcinated in air at 450 °C for 5 h [156]. The 0.5 wt% MWNT/doped TiO_2 nanocomposite exhibited complete

killing for *S. aureus* and *E. coli* under visible light irradiation for 180 and 300 min, respectively. However, nanocomposites with 0.3 wt% and 0.1 wt% MWNTs only showed 80% and 90% inhibition for *S. aureus*. In another study, Koli et al. prepared (0.1–0.5 wt%) MWNT/Fe-doped TiO_2 nanocomposites using the sol gel process. The 0.5 wt% MWNT/Fe-doped TiO_2 nanocomposite showed 100% inactivation for Gram-positive Bacillus subtilis under visible light illumination for 120 min. However, nanocomposites with 0.1 wt% and 0.3 wt% MWNTs exhibited complete inhibition at 180 min [157]. In the case of Gram-negative Pseudomonas aeruginosa, MWNT/Fe-doped TiO_2 nanocomposites with 0.1, 0.3 and 0.5 wt% MWNTs required 240 and 300 min, respectively, for complete bacterial killing. The photocatalytic inactivation of these bacterial strains derived from the effective generation of ROS under visible light irradiation.

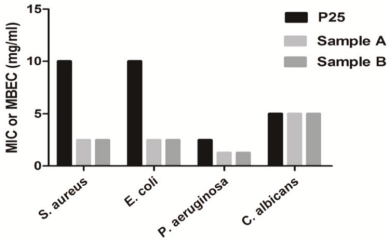

Figure 28. MIC and MBEC values of rGO/1%Fe-N-doped TiO_2 nanocomposites and commercial P25 TiO_2 treated with *S. aureus*, *E. coli*, *P. aeruginosa* and fungal C. albicans under visible light at 37 °C for 24 h. Reproduced with permission from [277]. Copyright MDPI, 2017.

5.4. Coupled Semiconductors

Limited studies are available in the literature on the visible-light photocatalytic bactericidal activity of oxide semiconductor heterojunctions [177,179]. Recently, Janczarek et al. studied the antibacterial performance of cuprous oxide/titania nanocomposites prepared by mechanically mixing Cu_2O with TiO_2 powders of different structures including pure anatase TiO_2 (8 nm), pure rutile TiO_2 (16 nm) and Aeroxide® TiO_2 P25 in an agate mortar [177]. Figure 29a–d shows the antibacterial performance of pure Cu_2O and Cu_2O/TiO_2 nanocomposites against *E. coli* in the dark, under UV and visible light irradiation, respectively. Pure Cu_2O displays high bactericidal activity under UV or visible light irradiation due to the intrinsic activity of Cu^+ ions (Figure 29a). Pure anatase TiO_2 NPs with a negative charge surface show little bacterial inactivation in the dark as they repel negatively charged bacteria to a lesser degree [44,57]. However, their antibacterial activity improves substantially under UV light irradiation as a result of the ROS generation. By coupling anatase TiO_2 with Cu_2O, the Cu_2O/anatase shows enhanced antibacterial activity in the dark, under UV or visible light irradiation (Figure 29b; solid curve). The bactericidal activity of Cu_2O/anatase in the dark is caused by the Cu^+ ions in Cu_2O. The enhanced bactericidal activity of this sample under visible light is attributed to the interfacial charge transfer of electrons from Cu_2O to TiO_2 across the heterojunction interface. This prolongs the lifetime of charge carriers, such that they can take part in photocatalytic reactions. Cu_2O generates electron–hole pairs readily under visible light irradiation due to its small bandgap of 2.17 eV. Under UV light irradiation, the interfacial charge transfer from TiO_2 to Cu_2O, and the inhibition of charge carriers' recombination contribute to an enhancement in bactericidal activity. In contrast, unmodified rutile and Cu_2O/rutile show slower antibacterial activity under UV or visible light irradiation (Figure 29d).

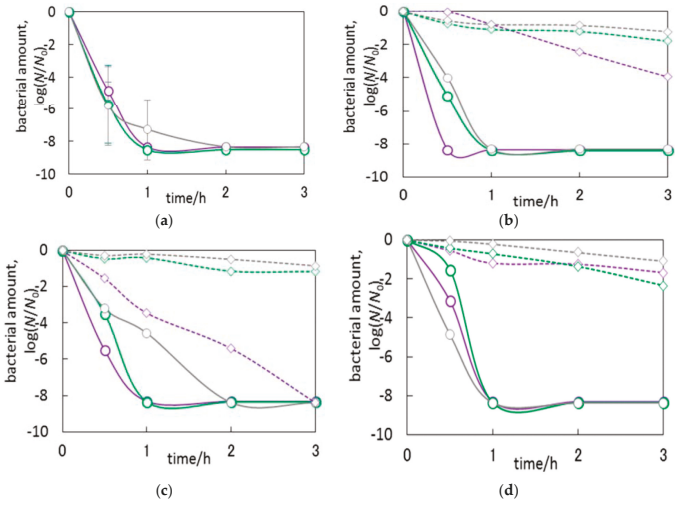

Figure 29. Survival of *E. coli* in CFU/mL treated with (**a**) Cu_2O, (**b**) Cu_2O/anatase TiO_2, (**c**) Cu_2O/P25, and (**d**) Cu_2O/rutile TiO_2 in solid curves with circle symbols; grey color (dark condition), violet (UV irradiation) and green (visible light). Umodified anatase TiO_2, P25 and rutile TiO_2 results are shown in dashed curves with diamond symbols in grey (dark condition), violet (UV irradiation) and green (visible light). Error bars in Cu_2O: standard deviation determined from two or three independent measurements. Reproduced with permission from [177]. Copyright MDPI, 2018.

5.5. Polymer/Titania Nanocomposites

Novel polymer nanocomposites with enhanced chemical, thermal and mechanical properties can be designed and developed by adding functional nanofillers of unique properties [26,26,68–72,280,281]. Such polymer nanocomposites show great potential for structural, electronic, environmental and biomedical engineering applications. The polymeric matrix of nanocomposites immobilizes nanofillers and offers protection to the fillers from mechanical damage. The extent of property enhancement in the polymer nanocomposites depends greatly on the homogeneous dispersion of the fillers, and good interfacial bonding between the filler and polymer matrix [280]. The polymers employed for forming nanocomposites can be either degradable or nondegradable, depending on their intended application. Degradable polymers such as PLA, polyvinyl alcohol (PVA), poly(ε-caprolactone) (PCL) and chitosan are generally used to form scaffolds and wound dressings [26,65,282–285]. These polymers should have the ability to degrade with time and to heal the wounds.

Titania nanomaterials have been incorporated into polymers to form antibacterial coatings, food packaging materials, medical implants, wound dressings and scaffolds [59–65,229,286,287]. However, those studies are mainly focused on the bactericidal properties of the polymer nanocomposites with TiO_2 nanomaterials under UV irradiation. However, it is impractical to use a UV source to excite electron–hole pairs in the polymer–TiO_2 NP system for applications in theb medical sector and food industry. Therefore, the development of visible-light active polymer–TiO_2 nanocomposites is considered of technological interest and practical importance [288–293].

The bactericidal activity of polymer–TiO_2 nanocomposites under visible light also depends on the type of polymers employed. In particular, natural chitosan (CS) with biodegradable behavior can bind to TiO_2 NPs through its amino and hydroxyl groups, thereby extending the optical absorption of TiO_2 NPs into the visible region. The CS/TiO_2 nanocomposites exhibit a red shift in absorption in their UV-vis spectra [289,292,294]. The bandgap of TiO_2 NPs in CS/TiO_2 nanocomposites is then reduced from 3.20 to 3.00 eV [292]. As such, CS/TiO_2 nanocomposites exhibit the photocatalytic inactivation of microorganisms under visible light. Accordingly, CS/TiO_2 films find useful application

as antimicrobial wrapping films for vegetables and fruits under visible light. Thus, TiO_2 nanofillers can delay the ripening process of fresh produce [289,295]. Very recently, Zhang et al. fabricated a CS/TiO_2 nanocomposite film for wrapping red grapes. They assessed the antimicrobial activity of the film against food-borne pathogenic microbes, including *E. coli*, *S. aureus*, C. albicans, and Aspergillus niger (mold) [289]. They found that the film exhibited a good microbial inactivation effect, with complete sterilization for all microbial strains within 12 h. The composite film was very effective in protecting red grapes from microbial attack, thereby extending their shelf-life and improving the quality of fresh fruit accordingly (Figure 30a–c). Moreover, pure CS film also shows antibacterial effect to a certain degree. In contrast, grapes were spoiled and mouldy in the plastic wrap, as expected.

Figure 30. Photographs showing the preservation of red grapes wrapped with (**a**) plastic film, (**b**) chitosan film, and (**c**) chitosan-TiO_2 film at 37 °C for six days. Reproduced with permission from [289]. Copyright Elsevier, 2017.

It is noteworthy that CS/TiO_2 nanocomposites also find medical applications as antibacterial scaffolds in the presence of visible light. Biodegradable chitosan has been used as a scaffold in orthopedics, particularly for bone tissue engineering. The hydrophilic behavior of CS facilitates the adhesion and growth of bone cells (osteoblasts) on its surface [296]. However, a pure chitosan scaffold suffers from poor mechanical strength, so it is unable to provide sufficient mechanical support for the proliferation of osteoblasts during the bone healing process. Therefore, TiO_2 NPs and AgNPs are added to CS to improve mechanical strength [65]. Recently, Raut et al. enhanced the visible-light bacterial inactivation of the CS/TiO_2 NPs nanocomposite by including a Cu dopant into TiO_2 NPs (denoting as CT) through the sol-gel process. The CT nanofillers were then solution-mixed with CS to yield CS/Cu-doped TiO_2, denoted as CS-CT [288]. Figure 31a shows the bactericidal activity of CS, CT and CS–CT samples against *E. coli* under visible light. A 100% bacterial inactivation time is achieved in 240 min by CT and 120 min by CS–CT. Therefore, a synergistic effect exists between Cu-doped TiO_2 NPs (CT) and C, thereby giving rise to a faster bacterial reduction time of 120 min. Figure 31b shows the effect of an *OH radical, generated by the photoexcitation of an electron–hole pair, in destroying *E. coli*.

Antibacterial polymer/TiO_2 nanocomposites also find attractive applications in textile industries for producing odorless and self-cleaning fabrics. Clothing fabrics are prone to microbial contamination, and can spread infections accordingly. The clothes generate a warm and humid environment on human skin, causing the secretion of sweat and bacterial growth [297]. Cotton consists of natural cellulosic fibers that absorb more sweat than synthetic polymer fabrics. Thus, cotton clothes tend to keep the body dry while absorbing sweat. Very recently, Zahid et al. prepared Mn-doped TiO_2 NPs (150 nm) by the sol-gel method, and then applied the spray coating technique to apply Mn-doped TiO_2 NPs on cotton fabrics. NPs0, NPs10, NPs25 and NPs50 were designated to the cotton fabrics with zero, 10, 25 and 50 wt% Mn-doped TiO_2 NPs, respectively [298]. The fabrics with and without Mn-doped TiO_2 NPs in the dark exhibited no bactericidal effect because no photocatalytic excitation occurred in the absence of light. The NPs10 and NPs 25 reduced the *S. aureus* population by 80% and 90% within the first 60 min, respectively, while NPs50 and NPs50W reduced nearly ~100% *S. aureus* population in the same period under sunlight (Figure 32a). A lower bacterial inactivation rate was found for the fabrics with Mn-doped TiO_2 NPs and treated with *K. pneumoniae* in the first 60 min (Figure 32b). The presence of Mn ions dopant promoted the generation of an electron–hole pair in TiO_2 fillers for creating ROS under visible light, as shown in Figure 32a,c. Apart from its antimicrobial activity, the photocatalytic

effect also removed or degraded color stains on the fabrics, thus performing self-cleaning, as shown in Figure 32c. The visible-light antibacterial activity of modified titania nanomaterials is summarized in Table 2.

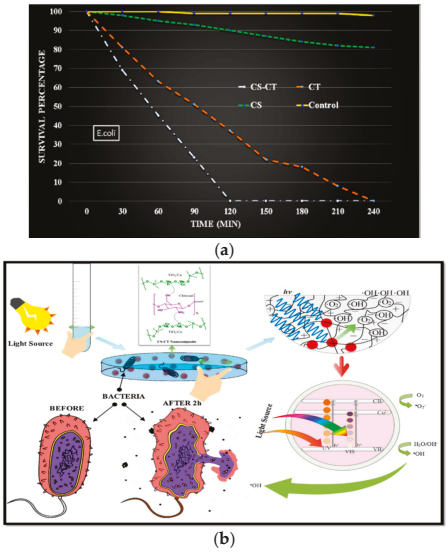

(**a**)

(**b**)

Figure 31. (**a**) Antibacterial activity of CS, CT and CS–CT samples against *E. coli* under visible light illumination. (**b**) Mechanism of antibacterial activity of CS/Cu-doped TiO_2 nanocomposite. Reproduced with permission from [288]. Copyright Elsevier, 2011.

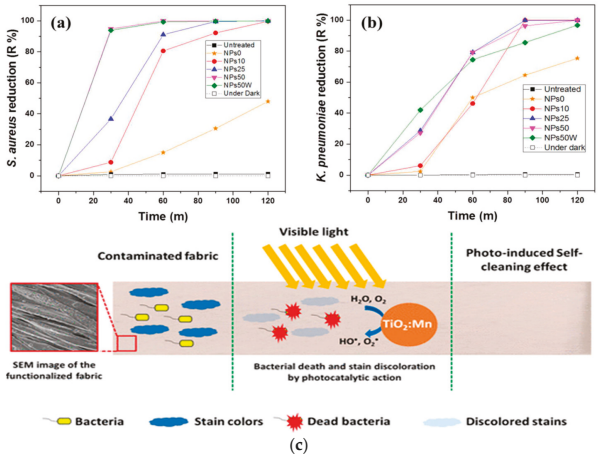

(**c**)

Figure 32. Bacterial reduction in percentage of (**a**) *S. aureus* and (**b**) *K. pneumoniae* on cotton fabrics with and without Mn-doped TiO_2 NPs in the dark and under natural sunlight. NPs0, NPs10, NPs25 and NPs50 are cotton fabrics with zero, 10, 25 and 50 wt% Mn-doped TiO_2 NPs; NPs50W is the NPS50 after 10 washing cycles. (**c**) Schematic of visible light induced the photocatalytic inactivation of bacteria and degradation of stain residues on contaminated fabric with Mn-doped TiO_2 NPs. Reproduced with permission from [298]. Copyright American Chemical Society, 2018.

Table 2. Bactericidal performance of modified titania nanoparticles under visible light.

Material	Size, nm	Bacteria	Complete Inactivation Time	Ref.
(1–3 mol%) Ni/TiO_2 NPs	8–10	*E. coli* *S. aureus* *Samonella abony*	>300 min (3% Ni dopant) >240 min (3% Ni dopant) >360 min (3% Ni dopant)	[248]
(1–3 mol%) Cu/TiO_2 NPs	9–10	*E. coli* *S. aureus*	240 min (3% Cu dopant) 120 min (3% Cu dopant)	[247]
0.5%Cu/TiO_2 NPs	28.84	*E. coli* *S. aureus*	30 min 30 min	[109]
Ag/TiO_2 NPs	AgNPs: 0.9; TiO_2 NPs: 8	*E. coli*	60 min	[124]
N/TiO_2 NPs	10–30	*E. coli* *S. aureus*	420 min 360 min	[161]
F-N doped P25	70	*E. coli*	60 min	[270]
F-N doped TiO_2	21.3	*E. coli*	60 min	[271]
(0.5–2.5%) rGO/TiO_2 NPs	17–18	*E. coli*	75 min (1.5% rGO/TiO_2 NPs)	[101]
(0.1–0.5%) MWNT/TiO_2 NPs	TiO_2 NPs: 8–15 MWNT diameter: 20–45	*E. coli* *S. aureus*	300 min (0.5% MWNT/TiO_2) 180 min (0.5% MWNT/TiO_2)	[156]
0.5 wt% MWNT/Fe-doped TiO_2	Fe-doped TiO_2: 15–20 MWNT diameter: 20–45	*B. subtilis* *P. aeruginosa*	120 min 240 min	[157]
Cu_2O/TiO_2	TiO_2 NPs: 8	*E. coli*	60 min	[177]
CS/Cu-doped TiO_2	16	*E. coli*	120 min	[288]
Cotton/(10–50%) Mn-doped TiO_2	Mn-doped TiO_2: 150	*S. aureus* *K. pneumoniae*	90 min (25 wt% Mn dopant) 90 min (25 wt% Mn dopant)	[298]
Cotton/(10–50%) Mn-doped TiO_2	Mn-doped TiO_2: 150	*S. aureus* *K. pneumoniae*	60 min (50 wt% Mn dopant) 120 min (50 wt% Mn dopant)	[298]

6. Biocompatibility and Cytotoxicity

Antibacterial materials and coatings have been a focus of global research topics for the past decade in orthopedics, due to an increasing incidence of implant-related infections caused by MDR bacteria [299]. Medical devices and implants are easily contaminated with microorganisms, leading to the formation of biofilms on their surfaces. Therefore, titania coating is an attractive solution for controlling implant infection by decreasing bacteria adhesion through the introduction of metal nanoparticles (e.g., AgNPs or CuNPs) to the coating [300,301]. Furthermore, titania coating formed on the medical devices should exhibit good biocompatibility with the host tissues. As an example, titania film deposited on polyetheretherketone (PEEK) spinal implant exhibits superior compatibility compared to uncoated PEEK in terms of osteoblastic adhesion, proliferation, and differentiation [302]. Similarly, anodic TNTs of large surface areas formed on Ti-based alloys have been reported to provide anchoring sites for osteoblasts and fibroblasts, thereby promoting cell proliferation effectively [217–219,303–305]. Ti-based alloys (e.g., Ti-6%Al-4%V and Ti-6%Al-7%Nb) are commonly used as the load-bearing prostheses in orthopedics and tooth implants in dentistry. The optimal diameter of TNTs for osteoblastic adhesion and growth is typically below 100 nm [217,218]. Recently, Radtke et al. reported that anodic TNTs formed on the Ti-6%Al-4%V alloy, especially at lower anodic potentials with diameters of 25–35 nm, were effective in promoting the growth of murine fibroblasts L929 [303]. Xu et al. investigated the

biocompatibility of periodontal ligament cells on anodized TNTs of different diameters. Periodontal ligament cells (PDLCs) are the key cells responsible for periodontal tissue regeneration [304]. They demonstrated that the TNTs formed on thin Ti foil substrate favor the adhesion and growth of PDLCs. Furthermore, TNTs promoted the osseointegration of Ti substrate more effectively than untreated Ti foil, as evidenced by the high gene expression levels of alkaline phosphatase, osteocalcin and osteopontin.

6.1. Cytotoxicity

Advanced nanomaterials, prepared by emerging nanotechnology, pose toxicity to humans to a large/lesser extent depending on their structure, chemical composition, shape, distribution, etc. [14,15,306]. Wadhwa et al. reported that hydrothermally synthesized TNTs and TiO_2 NPs exhibit no toxic effect towards the human alveolar carcinoma epithelial cell line (A549) [307]. Standalone and detached TNTs from Ti foil substrate were toxic to human dermal fibroblasts as a result of the ROS generation, leading to DNA damage and chromosomal aberration [308]. Allegri et al. reported that electrospun TiO_2 nanofibers were toxic towards A549 and murine macrophage cell lines (Raw 264.7). The cytotoxic effects were dose-dependent, with larger effects on A549 than on Raw 264.7. However, TiO_2 NPs exert no cytotoxic effect on these two cell lines [309].

As mentioned, TiO_2 NPs have been produced commercially in large quantities for applications in paints, pharmaceutical, food, drug and cosmetic industries [39–56]. The synthesis and handling of TiO_2 NPs during the production process can release a tremendous amount of these nanomaterials into the environment, including air, soil and water. The wastewater of titania production plants is the major source pollutant that leaks into the environment. The nanomaterials are discharged in the sewage sludge and can enter the soil and water ecosystem [310]. Therefore, the disposal and treatment of wasterwater, as well as the recycling of titania from water treatment plants, are considered of technological importance [311]. Moreover, the widespread use of products with TiO_2 NPs would also release such nanoparticles into the environment. For instance, auto-manufacturing plants consume large quantities of titania pigment paints for coating car bodies. Therefore, plaint sludge is always found in the paint-bearing wastewaters. The recycling and reproduction of TiO_2 NPs from the paint sludge are beneficial to both the environmental and industrial sectors for minimizing pollution [312]. Furthermore, embedded TiO_2 NPs in the paint of buildings, bridges and traffic railings could be lost and released into the aquatic environment due to a lengthy outdoor weathering [313]. Some consumer titania products such as food-packages and textiles could also end up as waste, and are disposed of in incinerators and landfills [314]. The wastewater treatment plants remove most TiO_2 NPs in the influent sewage; however, the residual nanoparticles would discharge to natural water ecosystems. In this respect, TiO_2 NPs could potentially induce harmful effects to aquatic organisms, such as impaired metamorphosis and growth, teratogenicity, and mortality of fish larvae [315,316].

6.1.1. Neat TiO_2 NPs

TiO_2 NPs can enter the human body through exposure to workplace atmospheres, the use of commercial products, the ingestion of food and pharmaceuticals. The main routes of entry include skin contact, inhalation, ingestion and medical implants [317]. Accordingly, public concerns have been raised related to the safe use of TiO_2 NPs, and their effects on human health and the environment. Conflicting results are reported in the literature regarding the biocompatibility and cytotoxicity of TiO_2 NPs. Some studies indicate a good biocompatibility of TiO_2 NPs with mammalian cells [166,201,309,318], while others reveal the toxic effects of TiO_2 NPs [319–325]. The discrepancy is attributed to the biological and materials factors involved during in vitro studies. The former factors include the type of culture cells, cell cultivation time and cell-based assays used, while the latter factors include the size, shape, crystal structure (anatase or rutile), and dose of TiO_2 NPs in the assay tests [326].

Wang et al. investigated cytotoxicity in A549 cells induced by TiO_2 NPs (5 nm) using 3-(4,5-dimethylthiazol-2-yl)-2,5-diphenyltetrazolium bromide (MTT), quantitative real-time PCR (qRT-PCR) and comet assays, as well as rhodamine 123 staining [323]. From the MTT results, the

cytotoxic effect of TiO_2 NPs was time- and concentration-dependent (in a range from 50 to 200 μg/mL). Comet assay revealed DMA damage in cells exposed to 50 to 200 μg/mL TiO_2 NPs for 48 h. TiO_2 NPs also decreased the mitochondrial membrane potential as determined by rhodamine 123 (Rh123) staining. The qRT-PCR analysis demonstrated that the expression of caspase-3 and caspase-9 messenger RNA (mRNA) increased dramatically upon exposure to 100 and 200 μg/mL TiO_2 NPs for 48 h. As is known, caspases play the key role in executing apoptosis. Caspase-3 tends to induce DNA bond cleavage and inactivate cytoskeletal proteins. From this perpective, TiO_2 NPs inhibit A549 proliferation, and induce DNA damage and eventual cell apoptosis through the activation of the intrinsic mitochondrial pathway [323].

TiO_2 NPs can penetrate the human body through inhalation, then translocate from the lungs into the bloodstream, and the subsequent uptake in other organs like the heart, liver, spleen and brain. Huerta-Garcia et al. investigated the in vitro toxicity of TiO_2 NPs on rat cardiomyoblasts (H9c2) [327]. They found that the cellular uptake of TiO_2 NPs by H9c2 cells reduces their metabolic activity and cell growth, thus causing mitochondrial dysfunction due to a marked reduction in mitochondrial membrane potential. Furthermore, TiO_2 NPs increase the ROS level and membrane permeability of H9c2 cells greatly, leading to final cell death. Therefore, the internalization and building up of TiO_2 NPs in cardiomyoblasts would induce cardiac damage and pose threats to human health upon inhalation of those nanoparticles. More recently, Mottola et al. studied the genotoxic effect of TiO_2 NPs on human amniotic fluid cells in vitro. The TiO_2 NPs exposure caused DNA strand fragmentation, a loss of viability, and apoptosis of the cells [325].

Yin et al. studied the phototoxicity of TiO_2 NPs (<25 nm, 31 nm, <100 nm, and 325 nm) in human skin keratinocytes (HaCaT) under UVA irradiation [328]. TiO_2 NPs induced photocytotoxicity and cell membrane damage in a UVA dose- and TiO_2 NPs dose-dependent manner. The smaller the size of TiO_2 NPs, the higher the cell damage was. The induced photocytotoxic damage was attributed to the ROS generation during UVA irradiation, leading to lipid peroxidation of the plasma membrane. TiO_2 NPs with a large surface-to-volume ratio enhanced biological reactivity by generating ROS. The degree of photocytotoxicity and cell membrane damage depends greatly on the level of ROS generated. More recently, Ren et al. also reported a similar finding on the phototoxicity of TiO_2 NPs in HaCaT cells under UV irradiation [329].

The adverse effects of TiO_2 NPs on mammalian cells, such as DNA damage, the generation of ROS, and apoptosis, addressed in in vitro studies, are supported by in vivo animal models [330–334]. Grassian et al. exposed mice to TiO_2 NPs (2–5 nm; 8.88 mg/m^3; 4 h/day for 10 days) through inhalation. Exposure for 1–2 weeks led to pulmonary inflammation with high cell counts of alveolar macrophages in bronchoalveolar lavage (BAL) fluid [330]. To evaluate the potential respiratory system toxicity, Liu et al. studied the biodistribution of TiO_2 NPs (5, 21 and 50 nm) in rats via intratracheally instillation at doses of 0.5, 5, and 50 mg/kg body weight (bw). Rats were then sacrificed one week post-instillation [331]. Histopathological evaluation of lung tissues revealed a dose-dependent inflammatory lesion. At a specific dose, the pulmonary toxicity induced by 5 nm TiO_2 NPs was more severe than that caused by 21 and 50 nm TiO_2 NPs. In the case of dermal exposure, Wu et al. reported that TiO_2 NPs can penetrate through the skin of hairless mice, and finally reach the liver following a prolonged exposure of 60 days. This led to a remarkable change in malondialdehyde (MDA) level [332]. MDA is a marker of liquid peroxidation and oxidation stress of cells. Therefore, an increase in free radicals produces high levels of MDA. Disdier et al. intravenously administrated P25 TiO_2 NPs of 1 mg/kg into male Fisher F344 rats. They analyzed the biodistribution of Ti level in internal organs of rats using inductively coupled plasma mass spectrometry [333]. Biopersistence of Ti in the main target organs, i.e., the liver, lungs, spleen and kidneys, was observed after intravenous administration for up to 365 days (Figure 33a–d). Jia et al. intraperitoneally injected TiO_2 NPs (5, 10, 60, 90 nm) and TiO_2 microparticles at doses of 5, 10, 50, 100, 150, and 200 mg/kg (once a day for 14 days) into rats (half male and half female). TiO_2 NPs were found to accumulate in the liver, kidney, spleen, lung, brain, and heart through the circulatory system [335]. The liver was damaged seriously due to mitochondrial dysfunction and the ROS generation at TiO_2

NPs doses ≥10 mg/kg, leading to hepatocyte apoptosis. Furthermore, TiO_2 NPs were more toxic than TiO_2 microparticles, as expected. The distribution of TiO_2 NPs in the brain tissue suggested that nanoparticles can enter directly into the central nervous system without crossing the blood–brain barrier. Finally, TiO_2 NPs also caused genotoxicity in the ex vivo mouse embryo models [335].

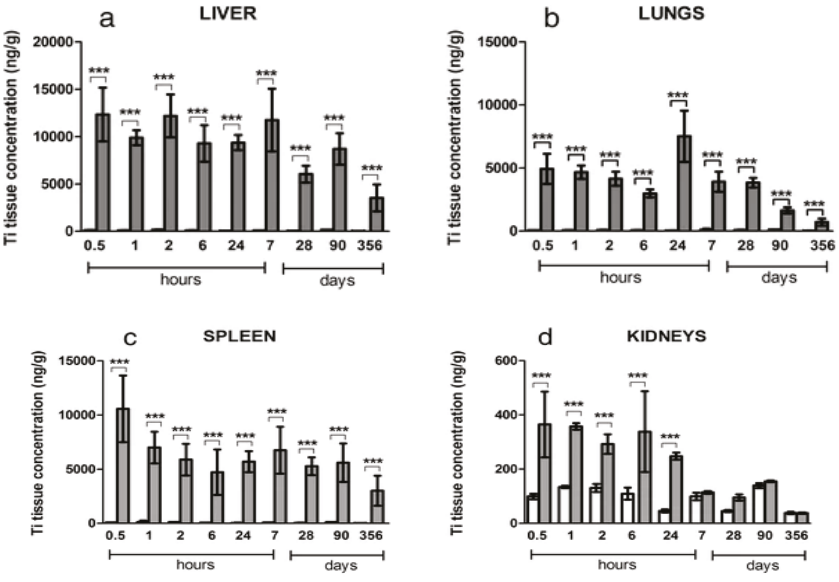

Figure 33. Biopersistence of titanium level in (**a**) liver, (**b**) lungs, (**c**) spleen and (**d**) kidneys after intravenous injection of 1 mg/kg TiO_2 NPs in rats for 365 days. Grey and white bars are treated and control mice, respectively. Error bars represent the mean ± SD and $n = 6$. Statistical comparison is performed by two-way ANOVA, * $p < 0.05$; ** $p < 0.01$; *** $p < 0.001$. Reproduced with permission from [333]. Copyright BioMed Central, 2015.

6.1.2. Metal-Doped TiO_2 NPs

We now consider the effect of metal doping on the cytotoxicity of TiO_2 NPs in human cells. Doping TiO_2 NPs with transition metals and noble metals is an efficient strategy for improving the photocatalytic inactivation of bacteria in the visible region. However, this approach has its own drawback as metal dopants can induce cytotoxicity in human cells. Therefore, metal-doped TiO_2 NPs photocatalysts can fulfill the requirement of bactericidal performance, but they pose potential human health and safety hazards following long-term exposure. Recently, Ahamed et al. employed MTT and neutral red uptake (NRU) assays to assess the metabolic and lysosomal activities of human liver cancer (HepG2) cells exposed to Ag (0.5–5%)-doped TiO_2 NPs [318]. Their results showed that Ag-doped TiO_2 NPs reduce the cell viability in a dose-dependent manner, as shown in Figure 34a,b. Apparently, TiO_2 NPs display no toxic effect to the HepG2 cell. In contrast, Ag (0.5–5%)-doped TiO_2 NPs are toxic, as the Ag-dopant can release zero valent Ag^0 or Ag^+ ion to reduce cell viability through ROS generation [15]. This leads to the leakage of intracellular components at Ag (0.5–5%)-doped TiO_2 NPs doses of ≥25 μg/mL, as evidenced by lactate dehydrogenase (LDH) assay (Figure 34c). Furthermore, cell viability decreases with increasing Ag content in Ag-doped TiO_2 NPs, from 0.5% to 5%, while the ROS level increases with increasing Ag content (Figure 34d).

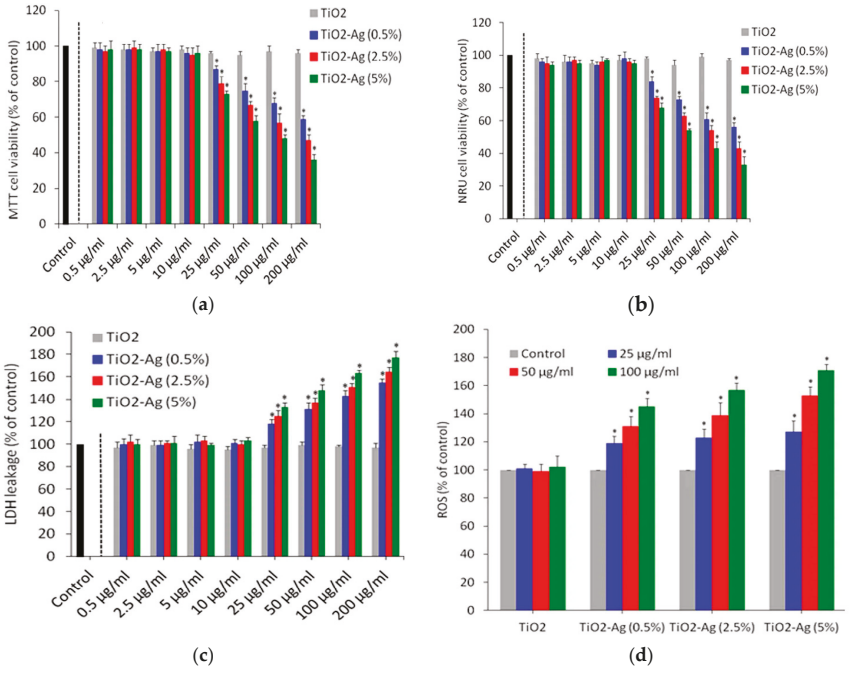

Figure 34. (**a**) MTT, (**b**) NRU, and (**c**) lactase dehydrogenase leakage results of human liver cancer (HepG2) cells exposed to TiO_2 NPs and Ag-doped TiO_2 NPs of different concentrations. (**d**) ROS level of HepG2 cells exposed to pure TiO_2 NPs and Ag-doped TiO_2 NPs of 25, 50 and 100 µg/mL. Reproduced with permission from [318], Copyright Nature Publishing Group, 2017.

6.1.3. rGO-Modified TiO_2 NPs

Jin et al. demonstrated that rGO/TiO_2 NPs would separate independently into TiO_2 NPs and GO after entering A549 cells. The rGO/TiO_2 NPs composite could induce cytotoxicity in A549 due to the generation of oxidative stress [336]. More recently, Prakash et al. prepared rGO (10–50%)/TiO_2 nanocomposites using hydrothermal synthesis, and studied their toxicity in zebrafish embryos and larvae [337]. The toxicity of rGO (10–50%)/TiO_2 nanocomposites was highly dependent on the rGO concentrations and doses. At low concentration and dose levels (10%, 20%, and 30% rGO; 0.25–30 µg/mL), rGO (10–30%)/TiO_2 nanocomposites exhibited no toxicity to the zebrafish embryos. At high doses of 0.125–1.0 mg/mL, all the rGO (10–50%)/TiO_2 nanocomposites induced teratogenicity and cardiotoxicity due to the generation of ROS. Zebrafish (Danio rerio) are aquatic species commonly employed to detect toxicological effects due to their known physiology having a high degree of genetic similarity with mammals, and the optical transparency of the tissues.

7. Prospects and Challenges

Titania has been considered an inert and nontoxic material. It is typically used as a color additive for foods up to 1 wt%, and was approved by the Food and Drug Agency of the United States under Title 21 of the Code of Federal Regulations [338]. The additive contains TiO_2 NPs as described by the E171, European Food Safety Authority (EFSA) of the European Union [339]. Titania is also widely used in toothpaste as a white pigment with a small fraction of TiO_2 NPs. These nanoparticles are also detected in sweets containing E 171, e.g., chewing gum, colored candy, chocolate and cake-icing. The approximate oral ingestion of TiO_2 NPs for the Dutch is 0.19 mg/kg bw/day for elderly, 0.55 mg/kg bw/day for 7–69 year old people, and 2.16 mg/kg bw/day for young children [340]. Very recently,

Hwang et al. demonstrated that commercial TiO_2 additive as outlined by the E171 contains particles with mean size values of 118–169 nm. The TiO_2 additive created ROS and inhibited long-term colony formation in human intestinal epithelial Caco-2 cells at concentrations >125 μg/mL. The additive slightly induced apoptosis at a very high content of 1000 μg/mL upon exposure for 24 h [341]. This result raises a safety concern about the toxic impact of TiO_2 food additives on human health [342]. Heringa et al. reported the presence of TiO_2 NPs in 15 post-mortem human livers and spleens of Caucasians. Those human subjects followed a West European diet and used toothpaste, so this may have resulted from oral intake of TiO_2 NPs [343].

Most in vitro cell cultivation and in vivo animal models tests clearly indicate that TiO_2 NPs are toxic to mammalian cells, since they induce DNA damage, ROS generation, and apoptosis. In particular, Ag-doped TiO_2 NPs act as a double-edged sword, having beneficial and adverse effects. The plasmonic effect of surface electrons of AgNP-decorated TiO_2 NPs promotes light-harvesting in the visible region, as mentioned previously. This inhibits bacterial growth of *E. coli* and *S. aureus* effectively when compared to pure TiO_2 NPs, as shown in Figure 20. Therefore, there exists a synergistic bactericidal effect of TiO_2 and AgNPs through the photocatalytic reaction and Ag^0/Ag^+ species released from the AgNPs. However, metallic Ag^0 and ionic Ag^+ released from AgNPs can elicit a toxic effect on HepG2 cells through ROS generation (Figure 34). Furthermore, AgNPs have been found to induce a toxic effect on mammalian cells in a dose-, size- and time-dependent manner. In vivo animal studies reveal that AgNPs locate preferentially in murine target organs including the liver, spleen, kidney and brain after intratracheal instillation, intravenous or intraperitoneal injection [15].

Standalone and detached TNTs exhibit poor compatibility to human dermal fibroblasts due to ROS generation, leading to DNA damage and chromosomal aberration [308]. Ultrasonication was employed to detach TNTs from the Ti substrate. Standalone TNTs were able to pierce and penetrate through the membrane of fibroblasts, resulting in cytotoxicity. Without ultrasonication, intact TNTs adhered firmly on the Ti substrate, acting as the adhesion and growth sites for murine osteoblasts (MC3T3-E1) and human fibroblasts [226,261]. As such, anodic TNTs exhibited higher osteoblastic viability than pure Ti (Figure 35). After sputtered coating TNTs with silver for 60, 120 and 180 s (designated as ANS 60, ANS 120 and ANS 180), the ANS 60 sample still showed better biocompatibity than pure Ti. However, the cell viability of ANS 120 and ANS 180 samples decreased markedly because a longer sputtering time favored more AgNP formation on the nanotubes. Thus the ANS 180 sample exhibited the lowest cell proliferation. From Figure 21, ANS 60 showed a similar antibacterial actitvity to ANS 120 and ANS 180 samples. Therefore, a balance between bactericidal activity and cellular viability can be reached by monitoring the Ag content in ANS 60. In general, Ti-based alloy implants have inadequate antibacterial activity, so much effort has been made to improve their compatibility and antibacterial properties for clinical applications. Ti-based alloy implants with enhanced antibacterial activity and biocompatibility can be achieved by forming an Ag-doped TNTs surface layer with an optimal Ag content through anodization and sputtering. The modified TNTs formed on Ti-based implants can reduce bacterial colonization on their surfaces accordingly. Alternatively, antibacterial CuNPs can be used to replace AgNPs for doping TNTs with improved biocompatibility [98,99]. CuNPs are less toxic than AgNPs to human and bovine mammary epithelial cells [344].

However, it remains a big challenge for chemists and materials scientists to design novel nanomaterials for technological and medical applications utilizing TiO_2 NPs and doped TiO_2 NPs. With the increasing need for antibacterial scaffolds and wound dressings in tissue engineering, biodegradable polymers are ideal materials to immobilize TiO_2 NPs to form polymer nanocomposites with improved biocompatibility and photocatalytic activity. It is of primary importance to select a proper polymeric material, suitable for those applications. As previously mentioned, mixing chitosan with TiO_2 NPs can yield a biodegradable plastic film with visible light photocatalytic bactericidal activity. The film functions effectively for preserving fresh fruits and vegetables, and for prolonging shelf-life [289]. Such a plastic film can also be used as a food packaging material for killing pathogenic bacteria that causes food poisoning or food spoilage. In addition, biodegradable CS-TiO_2 NPs

film also finds potential applications as antibacterial scaffolds and wound dressings in orthopedics. By incorporating Cu dopant into TiO_2 NPs, the resulting CS/Cu-doped TiO_2 NPs shows higher photocatalytic bactericidal activity, as expected [288].

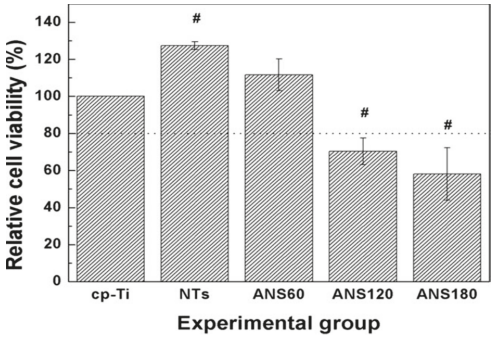

Figure 35. The viability of MC3T3-E1 murine osteoblasts obtained from the MTT assay. Error bars indicate the standard deviation ($n = 5$); # $p < 0.05$ compared with commercial pure Ti (cp-Ti). Reproduced with permission from [261]. Copyright Wiley, 2014.

Finally, antibacterial and self-cleaning fabrics have received considerable attention in hospitals and clinics due to the increased risk of healthcare-associated infections. Those fabrics are particularly useful against nosocomial bacteria to protect patients from harmful microorganisms [298,345]. The fabrics made from cotton/Mn-doped TiO_2 NPs have been reported to exhibit full inactivation of *S. aureus* and *K. pneumoniae* within 120 min under sunlight (Figure 32a,b) [298]. However, one can see that such fabrics need at least 25 wt% Mn-doped TiO_2 NPs for achieving antibacterial properties. Those fillers can be removed from the fabrics upon several washing cycles, and then discharged into rivers and lakes. The recent literature data indicate the toxicity of rGO/TiO_2 NPs in inducing teratogenic effects on zebrafish, although at doses considerably higher than those in aquatic environments [337]. The release of large amounts of Mn-doped TiO_2 NPs would inevitably pollute the aquatic environment, and harm aquatic life in the ecosystem [346]. Moreover, Mn is a heavy metal that is toxic to mammalian cells. Manganese can induce toxicity in human bronchial epithelial cells, leading to caspase-9-mediated cell death [347,348]. Therefore, non-noble metal doped TiO_2 NPs such as the N-doped TiO_2 NPs photocatalyst is considere a potential replacement for Mn-doped TiO_2 NPs for reducing environmental toxicity.

Thanks to the efforts of researchers, visible-light active TiO_2 NPs and their nanocomposites have been found to exhibit a bactericidal effect against drug-resistant bacteria including salmonella abony, *S. aureus*, *K. pneumoniae*, *P. aeruginosa* and anthrax. However, it still requires substantial time and effort to develop visible-light active TiO_2 NPs photocatalysts with both antibacterial activity and good cytocompatibility. Long-term, in vivo animal studies relating to the biocompatibility and cytotoxicity of those photocatalysts are required. More research studies are needed to design the toxic free, green synthesis of visible-light active TiO_2 NPs with bactericidal activity for industrial, environmental and medical applications.

8. Conclusions

This review gives a summary of the synthesis, photocatalytic bacterial inactivation, biocompatibility and cytotoxic effects of visible-light active TiO_2 NPs and their nanocomposites, especially over the past five years. The photocatalytic bactericidal effect of TiO_2 NPs with a wide bandgap depends on the creation of an electron–hole pair under UV irradiation to generate ROS. The created radicals then interact with microorganisms, causing damage to the structure of the cell membrane and the subsequent leakage of intracellular components. However, UV-responsive TiO_2 NPs

exhibit poor photocatalytic efficiency under visible light. It is of practical importance to employ visible light to induce the photocatalytic bactericidal activity of TiO_2 NPs. Considerable progress has recently been made in the development of TiO_2 nanostuctures with good photocatalytic bactericidal activity under visible light irradiation. Visible-light active TiO_2 nanomaterials can be synthetized through several techniques including sol-gel, hydrothermal/solvothermal, electrochemical anodization, and electrospinning. Among these, sol-gel is commonly used for preparing TiO_2 NPs, while electrochemical anodization is an effective method for fabricating TNTs.

Doping TiO_2 NPs with metal and non-metal elements can lead to a red shift in the optical absorption edge into the visible region, resulting in a reduction of the bandgap accordingly. Transition metal elements, such as Mn, Fe, V and Cu, can create a localized d-electron state in the bandgap of TiO_2 NPs, thereby promoting the separation of photogenerated electron–hole pair and suppressing the recombination of charge carriers. However, defect states in the bandgap of titania would also serve as charge recombination centers under experimental conditions of high dopant concentrations. Noble metal dopants such as AgNPs exhibit plasmonic oscillation of surface electrons under visible light irradiation. As such, hot-electron transfer from excited AgNPs into the conduction band of TiO_2 NPs creates ROS for bactericidal activity. In addition to photocatalytic bactericidal activity, AgNPs of Ag-doped TiO_2 NPs can inactivate bacteria through the release of Ag^+ ions. These cations strongly interact with the thiol groups of microorganisms and inhibit DNA replication, resulting in apoptosis. Furthermore, AgNPs also induce a toxic effect on human cells. In this respect, we must be cautious when using AgNPs as a dopant for TiO_2 NPs. Taking account of the adverse effects of metal dopants, visible-light active, anion-doped TiO_2 NPs using non-metal elements have attracted increasing attention as agents against pathogenic bacteria.

Given the important uses of visible-light active TiO_2 NPs for various applications, their impact on human health poses a serious concern worldwide. In vitro cell cultivation and in vivo animal models studies have reported the cytotoxic effects of TiO_2 NPs and Ag-doped TiO_2 NPs in mammalian cells by inducing an inflammatory response, DNA damage, ROS generation, and apoptosis. For long-term safety, more research studies are needed to properly design a toxic free, green synthesis of visible-light active TiO_2 NPs with bactericidal activity.

Author Contributions: S.C.T. conceived and directed the research. C.L., Y.L. and S.C.T. contributed to the writing of this review article. All authors have read and agree to the published version of the manuscript.

Funding: National Youth Science Foundation, China (Grant Number: 21703096), and Natural Science Foundation of Shandong Province, China (Grant Number: ZR2019MB053) provided the funding of this research.

Conflicts of Interest: The authors declare no conflict of interest.

References

1. Economou, V.; Gousia, P. Agriculture and food animals as a source of antimicrobial-resistant bacteria. *Infect. Drug Resist.* **2015**, *8*, 49–61. [CrossRef] [PubMed]
2. Rousham, E.K.; Unicomb, L.; Aminul, M. Human, animal and environmental contributors to antibiotic resistance in low-resource settings: Integrating behavioural, epidemiological and one health approaches. *Proc. R. Soc. B Biol. Sci.* **2018**, *285*, 20180332. [CrossRef] [PubMed]
3. Li, B.; Webster, T.J. Bacteria antibiotic resistance: New challenges and opportunities for implant-associated orthopedic infections. *J. Orthop. Res.* **2018**, *36*, 22–32. [CrossRef] [PubMed]
4. Kavanagh, N.; Ryan, E.J.; Widaa, A.; Sexton, G.; Fennell, J.; O'Rourke, S.; Cahill, K.C.; Kearney, C.J.; O'Brien, F.J.; Kerrigan, S.W. Staphylococcal osteomyelitis: Disease progression, treatment challenges, and future directions. *Clin. Microbiol. Rev.* **2018**, *31*, e00084-17. [CrossRef] [PubMed]
5. Collignon, P.J.; McEwen, S.A. One health—Its importance in helping to better control antimicrobial resistance. *Trop. Med. Infect. Dis.* **2019**, *4*, 22. [CrossRef] [PubMed]
6. Huh, A.J.; Kwon, Y.J. Nanoantibiotics: A new paradigm for treating infectious diseases using nanomaterials in the antibiotics resistant era. *J. Control. Release* **2011**, *156*, 128–145. [CrossRef] [PubMed]

7. Shaikh, S.; Nazam, N.; Rizvi, S.M.; Ahmad, K.; Baig, M.H.; Lee, E.J.; Choi, I. Mechanistic insights into the antimicrobial actions of metallic nanoparticles and their implications for multidrug resistance. *Int. J. Mol. Sci.* **2019**, *20*, 2468. [CrossRef]
8. Jesline, A.; John, N.P.; Narayanan, P.M.; Vani, C.; Murugan, S. Antimicrobial activity of zinc and titanium dioxide nanoparticles against biofilm-producing methicillin-resistant *Staphylococcus aureus*. *Appl. Nanosci.* **2015**, *5*, 157–162. [CrossRef]
9. Chen, C.; Li, S.; Thomas, A.; Kotov, N.A.; Haag, R. Functional graphene nanomaterials based architectures: Biointeractions, fabrications, and emerging biological applications. *Chem. Rev.* **2017**, *117*, 1826–1914. [CrossRef]
10. Tjong, S.C.; Chen, H. Nanocrystalline materials and coatings. *Mater. Sci. Eng. R Rep.* **2004**, *45*, 1–88. [CrossRef]
11. Tjong, S.C. *Nanocrystalline Materials: Their Synthesis-Structure-Property Relationships and Applications*, 2nd ed.; Elsevier: London, UK, 2013; ISBN 9780124077966.
12. He, L.X.; Tjong, S.C. Nanostructured transparent conductive films: Fabrication, characterization and applications. *Mater. Sci. Eng. R Rep.* **2016**, *109*, 1–101. [CrossRef]
13. He, L.X.; Tjong, S.C. Aqueous graphene oxide-dispersed carbon nanotubes as inks for the scalable production of all-carbon transparent conductive films. *J. Mater. Chem. C* **2016**, *4*, 7043–7051. [CrossRef]
14. Liao, C.; Li, Y.; Tjong, S.C. Graphene nanomaterials: Synthesis, biocompatibility, and cytotoxicity. *Int. J. Mol. Sci.* **2018**, *19*, 3564. [CrossRef] [PubMed]
15. Liao, C.; Li, Y.; Tjong, S.C. Bactericidal and cytotoxic properties of silver nanoparticles. *Int. J. Mol. Sci.* **2019**, *20*, 449. [CrossRef]
16. He, L.; Liao, C.; Tjong, S.C. Scalable fabrication of high-performance transparent conductors using graphene oxide-stabilized single-walled carbon nanotube inks. *Nanomaterials* **2018**, *8*, 224. [CrossRef]
17. Graves, J.L., Jr.; Thomas, M.; Ewunkem, J.A. Antimicrobial nanomaterials: Why evolution matters. *Nanomaterials* **2017**, *7*, 283. [CrossRef]
18. Gupta, A.; Mumtaz, S.; Li, C.H.; Hussain, I.; Rotello, V.M. Combatting antibiotic-resistant bacteria using nanomaterials. *Chem. Soc. Rev.* **2019**, *48*, 415–427. [CrossRef]
19. Küünal, S.; Visnapuu, M.; Volubujeva, O.; Soares Rosario, M.; Rauwel, P.; Rauwel, E. Optimisation of plant mediated synthesis of silver nanoparticles by common weed Plantago major and their antimicrobial properties. *IOP Conf. Ser. Mater. Sci. Eng.* **2019**, *613*, 012003. [CrossRef]
20. Küünal, S.; Rauwel, P.; Rauwel, E. Plant extract mediated synthesis of nanoparticles. In *Emerging Applications of Nanoparticles and Architectural Nanostructures: Current Prospects and Future Trends*; Barhoum, A., Makhlouf, A.S., Eds.; Elsevier: Amsterdam, The Netherlands, 2018; Chapter 14; pp. 411–416. [CrossRef]
21. Collin, F. Chemical basis of reactive oxygen species reactivity and involvement in neurodegenerative diseases. *Int. J. Mol. Sci.* **2019**, *20*, 2407. [CrossRef]
22. Regmi, C.; Joshi, B.; Ray, S.K.; Gyawali, G.; Pandey, R.P. Understanding mechanism of photocatalytic microbial decontamination of environmental wastewater. *Front. Chem.* **2018**, *6*, 33. [CrossRef]
23. Ballottin, D.; Fulaz, S.; Cabrini, F.; Tsukamoto, J.; Duran, N.; Alves, O.L.; Tasic, L. Antimicrobial textiles: Biogenic silver nanoparticles against Candida and Xanthomonas. *Mater. Sci. Eng. C* **2017**, *75*, 582–589. [CrossRef] [PubMed]
24. Chernousova, S.; Epple, M. Silver as antibacterial agent: Ion, nanoparticle and metal. *Angew. Chem. Int. Ed.* **2013**, *52*, 1636–1653. [CrossRef]
25. Kedziora, A.; Speruda, M.; Krzyzewska, E.; Rybka, J.; LukowiK, A.; Bugla-Płoskonska, G. Similarities and differences between silver ions and silver in nanoforms as antibacterial agents. *Int. J. Mol. Sci.* **2018**, *19*, 444. [CrossRef] [PubMed]
26. Liu, C.; Shen, J.; Yeung, K.W.K.; Tjong, S.C. Development and antibacterial performance of novel polylactic acid-graphene oxide-silver nanoparticle hybrid nanocomposite mats prepared by electrospinning. *ACS Biomater. Sci. Eng.* **2017**, *3*, 471–486. [CrossRef]
27. Liu, C.; Shen, J.; Liao, C.Z.; Yeung, K.W.; Tjong, S.C. Novel electrospun polyvinylidene fluoride-graphene oxide-silver nanocomposite membranes with protein and bacterial antifouling characteristics. *Express Polym. Lett.* **2018**, *12*, 365–382. [CrossRef]
28. Hanaor, D.A.; Sorrell, C.C. Review of the anatase to rutile phase transformation. *J. Mater. Sci.* **2011**, *46*, 855–874. [CrossRef]

29. Sarkar, A.; Khan, G.G. The formation and detection techniques of oxygen vacancies in titanium oxide-based nanostructures. *Nanoscale* **2019**, *11*, 3414–3444. [CrossRef]
30. Pesci, F.M.; Wang, G.; Klug, D.R.; Li, Y.; Cowan, A.J. Efficient suppression of electron-hole recombination in oxygen-deficient hydrogen-treated TiO_2 nanowires for photoelectrochemical water splitting. *J. Phys. Chem. C* **2013**, *117*, 25837–25844. [CrossRef]
31. Zhao, H.; Pan, F.; Li, Y. A review on the effects of TiO_2 surface point defects on CO_2 photoreduction with H_2O. *J. Mater.* **2017**, *3*, 17–32. [CrossRef]
32. Shwetharani, R.; Sakar, M.; Fernando, C.A.; Binas, V.; Balakrishna, R.G. Recent advances and strategies to tailor the energy levels, active sites and electron mobility in titania and its doped/composite analogues for hydrogen evolution in sunlight. *Catal. Sci. Technol.* **2019**, *9*, 12–46. [CrossRef]
33. Rauwel, E.; Galeckas, A.; Rauwel, P. Photoluminescent cubic and monoclinic HfO_2 nanoparticles: Effects of temperature and ambient. *Mater. Res. Express* **2014**, *1*, 015035. [CrossRef]
34. Wang, B.; Huang, W.; Chi, L.; Al-Hashimi, M.; Marks, T.J.; Facchetti, A. High-k gate dielectrics for emerging flexible and stretchable electronics. *Chem. Rev.* **2018**, *118*, 5690–5754. [CrossRef] [PubMed]
35. Markov, S.L.; Vidaković, A.M. Testing methods for antimicrobial activity of TiO_2 photocatalyst. *Acta Period Technol.* **2014**, *45*, 141–152. [CrossRef]
36. Rajh, T.; Dimitrijevic, N.M.; Bissonnette, M.; Koritarov, T.; Konda, V. Titanium dioxide in the service of the biomedical revolution. *Chem. Rev.* **2014**, *114*, 10177–10216. [CrossRef] [PubMed]
37. Matsunaga, T.R.; Tomoda, Y.; Nakajima, T.; Wake, H. Photoelectrochemical sterilization of microbial cells by semiconductor powders. *FEMS Microbiol. Lett.* **1985**, *29*, 211–214. [CrossRef]
38. Bogdan, J.; Zarzynska, J.; Plawinska-Czarnak, J. Comparison of infectious agents susceptibility to photocatalytic effects of nanosized titanium and zinc oxides: A practical approach. *Nanoscale Res. Lett.* **2015**, *10*, 309. [CrossRef] [PubMed]
39. Wang, Y.; Wu, T.; Zhou, Y.; Meng, C.; Zhu, W.; Liu, L. TiO_2-based nanoheterostructures for promoting gas sensitivity performance: Designs, developments, and prospects. *Sensors* **2017**, *17*, 1971. [CrossRef]
40. Abbas, M.; Iftikhar, H.; Malik, M.H.; Nazir, A. Surface coatings of TiO_2 nanoparticles onto the designed fabrics for enhanced self-cleaning properties. *Coatings* **2018**, *8*, 35. [CrossRef]
41. Huang, Y.; Mei, L.; Chen, X.; Wang, Q. Recent developments in food packaging based on nanomaterials. *Nanomaterials* **2018**, *8*, 830. [CrossRef]
42. Haggerty, J.E.S.; Schelhas, L.T.; Kitchaev, D.A.; Mangum, J.S.; Garten, L.M.; Sun, W.; Stone, K.H.; Perkins, J.D.; Toney, M.F.; Ceder, G.; et al. High-fraction brookite films from amorphous precursors. *Sci. Rep.* **2017**, *7*, 15232. [CrossRef]
43. Diebold, U. The surface sicence of titanium dioxide. *Surf. Sci. Rep.* **2003**, *48*, 53–229. [CrossRef]
44. Lin, X.; Li, J.; Ma, S.; Liu, G.; Yang, K.; Tong, M.; Lin, D. Toxicity of TiO_2 nanoparticles to Escherichia coli: Effects of particle size, crystal phase and water chemistry. *PLoS ONE* **2014**, *9*, e110247. [CrossRef] [PubMed]
45. Maziarz, W.; Kursior, A.; Trenczek-Zajac, A. Nanostructured TiO_2-based gas sensors with enhanced sensitivity to reducing gases. *Beilstein J. Nanotechnol.* **2016**, *7*, 1718–1726. [CrossRef] [PubMed]
46. Raghu, A.V.; Karuppanan, K.K.; Nampoothin, J.; Pullithadathil, B. Wearable, flexible ethanol gas sensor based on TiO_2 nanoparticles-grafted 2D-titanium carbide nanosheets. *ACS Appl. Nano Mater.* **2019**, *2*, 1152–1163. [CrossRef]
47. Liu, G.; Yang, H.G.; Pan, J.; Yang, Y.Q.; Lu, G.Q.; Cheng, H.M. Titanium dioxide crystals with tailored facets. *Chem. Rev.* **2014**, *114*, 9559–9612. [CrossRef] [PubMed]
48. Al-Attafi, K.; Nattestad, A.; Wu, Q.; Ide, Y.; Yamauchi, Y.; Dou, S.X.; Kim, J.H. The effect of amorphous TiO_2 in P25 on dye-sensitized solar cell performance. *Chem. Commun.* **2018**, *54*, 381–384. [CrossRef]
49. Truppi, A.; Petronella, F.; Placido, T.; Striccoli, M. Visible-light-active TiO_2-based hybrid nanocatalysts for environmental applications. *Catalysis* **2018**, *7*, 100. [CrossRef]
50. Tobaldi, D.M.; Piccirillo, C.; Pullar, R.C.; Gualtieri, A.F.; Seabra, M.P.; Castro, P.M.; Labrincha, J.A. Silver-modified nano-titania as an antibacterial agent and photocatalyst. *J. Phys. Chem. C* **2014**, *118*, 4751–4766. [CrossRef]
51. Ali, T.; Ahmed, A.; Alam, U.; Uddin, I.; Tripathi, P.; Muneer, M. Enhanced photocatalytic and antibacterial activities of Ag-doped TiO_2 nanoparticles under visible light. *Mater. Chem. Phys.* **2018**, *212*, 325–335. [CrossRef]

52. Moongraksathum, B.; Chen, Y.W. Anatase TiO_2 co-doped with silver and ceria for antibacterial application. *Catal. Today* **2018**, *310*, 68–74. [CrossRef]
53. Viet, P.V.; Phan, B.T.; Mott, D.; Maenosono, S.; Sang, T.T.; Thi, C.M.; Hieu, L.V. Silver nanoparticle loaded TiO_2 nanotubes with high photocatalytic and antibacterial activity synthesized by photoreduction method. *J. Photochem. Photobiol. A* **2018**, *352*, 106–112. [CrossRef]
54. Ahmad, R.; Mohsin, M.; Ahmad, D.; Sardar, M. Alpha amylase assisted synthesis of TiO_2 nanoparticles: Structural characterization and application as antibacterial agents. *J. Hazard. Mater.* **2015**, *283*, 171–177. [CrossRef] [PubMed]
55. Lorenzetti, M.; Gongadze, E.; Kulkarni, M.; Junkar, I.; Iglic, A. Electrokinetic properties of TiO_2 nanotubular surfaces. *Nanoscale Res. Lett.* **2016**, *11*, 378. [CrossRef] [PubMed]
56. Jiang, X.; Lv, B.; Wang, Y.; Shen, Q.; Wang, X. Bactericidal mechanisms and effector targets of TiO_2 and Ag-TiO_2 against Staphylococcus aureus. *J. Med. Microbiol.* **2017**, *66*, 440–446. [CrossRef]
57. Pagnout, C.; Jomini, S.; Dadhwal, M.; Caillet, C.; Thomas, F.; Bauda, P. Role of electrostatic interactions in the toxicity of titanium dioxide nanoparticles toward Escherichia coli. *Colloids Surf. B Biointerfaces* **2012**, *92*, 315–321. [CrossRef]
58. Liou, J.W.; Chang, H.H. Bactericidal effects and mechanisms of visible light responsive titanium dioxide photocatalysts on pathogenic bacteria. *Arch. Immunol. Ther. Exp.* **2012**, *6*, 267–275. [CrossRef]
59. Charpentier, P.A.; Burgess, K.; Wang, L.; Chowdhury, R.R.; Lotus, A.F.; Moula, G. Nano-TiO_2/polyurethane composites for antibacterial and self-cleaning coatings. *Nanotechnology* **2012**, *23*, 425606. [CrossRef]
60. Santhosh, S.M.; Kandasamy, N. Antibiofilm activity of epoxy/Ag-TiO_2 polymer nanocomposite coatings against *Staphylococcus aureus* and *Escherichia coli*. *Coatings* **2015**, *5*, 95–114. [CrossRef]
61. Khorshidi, B.; Biswas, I.; Ghosh, T.; Thundat, T.; Sadrzadeh, M. Polyamide-TiO_2 nanocomposite membranes with enhanced thermal stability and anti-biofouling propensity. *Sci. Rep.* **2018**, *8*, 784. [CrossRef]
62. Zhang, S.; Liang, X.; Gadd, G.M.; Zhao, Q. Advanced titanium dioxide-polytetrafluorethylene (TiO_2-PTFE) nanocomposite coatings on stainless steel surfaces with antibacterial and anti-corrosion properties. *Appl. Surf. Sci.* **2019**, *490*, 231–241. [CrossRef]
63. Ahmadi, R.; Tanomand, A.; Kazeminawa, F.; Kamounah, F.S.; Ayaseh, A.; Ganbarov, K.; Yousefi, M.; Katourani, A.; Yousefi, B.; Kafil, H.S. Fabrication and characterization of a titanium dioxide (TiO_2) reinforced with bio-nanocomposite containing Miswak (*Salvadora percica* L.) extract–the antimicrobial, thermophysical, and barrier properties. *Int J. Nanomedic.* **2019**, *14*, 3439–3454. [CrossRef] [PubMed]
64. Hegedus, P.; Szabó-Bárdos, E.; Horvath, O.; Szabo, P.; Horvath, K. Investigation of a TiO_2 photocatalyst immobilized with poly(vinyl alcohol). *Catal. Today* **2017**, *284*, 179–186. [CrossRef]
65. Bui, V.K.; Park, D.; Lee, Y.C. Chitosan combined with ZnO, TiO_2 and Ag nanoparticles for antimicrobial wound healing applications: A mini review of the research trends. *Polymers* **2017**, *9*, 21. [CrossRef] [PubMed]
66. Meng, Y.Z.; Tjong, S.C. Rheology and morphology of compatibilized polyamide 6 blends containing liquid crystalline copolyesters. *Polymer* **1998**, *39*, 99–107. [CrossRef]
67. Meng, Y.Z.; Tjong, S.C.; Hay, A.S.; Wang, S.J. Synthesis and proton conductivities of phosphonic acid containing poly-(arylene ether)s. *J. Polym. Sci. A Polym. Chem.* **2001**, *39*, 3218–3226. [CrossRef]
68. Liu, C.; Chan, K.W.; Shen, J.; Liao, C.; Yeung, K.W.K.; Tjong, S.C. Polyetheretherketone hybrid composites with bioactive nanohydroxyapatite and multiwalled carbon nanotube fillers. *Polymers* **2016**, *8*, 425. [CrossRef]
69. Chan, K.W.; Liao, C.; Wong, H.M.; Yeung, K.W.K.; Tjong, S.C. Preparation of polyetheretherketone composites with nanohydroxyapatite rods and carbon nanofibers having high strength, good biocompatibility and excellent thermal stability. *RSC Adv.* **2016**, *6*, 19417–19429. [CrossRef]
70. Liao, C.; Li, K.; Wong, H.M.; Tong, W.Y.; Yeung, K.W.K.; Tjong, S.C. Novel polypropylene biocomposites reinforced with carbon nanotubes and hydroxyapatite nanorods for bone replacements. *Mater. Sci. Eng. C* **2013**, *13*, 1380–1388. [CrossRef]
71. Liao, C.; Wong, H.M.; Yeung, K.W.K.; Tjong, S.C. The development, fabrication and material characterization of polypropylene composites reinforced with carbon nanofiber and hydroxyapatite nanorod hybrid fillers. *Int. J. Nanomed.* **2014**, *9*, 1299–1310. [CrossRef]
72. Liu, C.; Wong, H.M.; Yeung, K.W.; Tjong, S.C. Novel electrospun polylactic acid nanocomposite fiber mats with hybrid graphene oxide and nanohydroxyapatite reinforcements having enhanced biocompatibility. *Polymers* **2016**, *8*, 287. [CrossRef]

73. Horn, M.; Schwerdtfeger, C.F.; Meagher, E.P. Refinement of the structure of anatase at several temperatures. *Z. Krist.* **1972**, *136*, 273–281. [CrossRef]
74. Baur, W.H.; Khan, A.A. Rutile-type compounds. IV. SiO_2, GeO_2 and a comparison with other rutile-type structures. *Acta Crystallogr. B* **1971**, *27*, 2133–2139. [CrossRef]
75. Fagan, R.; Synnott, D.W.; McCormack, D.E.; Pillai, S.C. An effective method for the preparation of high temperature stable anatase TiO_2 photocatalysts. *Appl. Surf. Sci.* **2016**, *371*, 447–452. [CrossRef]
76. Higashimoto, S. Titanium-dioxide-based visible-light-sensitive photocatalysis: Mechanistic insight and applications. *Catalysts* **2019**, *9*, 201. [CrossRef]
77. Lu, Y.; Zang, Y.; Zhang, H.; Zhang, Y.; Wang, G.; Zhao, H. Meaningful comparison of photocatalytic properties of {001} and {101} faceted anatase TiO_2 nanocrystals. *Sci. Bull.* **2016**, *61*, 1003–1012. [CrossRef]
78. Sajan, C.P.; Wageh, S.; Al-Ghamdhi, A.A.; Yu, J.; Cao, S. TiO_2 nanosheets with exposed {001} facets for photocatalytic application. *Nano Res.* **2016**, *9*, 3–27. [CrossRef]
79. Liu, X.; Du, G.; Li, M. True photoreactivity origin of Ti^{3+}-doped anatase TiO_2 crystals with respectively dominated exposed {001}, {101}, and {100} facets. *ACS Omega* **2019**, *4*, 14902–14912. [CrossRef]
80. Li, M.; Yin, J.J.; Wamer, W.G.; Lo, Y.M. Mechanistic characterization of titanium dioxide nanoparticle-induced toxicity using electron spin resonance. *J. Food Drug Anal.* **2014**, *22*, 76–85. [CrossRef]
81. Xue, C.; Wu, J.; Lan, F.; Liu, W.; Yang, X.; Zeng, F.; Xu, H. Nano titanium dioxide induces the generation of ROS and potential damage in HaCaT cells under UVA irradiation. *J. Nanosci. Nanotechnol.* **2010**, *10*, 8500–8507. [CrossRef]
82. Bartlet, K.; Movafaghi, S.; Dasi, L.P.; Kota, A.K.; Popat, K.C. Antibacterial activity on superhydrophobic titania nanotube arrays. *Colloids Surf. B Biointerfaces* **2018**, *166*, 179–186. [CrossRef]
83. Dong, H.; Zeng, G.; Tang, L.; Fan, C.; Zhang, C.; He, X. An overview on limitations of TiO_2-based particles for photocatalytic degradation of organic pollutants and the corresponding countermeasures. *Water Res.* **2015**, *79*, 128–146. [CrossRef] [PubMed]
84. Pelaez, M.; Nolan, N.; Pillai, S.; Seery, M.; Falaras, P.; Kontos, A.G.; Dunlop, P.S.; Hamilton, J.W.; Byrne, J.A.; O'Shea, K.; et al. A review on the visible light active titanium dioxide photocatalysts for environmental applications. *Appl. Catal. B Environ.* **2012**, *125*, 331–349. [CrossRef]
85. Schneider, J.; Matsuoka, M.; Takeuchi, M.; Zhang, J.; Horiuchi, Y.; Anpo, M.; Bahnemann, D.W. Understanding TiO_2 photocatalysis: Mechanisms and materials. *Chem. Rev.* **2014**, *114*, 9919–9986. [CrossRef] [PubMed]
86. Moma, J.; Baloyi, J. Modified Titanium Dioxide for Photocatalytic Applications. In *Photocatalysts—Applications and Attributes*; Khan, S.B., Akhtar, K., Eds.; Intech Open: London, UK, 2019; Chapter 3; pp. 37–56. [CrossRef]
87. Kang, X.; Liu, S.; Dai, Z.; He, Y.; Song, X.; Tang, Z. Titanium dioxide: From engineering to applications. *Catalysis* **2019**, *9*, 191. [CrossRef]
88. Lin, W.C.; Lin, Y.J. Effect of vanadium (IV)-doping on the visible light-induced catalytic activity of titanium dioxide catalysts for methylene blue degradation. *Environ. Eng. Sci.* **2012**, *29*, 447–452. [CrossRef]
89. Yu, J.H.; Nam, S.H.; Lee, J.W.; Kim, D.I.; Boo, J.H. Oxidation state and structural studies of vanadium-doped titania particles for the visible light-driven photocatalytic activity. *Appl. Surf. Sci.* **2019**, *472*, 46–53. [CrossRef]
90. Lv, T.; Zhao, J.; Chen, M.; Shen, K.; Zhang, D.; Zhang, J.; Zhang, G.; Liu, Q. Boosted visible-light photodegradation of methylene blue by V and Co co-doped TiO_2. *Materials* **2018**, *11*, 1946. [CrossRef]
91. Khatun, N.; Rini, E.G.; Shirage, P.; Rajput, P.; Jha, S.N.; Sen, S. Effect of lattice distortion on bandgap decrement due to vanadium substitution in TiO_2 nanoparticles. *Mater. Sci. Semicond. Process.* **2016**, *50*, 7–13. [CrossRef]
92. Binas, V.; Venieri, D.; Kotzias, D.; Kiriakidis, D. Modified TiO_2 based photocatalysts for improved air and health quality. *J. Mater.* **2017**, *3*, 3–16. [CrossRef]
93. Moradi, H.; Eshaghi, A.; Hosseini, S.R.; Ghani, K. Fabrication of Fe-doped TiO_2 nanoparticles and investigation of photocatalytic decolorization of reactive red 198 under visible light irradiation. *Ultrason. Sonochem.* **2016**, *32*, 314–319. [CrossRef] [PubMed]
94. Crisan, M.; Mardare, D.; Ianculescu, A.; Dragan, N.; Nitoi, I.; Crisan, D.; Voicescu, M.; Todan, L.; Oancea, P.; Adomnitei, C.; et al. Iron doped TiO_2 films and their photoactivity in nitrobenzene removal from water. *Appl. Surf. Sci.* **2018**, *455*, 201–215. [CrossRef]
95. Daghrir, R.; Drogui, P.; Robert, D. Modified TiO_2 for environmental photocatalytic applications: A review. *Ind. Eng. Chem. Res.* **2013**, *52*, 3581–3599. [CrossRef]
96. Li, W. Influence of electronic structures of doped TiO_2 on their photocatalysis. *Phys. Status Solidi Rapid Res. Lett.* **2014**, *9*, 10–27. [CrossRef]

97. Ivanov, S.; Barylyak, A.; Besaha, K.; Bund, A.; Wojnarowska-Nowak, R.; Yaremchuk, I.; Kus-Liśkiewicz, M. Synthesis, characterization, and photocatalytic properties of sulfur- and carbon-codoped TiO_2 nanoparticles. *Nanoscale Res. Lett.* **2016**, *11*, 140. [CrossRef]
98. Koklic, T.; Pintaric, S.; Zdovc, I.; Golob, M.; Umek, P.; Mehle, A.; Dobeic, M.; Strancar, J. Photocatalytic disinfection of surfaces with copper doped TiO_2 nanotube coatings illuminated by ceiling mounted fluorescent light. *PLoS ONE* **2018**, *13*, e0197308. [CrossRef] [PubMed]
99. Syrek, K.; Grudzień, J.; Sennik-Kubiec, A.; Brudzisz, A.; Sulka, G.D. Anodic titanium oxide layers modified with gold, silver, and copper nanoparticles. *J. Nanomater.* **2019**, *2019*, 9208734. [CrossRef]
100. Janczarek, M.; Wei, Z.; Endo, M.; Ohtani, B.; Kowalska, E. Silver- and copper modified decahedral anatase titania particles as visible light-responsive plasmonic photocatalyst. *J. Photon. Energy* **2016**, *7*, 012008. [CrossRef]
101. Wanag, A.; Rokicka, P.; Kusiak-Nejman, E.; Kapica-Kozar, J.; Wrobel, R.J.; Markowska-Szczupak, A.; Morawski, A.W. Antibacterial properties of TiO_2 modified with reduced graphene oxide. *Ecotoxicol. Environ. Saf.* **2018**, *147*, 788–793. [CrossRef]
102. Raja, A.; Selvakumar, K.; Rajasekaran, P.; Arunpandian, M.; Ashokkumar, S.; Kaviyarasu, K.; Asath Bahadur, S.; Swaminathan, M. Visible active reduced graphene oxide loaded titania for photodecomposition of ciprofloxacin and its antibacterial activity. *Colloids Surf. A* **2019**, *564*, 23–30. [CrossRef]
103. Tayel, A.; Ramadan, A.R.; El Seoud, O.A. Titanium dioxide/graphene and titanium dioxide/graphene oxide nanocomposites: Synthesis, characterization and photocatalytic applications for water decontamination. *Catalysts* **2018**, *8*, 491. [CrossRef]
104. Rauwel, P.; Galeckas, A.; Salumaa, M.; Ducroquet, F.; Rauwel, E. Photocurrent generation in carbon nanotube/cubic-phase HfO_2 nanoparticle hybrid nanocomposites. *Beilstein J. Nanotechnol.* **2016**, *7*, 1075–1085. [CrossRef] [PubMed]
105. Choi, W.; Termin, A.; Hoffmann, M.R. The role of metal ion dopants in quantum-sized TiO_2: Correlation between photoreactivity and charge carrier recombination dynamics. *J. Phys. Chem.* **1994**, *98*, 13669–13679. [CrossRef]
106. Fang, W.Z.; Xing, M.Y.; Zhang, J.L. A new approach to prepare Ti^{3+} self-doped TiO_2 via $NaBH_4$ reduction and hydrochloric acid treatment. *Appl. Catal. B Environ.* **2014**, *160–161*, 240–246. [CrossRef]
107. Wan, Z.; Huang, G.F.; Huang, W.Q.; Jiao, C.; Yan, X.G.; Yang, Z.M.; Zhang, Q.L. The enhanced photocatalytic activity of Ti^{3+} self-doped TiO_2 by a reduction method. *Mater. Lett.* **2014**, *122*, 33–36. [CrossRef]
108. Jayashree, S.; Ashokkumar, M. Switchable intrinsic defect chemistry of titania for catalytic applications. *Catalysts* **2018**, *8*, 601. [CrossRef]
109. Mathew, S.; Ganguly, P.; Rhatigan, S.; Kumaravel, V.; Byrne, C.; Hinder, S.J.; Bartlett, J.; Nolan, M.; Pillai, S.C. Cu-doped TiO_2: Visible light assisted photocatalytic antimicrobial activity. *Appl. Sci.* **2018**, *8*, 2067. [CrossRef]
110. Manzoor, M.; Rafiq, A.; Ikram, M.; Nafees, M.; Ali, S. Structural, optical, and magnetic study of Ni-doped TiO_2 nanoparticles synthesized by sol–gel method. *Int. Nano Lett.* **2018**, *8*, 1–8. [CrossRef]
111. Huang, J.G.; Guo, X.T.; Wang, B.; Li, L.Y.; Zhao, M.X.; Dong, L.L.; Liu, X.J.; Huang, Y.T. Synthesis and photocatalytic activity of Mo-doped TiO_2 nanoparticles. *J. Spectrosc.* **2015**, *2015*, 681850. [CrossRef]
112. Avilés-García, O.; Espino-Valencia, J.; Romero, R.; Rico-Cerda, J.L.; Arroyo-Albiter, M.; Natividad, R. W and Mo doped TiO_2: Synthesis, characterization and photocatalytic activity. *Fuel* **2017**, *198*, 31–41. [CrossRef]
113. Shi, Z.; Lai, H.; Yao, S.; Wang, S. Photocatalytic activity of Fe and Ce co-doped mesoporous TiO_2 catalyst under UV and visible light. *J. Chin. Chem. Soc.* **2012**, *59*, 614–620. [CrossRef]
114. Aviles-Garcia, O.; Espino-Valencia, J.; Romero-Romero, R.; Rico-Cerda, J.L.; Arroyo-Albiter, M.; Solis-Casados, D.A.; Navitidad-Rangel, R. Enhanced photocatalytic activity of titania by co-doping with Mo and W. *Catalysts* **2018**, *8*, 631. [CrossRef]
115. El Mragui, A.; Logvina, Y.; Pinto da Silva, L.; Zegaoui, O.; Estevesda Silva, J.C.G. Synthesis of Fe- and Co-doped TiO_2 with improved photocatalytic activity under visible irradiation toward carbamazepine degradation. *Materials* **2019**, *12*, 3874. [CrossRef] [PubMed]
116. Nadolna, J.; Grzyb, G.; Sobczak, J.W.; Lisowski, W. Visible light activity of rare earth metal doped (Er^{3+}, Yb^{3+} or Er^{3+}/Yb^{3+}) titania photocatalysts. *Appl. Catal. B Envorin.* **2015**, *163*, 40–49. [CrossRef]
117. Rozman, N.; Tobaldi, D.M.; Cvelbar, U.; Puliyalil, H.; Labrincha, J.A.; Legat, A.; Skapin, A.S. Hydrothermal synthesis of rare-earth modified titania: Influence on phase composition, optical properties, and photocatalytic activity. *Materials* **2019**, *12*, 713. [CrossRef] [PubMed]

118. Mazierski, P.; Lisowski, W.; Grzyb, T.; Winiarski, M.J.; Klimczuk, T.; Mikołajczyk, A.; Flisikowski, J.; Hirsch, A.; Kolakowska, A.; Puzyn, T.; et al. Enhanced photocatalytic properties of lanthanide-TiO_2 nanotubes: An experimental and theoretical study. *Appl. Catal. B Environ.* **2017**, *205*, 376–385. [CrossRef]
119. Xie, K.; Jia, Q.; Wang, Y.; Zhang, W.; Xu, J. The electronic structure and optical properties of anatase TiO_2 with rare earth metal dopants from first-principles calculations. *Materials* **2018**, *11*, 179. [CrossRef]
120. Makdee, A.; Unwiset, P.; Chanapattharapol, K.C.; Kidkhunthod, P. Effects of Ce addition on the properties and photocatalytic activity of TiO_2, investigated by X-ray absorption spectroscopy. *Mater. Chem. Phys.* **2018**, *213*, 431–443. [CrossRef]
121. Kasinathan, K.; Kennedy, J.; Elayaperumal, M.; Henini, M.; Malik, M. Photodegradation of organic pollutants RhB dye using UV simulated sunlight on ceria based TiO_2 nanomaterials for antibacterial applications. *Sci. Rep.* **2016**, *6*, 38064. [CrossRef]
122. Choudhury, B.; Borah, B.; Choudhury, A. Extending photocatalytic activity of TiO_2 nanoparticles to visible region of illumination by doping of cerium. *Photochem. Photobiol.* **2012**, *88*, 257–264. [CrossRef]
123. Li, J.; Zhou, H.; Qian, S.; Liu, Z.; Feng, J.; Jin, P.; Liu, X. Plasmonic gold nanoparticles modified titania nanotubes for antibacterial application. *Appl. Phys. Lett.* **2014**, *104*, 261110. [CrossRef]
124. Endo, M.; Wei, Z.; Wang, K.; Karabiyik, B.; Yoshiiri, K.; Rokickka, P.; Ohtani, B.; Markowska-Szczupak, A.; Kowalska, E. Noble metal-modified titania with visible-light activity for the decomposition of microorganisms. *Beilstein J. Nanotechnol.* **2018**, *9*, 829–841. [CrossRef] [PubMed]
125. Wysocka, I.; Kowalska, E.; Ryl, J.; Nowaczyk, G.; Zielińska-Jurek, A. Morphology, photocatalytic and antimicrobial properties of TiO_2 modified with mono- and bimetallic copper, platinum and silver nanoparticles. *Nanomaterials* **2019**, *9*, 1129. [CrossRef]
126. Petica, A.; Florea, A.; Gaidau, C.; Balan, D.; Anicai, L. Synthesis and characterization of silver-titania nanocomposites prepared by electrochemical method with enhanced photocatalytic characteristics, antifungal and antimicrobial activity. *J. Mater. Res. Technol.* **2019**, *8*, 41–53. [CrossRef]
127. Krajczewski, J.; Kolataj, K.; Kudelski, A. Plasmonic nanoparticles in chemical analysis. *RSC Adv.* **2017**, *7*, 17559–17576. [CrossRef]
128. Kim, M.; Lin, M.; Son, J.; Xu, H.; Nam, J.M. Hot-electron-mediated photochemical reactions: Principles, recent advances, and challenges. *Adv. Opt. Mater.* **2017**, *5*, 1700004. [CrossRef]
129. Furube, A.; Hashimoto, S. Insight into plasmonic hot-electron transfer and plasmon molecular drive: New dimensions in energy conversion and nanofabrication. *NPG Asia Mater.* **2017**, *9*, e454. [CrossRef]
130. Zhang, Z.; Zhang, C.; Zheng, H.; Xu, H. Plasmon-driven catalysis on molecules and nanomaterials. *Acc. Chem. Res.* **2019**, *52*, 2506–2515. [CrossRef]
131. Hartland, G.V.; Besteiro, L.V.; Johns, P.; Govorov, A.O. What's so hot about electrons in metal nanoparticles? *ACS Energy Lett.* **2017**, *2*, 1641–1653. [CrossRef]
132. Kim, J.; Son, H.Y.; Nam, Y.S. Multilayered plasmonic heterostructure of gold and titania nanoparticles for solar fuel production. *Sci. Rep.* **2018**, *8*, 10464. [CrossRef]
133. Wu, N. Plasmonic metal–semiconductor photocatalysts and photoelectrochemical cells: A review. *Nanoscale* **2018**, *10*, 2679–2696. [CrossRef]
134. Clavero, C. Plasmon-induced hot-electron generation at nanoparticle/metal-oxide interfaces for photovoltaic and photocatalytic devices. *Nat. Photonics* **2014**, *8*, 95–103. [CrossRef]
135. Khan, M.R.; Chowdhurya, M.N.; Chuan, T.W.; Cheng, C.K. Schottky barrier and surface plasmonic resonance phenomena towards the photocatalytic reaction: Study of their mechanisms to enhance the photocatalytic activity. *Catal. Sci. Technol.* **2015**, *5*, 2522–2531. [CrossRef]
136. Yao, G.Y.; Liu, Q.L.; Zhao, Z.Y. Studied localized surface plasmon resonance effects of Au nanoparticles on TiO_2 by FDTD simulations. *Catalysts* **2018**, *8*, 236. [CrossRef]
137. Michalas, L.; Khiat, A.; Stathopoulos, S.; Prodromakis, T. Electrical characteristics of interfacial barriers at metal—TiO_2 contacts. *J. Phys. D Appl. Phys.* **2018**, *51*, 425101. [CrossRef]
138. Hankodo, C.T.; Moustakas, N.G.; Peppel, T.; Springer, A.; Oropeza, F.E.; Huda, A.; Bustan, M.D.; Yudono, B.; Gulo, F.; Strunk, J. Characterization and effect of Ag(0) vs. Ag(I) species and their localized plasmon resonance on photochemically inactive TiO_2. *Catalysts* **2019**, *9*, 323. [CrossRef]
139. Ma, Y.; Zhi, L. Graphene-based transparent conductive films: Material systems, preparation and applications. *Small Methods* **2019**, *3*, 1800199. [CrossRef]

140. Nair, R.R.; Blake, P.; Grigorenko, A.N.; Novoselov, K.S.; Booth, T.J.; Stauber, T.; Peres, N.M.; Geim, A.K. Fines structure constant defines visual transparency of graphene. *Science* **2008**, *320*, 1308. [CrossRef]
141. Kim, C.H. Nanostructured graphene: An active component in optoelectronic devices. *Nanomaterials* **2018**, *8*, 328. [CrossRef]
142. Kumar, P.; Huo, P.; Zhang, R.; Liu, B. Antibacterial properties of graphene-based nanomaterials. *Nanomaterials* **2019**, *9*, 737. [CrossRef]
143. Karahan, H.E.; Wiraja, C.; Xu, C.; Wei, J.; Wang, Y.; Wang, L.; Liu, F.; Chen, Y. Graphene materials in antimicrobial nanomedicine: Current status and future perspectives. *Adv. Healthc. Mater.* **2018**, *7*, 1701406. [CrossRef]
144. Gillespie, N.O.; Martsinovich, N. Origin of charge trapping in TiO_2/reduced graphene oxide photocatalytic composites: Insights from theory. *ACS Appl. Mater. Interf.* **2019**, *11*, 31909–31922. [CrossRef] [PubMed]
145. Tang, B.; Chen, H.; Peng, H.; Wang, Z.; Huang, W. Graphene modified TiO_2 composite photocatalysts: Mechanism, progress and perspective. *Nanomaterials* **2018**, *8*, 105. [CrossRef] [PubMed]
146. Tan, L.L.; Ong, W.J.; Chai, S.P.; Mohamed, A.R. Reduced graphene oxide-TiO_2 nanocomposite as a promising visible-light-active photocatalyst for the conversion of carbon dioxide. *Nanoscale Res. Lett.* **2013**, *8*, 465. [CrossRef] [PubMed]
147. Polat, E.O.; Balci, O.; Kakenov, N.; Uzlu, H.B.; Kocabas, C.; Dahiya, R. Synthesis of large area graphene for high performance in flexible optoelectronic devices. *Sci. Rep.* **2015**, *5*, 16744. [CrossRef] [PubMed]
148. Guerrero-Contreras, J.; Caballero-Briones, F. Graphene oxide powders with different oxidation degree, prepared by synthesis variations of the Hummers method. *Mater. Chem. Phys.* **2015**, *153*, 209–220. [CrossRef]
149. Dreyer, D.R.; Park, S.; Bielawski, C.W.; Ruoff, R.S. The chemistry of graphene oxide. *Chem. Soc. Rev.* **2010**, *39*, 228–240. [CrossRef]
150. Park, S.; An, J.; Potts, J.R.; Velamakanni, A.; Murali, S.; Ruoff, R.S. Hydrazine-reduction of graphite- and graphene oxide. *Carbon* **2011**, *49*, 3019–3023. [CrossRef]
151. Xu, C.; Shi, X.; Ji, A.; Shi, L.; Zhou, C.; Cui, Y. Fabrication and characteristics of reduced graphene oxide produced with different green reductants. *PLoS ONE* **2015**, *10*, e0144842. [CrossRef]
152. Yeh, T.F.; Teng, T.C.; Chen, L.C.; Teng, H. Graphene oxide-based nanomaterials for efficient photoenergy conversion. *J. Mater. Chem. A* **2016**, *4*, 2014–2048. [CrossRef]
153. Giovannetti, R.; Rommozzi, E.; Zannotti, M.; D'Amato, C.A. Recent advances in graphene based TiO_2 nanocomposites ($GTiO_2Ns$) for photocatalytic degradation of synthetic dyes. *Catalysts* **2017**, *7*, 305. [CrossRef]
154. Rauwel, P.; Galeckas, A.; Ducroquet, F.; Rauwel, E. Selective photocurrent generation in HfO_2 and carbon nanotube hybrid nanocomposites under Ultra-Violet and visible photoexcitations. *Mater. Lett.* **2019**, *246*, 45–48. [CrossRef]
155. Akhavan, O.; Azimirad, R.; Safa, S.; Larijani, M.M. Visible light photo-induced antibacterial activity of CNT–doped TiO_2 thin films with various CNT contents. *J. Mater. Chem.* **2010**, *20*, 7386–7392. [CrossRef]
156. Koli, V.B.; Dhodamani, A.G.; Raut, A.V.; Thorat, N.D.; Pawar, S.H.; Delekar, S.D. Visible light photo-induced antibacterial activity of TiO_2-MWCNTs nanocomposites with varying the contents of MWCNTs. *J. Photochem. Photobiol. A* **2016**, *328*, 50–58. [CrossRef]
157. Koli, V.B.; Delekar, S.D.; Pawar, S.H. Photoinactivation of bacteria by using Fe-doped TiO_2-MWCNTs nanocomposites. *J. Mater. Sci. Mater. Med.* **2016**, *27*, 177. [CrossRef]
158. Choi, J.; Park, H.; Hoffmann, M.R. Effects of single metal-ion doping on the visible-light photoreactivity of TiO_2. *J. Phys. Chem. C* **2010**, *114*, 783–792. [CrossRef]
159. Nagpure, S.; Kim, D.Y.; Rankin, S.E. Synthesis and catalytic applications of non-metal doped mesoporous titania. *Inorganics* **2017**, *5*, 15. [CrossRef]
160. Valentin, C.D.; Pacchioni, G. Trends in non-metal doping of anatase TiO_2: B, C, N and F. *Catal. Today* **2013**, *206*, 12–18. [CrossRef]
161. Ananpattarachai, J.; Boonto, Y.; Kajitvichyanukul, P. Visible light photocatalytic antibacterial activity of Ni-doped and N-doped TiO_2 on Staphylococcus aureus and Escherichia coli bacteria. *Environ. Sci. Pollut. Res.* **2016**, *23*, 4111–4119. [CrossRef]
162. Zener, B.; Matoh, L.; Carraro, G.; Miljevic, B.; Korosec, R.C. Sulfur-, nitrogen- and platinum-doped titania thin films with high catalytic efficiency under visible-light illumination. *Beilstein J. Nanotechnol.* **2018**, *9*, 1629–1640. [CrossRef]

163. Cravanzola, S.; Cesano, F.; Gaziano, F.; Scarano, D. Sulfur-doped TiO_2: Structure and surface properties. *Catalysts* **2017**, *7*, 214. [CrossRef]
164. Banerjee, S.; Pillai, S.C.; Falaras, P.; O'Shea, K.E.; Byrne, J.A.; Dionysiou, D.D. New insights into the mechanism of visible light photocatalysis. *J. Phys. Chem. Lett.* **2014**, *5*, 2543–2554. [CrossRef]
165. Yu, J.C.; Yu, J.; Ho, W.; Jiang, Z.; Zhang, L. Effects of F- doping on the photocatalytic activity and microstructures of nanocrystalline TiO_2 powders. *Chem. Mater.* **2002**, *14*, 3808–3816. [CrossRef]
166. Asahi, R.; Morikawa, T.; Ohwaki, T.; Aoki, K.; Taga, Y. Visible-light photocatalysis in nitrogen-doped titanium oxides. *Science* **2001**, *13*, 269–271. [CrossRef] [PubMed]
167. Varley, J.B.; Janotti, A.; van de Walle, C.G. Mechanism of visible-light photocatalysis in nitrogen-doped TiO_2. *Adv. Mater.* **2011**, *23*, 2343–2347. [CrossRef] [PubMed]
168. Ansari, S.A.; Khan, M.M.; Ansari, M.O.; Cho, M.H. Nitrogen-doped titanium dioxide (N-doped TiO_2) for visible light photocatalysis. *New J. Chem.* **2016**, *40*, 3000–3009. [CrossRef]
169. Yang, K.; Dai, Y.; Huang, B.; Whangbo, M.H. Density functional characterization of the visible-light absorption in substitutional C-anion- and C-cation-doped TiO_2. *J. Phys. Chem. C* **2009**, *113*, 2624–2629. [CrossRef]
170. Di Valentin, C.; Pacchioni, G.; Selloni, A. Theory of carbon doping of titanium dioxide. *Chem. Mater.* **2005**, *17*, 6656–6665. [CrossRef]
171. Geng, H.; Yin, S.; Yang, X.; Shuai, Z.; Liu, B. Geometric and electronic structures of the boron-doped photocatalyst TiO_2. *J. Phys. Condens. Matter* **2006**, *18*, 87–96. [CrossRef]
172. Patel, N.; Dashora, A.; Jaiswal, R.; Fernandes, R.; Yadav, M.; Kothari, D.C. Experimental and theoretical investigations on the activity and stability of substitutional and interstitial boron in TiO_2 photocatalyst. *J. Chem. Phys.* **2015**, *119*, 18581–18590. [CrossRef]
173. Sotelo-Vazquez, C.; Noor, N.; Kafizas, A.; Quesada-Cabrera, R.; Scanlon, D.O.; Taylor, A.; Durrant, J.R.; Parkin, I.P. Multifunctional P-doped TiO_2 films: A new approach to self-cleaning, transparent conducting oxide materials. *Chem. Mater.* **2015**, *27*, 3234–3242. [CrossRef]
174. Gopal, N.O.; Lo, H.H.; Ke, T.F.; Chou, C.C.; Wu, J.D.; Sheu, S.C.; Ke, S.C. Visible light active phosphorus-doped TiO_2 nanoparticles: An EPR evidence for the enhanced charge separation. *J. Phys. Chem. C* **2012**, *116*, 16191–16197. [CrossRef]
175. Li, D.; Haneda, H.; Hishita, S.; Labhsetwar, N.K. Fluorine-doped TiO_2 powders prepared by spray pyrolysis and their improved photocatalytic activity for decomposition of gas-phase acetaldehyde. *J. Fluor. Chem.* **2005**, *126*, 69–77. [CrossRef]
176. Yang, G.; Wang, T.; Yang, B.; Yan, Z.; Ding, S.; Xiao, T. Enhanced visible-light activity of F-N co-doped TiO_2 nanocrystals via nonmetal impurity, Ti^{3+} ions and oxygen vacancies. *Appl. Surf. Sci.* **2013**, *287*, 135–142. [CrossRef]
177. Janczarek, M.; Endo, M.; Zhang, D.; Wang, K.; Kowalska, E. Enhanced photocatalytic and antimicrobial performance of cuprous oxide/titania: The effect of titania matrix. *Materials* **2018**, *11*, 2069. [CrossRef]
178. Haque, F.; Daeneke, T.; Kalantar Zadeh, K.; Ou, J. Two-dimensional transition metal oxide and chalcogenide-based photocatalysts. *Nano-Micro Lett.* **2018**, *10*, 23. [CrossRef]
179. Kiwi, J.; Rtimi, S. Mechanisms of the antibacterial effects of TiO_2–FeOx under solar or visible light: Schottky barriers versus surface plasmon resonance. *Coatings* **2018**, *8*, 391. [CrossRef]
180. Bera, S.; Won, D.I.; Rawal, S.B.; Kang, H.J.; Lee, W.I. Design of visible-light photocatalysts by coupling of inorganic semiconductors. *Catal. Today* **2019**, *335*, 3–19. [CrossRef]
181. Phung, H.N.; Tran, V.N.; Nguyen, L.T.; Phan, L.K.; Duong, P.A.; Le, H.V. Investigating visible-photocatalytic activity of MoS_2/TiO_2 heterostructure thin films at various MoS_2 deposition times. *J. Nanomater.* **2017**, *2017*, 3197540. [CrossRef]
182. Liao, Y.; Deng, P.; Wang, X.; Zhang, D.; Li, F.; Yang, Q.; Zhang, H.; Zhong, Z. A Facile method for preparation of Cu_2O-TiO_2 NTA heterojunction with visible-photocatalytic activity. *Nanoscale Res. Lett.* **2018**, *13*, 221. [CrossRef]
183. Li, G.; Huang, J.; Chen, J.; Deng, Z.; Huang, Q.; Liu, Z.; Guo, W.; Cao, R. Highly active photocatalyst of Cu_2O/TiO_2 octahedron for hydrogen generation. *ACS Omega* **2019**, *4*, 3392–3397. [CrossRef]
184. Zhu, X.; Gu, P.; Wu, H.; Yang, D.; Sun, H.; Wangyang, P.; Li, J.; Tian, H. Influence of substrate on structural, morphological and optical properties of TiO_2 thin films deposited by reaction magnetron sputtering. *AIP Adv.* **2017**, *7*, 125326. [CrossRef]

185. Orlianges, J.C.; Crunteanu, A.; Pothier, A.; Merie-Mejean, T.; Blondy, P.; Champeaus, C. Titanium dioxide thin films deposited by pulsed laser deposition and integration in radio frequency devices: Study of structure, optical and dielectric properties. *Appl. Surf. Sci.* **2012**, *263*, 111–114. [CrossRef]
186. Vahl, A.; Veziroglu, S.; Henkel, B.; Strunskus, T.; Polonskyi, O.; Aktas, O.C.; Fuapel, F. Pathways to tailor photocatalytic performance of TiO_2 thin films deposited by reactive magnetron sputtering. *Materials* **2019**, *12*, 2840. [CrossRef] [PubMed]
187. Johari, N.D.; Rosli, J.M.; Juoi, J.M.; Yazid, S.A. Comparison on the TiO_2 crystalline phases deposited via dip and spin coating using green sol–gel route. *J. Mater. Res. Technol.* **2019**, *8*, 2350–2358. [CrossRef]
188. Manoj, P.K.; Koshy, P.; Vaidyan, V.K. Transparent anatase titania films: A critical study on optical properties. *Prog. Nat. Sci. Mater. Int.* **2012**, *22*, 79–85. [CrossRef]
189. Bai, Y.; Mora-Sero, I.; De Angelis, F.; Bisquert, J.; Wang, P. Titanium dioxide nanomaterials for photovoltaic applications. *Chem. Rev.* **2014**, *114*, 10095–10130. [CrossRef]
190. Rauwel, E.; Willinger, M.G.; Ducroquet, F.; Rauwel, P.; Matko, I.; Kiselev, D.; Pinna, N. Carboxylic acids as oxygen sources for the atomic layer deposition of high-κ metal oxides. *J. Phys. Chem. C* **2008**, *112*, 12754–12759. [CrossRef]
191. Correa, G.C.; Bao, B.; Strandwitz, N.C. Chemical stability of titania and alumina thin films formed by atomic layer deposition. *ACS Appl. Mater. Interfaces* **2015**, *7*, 14816–14821. [CrossRef]
192. Zhang, Y.; Utke, I.; Michler, J.; Ilari, G.; Rossell, M.D.; Erni, R. Growth and characterization of CNT–TiO_2 heterostructures. *Beilstein J. Nanotechnol.* **2014**, *5*, 946–955. [CrossRef]
193. Kumar, S.G.; Koteswara Rao, K.S. Polymorphic phase transition among the titania crystal structures in solution based approach: From precursor chemistry to nucleation process. *Nanoscale* **2014**, *6*, 11574–11632. [CrossRef]
194. Padmanabhan, S.C.; Pillai, S.C.; Colreavy, J.; Balakrishnan, S.; McCormack, D.E.; Perova, T.S.; Gunko, Y.; Hinder, S.J.; Kelly, J.M. A simple sol gel processing for the development of high-temperature stable photoactive anatase titania. *Chem. Mater.* **2007**, *19*, 4474–4481. [CrossRef]
195. Behnajady, M.A.; Eskandarloo, H. Preparation of TiO_2 nanoparticles by the sol–gel method under different pH conditions and modeling of photocatalytic activity by artificial neural network. *Res. Chem. Intermed.* **2015**, *41*, 2001–2017. [CrossRef]
196. Lusvard, G.; Barani, C.; Giubertoni, F.; Paganelli, G. Synthesis and characterization of TiO_2 nanoparticles for the reduction of water pollutants. *Materials* **2017**, *10*, 1208. [CrossRef] [PubMed]
197. Sharma, M.; Pathak, M.; Kapoor, P.N. The sol-gel method: Pathway to ultrapure and homogeneous mixed metal oxide nanoparticles. *Asian J. Chem.* **2018**, *30*, 1405–1412. [CrossRef]
198. Marami, M.B.; Farahmandjoum, M.; Khoshnevisan, B. Sol–gel synthesis of Fe-doped TiO_2 nanocrystals. *J. Electron. Mater.* **2018**, *47*, 3741–3748. [CrossRef]
199. Mogal, S.I.; Gandhi, V.G.; Mishra, M.; Tripathi, S.; Joshi, P.A.; Shah, D.O. Single-step synthesis of silver-doped titanium dioxide: Influence of silver on structural, textural, and photocatalytic properties. *Ind. Eng. Chem. Res.* **2014**, *53*, 5749–5758. [CrossRef]
200. Katoueizadeh, E.; Zebarjad, S.M.; Janghorban, K. Synthesis and enhanced visible-light activity of N-doped TiO_2 nano-additives applied over cotton textiles. *J. Mater. Res. Technol.* **2018**, *7*, 204–211. [CrossRef]
201. Nolan, T.; Synnot, D.; Seery, M.; Hider, S.; Van Wassenhaven, A.; Pillai, S. Effect of N-doping on the photocatalytic activity of sol-gel TiO_2. *J. Hazard. Mater.* **2012**, *211–212*, 88–94. [CrossRef]
202. Zane, A.; Zuo, R.; Villamena, F.A.; Rockenbauer, A.; Foushee, A.M.; Flores, K.; Dutta, P.K.; Nagy, A. Biocompatibility and antibacterial activity of nitrogen-doped titanium dioxide nanoparticles for use in dental resin formulations. *Int. J. Nanomed.* **2016**, *11*, 6459–6470. [CrossRef]
203. Qin, H.L.; Gu, G.B.; Liu, S. Preparation of nitrogen-doped titania with visible-light activity and its application. *C. R. Chim.* **2008**, *11*, 95–100. [CrossRef]
204. Livraghi, S.; Chierotti, M.R.; Giamello, E.; Magnacca, G.; Paganini, M.C.; Cappelletti, G.; Bianchi, C.L. Nitrogen-doped titanium dioxide active in photocatalytic reactions with visible light: A multi-technique characterization of differently prepared materials. *J. Phys. Chem. C* **2008**, *112*, 17244–17252. [CrossRef]
205. Yanagisawa, K.; Ovenstone, J. Crystallization of anatase from amorphous titania using the hydrothermal technique: Effects of starting material and temperature. *J. Phys. Chem. B* **1999**, *103*, 7781–7787. [CrossRef]

206. Stride, J.A.; Tuong, N.T. Controlled Synthesis of Titanium Dioxide Nanostructures. In *Solid State Phenomena: Solid State Chemistry and Photocatalysis of Titanium Dioxide*; Nowotny, M.K., Nowotny, J., Eds.; Trans Tech Publications Ltd.: Zurich, Switzerland, 2010; Volume 162, pp. 261–294.
207. Morais, A.; Longo, C.; Araujo, J.; Barroso, M. Nanocrystalline anatase TiO_2/reduced graphene oxide composite films as photoanodes for photoelectrochemical water splitting studies: The role of the reduced graphene oxide. *Phys. Chem. Chem. Phys.* **2015**, *18*, 2608. [CrossRef]
208. De Marco, L.; Manca, M.; Giannuzzi, R.; Malara, F.; Melcarne, G.; Ciccarella, G.; Zama, I.; Cingolani, R.; Gigli, G. Novel preparation method of TiO_2-nanorod-based photoelectrodes for dye-sensitized solar cells with improved light-harvesting efficiency. *J. Phys. Chem. C* **2010**, *114*, 4228–4236. [CrossRef]
209. Falentin-Daudré, C.; Baumann, J.S.; Migonney, V.; Spadavecchia, J. Highly crystalline sphere and rod-shaped TiO_2 nanoparticles: A facile route to bio-polymer grafting. *Front. Lab. Med.* **2017**, *1*, 217–223. [CrossRef]
210. Roca, R.A.; Leite, E.R. Size and shape tailoring of titania nanoparticles synthesized by solvothermal route in different solvents. *J. Am. Ceram. Soc.* **2013**, *96*, 96–102. [CrossRef]
211. Zhang, S.; Li, Y.; Li, M. Facile Synthesis of anatase TiO_2 nanospheres as anode materials for sodium-ion batteries. *JOM* **2018**, *70*, 1411–1415. [CrossRef]
212. Dubey, R.S.; Krishnamurthy, K.V.; Singh, S. Experimental studies of TiO_2 nanoparticles synthesized by sol-gel and solvothermal routes for DSSCs application. *Results Phys.* **2019**, *14*, 102390. [CrossRef]
213. Tjong, S.C.; Hoffman, R.W.; Yeager, E.B. Electron and ion spectroscopic iron-chromium alloys. *J. Electrochem. Soc.* **1982**, *129*, 1662–1668. [CrossRef]
214. Tjong, S.C.; Yeager, E. ESCA and SIMS studies of the passive film on iron. *J. Electrochem. Soc.* **1981**, *128*, 2251–2254. [CrossRef]
215. Louarn, G.; Salou, L.; Hoonaert, A.; Layrolle, P. Nanostuctured surface coatings for titanium alloy implants. *J. Mater. Res.* **2019**, *34*, 1892–1899. [CrossRef]
216. Kulkarni, M.; Mazare, A.; Gongadze, E.; Perutkova, S.; Kralj-Iglič, V.; Milosev, I.; Schmuki, P.; Iglic, A.; Mozetic, M. Titanium nanostructures for biomedical applications. *Nanotechnology* **2015**, *26*, 062002. [CrossRef] [PubMed]
217. Minagar, S.; Wang, J.; Berndt, C.C.; Ivanova, E.P.; Wen, C. Cell response of anodized nanotubes on titanium and titanium alloys. *J. Biomed. Mater. Res. Part A* **2013**, *101*, 2726–2739. [CrossRef] [PubMed]
218. Su, E.; Justin, D.F.; Pratt, C.R.; Sarin, V.K.; Nguyen, V.S.; Oh, S.; Jin, S. Effects of titanium nanotubes on the osseointegration, cell differentiation, mineralisation and antibacterial properties of orthopaedic implant surfaces. *Bone Jt. J.* **2018**, *100* (Suppl. S1A), 9–16. [CrossRef]
219. Fu, Y.; Mo, A. A Review on the electrochemically self-organized titania nanotube arrays: Synthesis, modifications, and biomedical applications. *Nanoscale Res. Lett.* **2018**, *13*, 187. [CrossRef] [PubMed]
220. Liu, N.; Chen, X.; Zhang, J.; Schwank, J.W. A review on TiO_2-based nanotubes synthesized via hydrothermal method: Formation mechanism, structure modification, and photocatalytic applications. *Catal. Today* **2014**, *225*, 34–51. [CrossRef]
221. Ahmad, A.; Haq, E.U.; Akhtar, W.; Arshad, M.; Ahmad, Z. Synthesis and characterization of titania nanotubes by anodizing of titanium in fluoride containing electrolytes. *Appl. Nanosci.* **2017**, *7*, 701–710. [CrossRef]
222. Macak, J.M.; Tsuchiya, H.; Ghicov, A.; Yasuda, K.; Hahn, R.; Bauer, S.; Schmuki, P. TiO_2 nanotubes: Self-organized electrochemical formation, properties and applications. *Curr. Opin. Solid State Mater. Sci.* **2007**, *11*, 3–18. [CrossRef]
223. Do, T.C.; Nguyen, T.Q.; Nguyen, K.T.; Le, P.H. TiO_2 and Au-TiO_2 nanomaterials for rapid photocatalytic degradation of antibiotic residues in aquaculture wastewater. *Materials* **2019**, *12*, 2434. [CrossRef]
224. Lai, C.W. Surface morphology and growth of anodic titania nanotubes films: Photoelectrochemical water splitting studies. *J. Nanomater.* **2015**, *2015*, 820764. [CrossRef]
225. Nguyen, T.L.; Ung, T.D.; Nguyen, Q.L. Non-chapped, vertically well aligned titanium dioxide nanotubes fabricated by electrochemical etching. *Adv. Nat. Sci. Nanosci. Nanotechnol.* **2014**, *5*, 025016. [CrossRef]
226. Lan, M.Y.; Liu, C.P.; Huang, H.H.; Lee, S.W. Both enhanced biocompatibility and antibacterial activity in Ag-decorated TiO_2 nanotubes. *PLoS ONE* **2013**, *8*, e75364. [CrossRef] [PubMed]
227. Li, Y.; Liao, C.; Tjong, S.C. Electrospun polyvinylidene fluoride-based fibrous scaffolds with piezoelectric characteristics for bone and neural tissue engineering. *Nanomaterials* **2019**, *9*, 952. [CrossRef] [PubMed]
228. Al-Enizi, A.M.; Zagho, M.M.; Elzatahry, A.A. Polymer-based electrospun nanofibers for biomedical applications. *Nanomaterials* **2018**, *8*, 259. [CrossRef]

229. Feng, S.; Zhang, F.; Ahmed, S.; Liu, Y. Physico-mechanical and antibacterial properties of PLA/TiO_2 composite materials synthesized via electrospinning and solution casting processes. *Coatings* **2019**, *9*, 525. [CrossRef]
230. Xue, J.; Wu, T.; Dai, Y.; Xia, Y. Electrospinning and electrospun nanofibers: Methods, materials, and applications. *Chem. Rev.* **2019**, *19*, 5298–5415. [CrossRef]
231. Tekmen, C.; Susio, A.; Cocen, U. Titania nanofibers prepared by electrospinning. *Mater. Lett.* **2008**, *62*, 4470–4472. [CrossRef]
232. Mondal, K. Recent advances in the synthesis of metal oxide nanofibers and their environmental remediation applications. *Inventions* **2017**, *2*, 9. [CrossRef]
233. Albetran, H.; O'Connor, B.H.; Low, I.M. Effect of calcination on band gaps for electrospun titania nanofibers heated in air–argon mixtures. *Mater. Des.* **2016**, *92*, 480–485. [CrossRef]
234. Chapman, B.S.; Mishra, S.R.; Tracy, J.B. Direct electrospinning of titania nanofibers with ethanol. *Dalton Trans.* **2019**, *48*, 12822–12827. [CrossRef]
235. Pan, X.; Yang, M.Q.; Fu, X.; Zhang, N. Defective TiO_2 with oxygen vacancies: Synthesis, properties and photocatalytic applications. *Nanoscale* **2013**, *5*, 3601. [CrossRef] [PubMed]
236. Nasr, M.; Balme, S.; Eid, C.; Habchi, R.; Miele, P.; Bechelany, M. Enhanced visible-light photocatalytic performance of electrospun rGO/TiO_2 composite nanofibers. *J. Phys. Chem. C* **2017**, *121*, 261–269. [CrossRef]
237. Kiwi, J.; Rtimi, S.; Sanjines, R.; Pulgarin, C. TiO_2 and TiO_2-doped films able to kill bacteria by contact: New evidence for the dynamics of bacterial inactivation in the dark and under light irradiation. *Int. J. Photoenergy* **2014**, *2014*, 785037. [CrossRef]
238. Li, Y.; Zhang, W.; Niu, J.; Chen, Y. Mechanism of photogenerated reactive oxygen species and correlation with the antibacterial properties of engineered metal-oxide nanoparticles. *ACS Nano* **2012**, *6*, 5164–5173. [CrossRef]
239. Tsai, T.M.; Chang, H.H.; Chang, K.C.; Liu, Y.L.; Tseng, C.C. A comparative study of the bactericidal effect of photocatalytic oxidation by TiO_2 on antibiotic-resistant and antibiotic-sensitive bacteria. *J. Chem. Technol. Biotechnol.* **2010**, *85*, 1642–1653. [CrossRef]
240. Kubacka, A.; Diez, M.S.; Rojo, D.; Bargiela, R.; Ciordia, S.; Zapico, I.; Albar, J.P.; Barbas, C.; dos Santos, V.A.; Fernández-García, M.; et al. Understanding the antimicrobial mechanism of TiO_2-based nanocomposite films in a pathogenic bacterium. *Sci. Rep.* **2015**, *4*, 4134. [CrossRef]
241. Vatansever, F.; de Melo, W.C.; Avci, P.; Vecchio, D.; Sadasivam, M.; Gupta, A.; Chandran, R.; Karimi, M.; Parizotto, N.A.; Yin, R.; et al. Antimicrobial strategies centered around reactive oxygen species—Bactericidal antibiotics, photodynamic therapy and beyond. *FEMS Microbiol. Rev.* **2013**, *37*, 955–989. [CrossRef]
242. Sheng, H.; Nakamura, K.; Kanno, T.; Sasaki, K.; Niwano, Y. Bactericidal effect of photolysis of H_2O_2 in combination with sonolysis of water via hydroxyl radical generation. *PLoS ONE* **2015**, *10*, e0132445. [CrossRef]
243. Michels, H.T.; Keevil, C.W.; Salgado, C.D.; Schmidt, M.G. From laboratory research to a clinical trial: Copper alloy surfaces kill bacteria and reduce hospital-acquired infections. *Herd* **2015**, *9*, 64–79. [CrossRef]
244. Rtimi, S.; Pulgarin, C.; Kiwi, J. Recent developments in accelerated antibacterial inactivation on 2D Cu-titania surfaces under indoor visible light. *Coatings* **2017**, *7*, 20. [CrossRef]
245. Moongraksathum, B.; Shang, J.Y.; Chen, Y.W. Photocatalytic antibacterial effectiveness of Cu-doped TiO_2 thin film prepared via the peroxo sol-gel method. *Catalysts* **2018**, *8*, 352. [CrossRef]
246. Leyland, N.S.; Podporska-Carroll, J.; Browne, J.; Hinder, S.J.; Quilty, B.; Pillai, S.C. Highly efficient F, Cu doped TiO_2 anti-bacterial visible light active photocatalytic coatings to combat hospital-acquired infections. *Sci. Rep.* **2016**, *6*, 24770. [CrossRef] [PubMed]
247. Yadav, H.M.; Odari, S.V.; Koli, V.B.; Mali, S.S.; Hong, C.K.; Pawar, S.H.; Delekar, S.D. Preparation and characterization of copper-doped anatase TiO_2 nanoparticles with visible light photocatalytic antibacterial activity. *J. Photochem. Photobiol. A* **2014**, *280*, 32–38. [CrossRef]
248. Yadav, H.M.; Odari, S.V.; Bohara, R.A.; Mali, S.S.; Pawar, S.H.; Delekar, S.D. Synthesis and visible light photocatalytic antibacterial activity of nickel-doped TiO_2 nanoparticles against Gram-positive and Gram-negative bacteria. *J. Photochem. Photobiol. A* **2014**, *294*, 130–136. [CrossRef]
249. Vollmer, W.; Blanot, D.; De Pedro, M.A. Peptidoglycan structure and architecture. *FEMS Microbiol. Rev.* **2008**, *32*, 149–167. [CrossRef] [PubMed]
250. Bertani, B.; Ruiz, N. Function and biogenesis of lipopolysaccharides. *EcoSal Plus* **2018**. [CrossRef] [PubMed]

251. Botos, I.; Noinaj, N.; Buchanan, S.K. Insertion of proteins and lipopolysaccharide into the bacterial outer membrane. *Philos. Trans. R. Soc. B* **2017**, *372*, 20160224. [CrossRef] [PubMed]
252. Polissi, A.; Sperandeo, P. The lipopolysaccharide export pathway in Escherichia coli: Structure, organization and regulated assembly of the Lpt machinery. *Mar. Drugs* **2014**, *12*, 1023–1042. [CrossRef]
253. Dakal, T.C.; Kumar, A.; Majumdar, R.S.; Yadav, V. Mechanistic basis of antimicrobial actions of silver nanoparticles. *Front. Microbiol.* **2016**, *7*, 1831. [CrossRef]
254. Hsueh, Y.H.; Lin, K.S.; Ke, W.J.; Hsieh, C.T.; Chiang, C.L.; Tzou, D.Y.; Liu, S.T. The antimicrobial properties of silver nanoparticles in Bacillus subtilis are mediated by released Ag^+ ions. *PLoS ONE* **2015**, *10*, e0144306. [CrossRef]
255. Riaz Ahmed, K.B.; Nagy, A.M.; Brown, R.P.; Zhang, Q.; Malghan, S.G.; Goering, P.L. Silver nanoparticles: Significance of physicochemical properties and assay interference on the interpretation of in vitro cytotoxicity studies. *Toxicol. In Vitro* **2017**, *38*, 179–192. [CrossRef] [PubMed]
256. Gupta, K.; Singh, R.P.; Pandey, A.; Pandey, A. Photocatalytic antibacterial performance of TiO_2 and Ag-doped TiO_2 against *S. aureus*, *P. aeruginosa* and *E. coli*. *Beilstein J. Nanotechnol.* **2013**, *4*, 345–351. [CrossRef] [PubMed]
257. Garvey, M.; Panaitescu, E.; Menon, L.; Byrne, C.; Dervin, S.; Hinder, S.J.; Pillai, S.C. Titania nanotube photocatalysts for effectively treating waterborne microbial pathogens. *J. Catal.* **2016**, *344*, 631–639. [CrossRef]
258. Nguyen, N.T.; Ozkan, S.; Tomanec, O.; Zboril, A.; Schmuki, P. Spaced titania nanotube arrays allow the construction of an efficient N-doped hierarchical structure for visible light harvesting. *ChemistryOpen* **2018**, *7*, 131–135. [CrossRef]
259. Podporska-Carroll, J.; Panaitescu, E.; Quilty, B.; Wang, L.; Menon, L.; Pillai, S.C. Antimicrobial properties of highly efficient photocatalytic TiO_2 nanotubes. *Appl. Catal. B Environ.* **2015**, *176*, 70–75. [CrossRef]
260. Hajjaji, A.; Elabidi, M.; Trabelsi, K.; Assadi, A.A.; Bessais, B.; Rtimi, S. Bacterial adhesion and inactivation on Ag decorated TiO_2-nanotubes under visible light: Effect of the nanotubes geometry on the photocatalytic activity. *Colloids Surf. B* **2018**, *70*, 92–98. [CrossRef]
261. Uhm, S.H.; Song, D.H.; Kwon, J.S.; Lee, S.B.; Han, J.G.; Kim, K.N. Tailoring of antibacterial Ag nanostructures on TiO_2 nanotube layers by magnetron sputtering. *J. Biomed. Mater. Res. Part B* **2014**, *102*, 592–603. [CrossRef]
262. Dunnill, C.W.; Aiken, Z.A.; Kafizas, A.; Pratten, J.; Wilson, M.; Morgan, D.J.; Parkin, I.P. White light induced photocatalytic activity of sulfur-doped TiO_2 thin films and their potential for antibacterial application. *J. Mater. Chem.* **2009**, *19*, 8747–8754. [CrossRef]
263. Xue, X.; Wang, Y.; Yang, H. Preparation and characterization of boron-doped titania nano-materials with antibacterial activity. *Appl. Surf. Sci.* **2013**, *264*, 94–99. [CrossRef]
264. Sun, D.S.; Kau, J.H.; Huang, H.H.; Tseng, Y.H.; Wu, W.S.; Chang, H.H. Antibacterial properties of visible-light-responsive carbon-containing titanium dioxide photocatalytic nanoparticles against anthrax. *Nanomaterials* **2016**, *6*, 237. [CrossRef]
265. He, P.; Tao, J.; Huang, X.; Xue, J. Preparation and photocatalytic antibacterial property of nitrogen doped TiO_2 nanoparticles. *J. Sol-Gel Sci. Technol.* **2013**, *68*, 213–218. [CrossRef]
266. Fagan, R.; McCormack, D.E.; Hinder, S.; Pillai, S.C. Improved high temperature stability of anatase TiO_2 photocatalysts by N, F, P co-doping. *Mater. Des.* **2016**, *96*, 44–53. [CrossRef]
267. Li, C.; Sun, Z.; Ma, R.; Xue, Y.; Zheng, S. Fluorine doped anatase TiO_2 with exposed reactive (001) facets supported on porous diatomite for enhanced visible-light photocatalytic activity. *Microporous Mesoporous Mater.* **2017**, *243*, 281–290. [CrossRef]
268. Hamilton, J.W.J.; Byrne, J.A.; Dunlop, P.S.M.; Dionysiou, D.D.; Pelaez, M.; O'Shea, K.; Synnott, D.; Pillai, S.C. Evaluating the mechanism of visible light activity for N,F-TiO_2 using photoelectrochemistry. *J. Phys. Chem. C* **2014**, *118*, 12206–12215. [CrossRef]
269. Abdullah, A.M.; Gracia-Pinilla, M.A.; Pillai, S.C.; O'Shea, K. UV and visible light-driven production of hydroxyl radicals by reduced forms of N, F, and P codoped titanium dioxide. *Molecules* **2019**, *24*, 2147. [CrossRef] [PubMed]
270. Milosevic, I.; Jayaprakash, A.; Greenwood, B.; van Driel, B.; Rtimi, S.; Bowen, P. Synergistic effect of fluorinated and N doped TiO_2 nanoparticles leading to different microstructure and enhanced photocatalytic bacterial inactivation. *Nanomaterials* **2017**, *7*, 391. [CrossRef]

271. Milosevic, I.; Rtimi, S.; Jayaprakash, A.; van Driel, B.; Greenwood, B.; Aimable, A.; Senna, M.; Bowen, P. Synthesis and characterization of fluorinated anatase nanoparticles and subsequent N-doping for efficient visible light activated photocatalysis. *Colloids Surf. B* **2018**, *171*, 445–450. [CrossRef]
272. Akhavan, O.; Ghaderi, E. Toxicity of graphene and graphene oxide nanowalls against bacteria. *ACS Nano* **2010**, *4*, 5731–5736. [CrossRef]
273. Akhavan, O.; Ghaderi, E.; Esfandiar, A. Wrapping bacteria by graphene nanosheets for isolation from environment, reactivation by sonication and inactivation by near-infrared irradiation. *J. Phys. Chem. B* **2011**, *115*, 6279–6288. [CrossRef]
274. Lu, X.; Feng, X.; Werber, J.R.; Chu, C.; Zucker, I.; Kim, J.H.; Osuji, J.O.; Elimelech, M. Enhanced antibacterial activity through the controlled alignment of graphene oxide nanosheets. *Proc. Natl. Acad. Sci. USA* **2017**, *114*, E9793–E9801. [CrossRef]
275. Linklater, D.P.; Baulin, V.A.; Juodkazis, S.; Ivanova, E.P. Mechano-bactericidal mechanism of graphene nanomaterials. *Interface Focus* **2018**, *8*, 20170060. [CrossRef] [PubMed]
276. Akhavan, O.; Ghaderi, E. Photocatalytic reduction of graphene oxide nanosheets on TiO_2 thin film for photoinactivation of bacteria in solar light irradiation. *J. Phys. Chem. C* **2009**, *113*, 20214–20220. [CrossRef]
277. Nica, I.C.; Stan, M.S.; Popa, M.; Chifiriuc, M.C.; Pircalabioru, G.G.; Lazar, V.; Dumitrescu, I.; Diamandescu, L.; Feder, M.; Baibarac, M.; et al. Development and biocompatibility evaluation of photocatalytic TiO_2/reduced graphene oxide-based nanoparticles designed for self-cleaning purposes. *Nanomaterials* **2017**, *7*, 279. [CrossRef]
278. Andrews, J.M. Determination of minimum inhibitory concentration. *J. Antimicrob. Chemother.* **2002**, *49*, 1049. [CrossRef]
279. Macia, M.D.; Rojo-Molinero, E.; Oliver, A. Antimicrobial susceptibility testing in biofilm-growing bacteria. *Clin. Microbiol. Infect.* **2014**, *20*, 981–990. [CrossRef] [PubMed]
280. Tjong, S.C. Structural and mechanical properties of polymer nanocomposites. *Mater. Sci. Eng. R Rep.* **2006**, *53*, 73–197. [CrossRef]
281. Jamróz, E.; Kulawik, P.; Kopel, P. The effect of nanofillers on the functional properties of biopolymer-based films: A review. *Polymers* **2019**, *11*, 675. [CrossRef]
282. Gao, T.; Jiang, M.; Liu, X.; You, G.; Wang, W.; Sun, Z.; Ma, A.; Chen, J. Patterned polyvinyl alcohol hydrogel dressings with stem cells seeded for wound healing. *Polymers* **2019**, *11*, 171. [CrossRef]
283. Mochane, M.J.; Motsoeneng, T.S.; Sadiku, E.R.; Mokhena, T.C.; Sefadi, J.S. Morphology and properties of electrospun PCL and its composites for medical applications: A mini review. *Appl. Sci.* **2019**, *9*, 2205. [CrossRef]
284. Liao, C.; Li, Y.; Tjong, S.C. Antibacterial activities of aliphatic polyester nanocomposites with silver nanoparticles and/or graphene oxide sheets. *Nanomaterials* **2019**, *9*, 1102. [CrossRef]
285. Rescek, A.; Scetar, M.; Hrnjak-Murgić, Z.; Dimitrov, N.; Galic, K. Polyethylene/polycaprolactone nanocomposite films for food Packaging modified with magnetite and casein: Oxygen barrier, mechanical, and thermal properties. *Polym. Plast. Technol.* **2016**, *55*, 1450–1459. [CrossRef]
286. Xing, Y.; Li, X.; Zhang, L.; Xu, Q.; Che, Z.; Li, W.; Bai, Y.; Li, K. Effect of TiO_2 nanoparticles on the antibacterial and physical properties of polyethylene-based film. *Prog. Org. Coat.* **2012**, *73*, 219–224. [CrossRef]
287. Munoz-Bonilla, A.; Cerrada, M.L.; Fernández-Garcia, M.; Kubacla, A.; Ferrer, M.; Fernandez-Garcia, M. Biodegradable polycaprolactone-titania nanocomposites: Preparation, characterization and antimicrobial properties. *Int. J. Mol. Sci.* **2013**, *14*, 9249–9266. [CrossRef] [PubMed]
288. Raut, A.V.; Yadav, H.M.; Gnanamani, A.; Pushpavanam, S.; Pawar, S.H. Synthesis and characterization of chitosan-TiO_2: Cu nanocomposite and their enhanced antimicrobial activity with visible light. *Colloids Surf. B* **2011**, *148*, 566–575. [CrossRef] [PubMed]
289. Zhang, X.; Xiao, G.; Wang, Y.; Zhao, Y.; Su, H.; Tan, T. Preparation of chitosan-TiO_2 composite film with efficient antimicrobial activities under visible light for food packaging applications. *Carbohydr. Polym.* **2017**, *169*, 101–107. [CrossRef]
290. Li, J.; Xie, B.; Xia, K.; Li, Y.; Han, J.; Zhao, C. Enhanced antibacterial activity of silver doped titanium dioxide-chitosan composites under visible light. *Materials* **2018**, *11*, 1403. [CrossRef]
291. Jbeli, A.; Hamden, Z.; Bouattour, S.; Ferraria, A.M.; Conceicao, D.S.; Vieira Ferreira, L.F.; Chehimi, M.M.; do Rego, A.M.; Rei Vilar, M.; Boufi, S. Chitosan-Ag-TiO_2 films: An effective photocatalyst under visible light. *Carbohydr. Polym.* **2018**, *199*, 31–40. [CrossRef]

292. Saravanan, R.; Aviles, J.; Gracia, F.; Mosquera, E.; Gupta, V.K. Crystallinity and lowering band gap induced visible light photocatalytic activity of TiO_2/CS (chitosan) nanocomposites. *Int. J. Biol. Macromol.* **2018**, *109*, 1239–1245. [CrossRef]
293. Zhao, Y.; Tao, C.; Xiao, G.; Xu, H. Controlled synthesis and wastewater treatment of Ag_2O/TiO_2 modified chitosan-based photocatalytic film. *RSC Adv.* **2017**, *7*, 11211–11221. [CrossRef]
294. Hamden, Z.; Bouattour, S.; Ferraria, A.M.; Ferreira, D.P.; Vieira Ferreira, L.F.; Botelho do Rego, A.M.; Boufi, S. In situ generation of TiO_2 nanoparticles using chitosan as a template and their photocatalytic activity. *J. Photochem. Photobiol. A* **2016**, *321*, 211–222. [CrossRef]
295. Kaewklin, P.; Siripatrawan, U.; Suwanagul, A.; Lee, Y.S. Active packaging from chitosan-titanium dioxide nanocomposite film for prolonging storage life of tomato fruit. *Int. J. Biol. Macromol.* **2018**, *112*, 523–529. [CrossRef] [PubMed]
296. Lavengood, S.L.; Zhang, M. Chitosan-based scaffolds for bone tissue engineering. *J. Mater. Chem. B* **2014**, *7*, 3161–3184. [CrossRef] [PubMed]
297. Callewaert, C.; De Maeseneire, E.; Kerckhof, F.M.; Verliefde, A.; Van de Wiele, T.; Boon, N. Microbial odor profile of polyester and cotton clothes after a fitness session. *Appl. Environ. Microbiol.* **2014**, *80*, 6611–6619. [CrossRef] [PubMed]
298. Zahid, M.; Papadopoulou, E.L.; Suarato, G.; Binas, V.D.; Kiriakidis, G.; Gounaki, I.; Moira, O.; Venieri, D.; Bayer, I.S.; Athanassiou, A. Fabrication of visible light-induced antibacterial and self-cleaning cotton fabrics using manganese doped TiO_2 nanoparticles. *ACS Appl. Bio Mater.* **2018**, *1*, 1154–1164. [CrossRef]
299. Pfang, P.G.; García-Cañete, J.; García-Lasheras, J.; Blanco, A.; Aunon, A.; Parron-Cambero, R.; Macías-Valcayo, A.; Esteban, J. Orthopedic implant-associated infection by multidrug resistant Enterobacteriaceae. *J. Clin. Med.* **2019**, *8*, 220. [CrossRef]
300. Li, Y.; Yang, Y.; Li, R.; Tang, X.; Guo, D.; Qing, Y.; Qin, Y. Enhanced antibacterial properties of orthopedic implants by titanium nanotube surface modification: A review of current techniques. *Int. J. Nanomed.* **2019**, *14*, 7217–7236. [CrossRef]
301. Gollwitzer, H.; Haenie, M.; Mittelmeier, W.; Heidenau, F.; Harrasser, N. A biocompatible sol-gel derived titania coating for medical implants with antibacterial modification by copper integration. *AMB Express* **2018**, *8*, 24. [CrossRef]
302. Tsou, H.K.; Hsieh, P.Y.; Chi, M.H.; Chung, C.J.; He, J.L. Improved osteoblast compatibility of medical-grade polyetheretherketone using arc ionplated rutile/anatase titanium dioxide films for spinal implants. *J. Biomed. Mater. Res. Part A* **2012**, *100*, 2787–2792. [CrossRef]
303. Radtke, A.; Topolski, A.; Jędrzejewski, T.; Kozak, W.; Sadowska, B.; Więckowska-Szakiel, M.; Szubka, M.; Talik, E.; Nielsen, L.P.; Piszczek, P. The bioactivity and photocatalytic properties of titania nanotube coatings produced with the use of the low-potential anodization of Ti6Al4V alloy surface. *Nanomaterials* **2017**, *7*, 197. [CrossRef]
304. Xu, L.; Lv, K.; Yu, W.Q. Effect of TiO_2 nanotube layers thickness on periodontal ligament cells. *Dentistry* **2016**, *6*, 369. [CrossRef]
305. Piszczek, P.; Lewandowska, Z.; Radtke, A.; Jędrzejewski, T.; Kozak, W.; Sadowska, B.; Szubka, M.; Talik, E.; Flori, F. Biocompatibility of titania nanotube coatings enriched with silver nanograins by chemical vapor deposition. *Nanomaterials* **2017**, *7*, 274. [CrossRef] [PubMed]
306. Laux, P.; Tentschert, J.; Riebeling, C.; Braeuning, A.; Creutzenberg, O.; Epp, A.; Fessard, V.; Haas, K.H.; Haase, A.; Hund-Rinke, K.; et al. Nanomaterials: Certain aspects of application, risk assessment and risk communication. *Arch. Toxicol.* **2018**, *92*, 121–141. [CrossRef] [PubMed]
307. Wadhwa, S.; Rea, C.; O'Hare, P.; Mathur, A.; Roy, S.S.; Dunlop, P.S.M.; Byrne, J.A.; Burke, G.; Meenan, B.; McLaughlin, J.A. Comparative in vitro cytotoxicity study of carbon nanotubes and titania nanostructures on human lung epithelial cells. *J. Hazard. Mater.* **2011**, *191*, 56–61. [CrossRef] [PubMed]
308. Mohamed, M.A.; Torabi, A.; Paulose, M.; Sakthi Kumar, D.; Varghese, O.K. Anodically grown titania nanotube induced cytotoxicity has genotoxic origins. *Sci. Rep.* **2017**, *7*, 41844. [CrossRef] [PubMed]
309. Allegri, M.; Bianchi, M.G.; Chiu, M.; Varet, J.; Costa, A.L.; Ortelli, S.; Blosi, M.; Bussolati, O.; Poland, C.A.; Bergamaschi, E. Shape-related toxicity of titanium dioxide nanofibres. *PLoS ONE* **2016**, *11*, e0151365. [CrossRef] [PubMed]

310. Holden, P.A.; Gardea-Torresdey, J.L.; Klaessig, F.; Turco, R.; Mortimer, M.; Hund-Rinke, K.; Avery, D.; Barcelo, D.; Behra, R.; Cohen, Y.; et al. Considerations of environmentally relevant test conditions for improved evaluation of ecological hazards of engineered nanomaterials. *Environ. Sci. Technol.* **2016**, *50*, 6124–6145. [CrossRef]
311. Gupta, R.; Xie, H. Nanoparticles in daily life: Applications, toxicity and regulations. *J. Environ. Pathol. Toxicol. Oncol.* **2018**, *37*, 209–230. [CrossRef]
312. Khezri, S.M.; Shariat, S.M.; Tabibian, S. Evaluation of extracting titanium dioxide from water-based paint sludge in auto-manufacturing industries and its application in paint production. *Toxicol. Ind. Health* **2013**, *29*, 697–703. [CrossRef]
313. Al-Kattan, A.; Wichser, A.; Vonbank, R.; Brunner, S.; Ulrich, A.; Zuin, S.; Nowack, B. Release of TiO_2 from paints containing pigment-TiO_2 or nano-TiO_2 by weathering. *Environ. Sci. Process. Impacts* **2013**, *15*, 2186–2193. [CrossRef]
314. Kim, Y. Nanowastes treatment in environmental media. *Environ. Health Toxicol.* **2014**, *29*, e2014015. [CrossRef]
315. Shi, X.; Li, Z.; Chen, W.; Qiang, L.; Xia, J.; Chen, M.; Zhu, L.; Alvarez, P.J. Fate of TiO_2 nanoparticles entering sewage treatment plants and bioaccumulation in fish in the receiving streams. *NanoImpact* **2016**, *3–4*, 96–103. [CrossRef]
316. Clemente, Z.; Castro, V.L.; Moura, M.A.; Jonsson, C.M.; Fraceto, L.F. Toxicity assessment of TiO_2 nanoparticles in zebrafish embryos under different exposure conditions. *Aquat. Toxicol.* **2014**, *147*, 129–139. [CrossRef] [PubMed]
317. De Matteis, V. Exposure to inorganic nanoparticles: Routes of entry, immune response, biodistribution and in vitro/in vivo toxicity evaluation. *Toxics* **2017**, *5*, 29. [CrossRef] [PubMed]
318. Ahamed, M.; Khan, M.A.M.; Akhtar, M.J.; Alhadlaq, H.A.; Alshamshan, A. Ag-doping regulates the cytotoxicity of TiO_2 nanoparticles via oxidative stress in human cancer cells. *Sci. Rep.* **2017**, *7*, 17662. [CrossRef]
319. Kuku, G.; Culha, M. Investigating the origins of toxic response in TiO_2 nanoparticle-treated cells. *Nanomaterials* **2017**, *7*, 83. [CrossRef]
320. Batt, J.; Milward, M.; Chapple, I.; Grant, M.; Roberts, H.; Addison, O. TiO_2 nanoparticles can selectively bind CXCL8 impacting on neutrophil chemotaxis. *Eur. Cells Mater.* **2018**, *35*, 13–24. [CrossRef]
321. Ribeiro, A.; Gemini-Piperni, S.; Travassos, R.; Lemgruber, L.; Silva, R.C.; Rossi, A.L.; Farina, M.; Anselme, K.; Shokuhfar, T.; Shahbazian-Yassar, R.; et al. Trojan-like internalization of anatase titanium dioxide nanoparticles by human osteoblast cells. *Sci. Rep.* **2016**, *6*, 23615. [CrossRef]
322. Valentini, X.; Absil, L.; Laurent, G.; Robbe, A.; Laurent, S.; Muller, R.; Legrand, A.; Nonclercq, D. Toxicity of TiO_2 nanoparticles on the NRK52E renal cell line. *Mol. Cell. Toxicol.* **2017**, *13*, 419–431. [CrossRef]
323. Wang, Y.; Cui, H.; Zhou, J.; Li, F.; Wang, J.; Chen, M.; Liu, Q. Cytotoxicity, DNA damage, and apoptosis induced by titanium dioxide nanoparticles in human non-small cell lung cancer A549 cells. *Environ. Sci. Pollut. Res.* **2014**, *22*, 5519–5530. [CrossRef]
324. Shi, H.; Magaye, R.; Castranova, V.; Zhao, J. Titanium dioxide nanoparticles: A review of current toxicological data. *Part. Fibre Toxicol.* **2013**, *10*, 15. [CrossRef]
325. Mottola, F.; Iovine, C.; Santonastaso, M.; Romeo, M.L.; Pacifico, S.; Cobellis, L.; Rocco, L. NPs-TiO_2 and lincomycin coexposure induces DNA damage in cultured human amniotic cells. *Nanomaterials* **2019**, *9*, 1511. [CrossRef] [PubMed]
326. Golbamak, N.; Rasulev, B.; Cassano, A.; Marchese Robinson, R.L.; Benfenati, E.; Leszczynski, J.; Cronin, M.T. Genotoxicity of metal oxide nanomaterials: Review of recent data and discussion of possible mechanisms. *Nanoscale* **2015**, *7*, 2154–2198. [CrossRef] [PubMed]
327. Huerta-García, E.; Zepeda-Quiroz, I.; Sánchez-Barrera, H.; Colín-Val, Z.; Alfaro-Moreno, E.; Ramos-Godinez, M.D.P.; López-Marure, R. Internalization of titanium dioxide nanoparticles is cytotoxic for H9c2 rat cardiomyoblasts. *Molecules* **2018**, *6*, 1955. [CrossRef] [PubMed]
328. Yin, J.J.; Liu, J.; Ehrenshaft, M.; Roberts, J.E.; Fu, P.P.; Mason, R.P.; Zhao, B. Phototoxicity of nanotitanium dioxides in HaCaT keratinocytes—Generation of reactive oxygen species and cell damage. *Toxicol. Appl. Pharmacol.* **2012**, *263*, 81–88. [CrossRef]
329. Ren, Y.; Liu, X.; Geng, R.; Lu, Q.; Rao, R.; Tan, X.; Yang, X.; Liu, W. Increased level of α2,6-sialylated glycans on HaCaT cells induced by titanium dioxide nanoparticles under UV radiation. *Nanomaterials* **2018**, *8*, 253. [CrossRef] [PubMed]

330. Grassian, V.H.; O'Shaughnessy, P.T.; Adamcakova-Dodd, A.; Pettibone, J.M.; Thorne, P.S. Inhalation exposure study of titanium dioxide nanoparticles with a primary particle size of 2 to 5 nm. *Environ. Health Perspect.* **2007**, *115*, 397–402. [CrossRef]
331. Liu, R.; Yin, L.; Pu, Y.; Lian, G.; Zhang, J.; Su, Y.; Xia, Z.; Ye, B. Pulmonary toxicity induced by three forms of titanium dioxide nanoparticles via intratracheal instillation in rats. *Prog. Nat. Sci.* **2009**, *19*, 573–579. [CrossRef]
332. Wu, J.; Liu, W.; Xue, C.; Zhou, S.; Lan, F.; Bi, L.; Xu, H.; Yang, X.; Zeng, F. Toxicity and penetration of TiO_2 nanoparticles in hairless mice and porcine skin after subchronic dermal exposure. *Toxicol. Lett.* **2009**, *191*, 1–8. [CrossRef]
333. Disdier, C.; Devoy, J.; Cosnefroy, A.; Chalansonnet, M.; Herlin-Boime, N.; Brun, E.; Lund, A.; Mabondzo, A. Tissue biodistribution of intravenously administrated titanium dioxide nanoparticles revealed blood-brain barrier clearance and brain inflammation in rat. *Part. Fibre Toxicol.* **2015**, *12*, 27. [CrossRef]
334. Hong, J.; Zhang, Y.Q. Murine liver damage caused by exposure to nano-titanium dioxide. *Nanotechnology* **2016**, *27*, 112001. [CrossRef]
335. Jia, X.; Wang, S.; Zhou, L.; Sun, L. The potential liver, brain, and embryo toxicity of titanium dioxide nanoparticles on mice. *Nanoscale Res. Lett.* **2017**, *12*, 478. [CrossRef] [PubMed]
336. Jin, C.; Wang, F.; Tang, Y.; Zhang, X.; Wang, J.; Yang, Y. Distribution of graphene oxide and TiO_2-graphene oxide composite in A549 cells. *Biol. Trace Elem. Res.* **2014**, *159*, 393–398. [CrossRef] [PubMed]
337. Prakash, J.; Venkatesan, M.; Praksash, J.S.; Bharath, G.; Anwer, S.; Veluswamy, P.; Prema, D.; Venkataprasanna, K.S.; Venkatasubbu, G.D. Investigations on the in-vivo toxicity analysis of reduced graphene oxide/TiO_2 nanocomposite in zebrafish embryo and larvae (Danio rerio). *Appl. Surf. Sci.* **2019**, *481*, 1360–1369. [CrossRef]
338. Code of Federal Regulations (Annual Edition). Available online: https://www.govinfo.gov/app/collection/cfr (accessed on 8 January 2020).
339. European Food Safety Authority (EFSA). Re-evaluation of titanium dioxide (E 171) as a food additive. *EFSA J.* **2016**, *14*, 4545. [CrossRef]
340. Rompelberg, C.; Heringa, M.B.; van Donkersgoed, G.; Drijvers, J.; Roos, A.; Westenbrink, S.; Peters, R.; van Bemmel, G.; brand, W.; Oomen, A.G. Oral intake of added titanium dioxide and its nanofraction from food products, food supplements and toothpaste by the Dutch population. *Nanotoxicology* **2016**, *10*, 1404–1414. [CrossRef]
341. Hwang, J.S.; Yu, J.; Kim, H.M.; Oh, J.M.; Choi, S.J. Food additive titanium dioxide and its fate in commercial foods. *Nanomaterials* **2019**, *9*, 1175. [CrossRef]
342. Skocaj, M.; Filipic, M.; Petkovic, J.; Novak, S. Titanium dioxide in our everyday life; is it safe? *Radiol. Oncol.* **2011**, *45*, 227–247. [CrossRef]
343. Heringa, M.B.; Peters, R.J.B.; Bleys, R.L.A.; van der Lee, M.K.; Tromp, P.C.; van Kesteren, P.C.; van Eijkeren, J.C.; Undas, A.K.; Oomen, A.G.; Bouwmeester, H. Detection of titanium particles in human liver and spleen and possible health implications. *Part. Fibre Toxicol.* **2018**, *15*, 15. [CrossRef]
344. Kalinska, A.; Jaworski, S.; Wierzbicki, M.; Golebiewski, M. Silver and copper nanoparticles—An alternative in future mastitis treatment and prevention? *Int. J. Mol. Sci.* **2019**, *20*, 1672. [CrossRef]
345. Li, S.H.; Zhu, T.X.; Huang, J.Y.; Guo, Q.Q.; Chen, G.Q.; Lai, Y.K. Durable antibacterial and UV-protective Ag/TiO_2@fabrics for sustainable biomedical application. *Int. J. Nanomed.* **2017**, *12*, 2593–2606. [CrossRef]
346. Lammel, T.; Sturve, J. Assessment of titanium dioxide nanoparticle toxicity in the rainbow trout (*Onchorynchus mykiss*) liver and gill cell lines RTL-W1 and RTgill-W1 under particular consideration of nanoparticle stability and interference with fluorometric assays. *NanoImpact* **2018**, *11*, 1–19. [CrossRef]
347. Smith, M.R.; Fernandes, J.; Go, Y. Redox dynamics of manganese as a mitochondrial life-death switch. *Biochem. Biophys. Res. Commun.* **2017**, *482*, 388–398. [CrossRef] [PubMed]
348. Zhang, L.; Sang, H.; Liu, Y.; Li, J. Manganese activates caspase-9-dependent apoptosis in human bronchial epithelial cells. *Hum. Exp. Toxicol.* **2013**, *32*, 1155–1163. [CrossRef] [PubMed]

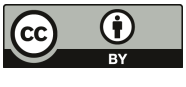

nanomaterials

MDPI

Letter

Deciphering the Roles of Interspace and Controlled Disorder in the Bactericidal Properties of Nanopatterns against *Staphylococcus aureus*

Khashayar Modaresifar [1,*,†], Lorenzo B. Kunkels [1,†], Mahya Ganjian [1], Nazli Tümer [1], Cornelis W. Hagen [2], Linda G. Otten [3], Peter-Leon Hagedoorn [3], Livia Angeloni [1,4], Murali K. Ghatkesar [4], Lidy E. Fratila-Apachitei [1] and Amir A. Zadpoor [1]

[1] Department of Biomechanical Engineering, Faculty of Mechanical, Maritime, and Materials Engineering, Delft University of Technology, 2628CD Delft, The Netherlands; lorenzo_k94@outlook.com (L.B.K.); m.ganjian@tudelft.nl (M.G.); n.tumer-1@tudelft.nl (N.T.); l.angeloni@tudelft.nl (L.A.); e.l.fratila-apachitei@tudelft.nl (L.E.F.-A.); a.a.zadpoor@tudelft.nl (A.A.Z.)

[2] Department of Imaging Physics, Faculty of Applied Sciences, Delft University of Technology, 2628CJ Delft, The Netherlands; c.w.hagen@tudelft.nl

[3] Department of Biotechnology, Faculty of Applied Sciences, Delft University of Technology, 2626HZ Delft, The Netherlands; l.g.otten@tudelft.nl (L.G.O.); p.l.hagedoorn@tudelft.nl (P.-L.H.)

[4] Department of Precision and Microsystems Engineering, Faculty of Mechanical, Maritime, and Materials Engineering, Delft University of Technology, 2628CD Delft, The Netherlands; m.k.ghatkesar@tudelft.nl

* Correspondence: k.modaresifar@tudelft.nl

† These authors contributed equally to this work.

Received: 10 December 2019; Accepted: 12 February 2020; Published: 18 February 2020

Abstract: Recent progress in nano-/micro-fabrication techniques has paved the way for the emergence of synthetic bactericidal patterned surfaces that are capable of killing the bacteria via mechanical mechanisms. Different design parameters are known to affect the bactericidal activity of nanopatterns. Evaluating the effects of each parameter, isolated from the others, requires systematic studies. Here, we systematically assessed the effects of the interspacing and disordered arrangement of nanopillars on the bactericidal properties of nanopatterned surfaces. Electron beam induced deposition (EBID) was used to additively manufacture nanopatterns with precisely controlled dimensions (i.e., a height of 190 nm, a diameter of 80 nm, and interspaces of 100, 170, 300, and 500 nm) as well as disordered versions of them. The killing efficiency of the nanopatterns against Gram-positive *Staphylococcus aureus* bacteria increased by decreasing the interspace, achieving the highest efficiency of 62 ± 23% on the nanopatterns with 100 nm interspacing. By comparison, the disordered nanopatterns did not influence the killing efficiency significantly, as compared to their ordered correspondents. Direct penetration of nanopatterns into the bacterial cell wall was identified as the killing mechanism according to cross-sectional views, which is consistent with previous studies. The findings indicate that future studies aimed at optimizing the design of nanopatterns should focus on the interspacing as an important parameter affecting the bactericidal properties. In combination with controlled disorder, nanopatterns with contrary effects on bacterial and mammalian cells may be developed.

Keywords: nanoscale additive manufacturing; surface nanopatterns; antibacterial effects; controlled disorder; interspace

1. Introduction

An increasing number of orthopedic implants are being implanted every year [1], resulting in a growing number of implant-associated infections (IAIs). Despite all efforts involved in preventing infections in clinical settings, IAIs still occur and are recognized as one of the most prevalent causes of

the failure of orthopedic implants [2,3]. Such infections usually necessitate either revision surgeries or the prolonged administration of antibiotics, which diminishes the patients' quality of life, causes major side effects, significantly increases the healthcare costs, and could lead to patient morbidity or even mortality [3,4]. *Staphylococci* bacteria are the most widespread infectious pathogens involved in IAIs [5]. While *Staphylococcus aureus* accounts for 20–30% of IAIs following fracture fixation and prosthetic joint infections [5–7], antibiotic treatment could act as a double-edged sword, particularly given the growing crisis of antibacterial resistance leading to the evolution of antibiotic-resistant species like Methicillin-resistant *staphylococcus aureus* (MRSA) [8]. Moreover, recent reports have shown that in addition to antibiotics, bacteria can develop resistance against other types of killing agents, such as silver nanoparticles [9]. Therefore, alternative approaches to the prevention of IAIs including those based on physical forces should be more seriously considered. In such approaches, specifically designed surface features kill the bacteria that reach the implant surface [10].

The recent progress in nano-/micro-fabrication techniques have made it feasible to develop surfaces ornamented with geometrical features (e.g., pillars) whose arbitrary shapes, sizes, and arrangements are precisely controlled [11]. Eukaryotic and prokaryotic cells are known to interact with these patterns in different ways ending up with distinct, and even contrary, cellular responses [12,13]. There are pieces of evidence suggesting that mechanobiological pathways trigger and control these responses [12,14,15]. At the same time, nature offers great examples of surfaces with nanoscale features (nanopatterns) that leave bacterial cells with no choice of response but death [10,16,17]. Therefore, studying the interactions between different types of cells and surface nanopatterns is of high interest, because, unlike larger length scales, nanopatterns can affect individual cell receptors, which stand first in the line for the transduction of mechanical signals [14,18].

Inspired by nature, many synthetic replicas of naturally occurring bactericidal nanopatterns have been designed, fabricated, and tested against a wide variety of bacterial strains [17,19]. Several design parameters such as the shape, dimensions (height, diameter, and the interspace between them), and arrangement highly influence the response of bacterial cells to surface nanopatterns [12,20]. For example, a specific range of dimensions is known to induce bactericidal properties (i.e., 100 nm < height < 900 nm; 20 nm < diameter < 207 nm; 9 nm < interspacing < 380 nm) [20].

The limited number of systematic studies has made it difficult to draw concrete conclusions regarding the isolated effects of each design parameter (i.e., height, diameter, or interspacing) on the bactericidal properties of surfaces. Similarly, while extensive data is available regarding the effects of disordered nanopatterns on the response of mammalian cells [21–23], a limited number of reports can be found on how disordered arrangement can affect the bactericidal properties of nanopatterns [24].

In the present study, we aimed to study the isolated effects of one specific design parameter (i.e., interspacing) as well as controlled disorder on the functionality of a bactericidal nanopattern. Pillar-shaped nanopatterns with an approximate height of 190 nm, a diameter of 80 nm, and an interspacing of 170 nm were chosen as the reference bactericidal nanopattern, which has been shown to be effective against both Gram-positive and Gram-negative bacteria [25]. Keeping the height and diameter constant, the interspacing of the nanopillars was changed to 100, 300, and 500 nm to create new nanopatterns. These values cover the full range of possible interspacing including one that was larger than all previously reported ones (i.e., 500 nm), one close to the maximum value reported before (i.e., 300 nm), and one smaller than the majority of the previous studies (i.e., 100 nm) [20]. The controlled disorder was the other studied parameter, creating a variant to each of the four abovementioned nanopatterns. Furthermore, *S. aureus* was used as the study organism because of its prevalence in IAIs. We used electron beam induced deposition (EBID) as a nanoscale additive manufacturing (3D printing) technique to fabricate the nanopatterns due to its high precision and controllability that make it an unrivaled single-step method for the direct printing of 3D surface physical features at the sub-10 nm nanoscale [25–27].

2. Materials and Methods

2.1. Nanopatterns Design, Fabrication, and Characterization

To introduce controlled disorder to the nanopatterns, the maximum distance at which nanopillars did not intersect when displaced towards each other was set as the maximum disorder distance. Having set the diameter of nanopatterns to 80 nm, the maximum disorder distance was defined for each nanopattern to be half of the difference between the interspacing and the diameter. Since such a small level of disorder does not substantially change the arrangement of the nanopatterns with an interspacing of 100 nm, the effects of disorder were not studied for that particular level of interspacing. The following nanopatterns were, therefore, included in the study: ordered nanopatterns with interspacings of 100, 170, 300, and 500 nm as well as disordered nanopatterns with interspacings of 170, 300, and 500 nm. We will call those patterns 100 *O*, 170 *O*, 170 *D*, 300 *O*, 300 *D*, 500 *O*, and 500 *D* where the first number corresponds to the interspacing of the nanopillars followed by a latter indicating whether the arrangement of nanopillars has been fully ordered (*O*) or included controlled disorder (*D*).

EBID was used to fabricate the desired nanopatterns on silicon substrates as described before [25]. Briefly, 1×1 cm^2 samples were prepared by cutting double-sided polished 4-inch (diameter = 10.16 cm) silicon wafers (thickness = 525 ± 25 μm, p-type), cleaning with nitric acid, and rinsing with deionized water subsequently.

A Helios Nano Lab 650 scanning electron microscope (SEM) (FEI company, Hillsboro, OR, USA) equipped with the apparatus required for EBID was used to create three nanopatterned areas of 20×20 μm^2 per specimen (Figure 1d). The precursor gas was Trimethyl(methylcyclopentadienyl)-platinum(IV), ($C_9H_{18}Pt$). The EBID process was performed using a working distance of 5 mm, an electron voltage of 17.8 kV, and a beam current of 0.40 nA. The background vacuum of the system was 8.82×10^{-7} mbar and the precursor gas flux was adjusted such that the total pressure was 2.33×10^{-6} mbar, after which the EBID process was started. Single-dot exposure was used as the writing strategy, using stream files generated through MATLAB (MathWorks, Natick, MA, USA) scripts.

The resulting nanopatterns were characterized by scanning electron microscopy (SEM) performing using the same equipment. The height and base diameter were measured for thirty different pillars per sample using 52° tilted SEM images. The center-to-center spacing was also measured from the top view images. The dimensions of the produced nanopatterns are reported as mean ± standard deviation (Table 1).

Table 1. The characteristics of the nanopatterns produced by EBID.

Pattern Type	Interspace (nm)	Disorder Distance (nm)	Height (nm)	Base Diameter (nm)	Aspect Ratio	Pillar Density (Number/μm^2)
100 *O*	100	0	198 ± 7	89 ± 4	2.2 ± 0.0	100.6
170 *D*	170	45	200 ± 13	73 ± 9	2.7 ± 0.2	35.5
170 *O*	170	0	188 ± 22	67 ± 13	2.8 ± 0.2	35.5
300 *D*	300	110	177 ± 13	73 ± 3	2.4 ± 0.1	11.9
300 *O*	300	0	190 ± 28	71 ± 2	2.7 ± 0.3	11.9
500 *D*	500	210	201 ± 15	76 ± 4	2.6 ± 0.1	4.5
500 *O*	500	0	184 ± 16	72 ± 3	2.6 ± 0.1	4.5

Given that the static water contact angles could not be measured directly (due to the small size of the patterned areas), we used the Cassie-Baxter wettability model to estimate the values corresponding to different designs [28,29]. To this aim, the contact angle of an EBID-fabricated Pt-C layer was measured by a DSA 100 drop shape analyzer (Krüss, Hamburg, Germany) using deionized water. A volume of 2 μL liquid with a falling rate of 1667 μL min^{-1} was placed on the surface and the average contact angle was recorded within 30 s after the droplet touched the surface. The measured contact angle was further used to calculate the Cassie-Baxter contact angle (Table 1) [25].

Furthermore, topography images of the nanopatterns were acquired in Quantitative Imaging (QI) mode using an AFM JPK Nanowizard 4 (Berlin, Germany) and a high aspect ratio probe (TESPA-HAR, Bruker, Germany). A set point of 20 nN, a Z length of 300 nm, and a pixel time of 10 ms were used as scanning parameters. The images were analysed by using the JPK SPM data processing software (JPK instruments, v6.1, Berlin, Germany) to obtain 3D images of the surface and the average roughness.

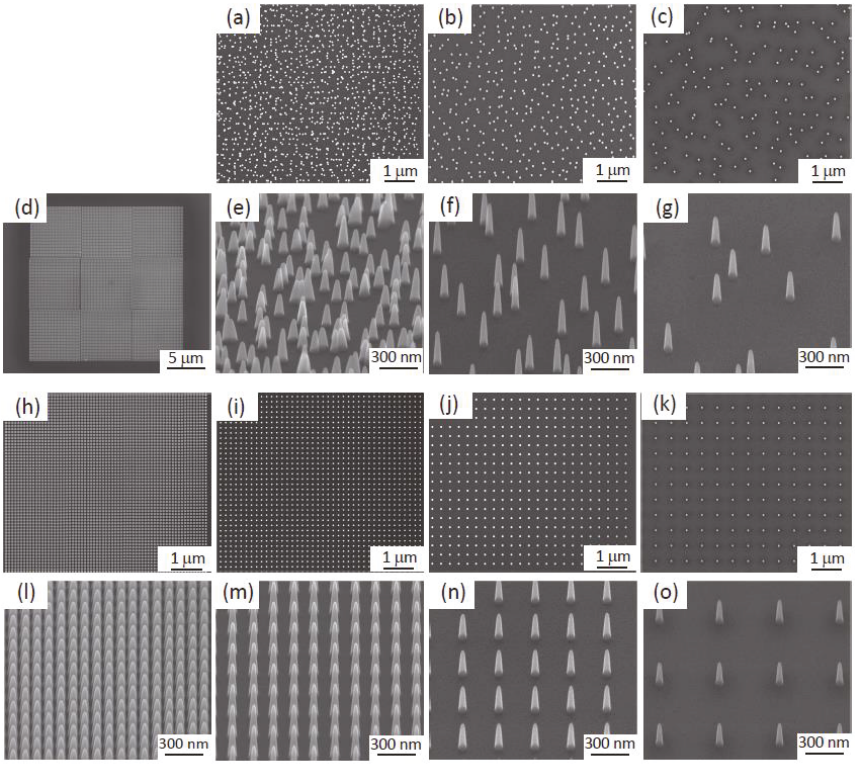

Figure 1. The scanning electron microscope (SEM) images of (**a**) the top view of the nanopillars with a height of 190 nm, a diameter of 80 nm, and an interspacing of 170 nm with 45 nm disorder distance (170 *D)*; (**b**) the top view of the nanopillars with an interspacing of 300 nm and 110 nm disorder distance (300 *D*); (**c**) the top view of the nanopillars with an interspacing of 500 nm and 210 nm disorder distance (500 *D*); (**d**) 20 × 20 μm^2 nanopatterned areas on a Si substrate; (**e**) the tilted view of 170 *D*; (**f**) the tilted view of 300 *D*; (**g**) the tilted view of 500 *D*; (**h**) the top view of the ordered nanopillars with an interspacing of 100 nm (100 *O*); (**i**) the top view of the ordered nanopillars with an interspacing of 170 nm (170 *O*); (**j**) the top view of the ordered nanopillars with an interspacing of 300 nm (300 *O*); (**k**) the top view of the ordered nanopillars with an interspacing of 500 nm (500 *O*); (**l**) the tilted view of 100 *O*; (**m**) the tilted view of 170 *O*; (**n**) the tilted view of 300 *O*; (**o**) the tilted view of 500 *O*.

2.2. Preparation of Bacterial Cultures

Gram-positive bacteria *Staphylococcus aureus* (RN0450 strain) (BEI Resources, VA, USA) was grown on brain heart infusion (BHI) (Sigma-Aldrich, MO, USA) agar plates at 37 °C overnight. A pre-culture of bacteria was prepared by inoculating a single colony in 10 mL autoclaved BHI, shaken at 140 rpm at 37 °C. The bacterial cells were collected at their logarithmic stage of growth and their optical density at 600 nm wavelength (OD_{600}) in the medium solution was adjusted to a value of 0.1 to be finally cultured on the specimens. Such OD is equivalent to 148 × 10^6 colony forming units (CFUs) per milliliter.

2.3. Investigation of Bactericidal Properties

Two independent sets of experiments were performed to evaluate the bactericidal properties of the nanopatterns. In each set of experiments, the nanopatterned areas of each specimen and the surrounding flat areas (Figure 1d) were considered as the study and control groups (all in triplicates) in the bacterial studies, respectively. The specimens were initially sterilized by through immersion in 70% ethanol and were exposed to UV light for 20 min prior to inoculation with 1 mL of the bacterial suspension in a 24-well plate (Cell Star, Germany). The specimens were then incubated at 37 °C for 18 h.

As previously explained [25], fabricating large areas of nanopatterned surfaces using EBID is not time-efficient yet, but patterning a small area would suffice for systematically studying the bactericidal effects of highly controlled nanopatterns. However, it hinders the use of certain assessment methods such as live/dead staining and CFU counting. We therefore exploited a method applied previously in several other studies [25,30–33] in which morphological evaluation of bacterial cells through SEM imaging is used to distinguish between disrupted and healthy bacterial cells. The validity of this technique has been demonstrated before in studies that have used and compared different evaluation techniques in determining the bactericidal properties of nanopatterned surfaces [30,33]. Therefore, to determine the killing efficiency of the nanopatterns, we first washed our specimens with phosphate-buffered saline (PBS) to remove any non-adherent bacteria. The adhered bacterial cells were then fixed by immersion in a PBS solution containing 4% formaldehyde (Sigma-Aldrich, St. Louis, MI, USA) and 1% glutaraldehyde (Sigma-Aldrich, St. Louis, MO, USA) at 4 °C for 1 h. Subsequently, the samples were dehydrated by a series of ethanol washing (50%, 70%, and 96% ethanol, respectively) and finally with hexamethyldisilazane (HMDS) (Sigma-Aldrich, St. Louis, MO, USA) for 30 min. After being air-dried, a thin layer of gold was sputtered on the specimens prior to being imaged by SEM at different magnifications and tilt angles of 0° and 52°. The killing efficiency was defined as the ratio of damaged cells to the total number of cells on the intended areas. Moreover, counting the total number of the bacterial cells attached to the nanopatterned and flat areas of each specimen enabled a comparison between the cell adhesion within the flat and nanopatterned surfaces.

2.4. Investigation of Nanopattern-Bacteria Interface

In order to further investigate the interactions between the bacterial cells and the nanopillars, and to analyse the possible killing mechanism of the nanopattern with the highest killing efficiency, focused ion beam scanning electron microscopy (FIB-SEM, FEI, Helios Nano Lab 650, OR, USA) was performed to acquire a cross-sectional view of the interface between cells and patterns. The specimen was tilted to 52°, at which angle the surface was milled using Gallium ions with a 7.7 pA ion beam (Z = 1.5 μm, operating voltage = 30 kV).

2.5. Statistical Analysis

To determine the statistical significance of the differences between the means of different experimental groups in terms of their bacterial cells attachment, a two-way ANOVA test was performed, followed by a Sidak's multiple comparisons test, which was performed using Prism version 8.0.1 (GraphPad, San Diego, CA, USA). Similarly, the killing efficiency of different nanopatterns was statistically analyzed using the Mann-Whitney test. A p-value below 0.05 was considered to indicate statistical significance.

3. Results

3.1. Characteristics of the Fabricated Nanopatterns

Nanopillar arrays with different types of arrangements and interspacing values were successfully fabricated in 20×20 μm^2 areas on each sample (Figure 1). Notwithstanding some slight variations, the intended dimensions were achieved for all the experimental groups (Table 1). The differences in the dimensions and arrangements of the nanopillars were clearly observed in SEM images (Figure 1)

and AFM images (Figure 2). The average roughness decreased by increasing the interspacing of both ordered nanopillars (from 46.8 ± 4.9 nm for 100 *O* to 39.1 ± 1.8 nm for 500 *O*) and disordered nanopillars (from 68.3 ± 4.9 nm for 170 *D* to 24.8 ± 2.3 nm for 500 *D*). The density of the nanopillars decreased by increasing the interspacing, from 100.6 pillars per μm^2 for 100 *O* to 4.5 pillars per μm^2 for 500 *O* and 500 *D*. The nanopatterned surfaces were hydrophobic, as estimated by using the Cassie-Baxter model, with water contact angles ranging from 154° to 176°.

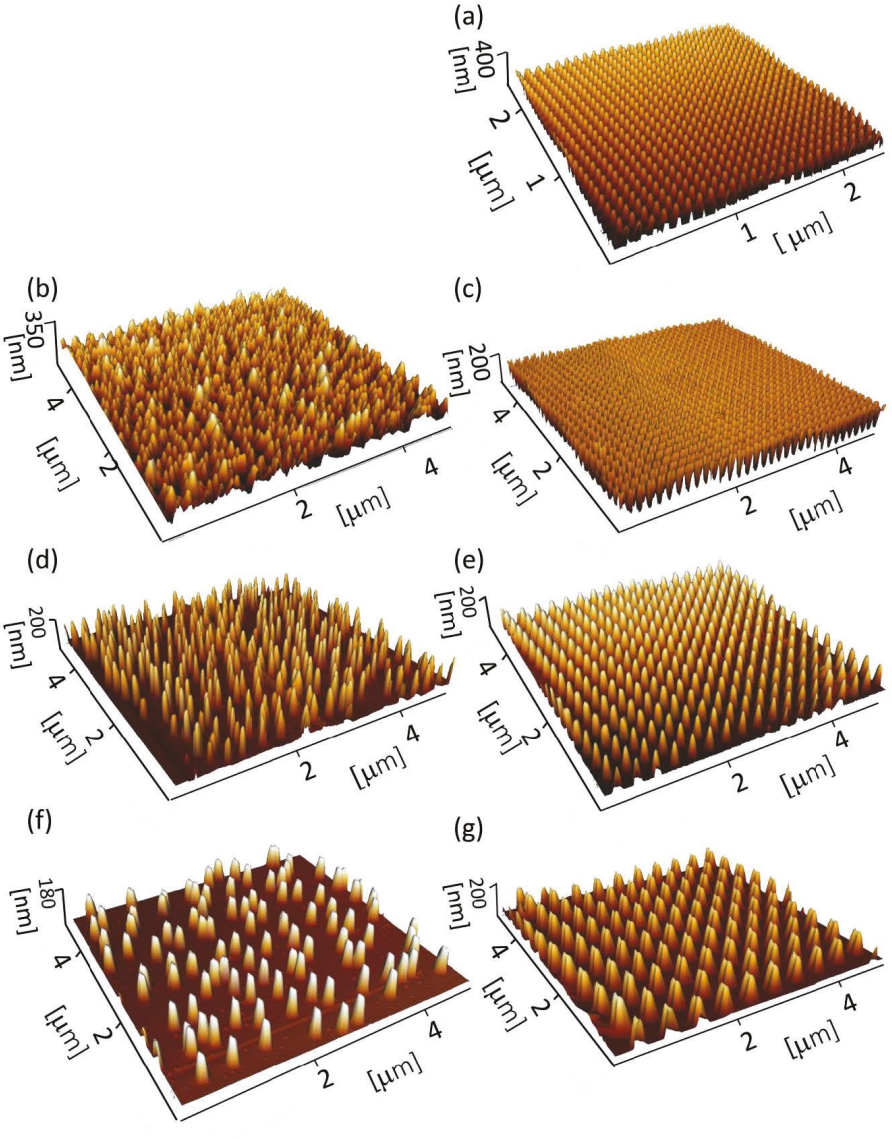

Figure 2. 3D AFM images of (**a**) 100 *O*; (**b**) 170 *D*; (**c**) 170 *O*; (**d**) 300 *D*; (**e**) 300 *O*; (**f**) 500 *D*; (**g**) 500 *O* nanopillars.

3.2. Effect of Interspacing on Bactericidal Properties

Before analyzing the effects of the selected parameters on the bactericidal activity of the nanopatterns, the bacterial adhesion to the specimens was studied to see whether any of the fabricated nanopatterns impairs the attachment of bacterial cells. Although care was taken to ensure seeding was as homogeneous as possible, there might be local differences in the number of the bacteria attached to the specimens. However, the ratio of the number of cells attached to the nanopatterned surfaces to those attached to a similar-sized flat area did not significantly vary between the specimens, meaning that bacterial cell adhesion was similar between all experimental groups (Figure 3a).

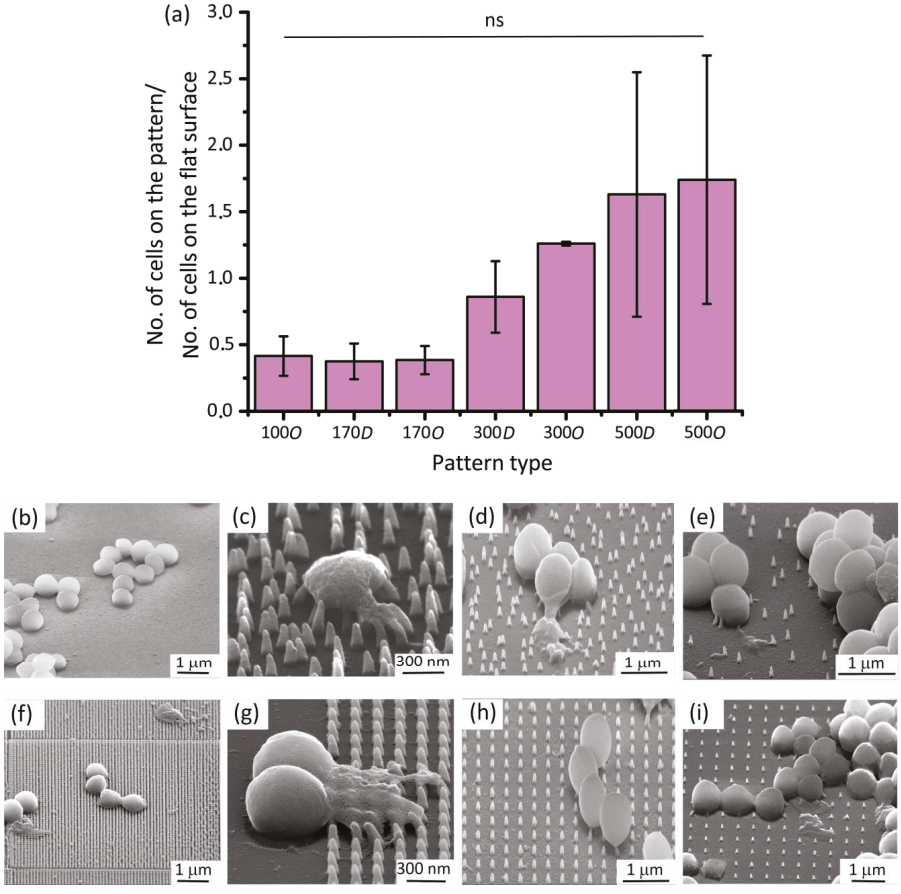

Figure 3. (**a**) The ratio of the bacterial cells attached to the nanopatterns to those attached to similar flat areas. No significant difference in that ratio for different types of nanopattern indicates that bacterial adhesion is similar between different groups; The SEM images of *S. aureus* bacteria on (**b**) the control Si surface; (**c**) 170 *D*; (**d**) 300 *D*; (**e**) 500 *D*; (**f**) 100 *O*; (**g**) 170 *O*; (**h**) 300 *O*; (**i**) 500 *O* at 52° tilted view. The damaged bacterial cells can be identified with irregular and unrecognizable morphologies as compared to normal cells on flat surfaces.

S. aureus cells showed their typical coccoid-shaped morphology on the flat areas with no significant sign of irregularity, disruption, or death (Figure 3b). On the contrary, ruptured bacterial cells with squashed morphologies were identified on the nanopatterned areas and were marked as damaged/dead

cells (Figure 3f–i). The ordered nanopatterns with larger interspacing values (i.e., 300 *O* and 500 *O*) displayed significantly lower bactericidal efficiencies against *S. aureus* (8.6 ± 4.2% and 3.7 ± 2.3%, respectively) as compared to 100 *O* and 170 *O* ($p < 0.01$) (Figure 4a). While there was a significant difference in the killing efficiency between 300 *O* and 500 *O* ($p < 0.05$), no significant differences were observed between 100 *O* and 170 *O*.

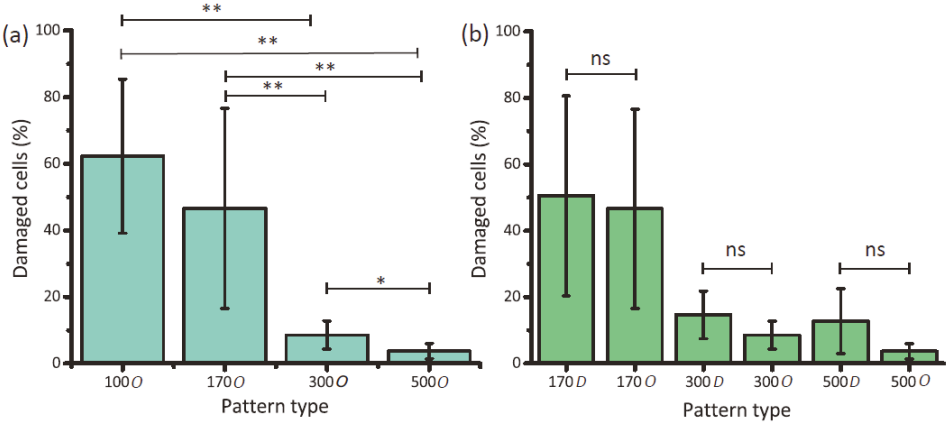

Figure 4. (**a**) The effects of interspacing on the bactericidal efficiency of nanopatterns (* $p < 0.05$ and ** $p < 0.01$); (**b**) The effects of controlled disorder on the bactericidal efficiency of nanopatterns. No significant differences were observed between the ordered and disordered nanopatterns but the value of interspacing.

3.3. The Effects of Controlled Disorder on Bactericidal Properties

The effects of controlled disorder on the bactericidal activity of the nanopatterned surfaces were evaluated by comparing the killing efficiency of the ordered and disordered nanopatterns with the same interspacing (Figure 3c–e). Although somewhat higher values of killing efficiencies were observed for the disordered nanopatterns with larger interspacing values (i.e., 300 *D* and 500 *D*) as compared to their ordered counterparts, the differences were not statistically significant (Figure 3b). The disordered nanopattern with the lower interspacing (i.e., 170 *D*) showed the same bactericidal efficiency as the ordered counterpart (Figure 4b).

3.4. Nanopattern-Bacteria Interface

Cross-sectional views showed that nanopatterns could penetrate the bacterial cell wall and cause their death by disrupting it (Figure 5). Moreover, the bending of the nanopillars underneath the bacterial cells (Figures 3 and 5) suggested significant amounts of reciprocal forces that cells and pillars exert on each other.

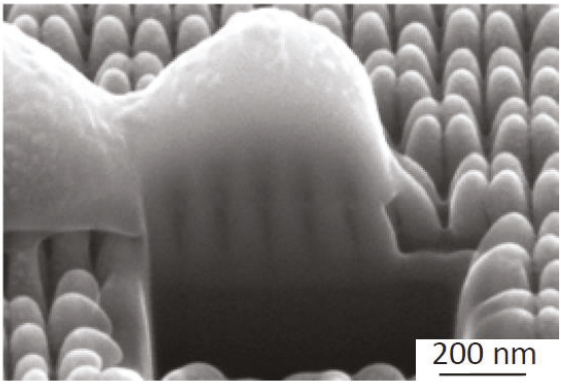

Figure 5. The SEM image of the interface between bacteria and the 100 *O* nanopattern. The depth of direct penetration of the nanopillars into the bacterial cell wall (about 100 nm) far exceeds the average cell wall thickness of *S. aureus* (i.e., 10–20 nm).

4. Discussion

The main contribution of this study was shedding light on how interspacing and controlled disorder could affect the bactericidal properties of nanopatterns. The height and diameter of the nanopatterns produced were, therefore, kept constant while the interspacing and the arrangement of nanopillars were systematically altered in seven different study groups.

In order to elucidate the effects of these two parameters on the bactericidal properties of nanopatterns, it is crucial to first consider their killing mechanisms. The main killing mechanism of nanopatterns is widely believed to be the direct penetration of high aspect-ratio nanopatterns into the bacterial cell wall and disrupting it by exerting a high enough force [20,31]. Since the thickness and composition of cell walls are different in Gram-negative and Gram-positive bacteria [34], the same force will not rupture different cell walls equally [16,35]. Moreover, other factors such as hydrostatic and gravitational forces should be also considered when studying the interactions between bacteria and nanopatterns [36].

The results of this study showed that the cell wall of *S. aureus* could be mechanically penetrated by nanopatterns (Figure 5) and be severely damaged with an unrecognizable morphology (Figure 3), as reported previously [25,30,37]. However, changing the interspacing of nanopatterns could drastically affect the percentage of the damaged cells. Although aspect-ratio is a crucial design parameter of bactericidal nanopatterns, this effect seems to overshadow the effects of the nanopatterns aspect-ratio, which is corroborated by other studies in the literature. Linklater et al. showed that nanopillars with a diameter of 80.3 nm, an interspacing of 99.5 nm (similar to 100 *O* in the present study), and a height of around 430 nm (much higher than 100 *O*), exhibit a comparable level of bactericidal activity against *S. aureus* [38]. Similarly, another study [39] showed that naturally occurring nanopillars with the approximate height of 430 nm, the approximate tip diameter of 48 nm, and an interspacing of around 116 nm (i.e., larger height than 100 *O* but comparable interspacing), exhibit a killing efficiency of 39.4 ± 20.3% against *S. aureus* after 18 h. Computational simulations have also demonstrated that, as compared to the height, the interspacing has a substantially greater effect on the bactericidal properties of nanopillars [40]. It is plausible that a smaller interspacing and a higher density of nanopatterns result in more contact points between the bacteria and nanopatterns. This, in turn, leads to more physicomechanical interactions and higher chances of bacteria being ruptured [41], however, further studies are required to determine the minimum number of contact points that exert enough force to rupture the cell wall of different types of bacteria. According to the literature, the majority of bactericidal nanopatterns have an interspacing below 300 nm [20]. The reported values make more sense when it comes to bactericidal activity against *S. aureus*, which has a coccoid shape with a diameter

larger than 500 nm [42]. For an interspacing exceeding the diameter of *S. aureus*, it is likely that bacterial cells land in between the nanopillars, thereby escaping the deadly spikes (Figure 3h,i).

An increased number of contact points for the lower values of interspacing could also contribute to some other proposed killing mechanisms. Bandara et al. [43] have argued that nanopillars do not directly interact with the bacterial cell membrane and showed that bacterial cells attach to surface nanopatterns via the expression of extracellular polymeric substances (EPS). Further movement of the bacteria on the surface on the one hand and strong EPS-mediated adhesion forces on the other lead to the stretching of the cell membrane beyond its rupture point. Considering this theory, an increased number of adhesion sites between surface features and expressed EPS could potentially amplify such a stretching mechanism. Although the bending of the nanopillars underneath the bacterial cells could be due to that movement rather than the bacteria weight only, further evaluations such as live imaging for real-time tracking of the bacteria on the surface, are required to confirm such a mechanism. Additionally, AFM measurements in another study have shown that the adhesion force of an EPS-producing *S. aureus* strain attached to nanopatterns does not significantly change due to differences in interspacing [44]. Altogether, the results of the present study are more consistent with the direct penetration theory, as it can be seen that nanopatterns have actually intruded about 101 nm (SD 9 nm) (Figure 5) into the bacterial cells, which is much larger than the cell wall thickness of *S. aureus* (i.e., 10–20 nm) [45].

Deviation from an ordered arrangement in nanopatterns has been shown to effectively influence the differentiation of the human mesenchymal stem cells [22] and the response of osteoblast cells [21]. Biochemical mechanotransduction pathways have been shown to be involved in translating mechanical cues (e.g., disordered nanopatterns) into biochemical responses (proteomic changes) [46]. An intricate network of cellular components is associated with receiving, transducing, and interpreting the mechanical cues [14]. In contrast, the bacterial mechanotransduction mechanisms seem to be simpler since the structure and components of bacterial cells are not as complex as those of mammalian cells [15]. Moreover, the information over the influence of nanopatterns disorder on the bacterial mechanotransduction is scarcely available in the literature. Further studies are, therefore, needed to elucidate the possible mechanobiological pathways pertaining to the interactions of bacteria and nanopatterns. Similar to another study that used *E. coli* [24], our results showed no significant difference between the bactericidal efficiencies of ordered and disordered nanopatterns against *S. aureus* as long as the interspacing is kept constant. Given the killing mechanism observed in this study, it can be concluded that introducing controlled disorder either does not change the mechanical force that bacteria experience or does not increase it beyond the threshold required for cell wall rupture. The findings of this study indicate that interspacing is a highly promising design parameter that should be further optimized to achieve nanopatterned surfaces with the highest potential of bactericidal activity. In combination with controlled disorder, nanopatterns with contrary effects on bacterial and mammalian cells may be developed in order to achieve selective biocidal activity.

5. Conclusions

The effects of interspacing and controlled disorder, as two design parameters, on the bactericidal properties of nanopatterns were systematically studied. Nanopatterns with constant heights and diameters of 190 nm and 80 nm, respectively, and different values of interspacing (i.e., 100, 170, 300, and 500 nm) were fabricated using EBID. A controlled disordered version of the nanopatterns with interspacings of 170, 300, and 500 nm was also fabricated. Quantifying the number of damaged *S. aureus* cells cultured on the nanopatterns for 18 h, showed that decreasing the interspacing significantly increased the bactericidal efficiency and the nanopatterns with 100 nm interspacing exhibited the highest efficiency (62.3 ± 23.1%). The nanopatterns with controlled disorder did not enhance the bactericidal efficiency compared with the ordered counterparts. Moreover, the direct penetration of nanopatterns into the bacterial cell wall and its eventual rupture due to the forces applied to it was shown to be the dominant killing mechanism of these nanopatterns which is consistent with the

majority of the previous studies. Further research is required to elucidate whether interspacing and controlled disorder could affect the biochemical mechanotransduction pathways in bacteria.

Funding: This research has received funding from the European Research Council under the ERC grant agreement n° [677575].

Conflicts of Interest: The authors declare no conflict of interests.

References

1. Kurtz, S.; Ong, K.; Lau, E.; Mowat, F.; Halpern, M. Projections of primary and revision hip and knee arthroplasty in the United States from 2005 to 2030. *J. Bone Joint Surg.* **2007**, *89*, 780–785. [CrossRef]
2. Zimmerli, W.; Trampuz, A.; Ochsner, P.E. Prosthetic-joint infections. *N. Engl. J. Med.* **2004**, *351*, 1645–1654. [CrossRef]
3. Moriarty, T.F.; Kuehl, R.; Coenye, T.; Metsemakers, W.-J.; Morgenstern, M.; Schwarz, E.M.; Riool, M.; Zaat, S.A.; Khana, N.; Kates, S.L.; et al. Orthopaedic device-related infection: Current and future interventions for improved prevention and treatment. *EFORT Open Rev.* **2016**, *1*, 89–99. [CrossRef]
4. Steckelberg, J.M.; Osmon, D.R. *Prosthetic Joint Infections, Infections Associated with Indwelling Medical Devices*, 3rd ed.; American Society of Microbiology: Washington, DC, USA, 2000; pp. 173–209.
5. Montanaro, L.; Speziale, P.; Campoccia, D.; Ravaioli, S.; Cangini, I.; Pietrocola, G.; Giannini, S.; Arciola, C.R. Scenery of Staphylococcus implant infections in orthopedics. *Future Microbiol.* **2011**, *6*, 1329–1349. [CrossRef]
6. Trampuz, A.; Zimmerli, W. Diagnosis and treatment of infections associated with fracture-fixation devices. *Injury* **2006**, *37*, S59–S66. [CrossRef]
7. Corvec, S.; Portillo, M.E.; Pasticci, B.M.; Borens, O.; Trampuz, A. Epidemiology and new developments in the diagnosis of prosthetic joint infection. *Int. J. Artif. Organs* **2012**, *35*, 923–934. [CrossRef]
8. Turner, N.A.; Sharma-Kuinkel, B.K.; Maskarinec, S.A.; Eichenberger, E.M.; Shah, P.P.; Carugati, M.; Holland, T.L.; Fowler, V.G. Methicillin-resistant Staphylococcus aureus: An overview of basic and clinical research. *Nat. Rev. Genet.* **2019**, *17*, 203–218. [CrossRef]
9. Panáček, A.; Kvítek, L.; Smékalová, M.; Večeřová, R.; Kolář, M.; Röderová, M.; Dyčka, F.; Šebela, M.; Prucek, R.; Tomanec, O. Bacterial resistance to silver nanoparticles and how to overcome it. *Nat. Nanotechnol.* **2018**, *13*, 65. [CrossRef]
10. Hasan, J.; Crawford, R.J.; Ivanova, E.P. Antibacterial surfaces: The quest for a new generation of biomaterials. *Trends Biotechnol.* **2013**, *31*, 295–304. [CrossRef]
11. Gates, B.D.; Xu, Q.; Stewart, M.; Ryan, D.; Willson, C.G.; Whitesides, G.M. New approaches to nanofabrication: Molding, printing, and other techniques. *Chem. Rev.* **2005**, *105*, 1171–1196. [CrossRef]
12. Anselme, K.; Davidson, P.; Popa, A.; Giazzon, M.; Liley, M.; Ploux, L. The interaction of cells and bacteria with surfaces structured at the nanometre scale. *Acta Biomater.* **2010**, *6*, 3824–3846. [CrossRef]
13. Ploux, L.; Anselme, K.; Dirani, A.; Ponche, A.; Soppera, O.; Roucoules, V. Opposite responses of cells and bacteria to micro/nanopatterned surfaces prepared by pulsed plasma polymerization and UV-irradiation. *Langmuir* **2009**, *25*, 8161–8169. [CrossRef]
14. Sun, Y.; Chen, C.S.; Fu, J. Forcing stem cells to behave: A biophysical perspective of the cellular microenvironment. *Annu. Rev. Biophys.* **2012**, *41*, 519–542. [CrossRef]
15. Persat, A. Bacterial mechanotransduction. *Curr. Opin. Microbiol.* **2017**, *36*, 1–6. [CrossRef]
16. Hasan, J.; Webb, H.K.; Truong, V.K.; Pogodin, S.; Baulin, V.A.; Watson, G.S.; Watson, J.A.; Crawford, R.J.; Ivanova, E.P. Selective bactericidal activity of nanopatterned superhydrophobic cicada Psaltoda claripennis wing surfaces. *Appl. Microbiol. Biotechnol.* **2013**, *97*, 9257–9262. [CrossRef]
17. Elbourne, A.; Crawford, R.J.; Ivanova, E.P. Nano-structured antimicrobial surfaces: From nature to synthetic analogues. *J. Colloid Interface Sci.* **2017**, *508*, 603–616. [CrossRef]
18. Dalby, M.J.; Gadegaard, N.; Oreffo, R.O.C. Harnessing nanotopography and integrin-matrix interactions to influence stem cell fate. *Nat. Mater.* **2014**, *13*, 558–569. [CrossRef]
19. Hasan, J.; Roy, A.; Chatterjee, K.; Yarlagadda, P.K.D.V. Mimicking insect wings: The roadmap to bioinspiration. *ACS Biomater. Sci. Eng.* **2019**, *5*, 3139–3160. [CrossRef]
20. Modaresifar, K.; Azizian, S.; Ganjian, M.; Fratila-Apachitei, L.E.; Zadpoor, A.A. Bactericidal effects of nanopatterns: A systematic review. *Acta Biomater.* **2018**, *83*, 29–36. [CrossRef]

21. Allan, C.; Ker, A.; Smith, C.-A.; Tsimbouri, P.M.; Borsoi, J.; O'Neill, S.; Gadegaard, N.; Dalby, M.J.; Meek, R.M.D. Osteoblast response to disordered nanotopography. *J. Tissue Eng.* **2018**. [CrossRef]
22. Dalby, M.J.; Gadegaard, N.; Tare, R.; Andar, A.; Riehle, M.O.; Herzyk, P.; Wilkinson, C.D.W.; Oreffo, R.O.C. The control of human mesenchymal cell differentiation using nanoscale symmetry and disorder. *Nat. Mater.* **2007**, *6*, 997–1003. [CrossRef]
23. Dobbenga, S.; Fratila-Apachitei, L.E.; Zadpoor, A.A. Nanopattern-induced osteogenic differentiation of stem cells—A systematic review. *Acta Biomater.* **2016**, *46*, 3–14. [CrossRef]
24. Widyaratih, D.S.; Hagedoorn, P.-L.; Otten, L.G.; Ganjian, M.; Tümer, N.; Apachitei, I.; Hagen, C.W.; Fratila-Apachitei, L.; Zadpoor, A.A.; Tumer, N.; et al. Towards osteogenic and bactericidal nanopatterns? *Nanotechnology* **2019**, *30*. [CrossRef]
25. Ganjian, M.; Modaresifar, K.; Ligeon, M.R.; Kunkels, L.B.; Tümer, N.; Angeloni, L.; Hagen, C.W.; Otten, L.G.; Hagedoorn, P.L.; Apachitei, I. Nature helps: Toward bioinspired bactericidal nanopatterns. *Adv. Mater. Interfaces* **2019**. [CrossRef]
26. Van Dorp, W.F.; Van Someren, B.; Hagen, C.W.; Kruit, P.; Crozier, P.A. Approaching the resolution limit of nanometer-scale electron beam-induced deposition. *Nano Lett.* **2005**, *5*, 1303–1307. [CrossRef]
27. Van Kouwen, L.; Botman, A.; Hagen, C.W. Focused electron-beam-induced deposition of 3 nm dots in a scanning electron microscope. *Nano Lett.* **2009**, *9*, 2149–2152. [CrossRef]
28. Bhushan, B.; Nosonovsky, M. The rose petal effect and the modes of superhydrophobicity. *Philos. Trans. R. Soc. A* **2010**, *368*, 4713–4728. [CrossRef]
29. Sun, M.; Watson, G.S.; Zheng, Y.; Watson, J.A.; Liang, A. Wetting properties on nanostructured surfaces of cicada wings. *J. Exp. Boil.* **2009**, *212*, 3148–3155. [CrossRef]
30. Ivanova, E.P.; Hasan, J.; Webb, H.K.; Gervinskas, G.; Juodkazis, S.; Truong, V.K.; Wu, A.H.; Lamb, R.N.; Baulin, V.A.; Watson, G.S.; et al. Bactericidal activity of black silicon. *Nat. Commun.* **2013**, *4*, 2838. [CrossRef]
31. Linklater, D.P.; Juodkazis, S.; Rubanov, S.; Ivanova, E.P. Comment on "bactericidal effects of natural nanotopography of dragonfly wing on escherichia coli". *ACS Appl. Mater. Interfaces* **2017**, *9*, 29387–29393. [CrossRef]
32. Linklater, D.P.; De Volder, M.; Baulin, V.A.; Werner, M.; Jessl, S.; Golozar, M.; Maggini, L.; Rubanov, S.; Hanssen, E.; Juodkazis, S.; et al. High aspect ratio nanostructures kill bacteria via storage and release of mechanical energy. *ACS Nano* **2018**, *12*, 6657–6667. [CrossRef]
33. Linklater, D.P.; Juodkazis, S.; Crawford, R.J.; Ivanova, E.P.; Crawford, R. Mechanical inactivation of staphylococcus aureus and pseudomonas aeruginosa by titanium substrata with hierarchical surface structures. *Materialia* **2019**, *5*, 100197. [CrossRef]
34. Brown, L.; Wolf, J.M.; Prados-Rosales, R.; Casadevall, A. Through the wall: Extracellular vesicles in Gram-positive bacteria, mycobacteria and fungi. *Nat. Rev. Genet.* **2015**, *13*, 620–630. [CrossRef]
35. Pogodin, S.; Hasan, J.; Baulin, V.A.; Webb, H.K.; Truong, V.K.; Nguyen, T.H.P.; Boshkovikj, V.; Fluke, C.J.; Watson, G.S.; Watson, J.A.; et al. Biophysical model of bacterial cell interactions with nanopatterned cicada wing surfaces. *Biophys. J.* **2013**, *104*, 835–840. [CrossRef]
36. Xue, F.; Liu, J.; Guo, L.; Zhang, L.; Li, Q. Theoretical study on the bactericidal nature of nanopatterned surfaces. *J. Theor. Boil.* **2015**, *385*, 1–7. [CrossRef]
37. Jaggessar, A.; Yarlagadda, P.K. Modelling the growth of hydrothermally synthesised bactericidal nanostructures, as a function of processing conditions. *Mater. Sci. Eng. C* **2019**, *108*, 110434. [CrossRef]
38. Linklater, D.P.; Nguyen, H.K.D.; Bhadra, C.M.; Juodkazis, S.; Ivanova, E.P. Influence of nanoscale topology on bactericidal efficiency of black silicon surfaces. *Nanotechnology* **2017**, *28*, 245301. [CrossRef]
39. Truong, V.K.; Geeganagamage, N.M.; Baulin, V.A.; Vongsvivut, J.; Tobin, M.J.; Luque, P.; Crawford, R.J.; Ivanova, E.P. The susceptibility of Staphylococcus aureus CIP 65.8 and Pseudomonas aeruginosa ATCC 9721 cells to the bactericidal action of nanostructured calopteryx haemorrhoidalis damselfly wing surfaces. *Appl. Microbiol. Biotechnol.* **2017**, *101*, 4683–4690. [CrossRef]
40. Mirzaali, M.J.; Van Dongen, I.C.P.; Tumer, N.; Weinans, H.; Yavari, S.A.; Zadpoor, A.A.; Van Dongen, I. In-silico quest for bactericidal but non-cytotoxic nanopatterns. *Nanotechnology* **2018**, *29*. [CrossRef]
41. Hazell, G.; Fisher, L.E.; Murray, W.A.; Nobbs, A.H.; Su, B. Bioinspired bactericidal surfaces with polymer nanocone arrays. *J. Colloid Interface Sci.* **2018**, *528*, 389–399. [CrossRef]

42. Harris, L.G.; Foster, S.J.; Richards, R.G. An introduction to Staphylococcus aureus, and techniques for identifying and quantifying S. aureus adhesins in relation to adhesion to biomaterials: Review. *Eur. Cell Mater.* **2002**, *4*, 39–60. [CrossRef]
43. Bandara, C.D.; Singh, S.; Afara, I.O.; Wolff, A.; Tesfamichael, T.; Ostrikov, K.; Oloyede, A. Bactericidal effects of natural nanotopography of dragonfly wing on escherichia coli. *ACS Appl. Mater. Interfaces* **2017**, *9*, 6746–6760. [CrossRef]
44. Hizal, F.; Choi, C.-H.; Busscher, H.J.; Van Der Mei, H.C. Staphylococcal adhesion, detachment and transmission on nanopillared Si surfaces. *ACS Appl. Mater. Interfaces* **2016**, *8*, 30430–30439. [CrossRef]
45. Wyatt, P.J. Cell wall thickness, size distribution, refractive index ratio and dry weight content of living bacteria (stapylococcus aureus). *Nature* **1970**, *226*, 277–279. [CrossRef]
46. Kantawong, F.; Burgess, K.E.; Jayawardena, K.; Hart, A.; Burchmore, R.J.; Gadegaard, N.; Oreffo, R.O.; Dalby, M.J. Whole proteome analysis of osteoprogenitor differentiation induced by disordered nanotopography and mediated by ERK signalling. *Biomaterials* **2009**, *30*, 4723–4731. [CrossRef]

nanomaterials

MDPI

Article

Metal Nanoparticles for Improving Bactericide Functionality of Usual Fibers

George Frolov [1], Ilya Lyagin [2,3], Olga Senko [2,3], Nikolay Stepanov [2,3], Ivan Pogorelsky [4] and Elena Efremenko [2,3,*]

1 National Research Technological University "MISIS", Leninsky ave. 4, 119049 Moscow, Russia; georgifroloff@yandex.ru
2 Faculty of Chemistry, Lomonosov Moscow State University, Lenin Hills 1/3, 119991 Moscow, Russia; lyagin@mail.ru (I.L.); senkoov@gmail.com (O.S.); na.stepanov@gmail.com (N.S.)
3 N.M. Emanuel Institute of Biochemical Physics RAS, Kosygin str. 4, 119334 Moscow, Russia
4 48 Central Scientific Research Institute of the Ministry of Defense of the Russian Federation, Oktyabrsky ave. 121, 610017 Kirov, Russia; ipogorelsky@inbox.ru
* Correspondence: elena_efremenko@list.ru; Tel.:+7-(495)-939-3170; Fax: +7-(495)-939-5417

Received: 5 August 2020; Accepted: 29 August 2020; Published: 31 August 2020

Abstract: A wide variety of microbiological hazards stimulates a constant development of new protective materials against them. For that, the application of some nanomaterials seems to be very promising. Modification of usual fibers with different metal nanoparticles was successfully illustrated in the work. Tantal nanoparticles have shown the highest antibacterial potency within fibrous materials against both gram-positive (*Bacillus subtilis*) and gram-negative (*Escherichia coli*) bacteria. Besides, the effect of tantal nanoparticles towards luminescent *Photobacterium phosphoreum* cells estimating the general sample ecotoxicity was issued for the first time.

Keywords: metal nanoparticles; fiber material; antibacterial activity; bioluminescent cells

1. Introduction

Multiple metal-containing nanomaterials are of great interest since they possess explicit antimicrobial action and could possibly result in absence of microbial resistance to them [1]. This antimicrobial activity (e.g., bacteriostatic and bactericide) of nanomaterials was established to be predetermined by their chemical composition, particle size, shape, morphology, etc. [2]. Further, such antimicrobial functionality can be utilized to produce novel special materials for the food and textile industries, medicine, etc. [3,4].

Various fibrous materials are used in the textile industry, and thus, efficiency of their modification by different nanomaterials can vary significantly. Even micro- [5] and nanofibers [6] were suggested as carriers, though such novel materials certainly can be implemented in a distant future. The fibers currently used in protective outfits are much more common and produced on the basis of synthetic, semi-synthetic, natural polymers, and combinations thereof. Notably, the paradigm of multipurpose functionalization of textiles [7] could be applied for antimicrobial activity also [8].

It should be noted that antimicrobial activity of functionalized materials are usually determined with suspension or solid culture assay. However, both assays appeared to be poorly suited for such materials since: (i) either bacteriostatic or bactericide effect is caused by diffusion of active compound(s) from materials into medium (i.e., ability to diffuse is mostly measured); (ii) cell viability was not issued within materials (i.e., no data about real life application of protective outfits are provided). To solve the issue, specific dyes [9] or even a panel of direct detection bioassays [10] could be adapted. Alternatively, the concentration of intracellular adenosine triphosphate (ATP) [11,12] could be measured to produce highly reproducible and relevant results with nanomaterials [13].

Thus, the purpose of this work was the development of novel fibrous materials functionalized by metal nanoparticles which have antibacterial activity towards both gram-negative and gram-positive bacteria. For that, nanoparticles of various metals (Zn, Fe, Ti, and Ta) were produced, characterized, and deposited onto fibrous materials under varying conditions. Textiles with stable antibacterial activity within the bulk matrix were of special interest.

2. Materials and Methods

2.1. Preparation of Metal Nanoparticles

Metal nanoparticles were obtained using a unique laboratory device in a plasma electric arc discharge [14]. The main elements of the installation were a power supply unit, a capacitor unit, an air discharger, an electrode unit, a resistance unit, a pressure pump, and a control unit. The installation has the following variable parameters: 5–7 kV voltage supplied to metal electrodes; up to 3000 A current strength (the amplitude of the first half-wave); up to 15 μs electric pulse duration; ca. 100 V residual voltage across the capacitor unit; 0.2–0.3 ms capacitor recharging time; 300–500 Hz frequency of working discharges; 60 rpm rotation rate of the movable electrode relative to the stationary one; up to 10 L/h peristaltic pump performance; 1 bar peristaltic pump pressure; 100–800 μm spark length; and 800–10,200 pF capacitance of the capacitor unit. Specifically, metal nanoparticles were synthesized using a capacitor of 2200 pF, and the air gap in discharger was 500–550 μm (in the case of organic solvents) and 600–650 μm (in the case of distilled water) at ca. 12,000–15,000 K.

Different discharge modes allow the control of the composition and dispersion of nanoparticles. The concentration of nanoparticles was regulated by the performance of the peristaltic pump and by the multiplicity of treatment of the same solution. A single discharge treatment has resulted in metal concentrations of up to 40 μg/mL. The elemental composition of nanoparticles can be controlled by the chemical composition of the electrodes (including multiphase systems) and by the corresponding dispersion medium.

2.2. Characterization of Metal Nanoparticles

To determine the size of metal nanoparticles, a transmission electron microscope (TEM), LEO 912 AB OMEGA (Carl Zeiss, Oberkochen, Germany), with energy filter and Keller system was used. A drop of nanoparticle solution was placed on a standard TEM copper grid, coated with a thin film of polyvinyl formal, and dried at 296 ± 2 K for 15 min. The qualitative composition of metal nanoparticles was established by the electron diffraction patterns (Supplementary Figures S1 and S2).

Nanoparticle size distribution and their ζ-potential were analyzed by dynamic light scattering with a Zetasizer Nano ZS (Malvern Instruments, Worcestershire, UK). Measurements were realized in a 1-mL quartz cuvette or universal U-shape polystyrene cuvette at 25 °C (He-Ne laser, wavelength 633 nm) in triplicate.

To determine the mass concentration of metals in dispersed phase, they were completely ionized by concentrated HNO_3 for 3–4 min immediately before measurement. Metal concentration was analyzed using an atomic-emission spectrometer, iCAP 6300 Radial View (Thermo Fisher Scientific Inc., Waltham, MA, USA), with inductively coupled plasma. The instrument was calibrated with standard solutions of Ag^+ (328.07 nm), Ta^{5+} (240.06 nm), Cu^{2+} (324.75 nm), Fe^{3+} (238.20 nm), Ti^{2+} (323.45 nm), and Zn^{2+} ions (206.20 nm), and a 3 vol.% HNO_3 was used as a background. A shift of calibration curves was checked every 15 min.

2.3. Fibrous Materials and Their Characteristics

The fibrous materials, according to the manufacturer, contains 30% cotton and 70% meta polyaramide fiber fabric and is covered by poly(vinylidene difluoride)-*co*-poly(tetrafluoroethylene) membrane (Teks-Centre Ltd., Moscow, Russia). The percentage of surface coverage by a membrane was determined using a scanning electron microscope, Vega3 SB (Tescan, Brno, Czech Republic).

The structure of fibrous materials before and after application of metal nanoparticles were studied using a scanning electron microscope, Vega3 SB (Tescan, Brno, Czech Republic), with an energy-dispersive analyzer, X-Act 10 mm^2 SDD Detector (Oxford Instruments, Abingdon-on-Thames, United Kingdom). The linear profiles and two-dimensional maps of the spatial distribution of individual elements were revealed from X-ray spectrum of characteristic lines (or photon energies) of the elements present with an accuracy of about 1% and a detection limit of 0.01%. Analysis of the images was realized using a package, Fiji (a distribution of ImageJ, freely available at https://imagej.net/Fiji/Downloads).

The water vapor transmission rate through material was determined according to ISO 2528:2017.

Metal nanoparticles were deposited onto material dropwise and then dried at a room temperature within Petri dishes. To limit unnecessary losses, the maximum loading volume of the single deposition was limited to a 50 μL/cm^2. Alternatively, material was immersed into the nanoparticle solution as a whole until steeped in, and then removed and dried.

2.4. Investigation of Bactericide Activity

Cytotoxicity of nanoparticles towards mammalian cells was analyzed by MTT assay [15] with a mouse fibroblast NIH/3T3 (ATCC CRL-1658). Briefly, cells were cultured and diluted using a complete growth medium (DMEM with the addition of 10 vol.% fetal bovine serum and antibiotics). The grown cells at a concentration of 2×10^5 cells/mL were placed in a 96-well microplate and incubated for 24 h at 37 °C for adhesion to the surface. Further, a 150 μL of nanoparticle solution diluted to a concentration of 0.125–8.0 μg/mL was added and incubated for 24 h at 37 °C. After that, a 10 μL of MTT solution (5 mg/mL in DPBS buffer) was added to each well and incubated for 1 h. Next, the medium was gently decanted, and a 100 μL of DMSO was added to the each well. The optical density of the samples in the wells was measured on a microplate reader at 492 nm. Each experiment was carried out in triplicate; wells without metal nanoparticles were used as a control.

Biocide activity of metal nanoparticles towards luminescent bacteria were measured using the known method [16] with a *Photobacterium phosphoreum* B-1717 (All-Russian Collection of Industrial Microorganisms) immobilized in a poly(vinyl alcohol) cryogel. Briefly, the granules of immobilized bacteria were placed into a 100 μL of 0.3–30,000 ng/mL metal nanoparticle in a 2% NaCl water solution and incubated at 10 ± 1 °C for 30 min. The residual intensity of bioluminescence (I/I_0) was analyzed with a Microluminometr 3560 (New horizons diagnostics, Arbutus, MD, USA). Control granules were treated analogously but without nanoparticle addition.

The standard disk diffusion test was applied to a *Bacillus cereus* 8035 (ATCC 10702) and *Staphylococcus aureus* subsp. aureus (ATCC 25178) onto agar medium based on the Hottinger broth. Samples of fiber materials were aseptically deposited via backside or front face onto agar immediately after its inoculation by bacteria. After that, Petri dishes were incubated for 24 h at 37 °C and the growth inhibition zone was measured. Fiber material without nanoparticles was used in the same way as a control.

To quantitatively determine the bactericide activity of metal nanoparticles, the original method was applied to cells of gram-negative bacteria *Escherichia coli* DH5α (Thermo Fisher Scientific, Waltham, MA, USA) and gram-positive bacteria *Bacillus subtilis* B-522 (All-Russian Collection of Microorganisms, Russia). Cells were cultured in Luria–Bertani (LB) growth medium on a thermostatically controlled shaker, Adolf Kuhner AG (Basel, Switzerland), at 37 °C and agitation of 150 rpm. Cell growth was monitored using a spectrophotometer, Agilent UV-8453 (Agilent Technology, Waldbronn, Germany), at 540 nm. Bacterial cells were grown for 18–20 h and then sterilely separated from the culture broth by centrifugation at 8000× *g* for 10 min (Avanti J25, Beckman, Miami, FL, USA). Cell biomass was resuspended in a sterile 0.9% NaCl to a concentration of 10^6 cells/mL.

A 100 μL of the cell suspension was added to a 100 μL of 0–10 μg/mL of metal nanoparticles (with preliminary organic solvent evaporation) and incubated at 36 ± 2 °C for 3 h. The minimum bactericidal concentration (MBC) was assumed as the lowest concentration of metal nanoparticles, which completely inhibited the growth of bacteria (i.e., the concentration of intracellular ATP is equal

to 0). Benzethonium and benzalkonium chlorides were used as reference compounds in MBC detection. The concentration of intracellular ATP was determined by the known luciferin-luciferase method [12] with a Microluminometr 3560 (New horizons diagnostics, Arbutus, MD, USA) using a standard ATP reagent based on recombinant firefly luciferase (Lumtek LLC, Moscow, Russia). The data were linearized in semi-logarithm coordinates [11]. The mean and standard deviation (±SD) were calculated with SigmaPlot (ver. 12.5, Systat Software Inc., San Jose, CA, USA) from three independent experiments.

To study the bactericide activity of fibrous materials functionalized by nanoparticles, a new original method was used. Metal nanoparticles in various amounts (concentrations, volumes, application rates) were applied to the material samples (1 cm × 1 cm) and dried at room temperature for 20 h. Then, 50 μL of a suspension (10^6 cells/mL in a 0.9% NaCl) of *B.subtilis* B-522 or *E. coli* DH5α was applied to the materials and incubated for 24 h at room temperature. ATP was extracted by a 1 mL DMSO for 3 h and analyzed as described above. Samples without nanoparticles or with benzetonium chloride or benzalkonium chloride were used in the same way as controls. MBCs were calculated as previously described.

3. Results

3.1. Characteristics of Metal Nanoparticles and Their Deposition onto Fibrous Material

Metal nanoparticles obtained in electric arc have variable characteristics (Table 1). All of them tend to aggregate while increasing their concentration, and according to DLS measurements, they can grow up to μm size (Supplementary Table S1). Simultaneously their ζ-potential increases also.

Table 1. Size and ζ-potential of metal nanoparticles obtained in the media of ethanol, isopropanol and water. Some TEM images are presented on Supplementary Figures S1 and S2.

Metal	Size by TEM (nm)	ζ-potential (mV)	Concentration (μg/mL)
Fe^{EtOH}	2–3	1.4	7.8
Fe^{water}	2–3	–7.1	2.5
Ta^{EtOH}	1–3	2.7	18.3
Ta^{iPrOH}	1–3	0.05	15.1
Ta^{water}	2–3	68.7	5.1
Ti^{EtOH}	1–3	–0.8	5.7
Ti^{water}	1–2	–0.02	3.3
Zn^{EtOH}	2–5	6.2	71.7
Zn^{iPrOH}	4–10	1.3	53.1
Zn^{water}	3–5	8.1	7.2

To achieve high surface concentration of nanoparticles within fibrous material, it can be realized via different ways. Simultaneous synthesis and deposition of Cu nanoparticles was published previously [17]. However, it was inconvenient in this work due to application of preformed fibrous material. Alternatively, initial high enough concentration of nanoparticles and/or multiple deposition cycles were used to obtain necessary quantities of nanoparticles.

The outer hydrophobic polymer membrane was not continuous and covers ca. 50% of the surface of the fibrous materials used (Figure 1). Moreover, it has pores of 0.45–0.65 μm which ensure high water vapor transmission rate of ca. 480 g/(m^2 × d).

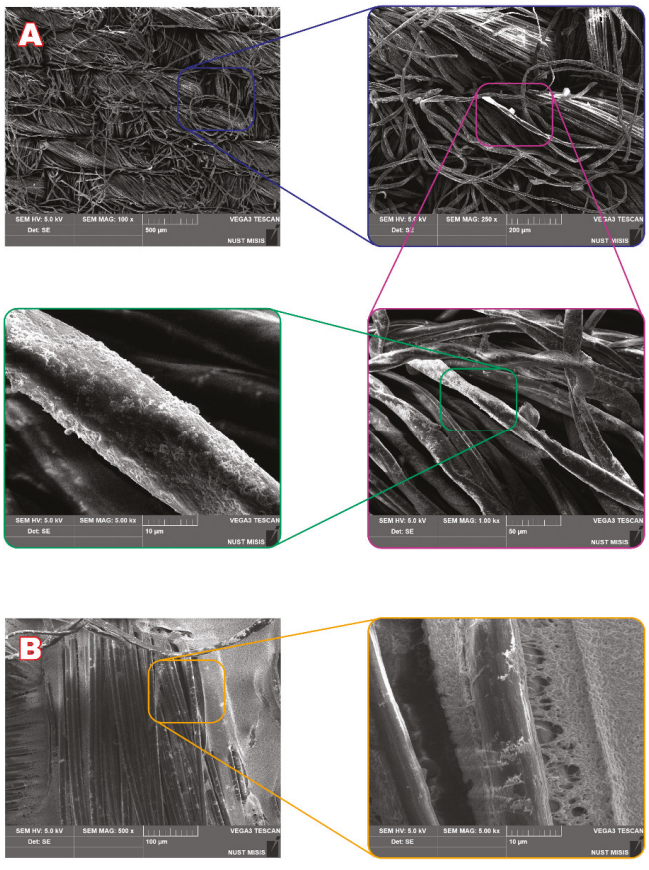

Figure 1. (**A**) SEM images of the front side of the fibrous material after deposition of Ta^{EtOH} nanoparticles. (**B**) SEM images of the back side of the fibrous material after deposition of Ta^{EtOH} nanoparticles. Initial material contained 30% of cotton and 70% of meta polyaramide fiber fabric and is covered by poly(vinylidene difluoride)-*co*-poly(tetrafluoroethylene) membrane from the back side.

Nanoparticles (for example, of Ta) were regularly distributed on the surface of fibrous material (Figure 2), though Ta aggregates tend to be accumulated in close proximity with phosphate and/or carboxy anions (Supplementary Figures S3–S5). Namely, the least quantity of 'free' aggregates (i.e., those which were not superimposed with other elements) of Ta^{EtOH} nanoparticles was in the case of oxygen (ca. 20–30%), followed by carbon (ca. 30–40%) and phosphorus (ca. 50%). Co-localization of Ta^{EtOH} nanoparticles with other elements issued was sparser.

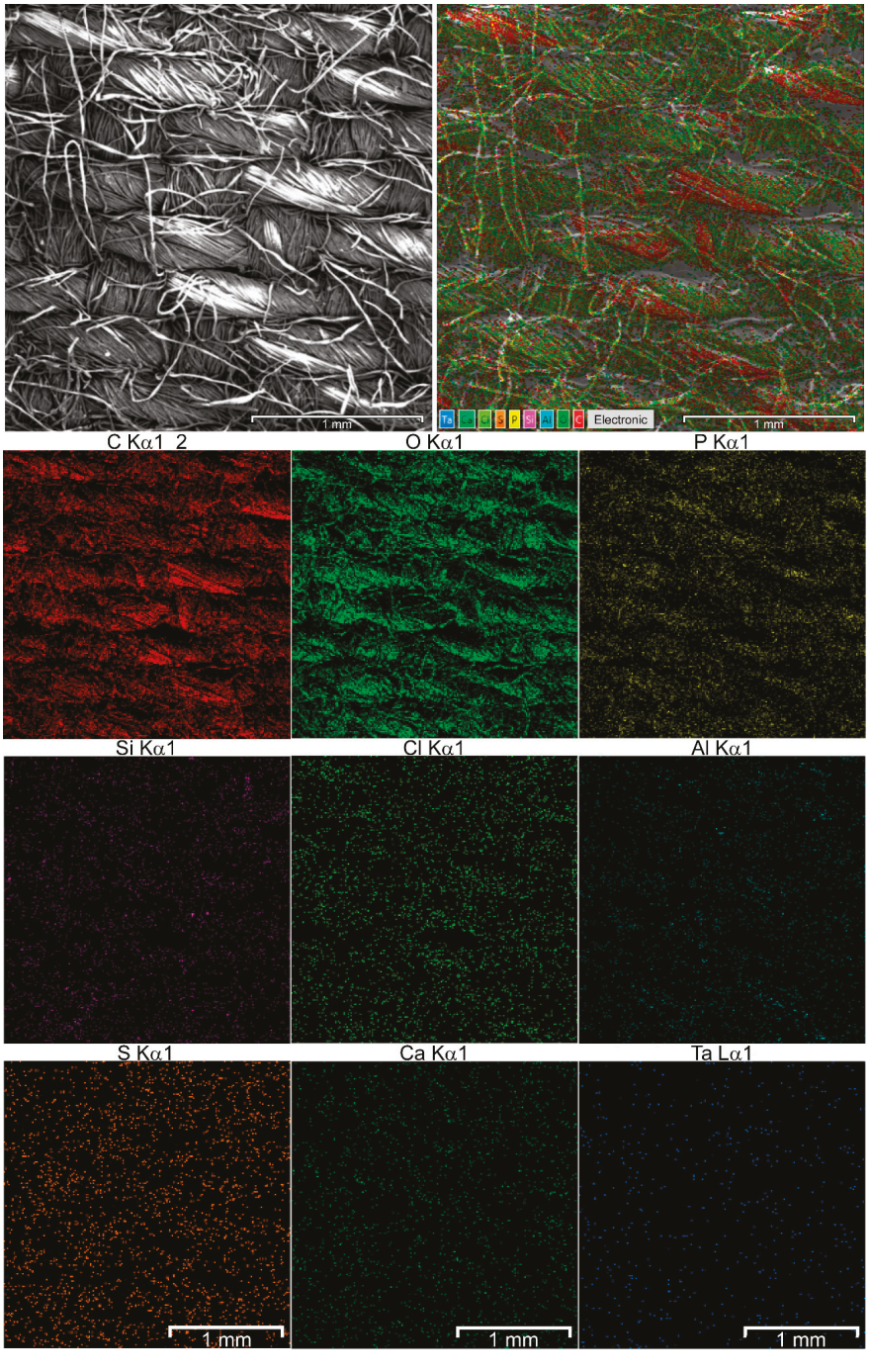

Figure 2. SEM and composite elemental images of fibrous material after deposition of Ta^{EtOH} nanoparticles. Elementwise chemical analysis is shown on inserts.

3.2. Analysis of Bactericide Activity

Initially no cytotoxicity of metal nanoparticles at concentrations of 0.125–8 μg/mL was revealed using MTT assay with mouse fibroblast NIH/3T3 cell line (Supplementary Figure S6).

After that, their cytotoxicity was issued with a luminescent *Photobacterium phosphoreum* immobilized within a poly(vinyl alcohol) cryogel [16,18]. Cytotoxic effect was variable, depending on the metal used (Figure 3), and was maximal for Ta and Zn nanoparticles.

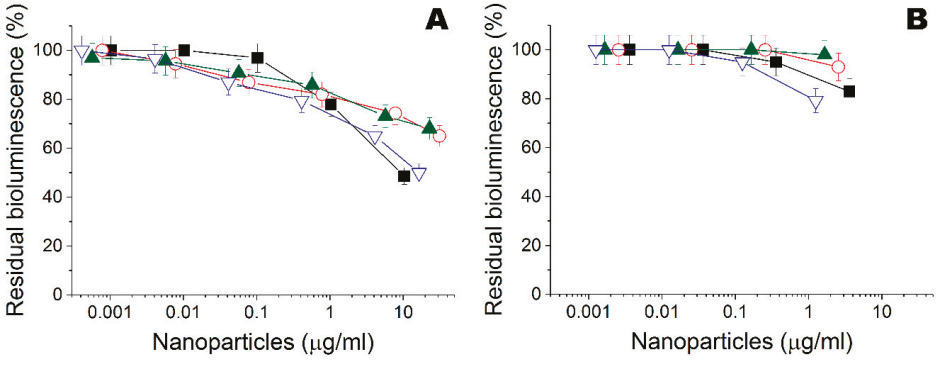

Figure 3. (**A**) Residual intensity of bioluminescence of immobilized cells *Photobacterium phosphoreum* treated by the Fe (○), Ta (▽), Ti (▲), and Zn (■) nanoparticles obtained in ethanol. (**B**) Residual intensity of bioluminescence of immobilized cells *P. phosphoreum* treated by the Fe (○), Ta (▽), Ti (▲), and Zn (■) nanoparticles obtained in water.

According to preliminary results with disk diffusion assay, functionalized materials had some bactericide activity towards both *Bacillus cereus* 8035 and *Staphylococcus aureus* subsp. aureus cells (Supplementary Figures S7–S10). However, this method appeared to be insufficient for the purposes of the work. Further bactericide activity of metal nanoparticles was analyzed against gram-negative (*Escherichia coli*) and gram-positive (*Bacillus subtilis*) bacteria using the original method (Figure 4). Gram-negative *E. coli* were more resistant, compared to gram-positive *B. subtilis*. Ta and Zn nanoparticles obtained both in ethanol and water had the best biocide potency and MBCs of 4–42 μg/mL and 10–27 μg/mL, respectively (Table 2). The difference of biocide activity between these nanoparticles obtained in ethanol or in water against gram-negative *E. coli* and gram-positive *B. subtilis* cells was not statistically significant: $p = 0.100$ and $p = 0.700$ in ethanol, and $p = 0.100$ and $p = 0.200$ in water according to ANOVA on ranks, respectively.

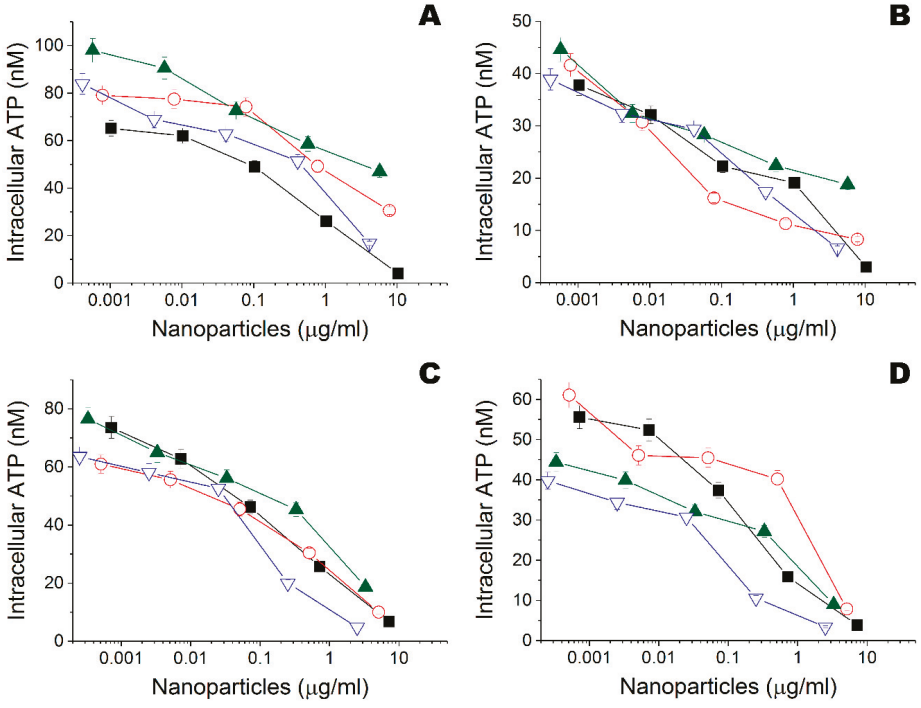

Figure 4. (**A**) Influence of Fe (○), Ta (▽), Ti (▲), and Zn (■) nanoparticles obtained in ethanol on intracellular ATP of *Escherichia coli* DH5α. (**B**) Influence of Fe (○), Ta (▽), Ti (▲), and Zn (■) nanoparticles obtained in ethanol on intracellular ATP of *Bacillus subtilis* B-522. (**C**) Influence of Fe (○), Ta (▽), Ti (▲), and Zn (■) nanoparticles obtained in water on intracellular ATP of *Escherichia coli* DH5α. (**D**) Influence of Fe (○), Ta (▽), Ti (▲), and Zn (■) nanoparticles obtained in water on intracellular ATP of *Bacillus subtilis* B-522.

Table 2. Minimal bactericidal concentrations (MBCs) of metal nanoparticles against gram-negative (*Escherichia coli*) and gram-positive (*Bacillus subtilis*) bacteria.

Nanoparticles	MBC (μg/mL)	
	E.coli	*B.subtilis*
Fe^{EtOH}	767 ± 139	36.6 ± 22.0
Ta^{EtOH}	41.9 ± 10.9	40.4 ± 22.0
Ti^{EtOH}	17,200 ± 15,200	2140 ± 1890
Zn^{EtOH}	20.3 ± 9.7	27.3 ± 14.2
Fe^{water}	34.4 ± 24.7	19.4 ± 5.6
Ta^{water}	4.0 ± 1.1	4.8 ± 2.7
Ti^{water}	66.6 ± 35.3	26.8 ± 17.1
Zn^{water}	23.9 ± 11.0	10.0 ± 3.9

Nanoparticles retained some (12.5–20%) of their bactericide activity after deposition onto fibrous material (Figure 5; Table 3), and Ta nanoparticles have demonstrated better performance. Under the same conditions, the usual antibacterials (benzalkonium and benzethonium chlorides) had MBCs of ca. 100–150 pg/cell that were orders of magnitude worse than values in suspension 0.6–16 pg/cell [19].

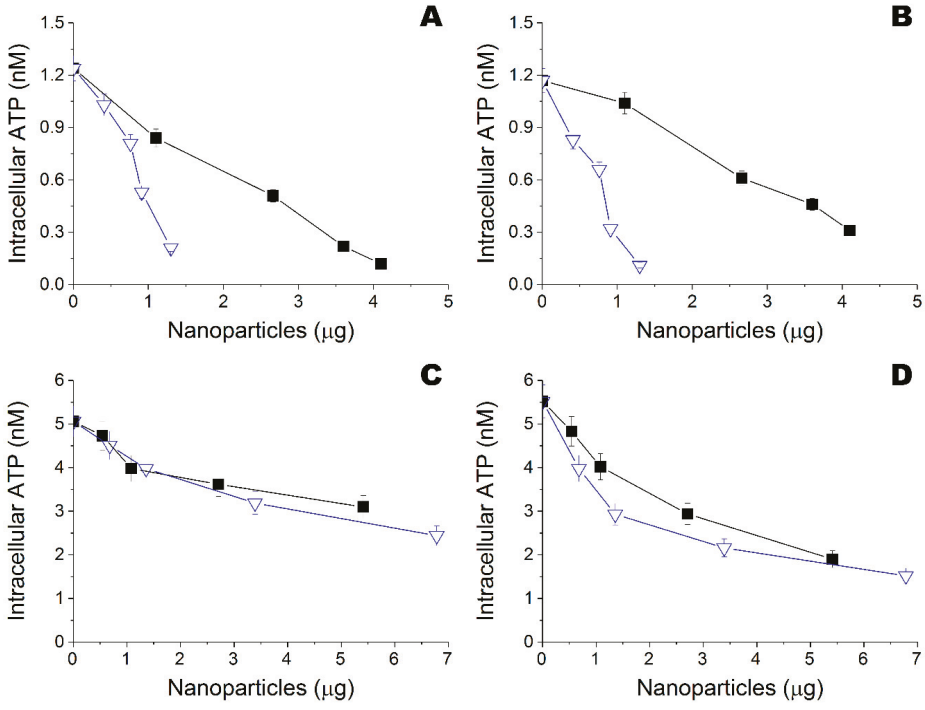

Figure 5. (**A**) Influence of Ta (▽) and Zn (■) nanoparticles obtained in ethanol and deposited onto fibrous material, on intracellular ATP of *Escherichia coli* DH5α. (**B**) Influence of Ta (▽) and Zn (■) nanoparticles obtained in ethanol and deposited onto fibrous material, on intracellular ATP of *Bacillus subtilis* B-522. (**C**) Influence of Ta (▽) and Zn (■) nanoparticles obtained in isopropanol and deposited onto fibrous material, on intracellular ATP of *Escherichia coli* DH5α. (**D**) Influence of Ta (▽) and Zn (■) nanoparticles obtained in isopropanol and deposited onto fibrous material, on intracellular ATP of *Bacillus subtilis* B-522.

Table 3. MBCs of various antibacterials deposited onto fibrous material (1 cm^2) against gram-negative (*Escherichia coli*) and gram-positive (*Bacillus subtilis*) bacteria.

Antibacterial Agent	Fibrous Material	MBC (pg/cell)	
		E. coli	*B. subtilis*
Zn^{EtOH} nanoparticles	−	20 ± 10	27 ± 14
	+	105 ± 11	161 ± 43
Ta^{EtOH} nanoparticles	−	42 ± 11	40 ± 22
	+	37 ± 4	31 ± 1
Zn^{iPrOH} nanoparticles	+	8970 ± 1290	518 ± 86
Ta^{iPrOH} nanoparticles	+	2220 ± 660	551 ± 229
Benzalkonium chloride	+	152 ± 16	133 ± 15
Benzethonium chloride	+	131 ± 13	106 ± 11

4. Discussion

Zn, Fe, and other nanoparticles are known to inhibit bioluminescence of *P. phosphoreum* and other luminescent bacteria [20,21]. However, to the best of our knowledge, there is no such information about Ta nanoparticles. Depending on the test microorganism used, variable sensitivity could be achieved [22].

Immobilized *P. phosphoreum* were quite sensitive and could recognize the most potent biocide nanoparticles at the preliminary step already. Interestingly, bioavailability of nanoparticles for immobilized cells seemed to depend on the solvent used to obtain them, being maximal in ethanol. It could be caused by increased ζ-potential of the most nanoparticles (except Fe) obtained in water (Table 1). On the one hand, biocide activity of nanoparticles towards suspension cells was usually enhanced at large ζ-potential [23]. On the other hand, these immobilized cells were shielded by additional polymer matrix which could tightly bind such strongly charged nanoparticles. The real example of a similar mode of action is a bacterial biofilm formation, which is known to protect cells against nanoparticles toxicity [24]. Thus, nanoparticles with lower ζ-potential could be more useful for treating complicated microbial community on the surface of some materials.

Various microorganisms have a differing susceptibility to nanoparticle biocides [10], and the modulation of reactive oxygen species (ROS) and/or heavy metal ions production are acknowledged as the main mechanisms of their antimicrobial action. Though other pathways, like enhanced penetration into cell [25] or influence on cell envelope [26], etc., are also possible.

Zn, Fe, and Ti nanoparticles are extensively investigated [27,28] but only few works deal with Ta nanoparticles. Previously Ta_2O_5 nanoparticles of 40–60 nm showed only limited bacteriostatic effect towards *Bacillus subtilis* at a dosage of 200 pg/cell [29], and no activity was detected against *Escherichia coli*, *Pseudomonas aeruginosa*, and *Staphylococcus aureus*. The efficiency of the commercial product was somehow increased by doping of Ta to ZnO nanoparticles then. However, the mechanism of antibacterial action was dramatically changed to ROS generation that is relevant to ZnO and differed from Ta alone.

Here, differently obtained Ta nanoparticles had a much more potency while comparing both with other metals (Fe and Ti) of the current work (Table 2) and with published data [29]. Only Zn nanoparticles have comparable bactericide activity in solution. Though their activity has dropped in five to six times while being applied on the fibers (Table 3). That was not happened in the case of Ta nanoparticles obtained in ethanol, but did occur for the benzalkonium and benzethonium chlorides. This again illustrates the importance of the bioavailability consideration, and support matrix could affect positively charged active compounds even more.

Highly hydrophobic carriers are supposed to cause additional limitations for biocide activity since they will decrease diffusion of the cells to the inner layers containing these active compounds. Thus, there is a balance between hydrophilic and hydrophobic characteristics of the carrier for maximal biocide efficiency. The current combination of Ta nanoparticles with cotton/polyaramide material is likely to be close to the optimal one.

5. Conclusions

Thus, novel fibrous materials functionalized by metal nanoparticles and having antibacterial activity towards gram-negative and gram-positive bacteria were developed. Ta^{EtOH} nanoparticles appeared to be the best choice for the maximal bactericide activity of resulting material. Moreover, viable cells were successfully determined directly onto treated fiber samples via applied ATP assay and could be recommended for other similar researches.

Supplementary Materials: The following are available online at http://www.mdpi.com/2079-4991/10/9/1724/s1, Table S1: Size distribution of aggregates of metal nanoparticles obtained in the media of ethanol, isopropanol and water, Figure S1: TEM and a Laue diffraction pattern images of metal nanoparticles obtained in water, Figure S2: TEM and a Laue diffraction pattern images of metal nanoparticles obtained in ethanol, Figure S3: Overlaying of Ta^{EtOH} nanoparticles with other chemical elements on the surface of fibrous material, Figure S4: Overlaying of Ta^{EtOH} nanoparticles with other chemical elements on the surface of fibrous material, Figure S5: Overlaying of Ta^{EtOH} nanoparticles with other chemical elements on the surface of fibrous material, Figure S6: Cytotoxicity of the Fe, Ta, Ti and Zn nanoparticles obtained in water towards mouse fibroblast NIH/3T3 cells, Figure S7: Results of preliminary zone inhibition test of various fiber materials deposited by different nanoparticles towards *Bacillus cereus* 8035 (ATCC 10702), Figure S8: Results of preliminary zone inhibition test of various fiber materials deposited by different nanoparticles towards *Staphylococcus aureus* subsp. aureus (ATCC 25178), Figure S9: Growth inhibition of *Bacillus cereus* 8035 (ATCC 10702) under samples of various fiber materials deposited by

different nanoparticles, Figure S10: Growth inhibition of *Staphylococcus aureus* subsp. aureus (ATCC 25178) under samples of various fiber materials deposited by different nanoparticles.

Author Contributions: Conceptualization, E.E.; methodology, G.F., N.S., and E.E.; validation, I.L.; formal analysis, I.L..; investigation, G.F., O.S., I.P., and N.S.; resources, O.S.; writing—original draft preparation, G.F. and N.S.; writing—review and editing, I.L. and E.E.; visualization, G.F., I.L., and I.P.; supervision, E.E.; project administration, E.E.; funding acquisition, E.E. All authors have read and agreed to the published version of the manuscript.

Funding: The work was financially supported by Russian Foundation for Basic Research (project 18-29-17069).

Conflicts of Interest: The authors declare no conflict of interest.

References

1. Gupta, A.; Mumtaz, S.; Li, C.-H.; Hussain, I.; Rotello, V.M. Combatting antibiotic-resistant bacteria using nanomaterials. *Chem. Soc. Rev.* **2019**, *48*, 415–427. [CrossRef]
2. Kumar, R.; Umar, A.; Kumar, G.; Nalwa, H.S. Antimicrobial properties of ZnO nanomaterials: A review. *Ceram. Int.* **2017**, *43*, 3940–3961. [CrossRef]
3. Yun, G.; Pan, S.; Wang, T.Y.; Guo, J.; Richardson, J.J.; Caruso, F. Synthesis of Metal Nanoparticles in Metal-Phenolic Networks: Catalytic and Antimicrobial Applications of Coated Textiles. *Adv. Healthc. Mater.* **2018**, *7*, e1700934. [CrossRef] [PubMed]
4. Burdușel, A.-C.; Gherasim, O.; Grumezescu, A.M.; Mogoantă, L.; Ficai, A.; Andronescu, E. Biomedical Applications of Silver Nanoparticles: An Up-to-Date Overview. *Nanomaterials* **2018**, *8*, 681. [CrossRef] [PubMed]
5. Konno, H.; Sasaki, S.; Nakasaka, Y.; Masuda, T. Facile Synthesis of Zeolitic Imidazolate Framework-8 (ZIF-8) Particles Immobilized on Aramid Microfibrils for Wastewater Treatment. *Chem. Lett.* **2018**, *47*, 620–623. [CrossRef]
6. Li, Z.; Zhou, G.; Dai, H.; Yang, M.; Fu, Y.; Ying, Y.; Li, Y. Biomineralization-mimetic preparation of hybrid membranes with ultra-high loading of pristine metal-organic frameworks grown on silk nanofibers for hazard collection in water. *J. Mater. Chem. A* **2018**, *6*, 3402–3413. [CrossRef]
7. Smith, M.K.; Mirica, K.A. Self-Organized Frameworks on Textiles (SOFT): Conductive Fabrics for Simultaneous Sensing, Capture, and Filtration of Gases. *J. Am. Chem. Soc.* **2017**, *139*, 16759–16767. [CrossRef]
8. Li, N.; Pranantyo, D.; Kang, E.-T.; Wright, D.S.; Luo, H.-K. *In Situ* Self-Assembled Polyoxotitanate Cages on Flexible Cellulosic Substrates: Multifunctional Coating for Hydrophobic, Antibacterial, and UV-Blocking Applications. *Adv. Funct. Mater.* **2018**, *28*, e1800345. [CrossRef]
9. Robertson, J.; McGoverin, C.; Vanholsbeeck, F.; Swift, S. Optimisation of the Protocol for the LIVE/DEAD®BacLight ™ Bacterial Viability Kit for Rapid Determination of Bacterial Load. *Front. Microbiol.* **2019**, *10*, e801. [CrossRef]
10. Aruoja, V.; Pokhrel, S.; Sihtmäe, M.; Mortimer, M.; Mädler, L.; Kahru, A. Toxicity of 12 metal-based nanoparticles to algae, bacteria and protozoa. *Environ. Sci. Nano* **2015**, *2*, 630–644. [CrossRef]
11. Ismayilov, I.T.; Stepanov, N.A.; Efremenko, E.N.; Abbasov, V.M. Evaluation of biocidal properties of vegetable oil-based corrosion inhibitors using bioluminescent enzymatic method. *Moscow Univ. Chem. Bull.* **2015**, *70*, 197–201. [CrossRef]
12. Stepanov, N.; Senko, O.; Perminova, I.; Efremenko, E. A new approach to assess the effect of various humic compounds on the metabolic activity of cells participating in methanogenesis. *Sustainability* **2019**, *11*, 3158. [CrossRef]
13. Piret, J.-P.; Bondarenko, O.M.; Boyles, M.S.P.; Himly, M.; Ribeiro, A.R.; Benetti, F.; Smal, C.; Lima, B.; Potthoff, A.; Simion, M.; et al. Pan-European inter-laboratory studies on a panel of *in vitro* cytotoxicity and pro-inflammation assays for nanoparticles. *Arch. Toxicol.* **2017**, *91*, 2315–2330. [CrossRef] [PubMed]
14. Leont'ev, V.K.; Pogorel'skii, I.P.; Frolov, G.A.; Karasenkov, Y.N.; Gusev, A.A.; Latuta, N.V.; Borozdkin, L.L.; Stefantsova, D.S. Antibacterial Properties of Aqueous Colloid Solutions of Metal and Metal Oxide Nanoparticles against Dental Plaque Bacteria. *Nanotechnol. Russ.* **2018**, *13*, 195–198. [CrossRef]
15. Efremenko, E.N.; Lyagin, I.V.; Klyachko, N.L.; Bronich, T.; Zavyalova, N.V.; Jiang, Y.; Kabanov, A.V. A simple and highly effective catalytic nanozyme scavenger for organophosphorus neurotoxins. *J. Control. Release* **2017**, *247*, 175–181. [CrossRef] [PubMed]

16. Senko, O.; Stepanov, N.; Maslova, O.; Akhundov, R.; Ismailov, A.; Efremenko, E. Immobilized luminescent bacteria for the detection of mycotoxins under discrete and flow-through conditions. *Biosensors* **2019**, *9*, 63. [CrossRef]
17. Shahidi, S.; Jamali, A.; Dalal Sharifi, S.; Ghomi, H. *In-situ* synthesis of CuO nanoparticles on cotton fabrics using spark discharge method to fabricate antibacterial textile. *J. Nat. Fibers* **2018**, *15*, 870–881. [CrossRef]
18. Efremenko, E.N.; Maslova, O.V.; Kholstov, A.V.; Senko, O.V.; Ismailov, A.D. Biosensitive element in the form of immobilized luminescent photobacteria for detecting ecotoxicants in aqueous flow-through systems. *Luminescence* **2016**, *31*, 1283–1289. [CrossRef]
19. Aragonès, L.; Escudé, C.; Visa, P.; Salvi, L.; Mocé-Llivina, L. New insights for rapid evaluation of bactericidal activity: A semi-automated bioluminescent ATP assay. *J. Appl. Microbiol.* **2012**, *113*, 114–125. [CrossRef]
20. Wang, D.; Gao, Y.; Lin, Z.; Yao, Z.; Zhang, W. The joint effects on *Photobacterium phosphoreum* of metal oxide nanoparticles and their most likely coexisting chemicals in the environment. *Aquat. Toxicol.* **2014**, *154*, 200–206. [CrossRef]
21. Mortimer, M.; Kasemets, K.; Heinlaan, M.; Kurvet, I.; Kahru, A. High throughput kinetic *Vibrio fischeri* bioluminescence inhibition assay for study of toxic effects of nanoparticles. *Toxicol. In Vitro* **2008**, *22*, 1412–1417. [CrossRef] [PubMed]
22. Deryabina, D.G.; Efremova, L.V.; Karimov, I.F.; Manukhov, I.V.; Gnuchikh, E.Y.; Miroshnikov, S.A. Comparative Sensitivity of the Luminescent *Photobacterium phosphoreum*, *Escherichia coli*, and *Bacillus subtilis* Strains to Toxic Effects of Carbon-Based Nanomaterials and Metal Nanoparticles. *Microbiology* **2016**, *85*, 198–206. [CrossRef]
23. Schwegmann, H.; Feitz, A.J.; Frimmel, F.H. Influence of the zeta potential on the sorption and toxicity of iron oxide nanoparticles on *S. cerevisiae* and *E. coli*. *J. Colloid Interface Sci.* **2010**, *347*, 43–48. [CrossRef]
24. Lara, H.H.; Romero-Urbina, D.G.; Pierce, C.; Lopez-Ribot, J.L.; Arellano-Jiménez, M.J.; Jose-Yacaman, M. Effect of silver nanoparticles on *Candida albicans* biofilms: An ultrastructural study. *J. Nanobiotechnol.* **2015**, *13*, e91. [CrossRef] [PubMed]
25. Kasemets, K.; Suppi, S.; Künnis-Beres, K.; Kahru, A. Toxicity of CuO nanoparticles to yeast *Saccharomyces cerevisiae* BY4741 wild-type and its nine isogenic single-gene deletion mutants. *Chem. Res. Toxicol.* **2013**, *26*, 356–367. [CrossRef] [PubMed]
26. Ivask, A.; Elbadawy, A.; Kaweeteerawat, C.; Boren, D.; Fischer, H.; Ji, Z.; Chang, C.H.; Liu, R.; Tolaymat, T.; Telesca, D.; et al. Toxicity mechanisms in *Escherichia coli* vary for silver nanoparticles and differ from ionic silver. *ACS Nano* **2014**, *8*, 374–386. [CrossRef]
27. Monteserín, C.; Blanco, M.; Murillo, N.; Pérez-Márquez, A.; Maudes, J.; Gayoso, J.; Laza, J.M.; Hernáez, E.; Aranzabe, E.; Vilas, J.L. Novel Antibacterial and Toughened Carbon-Fibre/Epoxy Composites by the Incorporation of TiO_2 Nanoparticles Modified Electrospun Nanofibre Veils. *Polymers* **2019**, *11*, 1524. [CrossRef] [PubMed]
28. Salat, M.; Petkova, P.; Hoyo, J.; Perelshtein, I.; Gedanken, A.; Tzanov, T. Durable antimicrobial cotton textiles coated sonochemically with ZnO nanoparticles embedded in an *in-situ* enzymatically generated bioadhesive. *Carbohydr. Polym.* **2018**, *189*, 198–203. [CrossRef] [PubMed]
29. Guo, B.L.; Han, P.; Guo, L.C.; Cao, Y.Q.; Li, A.D.; Kong, J.Z.; Zhai, H.-F.; Wu, D. The antibacterial activity of Ta-doped ZnO nanoparticles. *Nanoscale Res. Lett.* **2015**, *10*, e336. [CrossRef] [PubMed]

nanomaterials

MDPI

Article

Cu Nanoparticle-Loaded Nanovesicles with Antibiofilm Properties. Part I: Synthesis of New Hybrid Nanostructures

Lucia Sarcina [1], Pablo García-Manrique [2,3,4], Gemma Gutiérrez [3,4], Nicoletta Ditaranto [1], Nicola Cioffi [1], Maria Matos [3,4,*] and Maria del Carmen Blanco-López [2,4,*]

1 Department of Chemistry, Università degli Studi di Bari Aldo Moro, via Orabona 4, 70125 Bari, Italy; lucia.sarcina@uniba.it (L.S.); nicoletta.ditaranto@uniba.it (N.D.); nicola.cioffi@uniba.it (N.C.)
2 Department of Physical and Analytical Chemistry, University of Oviedo, Julián Clavería 8, 33006 Oviedo, Spain; garciampablo@uniovi.es (P.G.-M.); gutierrezgemma@uniovi.es (G.G.)
3 Department of Chemical and Environmental Engineering, University of Oviedo, Julián Clavería 8, 33006 Oviedo, Spain
4 Instituto Universitario de Biotecnología de Asturias, University of Oviedo, 33006 Oviedo, Spain
* Correspondence: matosmaria@uniovi.es (M.M.); cblanco@uniovi.es (M.d.C.B.-L.)

Received: 2 July 2020; Accepted: 4 August 2020; Published: 6 August 2020

Abstract: Copper nanoparticles (CuNPs) stabilized by quaternary ammonium salts are well known as antimicrobial agents. The aim of this work was to study the feasibility of the inclusion of CuNPs in nanovesicular systems. Liposomes are nanovesicles (NVs) made with phospholipids and are traditionally used as delivery vehicles because phospholipids favor cellular uptake. Their capacity for hydrophilic/hydrophobic balance and carrier capacity could be advantageous to prepare novel hybrid nanostructures based on metal NPs (Me-NPs). In this work, NVs were loaded with CuNPs, which have been reported to have a biofilm inhibition effect. These hybrid materials could improve the effect of conventional antibacterial agents. CuNPs were electro-synthesized by the sacrificial anode electrolysis technique in organic media and characterized in terms of morphology through transmission electron microscopy (TEM). The NVs were prepared by the thin film hydration method in aqueous media, using phosphatidylcholine (PC) and cholesterol as a membrane stabilizer. The nanohybrid systems were purified to remove non-encapsulated NPs. The size distribution, morphology and stability of the NV systems were studied. Different quaternary ammonium salts in vesicular systems made of PC were tested as stabilizing surfactants for the synthesis and inclusion of CuNPs. The entrapment of charged metal NPs was demonstrated. NPs attached preferably to the membrane, probably due to the attraction of their hydrophobic shell to the phospholipid bilayers. The high affinity between benzyl-dimethyl-hexadecyl-ammonium chloride (BDHAC) and PC allowed us to obtain stable hybrid NVs c.a. 700 nm in diameter. The stability of liposomes increased with NP loading, suggesting a charge-stabilization effect in a novel antibiofilm nanohybrid material.

Keywords: hybrid nanostructures; nanovesicles; nanoparticles; copper; antibiofilm

1. Introduction

A biofilm is commonly defined as a complex community of microorganisms adherent on a surface and organized in a polymeric matrix, usually containing exopolysaccharide [1–3]. These structures have a heterogenic network of aqueous compartments interposed between glycocalyx-enclosed microorganism in stalk- or mushroom-like structures [3], holding more than one single microbial species. The biofilm resistance issue could be considered phenotypic. Bacteria in biofilm present a higher antimicrobial resistance (AMR) compared to planktonic forms [3].

Prevention and destruction of biofilms is a challenging task requiring knowledge from several scientific research branches. Due to AMR mechanisms, there is an urgent need to search for novel efficient formulations. A reported effective strategy to develop more efficient materials to prevent/minimize biofilm formation is surface modification through the addition of metal particles (Cu, Zn, Ti, Ag) to polymeric blends [4–8] or biopolymers such as starch solutions [9]. Recent studies reported that carbon/copper nanoparticles (CuNP) hybrids were effective as biocides, with the carbon component in charge of capturing the bacteria and the CuNPs responsible for bacteria destruction. Moreover, the outer carbon layers protected the metallic copper from external oxidation [10]. It has been proved in the literature that, in order to have bactericidal inhibitory effect, a surface should be covered by relatively hydrophobic polymers that are positively charged [3].

Metal nanoparticles (Me-NPs) such as AuNPs, AgNPs or CuNPs display unique properties that make them suitable at surface science for the development of antimicrobial formulations. Previous studies investigated the integration of NPs in biomaterials showing unique recognition, catalytic, and inhibition properties [6,11–14]. Especially gold or silver NPs are largely used for biomedical application since they can be used as biomarkers and drug-delivery agents with a bactericidal effect [15]. The antibacterial action towards different microorganisms exerted by polymer nanocomposites loaded with copper NPs has already been proved [4,16–22], along with the possibility to tune the ionic copper release. It is possible to achieve efficient disinfection by simply changing the CuNP loading and/or the thickness and formulation of the surfactant shell. Indeed, as evident from the plots reported in Figure 1, when a stabilizer with four butyl alkyl chains is used to prepare CuNPs, the released plateau copper amount is around 1ppm. This value decreases as the length of the surfactant alkyl chains is increased, along with the slowdown of the kinetics and the kinetic constants. This could be explained by the increase in the shell thickness, which is able to modulate the copper ions' release from the surface of the NP core [21,23–25]. Moreover, in quaternary ammonium compounds (QAC), both the fatty-acyl chain length distributions and the degree of C–C saturation will significantly affect antimicrobial activity, with a maximized action against Gram positive bacteria when chain length is n = 12–14 and against Gram negative bacteria when n = 14–16 [26].

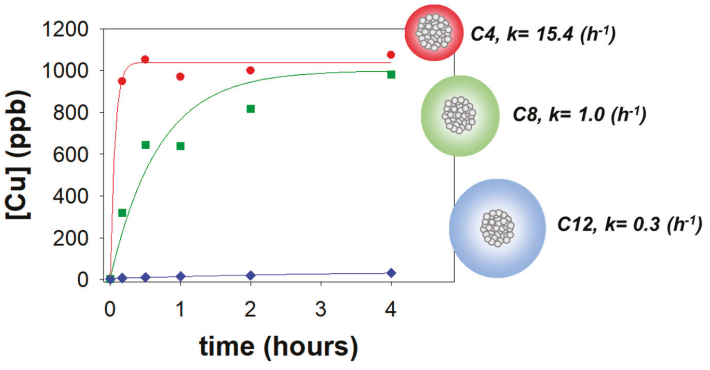

Figure 1. Effect of the alkyl chain length of the stabilizer on the copper release concentration and on the kinetic constant for copper nanocomposites with the same copper nanoparticle (CuNP) %*w*/*w* loading. Red: tetra butyl ammonium chloride (C4); green: tetra octyl ammonium chloride (C8); blue: tetra dodecyl ammonium chloride (C12).

Some of the reported modes of action of anti-biofilm molecules are inhibition via interference in the quorum sensing pathways, the adhesion mechanism, disruption of extracellular DNA, protein, lipopolysaccharides, exopolysaccharides and the secondary messengers involved in various signaling pathways [27]. It has been proved that novel nanostructures involving copper fusion increased antimicrobial activity against biofilms. This seems to be due to the release of copper ions, which inhibited

the quorum sensing in *Methylobacterium spp*. This resulted in inhibition of the expression of the genes that form biofilms [14].

Nanovesicles (NVs) are self-assembled structures of lipids enclosed in bilayers forming single (unilamellar) or concentric membranes (multilamellar), which divide hydrophilic and hydrophobic compartments. They can be considered as "soft nanoparticles" because of the interaction of their components resembling biological systems [28]. The most explored NV systems are liposomes and niosomes, which differ in terms of the components used for the NV membrane layer formation. The components mostly used are cationic lipids such as DOTMA (trimethyl [2,3-(dioleyloxy) propyl] ammonium chloride) or DPPC (DL-dipalmitoylphosphatidylcholine) and the nonionic sorbitan monostearate or trioleate, which resemble the structure of phospholipids that form biological membranes [28,29]. The choice of nanovesicle type affects the final shape and thickness of the membrane as well as supramolecular reorganization, permeability, elasticity and compatibility with biological materials [30–35].

Several techniques have been implemented to prepare NVs, depending on the specific requirement and technologic purposes. The procedure typically involves the following steps: drying down lipids from organic solvent, re-dispersing them in aqueous media, purifying liposomes, analyzing the morphology of the product and measuring, when possible, the encapsulation efficiency [36–38]. The selected method could affect some morphological factors such as size and size distribution, the physical instability of vesicles and their encapsulation efficiency.

Liposomes are meant to be stable and bio-related structures for the transport and the controlled release of drugs. Thus, the investigation of hybrid NP-loaded NVs could combine the bactericidal effect of metal NPs enforcing the efficacy of NVs for permeability and delivery. Park et al. (2005) demonstrated the formulation of gold-loaded liposomes including 3–4 nm NPs into lipid (DPPC) bilayers. Similar results were obtained for silver NP inclusion [15,39]. Moreover, it was found that the encapsulation of AgNPs into liposomes enhanced antibacterial efficacy, reducing the concentration of NPs necessary to achieve a complete inhibition of bacterial growth [40]. On the other hand, it has just recently been demonstrated that liposomes functionalized with quaternary ammonium compounds are able to inhibit bacterial adherence and biofilm formation [33]. Therefore, it could be expected that the combination of NVs and CuNPs in hybrid nanostructures could enhance antibiofilm properties.

Over the recent decades, the capability of using electrochemical methods for the synthesis of transition metal NPs [23,41], and its peculiarity to have notable control on particle size thanks to voltage control has been proved. The so-called sacrificial anode electrolysis (SAE) is based on the oxidation of the bulk anode-material and the subsequent reduction of the formed metal ions in the presence of a stabilizer in order to obtain core-shell NPs dispersed in the electrosynthesis solution.

The aim of the part I of this work was to study how NPs can be loaded in liposomes and to examine the behavior of these novel composite structures in terms of bilayers stability and fluidity. Their real antimicrobial capacity will be tested in part II. CuNPs were electro-synthesized by the SAE technique in organic media and characterized in terms of morphology through transmission electron microscopy (TEM). To assess NP inclusion in the lipid bilayer, the NVs were prepared by the thin film method in aqueous media, using phosphatidylcholine (PC) and cholesterol as a membrane stabilizer. This method promotes the formation of multilamellar vesicle structure [28,37], and it was chosen for this study to synthesize robust NVs with mechanical strength. The hybrid NP-loaded NVs were purified and their morphology was characterized by TEM. The particle size distribution and colloidal stability of the suspension were studied by dynamic light scattering (DLS), ζ-potential and multiple lights scattering (MLS). This study will open the path to novel nanohybrid materials with improved antibiofilm inhibition properties.

2. Materials and Methods

2.1. Materials

For CuNP preparation: two different surfactants were tested: tetra-dodecyl ammonium chloride (TDoAC), with four symmetric dodecyl alkyl chains, and benzyl-dimethyl-hexadecyl ammonium chloride (BDHAC), with four asymmetric alkyl chains. Both alkylammonium salts, chloroform ($CHCl_3$) and tetrahydrofuran (THF), were purchased from Merck KGaA (Darmstadt, Germany).

For vesicle preparation, the materials used were as follows: phosphatidylcholine (PC), from soybean (Phospholipon 90G) and cholesterol. PC was a kind gift from Lipoid (Ludwigshafen am Rhein, Germany), and cholesterol was purchased from Merck KGaA (Darmstadt, Germany).

2.2. Preparation of CuNPs

The synthesis of copper colloids was performed in a three-electrode cell equipped with a copper anode, a platinum cathode and a reference electrode made of $Ag/AgNO_3$ (0.1 M in Acetonitrile). The electrodes were dipped in a solution containing the surfactant which acted both as an electrolyte and a capping agent for NPs, providing a stable shell that prevented particle agglomeration, and avoided cathode metallization. Chloroform and tetrahydrofuran were used as solvents to let CuNPs disperse in the NVs. Two different surfactants were tested: tetra-dodecyl ammonium chloride (TDoAC), and benzyl-dimethyl-hexadecyl ammonium chloride (BDHAC).

The electrosynthesis was performed using the potentiostat CHI-1140 B (CH Instruments Inc., Austin, TX, USA). During the synthesis, an amperometric I-t curve was recorded, from which it was possible to read the total charge value useful to calculate the process yield. Finally, the colloid was characterized in order to determine particle size and morphology. At least three replicates were carried out for each experiment.

2.3. Characterization of CuNPs

Morphological analysis of the copper colloids was performed using an Tecnai Spirit G2 electron microscope (FEI Company, Hillsboro, OR, USA) with a LaB6 filament as its electron source (120 kV operating voltage). The transmission electron microscopy (TEM) images were used to measure the size and size distribution of the CuNPs using ImageJ software (Wayne Rasband (NIH), Bethesda, MD, USA). The histograms were prepared with SigmaPlot 12.0, plotting the frequency counts of the NP diameters vs. the NP size.

2.4. Preparation of Empty NVs and NP-Loaded NVs

The preparation of both empty NVs and hybrid CuNP-loaded NVs was carried out by using the thin film hydration method [37,42]. This well-established method for niosome or liposome technology is suitable for the effective encapsulation of additives (such as drugs) in the hydrophobic compartment [43]. Natural soybean phosphatidylcholine (PC) was used as the main lipid component and cholesterol as the membrane stabilizer. Several molar ratios were tested as reported in Table 1.

A Rotary evaporator Buchi R-205 was used for the preparation of both the empty and hybrid NVs. Firstly, the empty NVs were prepared by a 5 mM solution of PC in a mixture of chloroform and THF ($CHCl_3$:THF) in a 9:1 (*v*/*v*) ratio. Organic solvents were evaporated when setting the rotary evaporator. Experiments by modifying the temperature, rotation speed, evaporation time, and vacuum pressure were tested. After the evaporation of solvents, the film was left at 150 mbar under rotation for 1 h to enhance thinner formation, then the flask was filled with nitrogen and stored at room temperature overnight. The transparent and homogeneous film formed was hydrated by adding deionized water. The temperature of the deionized water, rotation speed and hydration time were optimized accordingly.

Table 1. Experimental parameter setting for the inclusion in nanovesicles (NVs) of CuNPs stabilized by tetra-dodecyl ammonium chloride (TDoAC—Cu@TDoAC) and benzyl-dimethyl-hexadecyl-ammonium chloride (BDHAC—Cu@BDHAC). The ratio of membrane components, phosphatidylcholine and cholesterol (PC:CHO), their lipid concentration and relative amount of lipid to nanoparticle composition (LIP:CuNPs) are listed for each test. Specifications of the solvents used, and temperature (T), pressure (P), rotation speed (R), and time (t) for evaporation and hydration steps are also reported.

TDoAC (Cu@TDoAC)												
	Membrane Components			**Solvents**		**Evaporation**				**Hydration P_{ATM}**		
	PC:CHO Molar Ratio	**Lipid (mM)**	**LIP:CuNPs (*w*/*w*)**	**$CHCl_3$:THF (*v*/*v*)**	**Vol (mL)**	**T °C**	**P (mbar)**	**R (rpm)**	**t (min)**	**T °C**	**R (rpm)**	**t (min)**
Test1	1:0	10	500:1	9:1	20	41	140	140	40	60	150	20
Test2	2:1	10	700:1	9:1	30	50	490	150	60	60	150	20
Test3	2:1	10	1500:1	9:1	15	52	180	150	90	55	150	30
BDHAC (Cu@BDHAC)												
	Membrane Components			**Solvents**		**Evaporation**				**Hydration P_{ATM}**		
	PC:CHO Molar Ratio	**Lipid (mM)**	**LIP:CuNPs (*w*/*w*)**	**$CHCl_3$:THF (*v*/*v*)**	**Vol (mL)**	**T °C**	**P (mbar)**	**R (rpm)**	**t (min)**	**T °C**	**R (rpm)**	**t (min)**
Test1	2:1	5	2000:1	9:1	25	53	150	150	60	50	150	5
Test2	2:1	5	1200:1	9:1	25	53	150	150	90	50	150	5
Test3	2:1	5	800:1	9:1	25	53	150	150	30	50	150	5

Table 1 shows the experimental parameters tested for the inclusion of both CuNPs stabilized by TDoAC (Cu@TDoAC) and by BDHAC (Cu@BDHAC).

2.5. Purification of NP-Loaded NVs

After the hydration, a purification step was implemented to separate CuNP–NV hybrids from non-encapsulated NPs. A red lipophilic dye (Fat Red Bluish) 0.5% (*w*/*w*) was used to better visualize the vesicles in a gel filtration PD10 empty column, in-house packed with Sepharose CL-4B. The Sepharose was kept at room temperature, then a solution was prepared with 13 mL of gel in 15 mL of milli-Q water. The solution was poured and left to pack over a 0.45 μm polyethylene frit previously washed in ethanol, and was then inserted in the column. Additionally, 2.5 mL of the sample was poured in the column; milli-Q-filtered water was added subsequently. The first 3 mL of the sample that dropped out, corresponding to the purified vesicles, was collected.

2.6. Characterization of Empty NVs and NP-Loaded NVs

Vesicle and hybrid colloid morphologic characterization was assessed with a JEM-1011 transmission electron microscope (TEM, JEOL, Akishima–Tokyo, Japan). The samples were diluted in a 1:100 ratio before placing a drop of the diluted suspension on a copper grid (TAAB, carbon coated 300 mesh). Since the NVs were transparent to the electron beam, it was necessary to perform a negative staining of the samples. After placing the samples containing the NVs on the grid, a drop of 2% (*w*/*w*) phosphotungstic acid solution was added on the grid and the excess was removed after ten seconds. The contact time with the staining agent was kept short enough to avoid an excessive darkening of the samples.

A Malvern Zetasizer Nano-ZS instrument, (Malvern, UK) was used for determining both size distribution of the empty NVs and hybrids by dynamic light scattering (DLS), and to estimate ζ-potential by laser Doppler velocimetry (LDV), which provides information concerning the stability of the empty liposomes and hybrid CuNP-loaded NVs. The samples were diluted in a 1:100 volume and the test was replicated three times for each composition, monitoring the stability over one week at 25 °C.

A Formulaction Turbiscan lab expert with an ageing station was also used to test the colloidal stability by verifying creaming, flocculation and precipitation in ageing conditions. Empty NVs prepared with PC and cholesterol were tested, as well as the hybrid NVs loaded with CuNPs and stabilized by BDHAC, with three different concentrations of the loaded copper colloids. The analysis lasted six days with a sampling time of two hours, and the samples were stored in the ageing station at 38 °C.

3. Results

3.1. Synthesis and Morphological Characterization of CuNPs

During the electrosynthesis of copper colloids, the current vs. time curve was recorded, hence the charge value. Comparing these experimental data with the weight change of electrodes, it was possible to estimate the percentage yield of the process and the concentration of copper in the final dispersion. Cu@TDoAC NPs were prepared using the surfactant concentration and the overpotential value already adjusted for this process (0.1 M, 1.5 V) [21].

When the asymmetric salt BDHAC was used as a stabilizer, the electrochemical parameters did not lead to the same optimal results, and fast precipitation and NP aggregation were observed. Therefore, an increased surfactant concentration was used with the aim of inducing a greater stabilizing effect and balancing the smaller steric hindrance of BDHAC as a shell-forming component [44]. Moreover, THF was tested as a single solvent to prevent phase separation during CuNP inclusion in the NVs.

Figure 2 reports the TEM images and the size distribution histograms of the Cu@TDoAC and Cu@BDHAC colloids.

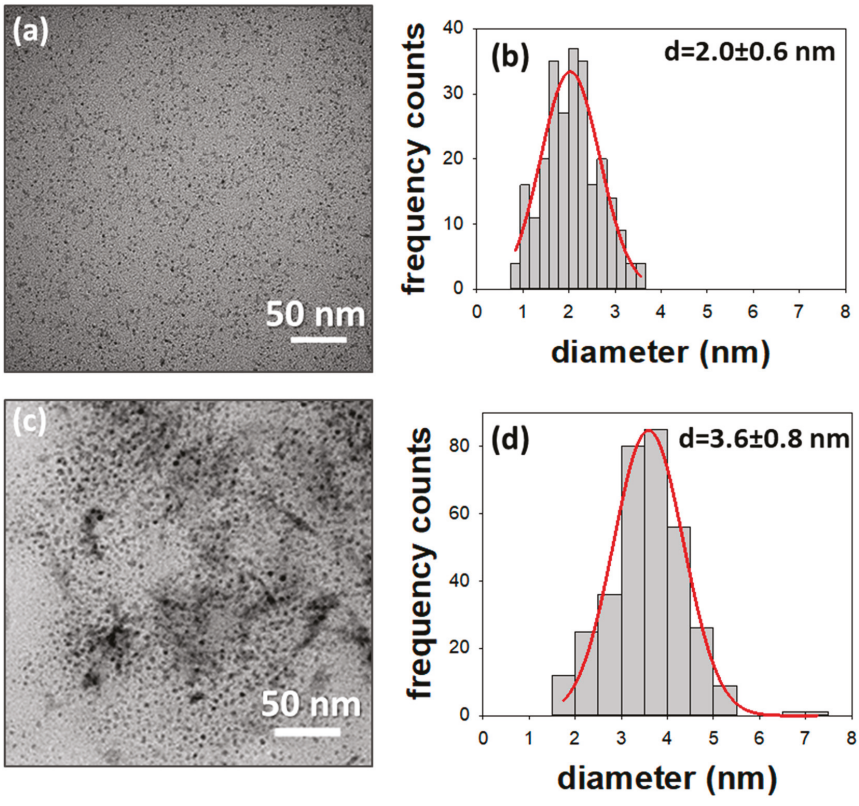

Figure 2. Transmission electron microscopy (TEM) images of the Cu@TDoAC colloid (**a**), and the Cu@BDHAC colloid (**c**), along with the size distribution histograms (**b**,**d**). Sample (**a**) d = 2.0 ± 0.6 nm, n = 250; sample (**c**) d = 3.6 ± 0.8 nm, n = 330.

In both cases, the images showed the presence of almost spherical NPs and an average diameter of a few nanometers with a homogeneous in-plane distribution, proving that the selected electrochemical parameters effectively yielded CuNPs with the desired morphology.

3.2. Preparation and Characterization of Empty NVs

The morphology of the empty NVs, studied through TEM analysis, is shown in Figure 3. Multilamellar structures (zoomed insert) and spherical structures with an average size of 100–1000 nm obtained as reported in literate for similar working conditions were observed [45,46]. The DLS characterization of the empty NVs presented only one peak, with a mean Z-average size of 1.6 ± 0.1 µm with a polydispersity index (PDI) of 0.18 ± 0.03. Some variations in size were observed after ageing; indeed, the NVs displayed an aggregation trend and precipitated after few hours as two peaks distribution appeared, with mean sizes of 1.90 ± 0.02 µm and 5.48 ± 0.01 µm. Therefore, PDI increased to 0.31 ± 0.01. NV ζ-potential measured by LDV was always found to be negative for all the replicates at c.a. −30 mV. As reported in the literature, a strong charged layer (positive or negative) can increase electrostatic repulsion between particles, thus, a value generally lower than −30 mV or higher than +30 mV for ζ-potential guarantees suspension stability [47].

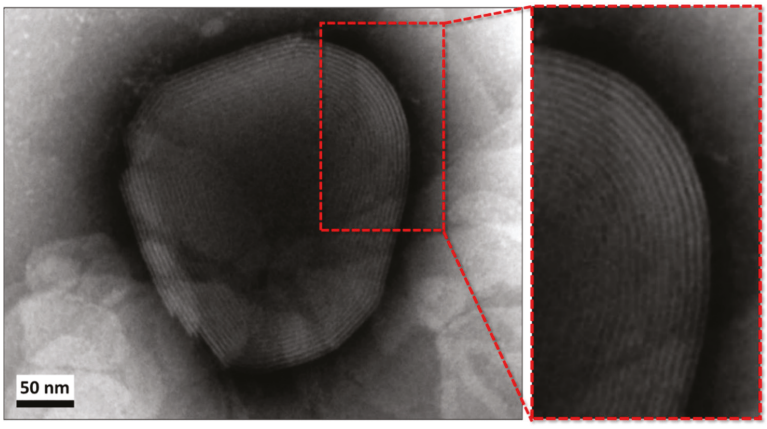

Figure 3. TEM images of the empty NVs. The inset highlights the obtained multilamellar structure.

3.3. Preparation and Characterization of NP-Loaded NVs

Cu@TDoAC showed the best colloidal stability and narrower size distribution, hence, it was chosen for the first NP inclusion test. On the other hand, Cu@BDHAC was selected—despite some partial aggregation occurring after a few days—because of its widely proven biocompatibility and antimicrobial properties [21], to exploit the synergistic effect with copper [44] when inserted in the NVs. The Cu@TDoAC- and Cu@BDHAC-loaded NVs were characterized and compared in order to further investigate a possible antibiofilm action exerted by the CuNPs combined with the disinfection properties of the quaternary ammonium compounds (part II). The preparation conditions for hybrid vesicles with Cu@TDoAC loading were optimized in test 3 (refer to Table 1). The characterization of this sample is reported in Figure 4 in regard to both TEM images and DLS analysis. The result was a dispersion of NVs with a wide size distribution in the 100–1000 nm diameter range, confirmed by both the characterization techniques. Some agglomeration also occurred, as an evident shift in the peaks' position was recorded during the three replicate DLS analyses. An adhesion of NPs limited to the surface of the NVs could be assumed, and/or some affinity between TDoAC and PC could lead to the agglomeration of hybrid systems [48].

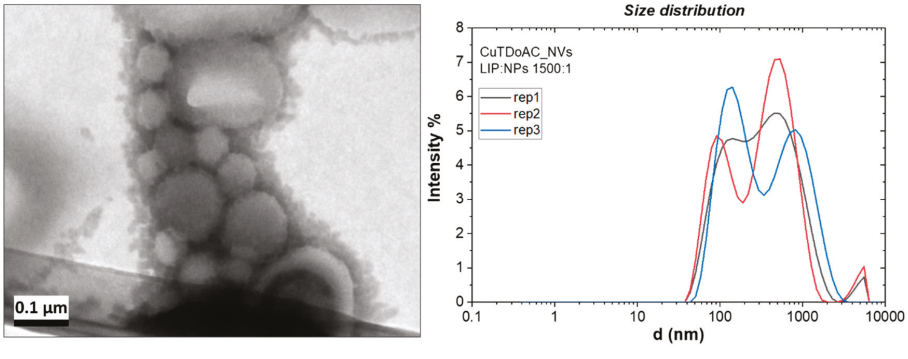

Figure 4. TEM image (**left**) and three dynamic light scattering (DLS) (**right**) replicate measurements of the Cu@TDoAC–NV hybrids prepared at optimized conditions: relative amount of lipid to nanoparticles(LIP:NPs) ratio 1500:1 *w*/*w*.

LDV analysis gave a ζ-potential value of 29 ± 2 mV for the Cu@TDoAC–NVs prepared with the highest Cu concentration (test 3), suggesting a positive charging of the sample due to the presence of copper NPs. Moreover, the ageing of the hybrids obtained in these conditions showed a broadening on the size distribution over time and a decrease in ζ-potential, whose value was measured after one week at 21 ± 4 mV.

The inclusion of the Cu@BDHAC colloid in lipid bilayers, tested in three different conditions (as stated in Table 1), was optimized by using colloids synthetized with THF as the sole solvent, which guarantees a uniform dispersion and controlled evaporation. Furthermore, the pressure control allowed a moderate evaporation speed, leading to a well-dried and transparent final film. This insured a more efficient hydration step and an NV dispersion in the sub-micron range with a narrow size distribution.

Figure 5 shows the TEM characterization of these hybrids, for which the formation of complex structures could be observed. NPs appeared to be assembled in clusters, only partially included in the NVs (Figure 5a,b). The presence of copper clusters in the range of 50–100 nm was confirmed by TEM analysis performed without negative staining (Figure 5c). This evidence could be explained by NP aggregation due to low stabilization of BDHAC and/or to a possible interaction of the surfactant with PC due to their similar molecular structure. Some works in the literature also suggest aggregation as a way for hybrids to minimize the strain in the bilayer caused by NP inclusion [49,50]. Moreover, from the DLS characterization (Figure 5d), two main peaks were observed centered at 91 nm and 712 nm. As the size of the empty NVs has been estimated to be in the micron range, it seems reasonable that the main DLS peak of the NP-loaded vesicles (712 nm) was probably attributable to the hybrids, while the peak at 91 nm could be ascribed to the free CuNP clusters.

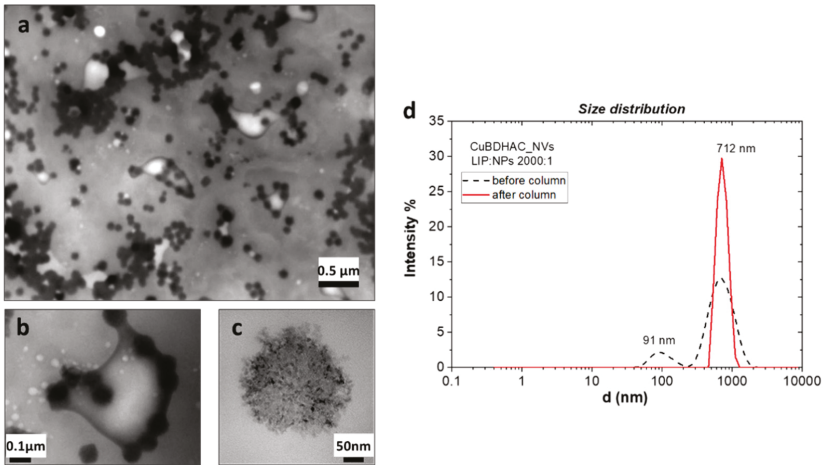

Figure 5. TEM image (**left**) and DLS (**right**) of the Cu@BDHAC–NV hybrids prepared at optimized conditions (LIP:NPs ratio 2000:1 *w*/*w*). Overview of complex structures (**a**) and zoom on a hybrid vesicle (**b**) and on one NP cluster (**c**). Size distribution recorded before and after sample filtration (**d**).

The filtration in the Sepharose-4B gel column was made to better understand if this peak assignment was confirmed and if an exclusion of cluster was possible. The red-full line in the graph (Figure 5d) refers to the DLS analysis after filtration. The purification excluded the smaller structures leading only higher sized vesicles to be selected. ζ-potential was evaluated for hybrids holding Cu@BDHAC colloids; a comparison between the empty and hybrid NVs is presented in Table 2. A more positive shift upon the increasing of the Cu colloid concentration loaded in the precursor solution was observed, as expected when introducing a positively charged species.

Table 2. Comparison of ζ-potential results obtained by laser Doppler velocimetry for the empty NVs and non-filtered hybrids with three increasing concentration of Cu@BDHAC.

SAMPLE	LIP:NPs (*w*/*w*)	ζ-Potential (mV)
NVs	–	−24 ± 5
Hybrid 1	2000:1	−11 ± 4
Hybrid 2	1200:1	5 ± 4
Hybrid 3	800:1	21 ± 6

Finally, colloidal stability of the empty NVs and hybrid suspension (Cu@BDHAC–NVs) was tested through the backscattering profile method acquired for non-filtered samples.

In Figure 6, the backscattering profiles are shown for the empty NVs and hybrid NVs with the highest concentration of the loaded Cu (test 3, corresponds to c.a. 72 μM for the used copper colloid).

The empty NVs (Figure 6a) presented a high peak at the bottom of the cell, indicating precipitation behavior after few hours of ageing, whereas hybrid nanocolloids did not exhibit precipitation. By comparing the backscattering profiles at different copper concentrations loaded into the hybrids (Figure 7), their suspension stability was confirmed. Indeed, small variation in backscattering values was observed along the cell, indicating a slight increase in the particle size with time. Nevertheless, the backscattering percentage after 6 days remains stable through the cell height, especially for a LIP:NPs ratio of 800:1. This means that an improved stability was obtained when increasing the copper loading.

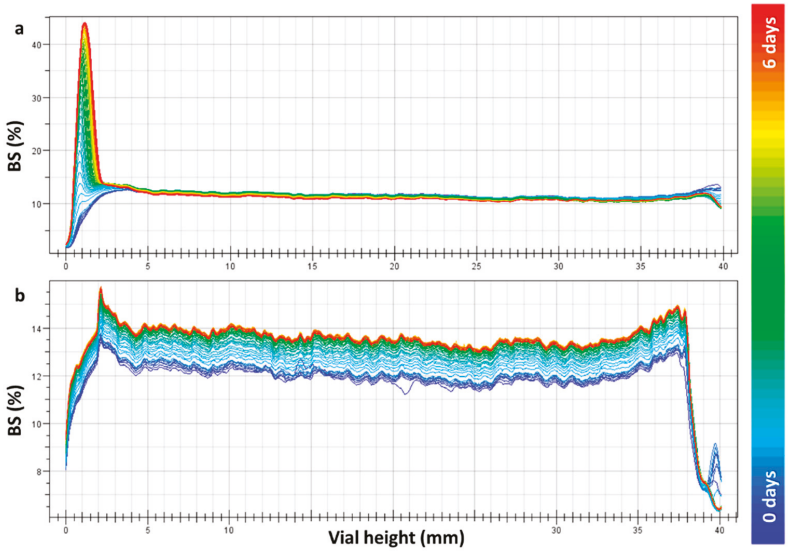

Figure 6. Backscattering profile vs. vials height acquired over 6 days. Signal comparison of the empty NVs (**a**) and Cu@BDHAC–NP-loaded NV hybrids (**b**) at a LIP:NPs ratio of 800:1 *w*/*w*.

The increasing colloidal stability observed for the highest CuNP loading could be related to major steric hindrance, as well as a sufficient charge-stabilizing effect induced by positively charged nanoparticles. Another major difference between the empty and hybrid NV is membranes fluidity. As the presence of NPs could increase fluidity, to avoid their subsequent escape, the presence of a membrane stabilizer is needed. The choice of cholesterol was essential, since it intercalates between lipid chains, balancing the increased volume of polar heads of membrane components [50,51]. The resulting

hybrid assembly show a promising stability, keeping its structure over ageing conditions without releasing NP clusters in the solution.

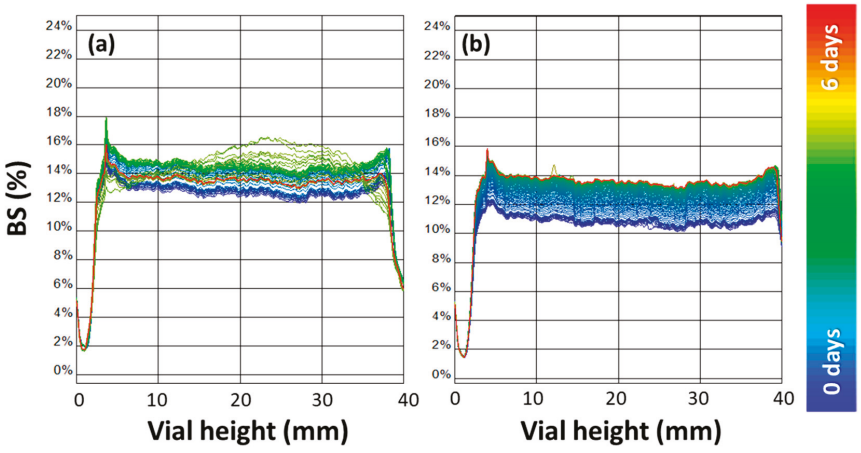

Figure 7. Backscattering profile (%) vs. vials height (mm) acquired over 6 days. Signal of the Cu@BDHAC–NP-loaded NV hybrids at a LIP:NPs ratio of 2000:1 *w/w* (**a**) and at a LIP:NPs ratio of 1200:1 *w/w* (**b**).

4. Conclusions

In the present work, the synthesis of hybrid systems based on electro-synthetized CuNPs was investigated. The largely known antibacterial properties of CuNPs and their application in materials and life science provided us the opportunity to work on new hybrid nanosystems with the aim of exploiting biochemical and physical properties of materials such as liposomes.

The inclusion of CuNPs stabilized by different quaternary ammonium compounds in vesicular systems made of phosphatidylcholine (PC) was demonstrated, indicating that the hydrophobic shell of the NP has a good affinity for vesicle bilayers.

Benzyl-dimethyl-hexadecyl-ammonium chloride (BDHAC) as a stabilizing surfactant of CuNPs was tested with the aim of developing a potentially synergistic antibacterial agent, combining in the same vesicle the effects of copper ions and BDHAC. A high affinity between this ammonium salt and PC was noticed, obtaining stable hybrid NVs 700–1000 nm in diameter. The stability of liposomes increased with NP loading with a maximum Cu concentration of 72 μM, suggesting a combined hindrance and charge-stabilization effect confirmed by dynamic light scattering, ζ-potential measurements and backscattering-monitored precipitation.

Preliminary experiments on antibiofilm efficacy were performed by testing our hybrid NPs against the proliferation of *Staphylococcus aureus* (Gram +), *Pseudomonas aeruginosa* (Gram −), and *Candida parapsilosis* (fungus). The inhibition effect was poor for the CuNP loading that we tested, therefore, further investigation will be carried out to assess the proper hybrid NV composition.

The application of the Cu-loaded nanosystems herein proposed is promising and will be investigated in bio-medical routes. The whole release of the NP cluster enclosed in the NVs could be avoided. Furthermore, these hybrid nanovesicles could provide a way to control the ionic release of copper through liposomes, which are already used for drug transport, and counteract the strong resistance of biofilms, subsequently leading to their destruction.

The application of our hybrid synergistic systems in the fight against antibiotic-resistant biofilms is envisaged, mostly in the cases where the use of vesicular systems might be beneficial when compared with the use of unprotected nanophases. While safety regulations are generally posing severe limits to

the use of ultrafine NPs [52], the same does not apply to NVs with sizes in the range of 100 to 1000 nm, like those of the present study.

Author Contributions: L.S.: investigation, data curation, writing—original draft preparation. P.G.-M.: investigation, data curation. G.G.: conceptualization, supervision, writing—review and editing. N.D.: visualization, supervision, writing—review and editing. N.C.: supervision, writing—review and editing, funding acquisition. M.M.: conceptualization, supervision, writing—original draft preparation. M.d.C.B.-L.: writing—review and editing, funding acquisition, project administration. All authors have read and agreed to the published version of the manuscript.

Funding: This research was funded by European Commission through European Union's Horizon 2020, Marie Skłodowska-Curie Innovative Training Networks (MSCA-ITN-ETN) under Grant number 813439-BREAK BIOFILMS. This research was also co-funded by Consejería de Educación y Ciencia del Principado de Asturias (Ref. IDI/2018/000185). L.S. acknowledges the financial support by the Global Thesis program from Università degli Studi di Bari Aldo Moro.

Conflicts of Interest: The authors declare no conflict of interest.

References

1. Smith, A.W. Biofilms and antibiotic therapy: Is there a role for combating bacterial resistance by the use of novel drug delivery systems? *Adv. Drug Deliv. Rev.* **2005**, *57*, 1539–1550. [CrossRef]
2. Hall-Stoodley, L.; Costerton, J.W.; Stoodley, P. Bacterial biofilms: From the natural environment to infectious diseases. *Nat. Rev. Microbiol.* **2004**, *2*, 95–108. [CrossRef]
3. Stoodley, P.; Sauer, K.; Davies, D.G.; Costerton, J.W. Biofilms as complex differentiated communities. *Annu. Rev. Microbiol.* **2002**, *56*, 187–209. [CrossRef]
4. Cioffi, N.; Torsi, L.; Ditaranto, N.; Tantillo, G.; Ghibelli, L.; Sabbatini, L.; Bleve-Zacheo, T.; D'Alessio, M.; Zambonin, P.G.; Traversa, E. Copper nanoparticle/polymer composites with antifungal and bacteriostatic properties. *Chem. Mater.* **2005**, *17*, 5255–5262. [CrossRef]
5. Sportelli, M.C.; Tütüncü, E.; Picca, R.A.; Valentini, M.; Valentini, A.; Kranz, C.; Mizaikoff, B.; Barth, H.; Cioffi, N.; Inhibiting, P. fluorescens biofilms with fluoropolymer-embedded silver nanoparticles: An in-situ spectroscopic study. *Sci. Rep.* **2017**, *7*, 1–13. [CrossRef]
6. Chari, N.; Felix, L.O.; Davoodbasha, M.A.; Sulaiman Ali, A.; Nooruddin, T. In vitro and in vivo antibiofilm effect of copper nanoparticles against aquaculture pathogens. *Biocatal. Agric. Biotechnol.* **2017**, *10*, 336–341. [CrossRef]
7. Galli, R.; Hall, M.C.; Breitenbach, E.R.; Colpani, G.L.; Zanetti, M.; de Mello, J.M.M.; Silva, L.L.; Fiori, M.A. Antibacterial polyethylene-ethylene vinyl acetate polymeric blend by incorporation of zinc oxide nanoparticles. *Polym. Test.* **2020**, *89*, 106554. [CrossRef]
8. Eltz, F.Z.; Vebber, M.C.; Aguzzoli, C.; Machado, G.; Da Silva Crespo, J.; Giovanela, M. Preparation, characterization and application of polymeric thin films containing silver and copper nanoparticles with bactericidal activity. *J. Environ. Chem. Eng.* **2020**, *8*, 103745. [CrossRef]
9. Khan, Z.; Al-Thabaiti, S.A. Biogenic silver nanoparticles: Green synthesis, encapsulation, thermal stability and antimicrobial activities. *J. Mol. Liq.* **2019**, *289*, 111102. [CrossRef]
10. Chen, H.; Wu, J.; Wu, M.; Jia, H. Preparation and antibacterial activities of copper nanoparticles encapsulated by carbon. *New Carbon Mater.* **2019**, *34*, 382–389. [CrossRef]
11. Brigger, I.; Dubernet, C.; Couvreur, P. Nanoparticles in cancer therapy and diagnosis. *Adv. Drug Deliv. Rev.* **2002**, *54*, 631–651. [CrossRef]
12. Tkachenko, A.G.; Xie, H.; Coleman, D.; Glomm, W.; Ryan, J.; Anderson, M.F.; Franzen, S.; Feldheim, D.L. Multifunctional gold nanoparticle-peptide complexes for nuclear targeting. *J. Am. Chem. Soc.* **2003**, *125*, 4700–4701. [CrossRef] [PubMed]
13. Beeton, M.L.; Aldrich-Wright, J.R.; Bolhuis, A. The antimicrobial and antibiofilm activities of copper(II) complexes. *J. Inorg. Biochem.* **2014**, *140*, 167–172. [CrossRef] [PubMed]
14. Seo, Y.; Hwang, J.; Lee, E.; Kim, Y.J.; Lee, K.; Park, C.; Choi, Y.; Jeon, H.; Choi, J. Engineering copper nanoparticles synthesized on the surface of carbon nanotubes for anti-microbial and anti-biofilm applications. *Nanoscale* **2018**, *10*, 15529–15544. [CrossRef]
15. Park, S.H.; Oh, S.G.; Mun, J.Y.; Han, S.S. Loading of gold nanoparticles inside the DPPC bilayers of liposome and their effects on membrane fluidities. *Colloids Surf. B Biointerfaces* **2006**, *48*, 112–118. [CrossRef]

16. Cioffi, N.; Torsi, L.; Ditaranto, N.; Sabbatini, L.; Zambonin, P.G.; Tantillo, G.; Ghibelli, L.; D'Alessio, M.; Bleve-Zacheo, T.; Traversa, E. Antifungal activity of polymer-based copper nanocomposite coatings. *Appl. Phys. Lett.* **2004**, *85*. [CrossRef]
17. Weir, E.; Lawlor, A.; Whelan, A.; Regan, F. The use of nanoparticles in anti-microbial materials and their characterization. *Analyst* **2008**, *133*, 835–845. [CrossRef]
18. Anyaogu, K.C.; Fedorov, A.V.; Neckers, D.C. Synthesis, characterization, and antifouling potential of functionalized copper nanoparticles. *Langmuir* **2008**, *24*, 4340–4346. [CrossRef]
19. Zare, Y.; Shabani, I. Polymer/metal nanocomposites for biomedical applications. *Mater. Sci. Eng. C* **2016**, *60*, 195–203. [CrossRef]
20. Sathiyavimal, S.; Vasantharaj, S.; Bharathi, D.; Saravanan, M.; Manikandan, E.; Kumar, S.S.; Pugazhendhi, A. Biogenesis of copper oxide nanoparticles (CuONPs) using Sida acuta and their incorporation over cotton fabrics to prevent the pathogenicity of Gram negative and Gram positive bacteria. *J. Photochem. Photobiol. B Biol.* **2018**, *188*, 126–134. [CrossRef]
21. Cioffi, N.; Ditaranto, N.; Torsi, L.; Picca, R.A.; De Giglio, E.; Sabbatini, L.; Novello, L.; Tantillo, G.; Bleve-Zacheo, T.; Zambonin, P.G. Synthesis, analytical characterization and bioactivity of Ag and Cu nanoparticles embedded in poly-vinyl-methyl-ketone films. *Anal. Bioanal. Chem.* **2005**, *382*, 1912–1918. [CrossRef] [PubMed]
22. Fuentes, S.; Alviña, R.; Zegarra, K.; Pérez, B.; Pozo, P. Antibacterial activities of copper nanoparticles in hybrid microspheres. *J. Nanosci. Nanotechnol.* **2019**, *19*, 4512–4519. [CrossRef] [PubMed]
23. Reetz, M.T.; Quaiser, S.A. A New method for the preparation of nanostructured metal clusters. *Angew. Chemie Int. Ed. English* **1995**, *34*, 2240–2241. [CrossRef]
24. Cioffi, N.; Ditaranto, N.; Sabbatini, L.; Torsi, L.; Zambonin, P.G. Nanomaterials for controlled metal release and process for their production. European Patent Application EP 2123797 B1, 12 August 2015.
25. Cioffi, N.; Ditaranto, N.; Sabbatini, L.; Tantillo, G.; Torsi, L.; Zambonin, P.G. Bioactive Metal Nanomaterials Stabilized by Bioactive Agents and Preparation Process. European Patent Application EP 2157211 B9, 2 March 2016.
26. Gilbert, P.; Moore, L.E. Cationic antiseptics: Diversity of action under a common epithet. *J. Appl. Microbiol.* **2005**, *99*, 703–715. [CrossRef]
27. Roy, R.; Tiwari, M.; Donelli, G.; Tiwari, V. Strategies for combating bacterial biofilms: A focus on anti-biofilm agents and their mechanisms of action. *Virulence* **2018**, *9*, 522–554. [CrossRef]
28. García-Manrique, P.; Matos, M.; Gutiérrez, G.; Estupiñán, O.R.; Blanco-López, M.C.; Pazos, C. Using factorial experimental design to prepare size-tuned nanovesicles. *Ind. Eng. Chem. Res.* **2016**, *55*, 9164–9175. [CrossRef]
29. Pando, D.; Gutiérrez, G.; Coca, J.; Pazos, C. Preparation and characterization of niosomes containing resveratrol. *J. Food Eng.* **2013**, *117*, 227–234. [CrossRef]
30. Liu, K.; Li, H.; Williams, G.R.; Wu, J.; Zhu, L.M. pH-responsive liposomes self-assembled from electrosprayed microparticles, and their drug release properties. *Colloids Surfaces A Physicochem. Eng. Asp.* **2018**, *537*, 20–27. [CrossRef]
31. Et-Thakafy, O.; Delorme, N.; Gaillard, C.; Mériadec, C.; Artzner, F.; Lopez, C.; Guyomarch, F. Mechanical properties of membranes composed of gel-phase or fluid-phase phospholipids probed on liposomes by atomic force spectroscopy. *Langmuir* **2017**, *33*, 5117–5126. [CrossRef]
32. Van Swaay, D.; Demello, A. Microfluidic methods for forming liposomes. *Lab Chip* **2013**, *13*, 752–767. [CrossRef]
33. Montefusco-Pereira, C.V.; Formicola, B.; Goes, A.; Re, F.; Marrano, C.A.; Mantegazza, F.; Carvalho-Wodarz, C.; Fuhrmann, G.; Caneva, E.; Nicotra, F.; et al. Coupling quaternary ammonium surfactants to the surface of liposomes improves both antibacterial efficacy and host cell biocompatibility. *Eur. J. Pharm. Biopharm.* **2020**, *149*, 12–20. [CrossRef] [PubMed]
34. Cui, H.; Li, W.; Li, C.; Vittayapadung, S.; Lin, L. Liposome containing cinnamon oil with antibacterial activity against methicillin-resistant Staphylococcus aureus biofilm. *Biofouling* **2016**, *32*, 215–225. [CrossRef]
35. Ardizzone, A.; Blasi, D.; Vona, D.; Rosspeintner, A.; Punzi, A.; Altamura, E.; Grimaldi, N.; Sala, S.; Vauthey, E.; Farinola, G.M.; et al. Highly stable and red-emitting nanovesicles incorporating lipophilic diketopyrrolopyrroles for cell imaging. *Chem. A Eur. J.* **2018**, *24*, 11386–11392. [CrossRef]
36. Pando, D.; Matos, M.; Gutiérrez, G.; Pazos, C. Formulation of resveratrol entrapped niosomes for topical use. *Colloids Surf. B Biointerfaces* **2015**, *128*, 398–404. [CrossRef] [PubMed]

37. Akbarzadeh, A.; Rezaei-Sadabady, R.; Davaran, S.; Joo, S.W.; Zarghami, N.; Hanifehpour, Y.; Samiei, M.; Kouhi, M.; Nejati-Koshki, K. Liposome: Classification, preparation, and applications. *Nanoscale Res. Lett.* **2013**, *8*, 102. [CrossRef]
38. Marchianò, V.; Matos, M.; Serrano-Pertierra, E.; Gutiérrez, G.; Blanco-López, M.C. Vesicles as antibiotic carrier: State of art. *Int. J. Pharm.* **2020**, *585*, 119478. [CrossRef] [PubMed]
39. Park, S.H.; Oh, S.G.; Mun, J.Y.; Han, S.S. Effects of silver nanoparticles on the fluidity of bilayer in phospholipid liposome. *Colloids Surf. B Biointerfaces* **2005**, *44*, 117–122. [CrossRef] [PubMed]
40. Eid, K.A.M.; Azzazy, H.M.E. Sustained broad-spectrum antibacterial effects of nanoliposomes loaded with silver nanoparticles. *Nanomedicine* **2014**, *9*, 1301–1310. [CrossRef]
41. Reetz, M.T.; Helbig, W. Size-selective synthesis of nanostructured transition metal clusters. *J. Am. Chem. Soc.* **1994**, *116*, 7401–7402. [CrossRef]
42. García-Manrique, P.; Machado, N.D.; Fernández, M.A.; Blanco-López, M.C.; Matos, M.; Gutiérrez, G. Effect of drug molecular weight on niosomes size and encapsulation efficiency. *Colloids Surf. B Biointerfaces* **2020**, *186*, 110711. [CrossRef]
43. Bothun, G.D. Hydrophobic silver nanoparticles trapped in lipid bilayers: Size distribution, bilayer phase behavior, and optical properties. *J. Nanobiotechnol.* **2008**, *6*, 1–10. [CrossRef]
44. Sportelli, M.C.; Longano, D.; Bonerba, E.; Tantillo, G.; Torsi, L.; Sabbatini, L.; Cioffi, N.; Ditaranto, N. Electrochemical preparation of synergistic nanoantimicrobials. *Molecules* **2020**, *25*, 49. [CrossRef]
45. Varona, S.; Martín, Á.; Cocero, M.J. Liposomal incorporation of lavandin essential oil by a thin-film hydration method and by particles from gas-saturated solutions. *Ind. Eng. Chem. Res.* **2011**, *50*, 2088–2097. [CrossRef]
46. Tsumoto, K.; Matsuo, H.; Tomita, M.; Yoshimura, T. Efficient formation of giant liposomes through the gentle hydration of phosphatidylcholine films doped with sugar. *Colloids Surf. B Biointerfaces* **2009**, *68*, 98–105. [CrossRef]
47. Becher, P. *Emulsions Theory and Practice*, 2nd ed.; Reinhold Publ. Corp. Chapman & Hall: New York, NY, USA, 1965.
48. Tischer, M.; Pradel, G.; Ohlsen, K.; Holzgrabe, U. Quaternary ammonium salts and their antimicrobial potential: Targets or nonspecific interactions? *ChemMedChem* **2012**, *7*, 22–31. [CrossRef]
49. Le Meins, J.F.; Schatz, C.; Lecommandoux, S.; Sandre, O. Hybrid polymer/lipid vesicles: State of the art and future perspectives. *Mater. Today* **2013**, *16*, 397–402. [CrossRef]
50. Schulz, M.; Olubummo, A.; Binder, W.H. Beyond the lipid-bilayer: Interaction of polymers and nanoparticles with membranes. *Soft Matter* **2012**, *8*, 4849–4864. [CrossRef]
51. Yang, S.-T.; Kreutzberger, A.J.B.; Lee, J.; Kiessling, V.; Tamm, L.K. The role of cholesterol in membrane fusion. *Chem. Phys. Lipids* **2016**, *199*, 136–143. [CrossRef]
52. Boros, B.V.; Ostafe, V. Evaluation of ecotoxicology assessment methods of nanomaterials and their effects. *Nanomaterials* **2020**, *10*, 610. [CrossRef]

nanomaterials

MDPI

Article

Influence of Polysaccharides' Molecular Structure on the Antibacterial Activity and Cytotoxicity of Green Synthesized Composites Based on Silver Nanoparticles and Carboxymethyl-Cellulose

María de los Ángeles Martínez-Rodríguez [1], Elizabeth Madla-Cruz [2], Victor H. Urrutia-Baca [3], Myriam A. de la Garza-Ramos [4], Virgilio A. González-González [1,5] and Marco A. Garza-Navarro [1,5,*]

1 Facultad de Ingeniería Mecánica y Eléctrica, Universidad Autónoma de Nuevo León, San Nicolás de los Garza 66455, Nuevo León, Mexico; angelesmttz@live.com.mx (M.A.M.-R.); virgilio.gonzalezgnz@uanl.edu.mx (V.A.G.-G.)

2 Facultad de Ciencias Biológicas, Laboratorio de Inmunología y Virología, Universidad Autónoma de Nuevo León, San Nicolás de los Garza 66455, Nuevo León, Mexico; elizabethmadla@hotmail.com

3 CHRISTUS—LATAM HUB Center of Excellence and Innovation, S.C. (CHRISTUS CEI), Monterrey 66260, Nuevo León, Mexico; vurrutia1990@gmail.com

4 Centro de Investigación y Desarrollo en Ciencias de la Salud, Universidad Autónoma de Nuevo León, Unidad de Odontología Integral y Especialidades, Monterrey 64460, Nuevo León, Mexico; myriam.garzarm@uanl.edu.mx

5 Centro de Innovación, Investigación y Desarrollo en Ingeniería y Tecnología, Universidad Autónoma de Nuevo León, Apodaca 66600, Nuevo León, Mexico

* Correspondence: marco.garzanr@uanl.edu.mx; Tel.: +52-(81)-8329-4000 (ext. 1641 or 1521)

Received: 13 May 2020; Accepted: 10 June 2020; Published: 14 June 2020

Abstract: In this paper we report on the influence of polysaccharides' molecular structure on the antibacterial activity and cytotoxicity of composites based on silver nanoparticles (AgNPs) immobilized into carboxymethyl-cellulose (CMC). These composites were green synthesized from the reduction of silver ions into aqueous solutions of the polysaccharide, using CMC with different degree of substitution (DS) and molecular weight (Mw). The composites were characterized by transmission electron microscopy (TEM), as well as infrared (ATR-FTIR), ultraviolet (UV-Vis), Raman, and X-ray photo-electron (XPS) spectroscopic techniques. The antibacterial activity was evaluated with minimum inhibitory concentration against *Enterococcus faecalis*. The cytotoxicity of composites was assessed against human gingival fibroblast. Experimental evidence suggests that particle size distribution and morphology of AgNPs change according to the quantity of silver precursor added to the reaction, as well as the DS and Mw of CMC used for composites preparation. This is related to the dispersion of silver precursor into aqueous solutions of the polysaccharide and the formation of Ag-O coordination bonds among AgNPs and COO^- moieties of CMC. Moreover, these coordination bonds modify the ability of nanoparticles to produce and release Ag^+ into aqueous dispersion, adjusting their antibacterial activity and the induction of cytotoxicity into the tested biological environments.

Keywords: silver nanoparticles; carboxymethyl-cellulose; composite; antibacterial activity; cytotoxicity

1. Introduction

In recent years, nanotechnology has impacted the development of new functional materials based on nanostructures. Among the so-called nanomaterials, silver nanoparticles (AgNPs) have emerged as

a promising specie to be used in biomedical and food packaging applications as a bactericide, fungicide, and antiviral [1–4]. There can be found studies regarding the effect of AgNPs on gram-negative bacteria, which indicate that nanoparticles with size between one and ten nanometers adhere to the surface of the bacteria cell membrane and disturb its permeability and respiration [5]. In addition, AgNPs dispersed into aqueous media can release Ag^+ ions that can be internalized by passive bacterial transport through the channels in the cell membrane of both Gram-negative and positive bacteria [6]. The Ag^+ ions inflict further damage to the bacteria due to its interaction with sulfur- and phosphorous-groups at the DNA, causing a loss in its ability to replicate; along with the deactivation of bacteria proteins, because of the interaction of Ag^+ ions with their thiol (R-SH) groups [7].

Nonetheless, the main concern about the use of AgNPs in biomedical and food packaging applications is their toxicity. It has been reported that AgNPs display a size-dependent cytotoxicity, related to the generation of reactive oxygen species (ROS) during their surface oxidation and subsequent release of Ag^+ ions into biological environments [8,9]. So, it is necessary to search for low-toxic AgNPs from methodologies that do not use nor produce toxic species. Accordingly, the "green" chemistry implies the design, development, and application of chemical products and process to reduce or eliminate the use or generation of hazardous substances to human health and the environment [10]. As has been reported in literature, the green chemistry routes for synthesis of AgNPs consider biopolymers such as chitosan, poly(lactic acid), sodium alginate, cellulose, and carboxymethyl-cellulose as both reducing and capping agents [11–16].

Among these biopolymers, the carboxymethyl-cellulose (CMC) emerges as a promising reducing and immobilization media for the green synthesis of AgNPs, due to its good chemical stability, as well as its biocompatible and biodegradable characteristics. The CMC is a semi-synthetic polysaccharide derived from the natural polymer cellulose, which undergoes the partial substitution of cellulose native hydroxymethyl (RCH_2OH) groups by carboxymethyl (RCOOH) groups [17]. The degree of substitution (DS) of RCH_2OH by RCOOH is reported as an average of carboxymethyl groups per monomer unit. The CMC is usually commercialized as a water-soluble sodium salt, which in aqueous solution can be loaded with metallic ions as Ag^+ by a simple displacement reaction of Na^+ [18]. Moreover, due to the abundant hydroxyl groups on its molecular structure, CMC has been successfully used as a reducing agent for the preparation of CMC-AgNPs composites [16,19]. From this approach is possible to get an outstanding particle size control and good efficiency over the silver ions reduction, without the use or generation of hazardous substances.

We previously reported on the ability of green synthesized CMC-AgNPs composites to inhibit the proliferation of Gram-positive and negative bacteria, such as *Streptococcus mutans* and *Porphyromonas gingivalis*, respectively, with a suitable cytotoxicity [20]. Nonetheless, currently, experimental evidence regarding the role of molecular structure of polysaccharides as CMC on the antibacterial activity and cytotoxicity of AgNPs-based composites does not exists. Consequently, in this work we report on the influence of polysaccharides' molecular structure on the antibacterial activity and cytotoxicity of CMC-AgNPs composites synthesized from a green chemistry route, by the use of CMC with different DS and molecular weight (Mw) as a reducing agent and immobilization media.

2. Materials and Methods

2.1. Synthesis and Characterization of CMC-AgNPs Composite

The CMC with DS = 0.7 and Mw = 90 kDa (0.7CMC), CMC with DS = 0.9 and Mw = 250 kDa (0.9CMC), CMC with DS = 1.2 and Mw = 250 kDa (1.2CMC) and silver nitrate ($AgNO_3$) were purchased from Sigma-Aldrich Co., Edo. de México, México, and used as received without any further treatment for the synthesis of CMC-AgNPs composites. Deionized water was used for the preparation of all solutions for this investigation (Barnstead EASYpure II system with ρ = 13 MΩ-cm).

The synthesis of CMC-AgNPs composites was performed following a previously reported route, with some modifications [19]. Briefly, aqueous CMC and $AgNO_3$ solutions were prepared at

concentrations of 15 mg/mL and 0.24, 0.48, 0.94, or 1.26 mg/mL, respectively, using deionized water. Then, 20 mL of CMC was added into a round-bottom three-neck flask (reactor) and stirred for 10 min under room conditions. Later, 10 mL of $AgNO_3$ solution was added to the reactor and the temperature was raised to 90 °C. The reaction was kept at this temperature for 24 h under reflux conditions. After 24 h, the resultant yellowish to reddish dispersions (depending on the concentration of $AgNO_3$ solution added to the reaction) was poured into a previously cooled round-bottom flask, in order to rapidly lower its temperature towards room temperature. These dispersions were frozen and then lyophilized. This process was performed using aqueous solutions of 0.7CMC, 0.9CMC, or 1.2CMC at a constant concentration of 15 mg/mL; as well as $AgNO_3$ solutions at the aforementioned concentrations of 0.24, 0.48, 0.94, or 1.26 mg/mL to obtain the composite samples 0.7/0.9/1.2Ag1, 0.7/0.9/1.2Ag2, 0.7/0.9/1.2Ag3, or 0.7/0.9/1.2Ag4, respectively. The Table 1 shows the CMC and $AgNO_3$ weights that were added to the reactor for the synthesis of each sample. Finally, dried samples were weighted and dissolved in deionized water to prepare CMC-AgNPs composites' dispersions for their further characterization.

Table 1. Reagents used for the synthesis of each composite sample.

Sample	$AgNO_3$ Weight (mg)	[$AgNO_3$] (mg/mL)	CMC Weight (mg)	[CMC] (mg/mL)	CMC/$AgNO_3$ Weight Ratio	CMC/Ag Weight Ratio
0.7Ag1	2.41	0.24	300	15.0	124.5	200.0
0.7Ag2	4.82	0.48	300	15.0	62.2	100.0
0.7Ag3	9.45	0.94	300	15.0	31.8	50.0
0.7Ag4	12.59	1.26	300	15.0	23.8	37.5
0.9Ag1	2.41	0.24	300	15.0	124.5	200.0
0.9Ag2	4.82	0.48	300	15.0	62.2	100.0
0.9Ag3	9.45	0.94	300	15.0	31.8	50.0
0.9Ag4	12.59	1.26	300	15.0	23.8	37.5
1.2Ag1	2.41	0.24	300	15.0	124.5	200.0
1.2Ag2	4.82	0.48	300	15.0	62.2	100.0
1.2Ag3	9.45	0.94	300	15.0	31.8	50.0
1.2Ag4	12.59	1.26	300	15.0	23.8	37.5

The crystalline and morphological features of CMC-AgNPs composites were examined by transmission electron microscopy (TEM) in a Field Emission Gun, FEI Titan G2 80-300 microscope, using electron microscopy techniques as bright field (BF) and Z-contrast (HAADF-STEM) imaging, as well as selected area electron diffraction (SAED). Particle size distribution of AgNPs was obtained from the measuring of at least 300 randomly selected particles in CMC-AgNPs samples using Graphic for Mac 3.1 software; and adjusting the experimental measuring data to the Gaussian statistic model in OriginPro 8.5.0 software, using tools as a descriptive statistic (frequency counts) and analysis (fitting). Ultraviolet-visible spectroscopy (UV-vis) studies of CMC-AgNPs composites as well as $AgNO_3$ precursor solution were performed in a Perkin-Elmer, Lambda 35, spectrometer to evaluate the reduction efficiency of the proposed synthesis route. Interactions between CMC molecules and AgNPs were examined using infrared spectroscopy (ATR-FTIR). ATR-FTIR spectra of pure 0.7CMC, 0.9CMC, 1.2CMC, as well as CMC-AgNPs samples were recorded in a Frontier MIR FT-IR, Universal ATR spectrometer. In addition, Raman spectroscopy was carried out in a Thermo Scientific, DXR Raman microscope. The spectra of selected composite samples were measured after 30 s of exposure and acquisition time of 60 s, using a radiation of 532 nm. Finally, X-Ray Photoelectron Spectroscopy (XPS) was perform for the measuring of C1s, O1s, and Ag3d spectra for pure 0.7CMC, 0.9CMC, and 1.2CMC, as well as for selected CMC-AgNPs samples in a Thermo-Scientific, K-Alpha spectrometer with monochromatized AlKα radiation (E = 1.5 keV), X-ray spot of 400 μm, and flood gun for charge compensation.

2.2. Antibacterial Assay

The antibacterial activity of CMC-AgNPs composites was examined using the standard broth dilution method. The minimal inhibitory concentration (MIC) was determined from 96-well flat-bottom plates containing 50 μL of CMC-AgNPs dilutions with concentrations [AgNPs] = 60 to 3.75 μg/mL in Brain Heart Infusion (BHI) medium (Becton Dickinson Bioxon, Edo. de México, México); and 50 μL of 1.0×10^8 CFU/mL of *Enterococcus faecalis* (ATCC® 29212™) (*E. faecalis*), up to a final volume of 100 μL per well. In addition, ampicillin at 5 μg/mL was used as a positive control for inhibition of bacterial growth; whereas BHI medium was employed as negative control. The prepared cultures were incubated at 37 °C for 24 h in an aerobic atmosphere. Bacterial growth was measured from the absorbance of the cultures at 595 nm using an iMark™ microplate reader (Bio-Rad laboratories, Hercules, CA, USA). Subsequently, the percentage of growth inhibition was calculated using:

$$\% \, inhibition = 100 - \left\{ \left[\frac{(Sample - Positive\ control)}{(Negative\ control - Positive\ control)} \right] \times 100 \right\} \quad (1)$$

The MIC value was defined as the lowest concentration of CMC-AgNPs that inhibited 99% of growth bacterial.

2.3. Cytotoxicity Assay

The cytotoxicity of CMC-AgNPs composites was evaluated against human gingival fibroblast cells (ATCC®PCS-201-018™), from 3-(4, 5-dimethylthiazol-2-yl)-2, 5-diphenyl tetrazolium (MTT) assay. The cell line was cultured in Dulbecco's modified Eagle's medium (DMEM), supplemented with 10% FBS, 1X antibiotic-antimycotic, and 6 mM L-glutamine (complete-DMEM) at 37 °C for 48 h in a humidified atmosphere of 5% CO_2. Later, 100 μL of complete-DMEM containing 5×10^4 cells were placed into each well of a flat-bottom 96-well plate and grown to approximately 90% confluence. Then, 100 μL of CMC-AgNPs dilutions at [AgNPs] = 60 to 3.75 μg/mL were added to each well and incubated for 24 h. Complete-DMEM and 2% Triton X-100 were used as negative and positive control, respectively. After incubation, supernatant was discarded, and the cells were carefully washed with PBS. Later, 100 μL of MTT diluted in complete-DMEM at 0.5 mg/mL were added to the wells and the cultures were incubated for 4 h. Subsequently, the supernatant was discarded, and the resulting formazan crystals were solubilized with 200 μL dimethyl sulfoxide. Finally, the absorbance of the cultures was recorded at 570 nm using a microplate reader. The percentage of cytotoxicity was calculated using:

$$\% \, cytotoxicity = 100 - \left\{ \left[\frac{(Sample - Positive\ control)}{(Negative\ control - Positive\ control)} \right] \times 100 \right\} \quad (2)$$

3. Results and Discussion

3.1. Morphological and Crystalline Features of CMC-AgNPs Composites

Figure 1 shows HAADF-STEM images taken from CMC-AgNPs composites that were synthesized using 0.7CMC as a reducing and immobilization agent. As Figure 1a displays, nanoparticles in sample 0.7Ag1 show a quasi-spherical morphology. There is also presented the adjustment of experimental data from particle size measuring to the Gaussian statistic model. The center of particle size distribution is 13.1 nm, showing a standard deviation of 5.3 nm. Nonetheless, the statistical distributions obtained for samples 0.7Ag2 and 0.7Ag3 depict centers at a larger particle size of 26 and 24.6 nm, respectively; as well as wider dispersions, with standard deviations of 17.7 and 17.0 nm, respectively (see Figure 1b,c). In addition, the nanoparticles in samples 0.7Ag2 and 0.7Ag3 show a change on their morphology from quasi-spherical to one that displays facets. The presence of faceted nanoparticles is also observed in sample 0.7Ag4, along with a large population of small nanoparticles with a mean size of 10.6 nm and standard deviation of 5.1 nm (see Figure 1d). The change in particle size distribution and morphology

of nanoparticles could be related to a decrease in the ability of CMC to control their growth as the weight content of $AgNO_3$ is increased (see Table 1).

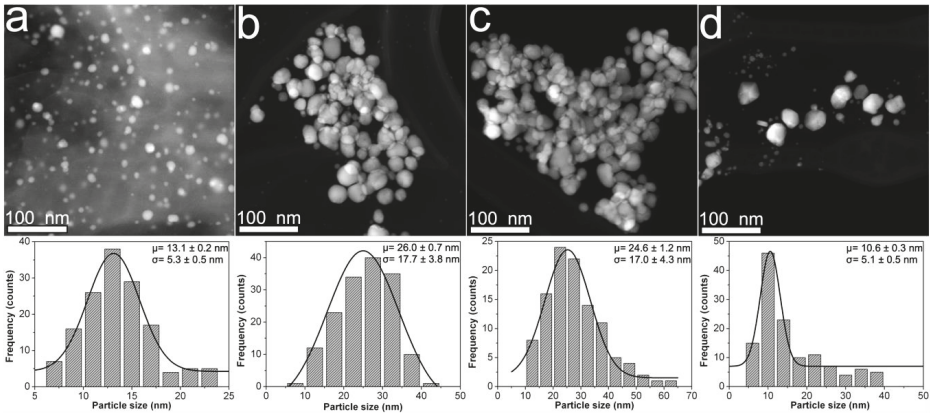

Figure 1. HAADF-STEM images obtained from composites samples: (**a**) 0.7Ag1; (**b**) 0.7Ag2; (**c**) 0.7Ag3; and (**d**) 0.7Ag4. The particle size distribution of each sample is shown just below its HAADF-STEM image.

The Figure 2 displays the morphological features of CMC-AgNPs samples that were obtained from 0.9CMC aqueous solutions. Herein we observed that mean particle size shows a small decrease from 32.6 to 28.3 nm as the weight content of $AgNO_3$ used for the synthesis of 0.9Ag1, 0.9Ag2, and 0.9Ag3 increases (see Table 1); as well as an increase in the standard deviation from 8.9 to 16.4 nm (see Figure 2a–c). Moreover, the nanoparticles in sample 0.9Ag4 display a remarkable increase in both mean particle size (44.1 nm) and standard deviation (28.8 nm) (see Figure 2d). The formation of aggregates from faceted nanoparticles in 0.9Ag4 is also noticeable. According to these results, the 0.7CMC reagent gives smaller mean particle size but larger standard deviation than 0.9CMC reagent when 2.41, 4.82, or 9.45 mg of $AgNO_3$ are used for the synthesis of samples.

Figure 3 shows the morphological characteristics for samples prepared with 1.2CMC reagent. For this case, the mean particle size tends to increase from 11 to 22.3 nm for samples 1.2Ag1, 1.2Ag2, and 1.2Ag3 (see Figure 3a–c) as the weight content of $AgNO_3$ increases (see Table 1). Nonetheless, this trend is not followed by 1.2Ag4, since it displays a mean particle size of 19.1 nm (see Figure 3d). The presence of nanoparticle aggregates that resemble those observed in the 0.9Ag4 sample is also seen in Figure 3d. Finally, the standard deviation for this experimental set varies in a direct proportion with the weight of $AgNO_3$ added for the synthesis of samples 1.2Ag1, 1.2Ag2, 1.2Ag3, and 1.2Ag4; and covers an interval from 4 to 14.8 nm. This evidence suggests that 1.2CMC reagent provides better control on particle size distribution than 0.7CMC and 0.9CMC reagents at the CMC/$AgNO_3$ weight ratios used for sample preparation (see Table 1). Table 2 reports the data from particle size distribution that were obtained for the synthesized composite samples.

Figure 4 resumes the crystalline features that were observed for nanoparticles prepared from aqueous solutions of 0.7CMC, 0.9CMC, and 1.2CMC. As Figure 4a,c,e display, the nanoparticles from samples 0.7Ag1, 0.9Ag1, and 1.2Ag1, respectively, depict a regular atomic arrangement, showing lattice fringes with a regular interplanar spacing of 2.4 Å. This spacing is congruent with that reported for family planes {111} of the crystalline structure of silver (see JCPDS: 04-0783). Furthermore, in the SAED patterns reported in Figure 4b,d,f we recognize diffraction rings related to family planes {111}, {200}, {220}, and {311} of the face-centered cubic (FCC) packing of silver (see JCPDS: 04-0783). This evidence confirms the formation of AgNPs in the synthesized samples.

However, in order to obtain a first approach regarding the reduction efficiency of Ag^+ from our synthesis route, we record UV-vis spectra for CMC-AgNPs composites and $AgNO_3$ solution used for their synthesis. As it can be observed in Figure 5, the spectra obtained from CMC-AgNPs composites do not show the absorption band related to the Ag^+ at 301 nm (see Figure 5a); instead, they display a well-defined band around 425–429 nm (see Figure 5b–d). According to the literature, this band is related to the characteristic surface plasmon resonance of AgNPs [21]. This result indicates that there are no detectable traces related to Ag^+ ions in the analyzed samples, suggesting full reduction of added Ag^+ into Ag^0. Accordingly, the CMC/AgNPs weight ratio could be calculated as 200, 100, 50, and 37.5 for the composites 0.7/0.9/1.2Ag1, 0.7/0.9/1.2Ag2, 0.7/0.9/1.2Ag3, and 0.7/0.9/1.2Ag4, respectively (see Table 1). Nonetheless, to get more information about the immobilization features of the different kind of CMC, it is necessary to evaluate the manner that the polysaccharide's chains interacts with the synthesized AgNPs. Consequently, we proceed to perform ATR-FTIR measures of CMC reagents and CMC-AgNPs samples.

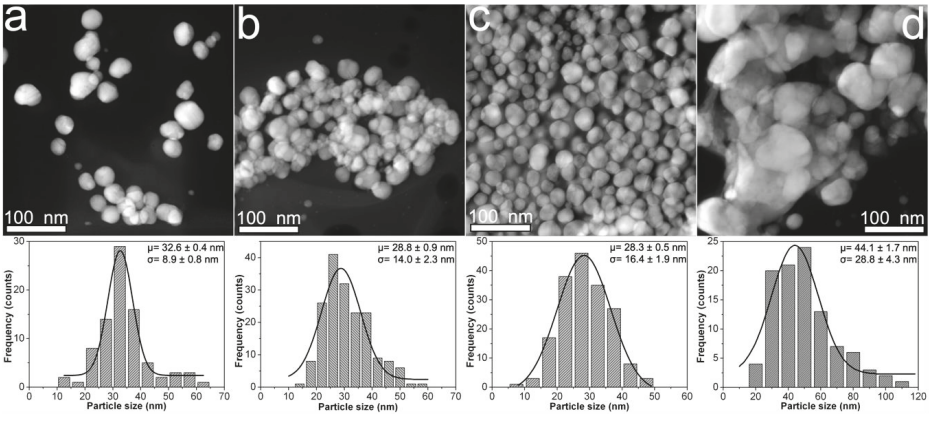

Figure 2. HAADF-STEM images obtained from composites samples: (**a**) 0.9Ag1; (**b**) 0.9Ag2; (**c**) 0.9Ag3; and (**d**) 0.9Ag4. The particle size distribution of each sample is shown just below its HAADF-STEM image.

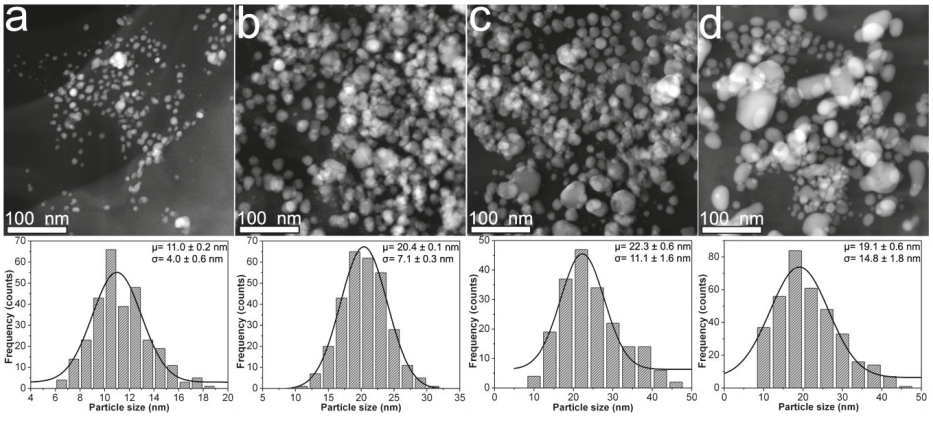

Figure 3. HAADF-STEM images obtained from composites samples: (**a**) 1.2Ag1; (**b**) 1.2Ag2; (**c**) 1.2Ag3; and (**d**) 1.2Ag4. The particle size distribution of each sample is shown just below its HAADF-STEM image.

Table 2. Data from particle size distribution obtained for composite samples.

Sample	Mean Particle Size (nm)	Standard Deviation (nm)
0.7Ag1	13.1	5.3
0.7Ag2	26.0	17.7
0.7Ag3	24.6	17.0
0.7 Ag4	10.6	5.1
0.9Ag1	32.6	8.9
0.9Ag2	28.8	14.0
0.9Ag3	28.3	16.4
0.9Ag4	44.1	28.8
1.2Ag1	11.0	4.0
1.2Ag2	20.4	7.1
1.2Ag3	22.3	11.1
1.2 Ag4	19.1	14.8

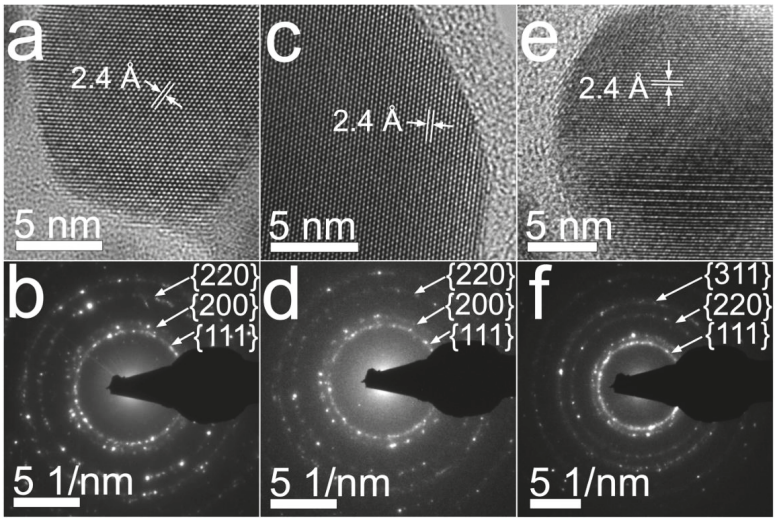

Figure 4. BF images and SAED patterns obtained from samples: (**a**) and (**b**) 0.7Ag1; (**c**) and (**d**) 0.9Ag1; (**e**) and (**f**) 1.2Ag1.

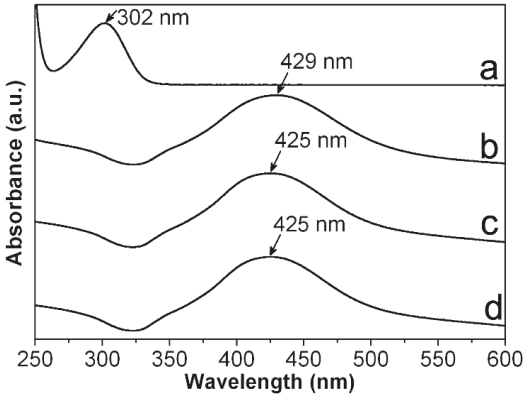

Figure 5. UV-vis spectra measured from (**a**) $AgNO_3$; (**b**) 0.7Ag4; (**c**) 0.9Ag4; and (**d**) 1.2Ag4.

3.2. Spectroscopic Characterization

Figure 6 shows the ATR-FTIR spectra obtained from powdered 0.7CMC, 0.9CMC, and 1.2CMC reagents, as well as those recorded from powdered CMC-AgNPs samples. Figure 6a displays the spectrum obtained for 0.7CMC, where it can recognize absorption bands related to [18,22,23]: symmetrical and asymmetrical stretching at O-H bond of hydroxyl groups (R-OH) at 3360 cm^{-1}; asymmetrical stretching at the C-H bond of the hydroxymethyl functional groups (R-CH_2OH) at 2911 cm^{-1}; asymmetrical and symmetrical stretching of -O-C = O bonds on the carboxymethyl functional groups (R-CH_2OCOO^-) at 1590 cm^{-1} and 1413 cm^{-1}, respectively; bending of -C-CH and O-CH- bonds on the R-CH_2OCOO^- groups at 1321 cm^{-1}; stretching of C-O bond on R-CH_2OCOO^- at 1269 and 1026 cm^{-1}; and stretching of C-O-C bonds on R-CH_2OCOO^- at 1099 and 1043 cm^{-1}. Figure 6a also shows the spectra recorded from samples 0.7Ag1, 0.7Ag2, 0.7Ag3, and 0.7Ag4. Herein we noticed a slight bathochromic shift in the position of the band related to asymmetrical stretching of O-C = O moieties at R-CH_2OCOO^-, from 1590 to 1586 cm^{-1}; along with a hypsochromic one from 1043 to 1053 cm^{-1} of the band associated to stretching on C-O-C bonds at the same functional groups.

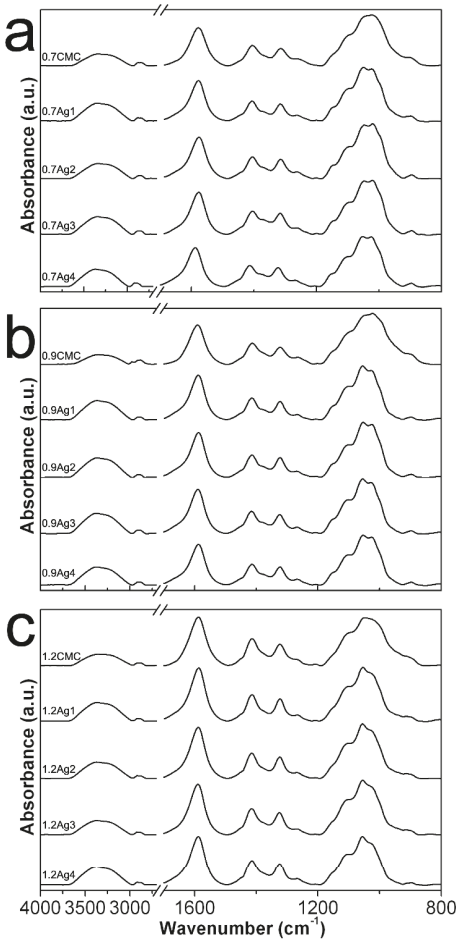

Figure 6. ATR-FTIR spectra obtained from (**a**) pure 0.7CMC and its composite samples; (**b**) pure 0.9CMC and its composite samples; (**c**) pure 1.2CMC and its composite samples.

In addition, Figure 6b depicts the spectrum obtained from powdered 0.9CMC, as well as those from composites 0.9Ag1, 0.9Ag2, 0.9Ag3, and 0.9Ag4. Likewise, bands related to vibrational modes of 0.9CMC molecules can be noticed, as the asymmetrical stretching of -O-C = O moieties at 1590 cm^{-1} and stretching of C-O-C bonds at 1044 cm^{-1}, which display bathochromic and hypsochromic shifts towards 1587 cm^{-1} and 1050 cm^{-1}, respectively, in the composites spectra. Moreover, this phenomenon also occurs for the samples 1.2Ag1, 1.2Ag2, 1.2Ag3, and 1.2 Ag4, since they display a noticeable shift on the band related to the stretching of C-O-C, from 1049 to 1055 cm^{-1}, with respect the position of this band in the spectrum recorded for 1.2CMC (see Figure 6c). These features suggest an interaction between CMC molecules and AgNPs for all the samples, which could be attributed to the adsorption of R-CH_2OCOO^- onto nanoparticles, as it has been reported elsewhere [24–26].

In order to corroborate the adsorption of CMC chains onto AgNPs, we record Raman spectra from selected powdered samples. Figure 7 shows the Raman spectra obtained from 0.7Ag1, 0.7 Ag4, 1.2Ag1, and 1.2Ag2. Here it is possible to identify bands associated with vibrational modes of CMC, such as stretching of C-H at 2916–2909 cm^{-1}; as well as asymmetrical and symmetrical stretching of O-C = O at 1588–1577 cm^{-1} and 1384–1376 cm^{-1}, respectively [25–28]. An increase in the intensity of Raman scattering in the bands attributed to stretching vibration in O-C = O can also be noticed, which seems to be related with the increase in the weight content of AgNPs in samples. The increase in intensity of both bands was evaluated taking as reference the intensity of the band attributed to C-H stretching vibration. As it has been documented in literature, the increase in the intensity of these bands can be related to the adsorption of COO^- moieties onto metal or semimetal nanoparticles; and occurs due to electric field induced surface enhanced Raman scattering (SERS) [29]. Moreover, there can be found a band at 234–228 cm^{-1}, attributed to the stretching vibration of Ag-O bond [30,31]. These results confirm the adsorption of CMC chains onto AgNPs and suggest the formation of a bond between Ag and O in the COO^- moieties of CMC, as it has been proposed elsewhere [30].

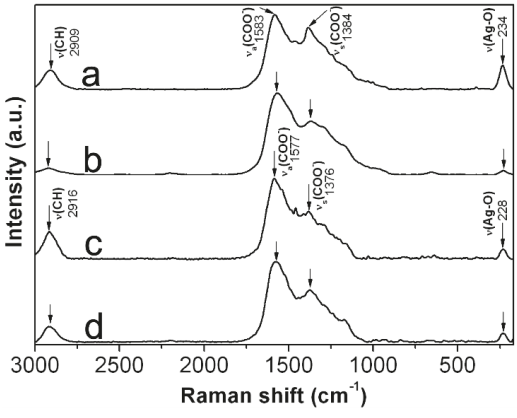

Figure 7. Raman spectra recorded from: (**a**) 0.7Ag1; (**b**) 0.7Ag4; (**c**) 1.2Ag1; and (**d**) 1.2Ag2.

In order to get further insight regarding the adsorption of RCH_2OCOO^- onto AgNPs surface, we proceed to measure C1s, O1s, and Ag3d XPS spectra from 0.7CMC, 0.9CMC, 1.2CMC reagents, as well as from some powdered samples. Peaks of the recorded XPS spectra were deconvoluted and fitted using a Gaussian approach in PeakFitV4.12 software. Accordingly, Figure 8a shows C1s and O1s spectra recorded from 0.7CMC. The C1s spectrum exhibits four peaks at 285.2, 287.0, 288.6, and 290.1 eV, which can be attributed to C in C-C, C-O, C = O, and O-C = O, respectively. Three peaks are observed in O1s spectrum that can be attributed to C = O, O-C = O and Auger electrons from Na at 531.5, 533.4, and 535.7 eV, respectively. Likewise, C1s spectra recorded from 0.9CMC and 1.2CMC were deconvoluted into four peaks at 285.0 eV (C-C), 286.7 eV (C-O), 288.2 eV (C = O), and 289.6 or

288.8 eV (O-C = O); whereas their O1s spectra show peaks at 531.4 eV (C = O), 533.1 eV (O-C = O), and 535.6 eV (Auger-Na) (see Figure 8b,c). The presence of these signals agrees with those expected from the molecular structure of these polysaccharides [32,33].

Figure 9 show C1s, O1s, and Ag3d spectra from samples 0.7Ag1, 0.9Ag1, and 1.2Ag1. C1s spectra of samples show peaks related to C-C, C-O, C = O, and O-C = O of the polysaccharide's chains, although they display changes in their binding energies with respect to that obtained from CMC reagents (see Figure 8); along with a change in the intensity of each peak (quantity of photoelectrons emitted from samples). Changes in binding energy occur into an interval from 0.2 to 0.9 eV, and are more obvious for emissions associated with C = O and O-C = O. In addition, O1s spectra show shifts in the binding energies related to emissions from C = O and O-C = O, into an interval between 0.4 and 0.9 eV. There is also observed Ag3d spectra of these samples that display peaks at 374.2–374.7 eV and 368.0–368.7 eV, which correspond to photoelectrons emitted from $3d_{3/2}$ and $3d_{5/2}$ states, respectively. The difference between the binding energies of such emissions is 6 eV for all cases, confirming that silver in samples is only Ag^0 [34–36]. Moreover, this experimental evidence is congruent with that obtained from UV-vis spectra regarding the full reduction of Ag^+ into Ag^0 (see Figure 5).

Likewise, Figure 10 shows the XPS spectra recorded from samples 0.7Ag2, 0.9Ag2, and 1.2Ag2. Herein, C1s and O1s spectra depict shifts in the binding energies related to C and O in C = O and O-C = O bonds that reach up 0.9 eV, with respect to those observed in Figure 8; as well as peaks around 374 and 368 eV in their Ag3d spectra, related to core emissions from $3d_{3/2}$ and $3d_{5/2}$, respectively. Thus, considering that the energy of photoelectrons emitted from discrete states as 1s is quite susceptible to change depending on the bonds that elements form, the fact that peaks related to C-C, C-O, O-C = O, and C = O display shifts on their binding energies indicates that AgNPs are immobilized in CMC by coordination bonds [36,37]. Moreover, taking into account the results obtained from Raman spectra, the coordination bonds can be attributed to those Ag-O among AgNPs and COO^- moieties of CMC.

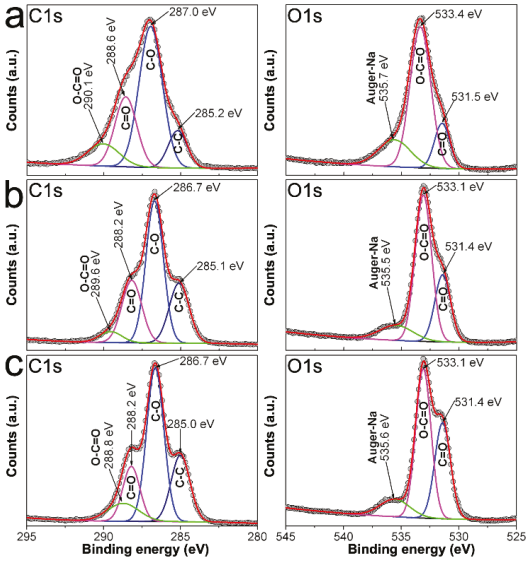

Figure 8. C1s and O1s spectra recorded by XPS from: (**a**) 0.7CMC; (**b**) 0.9CMC; and (**c**) 1.2CMC.

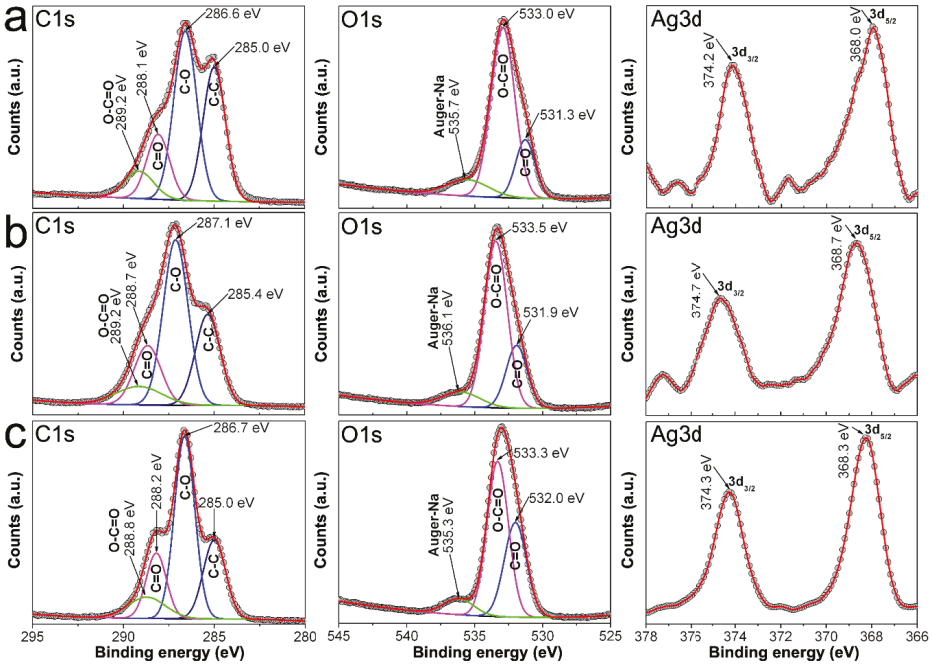

Figure 9. C1s and O1s spectra recorded by XPS from: (**a**) 0.7Ag1; (**b**) 0.9Ag1; and (**c**) 1.2Ag1.

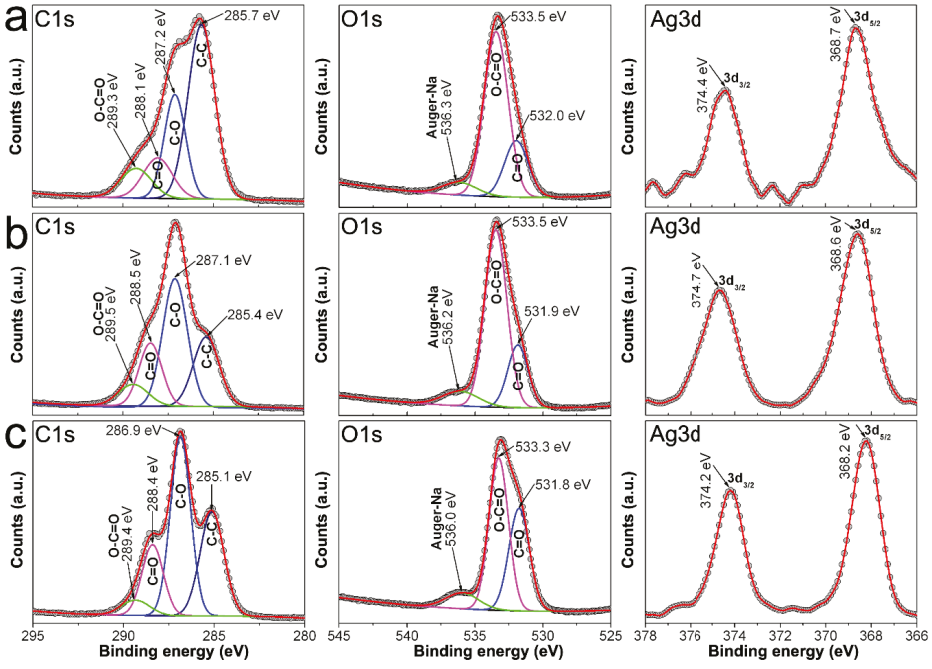

Figure 10. C1s, O1s and Ag3d spectra recorded by XPS from samples: (**a**) 0.7Ag2; (**b**) 0.9Ag2; and (**c**) 1.2Ag2.

Considering our experimental findings, the variation of the morphological features of AgNPs can be explained as follows. The CMC is capable of attracting Ag^+ ions to intermolecular sites nearby the negatively charged R-CH_2OCOO^- when both are diluted in aqueous media [18]. In these sites, the Ag^+ ions are reduced with the electrons realized from R–OH or R–CH_2OH groups of CMC at high temperature (i.e., 90 °C). Accordingly, the coalescence of Ag^0 conduces to the nucleation and subsequent growth of AgNPs, which will depend on the quantity of silver reagent added to the solution [19]. Hence, it is possible to state that when a CMC with a given DS and Mw is used for the synthesis of AgNPs, their particle size could increase as the weight content of $AgNO_3$ added to the reaction increases. This could explain the particle size distributions (mean size and standard deviation) obtained from almost the samples prepared from 0.9CMC and 1.2CMC aqueous solutions (see Figures 2 and 3). In addition, we observe that samples prepared with the same weight content of $AgNO_3$ but different CMC reagent display variations in their particle size distribution and morphology. According to our experimental evidence, the AgNPs are susceptible to form coordination bonds with COO^- moieties. Therefore, the particle size distribution and morphology of AgNPs will depend on the quantity of R-CH_2OCOO^- available for their immobilization. The quantity of R-CH_2OCOO^- available to restrict the size of AgNPs and avoid their secondary growth varies according to the DS of 0.9CMC and 1.2CMC (see Table 2).

This explanation seems to disagree with the morphological features of samples obtained from 0.7CMC aqueous solutions, since their particle size distributions (mean size and standard deviation) do not change in direct proportion with the weight of $AgNO_3$ added to each reaction; and they display smaller mean particle size than samples prepared with 0.9CMC reagent at the same weight content of $AgNO_3$ (see Table 2). In order to explain this phenomenon, we should consider the following. As Table 1 shows, all CMC aqueous solutions were prepared at the same concentration for the synthesis of samples. However, the 0.7CMC reagent has a lower Mw than 0.9CMC and 1.2CMC. It is well known that viscosity of a polymer solution varies in a direct proportion with its Mw at a given concentration. So, it is reasonable to think that, at the same weight content of $AgNO_3$, the dispersion of Ag^+ ions in 0.7CMC aqueous medium differs from that in 0.9CMC or 1.2CMC solutions. Moreover, considering the low DS of 0.7CMC, it is possible that some Ag^+ ions do not reach a site nearby the R-CH_2OCOO^- groups; hence, they could be reduced elsewhere. This implies that the coalescence of Ag^0, nucleation and subsequent growth of AgNPs also occur far from the R-CH_2OCOO^- groups. This could explain the high standard deviation obtained from samples 0.7Ag2 and 0.7Ag3, as well as the formation of large and faceted nanoparticles in sample 0.7Ag4 (see Figure 1). Nonetheless, the AgNPs are immobilized in CMC by coordination bonds, thus, it is possible to argue that these Ag-O bonds among AgNPs and COO^- moieties restrict the growth for a large number of nanoparticles when 0.7CMC reagent is used for preparation of composite samples (see Figure 1). This could explain the small mean particle size obtained at low weight content of $AgNO_3$ added for the preparation of 0.7Ag1 (see Table 2).

Therefore, it can be concluded that the key factor for the control of particle size distribution of synthesized AgNPs is the quantity of R-CH_2OCOO^- available for their immobilization. The quantity of these groups varies in direct proportion with the DS of CMC, which in general gives smaller particle sizes for CMC with higher DS. It is worth mentioning that the observed trends regarding the changes on standard deviation and morphology of AgNPs, as well as their plausible explanations, should be confirmed in further studies.

3.3. Antibacterial Activity

As we explain in Section 3.2, particle size distribution and morphology of the AgNPs mainly vary according to the DS of CMC used for their synthesis. This is related to the fact that nanoparticles are immobilized in CMC by the formation of Ag-O coordination bonds among AgNPs and COO^- moieties of the polysaccharide's chains. Thus, in order to address the effect of these bonds on the antibacterial activity of AgNPs, we proceed to test samples with similar particle size distributions but with nanoparticles immobilized into CMC with distinct DS, 0.7Ag1 and 1.2Ag1; along with the sample

0.9Ag4, which displays a different particle size distribution for nanoparticles immobilized into CMC with close DS to 1.2CMC. The antibacterial activity assays were performed by three replicates of three independent experiments using doses with a known concentration of AgNPs, [AgNPs]. As Figure 11 shows, an important antibacterial activity of CMC-AgNPs composites was observed at [AgNPs] = 60 μg/mL for the three tested samples. At this dose no statistical difference was observed compared to 5 μg/mL ampicillin ($p > 0.05$) for 0.9Ag4 and 1.2Ag1 samples. Therefore, [AgNPs] = 60 μg/mL can be established as the MIC value for our experimental setup, except for 0.7Ag1 sample. The sample 0.7Ag1 shows an inhibitory effect of 85.5 ± 2.3% at this dose. In addition, a residual inhibitory effect was observed at [AgNPs] = 30 μg/mL in 0.7Ag1, 0.9Ag4, and 1.2Ag1 with 26.3 ± 2.9%, 36.9 ± 5.7%, and 41.4 ± 8.3%, respectively (see Figure 11).

These results can be explained as follows. The antibacterial activity of AgNPs is believed to be related to the production and release of positive charged Ag ions from their surface in aqueous media [6]. Thus, smaller particle size leads to a large surface area, hence, to produce a higher amount of Ag^+ in aqueous solution than larger AgNPs [38]. The Ag^+ ions can be internalized by passive bacterial transport through the channels in the cell membrane bacteria and inflict damage due to their binding to cellular structural elements such as enzymes and proteins, particularly to their R-SH groups [6,7]. This binding diminishes the membrane permeability and leads to cell death [39]. Specifically, MIC value against gram-positive *E. faecalis* bacteria has been found in an interval between 500 and 0.19 μg/mL, depending on synthesis route, particle size, and surface modification [39–42]. Accordingly, the Ag-O coordination bonds among AgNPs and COO^- moieties of CMC do not blur the ability of nanoparticles to produce and release Ag^+ from their surface, thus, to display a remarkable antibacterial activity in aqueous media.

Moreover, it can be noticed that AgNPs with quite different particle size distribution but immobilized in CMC with close DS, as is the case for 0.9Ag4 and 1.2Ag1, display almost the same inhibition of bacteria growth (see Figure 11). This suggests that Ag-O coordination bonds among AgNPs and COO^- moieties of these polysaccharides enhance the antibacterial activity for CMC-AgNPs composites. This feature is congruent with the antibacterial activity observed for 0.7Ag1, since this sample presents a lower inhibitory effect than 1.2Ag1, even though both have a similar particle size distribution (see Table 2).

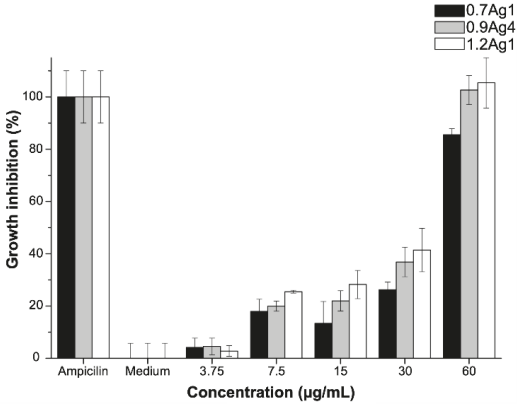

Figure 11. Antibacterial activity of CMC-AgNPs against *E. faecalis* growth. The data represent the percentage mean ± the percentage deviation.

3.4. Cytotoxicity

Considering the inhibitory effect on the bacteria growth of samples 0.7Ag1, 0.9Ag4, and 1.2Ag1, we proceed to evaluate their cytotoxicity at the same tested doses for the antibacterial assays. The

cytotoxicity assays were performed by three replicates of three independent experiments for the tested samples. As can be noticed in Figure 12, the highest cytotoxic effect occurs at [AgNPs] = 60 μg/mL for the three samples of CMC-AgNPs, showing a cytotoxicity greater than 95% after 24 h of treatment. However, the cytotoxic effect decreased in a dose dependent manner. At 30 μg/mL, 0.7Ag1 shows a lower cytotoxicity (60.5 ± 9.4%) than that from 0.9Ag4 and 1.2Ag1 of 100.3 ± 1.7% and 99.7 ± 5.9%, respectively. For subsequent dilutions, the decrease in cytotoxicity was more pronounced for 0.7Ag1 compared to the other two samples ($p < 0.001$). In addition, no cytotoxic effect was observed at a dilution of [AgNPs] = 3.75 μg/mL for the tested samples, since there are not statistical differences compared to the complete-DMEM control ($p > 0.05$). It is worth mentioning that at this dose no significant antibacterial activity was observed (see Figure 11).

In order to explain these results, we should consider the following. It is well known that AgNPs-mediated cytotoxicity in mammalian cells depends greatly on the nanoparticle size, shape, surface charge, dosage, oxidation state, and agglomeration condition as well as the cell type. Moreover, it has been demonstrated that antibacterial activity of AgNPs in aqueous media is related to oxidation of their surface and subsequent release of Ag^+ [43]. This oxidation conduces to the formation of reactive oxygen species (ROS) which trigger several negative effects on cell structures and their functions, inducing cytotoxicity [6,44]. Accordingly, the fact that 0.7Ag1 displays lower toxicity than 0.9Ag4 and 1.2Ag1 at all tested doses suggests that generation of ROS is diminished by the use of CMC with low DS for AgNPs immobilization. This is congruent with the results obtained from antibacterial activity assays regarding the inhibition of bacteria growth.

Hence, it can be concluded that Ag-O coordination bonds among AgNPs and COO^- moieties of CMC modify the ability of nanoparticles to produce and release Ag^+ into aqueous dispersion, adjusting their antibacterial activity and the induction of cytotoxicity into the tested biological environments. Finally, Table 3 summarize the results obtained from this work.

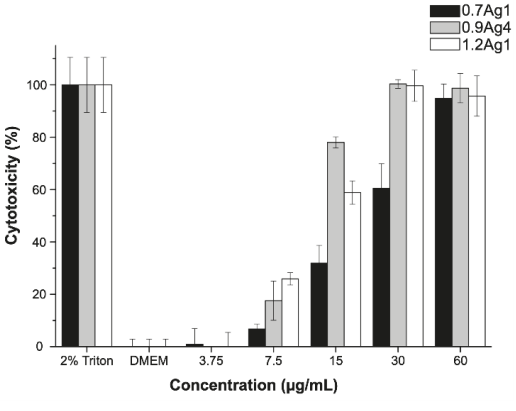

Figure 12. Cytotoxicity obtained from CMC-AgNPs composites against ATCC®PCS-201-018™ cell line. The data represent the percentage mean ± the percentage deviation.

Table 3. Summary of the results obtained from this work.

Characterization Technique	Obtained Results
HAADF-STEM imaging and particle size measuring	The particle size distribution change according to the weight of $AgNO_3$ added for the synthesis of nanoparticles, as well as the DS and Mw of CMC used as reducing agent and immobilization medium. The 1.2CMC reagent provides better control on particle size distribution than 0.7CMC and 0.9CMC reagents at the CMC/$AgNO_3$ weight ratios used for samples preparation.
BF imaging	The synthesized nanoparticles depict a regular atomic arrangement with an interplanar spacing that is congruent with the family planes {111} of silver.
SAED patterns	The synthesized nanoparticles show diffraction rings related to family planes {111}, {220}, {220} and {311} of the face-centered cubic (FCC) packing of silver.
UV-vis spectroscopy	The UV-Vis spectra obtained from CMC-AgNPs composites show that there are no detectable traces related to Ag^+ ions, suggesting full reduction of added Ag^+ to Ag^0.
ATR-FTIR spectroscopy	The ATR-FTIR spectra recorded from CMC-AgNPs composites suggest an interaction between CMC molecules and AgNPs, that could be attributed to the adsorption of R-CH_2OCOO^- groups onto nanoparticles.
Raman spectroscopy	The Raman spectra obtained from the selected samples confirms the adsorption of CMC chains onto nanoparticles and suggest the formation of a bond between Ag and O in the COO^- moieties of CMC.
XPS spectroscopy	The XPS spectra measured from selected composites confirms that the silver in samples is only Ag^0 and indicates that the AgNPs are immobilized into CMC by coordination bonds. Accordingly, these bonds are attributed to those Ag-O among AgNPs and COO^- moieties of CMC. Hence, the key factor for the control of particle size distribution of synthesized AgNPs is the quantity of R-CH_2OCOO^- available for their immobilization. The quantity of these groups varies in direct proportion with the DS of CMC.
Antibacterial activity and cytotoxicity assays	The antibacterial activity and cytotoxicity of the tested samples increase by the use of CMC with higher DS as AgNPs immobilization medium. Therefore, the Ag-O coordination bonds among AgNPs and COO^- moieties of CMC modify the ability of nanoparticles to produce and release Ag^+ into aqueous dispersion, adjusting their antibacterial activity and the induction of cytotoxicity into the tested biological environments.

4. Conclusions

The influence of polysaccharides' molecular structure on the antibacterial activity and cytotoxicity of green synthesized composites based on AgNPs immobilized into CMC was reported. The experimental evidence suggests that the particle size distribution and morphology of AgNPs mainly depend on the quantity of R-CH_2OCOO^- groups available for their immobilization. This is related to the fact that nanoparticles are immobilized in CMC by the formation of Ag-O coordination bonds among AgNPs and COO^- moieties of the polysaccharide's chains. Accordingly, the quantity of R-CH_2OCOO^- groups varies in direct proportion with the DS of CMC, which in general gives smaller particle size for CMC with higher DS. Moreover, the biological assays indicate that the antibacterial activity and cytotoxicity of the tested samples increase by the use of CMC with higher DS as AgNPs immobilization medium. Hence, it can be concluded that Ag-O coordination bonds among AgNPs and COO^- moieties of CMC modify the ability of nanoparticles to produce and release Ag^+ into aqueous dispersion, adjusting their antibacterial activity and the induction of cytotoxicity into the tested biological environments. Finally, it is worth mentioning that the width of the particle size distribution and morphology of AgNPs also depends on the weight of $AgNO_3$ added to the reaction and the Mw of CMC used for their synthesis. This could be related to the manner that silver ions are dispersed into the used CMC aqueous solutions for their reduction and subsequent nucleation and growth of AgNPs. Nonetheless, the observed trends regarding the variation of standard deviations and morphology, as well as their plausible explanations, should be confirmed in further studies.

Author Contributions: Conceptualization, M.A.d.l.G.-R. and V.A.G.-G.; data curation, M.A.M.-R. and E.M.-C.; formal analysis, V.H.U.-B. and M.A.G.-N.; investigation, M.A.M.-R., E.M.-C., and V.H.U.-B.; methodology, M.A.d.l.G.-R., and V.A.G.-G.; supervision, M.A.G.-N.; writing—original draft, M.A.M.-R., E.M.-C., V.H.U.-B., V.A.G.-G., and M.A.G.-N.; writing—review and editing, M.A.d.l.G.-R. and M.A.G.-N. All authors have read and agreed to the published version of the manuscript.

Funding: This research was founded by PAICYT-UANL, project number IT686-11. In addition, authors acknowledge to CHRISTUS—LATAM HUB Center of Excellence and Innovation, S.C. (CHRISTUS CEI) for financially supporting the study.

Conflicts of Interest: The authors declare no conflicts of interest. The funders had no role in the design of the study; in the collection, analyses, or interpretation of data; in the writing of the manuscript, or in the decision to publish the results.

References

1. Stathopoulou, M.-E.K.; Banti, C.N.; Kourkoumelis, N.; Hatzidimitriou, A.G.; Kalampounias, A.G.; Hadjikakou, S.K. Silver complex of salicylic acid and its hydrogel-cream in wound healing chemotherapy. *J. Inorg. Biochem.* **2018**, *181*, 41–55. [CrossRef] [PubMed]
2. Prucek, R.; Tuček, J.; Kilianová, M.; Panáček, A.; Kvítek, L.; Filip, J.; Kolář, M.; Tománková, K.; Zbořil, R. The targeted antibacterial and antifungal properties of magnetic nanocomposite of iron oxide and silver nanoparticles. *Biomaterials* **2011**, *32*, 4704–4713. [CrossRef] [PubMed]
3. Carbone, M.; Donia, D.T.; Sabbatella, G.; Antiochia, R. Silver nanoparticles in polymeric matrices for fresh food packaging. *J. King Saud Univ. Sci.* **2016**, *28*, 273–279. [CrossRef]
4. Farshchi, E.; Pirsa, S.; Roufegarinejad, L.; Alizadeh, M.; Rezazad, M. Photocatalytic/biodegradable film based on carboxymethyl cellulose, modified by gelatin and TiO2-Ag nanoparticles. *Carbohydr. Polym.* **2019**, *216*, 189–196. [CrossRef]
5. Morones, J.R.; Elechiguerra, J.L.; Camacho, A.; Holt, K.; Kouri, J.B.; Ramírez, J.T.; Yacaman, M.J. The bactericidal effect of silver nanoparticles. *Nanotechnology* **2005**, *16*, 2346–2353. [CrossRef]
6. Chernousova, S.; Epple, M. Silver as antibacterial agent: Ion, nanoparticle, and metal. *Angew. Chem. Int. Ed.* **2013**, *52*, 1636–1653. [CrossRef]
7. Feng, Q.L.; Wu, J.; Chen, G.Q.; Cui, F.Z.; Kim, T.N.; Kim, J.O. A mechanistic study of the antibacterial effect of silver ions on *Escherichia coli* and *Staphylococcus aureus*. *J. Biomed. Mater. Res.* **2000**, *52*, 662–668. [CrossRef]
8. Batchelor-McAuley, C.; Tschulik, K.; Neumann, C.C.M.; Laborda, E.; Compton, R.G. Why are silver nanoparticles more toxic than bulk silver? Towards understanding the dissolution and toxicity of silver nanoparticles. *Int. J. Electrochem. Sci.* **2014**, *9*, 1132–1138.
9. Bapat, R.A.; Chaubal, T.V.; Joshi, C.P.; Bapat, P.R.; Choudhury, H.; Pandey, M.; Gorain, B.; Kesharwani, P. An overview of application of silver nanoparticles for biomaterials in dentistry. *Mater. Sci. Eng. C* **2018**, *91*, 881–898. [CrossRef]
10. Moulton, M.C.; Braydich-Stolle, L.K.; Nadagouda, M.N.; Kunzelman, S.; Hussain, S.M.; Varma, R.S. Synthesis, characterization and biocompatibility of "green" synthesized silver nanoparticles using tea polyphenols. *Nanoscale* **2010**, *2*, 763–770. [CrossRef]
11. Shahid-ul-Islam; Butola, B.S.; Kumar, A. Green chemistry based in-situ synthesis of silver nanoparticles for multifunctional finishing of chitosan polysaccharide modified cellulosic textile substrate. *Int. J. Biol. Macromol.* **2019**. [CrossRef]
12. Senthilkumar, P.; Yaswant, G.; Kavitha, S.; Chandramohan, E.; Kowsalya, G.; Vijay, R.; Sudhagar, B.; Kumar, D.S.R.S. Preparation and characterization of hybrid chitosan-silver nanoparticles (Chi-Ag NPs); A potential antibacterial agent. *Int. J. Biol. Macromol.* **2019**, *141*, 290–297. [CrossRef] [PubMed]
13. Liao, C.; Li, Y.; Tjong, S.C. Antibacterial activities of aliphatic polyester nanocomposites with silver nanoparticles and/or graphene oxide sheets. *Nanomaterials* **2019**, *9*, 1102. [CrossRef]
14. Cavallaro, G.; Lazzara, G.; Milioto, S.; Parisi, F.; Evtugyn, V.; Rozhina, E.; Fakhrullin, R. Nanohydrogel formation within the halloysite lumen for triggered and sustained release. *Acs Appl. Mater. Interfaces* **2018**, *10*, 8265–8273. [CrossRef] [PubMed]
15. Basta, A.H.; El-Saied, H.; Hasanin, M.S.; El-Deftar, M.M. Green carboxymethyl cellulose-silver complex versus cellulose origins in biological activity applications. *Int. J. Biol. Macromol.* **2018**, *107*, 1364–1372. [CrossRef]

16. Martínez-Rodríguez, M.A.; Garza-Navarro, M.A.; Moreno-Cortez, I.E.; Lucio-Porto, R.; González-González, V.A. Silver/polysaccharide-based nanofibrous materials synthesized from green chemistry approach. *Carbohydr. Polym.* **2016**, *136*, 46–53. [CrossRef]
17. Chakraborty, T.; Chakraborty, I.; Ghosh, S. Sodium Carboxymethylcellulose−CTAB Interaction: A detailed thermodynamic study of polymer−surfactant interaction with opposite charges. *Langmuir* **2006**, *22*, 9905–9913. [CrossRef]
18. Nadagouda, M.N.; Varma, R.S. Synthesis of thermally stable carboxymethyl cellulose/metal biodegradable nanocomposites for potential biological applications. *Biomacromolecules* **2007**, *8*, 2762–2767. [CrossRef]
19. Garza-Navarro, M.A.; Aguirre-Rosales, J.A.; Llanas-Vázquez, E.E.; Moreno-Cortez, I.E.; Torres-Castro, A.; González-González, V.A. Totally ecofriendly synthesis of silver nanoparticles from aqueous dissolutions of polysaccharides. *Int. J. Polym. Sci.* **2013**, *2013*, 436021. [CrossRef]
20. Laredo-Naranjo, M.A.; Carrillo-Gonzalez, R.; De La Garza-Ramos, M.A.; Garza-Navarro, M.A.; Torre-Martinez, H.H.H.; Del Angel-Mosqueda, C.; Mercado-Hernandez, R.; Carrillo-Fuentevilla, R. Antimicrobial properties and dental pulp stem cell cytotoxicity using carboxymethyl cellulose-silver nanoparticles deposited on titanium plates. *Acta Biomater. Odontol. Scand.* **2016**, *2*, 60–67. [CrossRef]
21. Kemp, M.M.; Kumar, A.; Mousa, S.; Park, T.-J.; Ajayan, P.; Kubotera, N.; Mousa, S.A.; Linhardt, R.J. Synthesis of gold and silver nanoparticles stabilized with glycosaminoglycans having distinctive biological activities. *Biomacromolecules* **2009**, *10*, 589–595. [CrossRef] [PubMed]
22. He, F.; Zhao, D.; Liu, J.; Roberts, C.B. Stabilization of Fe−Pd nanoparticles with sodium carboxymethyl cellulose for enhanced transport and dechlorination of trichloroethylene in soil and groundwater. *Ind. Eng. Chem. Res.* **2007**, *46*, 29–34. [CrossRef]
23. Liu, J.; He, F.; Gunn, T.M.; Zhao, D.; Roberts, C.B. Precise seed-mediated growth and size-controlled synthesis of palladium nanoparticles using a green chemistry approach. *Langmuir* **2009**, *25*, 7116–7128. [CrossRef] [PubMed]
24. Donati, I.; Travan, A.; Pelillo, C.; Scarpa, T.; Coslovi, A.; Bonifacio, A.; Sergo, V.; Paoletti, S. Polyol synthesis of silver nanoparticles: Mechanism of reduction by alditol bearing polysaccharides. *Biomacromolecules* **2009**, *10*, 210–213. [CrossRef] [PubMed]
25. Ivleva, N.P.; Wagner, M.; Horn, H.; Niessner, R.; Haisch, C. In situ surface-enhanced Raman scattering analysis of biofilm. *Anal. Chem.* **2008**, *80*, 8538–8544. [CrossRef] [PubMed]
26. Wu, J.; Zhang, F.; Zhang, H. Facile synthesis of carboxymethyl curdlan-capped silver nanoparticles and their application in SERS. *Carbohydr. Polym.* **2012**, *90*, 261–269. [CrossRef] [PubMed]
27. Kaczmarska, K.; Grabowska, B.; Spychaj, T.; Zdanowicz, M.; Sitarz, M.; Bobrowski, A.; Cukrowicz, S. Effect of microwave treatment on structure of binders based on sodium carboxymethyl starch: FT-IR, FT-Raman and XRD investigations. *Spectrochim. Acta Part A Mol. Biomol. Spectrosc.* **2018**, *199*, 387–393. [CrossRef]
28. Ambjörnsson, H.A.; Schenzel, K.; Germgård, U. Carboxymethyl cellulose produced at different mercerization conditions and characterized by nir ft raman spectroscopy in combination with multivariate analytical methods. *BioResources* **2013**, *8*, 1918–1932. [CrossRef]
29. Lee, N.; Schuck, P.J.; Nico, P.S.; Gilbert, B. Surface enhanced raman spectroscopy of organic molecules on magnetite (Fe3O4) nanoparticles. *J. Phys. Chem. Lett.* **2015**, *6*, 970–974. [CrossRef]
30. Alee, K.S.; Kuladeep, R.; Rao, D.N. In-situ investigation of the formation of silver nanoparticles in polyvinyl alcohol through micro-Raman spectroscopy. *Opt. Commun.* **2013**, *293*, 69–74. [CrossRef]
31. Chang, S.; Ko, H.; Gunawidjaja, R.; Tsukruk, V.V. Raman markers from silver nanowire crossbars. *J. Phys. Chem. C* **2011**, *115*, 4387–4394. [CrossRef]
32. Li, L.; Wang, F.; Shao, Z.; Liu, J.; Zhang, Q.; Jiao, W. Chitosan and carboxymethyl cellulose-multilayered magnetic fluorescent systems for reversible protein immobilization. *Carbohydr. Polym.* **2018**, *201*, 357–366. [CrossRef] [PubMed]
33. Mansur, A.A.P.; de Carvalho, F.G.; Mansur, R.L.; Carvalho, S.M.; de Oliveira, L.C.; Mansur, H.S. Carboxymethylcellulose/ZnCdS fluorescent quantum dot nanoconjugates for cancer cell bioimaging. *Int. J. Biol. Macromol.* **2017**, *96*, 675–686. [CrossRef] [PubMed]
34. Xu, H.; Shi, X.; Ma, H.; Lv, Y.; Zhang, L.; Mao, Z. The preparation and antibacterial effects of dopa-cotton/AgNPs. *Appl. Surf. Sci.* **2011**, *257*, 6799–6803. [CrossRef]

35. Liu, H.; Lv, M.; Deng, B.; Li, J.; Yu, M.; Huang, Q.; Fan, C. Laundering durable antibacterial cotton fabrics grafted with pomegranate-shaped polymer wrapped in silver nanoparticle aggregations. *Sci. Rep.* **2014**, *4*, 5920. [CrossRef]
36. Xu, Q.; Ke, X.; Shen, L.; Ge, N.; Zhang, Y.; Fu, F.; Liu, X. Surface modification by carboxymethy chitosan via pad-dry-cure method for binding Ag NPs onto cotton fabric. *Int. J. Biol. Macromol.* **2018**, *111*, 796–803. [CrossRef]
37. Xu, Q.; Xie, L.; Diao, H.; Li, F.; Zhang, Y.; Fu, F.; Liu, X. Antibacterial cotton fabric with enhanced durability prepared using silver nanoparticles and carboxymethyl chitosan. *Carbohydr. Polym.* **2017**, *177*, 187–193. [CrossRef]
38. He, D.; Jones, A.M.; Garg, S.; Pham, A.N.; Waite, T.D. Silver nanoparticle−reactive oxygen species interactions: Application of a charging−discharging model. *J. Phys. Chem. C* **2011**, *115*, 5461–5468. [CrossRef]
39. Krishnan, R.; Arumugam, V.; Vasaviah, S.K. The MIC and MBC of silver nanoparticles against enterococcus faecalis a facultative anaerobe. *J. Nanomed. Nanotechnol.* **2015**, *6*, 1000285. [CrossRef]
40. Küp, F.Ö.; Çoşkunçay, S.; Duman, F. Biosynthesis of silver nanoparticles using leaf extract of Aesculus hippocastanum (horse chestnut): Evaluation of their antibacterial, antioxidant and drug release system activities. *Mater. Sci. Eng. C* **2020**, *107*, 110207. [CrossRef]
41. Dipankar, C.; Murugan, S. The green synthesis, characterization and evaluation of the biological activities of silver nanoparticles synthesized from Iresine herbstii leaf aqueous extracts. *Colloids Surf. B Biointerfaces* **2012**, *98*, 112–119. [CrossRef] [PubMed]
42. Odabaş, M.E.; Çinar, Ç.; Akça, G.; Araz, İ.; Ulusu, T.; Yücel, H. Short-term antimicrobial properties of mineral trioxide aggregate with incorporated silver-zeolite. *Dent. Traumatol.* **2011**, *27*, 189–194. [CrossRef] [PubMed]
43. Alcântara, M.T.S.; Lincopan, N.; Santos, P.M.; Ramirez, P.A.; Brant, A.J.C.; Riella, H.G.; Lugão, A.B. Simultaneous hydrogel crosslinking and silver nanoparticle formation by using ionizing radiation to obtain antimicrobial hydrogels. *Radiat. Phys. Chem.* **2019**, *165*, 108369. [CrossRef]
44. Fard, J.K.; Jafari, S.; Eghbal, M.A. A review of molecular mechanisms involved in toxicity of nanoparticles. *Adv. Pharm. Bull.* **2015**, *5*, 447–454. [CrossRef]

nanomaterials

MDPI

Article

ZnO Nanostructures with Antibacterial Properties Prepared by a Green Electrochemical-Thermal Approach

Maria Chiara Sportelli [1,2], Rosaria Anna Picca [1,2,*], Margherita Izzi [1], Gerardo Palazzo [1,2], Roberto Gristina [3], Massimo Innocenti [4], Luisa Torsi [1,2] and Nicola Cioffi [1,2]

[1] Chemistry Department, University of Bari "Aldo Moro", via E. Orabona 4, 70126 Bari, Italy; maria.sportelli@uniba.it (M.C.S.); margherita.izzi@uniba.it (M.I.); gerardo.palazzo@uniba.it (G.P.); luisa.torsi@uniba.it (L.T.); nicola.cioffi@uniba.it (N.C.)

[2] CSGI (Center for Colloid and Surface Science) c/o Dept. Chemistry, via Orabona 4, 70125 Bari, Italy

[3] Institute of Nanotechnology, National Research Council of Italy (CNR-NANOTEC), c/o Department of Chemistry, University of Bari "Aldo Moro", via Orabona 4, 70126 Bari, Italy; roberto.gristina@cnr.it

[4] Chemistry Department, University of Florence, Via Lastruccia 3-13, 50019 Sesto Fiorentino (FI), Italy; m.innocenti@unifi.it

* Correspondence: rosaria.picca@uniba.it

Received: 23 January 2020; Accepted: 29 February 2020; Published: 5 March 2020

Abstract: Zinc oxide (ZnO) nanostructures are widely applied materials, and are also capable of antimicrobial action. They can be obtained by several methods, which include physical and chemical approaches. Considering the recent rise of green and low-cost synthetic routes for nanomaterial development, electrochemical techniques represent a valid alternative to biogenic synthesis. Following a hybrid electrochemical-thermal method modified by our group, here we report on the aqueous electrosynthesis of ZnO nanomaterials based on the use of alternative stabilizers. We tested both benzyl-hexadecyl-dimetylammonium chloride (BAC) and poly-diallyl-(dimethylammonium) chloride (PDDA). Transmission electron microscopy images showed the formation of rod-like and flower-like structures with a variable aspect-ratio. The combination of UV–Vis, FTIR and XPS spectroscopies allowed for the univocal assessment of the material composition as a function of different thermal treatments. In fact, the latter guaranteed the complete conversion of the as-prepared colloidal materials into stoichiometric ZnO species without excessive morphological modification. The antimicrobial efficacy of both materials was tested against *Bacillus subtilis* as a Gram-positive model microorganism.

Keywords: zinc oxide; electrochemical synthesis; BAC; PDDA; nanorod; XPS; TEM; *B. subtilis*

1. Introduction

Semiconductor metal oxide nanostructures, and specifically ZnO ones, have received a great amount of interest in many areas due to their unique physical, chemical and optical properties [1]. Moreover, ZnO nanomaterials are well-known antimicrobial agents [2], which can be employed in several fields where pathogen spreading should be inhibited [3–5]. Besides the many physical [6–8] and chemical [9–11] methods for the production of such materials, scientific research has recently focused on green and simple electrochemical approaches [12,13]. These synthetic routes have the great advantage of being completely eco-friendly, using mainly aqueous solutions in the absence of reductants or other harmful chemicals [14]. Moreover, they can be easily scaled up for industrial purposes, and are cheap and easily reproducible [12,15]. Electrochemical approaches for the production of unsupported ZnO nanostructures (ZnONSs) are divided into three categories: electrochemical deposition under oxidative conditions (EDOC), electrolysis in alcohols, and electrolysis in the aqueous phase. EDOC [16] involves three stages: oxidation of a sacrificial anode, cathodic reduction of metal

ions, and oxidation of metal nanoclusters by means of the oxygen introduced into the cell, assisted by stabilization by surfactants. Electrolysis in alcohols consists in the electrochemical degradation of a Zn electrode at high potentials in an anhydrous environment [17,18]. This process was recently updated by Dhayagude et al. [19] using tetra-butyl-ammonium bromide (TBAB) as a stabilizer in a water/ethanol electrochemical medium. Regarding the synthesis in the aqueous alkali phase, a hybrid electrochemical-thermal method was proposed in 2010, which used an aqueous solution of $NaHCO_3$ to generate mixed carbonate and hydroxide Zn species, which were subsequently converted into ZnO by a calcination process at temperatures >300 °C [15,20]. In our group, we modified this method, in order to obtain a higher level of morphological control in the produced nanostructures. Both anionic [14,21] and cationic [22] stabilizers were dispersed in the electrochemical media and tested, and we demonstrated that we were able to produce various morphologies, ranging from spheroidal particles to rice-grain or rod-like structures.

Here, we propose a further upgrade of the aforementioned electrochemical process, which is run under mild galvanostatic conditions, using either benzyl-dimetylammonium chloride (BAC) or poly-diallyl-(dimethylammonium) chloride (PDDA) as a stabilizer. The first is a well-known disinfectant, and was used with the intent of producing nanostructures with enhanced antimicrobial properties [23,24]. The second one, a high charge density cationic polymer, is already used for the preparation of transistors and sensors, and as a coadjuvant in layer-by-layer deposition processes [25]. The gel-like products of the electrochemical step underwent a two-step thermal treatment: overnight desiccation at 120 °C and calcination at 450 °C for 1 h. Both the dried and the calcined samples, prepared with the two stabilizers, were characterized by transmission electron microscopy (TEM), and UV–Vis, infrared (FTIR) and *X*-ray photoelectron (XPS) spectroscopies. The critical role of temperature on the physicochemical properties of the final nanostructures was demonstrated. The antimicrobial activity of both the BAC- and PDDA-stabilized ZnONSs was demonstrated against a model Gram-positive microorganism, i.e., *B. subtilis*.

2. Materials and Methods

2.1. Materials

Zinc sheets (1 mm thick, 99.99+%) were purchased from Goodfellow Ltd and cut into 2×1 cm^2 pieces. Sodium bicarbonate ($NaHCO_3$, purum p.a., 99.0%), 2-propanol (IPA, Chromasolv® Plus, for HPLC, 99.9%), hydrochloric acid (HCl, ACS reagent, 37%), benzyl-hexadecyl-dimetylammonium chloride (BAC, pure cationic surfactant), potassium bromide (KBr, FTIR grade, >99% trace metals basis), poly-diallyl-(dimethylammonium) chloride (PDDA, with an average molecular weight MW of 200,000–350,000, 20 wt.% in H_2O), and Luria-Bertani (LB) broth (Miller, pH 6.8–7.2, 2.5% solution) were purchased from Merck-Sigma Aldrich (Milan, Italy). Aluminum oxide (Al_2O_3, purum p.a., 99.7%), for the mechanical polishing of zinc sheets, was obtained from Fluka Chemicals (Milan, Italy). Agar powder, meat extract, and peptone (from casein, pancreatic digest) were supplied by SIFIN Diagnostics Gmbh (Berlin, Germany). Milli-Q water was used in all experiments.

2.2. Synthesis of ZnONSs

A three-electrode setup was employed, using two zinc sheets as working (WE) and counter (CE) electrodes, and an Ag/AgCl (KCl sat.) as a reference electrode (RE). First, zinc electrodes were polished using sandpaper and afterward using alumina slurries with a different granulometry. Then, they underwent sonication, alternating between MilliQ water and IPA. Electrodes were finally activated in 1 M HCl for 30 s prior to use. The process yield (in terms of the mass of produced ZnONSs) was estimated by a differential weighting of the two zinc sheets before and after the process. The electrosynthesis was carried out in mild galvanostatic conditions, applying a current density of 10 mA/cm^2 with a CH-1140b potentiostat-galvanostat (CH Instruments, Bee Cave, TX, USA). The process was performed under continuous stirring for 1 h, at room temperature. The electrolytic

medium was composed of either 0.01 M BAC or 1 g/L PDDA, dissolved in 30 mM $NaHCO_3$ aqueous solution. pH was monitored at the beginning and the end of the synthesis. Afterward, the colloidal dispersion was centrifuged at 6000 rpm for 30 min, and the resulting precipitate was dried overnight at 120 °C. The obtained powder underwent calcination at 450 °C in a tubular muffle furnace for 1 h.

2.3. Morphological and Spectroscopic Characterizations

TEM microscopy was performed with an FEI Tecnai 12 (Hillsboro, OR, USA) instrument (high tension: 120 kV; filament: LaB_6), by dropping NP suspensions on a Formvar®-coated Cu grid (400 mesh, Agar Scientific, Stansted, UK).

UV–Vis spectroscopy was carried out with a Shimadzu UV-1601 double beam spectrometer, equipped with a silicon photodiode detector, from 200 to 700 nm, with 1-cm Quartz Suprasil® (Hellma Analytics, Jena, DE) cuvettes.

Infrared spectra were recorded on a Perkin Elmer Spectrum-Two (Milan, IT), in the spectral range of 4000–400 cm^{-1}, with a resolution of 1 cm^{-1}, averaging 8 consecutive scans. The samples were analyzed as KBr pellets by grinding a proper quantity of the ZnO nanopowder in an agate mortar.

XPS surface analysis was performed on a PHI (Chanhassen, MN, USA) Versaprobe II spectrometer. A monochromatized Al-Kα source (1486.6 eV) was used. Dual-beam charge neutralization was constantly applied during the analysis. Large-area XPS was performed, operating with a sampling area of 200 × 1400 μm^2. Samples were mounted onto the sample holder by means of double-sided tape. Survey scans (pass energy = 117.4 eV, step size = 1 eV) and high-resolution regions (pass energy = 58.7 eV, step size = 0.125 eV) relevant to C1s, O1s, N1s, Na1s, Cl2p, Zn2p, and ZnLMM were investigated. Detailed spectra processing was performed by CasaXPS® (v. 2.3.18PR1.0) software. Binding Energy (BE) referred to the aliphatic component of C1s at 284.8 eV. For estimating the proper peak positions and assignments in both IR and XPS analyses, a commercial ZnO powder, obtained from Sigma Aldrich (Milan, IT), was used.

Aqueous ZnONS suspensions of 0.5 g/L were also characterized by ζ-potential measurements, using a Zetasizer-Nano ZS from Malvern Instruments (Rome, IT). The cell holder was maintained at 25 °C by a Peltier element; Laser-Doppler electrophoresis (LDE) exploited forward scattering at 17°. The LDE measurements were performed in a disposable capillary cell, and the ζ-potential was evaluated from the electrophoretic mobility according to the Smoluchowski approximation.

2.4. Antimicrobial Activity of ZnONSs

BAC- and PDDA-ZnONSs were suspended in Milli-Q water at a concentration of 0.15% w/v and deposited by drop casting on sterilized circular glass slides (⌀ 12 mm, Agar Scientific). The *B. subtilis* isolated strain (MTCC 441) was provided by the Institute of Bioscience and Biology of the University of Bari. Fifty milliliters of fresh LB broth was inoculated with 1 mL of cell suspension and incubated at 30 °C. The bacterial culture at the beginning of the exponential growth phase, at a concentration of 10^7 CFU/mL (colony forming unit), was seeded (200 μL) on LB-agar Petri dishes. Then, circular glass slides covered with ZnONSs were put in contact with the seeded plates and incubated at 30 °C for 40 h. Experiments were performed in 5 replicates. The average values were used for calculation of the inhibition zone area. The minimum diameter of the inhibition zone was measured in mm.

A bare glass slide was used as a control sample.

3. Results and Discussion

3.1. Electrochemical Production of ZnONSs

This work follows the steps of the electrochemical-thermal hybrid method proposed by Chandrappa et al. [20], and improved by our group with the use of both cationic [22] and anionic [14,21] stabilizers. A colloidal suspension of hydroxides and zinc carbonates was produced in the presence of PDDA and BAC. As already shown [14,21,26], in fact, the final pH of the electrolytic medium is always

highly basic (>9), and species such as $Zn(OH)_2$, $[Zn(OH)_3]^-$ and $[Zn(OH)_4]^{2-}$ are thermodynamically stable in these conditions. The mixture is then converted into pure ZnO by thermal treatments. For each synthesis, the electrodes were weighed before and after the process, in order to calculate the mass variation and the experimental yield (Equation (1)).

$$m_{experimental} = \Delta m(WE) - \Delta m(CE) \quad (1)$$

The theoretical mass was calculated according to Faraday's law for a two-electron process, as expressed in Equation (2), where I is current intensity, Δt is process duration, M_{Zn} is Zn atomic mass, Z is the number of electrons involved in the process, and F is the Faraday constant:

$$m_{theoretical} = \frac{M_{Zn}\left(\frac{g}{mol}\right) \times \Delta t(s) \times I(A)}{Z(\#e^-) \times F\frac{C}{mol}} \quad (2)$$

The obtained results, for both stabilizers, are listed in Table 1.

Table 1. The process efficiency for the preparation of nanocolloids, expressed in terms of nanodispersed Zn masses, and % yields.

Stabilizer	Δm_{WE} (mg)	Δm_{CE} (mg)	$m_{experimental}$ (mg)	$m_{theoretical}$ (mg)	% Yield
BAC	19 ± 2	0 ± 2	19 ± 4	24.4	79
PDDA	17 ± 2	0 ± 2	17 ± 4	24.4	70

The synthesized products were first subjected to a desiccation treatment in an oven at 120 °C, which was carried out overnight, and a further thermal treatment at 450 °C for 1 h.

3.2. Morphological Characterization

Morphological analyses on both dried (120 °C) and annealed (450 °C) ZnONSs exhibited the influence of both stabilizers and thermal treatments. Figure 1 shows the TEM micrographs obtained on the ZnO nanostructures that were prepared in the presence of BAC.

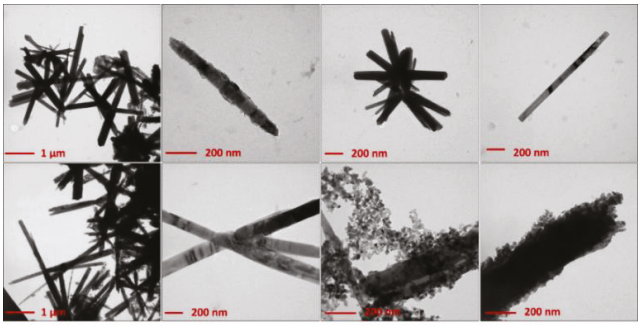

Figure 1. Transmission electron microscopy (TEM) images of electrosynthesized ZnO-based materials in the presence of benzyl-dimetylammonium chloride (BAC). Upper panels: ZnO dried at 120 °C overnight; lower panels: ZnO calcined at 450 °C for 1 h.

Rod-like and flower-like structures (with an average length of 1–2 µm) were obtained from samples dried at 120 °C. This morphology was preserved after calcination at 450 °C. However, a certain number of spheroidal nanoparticles (with an average diameter >5 nm) appeared after calcination, mainly at the wire tips. This phenomenon can be indicative of a possible mechanism of wire growth induced by calcination. In fact, the calcined samples showed slightly longer nanowires. The role of BAC in the growth mechanism of elongated rod-like structures may be tentatively explained by considering

certain similarities between the effect of BAC and that exerted by cetyltrimethylammonium bromide (CTAB), which is an asymmetric quaternary ammonium salt, as well [27]. It has been reported in the literature that CTA^+ ions, which have a structure of a charged tetrahedron with a long hydrophobic tail, can electrostatically interact with $[Zn(OH)_4]^{2-}$ (anion present in solution with a tetrahedral geometry, known to be the growth unit for ZnO), forming ion pairs [28–30]. In this way, the lateral growth is inhibited, whereas it is promoted along the *c*-axis ([0 0 0 1] direction), thus favoring the hexagonal (wurtzite) rod-like morphology [28]. Both CTAB and BAC promote the growth of ZnO crystallites in the form of wurtzite, the most thermodynamically stable ZnO crystalline form. Moreover, heating can favor assembly into flower-like shapes [28].

Analogously, Figure 2 reports images relevant to ZnO synthesized in the presence of PDDA.

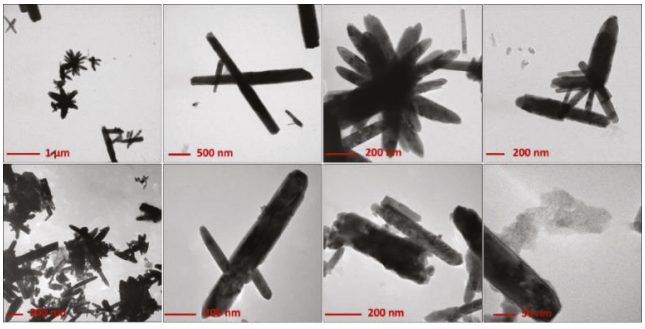

Figure 2. TEM images of electrosynthesized ZnO-based materials in the presence of poly-diallyl-(dimethylammonium) chloride (PDDA). Upper panels: ZnO dried at 120 °C overnight; lower panels: ZnO calcined at 450 °C for 1 h.

The latter promoted the formation of flower-like microstructures, with an average wire length of 200–500 nm. This morphology was also preserved after calcination, although the thermal deterioration of the polymer tended to produce more aggregates. In the case of PDDA, a growth mechanism involving lamellar superimposition can be hypothesized, as shown by the growth lines running along wires' length (Figure S1). Typically, the ZnO nanophases obtained by the proposed method show a crystalline, wurtzite structure, with a significant number of defects, as assessed by selected-area electron diffraction (SAED) analysis (Figure S2). Interestingly, other results indicate that calcination is not essential to obtain ZnO when using PDDA (vide infra).

3.3. FTIR and UV–Vis Characterizations

The FTIR spectra of all samples are presented in Figure 3.

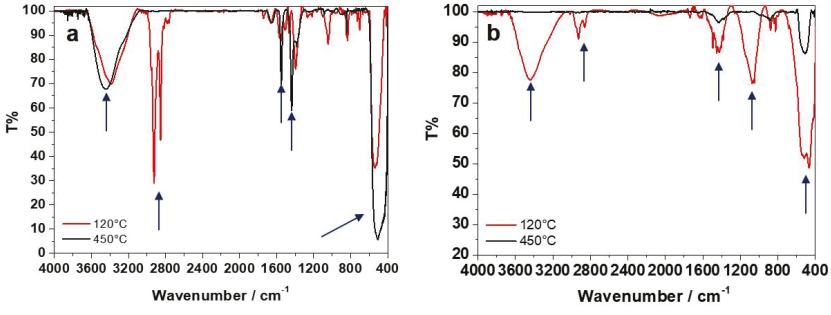

Figure 3. The FTIR spectra of dried (120 °C) and calcined (450 °C) samples: (**a**) ZnO-BAC; (**b**) ZnO-PDDA. The main IR modes are highlighted by arrows.

In the case of BAC (Figure 3a), IR data indicate that ZnO is already present in the 120 °C-dried samples, as highlighted by the characteristic IR band at 440–500 cm^{-1} attributed to the Zn-O stretching [22]; the conversion of Zn(II) species into stoichiometric ZnO is complete with calcination at 450 °C. The region between 1300 and 1600 cm^{-1} is typically associated with the presence of hydrozincite-like species ($Zn_x(CO_3)_y(OH)_z$) [31] and lowers after calcination. Furthermore, the increase in the treatment temperature also led to the disappearance of C-H stretching (3000–2800 cm^{-1}) signals [32]; on the contrary, hydroxyl (3500–3400 cm^{-1}) and styrene/carbonyl bands (1700–1500 cm^{-1}) slightly increase upon calcination, as the effect of a possible BAC degradation with temperature, forming burnt moieties.

Regarding PDDA (Figure 3b), the IR spectrum of the dried sample presented some characteristic bands of PDDA, not degraded by the thermal treatment. The absence of the two main absorptions related to the symmetric and asymmetric stretching modes (with the characteristic double-pointed shape) of the carbonates at 1389–1500 cm^{-1} [33] and of the other characteristic signals at 1047 cm^{-1}, 837 cm^{-1}, and 710 cm^{-1}, combined with the presence of the 3400-cm^{-1} band relative to O-H stretching (H_2O and hydroxides), indicates that Zn^{2+} is mainly present as hydroxide and not as hydrozincite. On the other hand, the IR spectrum of the calcined sample showed a stronger signal due to Zn-O stretching, whereas the hydroxide band decreased. Moreover, signals related to the polymeric stabilizer were no longer visible after calcination at 450 °C.

The UV–Vis spectra of all of the samples are presented in Figure 4. In the case of BAC (Figure 4a), the UV–Vis spectrum of the dried sample exhibited an absorption peak ascribable to ZnO (350–400 nm). The calcination process induced an increase in the peak intensity, due to pure ZnO and to a stronger absorption. For PDDA (Figure 4b), the band ascribable to ZnO showed a slight red shift from 374 nm to 382 nm with the increase in the treatment temperature, which could be related to a nanostructure size increase (a phenomenon generally reported in the literature) [14]. Broad absorption at higher wavelengths is attributed in the literature to crystal defects, especially oxygen vacancies in the sample [34].

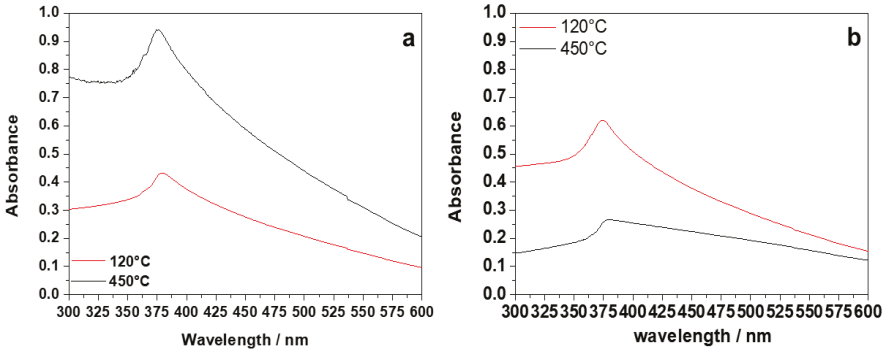

Figure 4. UV–Vis spectra of dried (120 °C) and calcined (450 °C) samples: (**a**) ZnO-BAC; (**b**) ZnO-PDDA.

3.4. XPS Characterization

XPS was useful in the univocal determination of zinc chemical speciation. Zn(II) species can be discriminated by means of the $ZnL_3M_{45}M_{45}$ Auger signal (expressed in kinetic energy, KE) and of the modified Auger parameter α′. In fact, the $Zn2p_{3/2}$ photoelectronic signal is uninformative as the chemical shift on this signal is small, compared to that on the corresponding Auger maximum. In fact, typical values for $Zn2p_{3/2}$ ranging between 1021 and 1023 eV are indifferently reported for zinc metal or Zn(II) [35]. All the analyzed samples presented $Zn2p_{3/2}$ positions in this range (Table 2). This means that the correct zinc speciation, based only on the main photoelectronic peak, is unreliable [36–38]. Considering that the typical value of α′ reported for ZnO is equal to 2010.2 ± 0.3 eV [14,22,26,35,39,40],

the Zn Auger signal was acquired and analyzed to assess the presence of zinc oxide in the investigated samples (Figure 5). The main component of $ZnL_3M_{4,5}M_{4,5}$ was used for the further calculation of α' and it is mainly ascribed to the ^1G final state transition, which is known to be the most probable [37,41]. In the case of BAC, XPS data revealed that the increase in the calcination temperature led to the increment of α' (Table 2), reaching values compatible with the presence of ZnO on the surface of the nanostructures. Dried samples presented a low value of α' (compatible with zinc hydroxides) [39], whereas it was around 2010.0 eV for 450 °C-calcined samples. These results are in agreement with the IR data. The XPS data on ZnO-BAC samples treated at 450 °C did not show any signal ascribable to nitrogen. This is indicative of the non-persistence of the cationic stabilizer on ZnONSs after calcination, and is in agreement with the IR results.

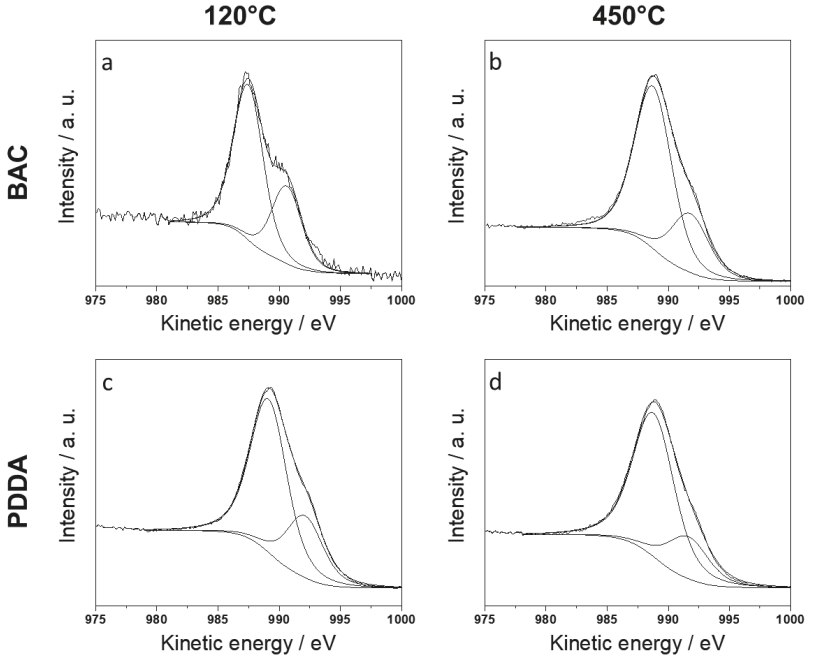

Figure 5. $ZnL_3M_{4,5}M_{4,5}$ XP spectra of dried (120 °C) and calcined (450 °C) samples. ZnO-BAC (**a**,**b**); ZnO-PDDA (**c**,**d**).

Table 2. Zn2p, $ZnL_3M_{4,5}M_{4,5}$ positions, and corresponding modified Auger parameter (α') for all of the samples, as a function of the stabilizer and of the thermal treatment.

	Thermal Treatment	$Zn2p_{3/2}$ BE (eV)	$ZnL_3M_{4,5}M_{4,5}$ KE (eV)	α' (eV)
BAC	120 °C	1022.0 ± 0.2	987.4 ± 0.2	2009.4 ± 0.3
	450 °C	1021.3 ± 0.2	988.8 ± 0.2	2010.1 ± 0.3
PDDA	120 °C	1021.1 ± 0.2	987.9 ± 0.2	2010.0 ± 0.3
	450 °C	1021.2 ± 0.2	988.8 ± 0.2	2010.0 ± 0.3

In a similar way, the XPS results on the PDDA-based samples are corroborated by the IR findings. The modified Auger parameter for zinc was compatible with the presence of ZnO, already in dried samples at 120 °C. The obtainment of pure ZnO in milder conditions with respect to the current state-of-the-art [14,21] makes ZnO-PDDA a highly appealing material. It is worth pointing out that, for the ZnO-PDDA treated at 120 °C, the N1s signal (Figure S3) that resulted is made up of two components: the first at a binding energy of 399.2 ± 0.2 eV, and the second at 402.2 ± 0.2 eV. They were

associated with the presence of free amine groups $-\underline{N}(CH_2)/-\underline{N}H_2$, and protonated groups (mainly $-\underline{N}(CH_3)_3{}^+/-\underline{N}H_3{}^+$) [35]. This evidence can be indicative that the quaternary nitrogen of the PDDA has partly been preserved and that the cationic character of the polymer has not been completely lost.

3.5. ζ-Potential Measurements

ζ-potential measurements (Figure 6) were performed on the most interesting samples in terms of chemical composition, morphology, and ease of preparation. From the characterizations reported above, it appears clear that ZnONSs prepared with BAC benefit from a calcination step when stoichiometric ZnO phases are desired. During this step, the stabilizing agent degrades and forms burnt carbonaceous moieties on nanostructures. This could be the reason why the calcined ZnONSs @BAC did not show any isoelectric point and had a highly negative ζ-potential in the pH range investigated here (Figure 6a).

In the case of ZnO-PDDA, a mild drying process at 120 °C is enough to obtain ZnO. Moreover, as demonstrated by XPS, the polyelectrolyte is retained on the ZnO surface after the thermal treatment at 120 °C. The persistence of the cationic NP stabilizer is consistent with the presence of a positive and almost constant ζ-potential, with a pH ranging from 5 to 11 (Figure 6b).

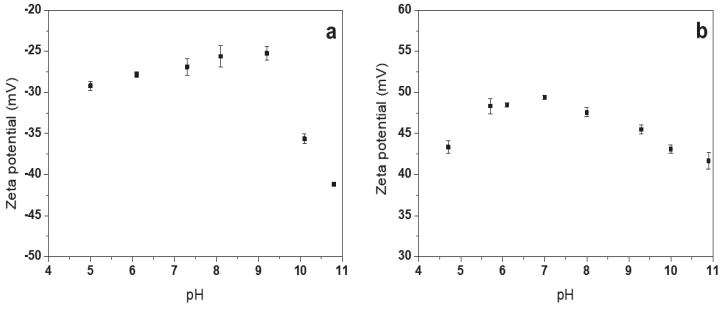

Figure 6. ζ-potential measurements as a function of pH: (**a**) calcined (450 °C) ZnO-BAC nanostructures; (**b**) dried (120 °C) ZnO-PDDA nanostructures.

3.6. Agar Disk Diffusion Tests

Antibacterial activity studies were carried out on both calcined (450 °C) ZnO-BAC nanostructures and dried (120 °C) ZnO-PDDA nanostructures. They showed consistent inhibition (>10 mm) [42] and no significant variation amongst stabilizers (Figure 7). In fact, the average inhibition diameters measured on five replicates resulted equal to 10.8 ± 0.6 mm for ZnO-BAC and 10.3 ± 1.2 mm for ZnO-PDDA. Slight differences in NP morphology and opposite ζ-potential values did not seem to have any influence on the NP antimicrobial behavior against a Gram-positive bacterial strain. No bacterial growth inhibition was found on the control samples.

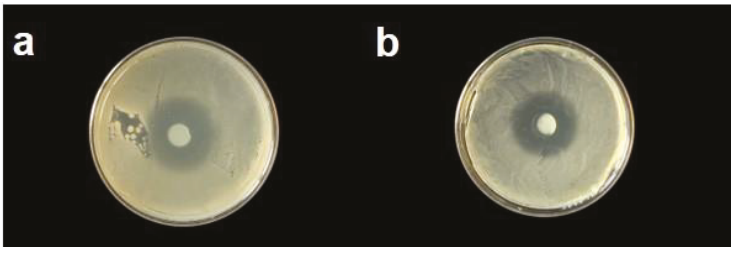

Figure 7. Evaluation of antibacterial action by an Agar diffusion test: (**a**) calcined (450 °C) ZnO-BAC nanostructures; (**b**) dried (120 °C) ZnO-PDDA nanostructures.

4. Conclusions

In summary, we proposed a green electrochemical strategy for the synthesis of ZnONSs in aqueous alkaline media with low-cost, non-toxic chemicals under mild conditions. ZnO rod- and flower-like structures were successfully synthesized by employing two different stabilizers, namely, BAC and PDDA. While for BAC a thermal treatment at temperatures ≥450 °C was necessary for the complete conversion of the as-prepared gel-like material into ZnO, PDDA allowed for the preparation of pure ZnONSs without the need for severe thermal treatment. In fact, both FTIR and XPS measurements confirmed the presence of stoichiometric ZnO after a simple drying step at 120 °C. In all cases, TEM analysis revealed the presence of elongated (or rod-like) structures, generally assembled into more complex and ordered aggregates after calcination at 450 °C. Both BAC- and PDDA-containing materials exhibited a consistent antimicrobial efficacy against *B. subtilis*, as demonstrated by agar diffusion tests. The approach presented here can be considered as an improvement of the current methodologies to produce elongated ZnO nanomaterials in an aqueous solution, employing cationic capping agents, thanks to higher yields and milder preparation conditions [22]. Application of these ZnO nanostructures in transistor devices (PDDA-capped) and for cultural heritage preservation (BAC-capped) is envisaged, and work is scheduled for the future in this field.

Supplementary Materials: The following are available online at http://www.mdpi.com/2079-4991/10/3/473/s1, Figure S1: TEM image of dried (120 °C) ZnO-PDDA sample. Figure S2: Selected area diffraction (SAED) image obtained on ZnONSs. Figure S3: N1s XP spectrum of ZnO-PDDA dried at 120 °C.

Author Contributions: M.C.S. performed TEM and spectroscopic characterizations, along with microbiological experiments, and wrote the first draft of the paper. R.A.P. developed the electrochemical approach and performed *X*-ray spectroscopic analyses. M.I. (Margherita Izzi) performed data treatment. G.P. performed ζ-potential measurements. R.G. developed microbiological protocols and supervised biological experimental activities. M.I. (Massimo Innocenti) and L.T. contributed to protocol development. N.C. supervised experimental activities. Authorship is limited to those who have contributed substantially to the work reported. All authors have read and agreed to the published version of the manuscript.

Funding: Partial financial support is acknowledged from the European Union's Horizon 2020 research and innovation program under the Marie Skłodowska-Curie Grant Agreement No. 813439, and from the Italian MIUR project "E-Design" ARS01_01158.

Acknowledgments: Vincenzo Villone, Thomas Centobelli, Romeo Lettini, and Marina Menga are acknowledged for their help in collecting some experimental data.

Conflicts of Interest: The authors declare no conflict of interest. The funders had no role in the design of the study; in the collection, analyses, or interpretation of data; in the writing of the manuscript, or in the decision to publish the results.

References

1. Özgür, Ü.; Alivov, Y.I.; Liu, C.; Teke, A.; Reshchikov, M.A.; Doğan, S.; Avrutin, V.; Cho, S.-J.; Morkoç, H. A comprehensive review of ZnO materials and devices. *J. Appl. Phys.* **2005**, *98*, 11. [CrossRef]
2. Sportelli, M.C.; Picca, R.A.; Cioffi, N. Nano-Antimicrobials Based on Metals. In *Novel Antimicrobial Agents and Strategies*; Wiley-VCH Verlag GmbH & Co. KgaA: Weinheim, Germany, 2014; pp. 181–218. ISBN 978-3-527-67613-2.
3. Ditaranto, N.; van der Werf, I.D.; Picca, R.A.; Sportelli, M.C.; Giannossa, L.C.; Bonerba, E.; Tantillo, G.; Sabbatini, L. Characterization and behaviour of ZnO-based nanocomposites designed for the control of biodeterioration of patrimonial stoneworks. *New J. Chem.* **2015**, *39*, 6836–6843. [CrossRef]
4. van der Werf, I.D.; Ditaranto, N.; Picca, R.A.; Sportelli, M.C.; Sabbatini, L. Development of a novel conservation treatment of stone monuments with bioactive nanocomposites. *Herit. Sci.* **2015**, *3*, 29. [CrossRef]
5. Ditaranto, N.; Picca, R.A.; Sportelli, M.C.; Sabbatini, L.; Cioffi, N. Surface characterization of textiles modified by copper and zinc oxide nano-antimicrobials. *Surf. Interface Anal.* **2016**, *48*, 505–508. [CrossRef]
6. Sportelli, M.C.; Valentini, M.; Picca, R.A.; Milella, A.; Nacci, A.; Valentini, A.; Cioffi, N. New Insights in the Ion Beam Sputtering Deposition of ZnO-Fluoropolymer Nanocomposites. *Appl. Sci.* **2018**, *8*, 77. [CrossRef]

7. Sportelli, M.C.; Nitti, M.A.; Valentini, M.; Picca, R.A.; Bonerba, E.; Sabbatini, L.; Tantillo, G.; Cioffi, N.; Valentini, A. Ion Beam Sputtering Deposition and Characterization of ZnO-Fluoropolymer Nano-Antimicrobials. *Sci. Adv. Mat.* **2014**, *6*, 1019–1025. [CrossRef]
8. He, X.X.; Li, H.Q.; Gu, J.B.; Wu, S.B.; Cao, B. *The Properties of ZnO Thin Films Fabricated by Ion Beam Sputtering and RF Magnetron Sputtering*; Shen, W., Chu, J., Eds.; SPIE digital library: Bellingham, WA, USA, 2008; p. 69842T.
9. Amizam, S.; Abdullah, N.; Rafaie, H.A.; Rusop, M.; Rusop, M.; Subban, R.Y.; Kamarulzaman, N.; Wui, W.T. *SEM and XRD Characterization of ZnO Nanostructured Thin Films Prepared by Sol-Gel Method with Various Annealing Temperatures*; AIP Publishing LLC: Mellville, NY, USA, 2010; pp. 37–41.
10. Benramache, S.; Benhaoua, B.; Chabane, F.; Guettaf, A. A comparative study on the nanocrystalline ZnO thin films prepared by ultrasonic spray and sol-gel method. *Optik Int. J. Light Electron Opt.* **2013**, *124*, 3221–3224. [CrossRef]
11. Ahmad, M.Z.; Sadek, A.Z.; Latham, K.; Kita, J.; Moos, R.; Wlodarski, W. Chemically synthesized one-dimensional zinc oxide nanorods for ethanol sensing. *Sens. Actuators B Chem.* **2013**, *187*, 295–300. [CrossRef]
12. Sportelli, M.C.; Scarabino, S.; Picca, R.A.; Cioffi, N. Recent trends in the electrochemical synthesis of zinc oxide nano-colloids. In *CRC Concise Encyclopedia of Nanotechnology*; CRC Press, LLC: Boca Raton, FL, USA, 2015; pp. 1158–1172. ISBN 978-1-4665-8034-3.
13. Izzi, M.; Sportelli, M.C.; Ditaranto, N.; Picca, R.A.; Innocenti, M.; Sabbatini, L.; Cioffi, N. Pros and Cons of Sacrificial Anode Electrolysis for the Preparation of Transition Metal Colloids: A Review. *ChemElectroChem* **2020**, *7*, 386–394. [CrossRef]
14. Picca, R.A.; Sportelli, M.C.; Hötger, D.; Manoli, K.; Kranz, C.; Mizaikoff, B.; Torsi, L.; Cioffi, N. Electrosynthesis and characterization of ZnO nanoparticles as inorganic component in organic thin-film transistor active layers. *Electrochim. Acta* **2015**, *178*, 45–54. [CrossRef]
15. Chandrappa, K.; Venkatesha, T.; Vathsala, K.; Shivakumara, C. A hybrid electrochemical–thermal method for the preparation of large ZnO nanoparticles. *J. Nanoparticle Res.* **2010**, *12*, 2667–2678. [CrossRef]
16. Dierstein, A.; Natter, H.; Meyer, F.; Stephan, H.-O.; Kropf, C.; Hempelmann, R. Electrochemical deposition under oxidizing conditions (EDOC): A new synthesis for nanocrystalline metal oxides. *Scr. Mater.* **2001**, *44*, 2209–2212. [CrossRef]
17. Starowicz, M.; Stypuła, B. Electrochemical Synthesis of ZnO Nanoparticles. *Eur. J. Inorg. Chem.* **2008**, *2008*, 869–872. [CrossRef]
18. Starowicz, M.; Stypuła, B.; Banaś, J. Electrochemical synthesis of silver nanoparticles. *Electrochem. Commun.* **2006**, *8*, 227–230. [CrossRef]
19. Dhayagude, A.C.; Nikam, S.V.; Kapoor, S.; Joshi, S.S. Effect of electrolytic media on the photophysical properties and photocatalytic activity of zinc oxide nanoparticles synthesized by simple electrochemical method. *J. Mol. Liq.* **2017**, *232*, 290–303. [CrossRef]
20. Chandrappa, K.G.; Venkatesha, T.V. Electrochemical Synthesis and Photocatalytic Property of Zinc Oxide Nanoparticles. *Nano-Micro Lett.* **2012**, *4*, 14–24. [CrossRef]
21. Sportelli, M.C.; Hötger, D.; Picca, R.A.; Manoli, K.; Kranz, C.; Mizaikoff, B.; Torsi, L.; Cioffi, N. Electrosynthesized Polystyrene Sulphonate-Capped Zinc Oxide Nanoparticles as Electrode Modifiers for Sensing Devices. In Proceedings of the Symposium K/RR—Synthesis, Characterization and Applications of Functional Materials—Thin Films and Nanostructures, San Francisco, CA, USA, 21–25 April 2014; Volume 1675.
22. Picca, R.A.; Sportelli, M.C.; Lopetuso, R.; Cioffi, N. Electrosynthesis of ZnO nanomaterials in aqueous medium with CTAB cationic stabilizer. *J. Sol-Gel Sci. Technol.* **2017**, *82*, 338–345. [CrossRef]
23. Sportelli, M.C.; Picca, R.A.; Cioffi, N. Recent advances in the synthesis and characterization of nano-antimicrobials. *TrAC Trends Anal. Chem.* **2016**, *84*, 131–138. [CrossRef]
24. Kumar, R.; Umar, A.; Kumar, G.; Nalwa, H.S. Antimicrobial properties of ZnO nanomaterials: A review. *Ceram. Int.* **2017**, *43*, 3940–3961. [CrossRef]
25. Sportelli, M.C.; Picca, R.A.; Manoli, K.; Re, M.; Pesce, E.; Tapfer, L.; Di Franco, C.; Cioffi, N.; Torsi, L. Surface analytical characterization of Streptavidin/poly(3–hexylthiophene) bilayers for bio-electronic applications. *Appl. Surface Sci.* **2017**, *420*, 313–322. [CrossRef]

26. Picca, R.A.; Manoli, K.; Luciano, A.; Sportelli, M.C.; Palazzo, G.; Torsi, L.; Cioffi, N. Enhanced stability of organic field-effect transistor biosensors bearing electrosynthesized ZnO nanoparticles. *Sens. Actuators B Chem.* **2018**, *274*, 210–217. [CrossRef]
27. Sarfraz, S.; Ali, S.; Khan, S.A.; Shah, K.H.; Amin, S.; Mujahid, M.; Jamil, S.; Janjua, M.R.S.A. Phase diagram and surface adsorption behavior of benzyl dimethyl hexadecyl ammonium bromide in a binary surfactant-water system. *J. Mol. Liq.* **2019**, *285*, 403–407. [CrossRef]
28. Rahman, Q.I.; Ahmad, M.; Misra, S.K.; Lohani, M.B. Hexagonal ZnO nanorods assembled flowers for photocatalytic dye degradation: Growth, structural and optical properties. *Superlattices Microstruct.* **2013**, *64*, 495–506. [CrossRef]
29. Sun, X.M.; Chen, X.; Deng, Z.X.; Li, Y.D. A CTAB-assisted hydrothermal orientation growth of ZnO nanorods. *Mater. Chem. Phys.* **2003**, *78*, 99–104. [CrossRef]
30. Maiti, U.N.; Nandy, S.; Karan, S.; Mallik, B.; Chattopadhyay, K.K. Enhanced optical and field emission properties of CTAB-assisted hydrothermal grown ZnO nanorods. *Appl. Surface Sci.* **2008**, *254*, 7266–7271. [CrossRef]
31. Hales, M.C.; Frost, R.L. Synthesis and vibrational spectroscopic characterisation of synthetic hydrozincite and smithsonite. *Polyhedron* **2007**, *26*, 4955–4962. [CrossRef]
32. Coblentz Society Inc. NIST Standard Reference Data: Reference Infrared Spectra. Available online: https://webbook.nist.gov/chemistry/ (accessed on 10 December 2019).
33. Dimakis, V.T.; Gavalas, V.G.; Chaniotakis, N.A. Polyelectrolyte-stabilized biosensors based on macroporous carbon electrode. *Anal. Chim. Acta* **2002**, *467*, 217–223. [CrossRef]
34. Pudukudy, M.; Yaakob, Z. Facile Synthesis of Quasi Spherical ZnO Nanoparticles with Excellent Photocatalytic Activity|SpringerLink. *J. Clust. Sci.* **2015**, *26*, 1187–1201. [CrossRef]
35. National Institute of Standards and Technology XPS Database. Available online: http://srdata.nist.gov/xps (accessed on 10 December 2019).
36. Winiarski, J.; Tylus, W.; Winiarska, K.; Szczygieł, I.; Szczygieł, B. XPS and FT-IR Characterization of Selected Synthetic Corrosion Products of Zinc Expected in Neutral Environment Containing Chloride Ions. *J. Spectrosc.* **2018**, *2018*, 2079278. [CrossRef]
37. Cocco, F.; Elsener, B.; Fantauzzi, M.; Atzei, D.; Rossi, A. Nanosized surface films on brass alloys by XPS and XAES. *RSC Adv.* **2016**, *6*, 31277–31289. [CrossRef]
38. Deroubaix, G.; Marcus, P. X-ray photoelectron spectroscopy analysis of copper and zinc oxides and sulphides. *Surface Interface Anal.* **1992**, *18*, 39–46. [CrossRef]
39. Dake, L.S.; Baer, D.R.; Zachara, J.M. Auger parameter measurements of zinc compounds relevant to zinc transport in the environment. *Surface Interface Anal.* **1989**, *14*, 71–75. [CrossRef]
40. Bera, S.; Dhara, S.; Velmurugan, S.; Tyagi, A.K. Analysis on Binding Energy and Auger Parameter for Estimating Size and Stoichiometry of ZnO Nanorods. *Int. J. Spectrosc.* **2012**, *2012*, 371092. [CrossRef]
41. Kowalczyk, S.P.; Pollak, R.A.; McFeely, F.R.; Ley, L.; Shirley, D.A. $L_{2,3}M_{45}M_{45}$ Auger Spectra of Metallic Copper and Zinc: Theory and Experiment. *Phys. Rev. B* **1973**, *8*, 2387. [CrossRef]
42. Supraja, N.; Prasad, T.N.V.K.V.; Gandhi, A.D.; Anbumani, D.; Kavitha, P.; Babujanarthanam, R. Synthesis, characterization and evaluation of antimicrobial efficacy and brine shrimp lethality assay of Alstonia scholaris stem bark extract mediated ZnONPs. *Biochem. Biophys. Rep.* **2018**, *14*, 69–77. [CrossRef]

nanomaterials

MDPI

Article

Enhanced Antifungal Activities of Eugenol-Entrapped Casein Nanoparticles against Anthracnose in Postharvest Fruits

Yang Xue, Shitong Zhou, Chenyue Fan, Qizhen Du * and Peng Jin *

The Key Laboratory for Quality Improvement of Agricultural Products of Zhejiang Province, The College of Agricultural and Food Sciences, Zhejiang a & F University, Hangzhou 311300, China; gxgxy0205@163.com (Y.X.); zst18846494139@163.com (S.Z.); fffffcy1021@163.com (C.F.)

* Correspondence: qizhendu@163.com (Q.D.); jinpeng@zafu.edu.cn (P.J.); Tel.: +86-571-63742176 (Q.D.); +86-18368187965 (P.J.); Fax: +86-571-88218710 (P.J.)

Received: 19 November 2019; Accepted: 11 December 2019; Published: 13 December 2019

Abstract: This study aims to improve the antifungal effects of eugenol through low-energy self-assembly fabrication and optimization of eugenol-casein nanoparticles (EC-NPs). Optimized EC-NPs (eugenol/casein ratio of 1:5) were obtained with a mean size of 307.4 ± 2.5 nm and entrapment efficiency of 86.3% ± 0.2%, and showed high stability under incubated at 20 and 37 °C for 48 h. EC-NPs exhibited satisfactory sustained-release effect at 20 °C or 37 °C, with remaining eugenols amounts of 79.51% and 53.41% after 72 h incubation, respectively, which were significantly higher than that of native eugenol (only 26.40% and 19.82% after the first 12 h). EC-NPs exhibited a greater antifungal activity (>95.7%) against spore germination of fungus that was greater than that of native eugenol, showed 100% inhibition of the anthracnose incidence in postharvest pear after 7 d. EC-NPs is potential as an environmental-friendly preservatives in the food industry.

Keywords: essential oil; encapsulation; bovine casein; antifungal activity; fruit preservation

1. Introduction

Up to now the low-cost and efficient of synthetic chemicals (i.e., inorganic salts, organic reagents, fungicides and pesticides) are widely used in the decay-controlling against postharvest diseases since the decay caused by spoilage microorganism invasion brings huge economic loss [1,2]. Considering to the food safety and human health, natural compounds that have low health or environmental impact are receiving wide attention [3,4]. Plant-derived bioactive substances have been applied as natural preservatives (e.g., essential oils, Base Natural, a commercial preservative) in the food industry due to their antifungal properties [5–7]. Eugenol (1,2-methoxy-4-(2-propenyl)-phenol), a principal component of the herbal essential oil from basil, has been classified as GRAS (generally recognized as safe) food additives, because reports indicated it has potential for the food field due to their antimicrobial properties against a wide range of microorganisms [8,9].

However, eugenol possesses high volatility and low water-solubility, which severely handicap its utilization due to the short timeliness for antibiosis [10]. In recent decades, the embedding and encapsulation has become a novel strategy to markedly offer numerous benefits for active compounds, for example, protection against oxidation, enhanced stability, retention of volatile ingredients and permeability [11]. Recently, encapsulation of eugenol showed enhanced bioactivity and stability [12,13]. However, the high-energy techniques or cumbersome processes for nano-formulation are difficult to scale-up for practical application. In addition, the preparation of some nanocarriers requires the addition of some chemical reagents, such as, dichloromethane [14], surfactant [15], which increases the risk of potential toxicity and safety that limit their applications in food industry [16]. Therefore,

eco-safe technologies for the nano-formulation of eugenol are needed to develop, so that they can be used in the food industry [17,18].

Caseins, the major component of milk proteins in bovine milk, is a low-cost and commercially available food-grade additive in food and beverage [19]. In the native state of caseins, they are very stable for high temperature and pressure (for example, treated by 100 °C and 100 MPa without losing their essential integrity). The natural caseins can self-assemble to the micellar structure in solution, with diameters in the approximate range 10–400 nm [20]. The amphiphilic nature of the caseins causes them to act more as block copolymers micelles of alternating charge and hydrophobicity, which are suitable for encapsulating the compounds of poor water solubility in the hydrophobic core of the micelle [21]. Therefore, caseins have been widely used as efficient nanocarriers for hydrophobic drug for controlled release [22]. Accordingly, the present study aims to prepare eugenol-entrapped casein nanoparticles through a low-energy and simple self-emulsifying technique, which will provide a promising alternate for nano-formulation of eugenol against postharvest decay of fruits and vegetables.

2. Materials and Methods

2.1. Materials

Bovine casein (>98%) and eugenol (99%) were obtained from Sigma–Aldrich, Chemical Co. (St. Louis, MO, USA). Ethanol was purchased from China National Pharmaceutical Industry Co. Ltd. (Beijing, China). All solutions were prepared by using deionized water (Millipore, Bedford, MA, USA). All other reagents were of analytical grade.

2.2. Preparation of Nanoparticles

Bovine casein used for the preparation of nanoparticles was fully dissolved in deionized water to form a final concentration of 20 mg/mL. Eugenol was dissolved into ethanol with a final concentration of 200 mg/mL. The casein solution (10 mL) in 50 mL glass beaker was stirred for 30 min at 500 rpm, and then eugenol solution was stepwisely added into the casein solution with a volume of 5 μL. After the addition of eugenol solution, the mixture solution was continued to stir for 30 min to yield eugenol-casein nanoparticle (EC-NP) dispersion. The denatured protein in the dispersion was removed through centrifugation at 12,000 rpm for 10 min. The EC-NPs samples were stored in a freezer (4 °C) for further use.

2.3. Characterization of EC-NPs

The size distribution of the fresh nanoparticles was determined as mentioned in our previous study [23]. In brief, 500 μL of the nanoparticles suspension were diluted into 5 mL of pre-filtered deionized water. The analysis was performed in dynamic light scattering using a Zetasizer ZS 90 instrument (Malvern Instruments, Malvern, UK) at 25 °C temperature, employing a nominal 5 mW He−Ne laser operating at a 633 nm wavelength and 173° scattering angle. The EE was obtained by determining the free eugenol in EC-NPs solution, which was separated by using an Amicon Ultra-7K centrifugal filter device (7000 MWCO, Millipore Corp., Billerica, MA, USA.). The quantitative analysis of eugenol was performed by a high-performance liquid chromatographic (HPLC) Shimadzu LC 20A system (Shimadzu, Kyoto, Japan), consisted of two LC-10A pumps, an SIL-10Avp autosampler, an SPD-M10Avp UV detector and a Symmetry C18 (5 μm, 4.6 mm × 250 mm) column. The mobile phase was composed of methanol/water (65:35) at a constant flow rate of 1 mL/min at 30 °C, and monitored at 282 nm [24]. All data were expressed as the mean value of three independent batches of the samples.

The entrapment efficiency (EE, in percent) of eugenol was calculated as the percentage of entrapped eugenol to total eugenol (as the following equation).

$$\text{EE\%} = \frac{\text{Total amount of eugenol} - \text{free eugenol amount}}{\text{Total amount of eugenol}} \times 100\%$$

The morphological characterization of eugenol nanoparticles was performed by transmission electron microscopy (TEM), (Hitachi, H-9500E, Tokyo, Japan) [25]. Briefly, a dispersion of NPs diluted with pure water was adsorbed onto a carbon-coated formvar film that was attached to a metal specimen grid. Excess sample was removed through blotting and the grid was covered with a small drop of staining solution (2% *w/v* phosphotungstic acid). The staining solution was left on the grid for a few min and then the excess solution was drained. The sample was allowed to air dry thoroughly and was then examined using a transmission electron microscope.

2.4. Stability Assessments of EC-NPs

To investigate the effects of temperatures on stability of the EC-NPs dispersions, 5 mL samples solution were placed in glass vials and stored at 4 °C, 20 °C and 37 °C, respectively. The entrapment efficiency (EE) of the dispersions was measured at predetermined time intervals (0, 2, 4, 8, 12, 24, 48 and 72 h) for the stability evaluation of the nanoparticles. After a treatment of the EC-NPs dispersion containing 4 mg/mL eugenol and 20 mg/mL caseins, the released eugenol and EE of EC-NPs were measured according to the above method. a mixture solution containing 4 mg/mL eugenol and 20 mg/mL caseins was used for a control. All samples were measured in triplicate.

2.5. Cell Culture

Luria−Bertani (LB) medium (g/L; 10 g tryptone, 5 g yeast extract and 10 g NaCl) added 1% glucose was used for the isolation and culture of spoilage microorganisms. Spoilage bacteria *Botrytis cinerea* [26] was isolated from decayed pear fruits. Mycelium was precultured on LB agar media at 30 °C for 5 d as the seed. The spore suspension was prepared as our previous description [23], by washing the 20-day seed cultures with sterile water containing 0.01% (v/v) Tween-80 and then diluting them to 1×10^5 spores/mL with the aid of a hemocytometer.

2.6. Determination of Antifungal Activity

The antifungal sensitivity of free eugenol and EC-NPs nanoparticles was determined by modified disc diffusion method [27]. Briefly, various amounts of free eugenol (1.00, 4.03, 8.04, 10.06, 15.08, 20.11, 25.13, 30.16, 35.19, 40.21 and 50.24 μg/mL) and equivalent eugenol-entrapped casein nanoparticles solution were uniformly smeared onto the LB agar media, respectively. Of the prepared spore suspension 5 μL was inoculated on the sterile filter paper at the center of the petri dish, and then incubated at 30 °C. The same manual tests were performed for control without eugenol. Finally, the inhibition rate of mycelium growth was calculated as a percentage of the control groups without eugenol. Minimum inhibitory concentration (MIC) is defined as the lowest concentration of eugenol or EC-NPs, which completely inhibits visible growth on solid media. To further quantitatively investigate the sustained-release effect of EC-NPs on the spore germination, the spore suspension was inoculated into 20 mL LB medium, added with an initial concentration of 40 μg/mL eugenol in both nanoencapsulated and nonencapsulated groups, respectively, and then cultured at 30 °C with shaking (200 rpm). The optical density at 600 nm (OD600) was used to monitor cell growth. The control was set without eugenol in the culture, and the entire experiment contained three replicates.

2.7. Effects of EC-NPs on Anthracnose Disease on Pear Fruit

The epidermis of pear fruits (a pear orchard in Hebei, China) was scrub with sterile saline, and then inoculated with 5 μL of *Botrytis cinerea* spore suspension (1×10^5 spores/mL) in the middle of each fruit with a sterile injection needle. An equivalent amount of eugenol (4 mg) of free eugenol (1 mL) and EC-NPs solution (1 mL) was sprayed onto the pear fruit surface. Each group contained three replicates of 25 pear fruits, and the control group was correspondingly treated with sterile distilled water (1 mL). Subsequently, all of the treated samples were stored at 25 °C in a sterile room. Disease incidence and lesion diameters were recorded. The incidence was defined as the appearance of decay spots and the

color changes of flesh at the inoculation hole. All data were analyzed by using Duncan's multiple range tests in the SPSS 13.0 software (IBM Corp., Armonk, NY, USA)

3. Results and Discussion

3.1. Characterization of Eugenol-Entrapped Casein Nanoparticles

Casein nanocarriers are widely used as delivery systems for hydrophobic drugs and bioactive compounds due to its excellent emulsification [28] and self-assembled ability [22]. In this work, eugenol-loaded casein nanoparticles (EC-NPs) were prepared through the pre-formation of spherical casein micelles followed by the stirring treatment of the mixture with eugenol, resulting in assemblies of casein/eugenol complexes at the nanometric scale. The effects of the eugenol concentration on the particle size, polydispersity (PDI), zeta potential, and entrapment efficiency were further studied as shown in Table 1. The increase of the eugenol amount from 1 to 6 mg/mL resulted in formation of larger nanoparticles from 249.3 to 333.8 nm. Similar results were observed in previous studies, in which the presence of antimicrobial agent yielded a more viscous dispersed phase, resulting in larger particles [13,14]. Meantime, PDI values of casein nanoparticles was found to in the range of 0.261–0.333, which indicates moderate size distribution [29]. Size and size distribution are important characteristic indexes because it is related to the release of active compound. Generally, spherical shape and better dispersity are beneficial to the release of active compound [30]. Zeta potential is also an important parameter to reflect the physicochemical and biological stabilities of nanoparticles in dispersion [31], which helps the formulation to enhance the long-term stability [32]. As shown in Table 1, the addition of eugenol slightly increased negative charges on the particle surface from −14.47 to −21.91 mV, which indicated that the nanoparticles with eugenol concentration of 4 mg/mL exhibited ideal particle stability.

Table 1. Effects of the concentration of eugenol on the particle size, zeta potential, polydispersity indexes (PDI) and entrapment efficiency (EE) of eugenol loading in casein nanoparticles.

Eugenol (mg/mL)	Size (nm)	PDI	Zeta (mV)	EE (%)
1	249.3 ± 3.3	0.261 ± 0.003	−14.47 ± 0.31	90.4 ± 0.8
2	278.3 ± 5.1	0.270 ± 0.012	−16.61 ± 0.11	91.1 ± 0.3
3	289.6 ± 1.8	0.283 ± 0.024	−20.64 ± 0.23	87.1 ± 0.6
4	307.4 ± 2.5	0.284 ± 0.033	−21.18 ± 0.67	86.3 ± 0.2
5	333.8 ± 4.8	0.311 ± 0.009	−21.91 ± 0.37	70.1 ± 1.2
6	326.9 ± 6.3	0.333 ± 0.007	−20.20 ± 0.26	67.1 ± 0.9

Entrapment efficiency (EE) is used to indicate the amount of compound entrapped into the polymeric matrix. The EE of the nanoparticles reached the maximum value of 91.1% when eugenol concentration was 2 mg/mL. However, with the eugenol rising from 2 to 6 mg/mL, the EE decreased from 91.1% to 67.1%. This result was in agreement with the nanoethosomes in our previous work [23]. The EC-NPs made of 2 mg/mL of eugenol exhibited a spherical shape (Figure 1a). Furthermore, to optimize the formulation of the nanoparticles, the antifungal effects of EC-NPs with consistent eugenol amount were evaluated in LB media against anthracnose strain *Botrytis cinerea*. As shown in Figure 1b, EC-NPs with 4 mg/mL eugenol showed the highest antifungal efficiency of 88.5% against anthracnose after 48 h of inoculation. There was a positive correlation between eugenol concentration and antifungal efficiency in this study. This result also showed that this increase in particle size did not compromise the antifungal action of the eugenol component-grafted EC-NPs.

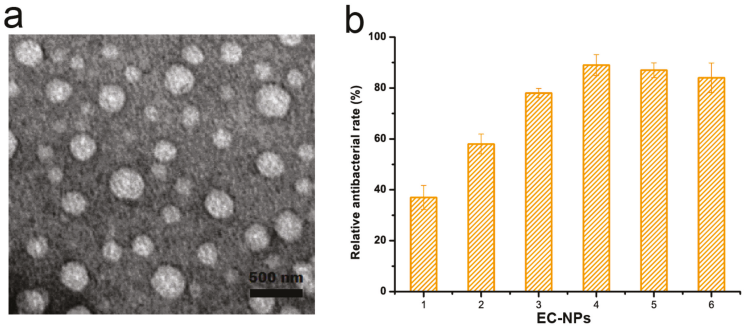

Figure 1. Characterization of eugenol nanoparticles. (**a**) Transmission electron microscopic image of eugenol-casein nanoparticles (EC-NPs). (**b**) Effects of eugenol concentration (mg/mL) on antifungal effect of eugenol-entrapped casein nanoparticles. The mean ± SD for three replicates are illustrated.

3.2. Release Assessment of Eugenol Nanoparticles

In order to study the stability effects of encapsulated eugenol compared with that of native eugenol, the eugenol residual amount of EC-NPs and free eugenol in solution was investigated for incubation at different temperatures. As shown in Figure 2, EC-NPs was stable for 72 h when incubated at 4 °C or 20 °C, with still 88.75% and 79.51% of remaining eugenol in the EC-NPs, respectively. Even after 72 h incubation at 37 °C, the EC-NPs showed a satisfactory slow release trend, possessing 53.41% of remaining eugenol. However, the unencapsulated eugenol solution gradually lose eugenol at 4 °C, only 21.09% of remaining eugenol after 72 h. As to 20 and 37 °C, the native eugenol possessed remaining eugenol amounts of only 26.4% and 19.82% after 12 h, respectively, and the eugenol lose about 80% of the initial amount, and especially the eugenol disappeared almost after 48 h. This result further clearly confirmed that native eugenol usually occurs with the burst effect dissipation and resulted in the short-term existence, which greatly compromised its long-lived antifungal effect [23]. The higher amounts of eugenol remaining in solution containing EC-NPs lead to the better lasting antifungal effect, which implied that the encapsulation of eugenol into casein nanoparticles could improve the stability and produce maintain-released effect of eugenol. Furthermore, the particle size, PDI and zeta potential of EC-NPs were further investigated for incubation at different temperatures (Table 2). These results showed that EC-NPs exhibited remarkable physical and chemical stability at 20 °C for 48 h though the size and PDI values present slight increase.

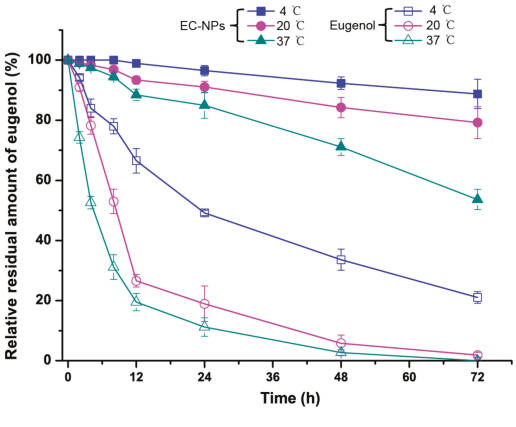

Figure 2. Effects of temperature on the eugenol stability in solution and in EC-NPs dispersion.

Table 2. Effects of the storage temperature on the particle size, zeta potential and polydispersity indexes (PDI) of EC-NPs nanoparticles after 48 h.

Temperature	Size (nm)	PDI	Zeta Potential (mV)
Control	307.4 ± 2.5	0.284 ± 0.033	−21.18 ± 0.67
4 °C	305.4 ± 1.9	0.289 ± 0.009	−21.01 ± 0.13
20 °C	310.3 ± 6.2	0.290 ± 0.008	−17.21 ± 0.32
37 °C	312.6 ± 4.2	0.303 ± 0.014	−17.32 ± 0.24

3.3. Antifungal Assessment of Eugenol Nanoparticles

The antifungal activity of eugenol and its potency were quantitatively assessed by determining the MIC. Table 1 show the MIC of free eugenol and EC-NPs nanoparticles against anthracnose in vitro. The difference in the mycelium diameter of the inhibition zone indicates the sensitivity of fungal strains to various concentrations of free eugenol or EC-NPs. The MIC values of EC-NPs against anthracnose were 40.21 μg/mL, which were slightly lower than those of free eugenol (50.24 μg/mL), which indicate EC-NPs possessed higher antifungal activity than free eugenol (Table 3). These results further show the property of eugenol and EC-NPs, i.e., they are potential to inhibit the growth of anthracnose in common fruit. Compared with the free form of eugenol, the antifungal ability of EC-NPs was compromised at the initial period of antifungal reactions [33], due to the slow release profile of the nanoencapsulated eugenol. This result was consistent with our previous work on the antifungal effect of eugenol nanoethosomes [23].

Table 3. Effects of eugenol formulation with various concentrations on the mycelial growth inhibition.

$C_{Eugenol}$ [a] (ug/mL)	Mycelial Growth Inhibition (%) [b]		
	Native Eugenol	Casein-Eugenol Mixture	EC-NPs
1.00	0.00	0.00	0.00
4.03	1.88 ± 0.67	2.38 ± 1.02	1.47 ± 0.76
8.04	8.41 ± 1.35	7.32 ± 1.03	7.57 ± 0.87
10.06	9.41 ± 0.87	10.91 ± 2.17	9.24 ± 0.39
15.08	17.62 ± 2.23	15.62 ± 1.98	14.67 ± 2.21
20.11	24.97 ± 2.62	27.27 ± 2.01	31.48 ± 1.62
25.13	28.34 ± 3.12	30.34 ± 1.36	36.98 ± 0.28
30.16	38.70 ± 1.26	37.40 ± 3.72	44.40 ± 1.31
35.19	68.21 ± 1.67	69.93 ± 0.89	87.9 ± 2.34
40.21	87.43 ± 3.17	89.21 ± 2.34	100 ± 0.00
50.24	100 ± 0.00	100 ± 0.00	100 ± 0.00

[a] The eugenol concentration is defined as all the eugenol amount in Luria–Bertani (LB) agar media. [b] The inhibition ratio is defined as a relative percentage of the control mycelial diameter after 72 h culture.

Evaluation of antifungal ability of EC-NPs was also performed by observing its inhibition effect on the mycelial diameter of anthracnose on LB agarose plate. As shown in Figure 3a, after incubation for 48 h, the mycelial growth was observed with significant differences between the EC-NPs group and other groups. Compared with the control, native eugenol and casein-eugenol mixture gave 50% inhibition of the mycelial growth. In contrast, the EC-NPs showed a completely inhibition on the fungal growth. Furthermore, the antifungal effects of EC-NPs were evaluated by calculating the inhibition rate on spore germination of fruit *Botrytis cinerea* pathogen fungus. As shown in Figure 3b, after 24 h of incubation, the spore germination rate of native eugenol group and casein-eugenol mixture group already reached to 51.8% and 61.1%, respectively, while the spore germination rate of EC-NPs were only 4.3% after 48 h and 38.7% after 72 h. Obviously, the fungal inhibition effect of EC-NPs was stronger than the native eugenol or casein-eugenol mixture, indicating that the nano-formulation of eugenol could effectively improve the fungal inhibition effectiveness, which should be contributed by the maintain-release of eugenol from EC-NPs, which prolonged the action time of eugenol against fungi. In the previous work

we have determined that native eugenol is usually volatile with a burst-effect release pattern, resulted in rapid dissipation during the initial period [23], while EC-NPs gave a maintain-release during a long time. In result, EC-NPs possess the potential for the antifungal application in post-harvest fruits.

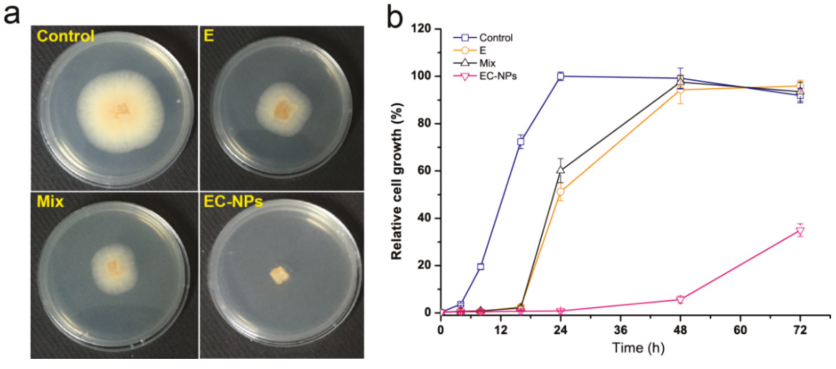

Figure 3. Evaluation of antifungal effects of eugenol nanoparticles. (**a**) Effects of native eugenol (E), casein-eugenol mixture (Mix) and eugenol-entrapped casein nanoparticles (EC-NPs) on the mycelial growth and (**b**) dynamic analyses of the spore germination in liquid media treated with the samples.

3.4. EC-NPs as Preservative against Fruit Corruption

EC-NPs was further determined the effectiveness on suppressing the anthracnose of fruits caused by the pathogenic invasion. Compared to the native eugenol, the rot of pear fruit caused by *Botrytis cinerea* strain was employed to test the effectiveness. After spore suspension (10 μL, 1×10^5 CFU/mL) was injected into epidermis of the pear fruit, the rot of pear fruit was observed by sprayed native eugenol or EC-NPs. As shown in Figure 4a, after being inoculated for 7 d, the obvious rots (black spot) were observed on the epidermis at the control group (treatment with sterilized water instead of preservatives), and minor wound decay occurred in native eugenol-treated group. In contrast, almost no any black spot and wound decay was observed in EC-NPs-treated group. After cutting open the inoculation site, we found that both the control group and native eugenol-treated group decayed in deep pulp while EC-NPs-treated group did not decay in deep pulp (Figure 4b). Obviously, EC-NPs completely suppressed the pathogen. As we known, nanoparticles possess excellent permeability for cortex [23,34]. Thus EC-NPs might get through the deeper pulp to deliver eugenol for antifungal. The disease incidences of control and native eugenol-treated groups reached 100% and 89% for 8 d incubation after inoculation, while that of EC-NPs group was only 23% (Figure 4c). In combination of the inhibition of the fruit rot and the disease incidences, we can conclude that EC-NPs significantly potentiate the antifungal efficacy of eugenol in inhibiting fruit anthracnose.

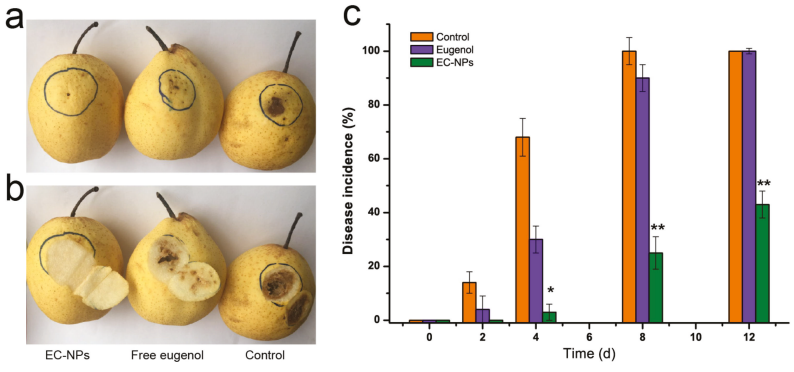

Figure 4. Effects of native eugenol and EC-NPs suppressing disease lesion of pear fruit inoculated with *Botrytis cinerea*. (**a**) Rot in the cuticular layer, (**b**) rot in pulp layer and (**c**) disease incidence of the pear fruit. Vertical bars represent the standard errors of the means of triplicate assays. The symbol * ($p < 0.05$) and ** ($p < 0.01$) indicate a significant difference between EC-NPs and native eugenol group.

4. Conclusions

Eugenol was encapsulated in casein micelles by simple process without any other additives. a mass ratio of 5:1 of caseins/eugenol yielded the highest encapsulation efficiency and stability for eugenol-casein nanoparticles (EC-NPs). EC-NPs significantly improve the antifungal efficacy against anthracnose. These results indicate that EC-NPs nanoparticles could be used as an economical and simple-manufactured preservative for postharvest fruits against microbial spoilage.

Author Contributions: P.J. and Q.D. designed the experiments, analyzed the data and wrote the paper. Y.X., S.Z. and C.F. performed the experiments.

Funding: This work was supported by the National Natural Science Foundation of China (grant numbers 31700078), the Key R&D Program Project of Zhejiang Province, China (Grant 2019C02072), the Zhejiang Agricultural and Forestry University for Talent Program (W20170029), and the Natural Science Foundation of Zhejiang Province, China (LY17C200018).

Conflicts of Interest: The authors declare no conflict of interest.

References

1. Deliopoulos, T.; Kettlewell, P.S.; Hare, M.C. Fungal disease suppression by inorganic salts: a review. *Crop Prot.* **2019**, *29*, 1059–1075. [CrossRef]
2. Qi, J.; Song, C.E.; Wang, B.; Zhou, J.; Kangasjärvi, J.; Zhu, J.; Gong, Z. Reactive oxygen species signaling and stomatal movement in plant responses to drought stress and pathogen attack. *J. Integr. Plant Biol.* **2018**, *60*, 805–826. [CrossRef] [PubMed]
3. Biesalski, H.-K.; Dragsted, L.O.; Elmadfa, I.; Grossklaus, R.; Müller, M.; Schrenk, D.; Walter, P.; Weber, P. Bioactive compounds: Safety and efficacy. *Nutrition* **2009**, *25*, 1206–1211. [CrossRef] [PubMed]
4. Yu, H.B.; Li, D.Y.; Zhang, H.F.; Xue, H.Z.; Pan, C.E.; Zhao, S.H.; Wang, L. Resveratrol inhibits invasion and metastasis of hepatocellular carcinoma cells. *J. Anim. Vet. Adv.* **2010**, *9*, 3117–3124. [CrossRef]
5. Chai, L.Q.; Meng, J.H.; Gao, J.; Xu, Y.; Wang, X.W. Identification of a crustacean β-1, 3-glucanase related protein as a pattern recognition protein in antibacterial response. *Fish Shellfish Immunol.* **2018**, *80*, 155–164. [CrossRef] [PubMed]
6. Dianella, S. Plant-derived antimicrobial compounds: Alternatives to antibiotics. *Future Microbiol.* **2012**, *7*, 979–990.
7. Zhang, H.; Li, M. Transcriptional profiling of ESTs from the biocontrol fungus Chaetomium cupreum. *Sci. World J.* **2012**, *2012*, 1–7.

8. Shah, B.; Davidson, P.M.; Zhong, Q. Nanodispersed eugenol has improved antimicrobial activity against *Escherichia coli* O157: H7 and Listeria monocytogenes in bovine milk. *Int. J. Food Microbiol.* **2013**, *161*, 53–59. [CrossRef]
9. Chen, F.; Shi, Z.; Neoh, K.; Kang, E. Antioxidant and antibacterial activities of eugenol and carvacrol-grafted chitosan nanoparticles. *Biotechnol. Bioeng.* **2009**, *104*, 30–39. [CrossRef]
10. Garg, A.; Singh, S. Enhancement in antifungal activity of eugenol in immunosuppressed rats through lipid nanocarriers. *Colloids Surf. B Biointerfaces* **2011**, *87*, 280–288. [CrossRef]
11. Zhu, Y.; Liu, C.; Xie, Z.; Liu, L.; Peng, C.; Xue, F. Botryoid-shaped nanoparticles-enhanced ELISA for ochratoxin A. *Food Agric. Immunol.* **2017**, *28*, 299–309. [CrossRef]
12. Woranuch, S.; Yoksan, R. Eugenol-loaded chitosan nanoparticles: I. Thermal stability improvement of eugenol through encapsulation. *Carbohydr. Polym.* **2013**, *96*, 578–585. [CrossRef] [PubMed]
13. Wang, L.; Zhang, Y. Eugenol nanoemulsion stabilized with zein and sodium caseinate by self-assembly. *J. Agric. Food Chem.* **2017**, *65*, 2990–2998. [CrossRef] [PubMed]
14. Gomes, C.; Moreira, R.G.; Elena, C.P. Poly (DL-lactide-co-glycolide)(PLGA) nanoparticles with entrapped trans-cinnamaldehyde and eugenol for antimicrobial delivery applications. *J. Food Sci.* **2011**, *76*, N16–N24. [CrossRef] [PubMed]
15. Ghosh, V.; Mukherjee, A.; Chandrasekaran, N. Eugenol-loaded antimicrobial nanoemulsion preserves fruit juice against, microbial spoilage. *Colloids Surf. B Biointerfaces* **2014**, *114*, 392–397. [CrossRef] [PubMed]
16. Wu, J.; Shi, M.; Li, W.; Zhao, L.; Wang, Z.; Yan, X.; Norde, W.; Li, Y. Pickering emulsions stabilized by whey protein nanoparticles prepared by thermal cross-linking. *Colloids Surf. B: Biointerfaces* **2015**, *127*, 96–104. [CrossRef]
17. McClements, D.J.; Rao, J. Food-grade nanoemulsions: Formulation, fabrication, properties, performance, biological fate, and potential toxicity. *Crit. Rev. Food Sci. Nutr.* **2011**, *51*, 285–330. [CrossRef]
18. Sokolik, C.G.; Rina, B.S.B.; Gedanken, A.; Lellouche, J.P. Proteinaceous microspheres as a delivery system for carvacrol and thymol in antibacterial applications. *Ultrason. Sonochem.* **2018**, *41*, 288–296. [CrossRef]
19. Dalgleish, D.G. On the structural models of bovine casein micelles—Review and possible improvements. *Soft Matter* **2011**, *7*, 2265–2272. [CrossRef]
20. Semo, E.; Kesselman, E.; Danino, D.; Livney, Y.D. Casein micelle as a natural nano-capsular vehicle for nutraceuticals. *Food Hydrocolloid.* **2007**, *21*, 936–942. [CrossRef]
21. Horne, D.S. Casein micelle structure: Models and muddles. *Curr. Opin. Colloid Interface Sci.* **2006**, *11*, 148–153. [CrossRef]
22. Bachar, M.; Mandelbaum, A.; Portnaya, I.; Perlstein, H.; Chen, S.E.; Barenholz, Y.; Danino, D. Development and characterization of a novel drug nanocarrier for oral delivery, based on self-assembled β-casein micelles. *J. Control. Release* **2012**, *160*, 164–171. [CrossRef] [PubMed]
23. Jin, P.; Yao, R.; Qin, D.; Chen, Q.; Du, Q. Enhancement in antibacterial activities of eugenol-entrapped ethosome nanoparticles via strengthening its permeability and sustained release. *J. Agric. Food Chem.* **2019**, *67*, 1371–1380. [CrossRef] [PubMed]
24. Liu, S.; Lin, Z.; Wang, H.; Chen, S. Quantification of eugenol and bancroftione in *Caryophylli Fructus* using high-performance liquid chromatography. *J. Chinses Pharm. Sci.* **2010**, *19*, 459–463. [CrossRef]
25. Zheng, Y.; Xiao, L.; Yu, C.; Jin, P.; Qin, D.; Xu, Y.; Yin, J.; Liu, Z.; Du, Q. Enhanced anti-arthritic efficacy by nanoparticles of (-)-Epigallocatechin gallate-glucosamine-casein. *J. Agric. Food Chem.* **2019**, *67*, 6476–6486. [CrossRef] [PubMed]
26. Gao, W.; Long, L.; Xu, L.; Lindsey, K.; Zhu, L. Suppression of the homeobox gene *HDTF1* enhances resistance to *Verticillium dahliae* and *Botrytis cinerea* in cotton. *J. Integr. Plant Biol.* **2016**, *58*, 503–513. [CrossRef]
27. Dhara, L.; Tripathi, A. Antimicrobial activity of eugenol and cinnamaldehyde against extended spectrum beta lactamase producing enterobacteriaceae by in vitro and molecular docking analysis. *Eur. J. Integr. Med.* **2013**, *5*, 527–536. [CrossRef]
28. Shapira, A.; Markman, G.; Assaraf, Y.G.; Livney, Y.D. β-casein–based nanovehicles for oral delivery of chemotherapeutic drugs: Drug-protein interactions and mitoxantrone loading capacity. *Nanomedicine* **2010**, *6*, 547–555. [CrossRef]
29. Huo, Q. Protein complexes/aggregates as potential cancer biomarkers revealed by a nanoparticle aggregation immunoassay. *Colloids Surf. B Biointerfaces* **2010**, *78*, 259–265. [CrossRef]

30. Silva, L.M.; Hill, L.E.; Figueiredo, E.; Gomes, C.L. Delivery of phytochemicals of tropical fruit by-products using poly (DL-lactide-co-glycolide)(PLGA) nanoparticles: Synthesis, characterization, and antimicrobial activity. *Food Chem.* **2014**, *165*, 362–370. [CrossRef]
31. Müller, R.; Jacobs, C.; Kayser, O. Nanosuspensions as particulate drug formulations in therapy: Rationale for development and what we can expect for the future. *Adv. Drug Del. Rev.* **2001**, *47*, 3–19. [CrossRef]
32. Li, B.; Du, W.; Jin, J.; Du, Q. Preservation of (−)-epigallocatechin-3-gallate antioxidant properties loaded in heat treated β-lactoglobulin nanoparticles. *J. Agric. Food Chem.* **2012**, *60*, 3477–3484. [CrossRef] [PubMed]
33. Wattanasatcha, A.; Rengpipat, S.; Supason, W. Thymol nanospheres as an effective anti-bacterial agent. *Int. J. Pharm.* **2012**, *434*, 360–365. [CrossRef] [PubMed]
34. Bédard, M.F.; Braun, D.; Sukhorukov, G.B.; Skirtach, A.G. Toward self-assembly of nanoparticles on polymeric microshells: Near-ir release and permeability. *ACS Nano.* **2008**, *2*, 1807–1816. [CrossRef]

nanomaterials

MDPI

Article

Layer by Layer Antimicrobial Coatings Based on Nafion, Lysozyme, and Chitosan

Ella N. Gibbons [1], Charis Winder [2], Elliot Barron [2], Diogo Fernandes [3], Marta J. Krysmann [1,*], Antonios Kelarakis [2,*], Adam V. S. Parry [4] and Stephen G. Yeates [4]

[1] School of Pharmacy and Biomedical Sciences, University of Central Lancashire, Preston PR1 2HE, UK; engibbons3@uclan.ac.uk
[2] UCLan Research Centre for Smart Materials, School of Physical Sciences and Computing, University of Central Lancashire, Preston PR1 2HE, UK; ciwinder@uclan.ac.uk (C.W.); ebarron93@live.co.uk (E.B.)
[3] Malvern Panalytical, Enigma Business Park, Grovewood Road, Malvern, Worcestershire WR14 1XZ, UK; dajfernandes@uclan.ac.uk
[4] School of Chemistry, University of Manchester, Manchester M13 9PL, UK; adam.parry@manchester.ac.uk (A.V.S.P.); stephen.yeates@manchester.ac.uk (S.G.Y.)
* Correspondence: mkrysmann@uclan.ac.uk (M.J.K.); akelarakis@uclan.ac.uk (A.K.)

Received: 14 October 2019; Accepted: 28 October 2019; Published: 4 November 2019

Abstract: The study focuses on the development of a new family of layer-by-layer coatings comprising Nafion, lysozyme and chitosan to address challenges related to microbial contamination. Circular dichroism was employed to gain insights on the interactions of the building blocks at the molecular level. Quartz crystal microbalance tests were used to monitor in real time the build-up of multilayer coatings, while atomic force microscopy, contact angle and surface zeta potential measurements were performed to assess the surface characteristics of the multilayer assemblies. Remarkably, the nanocoated surfaces show almost 100% reduction in the population of both *Escherichia coli* and *Staphylococcus aureus*. The study suggests that Nafion based synergistic platforms can offer an effective line of defence against bacteria, facilitating antimicrobial mechanisms that go beyond the concept of exclusion zone.

Keywords: antimicrobial; layer-by-layer; coatings; Nafion; multilayers

1. Introduction

The quest for advanced antimicrobial materials is driven by the large diversity of remarkably adaptable pathogens coupled with the alarming evolution of drug resistant strains that cause serious infections to humans and the ecosystem [1–4]. Despite preventive measures and increased public awareness, contiguous bacterial colonies are found on a variety of surfaces such as foodservice equipment, water distribution pipelines, swimming pools, lakes, rivers, public transport vehicles, toilets, door handles, home appliances, and air-conditioning filters. At the same time, bloodstream infections originating from catheters, implants, and surgical tools result in enormous costs for the healthcare system [5].

Layer by layer (LbL) assemblies, based on the alternated adsorption of oppositely charged molecules or nanoparticles, is a versatile approach that affords control at the nanoscale level, generating stable and robust coatings [6–8]. Based on those principles, a wide range of LbL antimicrobial coatings comprising polymers, nanoparticles, enzymes, peptides, biological molecules, and antibiotics as building units has been reported [9]. Their antimicrobial performance relies on bioadhesion resistance, contact-killing, release-killing, or a combination of those mechanisms [9].

Along those lines, the positively charged amidated ponericin G1, a strong antimicrobial against *Staphylococcus aureus* (*S. aureus*), was incorporated to hydrolytically degradable LbL coatings based on

poly (b-amino esters). The peptide was released from the film in a controlled manner and was effective in inhibiting bacteria attachment, thus demonstrating significant potential for implant materials and bandages [10]. In a contact-killing demonstration, LbL assemblies comprising poly (allylamine hydrochloride) and poly (sodium 4-styrene sulfonate) showed sufficient density of mobile cations that endowed significant antimicrobial activity [11]. In an anti-adhesion strategy, poly (L-lysine)/poly (L-glutamic acid) multilayers with the top bilayers bearing the pegylated polyanion drastically suppressed the adsorption of *Escherichia coli* (*E. coli*) [12].

In this work, we focus on LbL assemblies comprising two naturally occurring antimicrobials, namely lysozyme [13] and chitosan [14] along with Nafion, a synthetic ionomer with a robust, Teflon-like backbone bearing hydrophilic sulphonic acid groups. As a direct consequence of its chemical composition, Nafion forms proton exchange membranes with supreme structural and chemical stability that set the benchmark for fuel cell applications [15]. Moreover, Nafion has been shown to possess an exclusion zone against bacterial growth, an effect that has been attributed to repulsive forces between its negatively charged surface and the similarly charged cell membranes [16,17]. In this work, we demonstrate that, although the surface charges of Nafion have been neutralised (if not overcompensated) by the adsorption of positively charged molecules, the coatings show remarkable antimicrobial activity against *E. coli* and *S. aureus*. In that sense, our work paves the way for the development of a new family of Nafion-based nanostructured coatings with enhanced antimicrobial performance that do not necessarily rely on exclusion zone effects.

2. Materials and Methods

2.1. Materials

Nafion (DE 1021) (Chemours Company, Wilmington, DE, USA) with a total H^+ exchange capacity of 1.1 mequiv/g was obtained as a 10 wt% dispersion in water (Ion-Power) or as a 15 wt% dispersion in a mixture of low aliphatic alcohols (3-propanol, ethanol, and others) and water (Ion Power). Lysozyme (Buchs, Switzerland) from chicken eggs (106 U/mg) and medium molecular weight chitosan (Milwaukee, WI, USA) were obtained from Sigma Aldrich (Dorset, U.K). Chitosan was dispersed in water containing 0.1 wt% acetic acid.

2.2. Quartz Crystal Microbalance with Dissipation Monitoring (QCM-D)

The quartz crystal microbalance with dissipation monitoring (QCM-D) tests were performed using a Q-sense E1 unit (Biolin Scientific, Stockholm, Sweden) equipped with a Peltier-controlled flow cell (flow rate was set at 0.2 mL/min) with temperature accuracy of 0.02 °C. Au-modified crystals with a fundamental resonance frequency close to 5 MHz and diameter 150 nm were spin-coated (by depositing a drop of a 0.5 wt% Nafion solution in ethanol) and were then left at room temperature for at least seven days. All measurements included an initial equilibrium step of the crystal in the air to determine the fundamental resonant frequency, followed by an equilibrium step under constant flow of water to establish the baseline of the hydrated surface.

On the basis of Sauerbrey relation: $\Delta m = -(C/N)\,\Delta f$, deposition of a uniform layer with mass Δm reduces the resonant frequency of the crystal by Δf, where N is the overtone number (herein all values reported refer to $N = 3$) and C is the integrated crystal sensitivity that depends upon the intrinsic properties and the thickness of the crystal [18]. The dissipation factor D is defined as $D = E_d/(2\pi E_s)$, where E_d is the energy dissipated during one period of oscillation and E_s is the energy stored in the system [19].

2.3. Contact Angle Measurements

The contact angle of distilled water droplets (5 μL) deposited on the coated quartz crystals was determined by means of an OptoSigma (OptoSigma Corp., Santa Ana, CA, USA) optical tensiometer

using the standard sessile drop technique (Digidropmeter, GBX). The photos were captured 20 s following the deposition of the droplets. A minimum of five spots on each specimen were measured.

2.4. Circular Dichroism (CD) Spectrometry

Lysozyme solutions in the presence and absence of Nafion were inserted to a quartz cuvette of 0.1 cm light path length and their circular dichroism (CD) spectra at 25 °C were collected using a Jasco J-815 CD spectropolarimeter (Jasco, Tokyo, Japan). Each spectrum was collected for five accumulations, with a scanning range from 260 to 180 nm, a band width of 2 nm, data pitch of 0.5 nm, digital integration time of 1 s, and a scanning speed of 100 nm/min. Values for the baseline (measured without a cuvette) and the blank solutions (ultrapure water) were subtracted from test values. The CD spectra in terms of α-helix, β-sheet, and random structures were analysed using DichroWeb [20]. All samples had total concentration of 0.01 mg/mL, but varying f_{Lys} values, where f_{Lys} stands for weight of lysozyme/weight of Nafion.

2.5. Atomic Force Microscopy (AFM)

The samples were mounted on magnetic sample holders for AFM tests. The measurements were performed on a Park XE-100 (Parksystems, South Korea) in non-contact mode using a cantilever with spring constant of approximately 40 N/m. Images were taken with a 512 by 512 pixel resolution at a scan rate of between 0.2 and 0.5 Hz.

2.6. Surface Zeta Potential ($\zeta_{surface}$)

$(Naf/Lys)_6$, $(Naf/Chi)_6$, and $(Naf/Lys/Naf/Chi)_2$ coatings were deposited on Nafion-precoated aluminium foil and polypropylene substrates via standard dip-coating protocols. $\zeta_{surface}$ measurements were recorded at 25 °C in a surface zeta cell apparatus, at a forward angle of detection (13°) on a Zetasizer Nano ZS, (Malvern Panalytical, Malvern, UK). Data were recorded at different displacement distances from the surface which then allow for the surface zeta potential to be calculated, according to the equation below:

$$\zeta_{surface} = -\zeta_{intercept} + \zeta_{tracer\ particles} \quad (1)$$

where $\zeta_{intercept}$ is the zeta potential at displacement 0 from the surface, calculated from a linear regression fit. Four repeat measurements were recorded at each displacement of 1.25 μm from the previous point, with a total of four displacement points.

Polystyrene beads (DTS1235, −42 mV ± 10%) were used as the tracer particles and water was selected as the dispersant. The measured electrophoretic mobilities (U_E) were converted into ζ values assuming Smoluchowski approximation $F(ka) = 1.5$ for Henry's equation $U_E = 2\varepsilon\zeta F(ka)/3\eta$, where ε, η are the dielectric constant and the viscosity of the dispersant, respectively [21].

2.7. Antimicrobial Testing

A. Culturing Method. 250 mL Erlenmeyer flasks containing 25 mL nutrient broth were inoculated with a single loop of bacteria and incubated for 24 h in a SciQuip Incu-Shake MIDI orbital shaker (SciQuip Ltd, Newtown, Wem, Shropshire, UK) set to 200 rpm at 37 °C. Cultures were centrifuged at 4000 rpm for 10 min. Subsequently, the supernatant was discarded, 20 mL of 1/4 strength Ringer's solution was added, and the tubes were vortexed.

Tubes were centrifuged for a further 10 min at 4000 rpm and supernatant again discarded. 2 mL of $\frac{1}{4}$ strength Ringer's solution was added and tubes vortexed a final time. Resuspended cultures were diluted in nutrient broth to obtain an absorbance reading equivalent to a 0.5 McFarlane standard as recorded by Biochrom WPA S800 visible spectrophotometer (Biochrom Ltd, Cambridge, UK).

B. Disk testing method. Disk testing method was adapted from the literature [22]. Each disk was assigned to one of the twelve wells using a random number generator. Each of these wells was

lined with sterile aluminium foil, for ease of removal of disks and prevention of bacterial run-off. An additional well was filled with 1mL sterile distilled deionized water to prevent dehydration of samples.

200 μL bacterial culture was added to each disk and was incubated for 20 h at 37 °C. Following incubation, each disk was transferred along with the foil into 9.8 mL 1/4 strength Ringer's solution and sonicated for 10 min. Sonicated solutions were serially diluted 100 μL sample solution into 900 μL 1/4 strength Ringer's solution. A 100 μL respective sample was used to spread onto each nutrient agar plate, each dilution being plated in triplicate. Plates were incubated for 20 h at 37 °C, then counted for colonies. For each type of coating five crystals were tested and the average values were determined.

3. Results

The QCM-D sensogram shown in Figure 1a describes the build-up of four Nafion/lysozyme bilayers on a Nafion precoated crystal resonator. We note that Nafion combines a hydrophobic backbone with hydrophilic perfluoroether side chains terminated with sulphonic acid groups and, thus, it undergoes microphase separation into polar and nonpolar domains. In particular, Nafion is described as a network of parallel water-filled channels held in place by the cross-linking action of the crystalline domains [23].

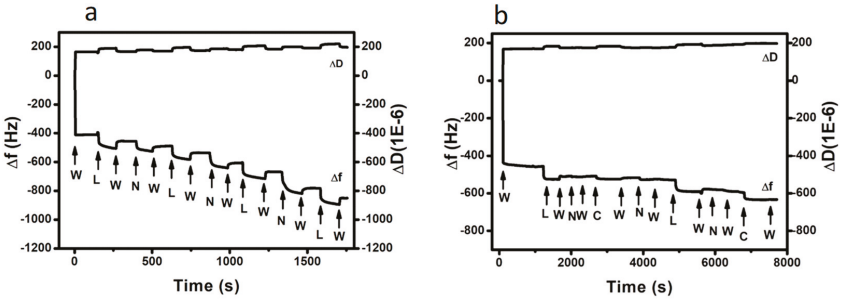

Figure 1. QCM-D sensograms at 25 °C monitoring the build-up of; (**a**) $(Naf/Lys)_4$ and (**b**) $(Naf/Lys/Naf/Chi)_2$. The letters "W", "N", "L", and "C" signify the injection of water, Nafion, lysozyme, and chitosan solution, respectively.

As seen in Figure 1a, injection of water results in a pronounced drop of the oscillating frequency coupled with a corresponding increase in the dissipation factor, indicating significant swelling of the ionic channels. The baseline recorded for the hydrated Nafion membrane remains stable, eliminating the possibility of even minor dissolution under water flow. Upon water exposure, Nafion's surface is reorganised with the sulphonic groups to be turned into the aqueous phase, a mechanism that gives rise to a large water contact angle hysteresis [24]. Owing to its amphiphilic nature Nafion has been shown to bind not only with charged polymers such as poly (oxyethylene) [25] and poly (oxypropylene) based diamines [26], but also with non-ionic surfactants via hydrogen bonding, hydrophobic interactions [27–29].

As evident by the significant drop in Δf (Figure 1a), lysozyme (at pH = 6.2), a ubiquitous enzyme widely used as food preservative, is massively adsorbed on the hydrated Nafion film. Given that lysozyme bears positive charges within the pH range 1–11 [30], it is strongly attracted to the negatively charged Nafion, so that subsequent rinsing with water removes only a limited amount of weakly bound lysozyme molecules. The Nafion/lysozyme deposition cycle was repeated for three more times in an identical fashion to generate an ultrathin LbL membrane denoted hereafter as $(Naf/Lys)_4$, while the deposition of two further bilayers led to $(Naf/Lys)_6$. Likewise, the $(Naf/Chi)_6$ LbL coating was assembled using chitosan, an aminopolysaccharide biopolymer with a broad antimicrobial spectrum that is extensively used to prevent bacterial contamination in food and drug packaging, as the positively charged layer. The QCM-D sensogram in Figure 1b describes the formation of a

$(Naf/Lys/Naf/Chi)_2$ assembly as a three-component coating that relies on the attractive Nafion/lysozyme and Nafion/chitosan forces. The action of those attractive forces is further confirmed by the spontaneous precipitation that takes place upon mixing 0.1 wt% Nafion with either 0.1 wt% lysozyme (pH = 6.2) or 0.1 wt% chitosan. Note that the injection of chitosan results in a rather limited drop in Δf compared to lysozyme, presumably due to enhanced steric hindrance.

Figure 2 displays AFM images of the Nafion, $(Naf/Lys)_6$, $(Naf/Chi)_6$, and $(Naf/Lys/Naf/Chi)_2$ coatings. It has been demonstrated that lysozyme adsorbed on a solid surface undergoes pronounced conformational reorganization driven by hydrophobic-hydrophobic interactions, ultimately resulting in the formation of aggregates that diffuse on the surface [31]. Chitosan molecules on a solid substrate follow similar clustering/agglomeration patterns, ultimately adopting significant levels of surface roughness [32]. At the same time, the topological characteristics of Nafion mirror the microphase separation of the bulk and are largely dependent on the relative humidity and the hydration levels [33].

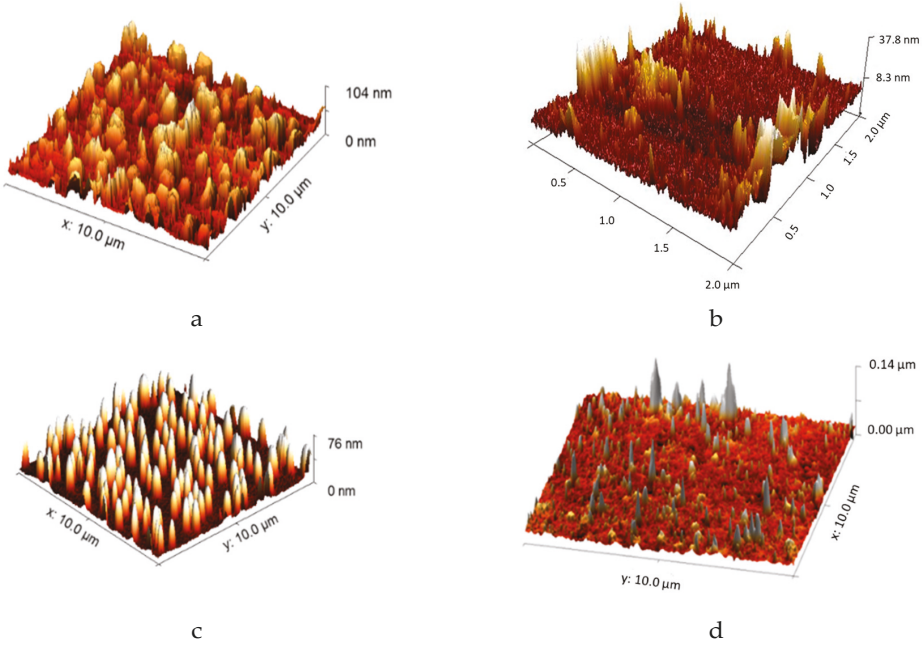

Figure 2. AFM images of the: (**a**) Nafion, (**b**) $(Naf/Lys)_6$, (**c**) $(Naf/Chi)_6$, and (**d**) $(Naf/Lys/Naf/Chi)_2$ coatings deposited on quartz crystal microbalance with dissipation monitoring (QCM-D) crystals.

As shown in Figure 3, the water contact angles for $(Naf/Lys)_6$, $(Naf/Chi)_6$, and $(Naf/Lys/Naf/Chi)_2$, were found to be 45.3°, 59.0°, and 65.1°, respectively, compared to 73.3° for a Nafion coated surface. It is generally accepted that hydrophobic surfaces are desirable for antimicrobial applications, however there is evidence to suggest that intermediate contact angles, as those found in the present systems, might also be compatible with advanced antimicrobial behaviour [34]. The above coatings were applied to polystyrene surfaces without compromising their optical transparency (Figure S1a), although the nanocoated surfaces showed enhanced UV-vis absorbance (Figure S1b). The development of transparent, yet UV blocking packaging materials with advanced antimicrobial properties are of supreme importance in the food industry and the coatings disclosed here point to this direction.

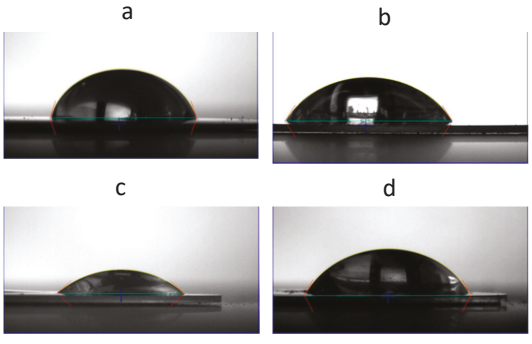

Figure 3. Water contact angles of: (**a**) Nafion, (**b**) $(Naf/Lys)_6$, (**c**) $(Naf/Chi)_6$, and (**d**) $(Naf/Lys/Naf/Chi)_2$ coatings deposited on QCM-D crystals.

As shown in Figure 4, the $(Naf/Lys)_6$, $(Naf/Chi)_6$, and $(Naf/Lys/Naf/Chi)_2$ coatings inhibit *E. coli* growth by 99.99%, 99.99%, and 99.95%, respectively, compared to 57.7% for the Nafion coated crystal. Moreover, the $(Naf/Lys)_6$, $(Naf/Chi)_6$, and $(Naf/Lys/Naf/Chi)_2$ coatings all inhibit *S. aureus* growth by 99.99%, compared to 57.1% for the Nafion coated crystal. For reference, $(Naf/Chi)_3$ and $(Naf/Lys/Naf/Chi)_1$ coatings reduce *E. coli* by 74.6% and 88.5%, respectively, and inhibit *S. aureus* growth by 99.9% and 83.4%, respectively (Figure S2).

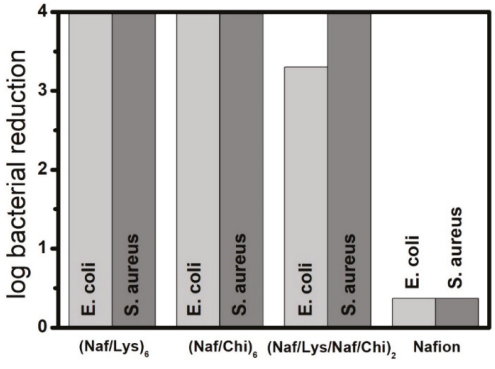

Figure 4. Reduction (in log scale) of the population of *E. coli* and *S. aureus* cultures exposed to $(Naf/Lys)_6$, $(Naf/Chi)_6$, $(Naf/Lys/Naf/Chi)_2$, and Nafion coated QCM-D crystals. (For each type of coating five crystals were tested and the average values are shown in this figure).

The photos displayed in Figure 5 clearly depict the significant advantages of the nanocoatings disclosed here. When *E. coli* and *S. aureus* cultures are exposed to uncoated QCM-D crystals (blank samples), no antimicrobial effect is observed. In contrast, when the same *E. coli* and *S. aureus* cultures are exposed to, otherwise identical, $(Naf/Lys)_6$, $(Naf/Chi)_6$, and $(Naf/Lys/Naf/Chi)_2$ coated QCM-D crystals, virtually all bacteria appear to be eliminated. Such a remarkable antimicrobial performance might reflect the synergistic effect of the contact-killing behaviour of lysozyme and chitosan, the bacteria-repelling behaviour of Nafion combined with contributions arising from surface roughness and wettability. Standard agar diffusion tests indicated the absence of bacteria inhibition zones around the coated crystals, confirming that the building blocks of the LbL assemblies are firmly fixed and do not diffuse into the agar.

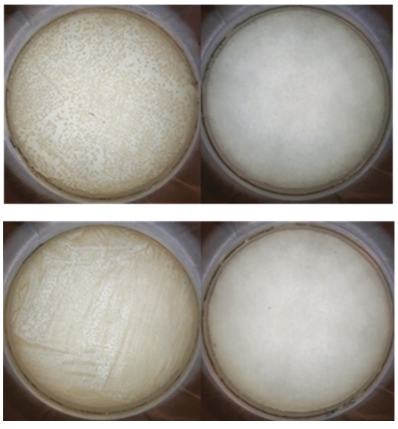

Figure 5. Photos of the petri dishes containing *E. coli* (upper photos) and *S. aureus* (lower photos) cultures. The petri dishes on the left have been exposed to uncoated QCM-D crystals, while those on the right have been exposed to $(Naf/Lys)_6$ coated discs, under otherwise identical conditions.

The antibacterial performance of lysozyme stems from its enzymatic activity to cleave 1,4 beta-linkages between N-acetylmuramic acid and N-acetyl-D-glucosamine that triggers peptidoglycan hydrolysis and, ultimately, cell lysis. Evidently, this mechanism is less effective for Gram-negative bacteria whose protective outer membranes prevents access to the enzyme [35]. Adjusting the pH of the lysozyme solution to 4 and 9 decreases the efficiency of $(Naf/Lys)_6$ against *E. coli* but leaves its ability to combat *S. aureus* essentially intact (Figure S2). It is noted that the lytic activity of lysozyme has been found to exhibit a maximum at pH 6.2 over a broad range of ionic strengths [36].

This supreme antimicrobial performance of lysozyme is only encountered on the condition that it's secondary structure is well preserved [37]. The CD spectrum of lysozyme shown in Figure 6 is dominated by two negative bands at 208 and 222 nm and suggests the presence of 71% α-helix and 10% β-sheet, consistent with data published previously [38]. Upon mixing with Nafion at $f_{Lys} = 0.9$ and $f_{Lys} = 0.3$, the secondary structure of lysozyme is modified to a small extent, given that the α-helix content decreases to 64% and 50% and the β-sheet content increases to 16% and 23%, respectively.

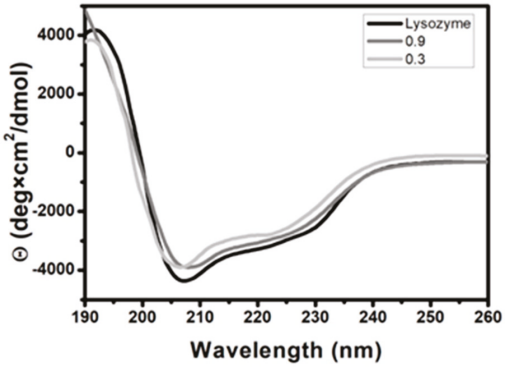

Figure 6. Circular dichroism (CD) spectra of aqueous solutions containing: Lysozyme and lysozyme/Nafion mixtures at $f_{Lys} = 0.9$ and $f_{Lys} = 0.3$ at 25 °C.

4. Discussion

A number of LbL assemblies employing lysozyme as a key antimicrobial ingredient has been reported in the literature. To that end, LbL assemblies comprising lysozyme and pectin deposited on cellulose mats were shown to induce a clear zone of bacterial inhibition, the more so when lysozyme is present at the outermost layer [39]. In a similar manner, lysozyme and gold nanoparticles were deposited on cellulose nanofibrous mats improving their antimicrobial performance against Gram-positive as well as Gram-negative model bacteria [40]. In addition, mechanically robust LbL membranes based on DNA-SWNT and lysozyme-SWNT (where SWNT stands for single-walled carbon nanotubes) were shown to exhibit long-term activity against *S. aureus* and *Micrococcus lysodeikticus*, however only when lysozyme is found on the outermost layer [41]. In our study, the effect of the outermost layer is minimal, given that both $(Naf/Lys)_3$ and $(Naf/Lys)_{3.5}$ coated crystals (with lysozyme at pH = 9) exhibit identical antimicrobial performance (Figure S2). Regarding the $(Naf/Lys)_6$, it appears that strong Nafion-protein electrostatic interactions keep lysozyme firmly fixed to the LbL assembly without compromising its secondary structure and while allowing its active sites to remain accessible by the bacteria.

The antimicrobial performance of chitosan critically depends upon intrinsic characteristics such as molecular weight and the degree of deacetylation and charge density, as well as external properties such as pH (enhanced activity at low pH), temperature (enhanced activity at higher temperatures) and ionic strength [42]. In general, three modes of action have been identified for chitosan: One arising from its polycationic nature that facilitates lysis of the microbial cell membranes, the second associated with its strong metal-chelating properties that deprives bacterial cells of essential nutrients, and the third stemming from its DNA-binding ability that inhibits protein and mRNA synthesis from the bacterial cells [14].

In analogy to lysozyme, a number of LbL antimicrobial membranes rely on the electrostatic immobilisation of chitosan. To that end, it has been reported that LbL assemblies based on chitosan/hyaluronic acid on PET show excellent activity against *E. coli* [43]. LbL assemblies based on chitosan/polyanionic lentinan sulphate on polyurethane showed 58% improvement against the opportunistic pathogen *P. aeruginosa* [44]. Moreover, LbL assemblies of chitosan and alginates on cotton samples were effective against *S. aureus* and *Klebsiella pneumonia* [45], while chitosan/lignosulphonates multilayers on cellulose fibres suppress *E. coli* growth up to 97% [46].

By comparison, only a limited body of work is centred around the antimicrobial activity of Nafion, even though Nafion coated stainless steel disks were shown to inhibit *E. coli* adhesion [22]. It is widely accepted that repulsive forces between the negatively charged Nafion and the similarly charged bacteria gives rise to a bacterial exclusion zone (EZ) at the Nafion-water interface. A recent study employed confocal laser scanning microscope to show that the EZ is a non-equilibrium phenomenon that diminishes with time, as van der Waals and acid-base forces start to dominate the Nafion-bacteria interactions [17]. Because of those forces, a significant number of cells are able to break the EZ barrier after 48 h of incubation, compared to rare and sporadic cell attachment after 24 h of incubation.

Interestingly, ζ for $(Naf/Lys)_6$, $(Naf/Chi)_6$, and $(Naf/Lys/Naf/Chi)_2$ deposited on the aluminium foil was found +2.8 mV, −22.2 mV, and −30.7 mV, respectively, compared to −52.1 mV for the Nafion coated aluminium foil surface and similar trends were recorded for the multilayers deposited on a polypropylene substrate. Although, Nafion's negative charges have been overcompensated in $(Naf/Lys)_6$ coatings, they exhibit exceptional antimicrobial behaviour that cannot be attributed solely to EZ effects. In that sense, our work demonstrates for the first time that Nafion based compositions exhibit supreme antimicrobial behaviour that goes beyond the concept of the EZ.

5. Conclusions

In conclusion, we report a systematic study on the structure-property relationships of a new series of antimicrobial coatings comprising Nafion, chitosan and lysozyme. The chemical composition, the topological characteristics and the wetting performance, are all important parameters that define

the superior antimicrobial behaviour of the ultrathin films. Our study provides solid evidence that coupling between Nafion and conventional antimicrobial agents can generate highly effective platform coatings to combat the colonization and spread of bacteria.

Supplementary Materials: The following are available online at http://www.mdpi.com/2079-4991/9/11/1563/s1, Figure S1: (i) Photos of UV-vis polystyrene cuvettes: Uncoated (A), $(Naf/Lys)_6$ (B), $(Naf/Chi)_6$ (C), $(Naf/Lys/Naf/Chi)_2$ (D), demonstrating their transparency levels. (ii) UV-vis spectra of polystyrene cuvettes coated with $(Naf/Lys)_6$, $(Naf/Chi)_6$, and $(Naf/Lys/Naf/Chi)_2$. Figure S2: Reduction of the population of E. coli and S. aureus cultures exposed to QCM-D crystals coated with $(Naf/Lys)_6$ (pH = 4), $(Naf/Lys)_6$ (pH = 9), $(Naf/Lys)_3$ (pH = 9), $(Naf/Lys)_{3.5}$ (pH = 9), $(Naf/Lys/Naf/Chi)_1$, and $(Naf/Chi)_3$.

Author Contributions: Conceptualization, A.K.; methodology, E.N.G., M.J.K., A.K.; resources, M.J.K., A.K., S.G.Y.; data curation, e.g., C.W., E.B., D.F., A.V.S.P.; writing-original draft preparation, A.K., M.J.K.; writing-review and editing, A.K.; supervision, A.K., M.J.K., S.G.Y.; project administration, A.K., M.J.K., S.G.Y.; revision: A.K., E.N.G.

Funding: This research received no external funding.

Conflicts of Interest: The authors declare no conflict of interest.

References

1. Costerton, J.W.; Stewart, P.S.; Greenberg, E.P. Bacterial biofilms: A common cause of persistent infections. *Science* **1999**, *284*, 1318–1322. [CrossRef] [PubMed]
2. Bergogne-Bérézin, E.; Decreé, D.; Joly-Guillou, M.L. Opportunistic nosocomial multiply resistant bacterial infections—Their treatment and prevention. *J. Antimicrob. Chemother.* **1993**, *32*, 39–47. [CrossRef] [PubMed]
3. Livermore, D.M. The need for new antibiotics. *Clin. Microbiol. Infect.* **2004**, *10*, 1–9. [CrossRef] [PubMed]
4. James, E.K.; Olivares, F.L. Infection and Colonization of Sugar Cane and Other Graminaceous Plants by Endophytic Diazotrophs. *Crit. Rev. Plant Sci.* **1998**, *17*, 77–119. [CrossRef]
5. Kang, C.I.; Kim, S.H.; Park, W.B.; Lee, K.D.; Kim, H.B.; Kim, E.C.; Oh, M.D.; Choe, K.W. Bloodstream infections caused by antibiotic-resistant gram-negative bacilli: Risk factors for mortality and impact of inappropriate initial antimicrobial therapy on outcome. *Antimicrob. Agents Chemother.* **2005**, *49*, 760–766. [CrossRef]
6. Hammond, P.T. Form and Function in Multilayer Assembly: New Applications at the Nanoscale. *Adv. Mater.* **2004**, *16*, 1271–1293. [CrossRef]
7. Tang, Z.; Wang, Y.; Podsiadlo, P.; Kotov, N.A. Biomedical Applications of Layer-by-Layer Assembly: From Biomimetics to Tissue Engineering. *Adv. Mater.* **2006**, *18*, 3203–3224. [CrossRef]
8. Richardson, J.J.; Cui, J.; Björnmalm, M.; Braunger, J.A.; Ejima, H.; Caruso, F. Innovation in Layer-by-Layer Assembly. *Chem. Rev.* **2016**, *116*, 14828–14867. [CrossRef]
9. Zhu, X.; Loh, X.J. Layer-by-layer assemblies for antibacterial applications. *Biomater. Sci.* **2015**, *3*, 1505–1518. [CrossRef]
10. Shukla, A.; Fleming, K.E.; Chuang, H.F.; Chau, T.M.; Loose, C.R.; Stephanopoulos, G.N.; Hammond, P.T. Controlling the release of peptide antimicrobial agents from surfaces. *Biomaterials* **2010**, *31*, 2348–2357. [CrossRef]
11. Lichter, J.A.; Rubner, M.F. Polyelectrolyte Multilayers with Intrinsic Antimicrobial Functionality: The Importance of Mobile Polycations. *Langmuir* **2009**, *25*, 7686–7694. [CrossRef] [PubMed]
12. Boulmedais, F.; Frisch, B.; Etienne, O.; Lavalle, P.; Picart, C.; Ogier, J.; Voegel, J.C.; Schaaf, P.; Egles, C. Polyelectrolyte multilayer films with pegylated polypeptides as a new type of anti-microbial protection for biomaterials. *Biomaterials* **2004**, *25*, 2003–2011. [CrossRef] [PubMed]
13. Hughey, V.L.; Johnson, E.A. Antimicrobial Activity of Lysozyme against Bacteria Involved in Food Spoilage and Food-Borne Disease. *Appl. Environ. Microbiol.* **1987**, *53*, 2165–2170. [PubMed]
14. Rabea, E.I.; Badawy, M.E.T.; Stevens, C.V.; Smagghe, G.; Steurbaut, W. Chitosan as antimicrobial agent: Applications and mode of action. *Biomacromolecules* **2003**, *4*, 1457–1465. [CrossRef] [PubMed]
15. Mauritz, K.A.; Moore, R.B. State of Understanding of Nafion. *Chem. Rev.* **2004**, *104*, 4535–4586. [CrossRef] [PubMed]
16. Klyuzhin, I.; Symonds, A.; Magula, J.; Pollack, G.H. New Method of Water Purification Based on the Particle-Exclusion Phenomenon. *Environ. Sci. Technol.* **2008**, *42*, 6160–6166. [CrossRef] [PubMed]

17. Cheng, Y.; Moraru, C.I. Long-range interactions keep bacterial cells from liquid-solid interfaces: Evidence of a bacteria exclusion zone near Nafion surfaces and possible implications for bacterial attachment. *Colloids Surf. B: Biointerfaces* **2018**, *162*, 16–24. [CrossRef] [PubMed]
18. Sauerbrey, G.Z. The use of quartz oscillators for weighing thin layers and for microweighing. *Für Phys.* **1959**, *155*, 206–222. [CrossRef]
19. Rodahl, M.; Höök, F.; Krozer, A.; Breszinski, P.; Kaseno, B. Quartz crystal microbalance setup for frequency and *Q*-factor measurements in gaseous and liquid environments. *Rev. Sci. Instrum.* **1995**, *66*, 3924–3930. [CrossRef]
20. Sreerama, N.; Woody, R.W. Estimation of protein secondary structure from circular dichroism spectra: Comparison of CONTIN, SELCON, and CDSSTR methods with an expanded reference set. *Anal. Biochem.* **2000**, *287*, 252–260. [CrossRef]
21. Kaszuba, M.; Corbett, J.; Watson, F.M.; Jones, A. High-concentration zeta potential measurements using light-scattering techniques. *Philos. Trans. R. Soc. A: Math. Phys. Eng. Sci.* **2010**, *368*, 4439–4451. [CrossRef] [PubMed]
22. Zhong, L.; Pang, L.; Che, L.; Wu, X.; Chen, X. Nafion coated stainless steel for anti-biofilm application. *Colloids Surf. B: Biointerfaces* **2013**, *111*, 252–256. [CrossRef] [PubMed]
23. Schmidt-Rohr, K.; Chen, Q. Parallel cylindrical water nanochannels in Nafion fuel-cell membranes. *Nat. Mater.* **2008**, *7*, 75–83. [CrossRef] [PubMed]
24. Goswani, S.; Klaus, S.; Benziger, J. Wetting and Absorption of Water Drops on Nafion Films. *Langmuir* **2008**, *24*, 8627–8633. [CrossRef]
25. Parthasarathy, M.; Kakade, B.A.; Pillai, V.K. Tuning the transport properties of Poly(oxyethylene)bisamine—Nafion polyelectrolyte complexes by dielectric manipulation. *Macromolecules* **2008**, *41*, 3653–3658. [CrossRef]
26. Ma, C.C.M.; Hsiao, Y.H.; Lin, Y.F.; Yen, C.Y.; Liao, S.H.; Weng, C.C.; Yen, M.Y.; Hsiao, M.C.; Weng, F.B. Effects and properties of various molecular weights of poly(propylene oxide) oligomers/Nafion® acid–base blend membranes for direct methanol fuel cells. *J. Power Sources* **2008**, *185*, 846–852. [CrossRef]
27. Kelarakis, A.; Giannelis, E.P. Nafion as cosurfactant: Solubilisation of Nafion in water in the presence of Pluronics. *Langmuir* **2011**, *27*, 554–560. [CrossRef]
28. Kelarakis, A.; Krysmann, M.J. Trivial and Non-Trivial Supramolecular Assemblies Based on Nafion. *Colloid Interface Sci. Commun.* **2014**, *1*, 31–34. [CrossRef]
29. Fernandes, D.; Kluska, W.; Stanislawska, J.; Board, B.; Krysmann, M.J.; Kelarakis, A. Novel hydrogels containing Nafion and poly(ethylene oxide) based block copolymers. *Polymer* **2017**, *114*, 73–78. [CrossRef]
30. Yu, G.; Liu, J.; Zhou, J. Mesoscopic coarse-grained simulations of hydrophobic charge induction chromatography (HCIC) for protein purification. *AIChE J.* **2015**, *61*, 2035–2047. [CrossRef]
31. Westwood, M.; Kirby, A.R.; Parker, R.; Morris, V.J. Combined QCMD and AFM studies of lysozyme and poly-L-lysine-poly-galacturonic acid multilayers. *Carbohydr. Polym.* **2012**, *89*, 1222–1231. [CrossRef] [PubMed]
32. Assis, O.B.G.; Bernardes-Filho, R.; Vieira, D.C.; Campana-Filho, S.P. AFM characterization of chitosan self-assembled films. *Int. J. Polym. Mater.* **2002**, *51*, 633–639. [CrossRef]
33. Aleksandrova, E.; Hiesgen, R.; Friedrich, K.A.; Roduner, E. Electrochemical atomic force microscopy study of proton conductivity in a Nafion membrane. *Phys. Chem. Chem. Phys.* **2007**, *9*, 2735–2743. [CrossRef] [PubMed]
34. Zhu, X.; Guo, S.; Jańczewski, D.; Velandia, F.J.P.; Teo, S.L.M.; Vancso, G.J. Multilayers of Fluorinated Amphiphilic Polyions for Marine Fouling Prevention. *Langmuir* **2014**, *30*, 288–296. [CrossRef]
35. Masschalck, B.; Michiels, C.W. Antimicrobial properties of lysozyme in relation to foodborne vegetative bacteria. *Crit. Rev. Microbiol.* **2003**, *29*, 191–214. [CrossRef]
36. Davies, R.C.; Neuberger, A.; Wilson, B.M. The dependence of lysozyme activity on pH and ionic strength. *Biochim. Biophys. Acta* **1969**, *178*, 294–305. [CrossRef]
37. Antonov, Y.A.; Moldenaers, P.; Cardinaels, R. Complexation of lysozyme with sodium caseinate and micellar casein in aqueous buffered solutions. *Food Hydrocoll.* **2017**, *62*, 102–118. [CrossRef]
38. Mohammadi, F.; Mahmudian, A.; Moeeni, M.; Hassani, L. Inhibition of amyloid fibrillation of hen egg-white lysozyme by the natural and synthetic curcuminoids. *RSC Adv.* **2016**, *6*, 23148–23160. [CrossRef]

39. Zhang, T.; Zhou, P.; Zhan, Y.; Shi, X.; Lin, J.; Du, Y.; Li, X.; Deng, H. Pectin/lysozyme bilayers layer-by-layer deposited cellulose nanofibrous mats for antibacterial application. *Carbohydr. Polym.* **2015**, *117*, 687–693. [CrossRef]
40. Zhou, B.; Li, Y.; Deng, H.B.; Hu, Y.; Li, B. Antibacterial multilayer films fabricated by layer-by-layer immobilizing lysozyme and gold nanoparticles on nanofibers. *Colloids Surf. B* **2014**, *116*, 432–438. [CrossRef]
41. Nepal, D.; Balasubramanian, S.; Simonian, A.L.; Davis, V.A. Strong Antimicrobial Coatings: Single-Walled Carbon Nanotubes Armored with Biopolymers. *Nano Lett.* **2008**, *8*, 1896–1901. [CrossRef] [PubMed]
42. Raafat, D.; Sahl, H.G. Chitosan and its antimicrobial potential—A critical literature survey. *Microb. Biotechnol.* **2009**, *2*, 186–201. [CrossRef] [PubMed]
43. Del Hoyo-Gallego, S.; Perez-Alvarez, L.; Gomez-Galvan, F.; Lizundia, E.; Kuritka, I.; Sedlarik, V.; Laza, J.M.; Vila-Vilela, J.L. Construction of antibacterial poly(ethylene terephthalate) films via layer by layer assembly of chitosan and hyaluronic acid. *Carbohydr. Polym.* **2016**, *143*, 35–43. [CrossRef]
44. Wang, Y.; Hong, Q.; Chen, Y.; Lian, X.; Xiong, Y. Surface properties of polyurethanes modified by bioactive polysaccharide-based polyelectrolyte multilayers. *Colloids Surf. B* **2012**, *100*, 77–83. [CrossRef] [PubMed]
45. Gomes, P.; Mano, J.F.; Queiroz, J.A.; Gouveia, I.C. Layer-by-layer deposition of antimicrobial polymers on cellulosic fibers: A new strategy to develop bioactive textiles. *Polym. Adv. Technol.* **2013**, *24*, 1005–1010. [CrossRef]
46. Li, H.; Peng, L. Antimicrobial and antioxidant surface modification of cellulose fibers using layer-by-layer deposition of chitosan and lignosulfonates. *Carbohydr. Polym.* **2015**, *124*, 35–42. [CrossRef]

nanomaterials

MDPI

Article

Influence of Preparation Procedure on Physicochemical and Antibacterial Properties of Titanate Nanotubes Modified with Silver

Manu Jose [1], Paulina Sienkiewicz [1], Karolina Szymańska [2], Dominika Darowna [1], Dariusz Moszyński [1], Zofia Lendzion-Bieluń [1], Kacper Szymański [1] and Sylwia Mozia [1,*]

[1] Institute of Inorganic Chemical Technology and Environment Engineering, Faculty of Chemical Technology and Engineering, West Pomeranian University of Technology, Szczecin, ul. Pułaskiego 10, 70-322 Szczecin, Poland; manu.jose@zut.edu.pl (M.J.); paulina.sienkiewicz@zut.edu.pl (P.S.); dominika.darowna@zut.edu.pl (D.D.); dariusz.moszynski@zut.edu.pl (D.M.); zofia.lendzion-bielun@zut.edu.pl (Z.L.-B.); kacper.szymanski@zut.edu.pl (K.S.)

[2] Nanomaterials Physicochemistry Department, Faculty of Chemical Technology and Engineering, West Pomeranian University of Technology, Szczecin, al. Piastów 45, 70-311 Szczecin, Poland; karolina.szymanska@zut.edu.pl

* Correspondence: sylwia.mozia@zut.edu.pl; Tel.: +48-91-449-47-30

Received: 7 May 2019; Accepted: 20 May 2019; Published: 23 May 2019

Abstract: Silver nanoparticles (NPs) are effective antibacterial agents; however, aggregation of NPs and uncontrolled release of Ag^+ affect their efficiency and may pose a risk to the environment. To overcome these disadvantages, immobilization of Ag onto titanate nanotubes (TNTs) was investigated. This paper describes the physicochemical and antibacterial properties of silver incorporated titanate nanotubes (Ag/TNTs) prepared using five procedures and containing different Ag amounts (0.11–30.85 wt.%). The methods were (i) sol-gel followed by a hydrothermal process; (ii) photodeposition under ambient conditions; (iii) photodeposition under an inert atmosphere; (iv) $NaBH_4$ reduction; and (v) electroless deposition after activation of TNTs with Sn^{2+}. Depending on the synthesis procedure, the presence of metallic Ag NPs, AgO or AgCl was observed. The electroless method led to an additional deposition of SnO_2 NPs. The antibacterial properties of Ag/TNTs were analyzed as a function of Ag content and released against *Escherichia coli* and *Staphylococcus epidermidis*. The best bactericidal properties exhibited Ag/TNTs prepared through the photodeposition process due to the higher interaction of exposed Ag NPs with bacteria. An increase of Ag loading resulted in improvement of antibacterial activity of Ag/TNTs although no direct correlation between silver content or release and inhibition of bacterial growth was found.

Keywords: titanate nanotubes; TNT; Ag; antibacterial; *Escherichia coli*; *Staphylococcus epidermidis*

1. Introduction

The presence of large concentrations of microorganisms such as bacteria, protozoans, and viruses in the majority of the world's water resources limits the use of a major portion of them as drinking water. According to the World Health Organization (WHO), 80% of diseases arise due to the consumption of contaminated water [1]. Hence, the development of new efficient technologies for the removal of harmful microorganisms from water will require much attention in the coming decades. Recently, nanomaterials with superior photoactivity, high surface-to-volume ratios, antibacterial properties, and good hydrophilicity have been explored for the inactivation of pathogenic microorganisms. Among them, silver NPs have gained much attention for their powerful antibacterial properties [2,3] which find application in wound dressing [4], textiles [5], and self-sterilizing surfaces

in food and pharmaceutical production [6]. The Ag NPs show good antimicrobial properties towards a broad spectrum of bacterial and fungal species including antibiotic-restraint strains [7,8].

Even though Ag NPs are known as promising biocidal agents due their distinctive physicochemical properties, their wide applicability is limited mainly due to the uncontrolled release of Ag^+ ions from the Ag NPs, which was found to have many toxic effects on the environment [9]. The high activity of Ag NPs arises from their ultra-small size and high mobility [8]. However, mobile Ag NPs are found to aggregate easily in the medium that alters their cytotoxicity, [10] and therefore, numerous studies have been conducted to improve their dispersion. To overcome these disadvantages of Ag NPs, their immobilization onto various supporting materials such as metal oxides, activated carbon, graphene oxide, polymers, etc., have been investigated [11]. Among various hybrid NPs, TiO_2 and TNTs modified with Ag NPs are being researched for their excellent antibacterial properties both in the presence and absence of light. The modification of TiO_2/TNTs with Ag NPs results in changes in the physicochemical characteristics such as size, shape, stability, and oxidation state of Ag NPs, which results in enhanced antibacterial, photocatalytic, and catalytic activities [12–16]. Wang et al. [17] observed improved and long-lasting antibacterial activity for Ag–polydopamine–TiO_2 nanotube composites which was attributed to the tethering of Ag NPs onto TNTs by polydopamine layers.

Important factors which affect the bactericidal activity of Ag NPs are their size, shape, surface functionalization, and stability [11]. The antibacterial properties of Ag NPs are found to increase with a decrease in their diameter, and the direct interaction of Ag NPs with bacteria mainly occurs when the diameters are around 1–10 nm [18,19]. Kubacka et al. [20] synthesized Ag/TiO_2 nanocomposites through impregnation and photodeposition methods with various Ag contents and studied their photocatalytic disinfection ability against *Escherichia coli*. They observed that below 1 wt.% of Ag, the disinfection activity of the samples obtained by the two methods was comparable while at higher silver content, the photo-deposited samples displayed improved performance. Also, they found that the presence of Ag NPs helps to improve the adhesion of bacteria onto nanocomposite surfaces and the Ag lixiviation can be controlled by optimizing the amount of Ag in the nanocomposite. Similar results were reported by other researchers [7,8]. It was also found that the Ag NPs changed the surface characteristics of TiO_2 such as the point of zero charge (PZC), which can influence bacterial attraction to the Ag/TiO_2 surface [20]. Es-Souni et al. [21] prepared Ag/TiO_2 nanocomposite coatings through a sol-gel approach and found that bactericidal actions rely on Ag^+ ion release, Ag NPs size, and hydrophilicity of the nanocomposites. Keleher et al. [22] observed higher antibacterial activity for Ag/TiO_2 than that of Ag metal, which was ascribed to the more available surface for Ag^+ ion release in solution. Sotiriou et al. [23] studied the leaching of Ag^+ ions from Ag/SiO_2 nanocomposites and reported that the amount of the released Ag^+ corresponded to the dissolution of 1–2 silver oxide monolayers present on the surface of Ag NPs, depending on their size. The authors also found that the reduction of silver oxide to metallic silver resulted in a significant minimization of Ag^+ ion leaching which was found to decrease the antibacterial activity against *E. coli*. The investigation on TNT ions exchanged with various metal ions presented by Rónavári et al. [24] revealed that only TNTs containing silver exhibited potential antibacterial and antifungal properties against different microbial species, which was ascribed to the release of ionic Ag^+ to the surrounding solution. In other research [14], it was observed that the controlled release of Ag^+ from Ag/TNTs nanocomposite through diffusion and osmosis effects provided extended antibacterial activities of this material. Rodríguez-González et al. [16], based on their research on antifungal properties of Ag/TNTs, concluded that due to the nanotubular morphology, the TNTs could easily damage cell walls and accelerate vacuolation and invagination which results in inactivation of fungi.

Silver NPs are predominantly synthesized from silver nitrate ($AgNO_3$) and silver acetate (CH_3COOAg) as the precursors [14–16,25]. Various reported methods for the preparation of Ag/TiO_2 nanocomposites are photoreduction [13], sol-gel [26], chemical reduction [27], template induced and solvothermal [28] methods. The Ag/TNTs are obtained through photoreduction [29], chemical reduction [30], ion exchange followed by calcination [31], microwave-assisted methods [32],

and hydrothermal processes [33]. The Ag/TNTs nanocomposites are mainly used as antibacterial nanomaterial [14], visible light photocatalyst [34], nanofiller in modified polymeric membranes [35], and as a multicolor photochromic material [36]. During the preparation of Ag-modified nanocomposites through a photoreduction approach, the physicochemical properties like size, uniformity, and density of photodeposited Ag NPs are depended upon solvent, silver precursor concentration, reaction atmosphere (ambient or inert), irradiation wavelength, and time or type of support (e.g., TiO_2, TNTs, etc.) used [13,37,38]. Ma et al. [30] reported that Ag NPs in the metallic form with a size range of 3–10 nm could be deposited onto TNTs by $NaBH_4$ reduction, whereas the reduction reaction carried out without the use of TNTs resulted in the formation of highly agglomerated Ag NPs with a size of 20–50 nm. The stability of the Ag NPs on TNTs was attributed to the strong bonding interaction between Ag NPs and the oxygen atoms of TNTs [30]. Priya et al. [27] demonstrated the synthesis of Ag_2O/Ag^0-loaded TiO_2 NPs by an electroless coating technique in which Ag^+ ions were reduced onto the TiO_2 using Sn^{2+}. Lai et al. [39] produced Ag/TiO_2 nanotubes by hydrothermal treatment of the sol-gel-processed Ag/TiO_2 NPs. The reduction of Ag^+ ions to metallic Ag occurred during the thermal treatment step of the sol-gel processed TiO_2 nanopowder. After the hydrothermal treatment, Ag NPs of sizes 4–8 nm were found to be well dispersed on the exterior of the nanotube surface with a small fraction of Ag NPs encapsulated in the interior of the TiO_2 nanotubes [39]. To the best of our knowledge, there are no reports on the application of the electroless technique to fabricate Ag-modified TNTs.

The physicochemical and antibacterial properties of Ag-modified TNTs are expected to vary with the adopted synthesis method. In view of this, the present study is focused on the evaluation of the influence of the preparation procedure on the properties and stability of Ag-modified titanate nanotubes (Ag/TNTs). Twelve types of Ag/TNTs were prepared with different Ag incorporation approaches and Ag contents. The synthetic procedures included (i) sol-gel followed by a hydrothermal process; (ii) photodeposition under ambient conditions; (iii) photodeposition under an inert atmosphere; (iv) $NaBH_4$ reduction; and (v) an electroless deposition process after activation of the TNTs' surface with various amounts of Sn^{2+} ions. The physicochemical properties of the hybrid Ag/TNTs were examined and discussed in detail. Moreover, the antibacterial performance of the composites against both Gram-positive and Gram-negative bacteria were evaluated under dark conditions.

2. Materials and Methods

2.1. Materials

Titanium(IV) isopropoxide (TTIP, Sigma–Aldrich, St. Louis, MO, USA, 97%) and anatase TiO_2 powder were purchased from Sigma–Aldrich Chemicals (St. Louis, MO, USA). HCl (35–38 wt.%), H_2SO_4 (96 wt.%), $AgNO_3$, $SnCl_2$, ammonia solution (25%), NaOH, Na_2HPO_4, and KH_2PO_4 were purchased from Avantor Performance Materials (Gliwice, Poland). $NaBH_4$ was supplied by Merck, (Darmstadt, Germany). 2-propanol, KCl, and NaCl were provided by Chempur (Piekary Śląskie, Poland).

Microbiological tests were carried out using Plate Count Agar (PCA) and Brain Heart Infusion (BHI) Agar (BIOMAXIMA, Lublin, Poland). Gram-negative *Escherichia coli* (strain K12, ATCC 29425, Manassas, VA, USA) and Gram-positive *Staphylococcus epidermidis* (ATCC 49461, Manassas, VA, USA) were used as model microorganisms. The initial concentration of bacteria suspension was set at 0.5 using McFarland scale (McFarland standards, bioMérieux, Marcy-l'Étoile, France).

In all experiments, pure (deionized) water (type 2, 0.066 μS cm^{-1}) from Elix 3 (Millipore, Burlington, MA, USA) was used, unless otherwise stated.

2.2. Preparation of TNTs

Titanate nanotubes were prepared by employing alkaline hydrothermal treatment of anatase TiO_2 powder. Initially, TiO_2 (2 g) was ultrasonicated with 60 mL of 10 M NaOH solution for 1 h at room temperature to obtain a homogeneous dispersion. The mixture was then transferred to a Teflon-lined stainless-steel autoclave and then heated at 140 °C for 24 h. After being cooled down to

room temperature, the product was first washed with 2 L of 0.1 M HCl and then with deionized water until the conductivity of the filtrate became ~1 $\mu S \cdot cm^{-1}$. Finally, the white product was dried at 80 °C in an oven for 12 h and stored.

2.3. Preparation of Hybrid Ag/TNTs

2.3.1. Preparation of Ag/TNTs by Sol-Gel Combined with Hydrothermal Process

Silver-modified nanocrystalline TiO_2 powders were synthesized by sol-gel process. First, 5.53 g of TTIP was dissolved in 100 mL of 2-propanol. A second solution was prepared by dissolving 50.96 and 254.8 mg of $AgNO_3$ (corresponding to Ag: Ti atomic ratios of 0.01 and 0.05, respectively) in a mixture of deionized water (50 mL) and 2-propanol (100 mL). Both solutions were sealed immediately and stirred thoroughly using the magnetic stirrer. The water part of the solution was then added drop-wise to the alkoxide part under continuous magnetic stirring. After the complete addition of the water part of the solution, the resulting suspension was stirred for 4 h before drying in an oven at 80 °C for the complete removal of residual water and the solvent. The dried powder was then ground well using a mortar and pestle and then calcined in a muffle furnace at 500 °C for 2 h at the heating rate of 5 °C min^{-1} for the crystallization of amorphous TiO_2. Such obtained Ag/TiO_2 powders containing various amount of Ag were then hydrothermally treated according to the procedure described above (see Section 2.2). The resulting hybrid products were denoted as Ag/TNT-1_SH and Ag/TNT-5_SH, where the "1" and "5" represented the initially used atomic ratio of Ag/Ti for the sol-gel synthesis of Ag/TiO_2 (Table 1).

Table 1. Summarizes the applied methods of Ag/titanate nanotube (TNT) synthesis, the corresponding concentrations of $AgNO_3$, and samples nomenclature.

No.	Method of Ag/TNTs Synthesis	Amount or Concentration of $AgNO_3$	Sample Name
1	Sol-gel and hydrothermal	0.01 (Ag/Ti)	Ag/TNT-1_SH
		0.05 (Ag/Ti)	Ag/TNT-5_SH
2	Photodeposition (Ambient atmosphere)	2.5 mM	Ag/TNT-2.5_AM
		100 mM	Ag/TNT-100_AM
3	Photodeposition (Inert atmosphere)	2.5 mM	Ag/TNT-2.5_IN
		100 mM	Ag/TNT-100_IN
4	$NaBH_4$ reduction	2.5 mM	Ag/TNT-2.5_NB
		100 mM	Ag/TNT-100_NB
5	Electroless reduction (0.1 g $SnCl_2$)	2.5 mM	Ag/TNT-2.5_EL (0.1)
		100 mM	Ag/TNT-100_EL (0.1)
6	Electroless reduction (1 g $SnCl_2$)	2.5 mM	Ag/TNT-2.5_EL (1)
		100 mM	Ag/TNT-100_EL (1)

2.3.2. Preparation of Ag/TNTs by Photodeposition

In this technique, 0.5 g of TNTs were dispersed into 50 mL of $AgNO_3$ solution (2.5 and 100 mM) with magnetic stirring (250 rpm) for 2 h in a glass reactor. The processes were carried out under either an ambient or inert (Ar) atmosphere. Afterward, the slurry was irradiated with a low-pressure mercury vapor lamp (TNN 15/32, Heraeus Noblelight GmbH, 15 W, λ_{max} = 254 nm) for 2 h with continuous stirring. The suspension was then collected by centrifugation and subsequently washed several times with deionized water for the complete removal of excess of Ag^+ ions. Finally, the products were dried at 80 °C in an oven for 12 h and stored. The samples were denoted later as Ag/TNT-2.5_AM and Ag/TNT-100_AM for ambient atmosphere, or Ag/TNT-2.5_IN and Ag/TNT-100_IN for inert atmosphere, where the numbers represented the concentration of $AgNO_3$ solution (Table 1).

2.3.3. Preparation of Ag/TNTs by $NaBH_4$ Reduction

The Ag^+ ions were reduced onto TNTs according to the procedure described elsewhere [30]. In a typical synthesis, 0.5 g of TNTs were dispersed into 50 mL of $AgNO_3$ solution (2.5 and 100 mM) and magnetically stirred for 2 h. The nanotubes were then separated from the solution by centrifugation at 3000 rpm. An ice-cold solution of $NaBH_4$ (5 mL, 0.1 M) was added drop-wise to the centrifuged sample. The product was then collected and washed with deionized water before drying at 80 °C in an

oven for 12 h. The samples were denoted later as Ag/TNT-2.5_NB and Ag/TNT-100_NB, where the numbers represented the concentration of $AgNO_3$ solution (Table 1).

2.3.4. Preparation of Ag/TNTs by Electroless Reduction

First, 0.5 g of TNTs were dispersed in 30 mL of deionized water. Then, a second solution was prepared by dissolving $SnCl_2$ (either 0.1 g or 1 g) in 20 mL of 0.2 M HCl. The two solutions were then mixed and stirred for 2 h at room temperature to obtain the surface sensitized TNTs. The suspension was subsequently centrifuged at 3000 rpm and washed three times with deionized water. The residue was then transferred to 50 mL of $AgNO_3$ solution (2.5 and 100 mM) and the resulting solution was made alkaline by the addition of 5 drops of aqueous NH_3 solution. The suspension was stirred for 1 h and the product was separated by centrifugation at 3000 rpm. After washing with deionized water, the nanomaterial was dried at 80 °C in an oven for 12 h. The samples were denoted later as Ag/TNT-2.5_EL (0.1) and Ag/TNT-100_EL (0.1) (for the samples processed using 0.1 g $SnCl_2$), and Ag/TNT-2.5_EL (1) and Ag/TNT-100_EL (1) (for the samples processed using 1 g $SnCl_2$), where the numbers 2.5 and 100 represented the concentration of $AgNO_3$ solution (Table 1).

2.4. Characterization Methods

The morphological analysis of pure TNTs and Ag/TNTs was carried out using a transmission electron microscope (TEM), FEI Tecnai F20. The elemental composition of the samples was studied with the usage of energy dispersive X-ray spectroscopy (EDS). The samples were prepared by sonication in ethanol followed by adding a drop of the suspension on a carbon-coated copper grid (300 mesh). The phase composition of the pure TNTs and Ag/TNTs was determined based on the X-ray diffraction (XRD) method (PANalytical Empyrean X-ray diffractometer) using CuKα radiation (λ = 1.54056 Å). Raman spectra were recorded with a 532 nm laser line (E_{laser} = 1.58eV) with a Renishaw in Via Raman micro-spectrometer. The isoelectric point (IEP) of the Ag/TNTs nanocomposites was measured using Zetasizer Nano-ZS (Malvern Instruments Ltd. Malvern, UK) equipped with a Multi-Purpose Titrator MPT-2 and a degasser. The samples were dispersed in ultrapure water and the pH was adjusted using HCl and NaOH solutions.

The composition of the Ag/TNTs surface was analyzed with use of the X-ray photoelectron spectroscopy (XPS). Measurements were conducted with Al K_a (h = 1486.6 eV) radiation in a Prevac system equipped with Scienta SES 2002 electron energy analyzer operating at constant transmission energy (E_p = 50 eV). The spectrometer was calibrated using the following photoemission lines (with reference to the Fermi level): EB Ag $3d_{5/2}$ = 368.3 eV and EB Au $4f_{7/2}$ = 84.0 eV. The analysis chamber was evacuated to the pressure below $1 \cdot 10^{-9}$ mbar. A powdered sample of the material was placed on a stainless-steel sample holder. The quantitative analysis of the surface composition was done on the basis of the peak area intensities using the sensitivity factor approach and assuming homogeneous composition of the surface layer.

Inductively coupled plasma optical emission spectrometry (ICP-OES) analysis was carried out using an Optima 5300DV spectrometer (Perkin Elmer, Waltham, MA, USA). To determine the real load of Ag in the Ag/TNTs, the samples were prepared by dissolution in a hot solution of $(NH_4)_2SO_4$ in concentrated H_2SO_4. After the solution cooled down, it was diluted with water.

To determine the release kinetics of Ag^+ ions from the different Ag/TNTs for seven days, 0.1 g of each nanocomposite was dispersed into 100 mL of deionized water and placed in a digital shaking water bath maintained at 30 °C. A defined number of samples was withdrawn after 1, 3, and 7 days and separated through a 0.2 μm filter. The concentration of Ag in the filtrate was analyzed using ICP-OES spectrometer and the given values were a mean from three repetitions.

2.5. Microbiological Study

2.5.1. Preparation of Culture Medium

First, the BHI and PCA solutions were prepared according to the instructions given by the manufacturer. Next, the Petri dishes were filled with an adequate solution and left to be solidified. Finally, the prepared agar plates were sterilized under UVC light for 20 min and then dried in the incubator for 3 days.

A NaCl solution was prepared by dissolving 8.5 g NaCl in 1 L of distilled water and then autoclaved.

Phosphate buffered saline (PBS, pH 7.2) was obtained by dissolution of 8 g NaCl, 0.2 g KCl, 1.44 g Na_2HPO_4, and 0.24 g of KH_2PO_4 in 1 L of distilled water, and the pH was adjusted using HCl. Before application, the solution was sterilized by autoclaving.

2.5.2. Antibacterial Study of Nanomaterials

A series of glass bottles filled with 100 mL of nanomaterial suspension (20 mg L^{-1}) in NaCl or PBS solutions containing *E. coli* or *S. epidermidis*, respectively, were prepared. The number of bacteria was set at 0.5 according to the McFarland scale. The control sample was prepared in the same way, but without addition of NPs. The bottles were incubated for 24 h at 37 °C with continuous stirring at 250 rpm. After that, the bacteria were counted using the serial decimal dilutions in NaCl and PBS solutions, respectively. 0.3 mL of a suitable diluted solution was put in the middle of a plate containing PCA or BHI and spread using a spreader. Three repetitions for each dilution were prepared. The plates with bacteria were incubated at 37 °C for 24 h. After that, the visible colonies of bacteria on agar plates were calculated by the counter (LKB 2002, POL-EKO, Wodzisław Śląski, Poland). The average colony forming unit (CFU) per mL values were evaluated according to Equation (1):

$$\text{CFU/mL} = \frac{N \times Y}{Z} \quad (1)$$

where: N—number of bacteria colonies visible on the Petri dish, Y—total dilution factor, and Z—volume of bacteria suspension put on the agar plate (0.3 mL).

The log reduction of bacterial growth was determined with reference to the blank sample using Equation (2):

$$\text{log reduction} = \log\left(\frac{A}{B}\right) \quad (2)$$

where: A—number of bacteria determined in control sample, i.e., without addition of NPs (CFU/mL), B—number of bacteria determined in the presence of NPs (CFU/mL).

3. Results and Discussion

3.1. ICP Compositional Analysis

The amount of Ag in the different Ag/TNTs nanocomposites was evaluated based on ICP-OES analysis, and the values are presented in Table 2.

Table 2. Amount of Ag in different Ag/TNTs nanocomposites measured by ICP-OES.

Sample Name	Ag (wt.%)	Sn (wt.%)	Sample Name	Ag (wt.%)	Sn (wt.%)
Ag/TNT-1_SH	0.11	-	Ag/TNT-2.5_NB	4.08	-
Ag/TNT-5_SH	3.56	-	Ag/TNT-100_NB	14.68	-
Ag/TNT-2.5_AM	3.77	-	Ag/TNT-2.5_EL (0.1)	2.33	5.17
Ag/TNT-100_AM	11.98	-	Ag/TNT-100_EL (0.1)	21.86	4.67
Ag/TNT-2.5_IN	3.11	-	Ag/TNT-2.5_EL (1)	2.97	20.01
Ag/TNT-100_IN	12.58	-	Ag/TNT-100_EL (1)	30.85	14.38

For all preparation procedures, the weight fraction of Ag in the nanocomposite was found to be increased with an increase in the initial concentration of $AgNO_3$. A minimum Ag content was observed for Ag/TNT-1_SH, and a maximum Ag loading was found in the case of Ag/TNT-100_EL (1). The amount of Ag was almost comparable for photodeposition (both inert and ambient atmosphere), and $NaBH_4$ reduction processes, with a moderately higher Ag loading observed for the latter approach. Silver/TNTs processed using an electroless method indicate the presence of Sn, originating from the $SnCl_2$ used as a reducing agent. The amount of Sn in the case of Ag/TNT-2.5_EL was found to be higher compared to Ag/TNT-100_EL samples for both 0.1 g and 1 g $SnCl_2$ loading, which confirms the role of Sn^{2+} ions in the reduction of Ag^+ to Ag^0 on the TNTs.

3.2. Morphological Analysis

Transmission electron microscopy was employed in order to determine the morphology of the Ag/TNTs and the size distribution of Ag NPs deposited on TNTs. The results are presented in Figure 1.

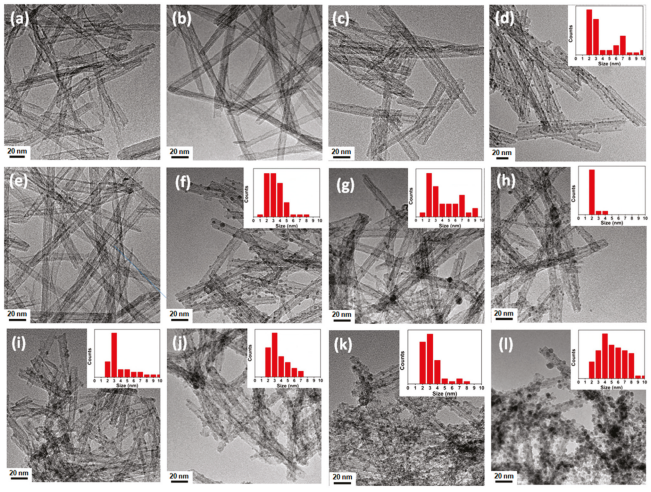

Figure 1. TEM images of Ag/TNTs and size distribution (inserted) of Ag nanoparticles (NPs) on TNTs: (**a**) Ag/TNT-1_SH, (**b**) Ag/TNT-5_SH, (**c**) Ag/TNT-2.5_AM, (**d**) Ag/TNT-100_AM, (**e**) Ag/TNT-2.5_IN, (**f**) Ag/TNT-100_IN, (**g**) Ag/TNT-2.5_NB, (**h**) Ag/TNT-100_NB, (**i**) Ag/TNT-2.5_EL (0.1), (**j**) Ag/TNT-100_EL (0.1), (**k**) Ag/TNT-2.5_EL (1), (**l**) Ag/TNT-100_EL (1).

The TEM images confirmed the formation of open-ended nanotubes with lengths in the range of ~50–200 nm and diameters of ~5–10 nm for all the Ag/TNTs. The sol-gel-assisted hydrothermal method of TNT modification did not result in the formation of Ag NPs within the used concentrations of the $AgNO_3$ solution. In the case of the photodeposition approach, the presence of the Ag NPs was observed when higher concentrations of $AgNO_3$ solution were applied, regardless of the atmosphere of the reaction. The ICP-OES compositional measurement (Table 2) also indicated low content of Ag for Ag/TNT-1_SH, Ag/TNT-5_SH, Ag/TNT-2.5_AM, and Ag/TNT-2.5_IN. Electroless and $NaBH_4$ reduction methods led to the creation of Ag NPs in the case of both lower and higher $AgNO_3$ solution concentration. The particle size distribution data in the insets in Figure 1d,f–l indicate the presence of NPs with sizes between 1–10 nm on TNTs. The sizes ranging from 2 to 10 nm, 1 to 8 nm, 1 to 9 nm and 2 to 4 nm corresponded to Ag NPs present in Ag/TNT-100_AM, Ag/TNT-100_IN, Ag/TNT-2.5_NB, Ag/TNT-100_NB, respectively. In the case of Ag/TNT-2.5_EL (0.1), Ag/TNT-100_EL (0.1), Ag/TNT-2.5_EL (1), and Ag/TNT-100_EL (1), the determined particle size (2 to 10 nm, 2 to 7 nm, 2 to 8 nm, and 2 to 10 nm, respectively) refers to both Ag and SnO_2 identified on the surface of the samples processed by the electroless method.

The TEM images also demonstrate the difference between physical and chemical Ag deposition processes (Supplementary Materials, Figure S1). The photoreduction approach led to creation of Ag NPs exclusively on the outer surface of TNTs, whereas chemical reduction techniques introduced Ag NPs both on the outer surface and inside the TNTs. This is because during UV irradiation, the outer region of the TNTs was more exposed to the action of the radiation, and hence, Ag^+ ion reduction preferably occurred in this area as observed in Figure S1a. For chemical reduction, the reducing agent had equal accessibility for the exterior and interior surfaces of the TNTs [40]. Hence, the Ag NPs could be deposited on either side of the TNTs as observed in Figure S1b,c. From particle size distribution analysis, it was observed that Ag/TNT-100_NB (inset of Figure 1h) contained almost exclusively Ag NPs with a size of 2 nm. The small size of the Ag NPs helped in the modification of both the inner and outer sides of the TNTs for this sample. However, for electroless deposition process, both surfaces of TNTs were found to be covered with an excess of NPs. This was due to the coexistence of both Ag and SnO_2 NPs with similar size making them indistinguishable from each other.

Based on TEM-EDS analysis (Figure S2), it was found that Ag/TNT-2.5_AM (Figure S2a) was characterized by a homogenous distribution of Ag all over the TNTs, despite the absence of NPs, as was found from Figure 1c. This suggests that Ag was built into the structure of nanotubes. In the case of Ag/TNT-5_SH (Figure S2b), an additional signal corresponding to Cl can be noticed, which indicates the presence of AgCl, possibly formed during the acid (HCl) washing step after the hydrothermal treatment. The EDS elemental mapping of Ag/TNT-2.5_EL (1), shown in Figure S2c, reveals the presence of Sn (red color) in addition to Ag (blue color). It can also be observed that Sn was uniformly distributed all over the TNTs in contrast to much smaller amounts of Ag concentrated in particular places. It is clear from the high resolution TEM (HRTEM) image of Ag/TNT-100_EL (1) shown in Figure S3 that the Ag and SnO_2 NPs were attached to the TNTs, and the interplanar spacing of NPs with distances 0.23 nm and 0.34 nm could be attributed to the (111) planes of Ag and (110) planes of SnO_2, respectively. Hence, the application of the electroless process resulted in the modification of TNTs with both Ag and SnO_2 NPs. From Table 2, it was observed that the Ag/TNT-2.5_EL (0.1) and Ag/TNT-2.5_EL (1) exhibited higher concentrations of Sn compared to Ag, therefore, it can be concluded that majority of NPs on the surface of TNTs for these materials are SnO_2 NPs.

3.3. XRD Analysis

The structural evolution from pure TNTs to different Ag/TNTs was studied by XRD measurements (Figure 2).

Figure 2a (i) shows the XRD pattern of pure TNTs, and it exhibited peaks at 2θ~9.7°, 24.3°, 27.8°, and 48°, which indicate the formation of layered titanates such as $H_2Ti_2O_5{\cdot}H_2O$, $H_2Ti_3O_7$ or $H_xTi_{2-x/4}\square_{x/4}O_4$ (x~0.7, □: vacancy) [31,41,42]. In comparison with pure TNTs, noticeable structural changes were observed in the XRD pattern of Ag/TNTs especially at higher Ag loading. The most perceptible change with Ag loading is the disappearance of the peak at 2θ~9.7° that resulted from the (100) plane of the TNTs. This was because during the synthesis of Ag/TNTs, Ag^+ ions first diffused to the TNTs' surface and deposited as silver hydrate intermediate ($Ag(OH)_n(H_2O)_m$), which upon dehydration with surface Ti–OH groups resulted in binding to the surface by sharing with surface oxygen atoms of the TiO_6 octahedron layers in the (100) planes of the TNTs. As a result, the (100) planes of the TNTs underwent drastic deformation, and hence loss of its X-ray diffraction pattern with Ag loading [43]. In addition, the X-ray diffraction peak at 2θ~24.3° was found to be distorted or weakened with Ag incorporation, which also resulted from the deformation at the surface of crystal lattice caused by the modification of the layered titanate structure [44]. This effect is maximal for Ag/TNT-100_NB, Ag/TNT-100_EL (0.1), Ag/TNT-2.5_EL (1), and Ag/TNT-100_EL (1). This is due to the presence of a high concentration of Ag and/or SnO_2 NPs, as shown by ICP-OES (Table 2) and TEM (Figure 1) analysis.

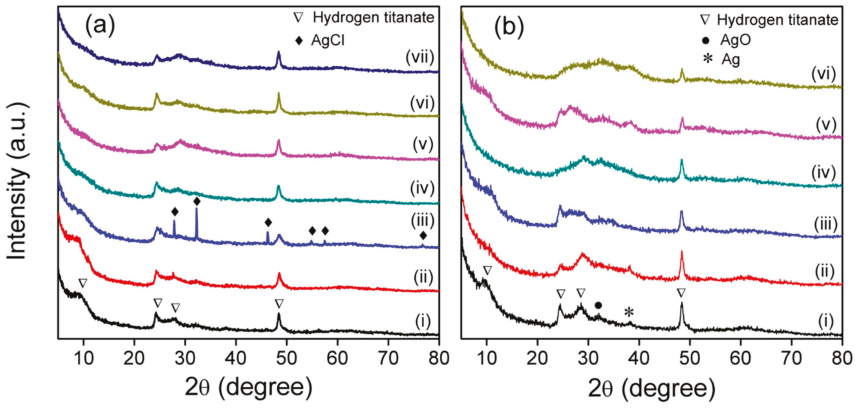

Figure 2. (**a**) XRD pattern of (i) pure TNTs, (ii) Ag/TNT-1_SH, (iii) Ag/TNT-5_SH, (iv) Ag/TNT-2.5_AM, (v) Ag/TNT-100_AM, (vi) Ag/TNT-2.5_IN, (vii) and Ag/TNT-100_IN. (**b**) XRD pattern of (i) Ag/TNT-2.5_NB, (ii) Ag/TNT-100_NB, (iii) Ag/TNT-2.5_EL (0.1), (iv) Ag/TNT-100_EL (0.1), (v) Ag/TNT-2.5_EL (1), and (vi) Ag/TNT-100_EL (1).

The XRD patterns of Ag/TNTs processed from sol-gel-derived Ag modified anatase TiO_2 (Ag/TNT-1_SH and Ag/TNT-5_SH) indicate the presence of AgCl (JCDPS 31-1238). The EDS mapping also suggested the presence of Cl in Ag/TNT-5_SH (Figure S2b). Furthermore, a higher fraction of Ag was found to be transformed to AgCl for Ag/TNT-5_SH compared to Ag/TNT-1_SH, which was directly related to the Ag content of the Ag–TiO_2 precursor used for hydrothermal treatment. The analysis of Ag/TNTs processed through electroless approach and $NaBH_4$ reduction method revealed two spikes at 2θ~32° and 2θ~38°, which can be assigned to silver oxide (AgO) (JCDPS 76-1489) and elemental Ag (JCDPS 04-0783), respectively.

3.4. Raman Spectra Analysis

Figure 3 shows the Raman spectra of the prepared TNTs and Ag/TNTs. Almost identical Raman vibration patterns were observed for both TNTs and Ag/TNTs, which consisted of mainly four very broad bands centered at 275, 450, 667, and 830 cm^{-1} that could be assigned to the protonated type of TNTs [34,45–47]. The occurrence of the peak at 149 cm^{-1} indicates the formation of a tetrahedron structure in the nanotubes with oxygen deficiencies [48]. The presence of Raman bands at 191, 275, 450, 667, 830, and 930 cm^{-1} confirmed the formation of $H_2Ti_3O_7$ nanotubes [41,49,50]. According to previous reports, the three Raman bands at around 270, 450, and 700 cm^{-1} are assigned to the A_g symmetric modes of Ti–O–Ti vibrations of layered titanates [41]. The bands at 830 cm^{-1} are assigned to the Ti–O–H symmetric stretching mode with short Ti–O distance [51], and the band at 930 cm^{-1} is due to the four coordinate Ti–O vibrations in the titanate structure [52]. Raman spectra of Ag/TNT-100_NB, Ag/TNT-100_EL (0.1), Ag/TNT-2.5_EL (1). and Ag/TNT-100_EL (1) also showed a loss characteristic vibration of TNTs due to the higher loading of NPs (both Ag and SnO_2). This indicate that higher metal loading drastically alters and/or diminishes the characteristic XRD and Raman vibration pattern of TNTs.

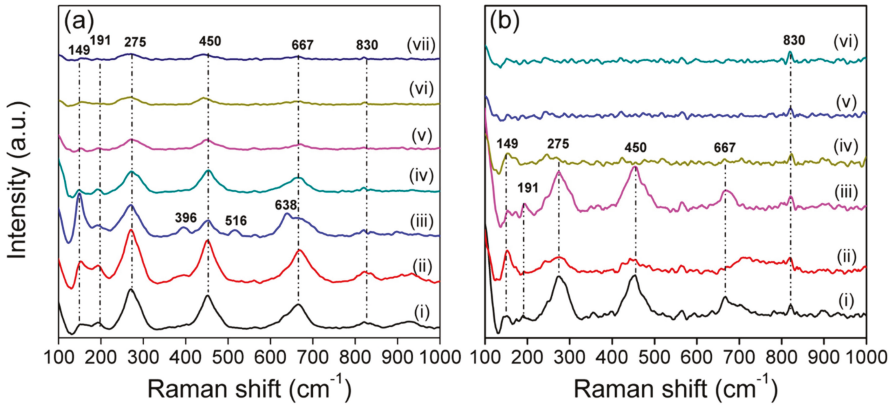

Figure 3. (**a**) Raman spectra of (i) pure TNTs, (ii) Ag/TNT-1_SH, (iii) Ag/TNT-5_SH, (iv) Ag/TNT-2.5_AM, (v) Ag/TNT-100_AM, (vi) Ag/TNT-2.5_IN, and (vii) Ag/TNT-100_IN. (**b**) Raman spectra of (i) Ag/TNT-2.5_NB, (ii) Ag/TNT-100_NB, (iii) Ag/TNT-2.5_EL (0.1), (iv) Ag/TNT-100_EL (0.1), (v) Ag/TNT-2.5_EL (1), and (vi) Ag/TNT-100_EL (1).

Different from the other samples, the spectra of Ag/TNTs prepared by sol-gel-assisted hydrothermal process show low intensity peaks at 396, 516, and 638 cm^{-1} which correspond to B_{1g}, A_{1g}, and E_{2g} vibration modes of anatase TiO_2, respectively [53]. Additionally, the intensity of the band at 149 cm^{-1} was found to be comparatively higher for this Ag/TNTs. This indicates that a small fraction of anatase TiO_2 remained unconverted after the hydrothermal process for these samples [32,49]. However, the presence of anatase TiO_2 could not be confirmed based on the XRD analysis (Figure 2) due to (i) the overlapping of the anatase TiO_2 peak with that of hydrogen titanate or (ii) too low content of anatase to be detected by this method.

Based on the XRD and Raman analyses, it can be concluded that the hydrogen titanate structure of Ag/TNTs remains unaffected at lower Ag loading and is affected when the Ag loading is higher.

3.5. XPS Analysis

The surface concentration of elements was measured with application of XPS analysis. Silver/TNT samples prepared by various methods using higher $AgNO_3$ content were selected (Table 3). The surface of all these samples consisted of titanium, oxygen, silver, and carbon atoms. The presence of Sn atoms was proven for the samples prepared by electroless reduction, Ag/TNT-100_EL (0.1) and Ag/TNT-100_EL (1). Sodium atoms were present on the surface of Ag/TNT-100_NB sample, which was confirmed by the Na KLL Auger peak. Unfortunately, the XPS Na 1s and Auger Ti LMM lines overlapped. Therefore, the XPS Na 1s peak's intensity could not be resolved and the concentration of sodium atoms was not considered in the calculation of the surface composition of Ag/TNT-100_NB sample.

Table 3. The surface concentration of elements identified by XPS on the surface of selected samples.

Element	Ti	O	C	Ag	Sn
Sample			**at.%**		
Ag/TNT-5_SH	23	73	4	traces	-
Ag/TNT-100_AM	19	63	15	3	-
Ag/TNT-100_IN	19	63	16	2	-
Ag/TNT-100_NB	18	61	18	3	-
Ag/TNT-100_EL (0.1)	16	59	15	5	5
Ag/TNT-100_EL (1)	11	60	9	9	11

In Table 3, the surface composition of the samples analyzed by XPS is shown. The calculations were employed with the assumption that the spatial distribution of all elements identified in a near-surface region was homogeneous.

In general, the Ti:O ratio observed for the investigated samples was close to 1:3. Therefore, the surface structure of Ti–O compounds was considered as a $TiO(OH)_2$ type rather than TiO_2 type. In samples Ag/TNT-100_EL (0.1) and Ag/TNT-100_EL (1), the Ti:O ratio was even smaller due to a significant concentration of oxygen atoms being a part of Sn–O compounds. Since the depth of detection for XPS was around 5–10 nm [54,55], the Ag NPs present on both the outer and inner TNTs walls were analyzed (Figure S1). This led to the similar Ag concentrations for Ag/TNT-100_AM, Ag/TNT-100_IN, and Ag/TNT-100_NB (2–3 at.%). A significant enrichment of the surface with silver atoms was observed for the samples obtained by the electroless reduction, especially in the sample Ag/TNT-100_EL (1). Considering that the surface concentration of silver w presented in atomic percent, the direct correlation of these data with the silver concentrations measured by ICP-OES method is not possible. However, a general relation of these concentrations between the samples is kept (Figure S4).

The high-resolution XPS spectra were analyzed to elucidate the chemical state of silver atoms formed by different types of preparation methods. The XPS Ag 3d spectra (Figure S5) have virtually identical positions of the maximum and a very symmetric spectrum envelope. They contained two spin-orbit components: $3d_{5/2}$ and $3d_{3/2}$ located at the binding energy of 368.3 eV and 374.3 eV, respectively. The full-width at half maximum (FWHM) of these components was also identical for all samples and amounted to 1.7 eV. Therefore, it is concluded that the chemical state of silver in all analyzed samples was identical. The binding energy of the maximum of XPS $3d_{5/2}$ component at 368.3 eV was characteristic for metallic silver [56]. The presence of silver oxides which can be considered in the context of Ag/TNTs materials should result in the XPS features located at the binding energy region between 367.3 eV and 368 eV.

3.6. Ag^+ Ion Release Measurement

One of the critical parameters which determines the antibacterial properties of nanocomposites modified with Ag NPs is Ag^+ ions' release ability [51]. Figure 4 shows the percentage of Ag^+ released from different Ag/TNTs for a period of one, three, and seven days of immersion in deionized water. The values were calculated with reference to the initial silver content in Ag/TNTs (Table 2).

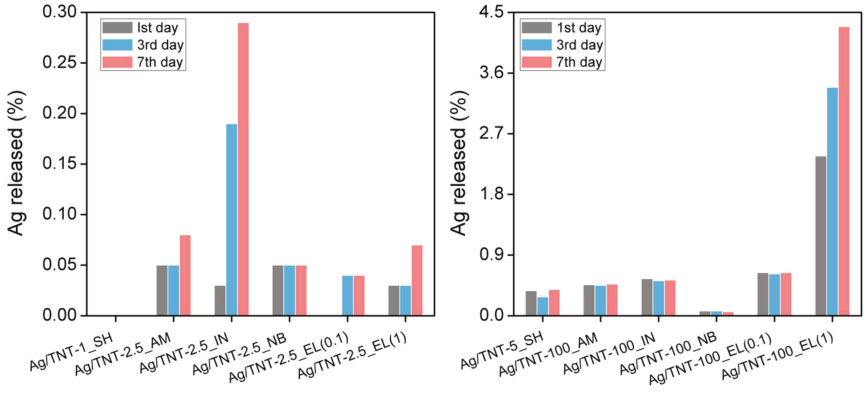

Figure 4. The percentage of Ag^+ released from different Ag/TNTs.

During a period of seven days, a very small amount of Ag^+ (<5%) was observed to be leached from the prepared Ag/TNTs which indicated their high stability. The amount of Ag^+ leaching from the NPs was found to increase with the increase in immersion time. However, for some Ag/TNTs, the amount of Ag released after the third day was slightly lower than after the first day (e.g., Ag/TNT-5_SH).

This could be explained by reincorporation of the released Ag^+ ions in the TNTs' structure by the ion-exchange process. The minimum Ag^+ release percentage was observed for Ag/TNT-1_SH and the maximum release exhibited the Ag/TNT-100_EL (1) which was directly related to the Ag content in the nanocomposite (Table 2). For Ag/TNTs with lower Ag content (less than 5 wt.%, Table 2), Ag/TNT-5_SH showed the highest Ag^+ release percentage. This sample was prepared by sol-gel followed by a hydrothermal process and was characterized by the presence of AgCl (almost insoluble in water, K_{sp} for AgCl at room temperature was 1.77×10^{-10} [57]) except from metallic Ag. In the case of this sample, no Ag NPs were identified on the surface (Figure 1b), although a uniform distribution of silver was confirmed by the TEM-EDS mapping (Figure S2b). Therefore, its low stability can be attributed to a dissolution of a silver layer covering the TNTs, a release of silver ions from AgCl or a removal of Ag^+ from titanate structure, where it was possibly built-in via the ion exchange process during the synthesis step. Except for Ag/TNT-100_NB, in the cases of all the other Ag/TNTs processed using a higher concentration of $AgNO_3$ (100 mM), the Ag^+ release percentage was directly related to the initial Ag content. The sample Ag/TNT-100_NB exhibited the maximum stability for Ag^+ leakage during the seven days of measurement which could be attributed to the presence of Ag NPs not only on the outer surface of the TNTs but also inside the nanotubes, as observed in Figure S1c–f. Such a structure can be regarded as a container (TNT) housing Ag NPs and serving as protection which hindered Ag^+'s release.

3.7. Surface Charge Measurements

On the basis of the zeta potential measurement as a function of pH, the isoelectric point (IEP) of the NPs was evaluated, and the corresponding values are summarized in Table 4.

Table 4. The isoelectric point (IEP) of the TNTs and Ag/TNTs.

Sample name	IEP	Sample name	IEP
TNTs	3.13(0.09)	Ag/TNT-100_IN	3.33(0.01)
TNTs (from sol-gel TiO2)	3.73(0.06)	Ag/TNT-2.5_NB	3.45(0.01)
Ag/TNT-1_SH	3.89(0.04)	Ag/TNT-100_NB	3.37(0.08)
Ag/TNT-5_SH	3.68(0.01)	Ag/TNT-2.5_EL (0.1)	3.39(0.01)
Ag/TNT-2.5_AM	3.39(0.08)	Ag/TNT-100_EL (0.1)	3.14(0.02)
Ag/TNT-100_AM	3.29(0.04)	Ag/TNT-2.5_EL (1)	3.69(0.03)
Ag/TNT-2.5_IN	3.38(0.03)	Ag/TNT-100_EL (1)	3.27(0.02)

Zeta potential describes the electrostatic interactions between the charged surface of a particle and the bulk of a liquid. There is an electrical double layer surrounding the particle. In the inner layer, the ions are strongly bound to the particle, and in the outer layer (diffuse layer) they are less firmly attached. The boundary between those regions is called the shear or slipping plane. The zeta potential is the potential between the dispersion medium and the stationary layer of the fluid attached to the particle. The zeta potential strongly depends on pH [58]. The pH at which the surface of the NPs has zero net charge is called the IEP [59]. When the pH is above the IEP, the surface sites become negatively charged either by adsorbing hydroxyl ions or by desorbing protons and vice versa. The value of the zeta potential of the nanomaterials could also affect their interactions with other species, such as microorganisms present in a liquid. The IEP of living *E. coli* and *S. epidermidis* are around 2.4 and 1.5–2.0, respectively [60,61]. Thus, the bacteria cells have positive charge only under very acidic conditions.

Both pure TNTs and Ag/TNTs show IEP in the range of ~3.1–3.9 and exhibit negative zeta potential above these values. The IEP of Ag/TNTs was found to be at higher pH than that of pure TNTs which could be attributed to (i) the presence of silver species, either in the form of Ag NPs or as Ag^+ ions replacing H^+ in TNTs structure, and (ii) the presence of SnO_2 NPs in case of the samples prepared by the electroless method. A similar trend in zeta potential was observed when the TiO_2 surface was modified with metals like Cu, Fe or Co [62]. However, for the same method of preparation, the Ag/TNTs with higher Ag content have slightly lower IEP values than that of Ag/TNTs with lower

Ag content. This is possibly because at a high Ag amount, the role of Ag NPs, which have an IEP of ~2.5 in deionized water, becomes more prominent [63].

3.8. Antibacterial Properties of Ag/TNTs

The antimicrobial properties of various Ag/TNTs were evaluated with reference to two types of bacteria: Gram-positive (*S. epidermidis*) and Gram-negative *(E. coli*). The results are presented in Figure 5. In general, for every type of Ag/TNTs synthesis approach, the samples obtained using lower $AgNO_3$ amount (i.e. 2.5 mM $AgNO_3$), and thus containing lower silver loading, were less active compared to the NPs synthesized with application of higher $AgNO_3$ concentration (i.e. 100 mM $AgNO_3$).

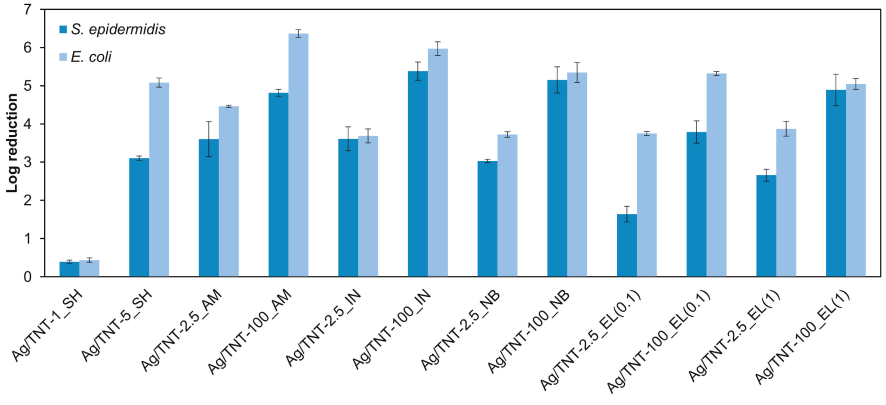

Figure 5. Antibacterial properties of Ag/TNTs towards *E. coli* and *S. epidermidis*.

Analyzing the results shown in Figure 5, it can also be observed that *S. epidermidis* was inactivated with lower efficiency than *E. coli*, regardless of the Ag/TNTs used. This phenomenon can be related with the composition of the bacteria cell wall. Gram-positive bacteria (i.e., *S. epidermidis*) have a relatively thick (20–80 nm), continuous cell wall, composed of peptidoglycan and covalently attached to other cell wall polymers (teichoic acids, polysaccharides, peptidoglycolipids) [64]. Such a structure results in a high rigidity of the bacterial cell as well as provides a very limited number of anchoring sites for Ag NPs and makes Ag NPs and ions difficult to penetrate [65,66]. On the other hand, Gram-negative bacteria possess a thin (5–10 nm) peptidoglycan layer, which in the case of *E. coli* is probably only a monolayer thick [64]. Outside the peptidoglycan layer, there is an outer membrane (7.5–10 nm). Despite the presence of many covalent bonds between polysaccharides and lipids in the outer membrane, the strength and rigidity of Gram-negative bacteria are low. Additionally, the presence of micro-channels known as porins responsible for bilateral transport of substances can facilitate transport of Ag^+ ions to the inner of bacteria cells [67].

The exact mechanism of action of nano-Ag as an antibacterial agent is not fully understood; however, in general, its antibacterial behavior is explained with the help of three approaches. First, due to the high binding affinity of Ag towards sulfur, Ag NPs attach to the bacterial cell membrane due to the presence of sulfur-containing proteins in it and cause many structural and functional changes to it [68,69]. Secondly, nano-Ag undergoes oxidation and the formed Ag^+ ions are released to the physiological environment which upon complexation with nucleic acids leads to DNA condensation and loss of replication ability [69]. Also, the Ag^+ ion has high affinity towards the thiol group of the cysteine residues of protein NADH dehydrogenases and causes disorder to the respiratory chain which finally leads to cell damage [70]. Thirdly, reactive oxygen species (ROS) like hydrogen peroxide (H_2O_2), hydroxyl radicals ($OH^\bullet$) or superoxide anions ($^\bullet O_2^-$) formed in the presence of Ag NPs also contribute to the bactericidal actions [71,72].

Based on the results presented in Figure 5, it can be observed that the method of preparation of Ag/TNTs had some influence on the antimicrobial action of the nanomaterials. Ivask et al. [73] investigated the relation between size and antibacterial activity of Ag NPs and suggested that the mechanism of action is mainly dependent upon Ag NPs size. When the Ag NP's diameter is above 10 nm, the antibacterial activity depends on the released Ag^+ ions, whereas when the size of Ag NP's diameter is below 10 nm, the interaction of NPs with the bacterial cell wall becomes more important. In the present investigations, the prepared Ag/TNTs contain Ag NPs with a size <10 nm, and hence, it can be expected that the antibacterial action occurs through direct interaction of Ag NPs present in the hybrid structures with the bacterial cell walls. From the morphological analysis (Figure S1), it was noticed that the Ag/TNTs processed through the photodeposition method contained Ag NPs which were mostly attached to the outer surface of TNTs. This led to the higher antibacterial activity of nanomaterials synthesized by the photoreduction approach than that of Ag/TNTs prepared by chemical reduction methods, using both $NaBH_4$ and $SnCl_2$ as reducing agents, even though they contained higher amounts of Ag (Table 2). Nonetheless, in the presence of SnO_2, the mechanism of antibacterial action of the NPs can differ from that of TNTs containing Ag only. The bactericidal potency of SnO_2 was investigated by Vidhu and Philip [74] who found formation of zones of inhibition in the presence of these nanoparticles. They attributed that to the mechanism typical for metal oxides, i.e., formation of reactive oxygen species and electrostatic interaction of nanostructures with bacterial cell walls. Furthermore, Kumar Nair et al. [75] reported a synergic antimicrobial action of Ag and SnO_2 towards *E. coli*. However, the authors applied UV irradiation to induce the antibacterial action. Nonetheless, the above data show that a direct comparison of Ag/TNTs containing solely Ag and those modified with both Ag and SnO_2 NPs is difficult and the explanation of the antimicrobial action of the NPs containing tin oxide needs further investigations. Nonetheless, in general, the obtained results revealed that the efficiency of inhibition of *E. coli* and *S. epidermidis* growth was lower when SnO_2 was present in the samples. Another mechanism of antibacterial action can be expected for the sol-gel-derived Ag/TNTs. In the case of these nanomaterials, no Ag NPs were detected during TEM analysis (Figure 1a,b); however, the XRD measurement confirmed the presence of the AgCl phase (Figure 2). Okkyoung et al. [76] in their work demonstrated that colloidal AgCl can be as important antibacterial agent as the other Ag forms, including Ag^+ ions. Taking the above into consideration the antibacterial properties of the discussed nanomaterials can be linked with the presence of AgCl.

In order to evaluate if there is any correlation between silver content in the hybrid Ag/TNTs and the log reduction values, the samples were divided into three groups, i.e., containing low (0.11 wt.%), medium (2.33–4.08 wt.%), and high (≥11.98 wt.%) amounts of Ag. Figure 6 summarizes the results. It can be observed that the nanomaterial with the lowest Ag content (0.11 wt.%) was characterized by the lowest antimicrobial activity against both bacteria. Analysis of the samples modified with a medium amount of Ag revealed that the antibacterial performance of the NPs containing between 2 and 4 wt.%Ag did not differ much, especially in terms of inhibition of *E. coli* growth. The highest log reduction with reference to both microorganisms (*E. coli*: 4.5 log reduction; *S. epidermidis*: 3.6 log reduction) exhibited Ag/TNT-2.5_AM, containing 3.77 wt.%Ag. A slightly better activity towards *E. coli* (5.1 log reduction) was observed in the case of Ag/TNT-5_SH (3.56 wt.%Ag); however, that sample was less efficient in terms of *S. epidermidis* inactivation (3.1 log reduction). In the discussed group of the NPs with medium Ag content, the lowest amount of silver was measured for Ag/TNT-2.5_EL (0.1) (2.33 wt.%), for which the sample exhibited the lowest activity with reference to the Gram-positive bacteria. The third group of Ag/TNTs covered samples with the highest Ag content. Amongst them, the best antibacterial performance against both *E. coli* and *S. epidermidis* revealed Ag/TNT-100_IN (6.0 and 5.4 log reduction, respectively), containing 12.58 wt.%Ag. No correlation between Ag content and antibacterial activity of the samples assigned to the third group was found. For example, the nanomaterial containing the highest Ag amount (30.85 wt.%) was less effective than the NPs with 12.58 wt.%Ag content. Such a phenomenon can be ascribed to the presence of Sn in the samples prepared by the electroless method (Table 2). Hassan et al. [77] observed that depending on SnO_2

content, the antibacterial activity of SnO_2/TiO_2 composites can be improved or decreased. Therefore, as was mentioned earlier, the antibacterial properties of TNTs modified with both Ag and Sn NPs need further detailed studies.

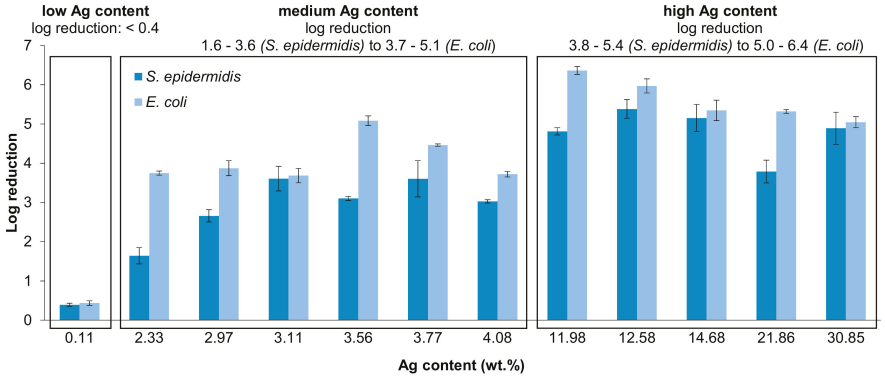

Figure 6. Antibacterial properties of Ag/TNTs with reference to Ag content in the hybrid nanomaterials.

Another attempt in explanation of antibacterial properties of the various Ag/TNTs was based on Ag^+ release from the NPs (Figure 4). The samples were again divided into three groups, i.e., characterized by low (≤0.05% versus total Ag content or ≤0.2 mg L^{-1} in solution), medium (0.07–0.55% or 0.11–0.55 mg L^{-1}) and high (≥0.64% or ≥1.13 mg L^{-1}) Ag^+ leakage (Figure S6). The lowest inhibition of bacterial growth was found for Ag/TNT-1_SH, in which case no Ag^+ leaching for seven days was observed. However, no correlation between Ag^+ release and antibacterial properties was noted. For example, the least stable Ag/TNT-100_EL (1), for which the concentration of the released Ag^+ was the highest (7.32 mg L^{-1}), exhibited a similar activity as Ag/TNT-100_NB with approximately 66 times lower Ag^+ leakage (0.11 mg L^{-1}).

The above analysis confirms that when the size of Ag NPs is less than 10 nm, the interaction of NPs with the bacterial cell is more important than Ag content or Ag^+ ion release. Nonetheless, in general, the samples containing higher Ag loading were more active than samples with low silver amount. Furthermore, the nanomaterials for which silver concentration in the solution was in the medium and high range were characterized by higher antibacterial activity than those exhibiting the lowest Ag^+ release. A comparison of the Ag/TNTs synthesis procedures analyzed in this study revealed that the photodeposition approach was the most effective technique to obtain nanomaterials with the best antibacterial properties.

4. Conclusions

Silver/TNTs with different Ag contents were synthesized through five different procedures including (i) sol-gel followed by a hydrothermal process; (ii) photodeposition under ambient conditions; (iii) photodeposition under an inert atmosphere; (iv) $NaBH_4$ reduction; and (v) an electroless deposition process after activation of TNTs' surface with various amounts of Sn^{2+} ions. The physicochemical characterization of various Ag/TNTs revealed the presence of Ag NPs in most samples. The NPs with size ~1–10 nm were uniformly deposited onto TNTs' surface. Moreover, the electroless deposition resulted in the additional decoration of TNTs with SnO_2 NPs. The presence of Ag NPs was not confirmed in case of nanomaterials obtained by the method (i), for which the AgCl phase was detected by the XRD analysis. Furthermore, no Ag NPs were observed in samples prepared from 2.5 mM $AgNO_3$ solution using the photodeposition approach. Nonetheless, the ICP-OES analysis confirmed that all samples contained Ag and its loading varied from 0.11 wt.% to 30.85 wt.%. For Ag/TNTs with higher Ag content, a maximum stability of the nanocomposite was shown by the sample prepared with $NaBH_4$ reduction method. It was noted that for the photoreduction process, the Ag NPs were

specifically deposited on the outer surface of the TNTs while chemical reduction led to the introduction of Ag NPs on both inner and outer surfaces. The antibacterial activity of different Ag/TNTs against both Gram-positive (*S. epidermidis*) and Gram-negative (*E. coli*) bacteria was evaluated under dark conditions. In general, Ag/TNTs with higher Ag content exhibited higher antibacterial activity compared to the nanomaterials with lower Ag loading. Also, *S. epidermidis* was inactivated with lower efficiency compared to *E. coli*, regardless of the hybrid NPs used. The Ag/TNTs obtained by the photodeposition approach were found to exhibit moderately higher antibacterial properties compared to samples prepared by other methods due to the higher interaction of Ag NPs present on the TNTs with bacterial cell walls.

Supplementary Materials: The following are available online at http://www.mdpi.com/2079-4991/9/5/795/s1, Figure S1: HRTEM image of (a) Ag/TNT-100_IN, (b) Ag/TNT-100_EL (0.1), and (c)–(f) Ag/TNT-100_NB (The circled regions in (e) and (f) represent the Ag NPs anchored to the inner surface of the TNTs. Moreover, in Figure S1(e) the Ag NP blocking the entrance to the TNT can be observed), Figure S2: EDS elemental mapping of (a) Ag/TNT-2.5_AM, (b) Ag/TNT-5_SH, (c) Ag/TNT-2.5_EL (1). Scanning transmission electron microscopy (STEM) images with red squares present the scanned area, Figure S3: HRTEM image of Ag/TNT-100_EL (1), Figure S4: The dependence between Ag content measured by XPS and ICP methods, Figure S5: XPS spectra of (i) Ag/TNT-5_SH, (ii) Ag/TNT-100_AM, (iii) Ag/TNT-100_IN, (iv) Ag/TNT-100_NB, (v) Ag/TNT-100_EL (0.1), and (vi) Ag/TNT-100_EL (1), Figure S6: Antibacterial properties of Ag/TNTs with reference to Ag release from the hybrid nanomaterial.

Author Contributions: Conceptualization, M.J. and S.M.; Funding acquisition, S.M.; Investigation, M.J., P.S., K.S. (Karolina Szymańska), D.D., D.M., Z.L.-B., K.S. (Kacper Szymański) and S.M.; Methodology, M.J., P.S., K.S. (Karolina Szymańska), D.D., D.M., Z.L.-B. and S.M.; Project administration, S.M.; Supervision, S.M.; Validation, M.J., P.S., K.S. (Kacper Szymański) and S.M.; Writing—original draft, M.J., P.S., K.S. (Karolina Szymańska), D.M. and S.M.

Funding: This work was supported by the National Science Centre, Poland under project No. 2016/21/B/ST8/00317.

Conflicts of Interest: The authors declare no conflict of interest.

References

1. Kumar, T.K.M.P.; Mandlimath, T.R.; Sangeetha, P.; Sakthivel, P.; Revathi, S.K.; Kumar, S.K.A.; Sahoo, S.K. Highly efficient performance of activated carbon impregnated with Ag, ZnO and Ag/ZnO nanoparticles as antimicrobial materials. *RSC Adv.* **2015**, *5*, 108034–108043. [CrossRef]
2. Yuan, X.; Setyawati, M.I.; Leong, D.T.; Xie, J.P. Ultrasmall Ag^{+}-rich nanoclusters as highly efficient nanoreservoirs for bacterial killing. *Nano Res.* **2014**, *7*, 301–307. [CrossRef]
3. Biswas, P.; Bandyopadhyaya, R. Synergistic antibacterial activity of a combination of silver and copper nanoparticle impregnated activated carbon for water disinfection, Environmental Science. *Nano* **2017**, *4*, 2405–2417.
4. Silver, S.; Phung, L.T.; Silver, G. Silver as biocides in burn and wound dressings and bacterial resistance to silver compounds. *J. Ind. Microbiol. Biotechnol.* **2006**, *33*, 627–634. [CrossRef]
5. Benn, T.M.; Westerhoff, P. Nanoparticle silver released into water from commercially available sock fabrics. *Environ. Sci. Technol.* **2008**, *42*, 4133–4139. [CrossRef] [PubMed]
6. Loher, S.; Schneider, O.D.; Maienfisch, T.; Bokorny, S.; Stark, W.J. Micro-organism-triggered release of silver nanoparticles from biodegradable oxide carriers allows preparation of self-sterilizing polymer surfaces. *Small* **2008**, *4*, 824–832. [CrossRef] [PubMed]
7. Agarwal, A.; Weis, T.L.; Schurr, M.J.; Faith, N.G.; Czuprynski, C.J.; McAnulty, J.F.; Murphy, C.J.; Abbott, N.L. Surfaces modified with nanometer-thick silver-impregnated polymeric films that kill bacteria but support growth of mammalian cells. *Biomaterials* **2010**, *31*, 680–690. [CrossRef]
8. Cao, H.; Liu, X.; Meng, F.; Chu, P.K. Biological actions of silver nanoparticles embedded in titanium controlled by micro-galvanic effects. *Biomaterials* **2011**, *32*, 693–705. [CrossRef] [PubMed]
9. Vazquez-Muñoz, R.; Borrego, B.; Juárez-Moreno, K.; García-García, M.; Morales, J.D.M.; Bogdanchikova, N.; Huerta-Saquero, A. Toxicity of silver nanoparticles in biological systems: Does the complexity of biological systems matter? *Toxicol. Lett.* **2017**, *276*, 11–20. [CrossRef]
10. Bélteky, P.; Rónavári, A.; Igaz, N.; Szerencsés, B.; Tóth, I.Y.; Pfeiffer, I.; Kiricsi, M.; Kónya, Z. Silver nanoparticles: Aggregation behavior in biorelevant conditions and its impact on biological activity. *Int. J. Nanomed.* **2019**, *14*, 667–687. [CrossRef] [PubMed]

11. Moritz, M.; Geszke-Moritz, M. The newest achievements in synthesis, immobilization and practical applications of antibacterial nanoparticles. *Chem. Eng. J.* **2013**, *228*, 596–613. [CrossRef]
12. Liu, S.X.; Qu, Z.P.; Han, X.W.; Sun, C.L. A mechanism for enhanced photocatalytic activity of silver-loaded titanium dioxide. *Catal. Today* **2004**, *93*, 877–884. [CrossRef]
13. Li, M.; Noriega-Trevino, M.E.; Nino-Martinez, N.; Marambio-Jones, C.; Wang, J.; Damoiseaux, R.; Ruiz, F.; Hoek, E.M.V. Synergistic bactericidal activity Ag-TiO_2 nanoparticles in both light and dark conditions. *Environ. Sci. Technol.* **2011**, *45*, 8989–8995. [CrossRef]
14. Wei, L.; Wang, H.; Wang, Z.; Yu, M.; Chen, S. Preparation and long-term antibacterial activity of TiO_2 nanotubes loaded with Ag nanoparticles and Ag ions. *RSC Adv.* **2015**, *5*, 74347–74352. [CrossRef]
15. Yang, D.; Yang, N.; Ge, J. Controlled deposition of ultra-small Ag particles on TiO_2 nanorods: Oxide/metal hetero-nanostructures with improved catalytic activity. *CrystEngComm* **2013**, *15*, 7230–7235. [CrossRef]
16. Rodríguez-González, V.; Domínguez-Espíndola, R.B.; Casas-Flores, S.; Patrón-Soberano, O.A.; Camposeco-Solis, R.; Lee, S.-W. Antifungal nanocomposites inspired by titanate nanotubes for complete inactivation of *Botrytis cinerea* isolated from tomato infection. *ACS Appl. Mater. Interfaces* **2016**, *8*, 31625–31637. [CrossRef]
17. Wang, H.; Wei, L.; Wang, Z.; Chen, S. Preparation, characterization and long-term antibacterial activity of Ag–poly (dopamine)–TiO_2 nanotube composites. *RSC Adv.* **2016**, *6*, 14097–14104. [CrossRef]
18. Martinez-Castanon, G.A.; Nino-Martinez, N.; Martinez-Gutierrez, F.; Martinez-Mendoza, J.R.; Ruiz, F. Synthesis and antibacterial activity of silver nanoparticles with different sizes. *J. Nanoparticle Res.* **2008**, *10*, 1343–1348. [CrossRef]
19. Morones, J.R.; Elechiguerra, J.L.; Camacho, A.; Holt, K.; Kouri, J.B.; Ramírez, J.T.; Yacaman, M.J. The bactericidal effect of silver nanoparticles. *Nanotechnology* **2005**, *16*, 2346. [CrossRef]
20. Kubacka, A.; Ferrer, M.; Martínez-Arias, A.; Fernández-García, M. Ag promotion of TiO_2-anatase disinfection capability: Study of *Escherichia coli* inactivation. *Appl. Catal. B Environ.* **2008**, *84*, 87–93. [CrossRef]
21. Es-Souni, M.; Fischer-Brandies, H.; Es-Souni, M. Versatile nanocomposite coatings with tunable cell adhesion and bactericidity. *Adv. Funct. Mater.* **2008**, *18*, 3179–3188. [CrossRef]
22. Keleher, J.; Bashant, J.; Heldt, N.; Johnson, L.; Li, Y. Photo-catalytic preparation of silver-coated TiO_2 particles for antibacterial applications. *World J. Microbiol. Biotechnol.* **2002**, *18*, 133–139. [CrossRef]
23. Sotiriou, G.A.; Meyer, A.; Knijnenburg, J.T.N.; Panke, S.; Pratsinis, S.E. Quantifying the origin of released Ag^+ ions from nanosilver. *Langmuir* **2012**, *28*, 15929–15936. [CrossRef]
24. Rónavári, A.; Kovács, D.; Vágvölgyi, C.; Kónya, Z.; Kiricsi, M.; Pfeiffer, I. Ion exchange defines the biological activity of titanate nanotubes. *J. Basic Microbiol.* **2016**, *56*, 557–565. [CrossRef]
25. Zhang, Y.; Liu, F.-M. Tunable optical properties of Ag–TiO_2 nanorod composites based on interparticle plasmon coupling. *Nano* **2016**, *11*, 1650110. [CrossRef]
26. Seery, M.K.; George, R.; Floris, P.; Pillai, S C. Silver doped titanium dioxide nanomaterials for enhanced visible light photocatalysis. *J. Photochem. Photobiol. A Chem.* **2007**, *189*, 258–263. [CrossRef]
27. Priya, R.; Baiju, K.V.; Shukla, S.; Biju, S.; Reddy, M.L.P.; Patil, K.; Warrier, K.G.K. Comparing ultraviolet and chemical reduction techniques for enhancing photocatalytic activity of silver oxide/silver deposited nanocrystalline anatase titania. *J. Phys. Chem. C* **2009**, *113*, 6243–6255. [CrossRef]
28. Ye, J.; Cheng, H.; Li, H.; Yang, Y.; Zhang, S.; Rauf, A.; Zhao, Q.; Ning, G. Highly synergistic antimicrobial activity of spherical and flower-like hierarchical titanium dioxide/silver composites. *J. Colloid Interface Sci.* **2017**, *504*, 448–456. [CrossRef]
29. Zhao, C.; Feng, B.; Li, Y.; Tan, J.; Lu, X.; Weng, J. Preparation and antibacterial activity of titanium nanotubes loaded with Ag nanoparticles in the dark and under the UV light. *Appl. Surf. Sci.* **2013**, *280*, 8–14. [CrossRef]
30. Ma, R.; Sasaki, T.; Bando, Y. Layer-by-Layer Assembled multilayer films of titanate nanotubes, Ag-or Au-loaded nanotubes, and nanotubes/nanosheets with polycations. *J. Am. Chem. Soc.* **2004**, *126*, 10382–10388. [CrossRef]
31. Cesano, F.; Bertarione, S.; Uddin, M.J.; Agostini, G.; Scarano, D.; Zecchina, A. Designing TiO_2 based nanostructures by control of surface morphology of pure and silver loaded titanate nanotubes. *J. Phys. Chem. C* **2009**, *114*, 169–178. [CrossRef]
32. Rodríguez-González, V.; Obregón-Alfaro, S.; Lozano-Sánchez, L.M.; Lee, S.-W. Rapid microwave-assisted synthesis of one-dimensional silver–$H_2Ti_3O_7$ nanotubes. *J. Mol. Catal. A Chem.* **2012**, *353*, 163–170. [CrossRef]

33. Yee, M.S.-L.; Khiew, P.S.; Lim, S.S.; Chiu, W.S.; Tan, Y.F.; Kok, Y.-Y.; Leong, C.-O. Enhanced marine antifouling performance of silver-titania nanotube composites from hydrothermal processing. *Colloids Surfaces A Physicochem. Eng. Asp.* **2017**, *520*, 701–711. [CrossRef]
34. Plodinec, M.; Gajović, A.; Jakša, G.; Žagar, K.; Čeh, M. High-temperature hydrogenation of pure and silver-decorated titanate nanotubes to increase their solar absorbance for photocatalytic applications. *J. Alloys Compd.* **2014**, *591*, 147–155. [CrossRef]
35. Mozia, S.; Jose, M.; Sienkiewicz, P.; Szymanski, K.; Darowna, D.; Zgrzebnicki, M.; Markowska-Szczupak, A. Polyethersulfone ultrafiltration membranes modified with hybrid Ag/titanate nanotubes: Physicochemical characteristics, antimicrobial properties, and fouling resistance. *Desalin. Water Treat* **2018**, *128*, 106–118. [CrossRef]
36. Miao, L.; Ina, Y.; Tanemura, S.; Jiang, T.; Tanemura, M.; Kaneko, K.; Toh, S.; Mori, Y. Fabrication and photochromic study of titanate nanotubes loaded with silver nanoparticles. *Surf. Sci.* **2007**, *601*, 2792–2799. [CrossRef]
37. Chan, S.C.; Barteau, M.A. Preparation of highly uniform Ag/TiO_2 and Au/TiO_2 supported nanoparticle catalysts by photodeposition. *Langmuir* **2005**, *21*, 5588–5595. [CrossRef]
38. Cozzoli, P.D.; Comparelli, R.; Fanizza, E.; Curri, M.L.; Agostiano, A.; Laub, D. Photocatalytic synthesis of silver nanoparticles stabilized by TiO_2 nanorods: A semiconductor/metal nanocomposite in homogeneous nonpolar solution. *J. Am. Chem. Soc.* **2004**, *126*, 3868–3879. [CrossRef]
39. Lai, Y.; Chen, Y.; Zhuang, H.; Lin, C. A facile method for synthesis of Ag/TiO_2 nanostructures. *Mater. Lett.* **2008**, *62*, 3688–3690. [CrossRef]
40. Bavykin, D.V.; Lapkin, A.A.; Plucinski, P.K.; Torrente-Murciano, L.; Friedrich, J.M.; Walsh, F.C. Deposition of Pt, Pd, Ru and Au on the surfaces of titanate nanotubes. *Top. Catal.* **2006**, *39*, 151–160. [CrossRef]
41. Kitano, M.; Wada, E.; Nakajima, K.; Hayashi, S.; Miyazaki, S.; Kobayashi, H.; Hara, M. Protonated titanate nanotubes with Lewis and Brønsted acidity: Relationship between nanotube structure and catalytic activity. *Chem. Mater.* **2013**, *25*, 385–393. [CrossRef]
42. Chen, Q.; Zhou, W.; Du, G.H.; Peng, L. Trititanate nanotubes made via a single alkali treatment. *Adv. Mater.* **2002**, *14*, 1208–1211. [CrossRef]
43. Yang, D.; Liu, H.; Liu, L.; Sarina, S.; Zheng, Z.; Zhu, H. Silver oxide nanocrystals anchored on titanate nanotubes and nanofibers: Promising candidates for entrapment of radioactive iodine anions. *Nanoscale* **2013**, *5*, 11011–11018. [CrossRef]
44. Huang, J.; Ding, L.; Xi, Y.; Shi, L.; Su, G.; Gao, R.; Wang, W.; Dong, B.; Cao, L. Efficient silver modification of TiO_2 nanotubes with enhanced photocatalytic activity. *Solid State Sci.* **2018**, *80*, 116–122. [CrossRef]
45. Hodos, M.; Horváth, E.; Haspel, H.; Kukovecz, Á.; Kónya, Z.; Kiricsi, I. Photosensitization of ion-exchangeable titanate nanotubes by CdS nanoparticles. *Chem. Phys. Lett.* **2004**, *399*, 512–515. [CrossRef]
46. Gajović, A.; Friščić, I.; Plodinec, M.; Iveković, D. High temperature Raman spectroscopy of titanate nanotubes. *J. Mol. Struct.* **2009**, *924*, 183–191. [CrossRef]
47. Kukovecz, Á.; Kordás, K.; Kiss, J.; Kónya, Z. Atomic scale characterization and surface chemistry of metal modified titanate nanotubes and nanowires. *Surf. Sci. Rep.* **2016**, *71*, 473–546. [CrossRef]
48. Qian, L.; Du, Z.-L.; Yang, S.-Y.; Jin, Z.-S. Raman study of titania nanotube by soft chemical process. *J. Mol. Struct.* **2005**, *749*, 103–107. [CrossRef]
49. Mozia, S.; Borowiak-Paleń, E.; Przepiórski, J.; Grzmil, B.; Tsumura, T.; Toyoda, M.; Grzechulska-Damszel, J.; Morawski, A.W. Physico-chemical properties and possible photocatalytic applications of titanate nanotubes synthesized via hydrothermal method. *J. Phys. Chem. Solids* **2010**, *71*, 263–272. [CrossRef]
50. Sallem, F.; Chassagnon, R.; Megriche, A.; El Maaoui, M.; Millot, N. Effect of mechanical stirring and temperature on dynamic hydrothermal synthesis of titanate nanotubes. *J. Alloys Compd.* **2017**, *722*, 785–796. [CrossRef]
51. Ren, N.; Li, R.; Chen, L.; Wang, G.; Liu, D.; Wang, Y.; Zheng, L.; Tang, W.; Yu, X.; Jiang, H.; et al. In situ construction of a titanate–silver nanoparticle–titanate sandwich nanostructure on a metallic titanium surface for bacteriostatic and biocompatible implants. *J. Mater. Chem.* **2012**, *22*, 19151–19160. [CrossRef]
52. Byeon, S.-H.; Lee, S.-O.; Kim, H. Structure and Raman spectra of layered titanium oxides. *J. Solid State Chem.* **1997**, *130*, 110–116. [CrossRef]

53. Pótári, G.; Madarász, D.; Nagy, L.; László, B.; Sápi, A.; Oszkó, A.; Kukovecz, A.; Erdőhelyi, A.; Kónya, Z.; Kiss, J. Rh-Induced support transformation phenomena in titanate nanowire and nanotube catalysts. *Langmuir* **2013**, *29*, 3061–3072. [CrossRef]
54. Bensebaa, F.; Zavaliche, F.; L'Ecuyer, P.; Cochrane, R.W.; Veres, T. Microwave synthesis and characterization of Co–ferrite nanoparticles. *J. Colloid Interface Sci.* **2004**, *277*, 104–110. [CrossRef]
55. Gilbert, J.B.; Rubner, M.F.; Cohen, R.E. Depth-profiling X-ray photoelectron spectroscopy (XPS) analysis of interlayer diffusion in polyelectrolyte multilayers. *Proc. Natl. Acad. Sci. USA* **2013**, *110*, 6651–6656. [CrossRef]
56. Moulder, J.F. *Handbook of X-ray Photoelectron Spectroscopy*; Perkin-Elmer Corp.: Eden Prairie, MN, USA, 1992.
57. Amiri, O.; Salavati-Niasari, M.; Farangi, M.; Mazaheri, M.; Bagheri, S. Stable plasmonic-improved dye sensitized solar cells by silver nanoparticles between titanium dioxide layers. *Electrochim. Acta* **2015**, *152*, 101–107. [CrossRef]
58. Hanaor, D.; Michelazzi, M.; Leonelli, C.; Sorrell, C.C. The effects of carboxylic acids on the aqueous dispersion and electrophoretic deposition of ZrO_2. *J. Eur. Ceram. Soc.* **2012**, *32*, 235–244. [CrossRef]
59. Torres Sánchez, R.M.; Tavani, E.L. Temperature effects on the point of zero charge and isoelectric point of a red soil rich in kaolinite and iron minerals. *J. Therm. Anal.* **1994**, *41*, 1129–1139. [CrossRef]
60. Kłodzińska, E.; Szumski, M.; Dziubakiewicz, E.; Hrynkiewicz, K.; Skwarek, E.; Janusz, W.; Buszewski, B. Effect of zeta potential value on bacterial behavior during electrophoretic separation. *Electrophoresis* **2010**, *31*, 1590–1596. [CrossRef]
61. Nuryastuti, T.; van der Mei, H.C.; Busscher, H.J.; Kuijer, R.; Aman, A.T.; Krom, B.P. recA mediated spontaneous deletions of the icaADBC operon of clinical *Staphylococcus epidermidis* isolates: A new mechanism of phenotypic variations. *Antonie van Leeuwenhoek* **2008**, *94*, 317–328. [CrossRef]
62. Di Paola, A.; García-López, E.; Marcí, G.; Martín, C.; Palmisano, L.; Rives, V.; Maria Venezia, A. Surface characterisation of metal ions loaded TiO_2 photocatalysts: Structure—Activity relationship. *Appl. Catal. B Environ.* **2004**, *48*, 223–233. [CrossRef]
63. Klitzke, S.; Metreveli, G.; Peters, A.; Schaumann, G.E.; Lang, F. The fate of silver nanoparticles in soil solution—Sorption of solutes and aggregation. *Sci. Total Environ.* **2015**, *535*, 54–60. [CrossRef]
64. Baron, S. *Medical Microbiology*; University of Texas Medical Branch: Galveston, TX, USA, 1996.
65. Fayaz, A.M.; Balaji, K.; Girilal, M.; Yadav, R.; Kalaichelvan, P.T.; Venketesan, R. Biogenic synthesis of silver nanoparticles and their synergistic effect with antibiotics: A study against gram-positive and gram-negative bacteria. *Nanomed. Nanotechnol. Biol. Med.* **2010**, *6*, 103–109. [CrossRef]
66. Kędziora, A.; Speruda, M.; Krzyżewska, E.; Rybka, J.; Łukowiak, A.; Bugla-Płoskońska, G. Similarities and differences between silver ions and silver in nanoforms as antibacterial agents. *Int. J. Mol. Sci.* **2018**, *19*, 444. [CrossRef]
67. Amato, E.; Diaz-Fernandez, Y.A.; Taglietti, A.; Pallavicini, P.; Pasotti, L.; Cucca, L.; Milanese, C.; Grisoli, P.; Dacarro, C.; Fernandez-Hechavarria, J.M.; et al. Synthesis, characterization and antibacterial activity against gram positive and gram negative bacteria of biomimetically coated silver nanoparticles. *Langmuir* **2011**, *27*, 9165–9173. [CrossRef]
68. Hatchett, D.W.; White, H.S. Electrochemistry of sulfur adlayers on the low-index faces of silver. *J. Phys. Chem.* **1996**, *100*, 9854–9859. [CrossRef]
69. Zhang, H.; Chen, G. Potent antibacterial activities of Ag/TiO_2 nanocomposite powders synthesized by a one-pot sol-gel method. *Environ. Sci. Technol.* **2009**, *43*, 2905–2910. [CrossRef]
70. AshaRani, P.V.; Low Kah Mun, G.; Hande, M.P.; Valiyaveettil, S. Cytotoxicity and genotoxicity of silver nanoparticles in human cells. *ACS Nano* **2009**, *3*, 279–290. [CrossRef]
71. Choi, O.; Hu, Z. Size dependent and reactive oxygen species related nanosilver toxicity to nitrifying bacteria. *Environ. Sci. Technol.* **2008**, *42*, 4583–4588. [CrossRef]
72. Le Ouay, B.; Stellacci, F. Antibacterial activity of silver nanoparticles: A surface science insight. *Nano Today* **2015**, *10*, 339–354. [CrossRef]
73. Ivask, A.; Kurvet, I.; Kasemets, K.; Blinova, I.; Aruoja, V.; Suppi, S.; Vija, H.; Kakinen, A.; Titma, T.; Heinlaan, M.; et al. Size-dependent toxicity of silver nanoparticles to bacteria, yeast, algae, crustaceans and mammalian cells in vitro. *PLoS ONE* **2014**, *9*, 1–14. [CrossRef]
74. Vidhu, V.K.; Philip, D. Biogenic synthesis of SnO_2 nanoparticles: Evaluation of antibacterial and antioxidant activities. *Spectrochim. Acta Part A Mol. Biomol. Spectrosc.* **2015**, *134*, 372–379. [CrossRef]
75. Kumar Nair, K.; Kumar, P.; Kumar, V.; Harris, R.A.; Kroon, R.E.; Viljoen, B.; Shumbula, P.M.; Mlambo, M.; Swart, H.C. Synthesis and evaluation of optical and antimicrobial properties of Ag-SnO_2 nanocomposites. *Phys. B Condens. Matter.* **2018**, *535*, 338–343. [CrossRef]

76. Choi, O.; Deng, K.K.; Kim, N.J.; Ross, L.; Surampalli, R.Y.; Hu, Z. The inhibitory effects of silver nanoparticle, silver ions, and silver chloride colloids on microbial growth. *Water. Res.* **2008**, *42*, 3066–3074. [CrossRef]
77. Hassan, S.M.; Ahmed, A.I.; Mannaa, M.A. Structural, Photocatalytic, Biological and catalytic properties of SnO_2/TiO_2 nanoparticles. *Ceram. Int.* **2018**, *44*, 6201–6211. [CrossRef]

nanomaterials

MDPI

Article

Boron Nitride Doped Polyhydroxyalkanoate/Chitosan Nanocomposite for Antibacterial and Biological Applications

Abdul Mukheem [1,*], Syed Shahabuddin [2,*], Noor Akbar [3], Azizi Miskon [1], Norazilawati Muhamad Sarih [4], Kumar Sudesh [5], Naveed Ahmed Khan [3], Rahman Saidur [2,6] and Nanthini Sridewi [1,*]

1 Department of Maritime Science and Technology, Faculty of Defence Science and Technology, National Defence University of Malaysia, Kuala Lumpur 57000, Malaysia; azizimis@gmail.com
2 Research Centre for Nano-Materials and Energy Technology (RCNMET), School of Science and Technology, Sunway University, Subang Jaya 47500, Malaysia; saidur@sunway.edu.my
3 Department of Biological Sciences, School of Science and Technology, Sunway University, Subang Jaya 47500, Malaysia; noormicrobiologist555@gmail.com (N.A.); naveedk@sunway.edu.my (N.A.K.)
4 Polymer Research Laboratory, Department of Chemistry, University of Malaya, Faculty of Science, Kuala Lumpur 50603, Malaysia; nmsarih@um.edu.my
5 Applied Microbiology and Ecobiomaterial Research Laboratory, School of Biological Sciences, Universiti Sains Malaysia, Penang 11800, Malaysia; ksudesh@usm.my
6 Department of Engineering, Lancaster University, Lancaster LA1 4YW, UK
* Correspondence: mukheembio@gmail.com (A.M.); syedshahab.hyd@gmail.com (S.S.); nanthini@upnm.edu.my (N.S.); Tel.: +60-124-675-320 (N.S.)

Received: 14 March 2019; Accepted: 10 April 2019; Published: 21 April 2019

Abstract: The present research focused on the fabrication of biocompatible polyhydroxyalkanoate, chitosan, and hexagonal boron nitride incorporated (PHA/Ch-hBN) nanocomposites through a simple solvent casting technique. The fabricated nanocomposites were comprehensively characterized by Fourier transform infrared spectroscope (FT-IR), field emission scanning electroscope (FESEM), and elemental mapping and thermogravimetric analysis (TGA). The antibacterial activity of nanocomposites were investigated through time-kill method against multi drug resistant (MDR) microbes such as methicillin-resistant *Staphylococcus aureus* (MRSA) and *Escherichia coli* (*E. coli*) K1 strains. In addition, nanocomposites have examined for their host cytotoxicity abilities using a Lactate dehydrogenase (LDH) assay against spontaneously immortalized human keratinocytes (HaCaT) cell lines. The results demonstrated highly significant antibacterial activity against MDR organisms and also significant cell viability as compared to the positive control. The fabricated PHA/Ch-hBN nanocomposite demonstrated effective antimicrobial and biocompatibility properties that would feasibly suit antibacterial and biomedical applications.

Keywords: boron nitride; chitosan; polyhydroxyalkanoate; nanocomposite; biocompatible; antibacterial

1. Introduction

In recent years, with the rapid development in biomedical field, many diseases have been discovered, and many have evolved due to various changes in the biological environment. Microbial infections are the key source of chronic diseases and mortality. There are few multi-drug resistant microbes, namely *E. coli* and *S. aureus*, which are generally responsible for infections such as wound in soft tissues, skin, and bloodstream diseases [1,2]. Antibiotics are the ideal treatment for bacterial infections because of their broad-spectrum effective outcomes [3]. However, many studies have

revealed that the extensive use and abuse of antibiotics has led to the emergence of multidrug resistant microbes, which is a major weakness of current antibiotic treatment [4]. Besides, cytocompatibility remains one of the most important features which has to be accounted for while proposing any antibiotic technique. Thus, the present scenario motivated scientists to develop biocompatible nanocomposites that feasibly exert better antibacterial and biocompatible properties including cost effectiveness.

Nanomaterials have multiple modes of action within microbial cells that lead to their death, all of which have been rays of hope for providing minimal death resistance compare to conventional antibiotics and anticancer drugs [5]. Many nanomaterials, for example graphene, silver, and gold, have demonstrated excellent antimicrobial properties which can be exploited in various biomedical applications [6,7]. Boron nitride (BN) is a strong carbon material formed by the bonding of boron and nitrogen elements. Furthermore, hBN has been extensively explored in biomedical applications and reported as biocompatible material in various biological applications [8,9]. In a study, an optimal viability of PC12 cells was noticed up to a 50 $\mu g\ mL^{-1}$ concentration of hBN, and there was no formation reactive oxygen species (ROS), cellular changes, or apoptosis for up to nine days of the experiment [10]. Biodegradable nanocomposites have also been designed by reinforcing hBN nanotubes, which have demonstrated significant enhancement in properties such as time, durability of scaffold, non-toxicity on osteoblasts and macrophages, and improved cell proliferation, which are apposite requirements for biomedical applications [11,12]. Merih et al. reported antibacterial and antibiofilm characteristics of hBN nanoparticles. The research revealed that *Streptococcus mutans* and *Staphylococcus pasteuri* obtained higher minimal inhibitory concentration value compared to *Streptococcus mutans* 3.3 and *Candida* species. [13]. Typically, *Streptococcus mutans* was known as an early resident that colonizes the tooth surface, forming dental plaque and the main pathogens for dental caries [13]. Thus, for the aforementioned potential of hBN, it must be further investigated for its broad spectrum antibacterial and host cytotoxicity effects, respectively.

Currently bio-based polymers are of great interest in biomedical research due to their inherent characteristics [14–16]. Biopolymers have been explored to achieve systemic improved therapeutics such as sustained drug release, even drug distribution, and set period degradation [17]. Polyhydroxyalkanoate is the class of novel biopolymers which belongs to the family of natural polyesters containing many different hydroxyl and carboxylic functional groups [18]. Furthermore, PHA is produced by several Gram-negative and Gram-positive microbes when fed with excess quantity of carbon under stressed growth conditions [19]. This unfavorable condition forced the microbe to store energy and carbon in the form of PHA macromolecules [19]. PHA has attracted a considerable scientific attention due to its biocompatible nature and biodegradability properties in a variety of applications ranging from nanotechnology, medical, tissue engineering, and packing industries [20–23]. However, PHA possesses limited applications in biomedical field due to its dissolution in toxic solvents such as chloroform, large crystals that cause brittleness and poor mechanical properties that are not suitable for biomaterials, wound management and packing [24,25]. Therefore, to improve the mechanical and thermal properties of PHA, its monomer side chain plays vital role and can be copolymerized with different monomers such as 3-hydroxyhexanoate (HHx), providing better flexibility, biodegradability, and mechanical properties, compared to bare PHA [24,26].

Furthermore, blending is one of the most suitable and easy methods of improving the incompatible properties of PHA by mixing with other biopolymers, a method which is hypothesized to have excellent physiochemical properties [24]. Chitosan is a natural cationic polysaccharide which has generated considerable interest due to its unique properties, and it is commonly used for the modification of drug formulations [27,28]. Saeed et al. reported that a Polyhydroxybutyrate chiotsan (PHB/Ch) matrix has demonstrated a more improved degradation rate than the individual efficacies of PHB. They found that dissolution of chitosan feasibly neutralizes the acidic nature of PHB degradation products [29]. Thus, chitosan's cross-linking ability helps to blend with various biocompatible polymers and nanoparticles in order to feasibly enhance composite properties such as surface morphology, contact angle length, and degradability [28].

The purpose of the present research is to evaluate the potential antibacterial effect and cell viability efficacy of fabricated PHA/Ch-hBN nanocomposites that were loaded with three different concentrations of hBN nanoparticles. Therefore, to achieve this purpose, the antibacterial activity of nanocomposites were analyzed against multi-drug resistant *E. coli* K1 and methicillin-resistant *Staphylococcus aureus* (MRSA). In addition, the cell cytotoxicity assays have also been examined through the LDH method. Additionally, in the present study nontoxic acetic acid was used to dissolve the PHA instead of a standard solvent chloroform to dissolve PHA [30].

2. Materials and Methods

Poly 3-hydroxybuterate-co-12mol% hydroxyhexanoate (P3HB-co-12mol%HHx) powder (350,000 Da) was provided by the KANEKA corporation, Osaka Japan. Chitosan powder of a medium molecular weight was obtained from Sigma-Aldrich, St. Louis, MO, USA. Hexagonal Boron Nitride (hBN) powder with an average particle size of 70 nm was procured from Lower Friction Company (Ontario, Canada). All the analytical grade reagents were used throughout the experiment. For antibacterial assays, stationary phase bacterial strains of methicillin-resistant *Staphylococcus aureus* (MRSA) and *E. coli* (K1) were used. Moreover, spontaneously immortalized human keratinocytes (HaCaT) cell lines were used for lactate dehydrogenase assay. A cytotoxicity detection kit was purchased from Roche Diagnostics, Indianapolis, IN, USA.

2.1. Preparation of Precursor Solution

A polymer solution with a concentration of 1 mg/mL of PHA in glacial acetic acid was prepared using a standard reflux setup. In a round bottom flask, PHA powder was mixed with glacial acetic acid and stirred for 5 min (300 rpm) at 118 °C on a magnetic stirrer. The solution was then allowed to cool down at room temperature. Simultaneously, a chitosan solution with a concentration of 1 mg/mL was prepared in 1% acetic acid, which was stirred for 24 h at room temperature on a magnetic stirrer. Furthermore, hBN nanoparticles with different weight percentages with respect to PHA (0.1, 0.5, and 1) were mixed in PHA solutions using a magnetic stirrer followed by ultra-sonication to dispersed the nanoparticles. The prepared chitosan solution (1 mg/mL) was added dropwise into the hBN-doped PHA solution to obtain a 10:1 ratio of PHA/Ch. The resultant PHA/Ch-hBN solution was ultra-sonicated for 30 min to distribute nanoparticles evenly within the polymer matrix. In this experiment, three nanocomposites were prepared with different concentrations of hBN nanoparticles.

2.2. Solvent Casting

A nanocomposite film was prepared from the polymer solution as illustrated in Figure 1. The solvent casting stage was prepared using a flat glass plate while the film size and thickness were controlled by standard microbiological glass slides (75 mm × 25 mm × 1 mm). A polymer solution was dispensed carefully onto the preheated (80 °C) glass platform with complete evaporation of solvent leading to the formation of uniformly thin film. PHA/Ch and PHA films were also prepared using a similar method. The resultant nanocomposites were dried at room temperature to remove any further residuals solvent.

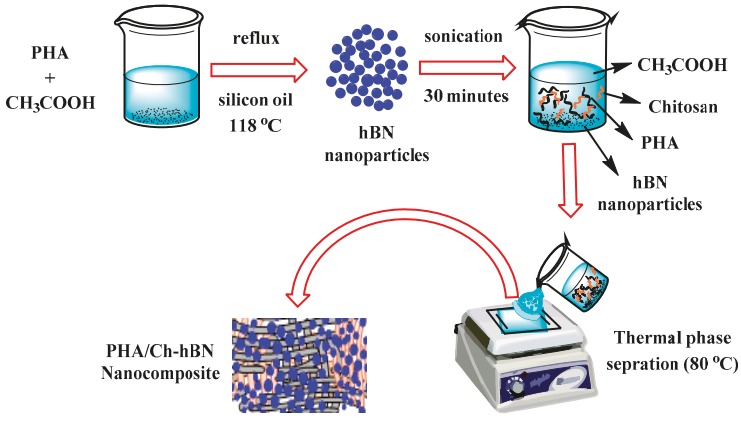

Figure 1. Schematic representation of the fabrication of film via solvent casting technique.

2.3. Antibacterial Assays

Antibacterial assays were performed to determine the percent bactericidal activity of different nanocomposites against multi-drug resistant bacteria. Briefly, 1×10^6 bacterial cells were incubated with PHA, PHA/Ch and PHA/Ch-hBN nanocomposites at 37 °C for 0, 2, 4, 6, and 24 h using the time-kill method. This method could be appropriate for the interaction between antibacterial agent and cultural broth. The clinical and laboratory standards institute (CLSI) has described this method as a well standardized technique to use for bacteria that is documented in M26-A of CLSI [31]. Bacterial cultures of MDR *E. coli* K1 and MRSA were grown over night, and the density of c. 1×10^8 CFU/mL was obtained through measuring 0.22 optical density (OD) at 595 nm [32]. About 10 µL, which is equal to c. 1×10^6 CFU/mL, was added in 100 µL nutrient broth containing the test samples of size 0.6 mm. The phosphate buffer saline was used to mark the total volume up to 200 µL. Next, cultures were ten-fold serially diluted to 10 µL, were plated on nutrient agar plates, and were incubated over night at 37 °C. For controls, bacteria incubated with gentamicin (100 µg/mL) as a positive, and PBS and PHA including PHA/Ch were used as negative control. The experiment was performed and analysed in triplicate.

2.4. Cytotoxicity Assays

HaCaT cell lines were grown in RPMI-1640 medium and supplemented with 10% (v/v) foetal bovine serum (FBS), 1% L-glutamine, 1% Penicillin-Streptomycin, and 1% minimal essential media nonessential amino acid (Life Technologies, California, CA, USA). The HaCaT cells were been seeded into the non-pyrogenic 24 well plate with the density of 5×10^3 per well and incubated at 37 °C with 5% CO_2, including 95% humidity, for 48 h. Briefly, a HaCaT cells monolayer was incubated with nanocomposites in a RPMI-1640 medium for 24 h at 37 °C in the presence of 5% CO_2 and 95% humidity. After this incubation, supernatant was aspirated to detect the cytotoxicity through measuring the release of lactate dehydrogenase (LDH), a schematic presentation of which is shown in Figure 2. Generally, the results of cytotoxicity were calculated applying the below formula:

$$\% \text{ cytotoxicity} = \frac{\text{sample value} - \text{control value}}{\text{total LDH release} - \text{control value}} \times 100$$

Whereas, to obtained the total LDH release, HaCaT cells were treated with 0.1% Triton X-100 at 37 °C for 30 min. Similarly, the cells incubated in RPMI-1640 were used as control values. In brief, the working principle of the assay was that LDH acted as catalyst for transforming lactate to pyruvate, thereby producing NADH and H^+. In next step, catalyst diaphorase converted H and H^+ to tetrazolium

salt that was then reduced to formazan dye. The relationship between metabolically active cells and formazan dye color provided precise quantification (cell death or proliferation) from the resultant supernatant. A dense purple color feasibly demonstrated the high enzyme activity due to the higher viable cells, and decrease in purple color signified the cytotoxicity.

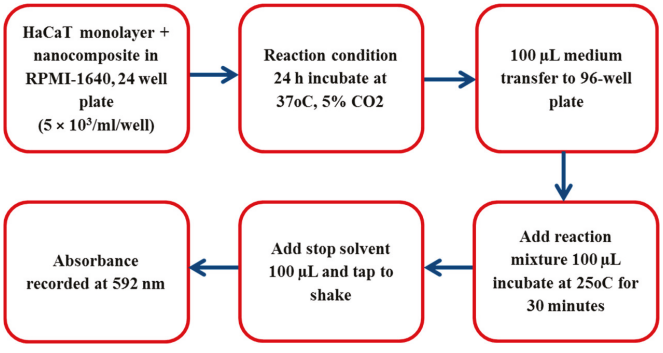

Figure 2. Schematic representation of measuring lactate dehydrogenase.

3. Results

3.1. Morphological Analysis

A surface morphological analysis of the hBN nanosheets, chitosan, and PHA/Ch-hBN nanocomposites were comprehensively evaluated through FESEM and TEM, as shown in Figure 3. Figure 3a represents the FESEM image of hBN which has depicted the discs like morphology in nano range where the 2D hBN flakes can be seen densely stacked onto each other. In addition, the obtained TEM image further confirm the disc-like morphology of hBN nanoflakes (Figure 3b). The stacked disc-like morphology of hBN, a characteristic of 2D, has been clearly established by FESEM and TEM analysis. The FESEM micrograph of chitosan is shown in Figure 3c, which demonstrates the cotton flakes like structures that is the characteristic morphology of chitosan [33]. Similar topology was also observed in nanocomposite depicted in Figure 3d, which is clearly revealing the formation of cross-linked polymeric networking of PHA/Ch. The morphology of the nanocomposites appears to be 2D layered type, which might be due to the interaction of polymeric chains with 2D hBN. However, from Figure 3d, it was found that the hBN nanoflakes were difficult to visualize within the nanocomposite since hBN nanodiscs were deeply embedded in the PHA polymeric matrix and difficult to visualize using FESEM imaging alone. Additionally, the amount of hBN is much less as compared to the bare polymer matrix, hence making its analysis further cumbersome through FESEM single-handedly. Therefore, the SEM elemental mapping analysis technique appears to be an appropriate method to demonstrate the presence and even distribution of hBN within the PHA/Ch matrix; this was further supported by energy dispersive X-ray EDX investigations.

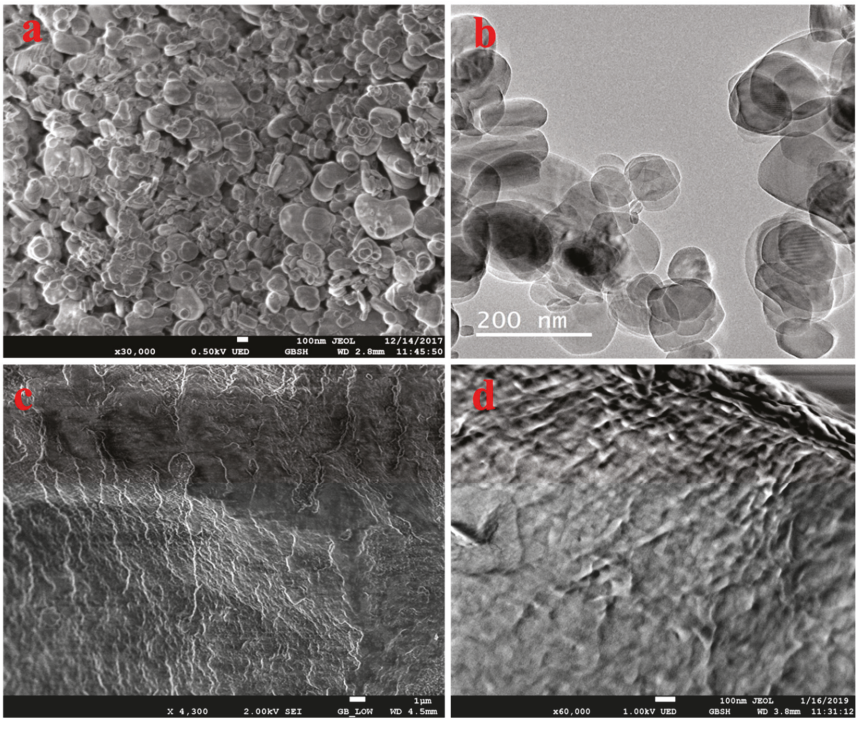

Figure 3. FESEM images of hBN (**a**), chitosan (**c**), and a PHA/Ch-hBN nanocomposite (**d**), as well as a TEM image of hBN (**b**).

Figure 4a,b illustrates the elemental mapping results of the composite PHA/Ch-hBN-5. As obvious from the obtained elemental mapping outcomes in Figure 4, hBN (Figure 4e,f) is present uniformly and homogeneously within the nanocomposites in addition with carbon (c) and oxygen (d), thereby confirming the successful formation of 2D hBN doped PHA/Ch nanocomposite. The elemental analysis was further found to be in a good agreement with the EDX data presented in Figure 4g, which clearly reveals the presence of B and N within the nanocomposite scaffold.

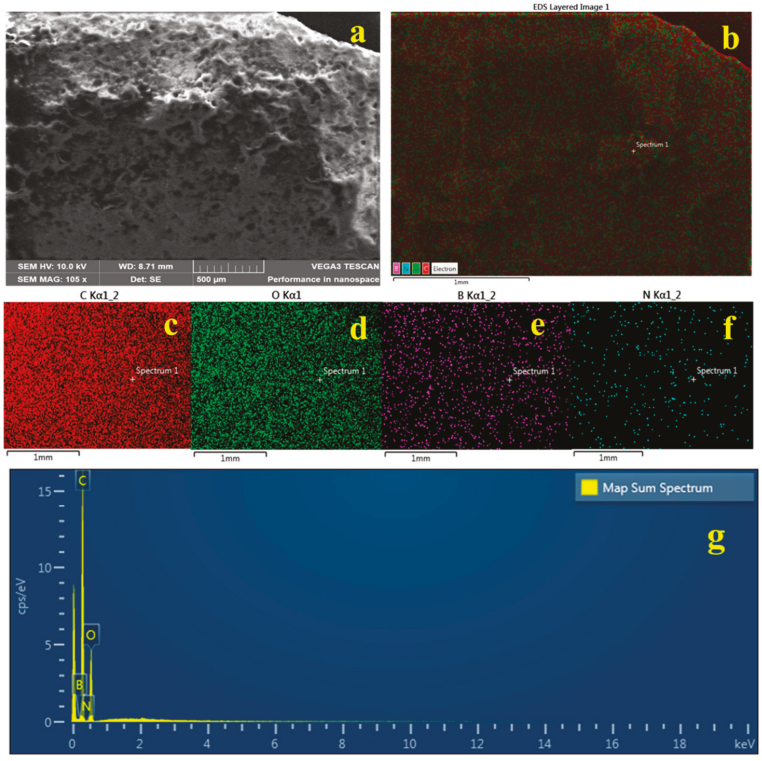

Figure 4. SEM image (**a**), EDX (**g**) and mapping (**b**–**f**) of PHA/Ch blend doped with 0.1% hBN nanocomposites.

3.2. FT-IR

The FT-IR spectra of PHA, Chitosan, hBN, PHA/Ch and PHA/Ch doped hBN nanocomposites are shown in Figure 5. The FT-IR spectrum of PHA is illustrated in Figure 5a. The IR peak appearing at 1700 cm^{-1} may be assigned to C=O (ester carbonyl) stretching of PHA polymer. The prominent bands at the spectral region of 1172 to 1280 cm^{-1} are associated C-O-C vibrations within the PHA polymeric chains. The IR bands appearing around at 3436 cm^{-1} can be assigned to -OH vibration in the carboxyl group present in copolymeric chains of PHA and P(3HB-co-3HHx). The prominent IR peak at 2933 cm^{-1} is the characteristic -C-H- vibrations of the methylene group present in the macromolecules of PHA (Figure 5a) [34,35]. Figure 5b exemplifies the FT-IR spectrum of chitosan. The broad IR bands at the range of 3352–3288 cm^{-1} may be assigned to stretching modes of the –OH and primary amine groups. The characteristic IR peaks appearing at 1640 cm^{-1} and 1588 cm^{-1} might be attributed to the C-N and C=O (amide) stretching modes. The C-H stretching and bending was ascribed to the bands at the spectral region of 2869 cm^{-1} and 1427 cm^{-1}, respectively (Figure 5b) [36]. From the hBN spectra shown in Figure 5c, the typical stretching vibration bands of B-N bond and B-N-B bending vibration were attributed around the spectral region of 1338 cm^{-1} and 767 cm^{-1} [37,38]. The IR spectrum of the various nanocomposites scaffolds are represented in Figure 5d. As obvious from the spectra of the nanocomposites, they comprise of the characteristic peaks and IR bands of PHA, chitosan, and hBN. As a result of an overlapping of the C-H stretching of chitosan in composites, the IR band at approximately 2877 cm^{-1} became less intense and was been slightly shifted to 2875 cm^{-1}. In addition, the C=O (amide) and C-N stretching bands in chitosan around at 1640 cm^{-1} and 1588 cm^{-1}, respectively, vanished in composites. The absorption bands at 2930 cm^{-1} and 1450 cm^{-1} in bare PHA and chitosan

showed slight shifts in the composites. The characteristic peaks at 1338 cm^{-1} and 767 cm^{-1} in hBN were detected at 1379 cm^{-1} and 738 cm^{-1} in hBN doped PHA/Ch nanocomposites. However, many IR peaks and bands have depicted significant changes shift as compared to the spectrum of of bare PHA, chitosan, and hBN signifying, the chemical associations or interactions with each other. Thus, the FT-IR spectrum suggests the formation of a PHA/Ch-hBN nanocomposite, which is in good agreement with the earlier analysis.

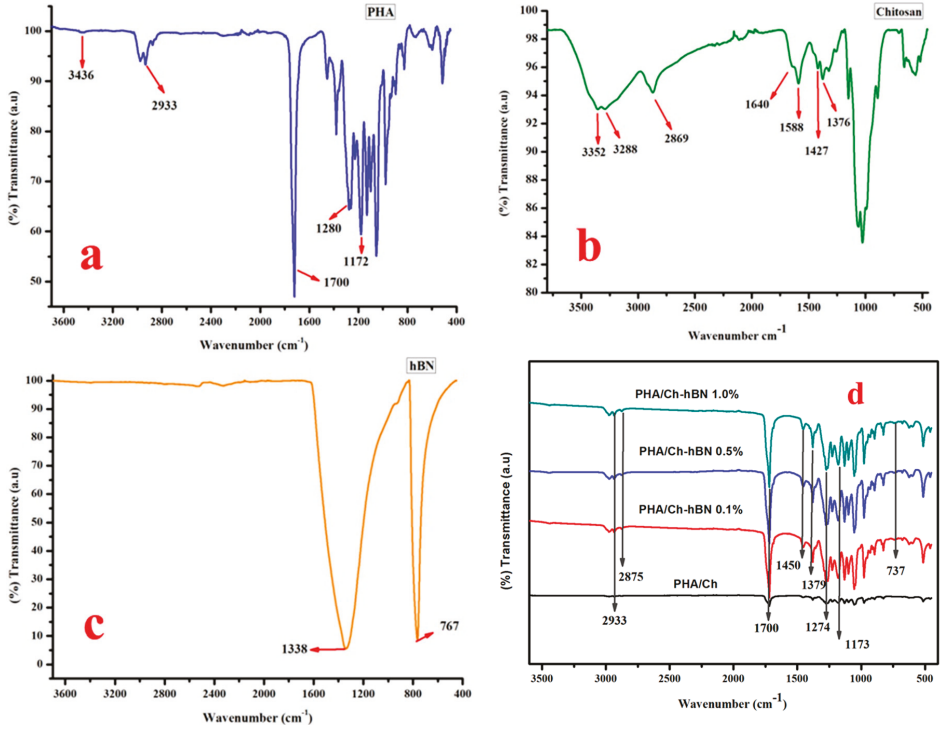

Figure 5. FT-IR (Fourier-transform infrared spectroscopy) spectrum of bare (**a**) PHA, (**b**) Chitosan, (**c**) hBN and, (**d**) nanocomposites.

3.3. Thermal Gravimetric Analysis (TGA)

Figure 6 represented the TGA results of PHA/Ch and PHA/Ch-hBN nanocomposites including bare PHA, chitosan, and hBN. The TGA analysis was performed under a nitrogen atmosphere at a temperature range of 30–500 °C for 10 °C/min. As apparent from the TGA thermogram of hBN, no weight loss pccured until 500 °C, which indicated a higher level of thermal stability. On the other hand, chitosan has revealed a 10% weight loss between 50–115 °C, which can be attributed to the loss of residual water and adsorbed moisture. The major weight loss in chitosan is observed at 250–343 °C, which may be assigned to the decomposition of ethereal groups, glucosamine moieties, and ring opening reactions. The thermogram of PHA reveals that it is thermally stable until 200 °C, the gradual weight loss has initiated around 250 °C, and a considerable weight loss of 98.6% was noted form 268–310 °C. This thermal degradation of PHA may be due to the degradation of unreacted free monomers and the decomposition of hydrocarbon polymeric chains. The blend of PHA/Ch has shown less thermal stability as bare compared to PHA but higher stability as compared to chitosan, which indicates some interactions and crosslinking between the two polymers. Though PHA has shown 100% decomposition till 500 °C, PHA/Ch has revealed 4% residue at 500 °C, thus signifying

some synergistic associations between tow biopolymers imparting thermal stability. Finally, the PHA/Ch-hBN nanocomposite revealed the improved thermal stability compared to PHA/Ch composite, which is possibly due to the addition more thermally stable hBN nanomaterial. Therefore, from the analysis, it was shown that the thermal stability of PHA/Ch-hBN nanocomposite has been improved as compared to PHA/Ch and can be applied in applications which require higher temperature (Up to 250 °C).

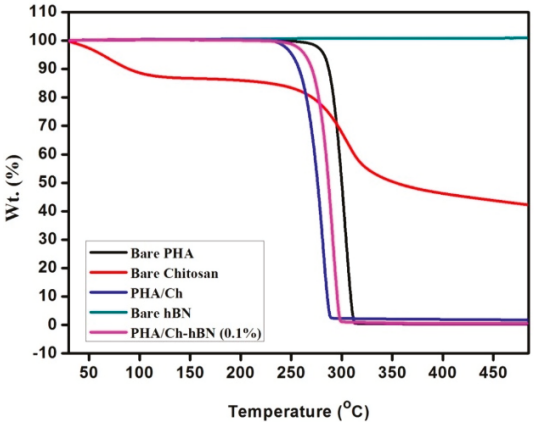

Figure 6. TGA thermogram of bare PHA, chitosan, hBN, and PHA/Ch, PHA/Ch-hBN nanocomposites.

4. Antibacterial Analysis

The antibacterial activities of fabricated nanocomposites were tested against MDR *E. coli* K1 and MRSA through the time-kill method. The results of PHA/Ch-hBN (hBN 0.1, 0.5 and 1.0 wt% wrt PHA) exhibited significant bactericidal activity against *E. coli* K1 ($p < 0.05$), which is represented in Figure 7a and Table 1. When tested against MRSA, the results revealed that nanocomposites significantly reduced the growth of bacteria (p-value) (<0.05) (Figure 7b and Table 1). The hBN nanocomposites remarkably reduce the percent viability of bacteria as compared to negative control (Figure 7a,b).

Table 1. PHA/Ch and hBN-doped PHA/Ch nanocomposite scaffolds antibacterial activity against *E. coli* K1and MRSA.

Test Samples	Antibacterial Activity against *E. coli* K1	Antibacterial Activity against MRSA
PHA/Ch	-	-
PHA/Ch-hBN (0.1 wt%)	+	+
PHA/Ch-hBN (0.5 wt%)	+	+
PHA/Ch-hBN (1 wt%)	+	+
Gentamicin	+	+

In brief, the antibacterial activity was assessed at different time intervals, and the first 2, 4, and 6 h of time points demonstrated effective bactericidal activity as compared to negative control (PHA/Ch), including 24 hours' time point. From the graph, it is hypothesized that the bactericidal activity was time dependent in this experiment, which was subjected to the morphology of nanocomposites. Furthermore, an increase in the concentration of hBN nanomaterial with the PHA/Ch composition has revealed the improved bactericidal ability. However, all the three concentrations of hBN nanocomposites have shown a significant reduction of *E. coli* K1 and MRSA for up to 24 h. The Gentamicin was applied as positive control, which killed 100% of the bacterial colonies. The statistical p-values were defined by applying two sample T-test distribution, while (*) is <0.05; (**) is <0.01; and (***) is <0.001, respectively.

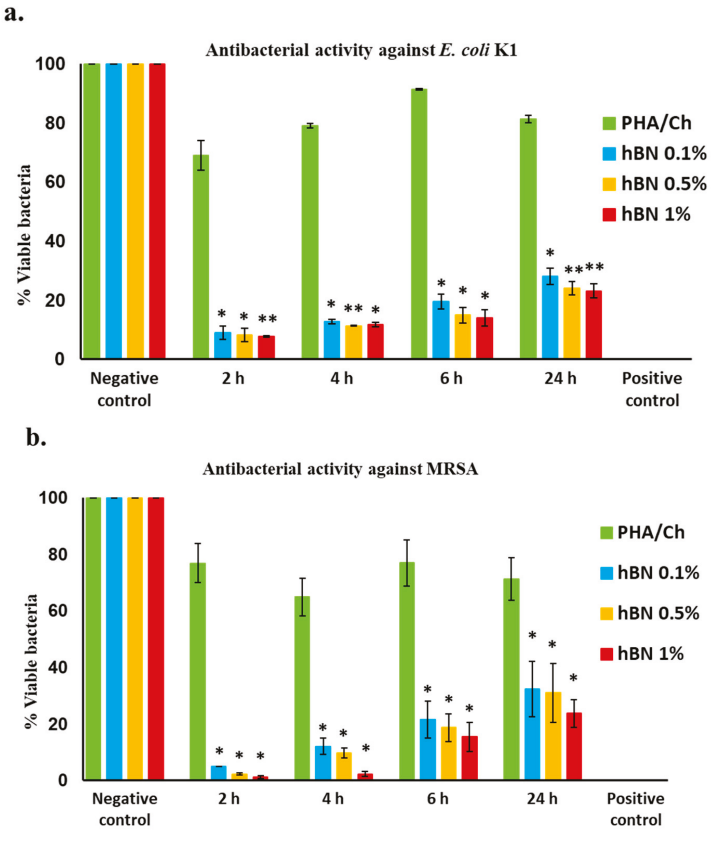

Figure 7. (**a**) Bactericidal activity of nanocomposites against *E. coli* K1 strain and (**b**) bactericidal activity against MRSA, shown significant bactericidal efficacy. (Using a two sample T-test, two-tailed distribution, (*) is <0.05; (**) is <0.01; and (***) is <0.001).

5. Cell Cytotoxicity Assay against HaCaT Cell Lines

For the biomedical applications, cell viability testing is an important step to determine the cellular effects of external toxicants and the biosafety of biomaterials. Therefore, the synthesized PHA/Ch-hBN nanocomposites were tested for their cytotoxic effects against HaCaT cell lines, and the cell viability was quantified through LDH assays. HaCaT cells have treated with test samples for up to 24 h, and the resultant cells have visualized by inverted microscope at 200X lens, which is presented in Figure 8.

The microscopic images have shown clearly that there was no decrease of confluent monolayer, which was treated with negative control (Figure 8a) and possessed complete destruction with a positive control, as depicted in Figure 8b (1% Trixton-100). Whereas both concentraions of the PHA/Ch-hBN (1.0% hBN wrt PHA) nanocomposite showed no cytotoxic effects against the HaCaT cell lines as shown in Figure 8c. Figure 9 illustrates the comprehensive percent cell cytotoxicity data.

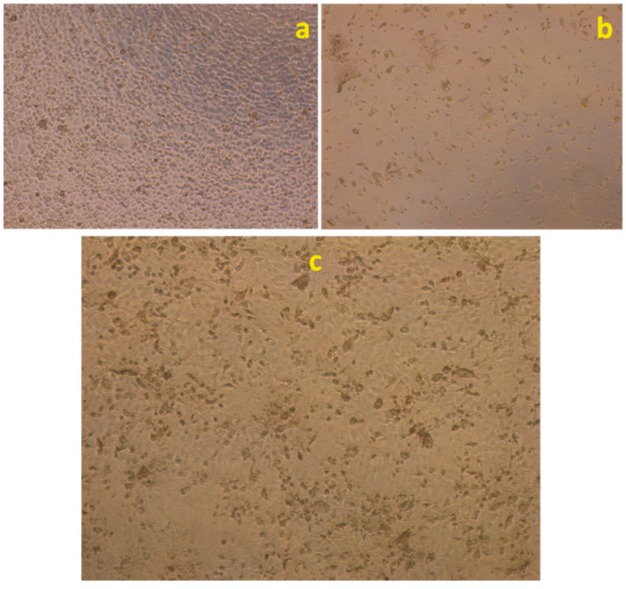

Figure 8. Effects of synthesized nanocomposites on the viability of HaCaT cell line, (**a–c**) represent the negative controls, positive controls, and PHA/Ch-hBN nanocomposite, respectively.

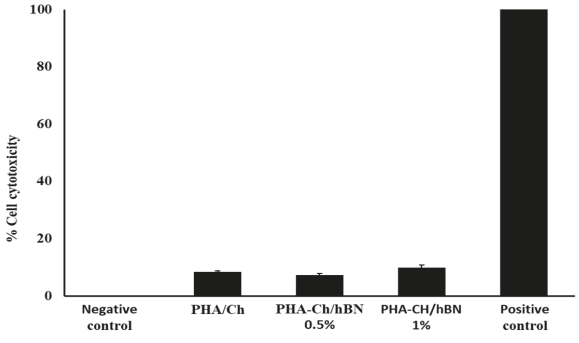

Figure 9. Representative cytotoxic effects of synthesized nanocomposites and positive control (1% Trixton-100) on a HaCaT cell line.

6. Comparison of Antibacterial Efficiencies

The antibacterial performance of the synthesized h-BN doped nanocomposite was compared with similar reported studies as illustrated in Table 2. In this investigation, the first two hours bactericidal activity of hBN was found to be 92% and 97% against *E. coli* K1 and MRSA, respectively, which is comparatively much enhanced as compared with other reports. As is apparent from the comparative data shown in Table 2, the synthesized hBN doped nanocomposite offers enhanced antibacterial efficiency and can thus be applicable for efficient in antibacterial treatments and biological applications.

Table 2. Comparative study of the antibacterial efficiencies of the different composites.

Nano Composites	Conc.	% Reduction		Time (h)	Proposed Applications	Ref.
		E.coli	MRSA			
BN/Ag	70 mg/L	100	-	3	Eternal catalyst and antibacterial	[39]
Gr-Pln	5 mg/mL	-	92	-	Antibacterial applications	[40]
BNAg/TiO_2	2 mg/mL	100	-	3	Photodegradation and antibacterial applications	[41]
Cu-Go/hBN	-	100	-	24	Biology and medical applications	[42]
PEI/BNNT	1 mg/mL	95	90	2	Nano vector for targeted drug delivery system	[43]
PHA/GAg	-	82	60	2	Antibacterial and sanitization application	[26]
PHA/Ch-hBN	1 mg/mL	92	97	2	Antibacterial and biological applications	This study

7. Conclusions

An PHA/Ch matrix and hBN nanodiscs-doped nanocomposite scaffolds have been efficaciously designed and fabricated through a facile solvent casting technique. hBN nanodiscs were effectively amalgamated within the inter-cross linked polymeric network of the PHA/Ch. The current examination indicated the synergistic consequence of the thermally stable hBN and the biopolymers, thus leading to the augmentation of the antibacterial activity of the nanocomposite against MDR *E. coli* K1 and MRSA. The fabricated polymeric scaffolds have exhibited superior bactericidal activity and killed pathogenic bacteria competently in a small time interval. Besides, nanocomposite has good cytocompatibility with human cells, as there was a minimal cytotoxicity observed. In conclusion, the multifunctional PHA/Ch-hBN nanocomposites have exhibited broad spectrum antibacterial efficiency and cytocompatibility within appropriate concentrations. Therefore, the synthesized nanocomposites can be considered as safe, efficient, and stable antibacterial scaffolds for biological applications.

Author Contributions: Conceptualization, S.S. and A.M. (Abdul Mukheem); methodology, S.S. and A.M. (Abdul Mukheem); software, S.S.; validation, S.S., A.M. (Abdul Mukheem), and N.A.; formal analysis, S.S., A.M. (Abdul Mukheem), and N.S.; investigation, S.S., A.M. (Abdul Mukheem), A.M. (Azizi Miskon), and N.A.; resources, S.S., R.S., N.K., N.M.S., K.S., and N.S.; writing—original draft preparation, S.S., A.M. (Abdul Mukheem), and N.S.; writing—review and editing, S.S., R.S., N.K., N.M.S., and N.S.; supervision, S.S., N.S., A.M. (Azizi Miskon), and K.S.; funding acquisition, S.S., and N.S.

Funding: This research was funded by the Ministry of Energy, Science, Technology, Environment and Climate Change (MESTECC), Malaysia through the Science Fund grant (No. 2014/03-01-19-SF0127) and Sunway University through internal grant (INT-2019-SST-RCNMET-02) for the research facilities and financial support.

Conflicts of Interest: The authors declare no conflict of interest.

References

1. Allocati, N.; Masulli, M.; Alexeyev, M.F.; Di Ilio, C. Escherichia coli in europe: An overview. *Int. J. Environ. Res. Public Health* **2013**, *10*, 6235–6254. [CrossRef] [PubMed]
2. Kobayashi, S.D.; Malachowa, N.; DeLeo, F.R. Pathogenesis of staphylococcus aureus abscesses. *Am. J. Pathol.* **2015**, *185*, 1518–1527. [CrossRef] [PubMed]
3. Paterson, I.K.; Hoyle, A.; Ochoa, G.; Baker-Austin, C.; Taylor, N.G. Optimising antibiotic usage to treat bacterial infections. *Sci. Rep.* **2016**, *6*, 37853. [CrossRef]
4. Fair, R.J.; Tor, Y. Antibiotics and bacterial resistance in the 21st century. *Perspect. Med. Chem.* **2014**, *6*, 25–64. [CrossRef]
5. Lakshminarayanan, R.; Ye, E.; Young, D.J.; Li, Z.; Loh, X.J. Recent advances in the development of antimicrobial nanoparticles for combating resistant pathogens. *Adv. Healthc. Mater.* **2018**, 1701400. [CrossRef] [PubMed]
6. Azam, A.; Ahmed, A.S.; Oves, M.; Khan, M.S.; Habib, S.S.; Memic, A. Antimicrobial activity of metal oxide nanoparticles against gram-positive and gram-negative bacteria: A comparative study. *Int. J. Nanomed.* **2012**, *7*, 6003. [CrossRef]
7. Sivakumar, P.; Lee, M.; Kim, Y.-S.; Shim, M.S. Photo-triggered antibacterial and anticancer activities of zinc oxide nanoparticles. *J. Mater. Chem. B* **2018**, *6*, 4852–4871. [CrossRef]
8. Merlo, A.; Mokkapati, V.R.; Pandit, S.; Mijakovic, I. Boron nitride nanomaterials: Biocompatibility and bio-applications. *Biomater. Sci.* **2018**, *6*, 2298–2311. [CrossRef]

9. Song, L.; Ci, L.; Lu, H.; Sorokin, P.B.; Jin, C.; Ni, J.; Kvashnin, A.G.; Kvashnin, D.G.; Lou, J.; Yakobson, B.I. Large scale growth and characterization of atomic hexagonal boron nitride layers. *Nano Lett.* **2010**, *10*, 3209–3215. [CrossRef] [PubMed]
10. Ciofani, G.; Danti, S.; D'Alessandro, D.; Ricotti, L.; Moscato, S.; Bertoni, G.; Falqui, A.; Berrettini, S.; Petrini, M.; Mattoli, V. Enhancement of neurite outgrowth in neuronal-like cells following boron nitride nanotube-mediated stimulation. *ACS Nano* **2010**, *4*, 6267–6277. [CrossRef] [PubMed]
11. Lahiri, D.; Rouzaud, F.; Richard, T.; Keshri, A.K.; Bakshi, S.R.; Kos, L.; Agarwal, A. Boron nitride nanotube reinforced polylactide–polycaprolactone copolymer composite: Mechanical properties and cytocompatibility with osteoblasts and macrophages in vitro. *Acta Biomater.* **2010**, *6*, 3524–3533. [CrossRef]
12. Lahiri, D.; Singh, V.; Benaduce, A.P.; Seal, S.; Kos, L.; Agarwal, A. Boron nitride nanotube reinforced hydroxyapatite composite: Mechanical and tribological performance and in-vitro biocompatibility to osteoblasts. *J. Mech. Behav. Biomed. Mater.* **2011**, *4*, 44–56. [CrossRef] [PubMed]
13. Kıvanç, M.; Barutca, B.; Koparal, A.T.; Göncü, Y.; Bostancı, S.H.; Ay, N. Effects of hexagonal boron nitride nanoparticles on antimicrobial and antibiofilm activities, cell viability. *Mater. Sci. Eng. C* **2018**, *91*, 115–124. [CrossRef] [PubMed]
14. Ulery, B.D.; Nair, L.S.; Laurencin, C.T. Biomedical applications of biodegradable polymers. *J. Polym. Sci. Part B Polym. Phys.* **2011**, *49*, 832–864.
15. Guo, B.; Glavas, L.; Albertsson, A.-C. Biodegradable and electrically conducting polymers for biomedical applications. *Prog. Polym. Sci.* **2013**, *38*, 1263–1286. [CrossRef]
16. Mohammed, I.A.; Shahabuddin, S.; Khanam, R.; Saidur, R. Synthesis, characterization and antibacterial activity of novel poly (silyl ether) s based on palm and soy oils. *Polímeros* **2018**. [CrossRef]
17. Kamaly, N.; Yameen, B.; Wu, J.; Farokhzad, O.C. Degradable controlled-release polymers and polymeric nanoparticles: Mechanisms of controlling drug release. *Chem. Rev.* **2016**, *116*, 2602–2663. [CrossRef] [PubMed]
18. Loo, C.Y.; Sudesh, K. Polyhydroxyalkanoates: Bio-based microbial plastics and their properties. *Malaysian Polym. J.* **2007**, *2*, 31–57.
19. Sudesh, K.; Abe, H.; Doi, Y. Synthesis, structure and properties of polyhydroxyalkanoates: Biological polyesters. *Prog. Polym. Sci.* **2000**, *25*, 1503–1555. [CrossRef]
20. Kourmentza, C.; Plácido, J.; Venetsaneas, N.; Burniol-Figols, A.; Varrone, C.; Gavala, H.N.; Reis, M.A. Recent advances and challenges towards sustainable polyhydroxyalkanoate (pha) production. *Bioengineering* **2017**, *4*, 55. [CrossRef] [PubMed]
21. Vijayendra, S.; Shamala, T. Film forming microbial biopolymers for commercial applications—A review. *Crit. Rev. Biotechnol.* **2014**, *34*, 338–357. [CrossRef] [PubMed]
22. Gumel, A.; Annuar, M. Nanocomposites of polyhydroxyalkanoates (phas). In *Polyhydroxyalkanoate (PHA) based Blends, Composites and Nanocomposites*; The Royal Society of Chemistry: London, UK, 2014; pp. 98–118.
23. Philip, S.; Keshavarz, T.; Roy, I. Polyhydroxyalkanoates: Biodegradable polymers with a range of applications. *J. Chem. Technol. Biotechnol. Int. Res. Process Environ. Clean Technol.* **2007**, *82*, 233–247. [CrossRef]
24. Li, Z.; Yang, J.; Loh, X.J. Polyhydroxyalkanoates: Opening doors for a sustainable future. *NPG Asia Mater.* **2016**, *8*, e265. [CrossRef]
25. Zhao, K.; Deng, Y.; Chen, J.C.; Chen, G.-Q. Polyhydroxyalkanoate (pha) scaffolds with good mechanical properties and biocompatibility. *Biomaterials* **2003**, *24*, 1041–1045. [CrossRef]
26. Mukheem, A.; Muthoosamy, K.; Manickam, S.; Sudesh, K.; Shahabuddin, S.; Saidur, R.; Akbar, N.; Sridewi, N. Fabrication and characterization of an electrospun pha/graphene silver nanocomposite scaffold for antibacterial applications. *Materials* **2018**, *11*, 1673. [CrossRef]
27. Saikia, C.; Gogoi, P.; Maji, T. Chitosan: A promising biopolymer in drug delivery applications. *J. Mol. Genet. Med. S* **2015**, *4*, 006. [CrossRef]
28. Shahabuddin, S.; Sarih, N.M.; Ismail, F.H.; Shahid, M.M.; Huang, N.M. Synthesis of chitosan grafted-polyaniline/co 3 o 4 nanocube nanocomposites and their photocatalytic activity toward methylene blue dye degradation. *RSC Adv.* **2015**, *5*, 83857–83867. [CrossRef]
29. Karbasi, S.; Khorasani, S.N.; Ebrahimi, S.; Khalili, S.; Fekrat, F.; Sadeghi, D. Preparation and characterization of poly (hydroxy butyrate)/chitosan blend scaffolds for tissue engineering applications. *Adv. Biomed. Res.* **2016**, *5*. [CrossRef]

30. Anbukarasu, P.; Sauvageau, D.; Elias, A. Tuning the properties of polyhydroxybutyrate films using acetic acid via solvent casting. *Sci. Rep.* **2015**, *5*, 17884. [CrossRef]
31. Balouiri, M.; Sadiki, M.; Ibnsouda, S.K. Methods for in vitro evaluating antimicrobial activity: A review. *J. Pharm. Anal.* **2016**, *6*, 71–79. [CrossRef] [PubMed]
32. Sagheer, M.; Siddiqui, R.; Iqbal, J.; Khan, N.A. Black cobra (naja naja karachiensis) lysates exhibit broad-spectrum antimicrobial activities. *Pathog. Global Health* **2014**, *108*, 129–136. [CrossRef] [PubMed]
33. Syed, S. Polyaniline based Nanocomposites as Adsorbents and Photocatalysts in the Removal of Organic dyes/Syed Shahabuddin. Ph.D. Thesis, University of Malaya, Kuala Lumpur, Malaysia, 2016.
34. Salim, Y.S.; Chan, C.H.; Sudesh, K.; Gan, S.N. Influence of Thermal Treatment on the Molecular Weights of Polyhydroxyalkanoate Containing 3-hydroxyhexanoate. *Adv. Mater. Res.* **2013**, *812*, 250–253. [CrossRef]
35. Shamala, T.; Divyashree, M.; Davis, R.; Kumari, K.L.; Vijayendra, S.; Raj, B. Production and characterization of bacterial polyhydroxyalkanoate copolymers and evaluation of their blends by fourier transform infrared spectroscopy and scanning electron microscopy. *Indian J. Microbiol.* **2009**, *49*, 251–258. [CrossRef]
36. Kisku, S.K.; Swain, S.K. Synthesis and characterization of chitosan/boron nitride composites. *J. Am. Ceram. Soc.* **2012**, *95*, 2753–2757. [CrossRef]
37. Salehirad, M.; Nikje, M.M.A. Synthesis and characterization of exfoliated polystyrene grafted hexagonal boron nitride nanosheets and their potential application in heat transfer nanofluids. *Iran. Polym. J.* **2017**, *26*, 467–480. [CrossRef]
38. Shahabuddin, S.; Khanam, R.; Khalid, M.; Sarih, N.M.; Ching, J.J.; Mohamad, S.; Saidur, R. Synthesis of 2d boron nitride doped polyaniline hybrid nanocomposites for photocatalytic degradation of carcinogenic dyes from aqueous solution. *Arab. J. Chem.* **2018**. [CrossRef]
39. Firestein, K.L.; Leybo, D.V.; Steinman, A.E.; Kovalskii, A.M.; Matveev, A.T.; Manakhov, A.M.; Sukhorukova, I.V.; Slukin, P.V.; Fursova, N.K.; Ignatov, S.G. Bn/ag hybrid nanomaterials with petal-like surfaces as catalysts and antibacterial agents. *Beilstein J. Nanotechnol.* **2018**, *9*, 250–261. [CrossRef]
40. Shoeb, M.; Mobin, M.; Rauf, M.A.; Owais, M.; Naqvi, A.H. In vitro and in vivo antimicrobial evaluation of graphene–polyindole (gr@ pin) nanocomposite against methicillin-resistant staphylococcus aureus pathogen. *ACS Omega* **2018**, *3*, 9431–9440. [CrossRef]
41. Nasr, M.; Soussan, L.; Viter, R.; Eid, C.; Habchi, R.; Miele, P.; Bechelany, M. High photodegradation and antibacterial activity of bn–ag/tio 2 composite nanofibers under visible light. *New J. Chem.* **2018**, *42*, 1250–1259. [CrossRef]
42. Parra, C.; Montero-Silva, F.; Henríquez, R.; Flores, M.; Garín, C.; Ramírez, C.; Moreno, M.; Correa, J.; Seeger, M.; Häberle, P. Suppressing bacterial interaction with copper surfaces through graphene and hexagonal-boron nitride coatings. *ACS Appl. Mater. Interfaces* **2015**, *7*, 6430–6437. [CrossRef] [PubMed]
43. Nithya, J.S.M.; Pandurangan, A. Aqueous dispersion of polymer coated boron nitride nanotubes and their antibacterial and cytotoxicity studies. *RSC Adv.* **2014**, *4*, 32031–32046. [CrossRef]

MDPI
St. Alban-Anlage 66
4052 Basel
Switzerland
Tel. +41 61 683 77 34
Fax +41 61 302 89 18
www.mdpi.com

Nanomaterials Editorial Office
E-mail: nanomaterials@mdpi.com
www.mdpi.com/journal/nanomaterials

MDPI
St. Alban-Anlage 66
4052 Basel
Switzerland

Tel: +41 61 683 77 34
Fax: +41 61 302 89 18

www.mdpi.com

ISBN 978-3-03943-960-7